**Title**
Polymer Electrolytes and the Limiting Current



**Author**
Grundy, Lorena Shannon

**Publication Date**
2022

Peer reviewed|Thesis/dissertation

# Polymer Electrolytes and the Limiting Current

by

Lorena Shannon Grundy

A dissertation submitted in partial satisfaction of the
requirements for the degree of

Doctor of Philosophy

in

Chemical Engineering

in the

Graduate Division

of the

University of California, Berkeley

Committee in charge:

Professor Nitash P. Balsara, Chair
Professor Jeffrey A. Reimer
Professor D. Kwabena Bediako

Summer 2022

# Abstract

Polymer Electrolytes and the Limiting Current

by

Lorena Shannon Grundy

Doctor of Philosophy in Chemical Engineering

University of California, Berkeley

Professor Nitash P. Balsara, Chair

Lightweight, safe energy storage options are a critical tool in enabling implementation of renewable energy options. Typical lithium-ion batteries use a liquid electrolyte composed of ethylene carbonate (EC), dimethyl carbonate (DMC), and a lithium salt, lithium hexafluorophosphate ($LiPF_6$). These batteries use graphite anodes, of which a large fraction is an electrochemically inactive support. One important direction in the energy storage field is to replace graphite anodes with solid lithium metal anodes to improve the energy density of the battery. However, lithium metal is incompatible with common electrolytes, and it is limited by its propensity for dendrite growth, which can lead to cell failure. Therefore, we are in search of an electrolyte that is safe against lithium metal and can prevent dendrite growth. We focus on polymer electrolytes, especially those based on poly(ethylene oxide) (PEO), including block copolymer electrolytes composed of PEO and polystyrene (PS), which microphase separate into PEO-rich ion-conducting regions and PS-rich mechanically-rigid regions that suppress dendrite growth.

In this Dissertation, a variety of techniques are used to characterize various electrolyte options, from liquids (Chapter 5), to homopolymers, which contain only one type of monomer (Chapter 6), to block copolymers, which contain two (Chapters 7-10). Chapter 1 provides a general introduction to polymers, polymer electrolytes, and characterization techniques. Chapters 2–4 detail the techniques used in this Dissertation. Nuclear magnetic resonance (NMR) spectroscopy (Chapter 2) probes the local environments of nuclei and can shed light on microphase separation in block copolymers, and pulsed-field gradient NMR measures the self-diffusion of nuclei, which is relevant to ion transport. Small angle X-ray scattering (SAXS) (Chapter 3) provides information about block copolymer morphology and phase behavior. Electrochemical characterization (Chapter 4)

probes the ion transport and thermodynamics of electrolytes and concentrated solution theory, developed by John Newman, enables theoretical prediction of electrolyte behavior.

In Chapter 5, we use oligomeric liquid glyme-based electrolytes to demonstrate the impact of local frictional interactions, quantified by Stefan-Maxwell diffusion coefficients calculated using concentrated solution theory, on ion transport. We define factors to quantify the importance of ion-ion and ion-solvent interactions, and find that in fluorinated electrolytes, ion-ion interactions dominate even at very low salt concentrations, bringing into question the validity of ideal solution assumptions even in dilute electrolytes. Chapter 6 applies these methods to solid systems with high-molecular weight PEO / LiTFSI electrolytes, providing the first characterization of such systems at salt concentrations above $r = 0.30$ lithium ions per ethylene oxide moiety. We observe a salt solubility limit at $r = 0.50$, impacting the maximum applicable current density—the limiting current—and a two-phase region between $r = 0.28$ and 0.50, the electrochemical consequences of which have not been explored previously.

Chapters 7 and 8 move into PS-*b*-PEO (SEO) / LiTFSI block copolymer electrolytes. In Chapter 7, we decouple grain growth from ionic conductivity during annealing, bringing to light the importance of thermal history and defect annihilation. In Chapter 8, we discover that strong magnetic fields macroscopically align the domains of a lamellar SEO / LiTFSI electrolyte, which produces $^{7}$Li NMR quadrupolar peak splitting which disappears at the order-to-disorder temperature, $T_{ODT}$, the temperature above which the polymer disorders. The presence of this peak splitting provides a new measure of $T_{ODT}$, which is typically detected using SAXS.

Chapters 9 and 10 combine SAXS and constant-current electrochemical polarization, which results in the salt accumulation at the positive electrode and depletion at the negative electrode. In Chapter 9, we study the local microstructure of a lamellar SEO / LiTFSI electrolyte, observing domain expansion at the salt-rich electrode and domain contraction at the salt-poor electrode. We discover that differently-oriented domains expand and contract to different extents, indicating that lamellae that do not provide direct conducting pathways between electrodes may still play an important role in ion transport by enabling the development of salt concentration gradients. In Chapter 10, we combine X-ray transmission with SAXS, and observe that the salt concentration of an SEO / LiTFSI electrolyte that initially has a body-centered cubic spherical (BCC) morphology fails to decrease below the salt concentration at which a transition to a hexagonally-packed cylindrical (HEX) morphology would have been expected. This suggests that the inability of polarization to induce morphological conditions can limit the development of salt concentration gradients, and therefore the applicable current.

Abstract

This work provides new insights into the local interactions, morphological factors, and external forces that impact the performance of polymer electrolytes. The goal of this Dissertation is to provide information that will contribute to an increased depth of understanding of ion transport in polymer electrolytes, enabling the rational design of future high-performance electrolytes.

"You shall love your crooked neighbour
With your crooked heart."

- W. H. Auden

# Table of Contents

Table of Contents

Table of Contents

Table of Contents

Table of Contents

# List of Figures

List of Figures

List of Figures

List of Figures

List of Figures

List of Figures

# List of Tables

# Nomenclature

| | |
|---|---|
| $A$ | electrochemically active electrode area |
| $a$ | fit parameter in Equation 5.5 |
| ac | alternating current |
| AgB | silver behenate SAXS calibrant |
| ALS | Advanced Light Source at LBNL |
| $B$ | magnetic field strength (T) |
| $b$ | fit parameter in Equation 5.5 |
| BCC | body-centered spherical morphology |
| $B_0$ | applied magnetic field strength (T) |
| $C_2$ | crystalline complex with 2 EO moieties per Li atom (see Chapter 6) |
| $c$ | salt concentration (mol/cm$^3$) |
| $c_{\mathrm{av}}$ | average salt concentration |
| $c_{\mathrm{av}}$ | salt concentration at the solubility limit |
| $c_{\mathrm{T}}$ | total concentration (mol/cm$^3$) ($c_0 + 2c$ for univalent salts) |
| $c_0$ | solvent concentration (mol/cm$^3$) |
| $D$ | salt mutual diffusion coefficient (cm$^2$/s) (see Equation 4.6) |
| $d$ | domain spacing (nm) |
| dc | direct current |
| DMC | dimethyl carbonate |
| DSC | differential scanning calorimetry |
| DSTE | double stimulated echo PFG-NMR pulse sequence |
| $D_{\mathrm{self}}$ | salt mutual diffusion coefficient estimated from NMR self-diffusion coefficient values (cm$^2$/s) (see Equation 5.11) |
| $D_{\mathrm{self},+}$ | cation self-diffusion coefficient measured by PFG-NMR (cm$^2$/s) |
| $D_{\mathrm{self},-}$ | anion self-diffusion coefficient measured by PFG-NMR (cm$^2$/s) |
| $D_{\mathrm{self},0}$ | solvent self-diffusion coefficient measured by PFG-NMR (cm$^2$/s) |
| $\mathfrak{D}$ | salt diffusion coefficient based on a thermodynamic driving force (cm$^2$/s) (see Equation 5.12) |
| $\mathfrak{D}_{\mathrm{ij}}$ | Stefan-Maxwell diffusion coefficient describing interactions between components $i$ and $j$, which can be the cation, anion, or solvent (cm$^2$/s) |
| $\mathfrak{D}_{0+}$ | Stefan-Maxwell diffusion coefficient describing interactions between cation and solvent (cm$^2$/s) (see Equation 4.14) |
| $\mathfrak{D}_{0-}$ | Stefan-Maxwell diffusion coefficient describing interactions between anion and solvent (cm$^2$/s) (see Equation 4.15) |
| $\mathfrak{D}_{+-}$ | Stefan-Maxwell diffusion coefficient describing interactions between cation and anion (cm$^2$/s) (see Equation 4.16) |

| | |
|---|---|
| $E$ | potential drop across the electrolyte (V) = $\Delta V - \Delta V_{int}$ |
| $E$ | NMR signal attenuation |
| EC | ethylene carbonate |
| EFG | electric field gradient |
| $F$ | Faraday's constant (96,485 C/mol) |
| $f$ | orientation parameter (see Chapter 9) |
| $FSI^-$ | bis(fluorosulfonyl)imide |
| FWHM | full peak width at half-maximum ($nm^{-1}$) |
| F4 | mixtures of C8-DMC and LiFSI salt (see Chapter 5) |
| $^{19}F$ | fluorine-19 atom |
| $g$ | magnetic field gradient strength (T/m) |
| GPC | gel permeation chromatography |
| GYR | gyroidal morphology |
| $h$ | Planck constant ($6.626\times10^{-34}$ J s) |
| $\hbar$ | reduced Planck constant ($h/2\pi = 1.0546\times10^{-34}$ J s) |
| HEX | hexagonally packed cylindrical morphology |
| H4 | mixtures of tetraglyme and LiTFSI salt (see Chapter 5) |
| $^1H$ | hydrogen-1 (proton) atom |
| $I$ | current (mA) |
| $I$ | scattering intensity |
| $I$ | NMR nuclear spin number ($I = 3/2$ for $^7Li$) |
| $i$ | current density ($mA/cm^2$) |
| $I_{blank}$ | SAXS intensity measured from an empty sample (see Equation 3.1) |
| $I_{dark}$ | SAXS intensity measured with beam off (see Equation 3.1) |
| $i_{lim}$ | maximum current density that can be sustained through the electrolyte ($mA/cm^2$) |
| $i_{lim,expt}$ | limiting current density measured experimentally ($mA/cm^2$) |
| $i_{lim,theory}$ | limiting current density predicted by concentrated solution theory ($mA/cm^2$) |
| $i_{lim}L$ | limiting current scaled by electrolyte thickness (mA/cm) |
| $Iq^2$ | scattering invariant |
| $I_{ss}$ | steady-state current (mA) |
| $I_s$ | scattered X-ray intensity |
| $I_0$ | incident X-ray intensity |
| $I_1$ | post-sample X-ray intensity |
| $I_{\sqrt{2}}$ | integrated intensity of the SAXS peak at $\sqrt{2}q^*$ (see Chapter 10) |
| $I_{\sqrt{3}}$ | integrated intensity of the SAXS peak at $\sqrt{3}q^*$ (see Chapter 10) |
| $I_\Omega$ | initial current calculated using Ohm's law (mA) ($I_\Omega = \Delta V/R_T$) |
| $J_1$ | collection of terms integrated to obtain salt concentration gradients, defined by Equations 4.19, 6.15, and 9.4 |

| | |
|---|---|
| $J_2$ | collection of terms integrated to obtain salt potential gradients, defined by Equation 9.6 |
| $K$ | constant in the Scherrer equation (Equation 7.4) |
| $k$ | Boltzmann constant ($1.381\times10^{-23}$ J/K) |
| $k_0$ | offset voltage (V) |
| $L$,$l$ | thickness of electrolyte (cm) |
| $L$ | grain size (see Equation 7.4) |
| LAM | lamellar morphology |
| $LAM_{\|\|}$ | lamellar morphology with PS/PEO interfaces oriented parallel to the current direction (see Chapter 9) |
| $LAM_{\perp}$ | lamellar morphology with PS/PEO interfaces oriented perpendicular to the current direction (see Chapter 9) |
| LiFSI | lithium bis(fluorosulfonyl)imide salt |
| $LiPF_6$ | lithium hexafluorophosphate salt |
| LiTFSI | lithium bis(trifluoromethanesulfonyl)imide salt |
| $Li^+$ | lithium cation |
| $^6Li$ | lithium-6 atom |
| $^7Li$ | lithium-7 atom |
| $m$ | salt molality, molal concentration (mol/kg) |
| $m$ | nuclear quantum number or spin state |
| $M_{EO}$ | molecular mass of ethylene oxide monomer (44.05 g/mol) |
| $M_i$ | molar mass of species $i$ (kg/mol) |
| $M_{PEO}$ | number-averaged molecular weight of poly(ethylene oxide) (kg/mol) |
| $M_{PS}$ | number-averaged molecular weight of polystyrene (kg/mol) |
| $M_S$ | molecular mass of styrene monomer (104.1 g/mol) |
| $N_i$ | number of atoms in spin state $i$ |
| NMP | *n*-methylpyrrolidone solvent |
| NMR | nuclear magnetic resonance spectroscopy |
| PDI | polydispersity index |
| PEEK | poly(ether ether ketone) |
| PEO | poly(ethylene oxide) |
| PFG-NMR | pulsed-field gradient nuclear magnetic resonance spectroscopy |
| PS | polystyrene |
| PyFAI | Python fast azimuthal integrator SAXS analysis package |
| $P_4$-*t*-Bu | *tert*-butyl phosphazene base |
| $Q$ | integration of $q^2I(q)$ (the scattering invariant) over the primary scattering peak |
| $Q$ | nuclear quadrupole moment |
| $q$ | scattering vector ($nm^{-1}$) |
| $q^*$ | scattering vector at the primary scattering peak ($nm^{-1}$) |
| $R$ | ideal gas constant (8.3145 J/mol K) |

| | |
|---|---|
| $r$ | molar salt concentration ([$Li^+$]/[EO]) |
| $r_{avg}$ | $r$ averaged over the entire volume of the electrolyte |
| $R_b$ | bulk cell resistance (Ω) |
| $R_i$ | interfacial cell resistance (Ω) |
| $R_{ss}$ | steady-state cell resistance (Ω) |
| $R_T$ | total cell resistance (Ω) |
| $R_0$ | initial cell resistance (Ω) |
| $S$ | nuclear angular momentum (see Chapter 2) |
| SANS | small-angle neutron scattering |
| SAXS | small-angle X-ray scattering |
| SEO | polystyrene-*block*-poly(ethylene oxide) |
| SEO(*xx*-*yy*) | SEO with *xx* kg/mol PS block and *yy* kg/mol PEO block |
| SSRL | Stanford Synchrotron Radiation Lightsource at SLAC |
| STE | stimulated echo PFG-NMR pulse sequence |
| $T$ | temperature (°C) |
| $t$ | time |
| $T_d$ | desired temperature (°C) (see Equations 3.4-3.6) |
| $TFSI^-$ | bis(trifluoromethanesulfonyl)imide anion |
| $T_f$ | electrolyte thermodynamic factor (see Equation 4.12) |
| THF | tetrahydrofuran solvent |
| $T_{ODT}$ | order-to-disorder transition temperature |
| $T_s$ | temperature setpoint (°C) (see Equations 3.4-3.6) |
| $t_{+,NMR}$ | transference number obtained using PFG-NMR |
| $t_+^0$ | cation transference number obtained using the Balsara and Newman method; referenced to the solvent frame (see Equation 4.8) |
| $t_-^0$ | anion transference number referenced to the solvent frame |
| $U$ | potential drop across the electrolyte (V) = $\Delta V - \Delta V_{int}$ |
| $U_{ss}$ | potential drop across the electrolyte at steady-state (V) |
| $v_i$ | molar volume of species or phase $i$ ($cm^3$/mol) |
| $x$ | axis parallel to current flow (see Figure 9.3a) |
| $x_{salt}$ | mole fraction of salt |
| $x/L$ | normalized cell position |
| $y$ | axis perpendicular to current flow and X-ray beam (see Figure 9.3a) |
| $z$ | axis parallel to X-ray beam (see Figure 9.3a) |
| $z_i$ | charge number of species $i$ |
| $Z_{Im}$ | imaginary component of impedance multiplied by $A$ (Ω$cm^2$) |
| $Z_{Re}$ | real component of impedance multiplied by $A$ (Ω$cm^2$) |
| $z_+$ | cation charge number (1 for univalent salts) |
| $z_-$ | anion charge number (-1 for univalent salts) |

## Greek

| | |
|---|---|
| $\beta_{\text{self}}$ | conductivity pre-factor from the Nernst-Einstein equation (Equation 5.1) |
| $\beta_0$ | conductivity pre-factor from Equation 5.22 |
| $\beta_{0,c}$ | conductivity pre-factor from Equation 5.23 |
| $\beta_{+-}$ | conductivity pre-factor from Equation 5.21 |
| $\gamma$ | gyromagnetic ratio (rad/sT) |
| $\gamma_{+-}$ | mean molal electrolyte activity coefficient |
| $\Delta$ | PFG-NMR diffusion delay (s) |
| $\Delta d$ | difference in domain spacing at time *t vs.* at $t = 0$ (nm) (see Chapter 9) |
| $\Delta E$ | energetic spacing between spin states (see Figure 2.5) |
| $\Delta V$ | potential drop at the potentiostat leads (V) |
| $\Delta V_{\text{int}}$ | potential drop across the electrolyte/electrode interface (V) |
| $\Delta\nu$ | NMR peak splitting (Hz) |
| $\delta$ | PFG-NMR magnetic field gradient pulse length (ms) |
| $\eta$ | viscosity (Pas) |
| $\theta$ | scattering angle |
| $\kappa$ | ionic conductivity (S/cm) |
| $\lambda$ | wavelength ($nm^{-1}$) |
| $\mu$ | nuclear magnetic moment |
| $\nu$ | total number of ions into which the salt dissociates (2 for univalent salts) |
| $\nu_i$ | number of species *i* into which a salt dissociates |
| $\nu_+$ | cations per molecule of salt (1 for univalent salts) |
| $\nu_-$ | anions per molecule of salt (1 for univalent salts) |
| $\pi$ | mathematical constant (3.14159) |
| $\rho$ | density ($g/cm^3$) |
| $\rho_c$ | conducting phase density |
| $\rho_+$ | current fraction obtained using the steady-state current method (see Equation 4.4) |
| $\tau$ | separator tortuosity (see Section 5.3.4) |
| $\tau, \tau_d, \tau_1, \tau_2$ | delays in PFG-NMR (s) |
| $\phi$ | azimuthal angle on the 2D SAXS detector (°) |
| $\phi_c$ | volume fraction of the conducting phase |
| $\phi_{\text{EO}}$ | volume fraction of the PEO phase |
| $\phi_{\text{EO/salt}}$ | volume fraction of the PEO/LiTFSI phase |
| $\chi$ | azimuthal angle on the 2D SAXS detector (°) |
| $\omega$ | frequency of precession (Hz) |

# Acknowledgements

One of my fundamental beliefs about scientific research is that it is not objective; it is shaped by who we are, where we sit, and with whom we sit. When I start a project, it is just as important for me to consider who will work with me along the way as it is to decide which questions to answer and with which experiments. I have been blessed with countless mentors, mentees, and people who are both at once, and I am proud to see their fingerprints throughout this Dissertation.

Nothing I have done would have been possible without Professor Nitash P. Balsara. Nitash, you taught me so much about polymers, electrochemistry, and X-rays. More importantly, you taught me how to turn a question asked into group meeting into a pile of data into a "bad draft" into a finished product. More importantly still, you shape and run your group in a way that is consistent with your scientific values. You care more about our learning and development as scientists than about our publication count, and I will always be grateful that you let me completely change the course of my Ph.D. in pursuit of the skills that I wanted to learn. You also know that the people determine the environment, and you have assembled a truly excellent group of people that make our lab a good environment.

Ksenia, Danielle, and Rita, you were on your way out the door when I was on my way in, but although we only overlapped briefly, you were my first examples of what it means to be a Balsara Lab member. Ksenia, despite being busy finishing up your projects and writing your own Dissertation, you took the time to teach me everything from how to bring a screwdriver into the glovebox (and back out, and in again…) to assembling NMR samples (and what to do when they break) to making quiche. I will always be grateful for your mentorship and friendship.

Deep, Jackie, and Whitney, you were the leaders of the group for two years in a row and played a large role in shaping my Berkeley experience. Deep, you made me feel welcome from the very beginning. I was always impressed by the way you balanced scientific collaboration and mentorship with fun and friendship, showing me that I belong in this group even when times are hard. Jackie, I am so grateful to call you my friend. During those hard times, you didn't give up on me, and we both grew into better labmates and, more importantly, close friends. I sincerely cherish everything I learned from you. Whitney, you took on so much (too much) for our group. You were always willing to take time to help others, and I couldn't even begin to list the things you taught me, from anionic synthesis to chemical inventory. Without you to help me remember to eat lunch, I probably would have starved somewhere in my second year. Thank you for loaning me both your couch and your cat for the writing of much of this Dissertation.

Acknowledgements

Gumi, I don't know what I would have done without you. You were a never-ending source of joy, patience, kindness, and empathy. You sometimes worried about whether you were a good enough mentor—I think that the fact that you were worried about it illustrates how much you cared about us. When I'm wondering how to support a labmate, I often ask myself, "what would Gumi say?" You are so patient, selfless, and kind, and I'm grateful for how much time I got to spend with you.

Mike, you took on a third-year who was lost at sea with no project and no electrochem skills and turned me into a fourth-year with more *in situ* SAXS data than I will ever be able to process. You always had answers to my naïve questions, and handled my many mistakes, even the big ones, with grace. Often, you commented that others in the group were much smarter than you, but you're one of the best, and smartest, scientists I know. Thank you for the time, mentorship, and kindness you gave me; my Balsara lab experience was a much calmer and happier place for having you in it.

Kevin, my favorite enemy, you quietly help all of us whenever we need it, and I see the care you put into leaving everything better than you found it. I am grateful for having the opportunity to work with you.

Zach, Alec, and Neel, Kevin and I are leaving the lab in good hands. You are all always eager to learn and just as eager to share that knowledge with others. Zach, you have taken every roadblock with patience and tenacity. No matter what you are going through, I always see you treating others with kindness and doing whatever it takes to help a friend. You make me feel like science is a team sport. Alec, you were a leader from the beginning, and you always seem to know what to do when something goes wrong, whether that means fixing a glovebox or going home and making some chocolate babka.

Darby, Morgan, Vivaan, and Karim, it has been an honor to watch you and work with you as you have transformed from new first-years into independent researchers. Despite a pandemic taking over your early time in the group, you immediately felt like part of the family. Darby, thank you for letting me dump new projects onto you and still being my friend after I gave you multiple new jobs. Lily, Michael, and Emily, you reassure me that the Balsara lab will only keep getting better. Emily, I can't imagine a better person to take over my project—you have learned so much already, and I can't wait to see what you will accomplish.

To the many postdocs who mentored me—Irune, Hee Jeung, Kim, Louise, Youngwoo, Saheli, David, Xiaopeng, Jaeyong—thank you. You have been the quiet backbones of the group, supporting and teaching us as we learn how to be scientists while also finishing your own projects.

Acknowledgements

I have been fortunate to have many advisors outside of my official group: Dr. Hasan Celik, Professor Louis Madsen, and Professor Jeff Reimer helped me make sense of my NMR data when I was a clueless first-year student and took me under their wings as if I was their own student. Dr. Chris Takacs does the work of at least ten people, and one of those—sometimes seemingly full-time—has been holding my hand as I wade through piles of SAXS scans. I can't imagine how I could have done anything I've worked on in the last two years without you.

The polymer physics community is a beautiful one, and I'm grateful for the life-long friends I've made. Lex, Emma, Konane, Melody, Danielle, Connor, and many more, thank you for being exemplary role models, and building the ladder down behind you as you've climbed to new heights, making it easier for me to follow you. Lex, even though we spent the first year of our friendship as faceless Twitter profiles, you have grown to be one of my closest friends. No matter what you're going through, you find a way to be there for me, and your future students will be so lucky to have such a supportive mentor; I know I am.

Easily the highlight of my Ph.D. has been the opportunity to teach, work with, and learn from the incredible undergraduate students at Berkeley. To the undergraduate researchers who have come through our group, especially Sean, Rohan, Hien, Andrew, Vijay, and Daniel, I am certain that I learned more from you than you learned from me. Tiffany Reardon, thank you for letting me be a part of the Pre-Engineering Program; it was an honor to be trusted to help our incoming engineers become Berkeley Chemists, and I so enjoyed working with them. Professors Marjorie Went, David Graves, Shannon Ciston, and Carlo Carraro, thank you for letting me be a teaching partner to each of you. You made me the educator that I am today, and you will continue to shape the educator that I will become.

One of the keys to surviving graduate school is having friends outside the lab who respond to a crisis by showing up with wine. Julie and Katie, you have been more of a life raft than you know. You listen to me vent when I need to vent, bring me wine when I need to stop venting, and take me on adventures when I need to escape. I couldn't have done it without you. Isaac, you have shown me a tremendous amount of care during these last few months, and I feel lucky to have you to be there for me when I don't always know how to be there for myself. It takes a village to raise a grad student: Julie R., Kyle, Darwin, Joe, Haefa, Elizabeth, Amaresh, Rebecca, David G., Sarah B., Chris, Bridgette, Elyse, Nat, Sarah Y., Lori, David B., Frankie, Angelo, Jeremy, Johnny, Jessica, Alison, Zach K., Adrian, Natalie, Emily, Ana, Helen, Grace, Chrissy, Mark, Tarini, Connie, Jade, Laleh, Sally, and many others, I wouldn't be the person I am today without you.

Acknowledgements

Graduate school is a long and difficult road, and it was not without its bumps. I owe many thanks to the doctors who helped me get to the end of it. From head to toe: Pat Dallacroce, Sameera Siddiqi, Kathy Tran, Andrew Sorensen, Harry Green, Allison Aiken, Amanda Ching-Wun Cheung, Mary Hawn, Sarah Minkow, Melanie Deal, Yuko Miyazaki, Rosemary Mann, and Sireesha Battula, thank you for taking me apart and putting me back together again.

Lastly and most importantly, my family. For as long as I can remember, my grandmother, Claire Henkin, always asked me what I was reading. She was an endless well of love and care, and I miss her every day. My grandparents Merriam and Francis Grundy loved and supported me every step of the way, and I am grateful to have had them in my corner. Mom and dad, I don't know where to start. You instilled in me a love of science from before I can remember, but supported all of my dreams along the way, whether I wanted to be a dancer or an author or a veterinarian. Cookies always show up on my doorstep when I need them most, and it is an infinite comfort to have you as my safety net and lifeline. I've fallen so many times, and you always catch me and stand me back on my feet. Thank you.

**Funding Acknowledgement**

This work was supported by the Joint Center for Energy Storage Research (JCESR), an Energy Innovation Hub funded by the U.S. Department of Energy, Office of Science, Office of Basic Energy Science, under Contract No. DE-AC02-06CH11357. Work at the the Molecular Foundry and the Advanced Light Source, which is a DOE Office of Science User Facility, was supported by Contract No. DE-AC02-05CH11231. Work at the Stanford Synchrotron Radiation Light Source, a user facility at SLAC National Accelerator Laboratory, was supported by the U.S. Department of Energy, Office of Science, Office of Basic Energy Science under Contract No. DE-AC02-76SF00515.

# Chapter 1: Introduction

An important part of the necessary worldwide shift to cleaner energy technologies must involve improved energy storage. One limitation of the current standard lithium-ion batteries is that their anode material is relatively low in energy per unit mass; using lithium metal as an anode is an attractive alternative due to its higher energy density. [1–3] However, the standard lithium-ion electrolyte, a liquid mixture of ethylene carbonate (EC), dimethyl carbonate (DMC), and lithium hexafluorophosphate salt ($LiPF_6$), is unstable against both lithium metal and state-of-the-art cathode materials. [4–8] In addition, the mixture is flammable, which is undesirable for safety reasons. Finally, lithium metal is prone to non-planar lithium deposition during battery cycling; in extreme cases, this can cause protrusion growth that leads to a cell short circuit. [9,10] It is desirable to use a solid electrolyte that can suppress lithium dendrite growth. [11] Thus, our ideal electrolyte would exhibit: (1) non-reactivity with lithium metal and novel cathode materials; (2) non-flammability; (3) mechanical rigidity; and (4) ion transport properties to enable sufficiently fast battery charging rates. This Dissertation presents insights into the morphology and transport properties of polymer electrolytes, which may bring us closer to meeting this goal.

## 1.1 Polymers

### *1.1.1 Introduction*

Polymers are chains of repeating chemical moieties. Two common polymers are poly(ethylene oxide) (PEO) and polystyrene (PS). Their structures are shown in Figures 1.1a and 1.1b, respectively. Polystyrene is mechanically rigid, while poly(ethylene oxide), when mixed with a lithium salt, exhibits high ionic conductivity but low mechanical rigidity.

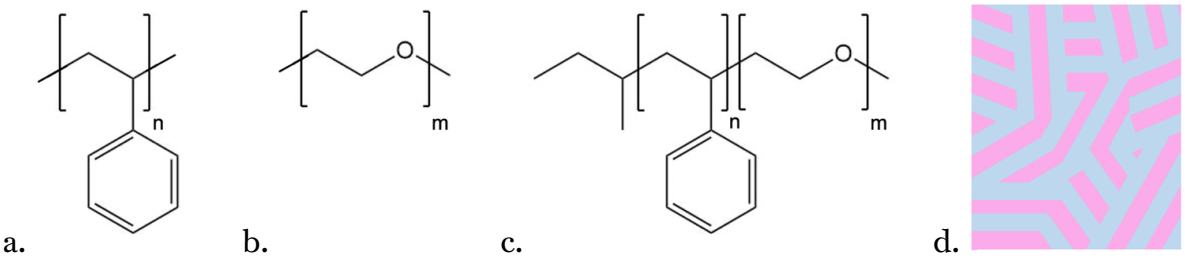


a. b. c. d.

Figure 1.1. Chemical structures of polystyrene (PS) (a) with *n* repeat units, poly(ethylene oxide) (PEO) with *m* repeat units (b), and polystyrene-*block*-poly(ethylene oxide) (PS-*b*-PEO or SEO) with *n* and *m* repeat units of PS and PEO, respectively, (c). Schematic of a lamellar block copolymer morphology (d).

### *1.1.2 Block Copolymers*

One way to attempt to combine the properties of two polymers is to form a block copolymer, which can be thought of as two polymer chains of different chemistries covalently bonded together. For example, polystyrene-*block*-poly(ethylene oxide) (PS-*b*-PEO or SEO) contains one PS chain and one PEO chain, with the length of each block controlled by the polymer synthesis procedure. The chemical structure of SEO is shown in Figure 1.1c.

Block copolymers can microphase separate into ordered morphologies, [12,13] resulting in, for SEO, PS-rich and PEO-rich domains. Microphase separation occurs through nucleation and growth, and therefore results in multiple ordered grains, usually randomly oriented, and grain boundaries. At high temperatures, ordering is disfavored as entropy dominates, and a disordered morphology is formed. The temperature of this order-to-disorder transition, $T_{ODT}$, depends on a variety of factors, including polymer chemistry, the lengths of each block, and, if salt is added, the salt concentration. [14,15]

## 1.2 SEO Block Copolymers

The detailed synthetic and purification procedures for polystyrene-*block*-poly(ethylene oxide) (SEO) has been presented elsewhere; [16–19] this Section will provide a brief, simplified overview. SEO is synthesized using living anionic polymerization, which requires air-free synthetic techniques [16] and dry and contaminant-free solvents and monomers. All synthesis is performed on the vacuum line, with some transfers done in the glovebox, and all glassware is thoroughly washed and flame-dried. Anionic synthesis involves multiple safety risks and should be thoroughly planned using standard operating procedures.

### *1.2.1 Monomer and Solvent Purification*

The solvents used are benzene and ethylbenzene. Benzene is stored in a solvent column, frozen and degassed on the vacuum line, and then brought into an Ar glovebox. To bond with any water present, *n*-butyllithium is added; styrene is added to form styrene oligomers which can be easily separated from the benzene. The polystyryl lithium chains cause the solution to turn red. The reactor is then returned to the vacuum line, and again frozen and degassed. Benzene distilled from the reactor into the polymerization vessel is clear, indicating that the polystyryl lithium chains have not been transferred. Ethylbenzene is purified through an analogous procedure.

Styrene is purchased anhydrous and pure; if inhibitor is present, it can be removed using filtration through alumina. Styrene is a liquid and can be pipetted into the polymerization reactor in an Ar glovebox. Ethylene oxide is a flammable, carcinogenic, and mutagenic gas; extreme safety precautions should be followed during use. In particular, over-

pressurization of vessels containing ethylene oxide can lead to vessel rupture and exposure. Ethylene oxide is dried by transferring, via the vacuum line, ethylene oxide from the as-received gas cylinder into a cooled flask. The flask is kept at -78 °C using a mixture of dry ice and isopropanol. After drying overnight, the ethylene oxide is distilled into ethylbenzene, where it can be kept safely at room temperature. Care must be taken when venting the vacuum line after any procedure involving the transfer of ethylene oxide, as residual ethylene oxide may remain in the line.

*1.2.2 Polymerization*

The first polymerization step is the initiation and polymerization of polystyrene. In the Ar glovebox, the polymerization reactor containing benzene is thoroughly stirred during the addition of the initiator and monomer to ensure monodispersity. The desired amount of *sec*-butyllithium is added to the polymerization reactor, followed by the desired amount of styrene monomer; the molar ratio of *sec*-butyllithium to styrene determines the length of the polystyrene block. The color changes to red, orange, or yellow, depending on the concentration of polystyryl lithium chains. Figure 1.2 [19] shows a schematic of the initiation and styrene polymerization steps.

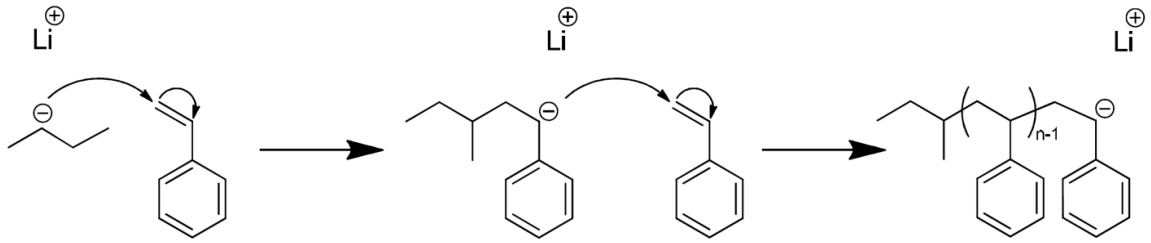


Figure 1.2. Schematic of initiation and polymerization of polystyryl chains.

For the next step, pure ethylene oxide is needed. Any procedure involving ethylene oxide is dangerous and extreme care should be taken. A small amount of ethylene oxide is distilled from the ethylbenzene vessel into a graduated ampoule kept on a dry ice and isopropanol mixture, and distilled again from that ampoule into the polymerization reactor, which is kept frozen on liquid nitrogen. Each chain will be end-capped with one ethylene oxide unit; further polymerization is inhibited by the association between the lithium cation from the *sec*-butyllithium with the oxyanion present upon ethylene oxide end-capping. At this stage the solution is clear, indicating the elimination of any carbanions. Figure 1.3 [19] shows a schematic of the end-capping step.

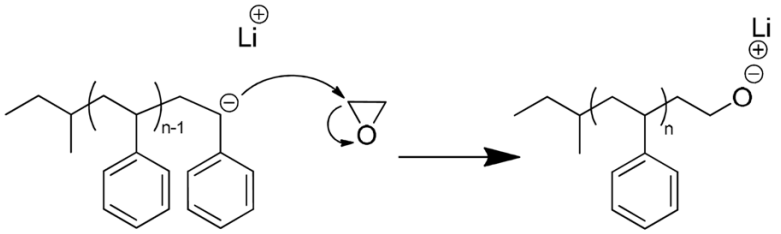


Figure 1.3. Schematic of the process of end-capping polystyryl chains with ethylene oxide.

To allow further ethylene oxide polymerization, the catalyst *tert*-butyl phosphazene ($P_4$-*t*-Bu) (Figure 1.4a) is added in the Ar glovebox; it associates with the lithium cations, freeing the anions for polymerization. The reactor is returned to the glovebox, frozen, and degassed. Ethylene oxide is again distilled into a graduated ampoule on dry ice and isopropanol, and the desired amount is carefully distilled into the polymerization reactor on liquid nitrogen. The polymerization is allowed to proceed for at least four days with constant stirring in an oil bath maintained at 45 °C. The growing oxyanion-terminated chains typically cause the reactor to take on a blue or purple color within several hours. Finally, the reactors are returned to the Ar glovebox and polymer chains are terminated using methanol. Figure 1.4b [19] shows a schematic of the ethylene oxide polymerization and termination steps. The final chemical structure of the polystyrene-*block*-poly(ethylene oxide) polymers is depicted in Figure 1.1c.

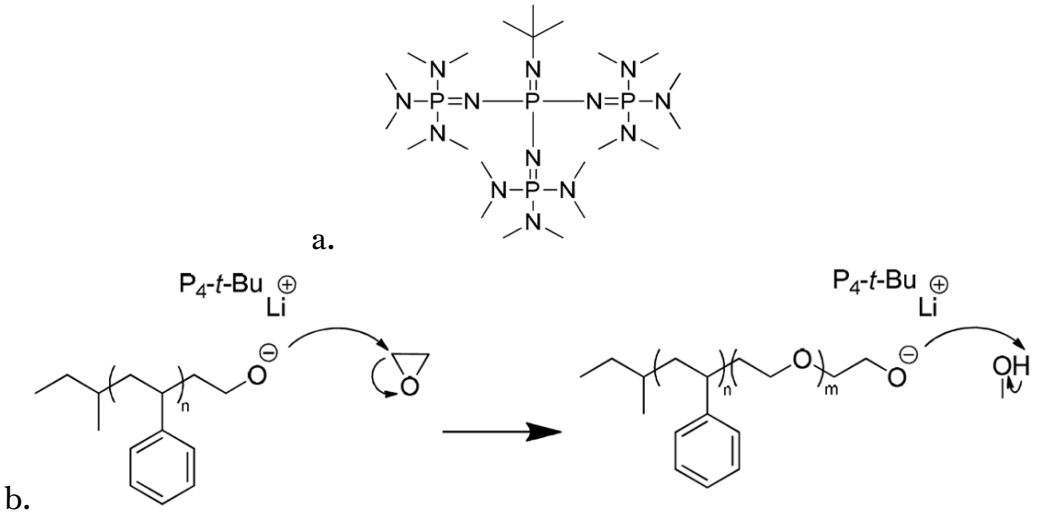


Figure 1.4. Chemical structure of *tert*-butyl phosphazene ($P_4$-*t*-Bu) (a) and schematic of the ethylene oxide polymerization and termination steps (b).

*1.2.3 Polymer Purification*

Polymers are purified by repeated precipitation using hexanes, filtration, and redissolution into benzene. They are also filtered through neutral alumina to remove any remaining phosphazene base. Particularly for low molecular weight polymers, where the

molar ratio of phosphazene base to polymer chains is high, many rounds of filtration may be required. Benzene is removed using a lyophilizer, leaving dry, white polymer powder, which is stored in a jar in a 4 °C refrigerator.

### *1.2.4 Polymer Characterization*

Before polymerization of ethylene oxide, gel permeation chromatography (GPC) using tetrahydrofuran (THF) is performed on the polystyrene homopolymer to determine its molecular weight and polydispersity index (PDI). After purification, GPC can be used to determine the final PDI. However, due to low solubility, *n*-methylpyrrolidone (NMP) is used as the solvent. Due to difficulty in calibrating GPC for block copolymers, in which chains of the same total length but with different ratios of the two blocks will exhibit different permeation times, this can only be used to determine the PDI, not the molecular weight. The molecular weight is determined using the known PS molecular weight and the mole ratio of ethylene oxide and styrene moieties determined using $^{1}$H NMR. The final polymers are denoted SEO*(xx-yy)*, where xx and yy are the molecular weights of the PS and PEO blocks, respectively. Anionic polymerization typically results in extremely narrow PDI, nearly always below 1.05.

### *1.2.5 Electrolyte Preparation*

Liquid electrolytes (Chapter 5) can be prepared by combining the solvent and salt in the desired ratio and stirring thoroughly. Because PEO and SEO are solids at room temperature, more complicated processes are required to achieve homogeneous electrolytes. PEO and LiTFSI are both soluble in THF, so PEO / LiTFSI electrolytes can be prepared by combining PEO and LiTFSI in the desired ratio, adding THF, stirring thoroughly until all polymer and salt are dissolved, and evaporating THF under vacuum at 120 °C overnight. SEO, however, is not soluble in THF; it is soluble in benzene, but LiTFSI is not. Therefore, electrolytes are prepared by preparing carefully-controlled solutions of SEO in benzene and LiTFSI in THF volumetrically. Separation of benzene from SEO is difficult, so it must be removed using an air-free lyophilizer.

## 1.3 Polymer Electrolytes

Polymer electrolytes are polymer chains mixed with salt. In this work, several different polymer chemistries—tetraglyme, C8-DMC (a fluorinated tetraglyme analog), PEO of varying molecular weights, and SEO of varying composition and molecular weight—are mixed with a lithium salt, typically lithium bis(trifluoromethanesulfonyl)imide salt (LiTFSI), but in one case lithium bis(fluorosulfonyl)imide (LiFSI). A large range of possible polymer-salt combinations is possible,[20] including mixtures of multiple polymers with salt[21] and single-ion conductors in which the anion is fixed to the polymer chain.[22]

### *1.3.1 Motivation*

As described at the beginning of this Chapter, in order to enable high energy density lithium metal batteries, novel electrolytes are needed that are stable against lithium metal, non-flammable, mechanically rigid, and ion conductive. Polymer electrolytes have long been considered a promising candidate: [20] they are generally non-flammable, and their properties can be tuned through manipulation of the salt concentration, molecular weight, and composition. [23] In particular, block copolymer electrolytes composed of a mechanically-rigid block and an ion-conducting block that preferentially solvates lithium ions can phase separate into mechanically rigid domains and ion conducting domains. [24] Depending on the molecular weight and composition of the polymers, different morphologies can be formed at different salt concentrations and temperatures. [12,15] There has been extensive work characterizing the morphology [15] and electrochemical behavior [25,23] of polymer electrolyte systems. However, much remains to be learned. The goal of this work is to better understand how various factors interact to influence polymer electrolyte performance in lithium-based electrochemical cells, in order to inform the rational design of future polymer electrolyte systems.

### *1.3.2 Research Questions*

In general, we seek to understand how polymer electrolytes behave in response to various stimuli, and in particular during battery cycling. How do intermolecular interactions contribute to electrochemical behavior? As salt concentrations develop, what limits the highest accessible current? How does thermal history or application of a magnetic field affect polymer morphology and electrochemical behavior? What happens to a block copolymer under the strain induced by cell polarization and the generation of a salt concentration gradient? How can we decouple salt concentration from morphology? What is the theory neglecting in predicting electrochemical behavior? What are the implications of these transitions and insights for electrolyte performance in electrochemical cells?

## 1.4 Nuclear Magnetic Resonance (NMR) Characterization

Nuclear Magnetic Resonance (NMR) spectroscopy is a nucleus-specific technique that capitalizes on the fact isotopes can be distinguished by their resonance frequencies, which in turn depend on their local environments. [26] Not all nuclei are NMR-active, but we are fortunate that there is at least one NMR-active nucleus in the polymer chains ($^{1}$H), cation ($^{7}$Li), and anion ($^{19}$F) of our polymer electrolyte systems. Details of NMR are explored in Chapter 2.

### *1.4.1 1D NMR*

In simple NMR experiments, the nucleus of interest (here, $^{1}$H, $^{7}$Li, or $^{19}$F) is selected via its characteristic frequency, and intensity peaks corresponding to atoms in that frequency range are measured in the presence of a large external magnetic field. The measured

frequency will depend on the nucleus via its characteristic gyromagnetic ratio, γ, as well as its local magnetic field, which is dominated by the applied field but is also influenced by the local environment, such as bonds. [26] Thus, the measured frequencies shed light on the environment of the atom. Further, peaks can split into multiplets, providing additional insight into interactions with neighboring atoms or local electric field gradients. See Sections 2.1-2.3 for more details; this will be exploited in Chapter 8 in the context of block copolymer electrolytes.

### *1.4.2 Pulsed-Field Gradient NMR (PFG-NMR)*

In pulsed-field gradient NMR (PFG-NMR), a series of pulses, including spatially-dependent magnetic field gradient pulses, are applied to distinguish atoms in different locations within the sample to measure their average displacement. This provides insight into the diffusion of various species and is particularly useful in combination with other techniques. See Section 2.4 for more details; the technique will be used in Chapter 5 in combination with electrochemical measurements and theory.

## 1.5 Morphological Characterization

Block copolymer electrolytes can microphase separate into a variety of ordered morphologies; most relevant to this work are, with increasingly asymmetric volume fractions, the lamellar, hexagonally packed cylindrical, and body-centered cubic spherical morphologies (Figure 1.5). The morphology of a block copolymer electrolyte significantly impacts its properties, and thus must be characterized in order to understand electrolyte performance. [23,27] Small-angle X-ray scattering (SAXS) provides morphological information.

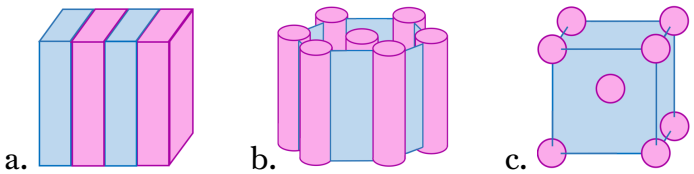


Figure 1.5. Cartoon of block copolymer morphologies relevant to this work: lamellar (LAM) (a), hexagonally packed cylindrical (HEX) (b), and body-centered cubic spherical (BCC) (c). The volume fraction of the blue phase increases from left to right.

### *1.5.1 Small-Angle X-Ray Scattering (SAXS)*

When exposed to an incident X-ray beam, samples absorb, transmit, and scatter radiation. The absorption is related to the concentration of different atomic species present, and thus can be used to calculate salt concentration if the densities are known. The scattering is quantified using the scattering vector, $q$. If the sample is ordered, an intensity peak will appear at a characteristic scattering vector, $q^*$, which is related to the domain spacing of the microstructure via Bragg's law, [28] while the morphology can be determined by the

locations of higher-order scattering peaks. The scattering pattern is also directional, allowing the user to attain insight into the behavior of differently-oriented ordered grains by examining different regions of the pattern. SAXS experiments can be performed *in situ* during battery cycling to learn how the application of a current affects the salt concentration profile and block copolymer morphology, which in turn sheds light on the failure mechanisms of electrochemical cells containing block copolymer electrolytes. SAXS is explained in more detail in Chapter 3 and applied in Chapters 7-11, and *in situ* SAXS and X-ray absorption are applied in Chapters 9-11.

## 1.6 Electrochemical Characterization

### *1.6.1 Parameters of Interest*

One of the key parameters controlling battery performance is the limiting current, $i_{\text{lim}}$, which is the maximum current a cell can sustain, and which therefore controls charging rates. During polarization of an electrolyte containing a mobile anion, salt concentration gradients develop, which impact cell efficiency and relate to the limiting current. These gradients can be measured experimentally using *in situ* X-ray techniques, and can be predicted by theory.

The ionic conductivity, $\kappa$, measures the electrolyte's tendency to transport charge, while the transference number, $t_+^0$, quantifies the fraction of initial charge transport, before salt concentration gradients develop, that can be attributed to the electrochemically active cation, relative to the solvent motion. The salt diffusion coefficient, $D$, relates salt flux to the salt concentration gradient, while the current fraction, $\rho_+$, measures the steady-state current relative to the initial current at constant potential, quantifying the effects of salt concentration gradient development on the current. The thermodynamic factor, $T_{\text{f}}$, measures the dependence of the mean molal activity coefficient, $\gamma_\pm$, on salt concentration. $T_{\text{f}}$ is used to relate concentration to electrochemical potential, and is unity in thermodynamically ideal systems. Finally, Stefan-Maxwell diffusion coefficients quantify inverse frictional interaction between components in the electrolyte, providing insight into molecular interactions; this is a key feature of Chapter 5.

### *1.6.2 Measurement Techniques*

Symmetric cells with stainless-steel blocking electrodes, which prevent electrode-electrolyte reactions, are used to measure the ionic conductivity. Lithium symmetric cells, containing non-blocking lithium metal electrodes, are used to measure $\rho_+$, $D$, and $i_{\text{lim}}$. Concentration cells are used to measure the dependence of electric potential on salt concentration, $\frac{dU}{d\ln m}$, where $U$ is the electric potential and $m$ is the molal salt concentration. From these measured parameters, $t_+^0$, $T_{\text{f}}$, and the Stefan-Maxwell diffusion coefficients can be calculated.

*1.6.3 Concentrated Solution Theory*

Concentrated solution theory, pioneered by John Newman, [29] is the framework used to allow the calculation of $t_+^0$, $T_f$, and the Stefan-Maxwell diffusion coefficients; $t_+^0$ depends on all of the aforementioned parameters, $T_f$ depends on $t_+^0$ and $\frac{dU}{d\ln m}$, and Stefan-Maxwell diffusion coefficients depends on $t_+^0$, $T_f$, and $\kappa$. The theory also enables prediction of concentration gradients, which can be compared with *in situ* SAXS experiments (Chapters 9-11), and the limiting current based on the concentration limits (Chapters 6 and 9-11). More detail is provided in Chapter 3, and concentrated solution theory is used throughout this Dissertation.

## 1.7 Structure of the Dissertation

The first four Chapters introduce the general background and approach of the Dissertation (Chapter 1), and three major experimental tools and their respective theory: nuclear magnetic resonance spectroscopy (NMR) (Chapter 2), small-angle X-ray scattering (SAXS) and absorption (Chapter 3), and full electrochemical characterization and modeling (Chapter 4). In Chapter 5, we start with liquid glyme-based systems, temporarily avoiding polymer and block copolymer-specific considerations to focus on the implications and applications of electrochemical characterization and PFG-NMR measurements. Chapter 6 continues with homopolymers, this time poly(ethylene oxide), exploring electrochemical characterization in the extreme high salt concentration limit, supported by additional characterization techniques, and the impact of salt solubility limits on the limiting current.

In Chapter 7, we transition to block copolymer electrolytes, beginning with a study of lamellar block copolymer grain structure and growth during thermal annealing, and its connection to ionic conductivity measurements. Continuing to explore the manipulation of grain structure, Chapter 8 describes magnetic field-induced preferential alignment of block copolymer grains measured using NMR and SAXS. Chapter 9 applies the previous insights—electrochemical characterization and theory, grain structure and alignment—to an *in situ* SAXS study of a partially-aligned lamellar SEO electrolyte that exhibits orientation-dependent structural changes during cycling. Due to the complex morphological effects of the concentration gradient development shown in Chapter 9, Chapter 10 explores using X-ray transmission to measure salt concentration as a function of position and time during cell cycling of an asymmetric block copolymer electrolyte, thus decoupling salt concentration and morphological changes; we learn that the inaccessibility of a phase transition limits the salt concentration, thus decreasing the limiting current. Chapter 11 summarizes the main points of the Dissertation and proposes directions for future study.

# Chapter 2: Nuclear Magnetic Resonance (NMR) Spectroscopy

Levitt's *Spin Dynamics* [26] is an excellent resource for an in-depth introduction to nuclear magnetic resonance spectroscopy (NMR). This chapter is intended for NMR beginners or non-users; I will provide a brief, over-simplified summary of only the basics of NMR relevant to understanding the rest of this Dissertation. Many of these ideas, and many more, are covered in much more detail in Levitt and other texts.

## 2.1 Nuclei, Spin, Angular Momentum, Magnetic Moments

### *2.1.1 Nuclear Fundamentals*

Nuclei have a property called spin, $I$, which determines, among other things, their NMR activity. If $I = 0$, as is the case for carbon-12, $^{12}C$, for example, the nucleus has no spin, and cannot be observed using NMR. However, if $I \neq 0$, the nucleus will have a non-zero angular momentum, $S$, and therefore a non-zero magnetic moment, $\mu = \gamma S$, where $\gamma$ is the gyromagnetic ratio, a property unique to each isotope.

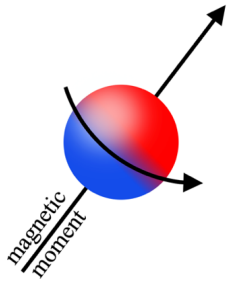


Figure 2.1. Vector illustration of the quantum mechanics of an NMR-active nucleus. The angular momentum is parallel to the magnetic moment.

### *2.1.2 Spin States*

The value of $I$ is quantized and must be a multiple of 1/2. It is documented for each nuclear isotope. The spin quantum number, $m$, also referred to as the "spin state," is also quantized, between -$I$ and $I$ in steps of size 1. In our systems, which are polymers mixed with lithium salts, there are several relevant nuclei. The only hydrogen-containing molecules are the polymer chains, so we will use hydrogen-1, $^{1}H$ (natural abundance 99.99%), to characterize the polymer chains. We will use lithium-6, $^{6}Li$ (natural abundance 7.59%), and lithium-7, $^{7}Li$ (natural abundance 92.41%), to characterize the lithium cation, and fluorine-19, $^{19}F$ (natural abundance 100.00%), to characterize the fluorine-containing salts, and, in some situations (see Chapter 5), fluorinated polymer chains. [30] The spin number, $I$, accessible spin states, $m$, gyromagnetic ratios, $\gamma$, and quadrupole moment, $Q$ (see Section 2.3), of the relevant nuclei are presented in Table 2.1.

Table 2.1. Spin number, $I$, accessible spin states, $m$, gyromagnetic ratio, $\gamma$, and quadrupole moment, $Q$, of relevant nuclei

| nucleus | spin number, $I$ [26] | possible spin states, $m$ | gyromagnetic ratio, $\gamma$ ($10^6$ rad $s^{-1}T^{-1}$) [26] | quadrupole moment, $Q$ (mb) [31] |
|---|---|---|---|---|
| $^{1}H$ | $1/2$ | $+1/2, -1/2$ | 267.522 | – |
| $^{6}Li$ | 1 | $+1, 0, -1$ | 39.372 | −0.808 |
| $^{7}Li$ | $3/2$ | $+3/2, +1/2, -1/2, -3/2$ | 10.398 | −40.1 |
| $^{19}F$ | $1/2$ | $+1/2, -1/2$ | 251.815 | – |

With no magnetic field present, the orientations of the magnetic moments of a collection of NMR-active nuclei will be random, with no net magnetic moment (Figure 2.2a). However, an applied external field (Figure 2.2b), here in the $z$-direction, provides a driving force for preferential alignment of the magnetic moments with the field, leading to a net magnetic moment parallel to the field. Note that the spins are still oriented in a variety of directions, but the slight preference for alignment with the field is sufficient for the generation of a net magnetic moment. Due to the inherent magnetic moment of the nuclei, this magnetic moment will precess around the applied field at a frequency

$$\omega = \gamma B \qquad (2.1)$$

in the radiofrequency range, where $\gamma$ is the gyromagnetic ratio of the nucleus and $B$ is the strength of the magnetic field experienced by the nucleus.

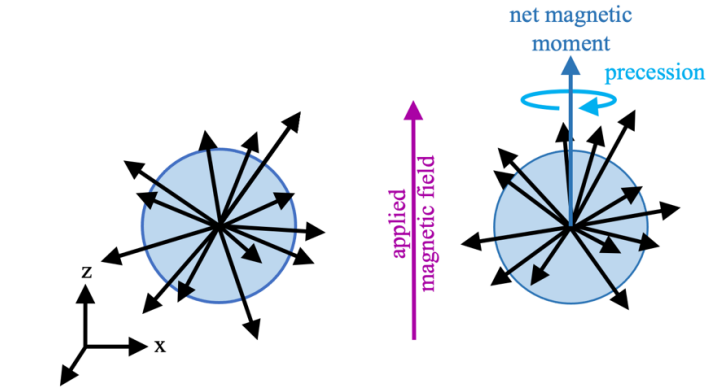


Figure 2.2. Two-dimensional projection illustrating several randomly oriented nuclear magnetic moments (a), and these magnetic moments in the presence of an external magnetic field along the $z$-axis (b), with a net preference for aligning with the applied field and precession about the field.

## 2.2 NMR

There are two different physical depictions of NMR. Both are applicable, but of differing utility in understanding different phenomena and experiments.

### *2.2.1 The Precession Conception of NMR*

The first conception of NMR, useful in understanding pulsed-field gradient (PFG) NMR (Section 2.4), relies on the concept of vector precession as described above. A constant large external magnetic field ($B_0$) is applied in the $z$-direction, generating a net magnetic moment parallel to the $B_0$ field (*i.e.,* in the $z$-direction) precessing at a frequency $\omega$ determined by Equation 2.1. Note that since $\omega$ depends on the gyromagnetic ratio, it is thus nucleus-specific.

In an NMR instrument, there is a coil that can both apply and measure oscillating magnetic fields along the $x$-axis. Because the net magnetic moment is along the $z$-axis, there is no net field in the $x$-direction. However, if a strong field is briefly applied in the $x$-direction at frequency $\omega$—typically a so-called 90° pulse—the net magnetic moment of the nuclei will (temporarily) align along the $xy$-plane. After the end of the pulse the magnetic moment will return to $z$-alignment through a process called "relaxation." Before the completion of the relaxation process and after the 90° pulse, the net magnetic moment will precess around the $z$-axis.

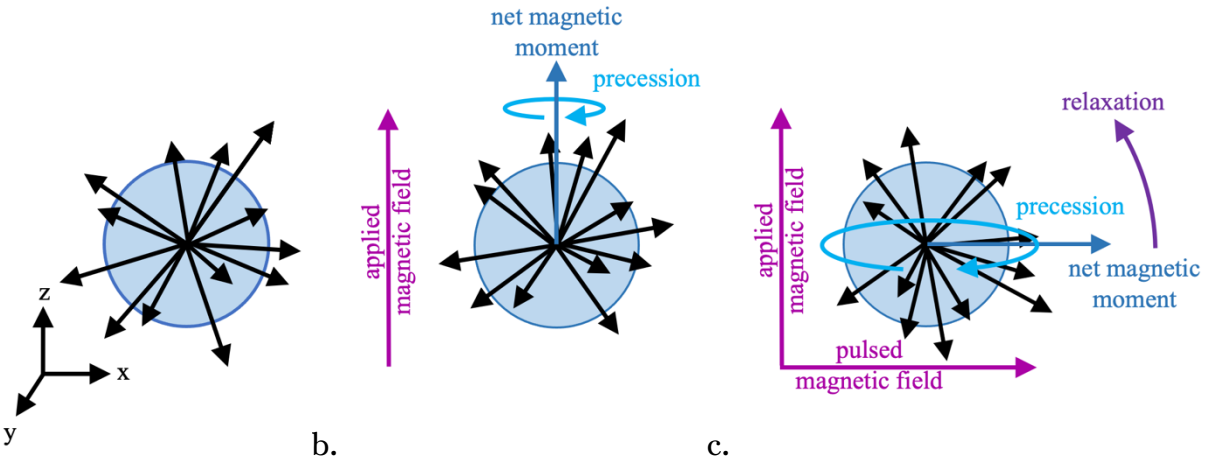


a. b. c.

Figure 2.3. Randomly oriented nuclear magnetic moments (a), and magnetic moments in the presence of an external magnetic field along the $z$-axis (b), with a net preference for aligning with the applied field and precession about the field. After a 90° magnetic field pulse in the $x$-direction, the net magnetic moment is along the $xy$-plane, but continues precessing about the $B_0$ field ($z$-axis) (c).

The 90° pulse results in a component of the net magnetic moment along the *xy*-plane which precesses around the *z*-axis. Physically, this is similar to a spinning top; when the top is perfectly upright, rotating around its axis of symmetry, it may appear not to be moving. However, if the top tilts to the side, de-aligning its axis of symmetry with its axis of precession, the rotation becomes visible (see Figure 2.4).

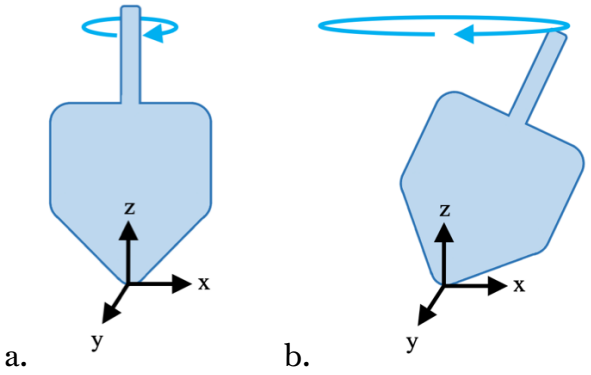


Figure 2.4. Mechanical metaphor for precession around the *z*-axis before (a) and after (b) application of a 90° pulse along the *x*-axis.

The precession around the *z*-axis along the *xy*-plane leads to an oscillating current in the coil along the *x*-axis. The frequency of this current is the frequency of precession, and can be extracted by performing a Fourier transform of the measured signal, leading to an intensity peak at frequency $\omega$. In Equation 2.1, $\omega$ is proportional to the total magnetic field experienced by the nucleus, $B$. A large component of that field will be the applied field, $B_0$, but the local environment of the atom also contributes, subtly shifting the measured frequency. Thus, different atoms of the same isotope in different local environments (for example, with different chemical bonds), will exhibit peaks at slightly different frequencies. NMR spectra of samples containing the examined nucleus in multiple environments will exhibit multiple peaks.

During the relaxation process, as the alignment of the net magnetic moment returns to alignment with the *z*-axis, the signal along the *xy*-plane decreases, and the peak intensity decreases. Even if nuclei are precessing at the same frequency, if they are slightly out of phase with each other, the peak intensity will also decrease. This will be essential in Section 2.4.

### *2.2.2 The Spin States Conception of NMR*

An alternate conception of NMR, useful in understanding peak splitting (Section 2.3), considers the spin states of the nuclei. The quantum mechanics of this explanation are complex,[26] but we can circumvent them with some simplifications.

Let us consider a spin-1/2 ($I = 1/2$) nucleus, like $^1$H. Such a nucleus has two possible spin states, $+{}^1/_2$ ("spin-up") and $-{}^1/_2$ ("spin-down"). One can think of the spin-up state as a magnetic moment parallel to the applied field and the spin-down state as a magnetic moment anti-parallel to the applied field at a very small energy difference $\Delta E$ from the spin-up state. This energy is related to the frequency measured by NMR through the Planck-Einstein relationship, $\Delta E = \hbar\omega$, where $\hbar$ is the reduced Planck constant $h/2\pi$. $\Delta E$ is proportional to the magnetic field:

$$\Delta E = \hbar\omega = \hbar\gamma B\,, \qquad (2.2)$$

such that, as in Section 2.2.1, the measured frequency depends on the magnetic field experienced by the nucleus, including contributions from the applied magnetic field, $B_0$, and the local atomic environment.

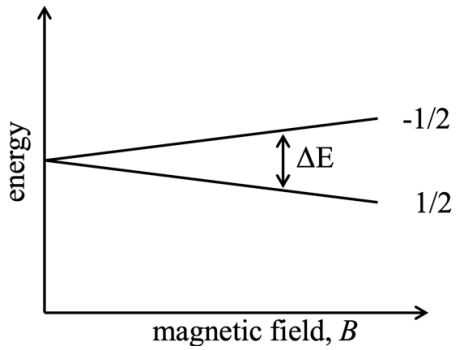


Figure 2.5. Illustration (with exaggerated $\Delta E$ for emphasis) of the energy differential between spin states increasing with the magnetic field experienced by a spin-1/2 nucleus.

For a non-spin-1/2 nucleus ($I \neq 1/2$), there are more than two spin states (see Table 2.1). However, under most circumstances, these spin states are evenly spaced, such that only one $\Delta E$, and thus one NMR frequency, are observed. An exception will be explored in the next Section.

## 2.3 Peak Splitting

### *2.3.1 Spin-spin Coupling*

As illustrated in Section 2.2, the observed NMR frequency depends on the local magnetic field experienced by the nucleus, including contributions from the applied field and the local environment. If another NMR-active nucleus, with its own magnetic moment, is near a given atom, then that magnetic moment will contribute to its local magnetic field. Just as our examined spin-1/2 nucleus can exist in two states, spin-up or spin-down, so can the neighboring nucleus. If we think of the spin-up state as a magnetic moment aligned

parallel to the field, then a neighboring nucleus in the spin-up state will slightly increase the local magnetic field, and thus the frequency of the peak. A neighboring nucleus in the spin-down state will slightly decrease the local magnetic field, and thus the frequency of the peak.

In NMR, we are never examining a single nucleus, but instead all nuclei in the examined frequency range. Thus, if some nuclei are near a spin-up neighbor, and some are near a spin-down neighbor, both effects will be observed. Recall that the spin-up state is preferred; however, $\Delta E$ is small, such that both states are approximately equally likely. Therefore, if the nuclei corresponding to a given NMR peak typically have one NMR-active neighbor, the peak will split into two peaks (or a "doublet" peak), corresponding to spin-up and spin-down neighbors, of equal intensities, since spin-up and spin-down neighbors are approximately equally likely.

If the nuclei typically have two NMR-active neighbors, there are three possibilities: spin-up/spin-up, with $B > B_0$, spin-up/spin-down or spin-down/spin-up, in which the magnetic moments cancel out and $B = B_0$, and spin-down/spin-down, with $B < B_0$ (Figure 2.6). Since there are two ways to achieve $B = B_0$ and only one way to achieve each of the others, the probabilities of these states are 1/4, 1/2, and 1/4, so the peak will split into three peaks (or a "triplet" peak), with the central peak at twice the intensity of the other (or "satellite") peaks; *i.e.*, a peak ratio of 1:2:1. This logic can be extended to increasing numbers of neighbors; for example, three NMR-active neighbors would lead to a quadruplet peak with a peak ratio of 1:3:3:1. This effect is referred to as "spin-spin coupling": the examined spin is affected by the spin of at least one neighboring nucleus. "Decoupling" excites nuclei at a chosen frequency to remove coupling, reducing the splitting of nuclei coupled with neighbors at that frequency to singlet peaks. [32]

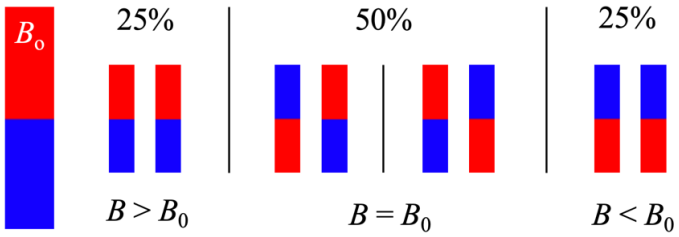


Figure 2.6. The possible spin states of two nuclei neighboring the examined nuclus, their resulting effects on the local magnetic field, and the corresponding probabilities of those effects.

### *2.3.1 Quadrupolar Splitting*

Non-spin-1/2 nuclei have more than two spin states. Because spin states are quantized, ranging between $+I$ and $-I$ in steps of size 1, a nucleus of spin $I$ will have $2I + 1$ accessible spin states, and thus $2I$ accessible transitions between spin states. Consider $^7$Li, $I = 3/2$:

accessible spin states are -3/2, -1/2, +1/2, and +3/2, and there are three corresponding transitions. As described in Section 2.2.1 and illustrated in Figure 2.7a, these transitions typically have the same $\Delta E$, and so only one NMR peak is observed. However, if the quadrupolar moment, $Q$, tabulated in Table 1, is non-zero, the quadrupolar moment of the nucleus can couple with a local electric field gradient (EFG), for example due to a highly polar environment, to shift the energies of the spin states (Figure 2.7b). The quantum mechanical details of the $Q$-EFG interaction are explored elsewhere. [26] The result of this coupling is that the three transitions (for a spin-3/2 nucleus) no longer exhibit the same $\Delta E$, and therefore no longer appear as a single NMR peak, but instead as three peaks (referred to as a "triplet" peak).

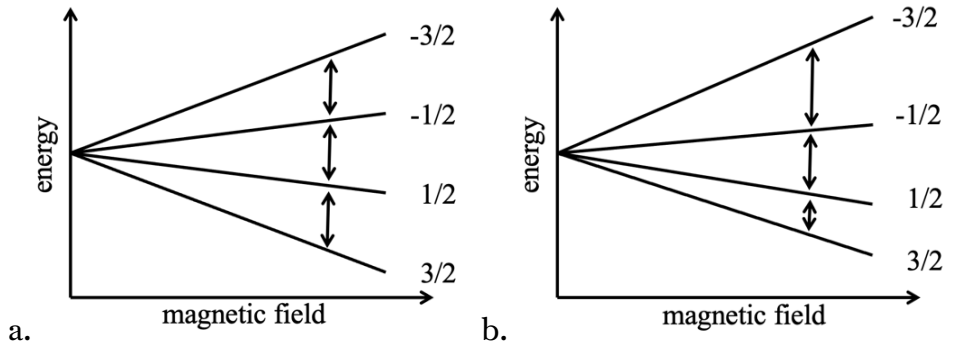


Figure 2.7. Illustration (with exaggerated transition energies) of spin state transitions of a spin-3/2 nucleus without (a) and with (b) the presence of a local electric field gradient (EFG).

As is a theme of this Chapter, the quantum mechanical physics of this shift, and in particular the peak intensity ratio of the resulting peaks, are complex and detailed elsewhere. [26] However, following the approach detailed in Philp *et al.*, [33] we can make an analogy to emission spectra to gain insight into the peak ratio. Boltzmann's law gives the population ratio of non-coupled spins at adjacent energy levels:

$$\frac{N_{i+1}}{N_i} = e^{\frac{-\Delta E}{kT}}, \qquad (2.2)$$

where $k$ is the Boltzmann constant and $T$ is the temperature. Because the $\Delta E$ is small, we can expand Equation 2.2 as a series and truncate it linearly:

$$\frac{N_{i+1}}{N_i} = 1 - \frac{\Delta E}{kT}. \qquad (2.2)$$

Thus,

$$N_2 = N_1\left(1 - \frac{\Delta E}{kT}\right),$$

$$N_3 = N_2\left(1 - \frac{\Delta E}{kT}\right) = N_1\left(1 - \frac{\Delta E}{kT}\right)^2, \qquad (2.3)$$

and so forth. These power series can be expanded, and, since $\Delta E$ is small, all terms with $\Delta E$ to a power of two or greater can be neglected. For four spin states, as is the case for a spin-3/2 nucleus, the result is:

$$N_2 = N_1\left(1 - \frac{\Delta E}{kT}\right),$$

$$N_3 = N_1\left(1 - 2\frac{\Delta E}{kT}\right),$$

$$\text{and } N_4 = N_1\left(1 - 3\frac{\Delta E}{kT}\right). \qquad (2.4)$$

It is clear from Equation 2.2 that the spacing in number of particles between each adjacent state is the same: $\frac{\Delta E}{kT}$. We can think of the acquisition of an NMR spectrum as exciting the nuclei from their natural Boltzmann distribution so that there are an equal number in all spin states ("saturation"), and then measuring how many spins make each energetic transition to return to the Boltzmann distribution. Since $\frac{\Delta E}{kT}$ is small, most spins will remain in their starting state and can be neglected. As an example, let us use $\frac{\Delta E}{kT} = 2$; the number chosen does not matter since we only care about the ratios. In that case, $N_i = N_{i+1} + 2$.

Figure 2.8a shows the number of excess spins at each energy level in the Boltzmann distribution. In Figure 2.8b, the spins have been saturated, *i.e.*, rearranged such that there are the same number in each level. First, we restore energy level (4) to its Boltzmann state; this requires allowing 3 spins (pink in Figure 2.8c) to make the 4 – 3 (spin state -3/2 to -1/2) transition. Next, 4 spins (pink in Figure 2.8d) make the 3 – 2 (spin state -1/2 to +1/2) transition to restore energy level (3) to its Boltzmann state. Finally, 3 spins (pink in Figure 2.8e) make the 2 – 1 (spin state +1/2 to +3/2) transition to restore the remaining energy levels to the Boltzmann transition (Figure 2.8f). Thus, the number of spins making each transition shown in Figure 2.7b are 3, 4, and 3, and the peak intensity ratio of the three corresponding peaks making up the quadrupolar triplet is 3:4:3. Similar

logic can be applied to determine the peak ratio of nuclei with other spin numbers—for example, a spin-1 nucleus like $^{6}$Li will have two peaks with equal intensities. [33] These saturation-transfer ratios are always applicable; however, the resultant peaks will only be distinguishable (*i.e.* at different frequencies) in the presence of an electric field gradient (EFG) at the position of the nucleus. The frequency spacing between the peaks ("peak splitting," Hz) increases with increasing magnitudes of the EFG and of the quadrupolar moment of the nucleus. [26] Thus, in the presence of an EFG, $^{7}$Li will exhibit a triplet peak of intensity ratio 3:4:3, and $^{6}$Li will exhibit a doublet peak with of intensity ratio 1:1. For the same EFG magnitude, $^{6}$Li will exhibit much narrower peak splitting due to its lower $Q$-value.

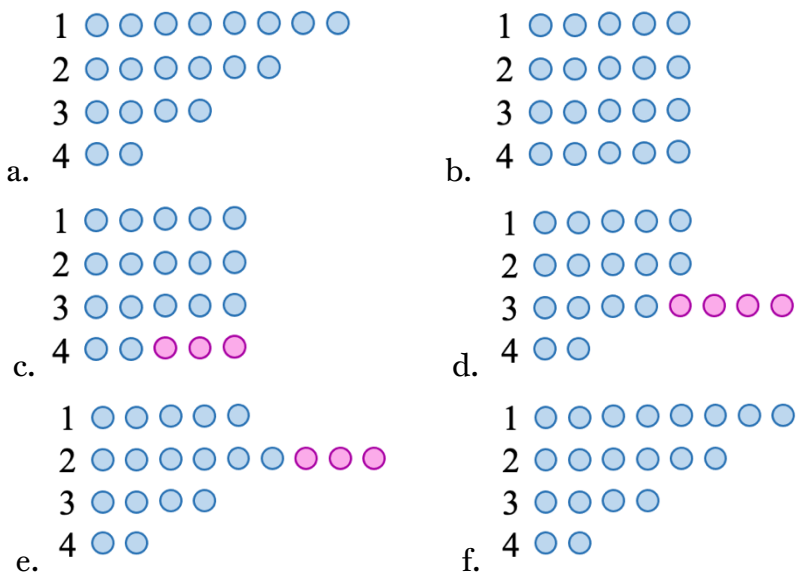


Figure 2.8. Illustration of the spin transfer process for a spin-3/2 nucleus from the Boltzmann distribution (a) to the excited equally-populated configuration (b) and back to the Boltzmann distribution (f). Three spins transfer from state (4) to state (3) (c), four from state (3) to state (3) (d), and three from state (2) to state (1). This results in a quadrupolar triplet peak ratio of 3:4:3 in the presence of an electric field gradient (EFG).

For a spin-3/2 nucleus, there are two possible origins of triplet peak splitting: spin-spin coupling with two NMR-active neighbors, or quadrupolar peak splitting due to the presence of an electric field gradient. However, in the first case, the peak ratio is 1:2:1, while in the second, the peak ratio is 3:4:3, and the two cases can be easily distinguished (see Chapter 8).

## 2.4 Pulsed-Field Gradient NMR

### *2.4.1 Introduction and Concepts*

Pulsed-field gradient nuclear magnetic resonance spectroscopy (PFG-NMR), so named because it involves short pulsed application of a magnetic field gradient, is used to measure the average displacement of NMR-active nuclei, and therefore the self-diffusion coefficient. The key work enabling this technique was performed by Stejskal and Tanner, [34] and Sinnaeve [35] is an excellent resource for detailed mathematical derivations. Other useful references include Johnson Jr. for theoretical aspects, [36] and Price for experimental details. [37] As with the previous Sections, this Section will provide a conceptual overview. It relies on the precession conception of NMR as detailed in Section 2.2.1.

First, recall that the precession frequency of a nucleus is proportional to the magnetic field that it experiences (Equation 2.1): if the magnetic field is increased, the precession frequency will increase. If the magnetic field is constant throughout the sample volume, after the application of an initial 90° pulse, all equivalent spins will precess at the same frequency and in phase with each other (Figure 2.9a). However, upon application of a magnetic field gradient, in which the applied field depends on position, spins at different positions in the sample will precess at different frequencies. In Figure 2.9b, a magnetic field that increases along the $+z$ direction is applied, causing the spins at higher $z$ positions to precess at a higher frequency. The pulse is brief, and after its application the spins again precess at the same frequency but are no longer in phase; the spins at higher $z$ positions are "ahead" of those at lower positions ("dephasing") (Figure 2.9b). Next, a 180° pulse (analogous to a 90° pulse as described above) is applied, inverting the accumulated phase difference; the spins at higher $z$ positions, which were "ahead" are now "behind" (Figure 2.9c). Now, the same magnetic field gradient pulse can be applied; the spins at higher $z$ positions will precess at a higher frequency during the application of the pulse, causing all spins to return to being in phase after the pulse (Figure 2.9d). However, if the atoms have diffused during the process (Figure 2.9e), then the strengths of the magnetic fields that a given atom experiences during the two magnetic field gradient pulses will be different, and rephasing will be incomplete (Figure 2.9f). This is referred to as a "spin-echo" experiment.

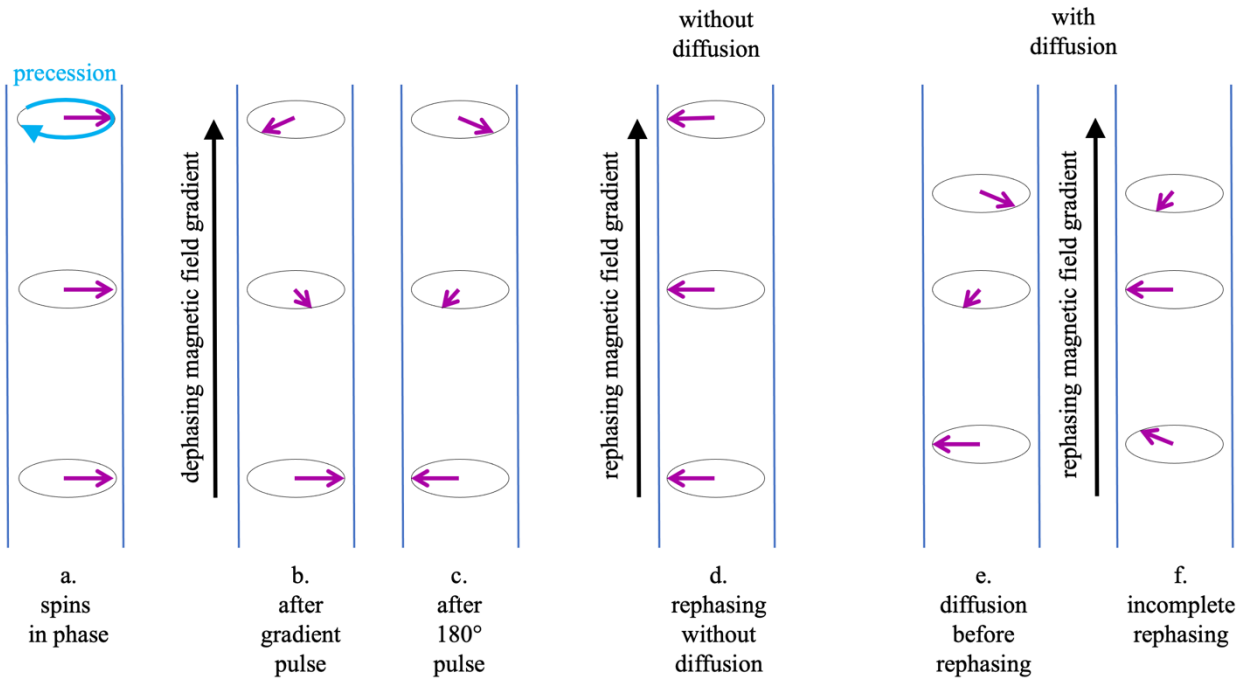


Figure 2.9. Illustration of the essential steps in PFG-NMR: spins start out in phase (a), are dephased by a magnetic field gradient pulse (b), reversed by a 180° pulse (c), and rephased by a second magnetic field gradient pulse (d). If diffusion has occurred between the two gradient pulses (e), rephasing is incomplete (f).

Dephasing results in a decrease in the NMR signal because the signal intensity is proportional to the vector sum of all spins; with dephasing, spins that are "ahead" cancel out spins that are "behind," reducing the total signal. With increased self-diffusion coefficient (*i.e.,* increased average displacement) or increased gradient strength (and therefore increased dephasing upon the first magnetic field gradient pulse), the dephasing at the end of the experiment will be greater, and therefore the signal intensity will be lower. The pulse sequence described above is the simplest PFG-NMR experiment and is illustrated in Figure 2.10; the gradient pulse is of length $\delta$, and the delay time, allowing for diffusion, between the two gradient pulses is of length $\Delta$.

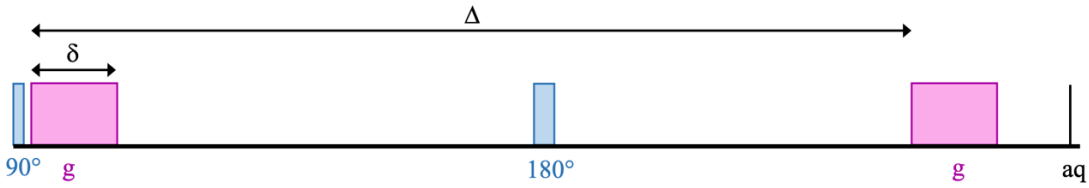


Figure 2.10. Illustration of the basic PFG diffusion experiment. 90° and 180° pulses are in blue, magnetic field gradient pulses, labeled "g," are in pink, and the point of acquisition is denoted "aq."

*2.4.2 The Stejskal-Tanner Equation*

The signal attenuation is described by the Stejskal-Tanner equation, [34] derived in Sinnaeve *et al.*: [35]

$$\frac{I}{I_0} = e^{-D\gamma^2\delta^2 g^2\left(\Delta-\frac{\delta}{3}\right)}, \qquad (2.5)$$

where $I$ is the integrated NMR peak intensity, $I_0$ is the integrated NMR peak intensity with no gradient applied, $D$ is the self-diffusion coefficient, $\gamma$ is the gyromagnetic ratio, $\delta$ is the length of the magnetic gradient pulse, $g$ is the strength of the magnetic field gradient (T/m), and $\Delta$ is the time delay between the two gradient pulses.

Typically, the experiment is repeated several times with varying values of $g$; with increasing $g$, the peak intensity will decrease (Figure 2.11a). Then, $\ln\left(\frac{I}{I_0}\right)$ can be plotted against the quantity $\gamma^2\delta^2 g^2\left(\Delta-\frac{\delta}{3}\right)$. The resulting curve is linear, and its slope is equal to the negative of the self-diffusion coefficient, $D$ (Figure 2.11b). This is referred to as a Stejskal-Tanner plot.

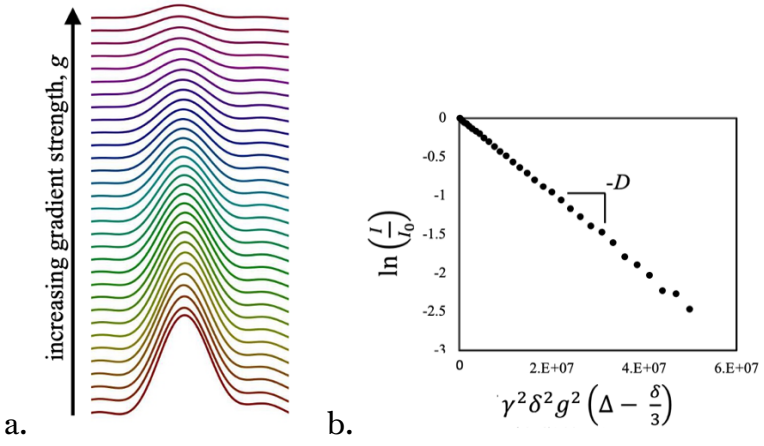


Figure 2.11. Example PFG-NMR data showing the decrease in signal intensity with increased magnetic field gradient strength, $g$ (a), and the corresponding Stejskal-Tanner plot (b).

*2.4.3 Advanced Pulse Sequences and Convection-Compensation*

One common extension to the basic PFG-NMR pulse sequence is the usage of bipolar gradient pulses. [38] A gradient pulse of length $\delta/2$ is applied, followed by a short time delay of length $\tau$, a 180° pulse, and a second gradient pulse of length $\delta/2$ in the opposite

direction of the first. Due to the 180° pulse, the second gradient pulse continues the dephasing begun by the first, and the total gradient pulse length is still δ. The usage of bipolar gradients reduces certain experimental artifacts such as so-called "eddy currents," equipment artifact caused by long gradient pulses, and static magnetic fields, for example due to sample inhomogeneities, which is of particular relevance for solid polymer samples. [35] In a stimulated echo (STE) experiment, two 90° pulses are used instead of a 180° pulse. [39] The result is that magnetization is stored along the *z*-axis through much of the Δ delay, significantly reducing the effects of relaxation and improving signal. These two modifications, along with a spoiler gradient described elsewhere, [35–37] are depicted in the pulse sequence shown in Figure 2.12.

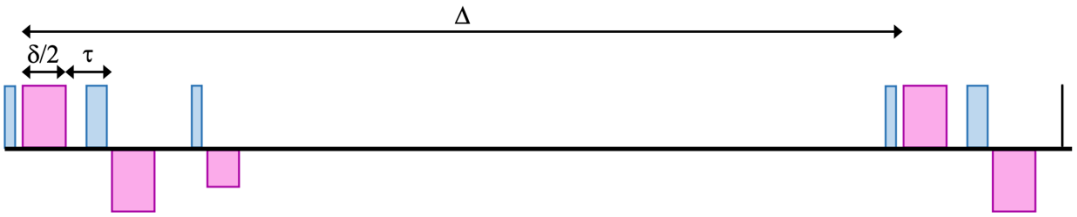


Figure 2.12. Stimulated echo (STE) pulse sequence including bipolar gradient pulses, stimulated echo, and a spoiler gradient. The color scheme is the same as in Figure 2.10.

For the pulse sequence described above and shown in Figure 2.12, Equation 2.5 can be modified to

$$\frac{I}{I_0} = e^{-D\gamma^2\delta^2 g^2\left(\Delta - \frac{\delta}{3} - \frac{\tau}{2}\right)}, \qquad (2.6)$$

where τ is the delay between the first and second gradient pulses. The analysis to obtain the self-diffusion coefficient, *D*, is analogous to that described above. [35]

One potential artifact in the use of PFG-NMR experiments to measure self-diffusion coefficients is convection, which can artificially increase atom displacements, and thus signal attenuation, leading to an over-estimation of the diffusion coefficient. The most common way to correct for this is by repeating the pulse sequence twice with opposite effective gradient directions, such that, if the local convection velocity is constant with time, its effects cancel out (Figure 2.13). This is called a double stimulated echo (DSTE) sequence. [40]

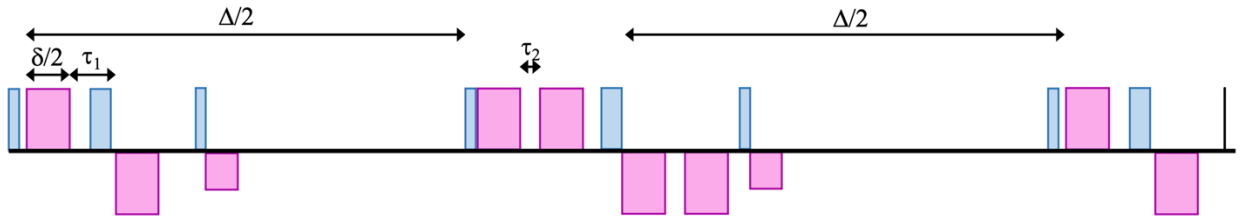


Figure 2.13. Double-stimulated echo (DSTE), convection-compensating pulse sequence. The color scheme is the same as that in Figures 2.10 and 2.12.

The resulting modified Stejskal-Tanner equation is:

$$\frac{I}{I_0} = e^{-D\gamma^2\delta^2 g^2\left(\Delta - \frac{2\delta}{3} - \frac{\tau_1+\tau_2}{2}\right)}, \qquad (2.7)$$

where $\tau_2$ is the additional delay between gradient pulses depicted in Figure 2.13. [35]

The disadvantage of the DSTE sequence is it results in significantly decreased signal intensity, and it should therefore be used only when necessary. One simple way to check whether convection is a factor is by performing several STE experiments with varying Δ. After analysis using Equation 2.6, the calculated $D$ for experiments with different Δ should be identical. If $D$ appears to increase with increasing Δ, this is a sign that it is possible that convection, which will be more pronounced with increased Δ, is artificially inflating $D$, and a convection-compensating sequence may be necessary.

Finally, the above illustrations and Stejskal-Tanner equations assume rectangular magnetic field gradient pulses, where the gradient strength is set to its maximum value, $g$, as quickly as possible at the start of the pulse. Often, to reduce eddy currents caused by rapid changes in $g$, a sine-shaped gradient pulse is used; the maximum attained gradient strength is still $g$, but this value is achieved less abruptly. In this case, Equations 2.5-2.7 become, respectively: [35]

$$\frac{I}{I_0} = e^{-D\gamma^2\delta^2 g^2 \frac{4}{\pi^2}\left(\Delta - \frac{\delta}{4}\right)}, \qquad (2.8)$$

$$\frac{I}{I_0} = e^{-D\gamma^2\delta^2 g^2 \frac{4}{\pi^2}\left(\Delta - \frac{5\delta}{16} - \frac{\tau}{2}\right)}, \qquad (2.9)$$

$$\text{and } \frac{I}{I_0} = e^{-D\gamma^2\delta^2 g^2 \frac{4}{\pi^2}\left(\Delta - \frac{5\delta}{8} - \frac{\tau_1+\tau_2}{2}\right)}, \qquad (2.10)$$

where the $\frac{4}{\pi^2}$ accounts for the fact that the integrated magnetic field strength for a sine-shaped magnetic field gradient pulse is a factor of $\frac{2}{\pi}$ smaller than that of a rectangular pulse. The values of *g* output from the Bruker instruments used for these studies account for this shape factor, and therefore the factor of $\frac{4}{\pi^2}$ can be omitted. In this work, bipolar sine-shaped gradients, and therefore Equations 2.9 and 2.10 with the omission of $\frac{4}{\pi^2}$ , are used.

### *2.4.4 Electrophoretic NMR*

Electrophoretic NMR (eNMR) is an extension of PFG-NMR. It uses similar pulse sequences, but with the application of an electric potential in a specially-designed NMR tube containing electrodes that can be connected to a potentiostat and synchronized with the application of the NMR and magnetic field gradient pulses. The potential causes a net velocity of the species affected by electrochemical activity; note that even non-charged species like polymer chains can exhibit a net velocity as they are displaced by charged species. As a result, the spins finish the experiment with a net phase shift due to migration, in addition to the signal attenuation due to self-diffusion which is detected by PFG-NMR. This phase shift can be measured and used to extract the velocity. [41] Notably, eNMR allows the determination of the velocities of different species independently due to its nucleus specificity, and also allows the determination of the sign of the velocity. These measurements have significant connections to electrochemical parameters, in particular the cation transference number, $t_+^0$. [42]

# Chapter 3: Small-Angle X-Ray Scattering

Small-angle X-ray scattering (SAXS) uses X-ray interactions with matter to gain insight into the composition and structure of materials. It provides a wealth of insight into electron density, morphology, orientation-dependent effects, and grain structure. We first explore SAXS *ex situ* (*i.e.,* without concurrent electrochemical experiments), and then extend the experiments to *in situ* applications, obtaining SAXS information as a function of position and time in an electrochemical cell during cycling.

## 3.1 *Ex Situ* Morphological Characterization

### *3.1.1 X-Ray Transmission*

In a typical SAXS experiment, the sample is exposed to an incident X-ray beam of intensity $I_0$ at wavelength $\lambda$. A small fraction (intensity $I_s$) of the beam is scattered at scattering angle $\theta$. The remainder is either transmitted through or absorbed by the sample (Figure 3.1). The transmitted and scattered X-rays reach a detector for measurement. Because the transmitted intensity is much higher than the scattered intensity, a beamstop is used to protect the region of the detector reached by the transmitted beam.

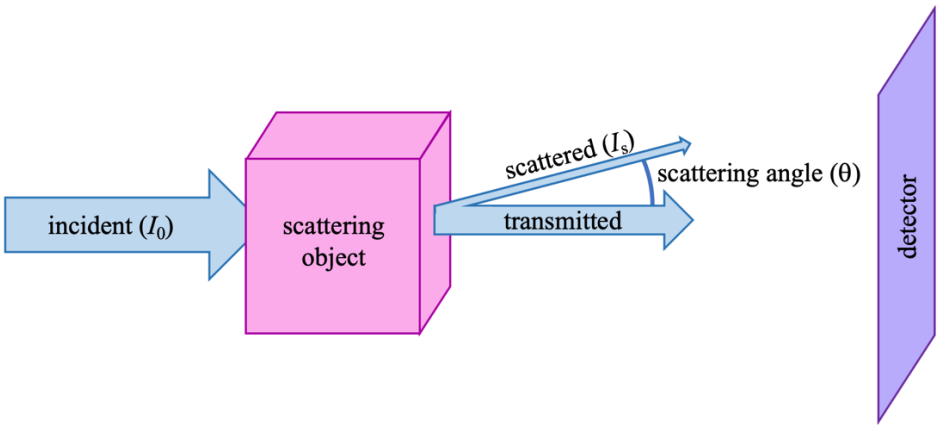


Figure 3.1. SAXS schematic. An incident X-ray beam ($I_0$) interacts with the scattering object. Much of the beam is transmitted, and a small amount ($I_s$) is scattered at scattering angle $\theta$. The remaining intensity is absorbed. Scattered X-rays are measured using a specialized detector.

The fraction of incident radiation that is absorbed depends only on the X-ray wavelength and the number and type of atom through which the beam passes. Therefore, if the density, molar composition, and thickness of the sample, along with the X-ray wavelength, are known, the X-ray absorption can be calculated using easily accessible online tools, for example one maintained by the Center for X-Ray Optics (cxro.org).[43] This is the case in block copolymer electrolytes with known salt concentration, allowing calculation of a

relationship between X-ray absorption and salt concentration. With accurate absorption measurements, the salt concentration can be calculated; this will be used in Chapter 10.

To measure absorption, ion counters are placed immediately before ($I_0$, measuring incident radiation, $I_0$) and after ($I_1$, measuring both scattered and transmitted radiation due to the small scattering angle) the sample. The *X-ray* transmission is then simply $I_1/I_0$, and the absorption is one minus the transmission. However, this measures the absorption of not only the sample but also the air and sample windows; to account for this, a blank sample with the same setup but without polymer sample must be measured. In addition, the ion counters may not have the correct baseline, and so a "dark" scan must be acquired to offset the ion counters. The sample absorption is then:

$$\text{transmission} = \frac{I_1}{I_0} = \frac{\left(I_{1,\text{sample}} - I_{1,\text{dark}}\right) \Big/ \left(I_{0,\text{sample}} - I_{0,\text{dark}}\right)}{\left(I_{1,\text{blank}} - I_{1,\text{dark}}\right) \Big/ \left(I_{0,\text{blank}} - I_{0,\text{dark}}\right)}. \qquad (3.1)$$

In some cases, the sample holders may scatter X-rays, and it is desirable to remove these effects from the final scattering data. The data is in the form of a 2D image (see Section 3.1.2), so it is simple to subtract the scattering of one sample (the blank) from another (the sample data) pixel-by-pixel. However, in the sample data, the scattering that can be attributed to the sample holder is attenuated by the sample itself (Figure 3.2). This can be accounted for by instead subtracting the blank data multiplied by the transmission of the sample as calculated in Equation 3.1. Additionally, scattering at larger scattering angles, $\theta$, is attenuated more, as it passes through a larger depth of sample (see Figure 3.2). This can be corrected by multiplying an additional factor of $\sec(\theta)$, where $\theta$ must be calculated for each pixel, by the subtracted term. The secant of the largest scattering angle for which subtraction is performed in this work is 1.00003, so this correction is omitted, but it can become an important factor in wide-angle experiments.

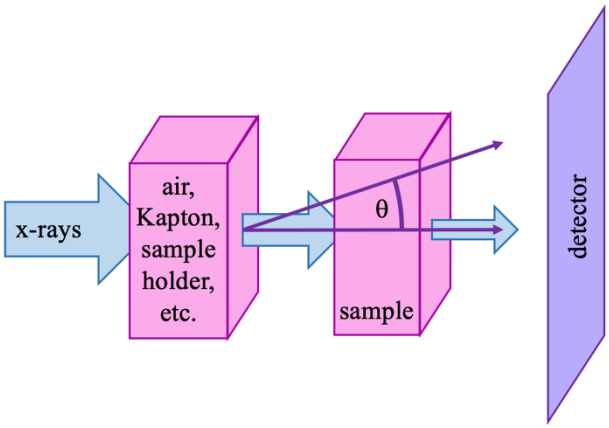


Figure 3.2. Illustration of the attenuation of the scattering signal of non-sample factors, such as air or sample holders, by the sample itself; this must be accounted for in subtracting the scattering signature. Signal at larger scattering angles passes through a larger depth of sample, and therefore is attenuated more than at small scattering angles.

### *3.1.2 X-Ray Scattering*

Scattering is directional. That is, if all grains are oriented along the *xy*-plane, scattering will be observed in the *z*-direction. If grains are oriented randomly, then the two-dimensional (2D) pattern observed on the detector will be isotropic, as depicted in Figure 3.3. Therefore, by examining different azimuthal angles (*i.e.*, different sectors of the 2D pattern), one can obtain morphological information about differently oriented grains. Often, when orientation effects are not of interest, the pattern is azimuthally averaged to obtain a one-dimensional curve.

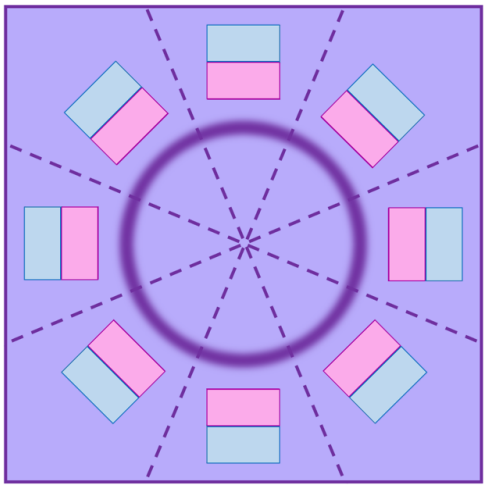

Figure 3.3. Illustration of a two-dimensional SAXS pattern divided into eight azimuthal sectors, with cartoons illustrating the orientation of a lamellar grain giving rise to scattering in that sector.

The scattering angle manifests in reciprocal space through a scattering vector $q$, defined as:

$$q = \frac{4\pi}{\lambda} \sin\left(\frac{\theta}{2}\right), \qquad (3.2)$$

with units of inverse nanometers. A 1D SAXS spectrum shows scattering intensity, $I$, as a function of $q$. Typically, the sample contains a microstructure—for example, the domains of a microphase-separated block copolymer—of some characteristic size, $d$. The X-ray scattering in this case is most intense at a critical $q$-value denoted $q^*$. The spacing, $d$, is related to $q^*$ through Bragg's law: [28]

$$d = \frac{2\pi}{q^*}. \qquad (3.3)$$

There are several block copolymer morphologies relevant to this work, and they are depicted in Figure 3.4. We will be using a polystyrene-*block*-poly(ethylene oxide) (PS-*b*-PEO or SEO) mixed with LiTFSI. The LiTFSI is preferentially solvated by the PEO, [24] resulting in a PEO-rich phase (pink) and a PEO/LiTFSI-rich phase (blue) when microphase separation occurs. The volume fraction of the PEO/LiTFSI phase is denoted $\phi_{EO/salt}$. When $\phi_{EO/salt}$ is near 0.5, a lamellar (LAM) morphology composed of alternating layers (Figure 3.4a) is formed. With increasing $\phi_{EO/salt}$, the morphology shifts to a PEO/LiTFSI matrix with hexagonally packed (HEX) PS cylinders (Figure 3.4b). Finally, at the highest vales of $\phi_{EO/salt}$, body-centered cubic (BCC) PS spheres within a PEO/LiTFSI matrix are formed (Figure 3.4c)

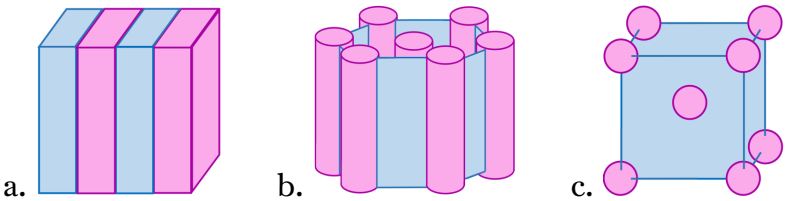


Figure 3.4. Cartoon of block copolymer morphologies relevant to this work: lamellar (LAM) (a); hexagonally packed cylindrical (HEX) (b); and body-centered cubic spherical (BCC) (c). Blue is the PEO/LiTFSI-rich phase, and pink is the PS-rich phase. The volume fraction of the PEO/LiTFSI phase (blue) increases from left to right.

Different morphologies can be distinguished by their scattering pattern. All will have a primary scattering peak, $q^*$, which can be related to the domain spacing using Equation 3.3. However, each will have additional peaks depending on the morphology (Table 3.1). A LAM sample will exhibit peaks at $q^*, 2q^*, 3q^*, 4q^*$, and so forth. A HEX sample will

exhibit peaks at $q^*, \sqrt{3}q^*, \sqrt{4}q^*, \sqrt{7}q^*$, and so forth. A BCC sample will exhibit peaks at $q^*, \sqrt{2}q^*, \sqrt{3}q^*, \sqrt{4}q^*$, and so forth. [44] For completeness, the gyroid morphology (GYR) is also included in Table 3.1, although it is not present in this work.

Table 3.1. Scattering peak locations for different block copolymer morphologies. [44]

| morphology | scattering peak locations |
|---|---|
| LAM | $q^*, 2q^*, 3q^*, 4q^*, 5q^*, 6q^*, \ldots$ |
| GYR | $q^*, \sqrt{\frac{4}{3}}q^*, \sqrt{\frac{7}{3}}q^*, \sqrt{\frac{8}{3}}q^*, \sqrt{\frac{10}{3}}q^*, \sqrt{\frac{11}{3}}q^* \ldots$ |
| HEX | $q^*, \sqrt{3}q^*, \sqrt{4}q^*, \sqrt{7}q^*, \sqrt{9}q^*, \sqrt{12}q^*, \ldots$ |
| BCC | $q^*, \sqrt{2}q^*, \sqrt{3}q^*, \sqrt{4}q^*, \sqrt{5}q^*, \sqrt{6}q^*, \ldots$ |

### *3.1.3 Sample Preparation*

Samples are prepared for SAXS measurements by melt-pressing polymer into a spacer with a thickness of 750 μm and an inner diameter of 3.18 mm. The spacer is then sandwiched between layers of X-ray (and visually) transparent Kapton windows and sealed in a custom-designed stainless steel sample holder to allow for air-free SAXS measurements (Figure 3.5). For calibration and subtraction purposes, silver behenate (AgB) and Kapton blank samples, respectively, are also prepared. At the beamline, samples are mounted into a controlled heating stage, also custom-built, for measurement.

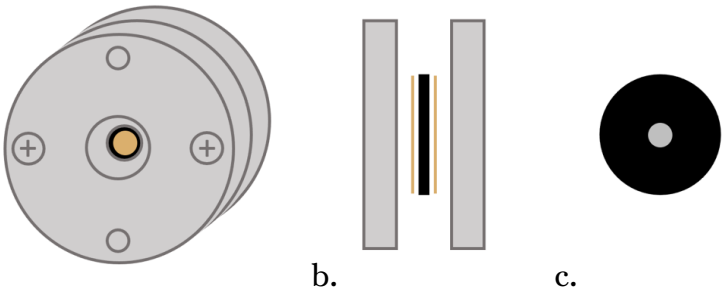

a. b. c.

Figure 3.5. Front (a) and side (b) views of SAXS sample holders comprised of a rubber spacer containing polymer sample (c) sandwiched between two transparent Kapton spacers and sealed in a stainless steel sample holder.

### *3.1.4 Temperature Calibration*

The setpoint of beamline stages does not necessarily correspond to the actual sample temperature. SAXS samples identical to those used for measurement were constructed with a thermocouple inserted to measure polymer temperature. Table 3.2 reports the actual temperature for various setpoints at beamline 7.3.3 at the ALS, beamline 1-5 at

SSRL, and the *in situ* SAXS heating stage that will be described in Section 3.2. It is clear that deviations from the desired temperature can be significant.

Table 3.2. Set *vs.* measured temperatures for the heating stages at beamline 7.3.3 at the ALS, beamline 1-5 at SSRL, and the *in situ* SAXS heating stage.

| setpoint (°C) | measured temperature at 7.3.3 (°C) | measured temperature at 1-5 (°C) | measured temperature for *in situ* stage (°C) |
|---|---|---|---|
| 40 | 37.5 | 39.6 | 38.6 |
| 50 | 46.9 | 49.9 | 48.3 |
| 60 | 56.3 | 60.3 | 57.6 |
| 70 | 65.7 | 70.6 | 67.1 |
| 80 | 75.1 | 80.9 | 76.3 |
| 90 | 84.5 | 91.2 | 86.3 |
| 100 | 93.9 | 101.5 | 95.8 |
| 110 | 103.3 | – | 105.3 |
| 120 | 112.7 | 122.1 | 114.8 |
| 130 | 122.1 | – | – |
| 140 | 131.5 | 142.8 | – |

From these data one can calculate what setpoint ($T_s$) should be chosen to achieve a desired temperature ($T_s$). Equations 3.4-3.6 show these relationships for beamline 7.3.3, beamline 1-5, and the *in situ* SAXS heating stage, respectively:

$$T_s = 1.06T_d + 0.07 \qquad (3.4)$$

$$T_s = 0.97T_d + 1.59 \qquad (3.5)$$

$$T_s = 1.05T_d - 0.90 \qquad (3.6)$$

For example, when using the *in situ* SAXS stage, the temperature should be set to 94 °C to achieve a sample temperature of 90 °C. Especially when comparing data acquired using multiple techniques on separate pieces of equipment, accurate temperature calibration and setting is essential.

### *3.1.5 Data Acquisition and Analysis*

Data are acquired using beamline software (beamline 7.3.3 at the Advanced Lightsource [ALS] at Lawrence Berkeley National Lab) and macros (at beamline 1–5 at the Stanford

Synchrotron Radiation Lightsource [SSRL] at SLAC National Accelerator Laboratory). The acquisition time, or the amount of time for which the sample is exposed to the beam, must be determined in order to maximize signal intensity without damaging the detector. Before the samples are heated, the scattering pattern for the AgB calibrant must be acquired at room temperature.

Simple data analysis can be performed using the Nika [45] macro in Igor Pro. The X-ray energy (and therefore wavelength) and detector pixel size are known for each beamline (for beamline 7.3.3 at the ALS, 10 keV and 0.172 mm × 0.172 mm, and for beamline 1-5 at SSRL, 12 keV and 0.079 mm × 0.079 mm). The AgB calibrant, which has a well-documented scattering pattern, can be used to determine the sample-to-detector distance and beam center position, correct for any rotation effects, and also to apply a mask to remove beamstop artifacts. Once the calibration parameters are known, Nika can be used to process 2D SAXS patterns, producing $I(q)$ curves by azimuthal or sector averaging; curve fitting can also be performed using Igor.

However, manually processing large numbers of scans can become cumbersome. The PyFAI [46] Python package is a useful tool for automating this process. After calibration similar to that described above, PyFAI functions can be incorporated into Python code to azimuthally or sector average large numbers of scans and perform peak fitting and further analysis. Sample code is provided in Appendix B.

## 3.2 *In Situ* SAXS Measurements

### *3.2.1 Motivation and Introduction*

During cycling of an electrochemical cell, if the transference number (see Chapter 4) is less than unity, a salt concentration gradient will develop, with salt accumulating near the positive electrode and becoming depleted near the negative electrode. With time, the salt concentration gradient will reach a steady-state or, if this is not possible, the cell will fail. Measurement of the salt concentration profile is therefore of significant interest in studying electrochemical performance, and while it can be predicted by theory (see Chapter 4), it is difficult to measure experimentally.

By acquiring SAXS scans at varying positions throughout the cell during *in situ* cell cycling, we can measure X-ray transmission and scattering as described above. The transmission measurements allow direct calculation of the local salt concentration within the beam profile, while the scattering data provide insight into morphology, orientation, and domain swelling and contraction during salt concentration changes. In general, we find that *in situ* SAXS scans of a given polymer electrolyte at a given salt concentration do not match equivalent *ex situ* measurements. This is because *ex situ* samples are equilibrated, while *in situ* measurements involve significant stresses and anisotropy due

to ion transport. Salt concentration, morphology, and domain spacing significantly impact ion transport in block copolymer electrolytes, [23] so it is important to have accurate conceptions of changes to these properties during cell cycling.

*3.2.2 Experimental Considerations*

Figure 3.6 depicts the custom-designed and machined poly(ether ether ketone) (PEEK) cells used for *in situ* SAXS measurement. The electrolyte (a) is between two stainless steel current collectors (b), each of which have lithium metal on the face that is in contact with the electrolyte. The cell thickness can be adjusted using the set screw (c); tightening the set screw during sample preparation also helps to ensure consistent melting throughout the electrolyte. Typical electrolyte thickness for these samples is approximately 1–1.5 mm. As built-in controls, two isolated sample holes are included. One contains the same electrolyte being studied (d), so that *in situ* and *ex situ* measurements can be done in parallel, and any shifts in sample-to-detector distance during the experiment can be corrected. Another contains no sample (e), which serves as the "blank" measurement needed for transmission calculations. Finally, the two halves of the cell are sealed with a rubber o-ring (f), screwed together (g), and sealed in pouch material. The beam is oriented normal to the face of the cell, and so shifting the samples spatially allows us to probe different positions between the two electrodes.

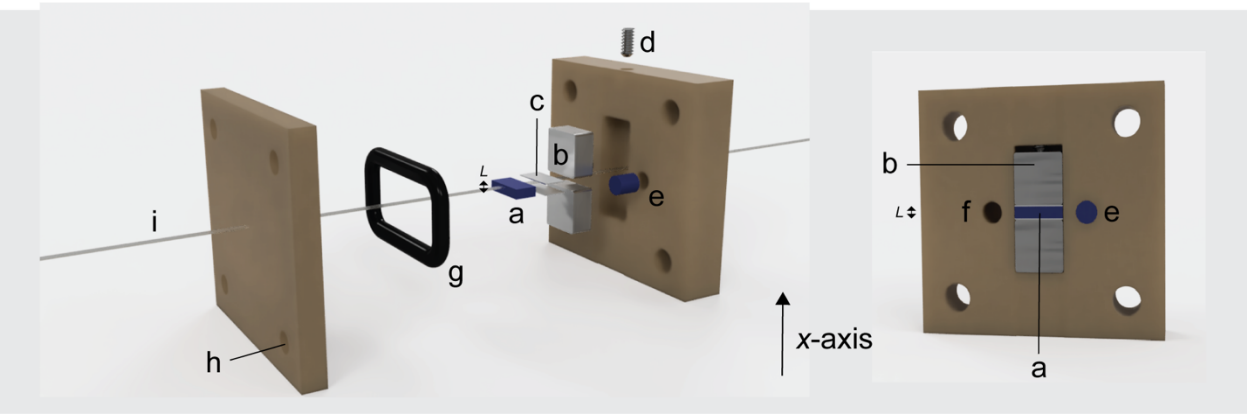


Figure 3.6. Schematic of *in situ* SAXS cell, side and front views. The electrolyte (a) is compressed between two stainless steel blocks (b). The lithium metal electrodes (c) are at the a / b boundaries. The electrolyte thickness, *L*, is controlled using a set screw (d). A reference (e) and a blank slot (f) are built in. The two halves of the cell are sealed with a rubber o-ring (g) and screwed together (h) before being sealed in pouch material. The X-ray beam (i) is shown to scale. The cell is constructed using PEEK.

Measuring the blank repeatedly through cycling experiments allows any drift in beam intensity and other factors to be compensated; for similar reasons, dark scans with no beam applied should be acquired regularly in order to account for any changes in the performance of the ion counters. The blank scans can also be transmission-corrected and

subtracted from the sample scans to remove any scattering from PEEK; see Section 3.1.1 for the mathematical details of transmission calculations.

We have observed that the scattering due to the pouch material changes with time at high temperatures. Therefore, the pouch material should be annealed prior to cell assembly so that the scattering from the pouch material is intransient during the experiments.

Because these samples contain lithium metal, it is important that all sample holder pieces be dry and solvent-free. PEEK absorbs water, so the PEEK cell components must be dried overnight at 120 °C before cell assembly.

In addition to these sample preparation considerations, *in situ* experiments pose challenges not encountered in *ex situ* SAXS experiments. Because we acquire scans constantly for time periods on the order of hours to days, the amount of data generated is large. It becomes essential to automate the data processing using tools like PyFAI, as described above. Sample Python analysis code is provided in Appendix B.

The long timescales of the experiments also result in the amplification of artifacts that are negligible in short *ex situ* experiments. For example, slow drifts in the beam center can accumulate over time and result in significant distortion of the data. It is useful to acquire calibration scans at time intervals throughout the experiment so that these effects can be mitigated. Periodic beam and slit re-alignment also reduce these effects.

Finally, the acquisition time must be carefully considered. Longer acquisition times result in higher SAXS signal, which can facilitate detection of higher order peaks, which is essential in analyzing non-lamellar block copolymers (Chapter 10). However, longer acquisition times also reduce temporal resolution, which is unfortunate when the goal is to observe changes with time. They can also increase the risk of beam damage due to repeated exposure to the X-ray radiation; it is advisable to dis-assemble cells in the glovebox after cycling and confirm that no white spots indicating possible beam damage are present. One solution is to use short acquisition times to increase temporal resolution and intersperse scans with longer acquisition times to ensure detection of higher-order peaks for accurate morphological characterization.

# Chapter 4: Electrochemical Characterization

## 4.1 Parameters of Interest

All electrolytes studied in this work contain a neutral polymer or solvent and a lithium salt, which dissociates into lithium cations and an anion; our most commonly-used salt, lithium bis(trifluoromethanesulfonyl)imide salt (LiTFSI), dissociates into $Li^+$ cations and $TFSI^-$ anions. In an electrochemical cell with a lithium anode, electrode reactions involving lithium will result in the passage of ionic current.

### *4.1.1 Limiting Current and Salt Concentration Gradients*

One important metric for electrolyte performance is the limiting current, $i_{lim}$, defined as the maximum current that can be stably accommodated by the cell. A higher limiting current corresponds to faster cell charging, a desirable property for practical applications. During cell polarization, a salt concentration gradient develops (Figure 4.1).[47] Initially, the salt concentration is constant throughout the cell. Upon the application of an electric current or potential, the cation migrates towards the anode while the anion migrates towards the cathode (Figure 4.1a). The anion cannot react, so it must accumulate at the cathode side, and charge neutrality dictates that the anion and cation concentration must be equal. This results in the development of a salt concentration gradient throughout the cell. At steady state (Figure 4.1b), the migration and diffusion of the anion are balanced, resulting in no net anion motion. For the cation, migration and diffusion both occur in the same direction. However, its concentration remains constant with time as it is consumed (plated, in the case of lithium metal electrodes, or intercalated, in the case of composite electrodes) at the anode and generated (stripped or deintercalated) at the cathode. At constant applied current, the corresponding potential increases until it plateaus as the steady-state concentration gradient is reached. If a steady-state concentration gradient cannot be reached, the potential will continue to increase until it diverges; the limiting current is defined as the current above which a steady-state cannot be reached.

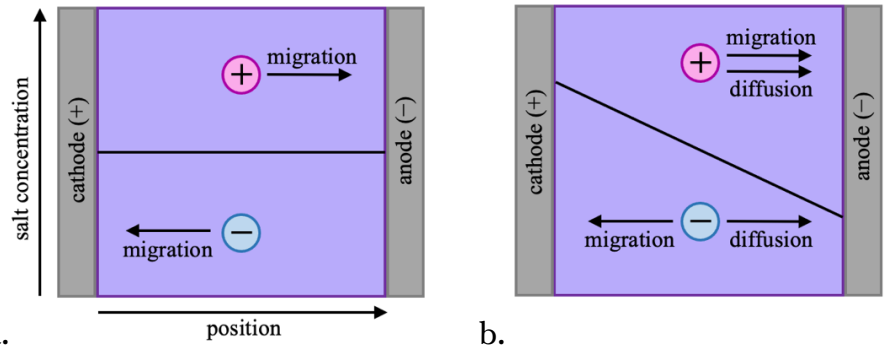


Figure 4.1. Illustration of a cell at the beginning of cell charging, when the salt

concentration is constant (a), and after the development of a steady-state salt concentration gradient (b). At steady-state, anion migration and diffusion are of equal magnitude, resulting in no net anion flux.

There are multiple possible reasons that this might occur. The most commonly-proposed reason is that the salt concentration reaches zero at the anode, preventing further lithium plating or intercalation. [48] Another more recently proposed mechanism is that if the salt concentration reaches the solubility limit at the cathode, it is impossible to dissolve more salt into the electrolyte via stripping or deintercalation. [49] These high salt concentration effects will be explored in PEO/LiTFSI in Chapter 5. However, there may be additional mechanisms; for example, the strain induced by forcing additional salt into pre-established block copolymer grains may limit increases in salt concentration despite the salt concentration being significantly less than the solubility limit and greater than zero. This will be explored in Chapters 9-11. Understanding the salt concentration gradient is critical to understanding limiting current behavior. It is not directly measurable electrochemically—hence the exploration of *in situ* X-ray techniques in Chapters 9-11—but it can be modeled if other electrochemical parameters have been measured.

### *4.1.2 Transport and Thermodynamic Parameters*

In order to model salt concentration gradients, and thereby gain insight into the limiting current, one must measure three transport parameters—ionic conductivity, $\kappa$, transference number, $t_+^0$, and salt diffusion coefficient, $D$—and the thermodynamic factor, $T_f = 1 + \frac{d\ln \gamma_\pm}{d\ln m}$. $D$ and $\kappa$ can be measured directly, while $t_+^0$ and $T_f$ are calculated based on the values of $D$, $\kappa$, the current fraction, $\rho_+$, and $\frac{dU}{d\ln m}$, where $U$ is the open circuit potential of a concentration cell, as described below, and $m$ is the molal salt concentration. [29]

The ionic conductivity, $\kappa$, measures the electrolyte's tendency towards transporting charge. Intuitively, one might believe that this would directly control charging rate and electrolyte performance; for this reason, and because of the ease of measurement, researchers tend to focus on conductivity in improving electrolytes. However, both cation and anion motion can contribute to the ionic conductivity, while only the cation is electrochemically active.

The transference number, $t_+^0$, describes the fraction of charge carried by the cation before concentration gradient development, with all ion motion relative to the solvent. Due to the electrochemical inactivity of the anion, ideally all charge would be carried by the cation, resulting in $t_+^0 = 1$. In this case, the anion is immobile—for example using a single-ion conductor in which the anion is covalently bonded to the polymer chain [22]—and therefore no concentration gradient is established. In practical systems, a wide range of transference numbers, including negative values, have been reported. [25,50]

A related parameter is the current fraction, $\rho_+$, which measures the ratio of the steady-state current under polarization to the initial current measured before salt concentration gradients are established. [51] This value has often been reported as the "transference number," based on the idea that the steady-state accounts for only motion of the cation, as there is no net anion motion, while the initial current includes contributions from both, and that therefore the ratio of the two currents is the fraction of charge carried by the cation. However, the cation velocity is not the same at steady-state as it is initially, so this logic is flawed. Nevertheless, while the current fraction is not a transference number, it still has important implications for understanding ion transport. [52]

The diffusion coefficient, $D$, also known as the mutual diffusion coefficient, relates the flux of the salt to the concentration gradient, *i.e.*, how quickly salt will diffuse down a concentration gradient. The thermodynamic factor, $T_\mathrm{f} = 1 + \frac{d\ln \gamma_\pm}{d\ln m}$, quantifies the dependence of the mean molal activity coefficient, $\gamma_\pm$, on the salt concentration. In a thermodynamically ideal electrolyte, $\gamma_\pm$ would be independent of salt concentration, and therefore $T_\mathrm{f}$ would be unity. With increasing salt concentrations, polymer electrolytes deviate significantly from ideality, [53] with $T_\mathrm{f}$ approaching 100 in extreme cases; this will be explored in Chapter 6.

### *4.1.3 Stefan-Maxwell Diffusion Coefficients*

The parameters described above provide valuable insight into macroscale ion transport, but on their own do little to elucidate the molecular interactions underpinning macroscale properties. Stefan-Maxwell diffusion coefficients, denoted $\mathfrak{D}_{ij}$, quantify the inverse frictional interactions between species $i$ and $j$. For an electrolyte composed of a solvent and a binary salt, there exist three such diffusion coefficients: $\mathfrak{D}_{0+}$ quantifies solvent-cation interactions, $\mathfrak{D}_{0-}$ quantifies solvent-anion interactions, and $\mathfrak{D}_{+-}$ quantifies cation-anion interactions. [29,54] For example, a small $\mathfrak{D}_{+-}$ indicates significant cation-anion frictional interactions. Stefan-Maxwell diffusion coefficients can be calculated from the aforementioned properties without additional measurements, and are used extensively in Chapter 5.

## 4.2 Measurement Techniques

### *4.2.1 Cell Assembly*

Three major types of cells are used in measuring electrochemical parameters. The first is a blocking electrode cell (Figure 4.2) used for conductivity measurements. In an argon glovebox, electrolyte is pressed into an annular spacer, sandwiched between stainless steel electrodes that are connected to nickel current collectors, and then sealed in an air-free pouch. When assembling the cells, it is important to ensure that the electrolyte is as

homogeneous as possible; however, accurate knowledge of the electrolyte dimensions (thickness, $L$, and area, $A$, of electrode contact) is also essential. Therefore, one must avoid excessive compression that may distort the spacer, and measure cell thickness after assembly. Because stainless steel is incompressible, it is best to measure the thickness of the electrode between electrodes and then subtract the known electrode thickness. Note that for liquid electrolytes, blocking electrode cells are not needed, as ionic conductivity can be measured using a conductivity probe (see Chapter 5).

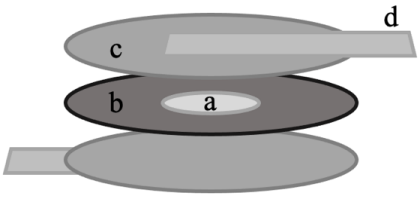


Figure 4.2. Schematic of a blocking electrode cell consisting of polymer electrolyte (a) in an annular spacer (b) sandwiched between stainless steel electrodes (c) and connected to electrochemical control via nickel current collectors (d). Air-free pouch is not shown.

Lithium symmetric cells are used for a wide range of electrochemical experiments. They are similar in geometry to blocking electrode cells, except that lithium metal electrodes are used. Lithium is very sensitive to air and water and therefore must be kept carefully isolated in an argon glovebox and brushed and pressed before use as an electrode. It should be uniformly shiny before use; white or black spots indicate reacted lithium. All cell pieces should be thoroughly cleaned and dried before contact with lithium metal. As with blocking electrode cells, accurate thickness and area information is needed. However, lithium is malleable and therefore not necessarily of known thickness. It is best to measure electrolyte thickness after it is pressed into the spacer material and before electrodes are added. These cells should be disassembled after use to check for changes in the appearance of the lithium, which may indicate undesired reactions or dendrite growth.

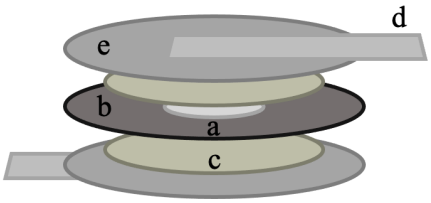


Figure 4.3. Schematic of a blocking electrode cell consisting of polymer electrolyte (a) in an annular spacer (b) sandwiched between lithium electrodes (c) and connected to electrochemical control via nickel current collectors (d), sometimes via stainless steel for convenience (e). Air-free pouch is not shown.

Finally, concentration cells are used to measure $\frac{dU}{d\ln m}$, which in turn is used to calculate other parameters, including $t_+^0$, $T_f$, and Stefan-Maxwell diffusion coefficients. A schematic

of a concentration cell is shown in Figure 4.4. The electrolyte of interest is pressed into one half of the spacer, while a reference electrolyte composed of the same polymer and salt but at a reference concentration is pressed into the other half. By convention, $r = 0.06$ is used as the reference concentration, but any concentration could be used provided it is kept constant across experiments. Lithium metal is attached to each electrolyte, connected to nickel current collectors, and the cell is sealed in an air-free pouch. For these experiments, electrolyte thickness and area and the fraction of the spacer occupied by each electrolyte do not impact the results. Instead, consistent contact must be maintained between the two electrolytes and between each electrolyte and the lithium electrode, and sufficient space (typically approximately 0.5 – 1 cm) must be left between the lithium electrodes and the electrolyte-electrolyte interface.

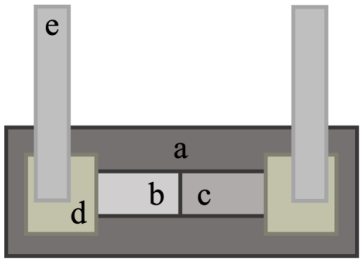


Figure 4.4. Schematic of a concentration cell. Spacer material (a) contains the electrolyte of interest (b) against a reference electrolyte composed of the same electrolyte at a reference salt concentration, typically $r = 0.06$ (c). Lithium metal (d) contacts both electrolytes and is connected to electrochemical control via nickel current collectors (e). Air-free pouch is not shown.

*4.2.2 Electrochemical Experiments*

All electrochemical experiments are performed on a BioLogic VMP3 potentiostat.

Blocking electrode cells are analyzed using alternating current (ac) impedance spectroscopy, typically with an amplitude of 80 mV and a frequency range of 1 MHz to 100 mHz and at least three points per frequency. Nyquist plots of the imaginary *vs.* real components of impedance ($Z_{Re}$ and $Z_{Im}$) are generated; an example showing typical behavior for polymer electrolyte blocking electrode cells, including the semicircle corresponding to bulk resistance at low frequencies and capacitive tail at high frequencies, is shown in Figure 4.5a. The data are fit to the equivalent circuit shown in Figure 4.5b, corresponding to Equation 4.1, to extract the bulk resistance, $R_b$. In Equation 5.1, $Z$ is the impedance, $R_{eq}$ and $L_{eq}$ are the resistance and inductance of the potentiostat equipment, $Q_b$ is the bulk capacitance, and $R_b$ is the bulk resistance.

$$Z = R_{eq} + L_{eq} + \frac{Q_b}{R_b} \qquad (5.1)$$

Cells must be allowed to equilibrate on the heating stage before analysis; Chapter 6 explores the effects of annealing time on conductivity measurements in block copolymer electrolytes. From the bulk resistance, the ionic conductivity, $\kappa$, can be calculated according to

$$\kappa = \frac{L}{R_b A}, \qquad (5.2)$$

where $L$ is the distance between the electrodes, $A$ is the area of electrode-electrolyte contact, and $R_b$ is the bulk resistance.

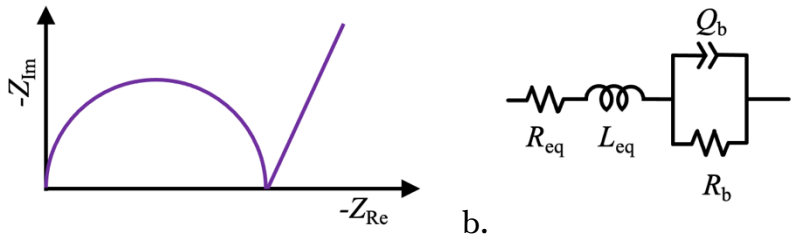


Figure 4.5. Illustration of a typical Nyquist plot, showing the imaginary *vs.* real components of complex impedance, generated using ac impedance spectroscopy of a polymer electrolyte cell with blocking electrodes (a) and corresponding equivalent circuit used for fitting resistance (b). $R_{eq}$ and $L_{eq}$ are the resistance and inductance of the potentiostat equipment, $Q_b$ is the bulk capacitance, and $R_b$ is the bulk resistance.

A wide variety of experiments are performed using lithium symmetric cells. However, the first step must be pre-conditioning, in which small amounts of current, usually approximately 20 mA/cm$^2$, are passed through the cell in order to stabilize the electrode-electrolyte interface. One conditioning cycle consists of passing current until the potential stabilizes, allowing the cell to relax at open circuit voltage (OCV), passing current in the opposite direction until the potential stabilizes, and again allowing the cell to relax. Conditioning cycles are repeated until the impedance stabilizes, for at least three cycles.

The same ac impedance experiment is performed on lithium symmetric cells as on blocking electrode cells, and an Nyquist plot showing typical results for a polymer electrolyte, with the first semicircle corresponding to bulk resistance and the second semicircle corresponding to interfacial resistance, is illustrated in Figure 4.6a. The equivalent circuit used for lithium symmetric cells is shown in Figure 4.6b, and the fit equation is given in Equation 4.3,

$$Z = R_{eq} + L_{eq} + \frac{Q_i}{R_i} + \frac{Q_b}{R_b}, \qquad (4.3)$$

where $Q_i$ and $R_i$ are the interfacial capacitance and resistance. In principle, $\kappa$ could be calculated using $R_b$ from lithium symmetric cells, removing the need for blocking electrode cells. However, lithium cells introduce interfacial effects and additional difficulty in accurate thickness measurements, so blocking electrode cells provide more accurate conductivity measurements.[52] Interfacial resistance should be monitored carefully during experiments; large increases in $R_i$ can indicate undesired reactions at the electrodes. The total cell resistance, $R_T$, is the sum of $R_b$ and $R_i$.

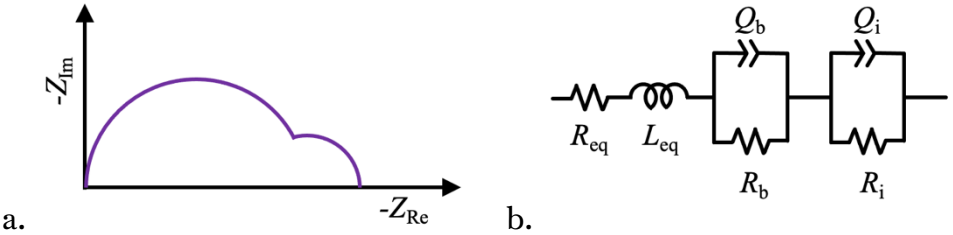


Figure 4.6. Illustration of a typical Nyquist plot, showing the imaginary vs real components of complex impedance, generated using using ac impedance spectroscopy of a polymer electrolyte cell with lithium electrodes (a) and corresponding equivalent circuit used for fitting resistance (b). $R_{eq}$ and $L_{eq}$ are the resistance and inductance of the potentiostat equipment, $Q_b$ and $R_b$ are the bulk capacitance and resistance, and $Q_i$ and $R_i$ are the interfacial capacitance and resistance.

Two parameters, the current fraction, $\rho_+$, and salt diffusion coefficient, $D$, can be extracted from a single experiment using a lithium symmetric cell. First, a small potential—typically the experiment is repeated with potentials, $\Delta V$, of 10, -10, 20, and -20 mV—is applied while measuring the ionic current and periodic impedance experiments. Upon application of the potential, the current immediately sharply increases, and then decreases before stabilizing at a steady-state value, $i_{ss}$ (Figure 4.7).

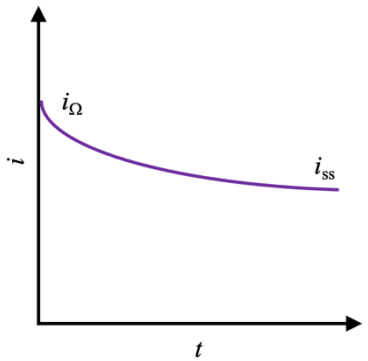


Figure 4.7. Illustration of typical *i vs.* time results from the constant potential experiment used to calculate the current fraction, $\rho_+$, in a lithium symmetric cell.

After the current stabilizes, the current fraction can be calculated according to Equation 4.4,

$$\rho_+ = \frac{i_{ss}\left(\Delta V - i_\Omega R_{i,0} A\right)}{i_\Omega\left(\Delta V - i_{ss} R_{i,ss} A\right)}, \qquad (4.4)$$

where $i_{ss}$ is the steady-state current, $\Delta V$ is the applied potential, $R_{i,0}$ is the initial interfacial resistance, $R_{i,ss}$ is the interfacial resistance at steady-state, and $A$ is the electrode area,. The initial current according to Ohm's law, [52] $i_\Omega$ is calculated according to Equation 4.5,

$$i_\Omega = \frac{\Delta V}{\frac{L}{\kappa} + R_{i,0} A}, \qquad (4.5)$$

where all variables are as defined above, and $L$ is the electrolyte thickness and $\kappa$ is the ionic conductivity measured using blocking electrodes. This method was first pioneered by Bruce and Vincent, [55] who reported $t_+ = \frac{i_{ss}}{i_0}$; additional corrections have been applied with time, and the result has come to represent the current fraction as opposed to a transference number. [52]

The application of this potential results in the generation of a salt concentration gradient; to measure the salt diffusion coefficient, $D$, via the restricted diffusion measurement, the open circuit potential, $U$, is measured while the cell is allowed to relax. [56] The potential is then fit to Equation 4.6,

$$-\frac{d\ln U}{dt} = \frac{\pi^2 D}{L^2}, \qquad (4.6)$$

to extract the diffusion coefficient. Typically, the first several minutes of relaxation are excluded to allow time for the discharging of the electric double layer, and the first 2 hours of relaxation after that point are fit to Equation 4.6; [25] in this region, the relationship between $lnU$ and $t$ is linear (Figure 4.8).

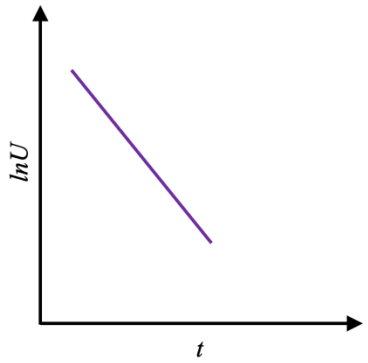


Figure 4.8. Illustration of typical *lnU vs.* time results from the relaxation experiment used to measure the salt restricted diffusion coefficient, *D*, in a lithium symmetric cell.

The limiting current can also be measured using lithium symmetric cells. In this experiment, a constant current is applied while the potential is monitored. Below the limiting current, the potential reaches a steady-state (the current is accessible), while above the limiting current, the potential diverges (the current is inaccessible). The limiting current is typically defined as the average of the highest accessible current and the lowest inaccessible current. [48] Figure 4.9 illustrates typical potential profiles at constant current above and below the limiting current.

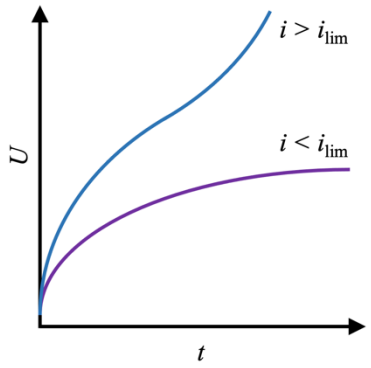


Figure 4.9. Illustration of typical potential *vs.* time results from the constant-current experiment used to measure the limiting current, $i_{lim}$, in a lithium symmetric cell. Below the limiting current (purple), the potential stabilizes over time, while above the limiting current (blue), the potential diverges.

The same cell can be used for multiple current experiments. It is important to allow the cell potential to fully relax before applying another current, and each current should be applied in the opposite direction from the last. Eventually, the repeated application of high currents can damage the electrode; growing interfacial resistances may indicate deleterious reactions at the electrode-electrolyte interface, while jagged potential measurements or a decrease in bulk resistance (indicating a possible decrease in effective

cell thickness), may be signs of dendrite growth. In either case, no further experiments should be run on the cell.

Finally, to extract $\frac{dU}{d\ln m}$, the open circuit voltage of concentration cells[54] is measured for at least 24 hours; an illustration of typical results is shown in Figure 4.10. Often, the potential is unpredictable during thermal and interfacial equilibration, then the potential is stable for at least several hours as the electrolytes mix, before eventually trending towards zero as the region of electrolyte mixing begins to reach the electrodes. Concentration cells are analyzed for several salt concentrations relative to the same reference salt concentration, typically $r = 0.06$; when the analyzed salt concentration is equal to the reference, the potential is zero. The potential is plotted *vs.* the log of the molal salt concentration, $m$, fit to a functional form, usually a power law, and the derivative is calculated as a function of $m$. The published relationship between $U$ and $m$ for PEO/LiTFSI at low salt concentration is

$$U = 100 - 74.9m^{0.84}, \qquad (4.7)$$

Where $U$ is units of millivolts, mV. See Chapter 6 for a discussion of this parameter at high salt concentrations approaching the salt solubility limit.

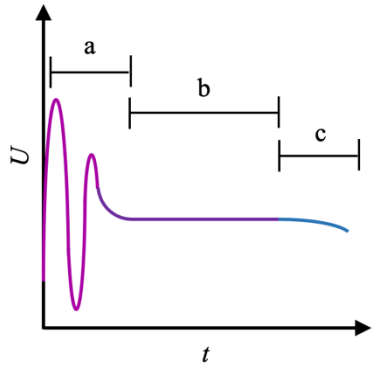


Figure 4.10. Illustration of typical potential *vs.* time results for a concentration cell. The potential is unstable initially during equilibration of the interfaces (a), then stable for a period of time (b), before decreasing towards zero as the region of electrolyte mixing reaches the electrodes (c).

## 4.3 Concentrated Solution Theory

### *4.3.1 Calculated Parameters*

As described in Section 4.2.2, the ionic conductivity, $\kappa$, the current fraction, $\rho_+$, the salt diffusion coefficient, $D$, and $\frac{dU}{d\ln m}$ can be measured directly from experimental data. Further parameters of interest, namely the transference number relative to the solvent velocity, $t_+^0$,

the thermodynamic factor, $T_f$, and Stefan-Maxwell diffusion coefficients, can be calculated based on these measured parameters using John Newman's concentrated solution theory.[29]

The transference number can be calculated according to Equation 4.8,

$$t_+^0 = 1 + \left(\frac{1}{\rho_+} - 1\right)\frac{z_+ \upsilon_+ FDc\phi_c}{\kappa}\left(\frac{dU}{d\ln m}\right)^{-1}, \qquad (4.8)$$

where $z_+$ is the charge of the cation, $\nu_+$ is the number of cations in the dissociated salt (both are equal to one for all salts in this study), $F$ is Faraday's constant (96,485 C/mol), $c$ is the molar salt concentration in the conducting phase (or the overall molar salt concentration in a one-phase system), and $\phi_c$ is the volume fraction of the conducting phase (one in a one-phase system).

In polystyrene-*block*-poly(ethylene oxide) (PS-*b*-PEO or SEO) electrolytes with a molar salt concentration of LiTFSI of $r$ lithium ions per ethylene oxide moiety, $\phi_c$ can be calculated according to Equation 4.9

$$\phi_c = \frac{v_c}{v_c + \frac{M_{PS}M_{EO}}{M_S M_{PEO}} v_S}, \qquad (4.9)$$

where $M_{PS}$ and $M_{PEO}$ are the molecular weights of the PS and PEO, respectively, blocks of the block copolymer, $M_S$ is the molar mass of the styrene repeat unit (104.1 g/mol), $M_{EO}$ is the molar mass of the ethylene oxide repeat unit (44.05 g/mol), $v_S$ is the molar volume of styrene (0.167 nm$^3$), and $v_c$ is the molar volume of the conducting (PEO/LiTFSI) phase,

$$v_c = \frac{M_{EO} + rM_{LiTFSI}}{\rho_c(r)}, \qquad (4.10)$$

where $M_{LiTFSI}$ is the molecular weight of LiTFSI (287.075 g/mol), and $\rho_c(r)$ is the density of PEO/LiTFSI mixtures as a function of $r$, which can be fit as

$$\rho_c = 1.714r + 1.161, \qquad (4.11)$$

where $\rho_c$ is in units of g/mL, using data published in the literature.[25] The molar salt concentration in the conducting phase, $c$, is equal to $1/v_c$.

Using the transference number, $t_+^0$, the thermodynamic factor can now be calculated: [29]

$$T_f = 1 + \frac{d\ln\gamma_\pm}{d\ln m} = -\frac{z_+\nu_+}{(\nu_+ + \nu_-)}\frac{F}{2RT(1-t_+^0)}\left(\frac{dU}{d\ln m}\right), \qquad (4.12)$$

where $\gamma_\pm$ is the mean molal activity coefficient, $m$ is the molal salt concentration, $z_+$ is the charge of the cation, $\nu_+$ and $\nu_-$ are the number of cations and anions, respectively, into which the salt dissociates, $F$ is Faraday's constant (96,485 C/mol), $R$ is the ideal gas constant (8.3145 J/mol K), $T$ is the absolute temperature, and $t_+^0$ and $\frac{dU}{d\ln m}$ have been calculated.

To calculate the Stefan-Maxwell diffusion coefficients, it is useful to first calculate $\mathfrak{D}$, the diffusion coefficient based on a thermodynamic driving force: [29]

$$D = \mathfrak{D}\frac{c_T}{c_0}\left(1 + \frac{\mathrm{d}\ln\gamma_\pm}{\mathrm{d}\ln m}\right), \qquad (4.13)$$

where $c_0$ is the solvent concentration, $c_T$ is the total concentration ($c_T = c_0 + 2c$, where $c$ is the salt concentration, for univalent salts), and the thermodynamic factor has been calculated previously. Then, the Stefan-Maxwell diffusion coefficients are: [29,50]

$$\mathfrak{D}_{0+} = \frac{-z_-}{z_+ - z_-}\frac{\mathfrak{D}}{1 - t_+^0}, \qquad (4.14)$$

$$\mathfrak{D}_{0-} = \frac{z_+}{z_+ - z_-}\frac{\mathfrak{D}}{t_+^0}, \qquad (4.15)$$

$$\text{and } \mathfrak{D}_{+-} = \left(\frac{-z_+z_-c_TF^2}{\kappa RT} - \frac{z_+ - z_-}{z_+\nu_+}\frac{c_0t_+^0(1 - t_+^0)}{c\mathfrak{D}}\right)^{-1}, \qquad (4.16)$$

where $z_-$ is the charge of the anion (-1 for LiTFSI) and all other terms have been defined previously. These coefficients, representing inter-species frictional interactions, will be discussed in detail in Chapter 5. Notably, the Stefan-Maxwell diffusion coefficients can also be related to the transference number according to: [29]

$$t_+^0 = \frac{z_+\mathfrak{D}_{0+}}{z_+\mathfrak{D}_{0+} - z_-\mathfrak{D}_{0-}}. \qquad (4.17)$$

*4.3.2 Modeling of Salt Concentration Gradients*

Newman's concentrated solution theory [29] can be used to model the steady-state salt concentration gradient in electrolytes ($r(x/L)$, where $r$ is the molar salt concentration, $x$ is the position in the cell, and $L$ is the cell thickness, such that $x/L$ ranges between zero and one) as a function of the applied current density, $i$, provided that the aforementioned parameters have been calculated.

The method, the details of which are provided elsewhere, [10,47,57] uses Equation 4.18 to calculate $r(x/L)$ based on $r(x/L = 0)$:

$$\int_{r\left(\frac{x}{L}=0\right)}^{r\left(\frac{x}{L}\right)} J_1(r)\,\mathrm{d}r = -\frac{iL}{F}\left(\frac{x}{L}\right), \qquad (4.18)$$

where

$$J_1(r) = \kappa\left(\frac{\mathrm{d}U}{\mathrm{dln}m}\right)\left[r\left(1-\frac{1}{\rho_+}\right)z_+\nu_+F\phi_c\right]^{-1}. \qquad (4.19)$$

$J_1(r)$ can be fit to a functional form based on previously-measured parameters as a function of $r$. For SEO/LiTFSI electrolytes, $\frac{\mathrm{d}U}{\mathrm{dln}m}(r)$ and $\rho_+(\mathrm{r})$ do not depend on polymer molecular weight or composition, [23] so for a new SEO polymer, only $\kappa$ must be measured, and $\phi_c$ calculated, to enable fitting of $J_1(r)$. Then, for a given current, $i$, a salt concentration at $x/L = 0$, $r(x/L = 0)$, is assumed, and Equation 4.18 is used to calculate $r(x/L)$ for all values of $x$, thus generating a salt concentration profile. This salt concentration profile can then be integrated to obtain the average salt concentration. If this is not equal to the known initial salt concentration, the guess for $r(x/L)$ is modified, and the process is completed until the salt concentration converges.

This method calculates the steady-state salt concentration gradient. The theory can be extended to model transient salt concentration gradients and species velocities. This is a powerful tool, and is applied in Chapter 10 in comparison with measured transient salt concentration gradients, but the computational techniques involved are outside the scope of this Dissertation; more detail can be found in references from computational collaborators. [58,59]

*4.3.3 Predictions of the Limiting Current*

As the applied current increases, the steady-state salt concentration gradient becomes steeper, with salt concentration decreasing at the negative electrode and increasing at the positive electrode (see Section 4.1.1). Traditionally, it has been assumed that the limiting

current is reached when the salt concentration reaches zero at the negative electrode, at which point further lithium plating / intercalation cannot occur and current cannot be passed. [29] Therefore, the limiting current is expected to increase with increasing salt concentration. Using this assumption, the salt concentration gradient can be calculated using the method described in Section 4.3.2, with increasing applied current densities until the salt concentration is calculated to reach zero at the negative electrode. At low salt concentrations, such predictions often agree well with measured limiting current densities. [10,47,57]

However, at high salt concentrations, the limiting current is found to decrease, a phenomenon not predicted by this model. It has been extended to account for the fact that if the salt concentration reaches the solubility limit at the positively charged electrode, further lithium stripping / deintercalation cannot occur, and current also cannot be passed. [49] With this addition, the theory predicts that limiting current increases with increasing salt concentration at low salt concentrations, where the mechanism for cell failure is the salt concentration reaching zero at the negative electrode, and decreases with increasing salt concentration at high salt concentrations, where the mechanism for cell failure is the salt concentration reaching the salt solubility limit at the positive electrode.

This model accounts for electrochemical factors contributing to the limiting current, and has been shown to accurately predict experimental values in some practical systems. [49,57] However, there may be non-electrochemical factors. For example, if block copolymer grains are equilibrated at one salt concentration, there may be a limit to the degree or rate of expansion or contraction of domains to accommodate changing salt concentration, even if it is between zero and the equilibrium solubility limit. This will be explored in Chapters 9-11.

# Chapter 5: Impact of Frictional Interactions on Conductivity, Diffusion, and Transference Number in Ether- and Perfluoroether-based Electrolytes*

## 5.1 Abstract

There is growing interest in fluorinated electrolytes due to their high-voltage stability. We use full electrochemical characterization based on concentrated solution theory to investigate the underpinnings of conductivity and transference number in tetraglyme/LiTFSI mixtures (H4) and a fluorinated analog, C8-DMC, mixed with LiFSI (F4). Conductivity is significantly lower in F4 than in H4, and F4 exhibits negative cation transference numbers, while that of H4 is positive at most salt concentrations. By relating Stefan-Maxwell diffusion coefficients, which quantify ion-solvent and cation-anion frictional interactions, to conductivity and transference number, we determine that at high salt concentrations, the origin of differences in transference number is differences in anion-solvent interactions. We also define new Nernst-Einstein-like equations relating conductivity to Stefan-Maxwell diffusion coefficients. In H4 at moderate to high salt concentrations, we find that all molecular interactions must be included. However, we demonstrate another regime, in which conductivity is controlled by cation-anion interactions. The applicability of this assumption is quantified by a pre-factor, $\beta_{+-}$, which is similar to the "ionicity" pre-factor that is often included in the Nernst-Einstein equation. In F4, $\beta_{+-}$ is unity at all salt concentrations, indicating that ionic conductivity is entirely controlled by the Stefan-Maxwell diffusion coefficient quantifying cation-anion frictional interactions.

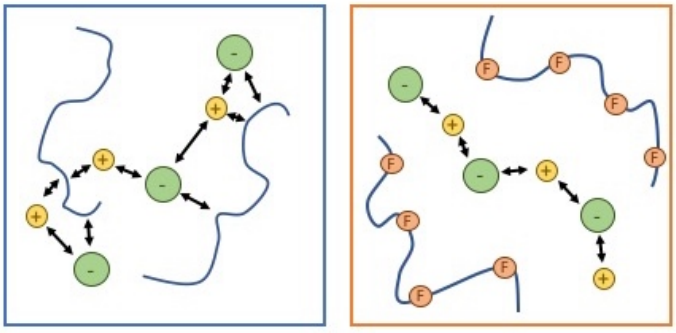


Figure 5.1. Cartoon illustrating the differences in interactions controlling conductivity in tetraglyme/LiTFSI (left) and the fluorinated C8-DMC/LiFSI system (right).

---

* This Chapter is adapted from Grundy, L. S.; Shah, D. B.; Nguyen, H. Q. *et al.* Impact of Frictional Interactions on Conductivity, Diffusion, and Transference Number in Ether and Perfluoroether-Based Electrolytes. *J. Electrochem. Soc.* **2020**, *167* (12), 120540. [230]

## 5.2 Introduction

The electrolyte used in current lithium-ion batteries is a mixture of ethylene carbonate (EC) and dimethyl carbonate (DMC), and a lithium salt, lithium hexafluorophosphate ($LiPF_6$). [4–6] There is growing interest in developing electrolytes for new battery chemistries that cannot be supported by this mixture. [60] One approach for improving the energy density of rechargeable batteries is by increasing the operating voltage of the cell. EC/DMC/$LiPF_6$ is neither stable against lithium metal nor is it stable against next-generation high-voltage lithium transition metal oxide cathode materials, in particular those with high nickel content. [4,7,61] There is thus considerable interest in ether-based electrolytes, such as poly(ethylene oxide) (PEO), which are stable against lithium metal. [62,63,20,64] Similarly, there is emerging interest in developing electrolytes based on fluorinated solvents due to their high-voltage stability. [65–69] Electrolyte performance depends crucially on ion solvation. In both carbonate- and ether-based electrolytes, the lithium cations are coordinated with the electronegative oxygen atoms on the solvent molecules. [62,20] Relatively little is known about the nature of ion solvation in fluorinated electrolytes. It is well-known that fluorinated compounds are highly soluble in one another, which is often referred to as the fluorous effect. [70] One might expect this effect to strengthen coordination between fluorinated anions and the fluorinated solvent. In addition to these effects, electrolyte performance depends on interactions between the non-coordinated ion and the solvent, and cation-anion interactions. [71,72]

### *5.2.1 Stefan-Maxwell Diffusion Coefficients*

At the continuum level, ion transport in binary electrolytes, which are composed of a solvent and two ions, is governed by three Stefan-Maxwell diffusion coefficients that quantify inverse frictional interactions between the cation and the solvent, $\mathfrak{D}_{0+}$, the anion and the solvent, $\mathfrak{D}_{0-}$, and the cation and the anion, $\mathfrak{D}_{+-}$, as well as a thermodynamic factor. [29] Methods to measure these quantities have been established in the literature and have been applied to several systems. [25,50,54] It is convenient to measure the thermodynamic factor and three related transport properties: ionic conductivity, $\kappa$, salt diffusion coefficient, $D$, and the transference number, $t_+^0$, and use well-established relationships to obtain Stefan-Maxwell diffusion coefficients from these measurements. [73]

### *5.2.2 The Nernst-Einstein Equation*

Measurements of ion self-diffusion coefficients, $D_{\mathrm{self},+}$ and $D_{\mathrm{self},-}$, by pulsed-field gradient NMR (PFG-NMR) have provided valuable insight into the underpinnings of ion transport. [74–82] In ideal, dilute electrolytes, wherein the activity coefficients of the ions are unity, the relationships between self-diffusion coefficients and ion transport coefficients are relatively simple. In this limit, ionic conductivity is given by the Nernst-Einstein equation, which is often modified to give Equation 5.1,

$$\kappa = \beta_{\text{self}} \frac{cF^2}{RT} \left( z_+^2 \nu_+ D_{\text{self},+} + z_-^2 \nu_- D_{\text{self},-} \right), \quad (5.1)$$

where $z_+$ and $z_-$ are the charge numbers, $\nu_+$ and $\nu_-$ are the number of cations and anions, $c$ is the salt concentration, and $F$ is Faraday's constant. [29] The parameter $\beta_{\text{self}}$ is a pre-factor that relates ion self-diffusion coefficients to conductivity. The inverse of $\beta_{\text{self}}$ is often referred to as the Haven ratio. [83,84] In ideal dilute electrolytes, $\beta_{\text{self}}$ is unity, and thus ionic conductivity is entirely dependent on the self-diffusion coefficients of the ions. In this limit, self-diffusion coefficients are inversely proportional to viscosity via the Stokes-Einstein relation. [85] If this relationship is assumed to hold at all salt concentrations, one obtains the Walden plot wherein data from different electrolytes collapse onto a line when conductivity is plotted against the reciprocal of viscosity. [77,86,87] In the literature, $\beta_{\text{self}}$ is often called ionicity, and is assumed to reflect the extent of salt dissociation in the electrolyte. [76–79,83,88–90] However, many lithium battery electrolytes are far from ideal, even in the dilute limit. It is therefore not surprising to find that experimentally-determined values of $\kappa$, $c$, $D_{\text{self},+}$, and $D_{\text{self},-}$ do not obey Equation 5.1, even in relatively dilute systems. [76–79,83,88–91]

### *5.2.3 Transference Number*

Many recent publications emphasize the importance of another transport property, the transference number. [9,52,75,79,92–97] In seminal work in 1987, Bruce and Vincent proposed a simple method for measuring the transference number. [51,55] They recognized that the transference number thus obtained is correct only in the case of ideal dilute electrolytes. In this case, the cation transference number obtained by the Bruce-Vincent method is identical to that based on self-diffusion coefficients, given in Equation 5.2,

$$t_{+,\text{NMR}} = \frac{z_+ D_{\text{self},+}}{z_+ D_{\text{self},+} - z_- D_{\text{self},-}}, \quad (5.2)$$

in which the subscript NMR is used because PFG-NMR is often used to measure the self-diffusion coefficients. One may consider Equation 5.1 and Equation 5.2 as characteristic of ideal dilute electrolytes. The rigorously-defined cation transference number with respect to the solvent velocity, $t_+^0$, however, is given by Equation 5.3, [29]

$$t_+^0 = \frac{z_+ \mathfrak{D}_{0+}}{z_+ \mathfrak{D}_{0+} - z_- \mathfrak{D}_{0-}}. \quad (5.3)$$

While $t_{+,\mathrm{NMR}}$ and that measured by the Bruce-Vincent method must be positive, there are several instances of negative $t_+^0$ values, as measured using electrochemical techniques [25,50,98,99] as well as using electrophoretic NMR. [75]

The objective of this paper is to quantify the relationships between the different ion transport properties introduced above. We have chosen two model systems: a conventional ether-based electrolyte comprised of tetraglyme and lithium bis(trifluoromethanesulfonyl)imide (LiTFSI), and a fluorinated analog, a perfluoroether-based electrolyte comprised of C8-DMC and lithium bis(fluorosulfonyl)imide (LiFSI). The chemical structures of the solvents and salts are shown in Figure 5.2. Both solvents contain four repeat units and differ mainly in the fact that C8-DMC is fluorinated. We thus refer to the two systems as "H4" and "F4," respectively. F4 is expected to have a lower dielectric constant than H4. [100] We note that the end-groups of H4 and F4 are different. Finally, we also note that different anions were used ($TFSI^-$ in H4 and $FSI^-$ in F4). FSI was chosen in F4 because it led to a higher ionic conductivity. [101] We compare thermodynamic factors, continuum transport properties, and self-diffusion coefficients measured in the two systems. Both systems are complex, and conductivity is not well-described by Equation 5.1. We use concentrated solution theory [29] to arrive at analogous equations that relate conductivity to Stefan-Maxwell diffusion coefficients rather than self-diffusion coefficients. These relationships are essential for understanding the origin of differences in ion transport in H4 and F4.

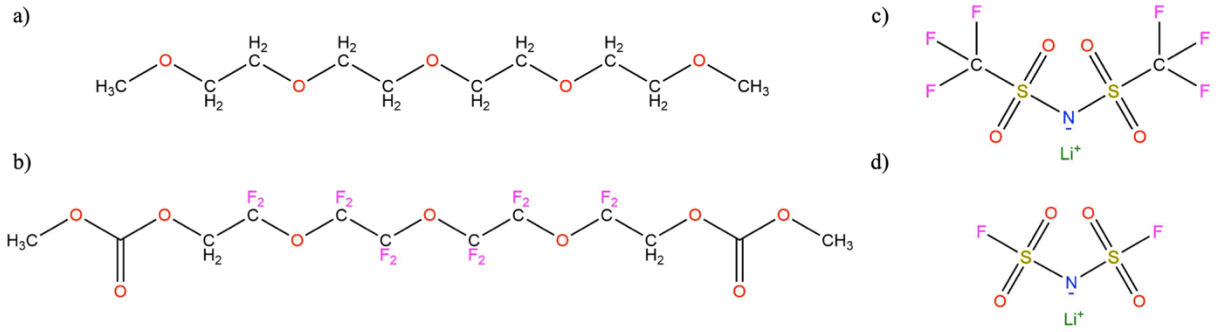


Figure 5.2. Chemical structures of tetraglyme (a), C8-DMC (b), LiTFSI (c), and LiFSI (d).

An important objective of this study is to answer the following questions:

(1) Are differences in conductivity in H4 and F4 related to differences in ion self-diffusion coefficients, $D_{\mathrm{self},+}$ and $D_{\mathrm{self},-}$, as anticipated by Equation 5.1?
(2) Are differences in conductivity in H4 and F4 related to differences in viscosity?
(3) Is $\beta_{\mathrm{self}}$ a measure of the extent of ion dissociation in H4 and F4?

## 5.3 Experimental Methods

### *5.3.1 Electrolyte Preparation*

C8-DMC was synthesized from a diol-terminated precursor as described elsewhere and has a molecular weight of 526 g/mol. [100,65] Tetraglyme was purchased from Sigma Aldrich. Both polymers were dried under dynamic vacuum at 50 °C for three days. LiFSI and LiTFSI were purchased from Oakwood Products, Inc. and Sigma Aldrich, respectively. Salts were dried under dynamic vacuum at 100 °C for three days. In an Ar glovebox, Li salt was added to the respective polymer by mass and mixed using a magnetic stirrer for at least 12 hours. Figure 5.2 shows the chemical structures of tetraglyme (a), C8-DMC (b), LiTFSI (c), and LiFSI (d). Mixtures of tetraglyme (a) and LiTFSI (c) are denoted as "H4" and mixtures of C8-DMC (b) and LiFSI (d) are denoted as "F4." LiFSI was used in F4 because previous work found it to be the salt that resulted in the highest conductivity in C8-DMC-based electrolytes. [101] Table 5.1 shows conversions between various salt concentration units in H4 and F4, including the mole fraction of salt, $x_{salt}$, weight percent salt, molality, and concentration in units of moles per cubic centimeter. The concentration of salt is denoted $c$, that of the solvent is denoted $c_0$, and the total concentration is $c_T = c_0 + 2c$, because each salt molecule contains two ions. The maximum concentrations studied were limited by the solubility limits. [98]

Table 5.1. Salt concentration in electrolytes in Chapter 5

| | $x_{salt}$ | wt% salt | molality (mol/kg) | density (g/L) | $c$ x10$^3$ (mol/cm$^3$) | $c_0$ x10$^3$ (mol/cm$^3$) | $c_T$ x10$^3$ (mol/cm$^3$) |
|---|---|---|---|---|---|---|---|
| H4 | 0.04 | 5.0 | 0.18 | 990 | 0.17 | 4.2 | 4.6 |
| | 0.24 | 29.3 | 1.44 | 1240 | 1.27 | 3.9 | 6.5 |
| | 0.46 | 52.1 | 3.78 | 1440 | 2.57 | 3.1 | 8.2 |
| | 0.55 | 60.8 | 5.39 | 1490 | 3.15 | 2.6 | 8.9 |
| F4 | 0.03 | 1.0 | 0.05 | 1490 | 0.08 | 2.8 | 2.9 |
| | 0.13 | 5.0 | 0.28 | 1450 | 0.39 | 2.6 | 3.4 |
| | 0.24 | 10.0 | 0.60 | 1660 | 0.89 | 2.8 | 4.6 |
| | 0.33 | 14.9 | 0.94 | 1680 | 1.36 | 2.7 | 5.4 |
| | 0.41 | 19.6 | 1.30 | 1630 | 1.70 | 2.5 | 5.9 |
| | 0.48 | 25.0 | 1.78 | 1760 | 2.36 | 2.5 | 7.2 |

### *5.3.2 Experimental Characterization*

All experiments were conducted at 30 °C. All error bars are standard deviations from at least three replicate measurements. In order to produce figure insets showing the ratio of properties in H4 and F4, linear interpolation was used to estimate the properties at the same salt concentrations in the two systems. Therefore, these insets should be regarded as approximations.

*5.3.3 Conductivity Measurements*

Ionic conductivity, denoted $\kappa$, of H4 and F4 was measured using a FiveEasy Conductivity Meter F30 (Mettler Toledo). Conductivity for the F4 system has been reported elsewhere.[52] Each measurement was carried out in triplicate.

*5.3.4 Electrochemical Characterization*

All other electrochemical techniques were performed as described by Shah *et al*,[98] and all results are tabulated in Table A5.1. Current fraction, $\rho_+$, previously referred to as ideal transference number, $t_{+,\mathrm{id}}$, was determined using polarization of lithium symmetric cells and Equation 5.4,

$$\rho_+ = \frac{I_{ss}}{I_\Omega}\left(\frac{\Delta V - I_\Omega R_0}{\Delta V - I_{\mathrm{ss}} R_{ss}}\right), \quad (5.4)$$

where $I_{ss}$ is the steady-state current, $I_\Omega = \Delta V/R_{\mathrm{T}}$ where $R_{\mathrm{T}}$ is the total resistance measured by ac impedance spectroscopy, $\Delta V$ is the applied polarization potential, $R_0$ is the initial interfacial resistance, and $R_{\mathrm{ss}}$ is the interfacial resistance at steady-state.

Restricted diffusion coefficients were determined by measuring the open-circuit potential, $U$, of lithium symmetric cells after polarization.[54] The relaxation profiles were fit to Equation 5.5,

$$U(t) = k_0 + ae^{-bt}, \quad (5.5)$$

where $k_0$ is an empirical offset voltage and $a$ and $b$ are fit parameters. The salt diffusion coefficient within the separator, $D$, is then determined by Equation 5.6,

$$D_s = \frac{l^2 b}{\pi^2}, \quad (5.6)$$

where $l$ is the thickness of the separator stack. Celgard 2500 separators (thickness 25 μm, diameter 19 mm) were soaked with the electrolyte. Three configurations were used for F4, with 5, 10, and 15 separators stacked to adjust the thickness of the electrolytes. Only one configuration was used for H4, with 20 separators stacked. The electrolyte diffusion coefficient, $D$, is then $\tau D_s$, where $\tau$ is the tortuosity of the separator ($\tau = 4.53 \pm 0.45$ as reported by Shah *et al.*[98]).

The open-circuit potential was measured using concentration cells with a *U*-cell design to determine the thermodynamic factor using Equation 5.7,

$$1 + \frac{\mathrm{d}\ln\gamma_{\pm}}{\mathrm{d}\ln m} = \frac{\kappa(z_+\nu_+)}{\nu RTDc\left(\frac{1}{\rho_+}-1\right)}\left(\frac{\mathrm{d}\,U}{\mathrm{d}\ln m}\right)^2, \quad (5.7)$$

where $z_+$ is the cation charge number, $\nu_+$ is the number of cations, $\nu$ is related to the stoichiometric factor, and $c$ is the salt concentration. For univalent salts, $z_+$ and $\nu_+$ are 1, and $\nu$ is 2. The thermodynamic factor can be used to calculate the transference number of the electrolyte phase, $t_+^0$, according to Equation 5.8,

$$t_+^0 = 1 - \sqrt{\frac{\frac{F^2Dc}{\nu\kappa RT}\left(\frac{1}{\rho_+}-1\right)}{1+\frac{\mathrm{d}\ln\gamma_{\pm}}{\mathrm{d}\ln m}}}. \quad (5.8)$$

*5.3.5 Viscosity*

Electrolyte viscosities were measured using an electromagnetically spinning viscometer (EMS-1000, Kyoto Instruments). Electrolytes were sealed in tubes in the glovebox, rendering the measurement air-free, and samples were maintained at 30 °C by the instrument. Bulk sample viscosity is determined from the rotation rate of an aluminum sphere within the solution as it is spun by an external applied magnetic field. No dependence on rotation rate was observed within instrument capabilities, and reported values were taken at a rate of 1,000 rpm. Error was estimated from at least 10 repeat measurements on the same sample.

*5.3.6 Pulsed-Field Gradient NMR*

Self-diffusion coefficients were measured using pulsed-field gradient NMR (PFG-NMR).[34] NMR samples were prepared under Ar in 5 mm tubes with high-pressure caps. Measurements on F4 were performed on a 600 MHz Bruker Avance III instrument using a broadband observe Smart probe (BBO) with a Z-gradient (maximum gradient strength 50 G/cm) and a variable temperature unit maintained at 30 °C. Diffusion data for the H4 samples were acquired on the same instrument but with a broadband observe Prodigy cryo-probe (BBO) with a Z-gradient (maximum gradient strength 67 G/cm). Measurements were performed at 233.23 MHz for $^7$Li, 565.63 MHz for $^{19}$F, and 600.13 MHz for $^1$H. For F4, $^{19}$F NMR was used to measure the diffusion of both the anion and the polymer backbone. The peak at 50 ppm was assigned to the anion.[98] For H4, due to the lack of fluorination of the polymer, $^1$H NMR was used to measure the diffusion of the polymer backbone.

For each nucleus at each salt concentration, inversion recovery experiments were used to measure $T_1$ relaxation constants in order to ensure that the recycle delay was maintained

above 5 times $T_1$. $T_1$ data for all measured nuclei in both systems as a function of salt concentration are shown in Figure A5.1. For all H4 samples, and all F4 samples below $x_{\text{salt}} = 0.4$, data were acquired using a double stimulated echo sequence [40] with bipolar gradients and convection compensation (Bruker pulse sequence dstebpgp3s). A stimulated echo sequence with bipolar gradients without convection correction (Bruker pulse sequence stebpgp1s) was used for F4 samples with $x_{\text{salt}} > 0.4$ due to low sensitivity. These samples have the highest viscosity (see Figure 5.3c), so it is reasonable to expect that convection is less likely to be significant. If convection is a factor, one would expect that larger diffusion delay times, Δ, would result in faster observed diffusion coefficients. Therefore, when convection correction was not used, experiments were conducted with a variety of diffusion delays and pulse lengths to confirm that convection was not a source of error. For F4, diffusion delays, Δ, from 0.5 to 1 s ($^7$Li) and 0.07 to 0.15 s ($^{19}$F), and magnetic field gradient pulse lengths, δ, from 16 to 40 ms ($^7$Li) and 2 to 11 ms ($^{19}$F) were used. For H4, Δ from 0.4 to 1.6 s ($^7$Li), 0.3 to 1 s ($^{19}$F), and 0.3 to 1.1 s ($^1$H), and δ from 1.6 to 4.4 ms ($^7$Li), 1.2 to 3.4 ms ($^{19}$F), and 0.8 to 2.8 ms ($^1$H) were used.

For the convection-compensated experiments, the signal attenuation was fit to Equation 5.9, [35]

$$E = e^{-\gamma^2 g^2 \delta^2 D_{\text{self,i}}\left(\Delta - \frac{5\delta}{8} - \tau_d\right)}, \quad (5.9)$$

where $E$ is the signal attenuation, $\gamma$ is the gyromagnetic ratio, $g$ is the pulsed field gradient strength, $D_{\text{self,i}}$ is the self-diffusion coefficient of species $i$, and $\tau_d$ is a delay for gradient recovery. For non-convection corrected experiments, $E$ was fit to Equation 5.10, [35]

$$E = e^{-\gamma^2 g^2 \delta^2 D_{\text{self,i}}\left(\Delta - \frac{\delta}{4}\right)}. \quad (5.10)$$

Both Equations 5.9 and 5.10 include corrections for sine-shaped gradient pulses. [35] For each diffusion measurement, 32 experiments with varying gradient strengths spaced linearly between 5% and 95% of the maximum gradient strength were performed, always resulting in linear signal attenuation on Stejskal-Tanner plots. [34] A representative Stejskal-Tanner plot is shown in Figure A5.2.

## 5.4 Results and Discussion

### *5.4.1 Electrochemical Characterization of H4 and F4*

Figure 5.3a shows the ionic conductivity of tetraglyme/LiTFSI (H4) and C8-DMC/LiFSI (F4) electrolytes as a function of salt mole fraction, $x_{\text{salt}}$. We chose to express salt concentration in terms of mole fraction rather than molality because the molar masses

of the solvents differ substantially; Table 5.1 can be used to convert between concentration units. Both systems exhibit similar trends, with the conductivity increasing with concentration at low concentration and reaching a shallow maximum at moderate concentration ($x_{salt}$ = 0.24 for H4 and 0.33 for F4) before decreasing at higher salt concentrations. However, the conductivity in H4 is one to two orders of magnitude higher than that of F4. In Figure 5.3 (and in subsequent Figures 5.4-5.6 and 5.8), we provide insets showing the ratio of the plotted parameters in H4 *vs.* F4. The ratio of conductivities shown in the inset in Figure 5.3a ranges from 210 at low salt concentration to 18 at high salt concentration. Our measured ionic conductivity for H4 is in excellent agreement with data in Yoshida *et al.* [76] and Schmidt *et al.* [79] Figure 5.3b shows the current fraction, $\rho_+$, measured by the Bruce-Vincent method. [51,55] $\rho_+$ decreases with salt concentration in both systems, but at all salt concentrations, $\rho_+$ is significantly higher in F4 than in H4. $\kappa$ and $\rho_+$ data for F4 are adapted from Shah *et al.* [98] by permission of the PCCP Owner Societies. Figure 5.3c shows viscosity in both systems, and these results are also shown in Table A5.2. Despite the similar chain lengths in H4 and F4, the viscosities differ by approximately an order of magnitude, with F4 being significantly more viscous. At high salt concentrations, the viscosity of F4 is a factor of 17 higher than that of H4. Our measured viscosities agree well with those reported in Yoshida *et al.* [76] for H4.

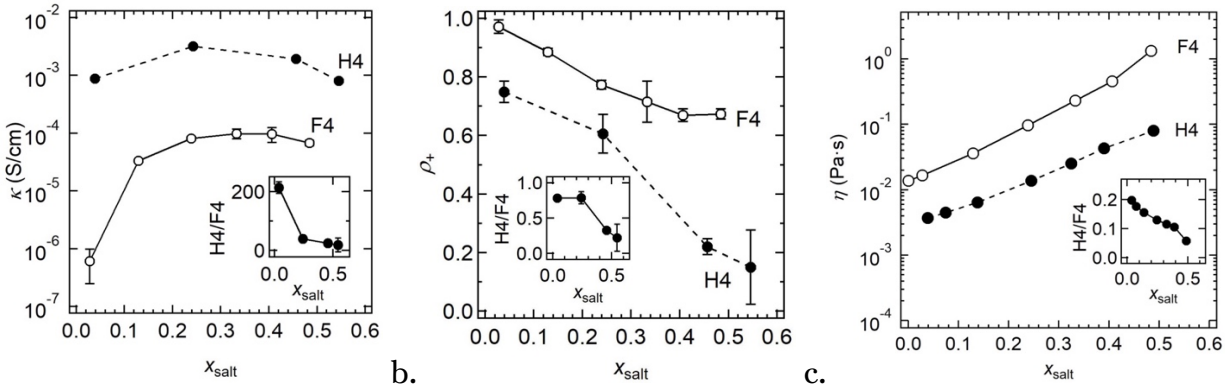


a. b. c.

Figure 5.3. Ionic conductivity, $\kappa$ (a), current fraction, $\rho_+$ (b), and viscosity, $\eta$ (c) as a function of salt concentration, $x_{salt}$, for H4 and F4. Insets show the ratios of properties in H4 *vs.* F4.

It is tempting to try to determine which electrolyte is "better" for lithium ion transport based on the data in Figure 5.3. If ionic conductivity were the only important parameter, then clearly H4 is the better electrolyte. However, in the limit of small dc currents, the efficacy of an electrolyte is given by the product $\kappa\rho_+$. [51,52,73,102,103] At high salt concentration in the vicinity of $x_{salt}$ = 0.5, the conductivity of H4 is higher than that of F4 by about an order of magnitude, but $\rho_+$ of H4 is lower than that of F4 by about the same factor. Using $\kappa\rho_+$ to evaluate efficacy thus suggests that H4 and F4 are equally

"good" electrolytes at high salt concentrations. Despite this observation, we expect the interactions between the ions and the solvent to be very different in H4 and F4. It is difficult, however, to determine what aspect of this difference affects $\kappa$ and $\rho_+$. In the discussion below, we illustrate that complete characterization (beyond $\kappa$ and $\rho_+$) is crucial for making inferences about lithium ion transport.

Figure 5.4 shows the salt diffusion coefficients, $D$, measured by the restricted diffusion method. [54] In both H4 and F4, $D$ decreases exponentially with increasing salt concentration. At all salt concentrations, $D$ is higher in H4 than in F4, consistent with the lower viscosity measured in H4. $D$ data for F4 is adapted from Shah *et al.* [98] by permission of the PCCP Owner Societies.

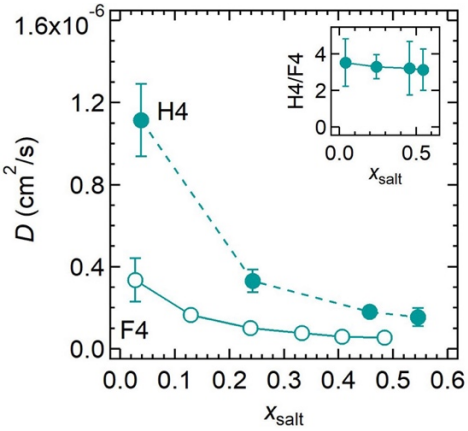


Figure 5.4. Salt diffusion coefficients, $D$, measured by the restricted diffusion technique. Inset shows the ratio of $D$ in H4 *vs.* F4.

*5.4.2 Self-Diffusion*

Figure 5.5 shows the self-diffusion coefficients of the cation, anion, and polymeric solvent, $D_{self,+}$, $D_{self,-}$, and $D_{self,0}$, respectively, measured by PFG-NMR. $D_{self,+}$ and $D_{self,-}$ for F4 are adapted from Shah *et al.* [98] by permission of the PCCP Owner Societies. In simple mixtures of non-interacting, uncharged molecules, self-diffusion coefficients are inversely proportional to molar mass. [85] For both H4 and F4, however, the polymer diffusion was found to be higher than that of either cation or anion. The molar masses of the polymeric solvents are 222 and 526 g/mol, that of the anions, $TFSI^-$ and $FSI^-$, are 280 and 180 g/mol for H4 and F4, respectively, and that of $Li^+$ is 7 g/mol. It may therefore be surprising that the diffusivities of the solvents are so much higher than those of the ions. The trends observed in Figure 5.5 are, however, consistent with data presented in Yoshida *et al.* [76] and Schmidt *et al.* [79] for H4. These results emphasize the importance of interactions between the ions and the polymer chains, as they cannot be explained without such interactions. In addition, the cation and anion self-diffusion coefficients are virtually

identical in F4, while in H4, $D_{\text{self},-}$ is higher than $D_{\text{self},+}$. This suggests that the nature of ion-polymer and ion-ion interactions are different in the two systems.

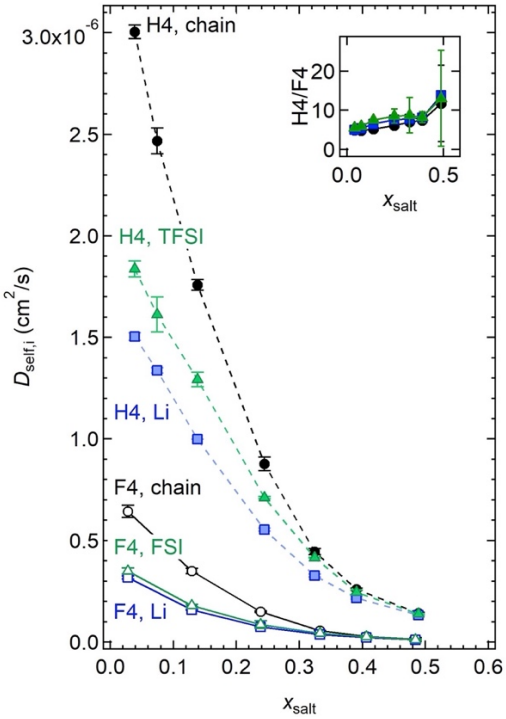


Figure 5.5. Self-diffusion coefficients of the cation (blue), anion (green), and polymeric solvent chain (black) in H4 (filled symbols) and in F4 (open symbols) as a function of salt concentration. The inset shows the ratio of the diffusivities in the two systems for the cation, anion, and chain.

The relationship between mutual and self-diffusion coefficients is often analyzed using the Nernst-Hartley relation, which gives a mutual diffusion coefficient in dilute electrolytes with dissociated salts. [104,105,106,107] However, the Nernst-Hartley relation does not include solvent diffusivity. We therefore define an analogous diffusion coefficient, $D_{\text{self}}$, which is similar in form to that defined by Nernst-Hartley but with the addition of a $D_{\text{self},0}$ term:

$$\frac{1}{D_{\text{self}}} = \frac{x_0}{D_{\text{self},0}} + \frac{x_+}{D_{\text{self},+}} + \frac{x_-}{D_{\text{self},-}}. \quad (5.11)$$

$D_{\text{self}}$, along with $D$ reproduced from Figure 5.4 for comparison, is shown as a function of salt concentration in Figure 5.6. As might be expected from the self-diffusion coefficient measurements (Figure 5.5), $D_{\text{self}}$ decreases exponentially with increasing salt concentration in both systems. In both systems, $D_{\text{self}}$ is higher than $D$ at low salt

concentrations and lower than $D$ at high salt concentrations. $D_{self}$ of H4 is about an order of magnitude larger than that of F4 at all salt concentrations.

### *5.4.3 The Stokes-Einstein Relationship*

For simple systems, such as dilute colloidal spheres suspended in a solvent, diffusion and viscosity are related by the Stokes-Einstein relationship, and this implies that the product $\eta D$ should be a constant.[108,109] In Figure 5.6b, we plot the product $\eta D_{self}$ as a function of salt concentration and observe remarkable agreement between the two systems. This product is approximately $10^{-8}$ $Pa \cdot cm^2$, and independent of salt concentration and the molecular structures of the anion and polymer. Figure 5.6b also shows the product $\eta D$ as a function of salt concentration. While the viscosity-corrected diffusion ($\eta D$) values agree well between H4 and F4 at low salt concentrations, they diverge at higher salt concentrations. For neither system is the product $\eta D$ independent of salt concentration. It is clear that viscosity does not explain the dependence of $D$ on salt concentration. Viscosity certainly affects ion transport, but more complex interactions must also come into play.

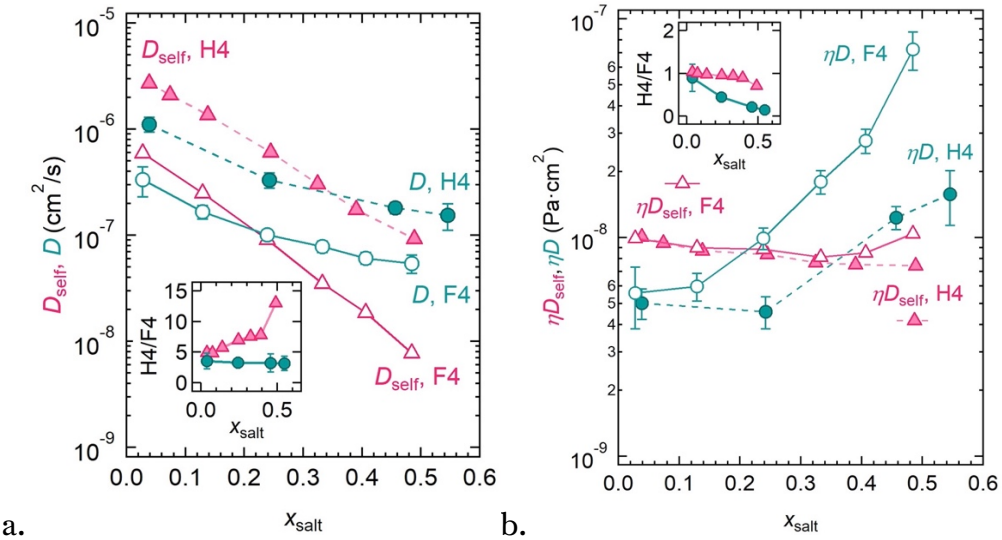


Figure 5.6. $D_{self}$ (Equation 5.11) (pink) and $D$ (reproduced from Figure 5.4 for comparison) (turquoise) (a), and $D_{self}$ (pink) and $D$ (turquoise) corrected by multiplication by viscosity (b) in H4 (filled symbols) and F4 (open symbols). Insets shows the ratio of $D_{self}$ and $D$, and $\eta D_{self}$ and $\eta D$, in H4 vs F4.

### *5.4.4 The Invalidity of the Nernst-Einstein Relationship*

The conductivity and self-diffusion coefficient data in Figures 5.3a and 5.5 enable calculation of $\beta_{self}$ using Equation 5.1. The results thus obtained for H4 and F4 are shown in Figure 5.7. If our electrolytes were thermodynamically ideal, which one might expect to be the case in the dilute limit, then $\beta_{self}$ would approach unity in the limit $x_{salt} \to 0$. In

H4 and F4, deviations from thermodynamic ideality are evident, even in the most dilute electrolytes we study. The qualitative dependence of $\beta_{self}$ on $x_{salt}$ is different in the two systems, with of $\beta_{self}$ in F4 increasing monotonically to its highest value ($\beta_{self} = 0.35$) at its highest salt concentration, while $\beta_{self}$ in H4 reaches a maximum ($\beta_{self} = 0.61$) at intermediate salt concentration ($x_{salt} = 0.46$). The data for H4 agree with reported data in Yoshida *et al.* [76] and Schmidt *et al.*; [79] however, these references only study salt concentrations below $x_{salt} = 0.5$, and therefore observe a monotonic increase in $\beta_{self}$. F4 could not be studied at higher salt concentrations due to its solubility limit. [98] $\beta_{self}$ values in H4 and F4 are also quantitatively different, particularly at low salt concentration; the lowest $\beta_{self}$ in F4 is 0.003, and H4 the minimum is 0.42. This difference is obtained despite the similarity of the dependence of ion self-diffusion coefficients and conductivity on $x_{salt}$.

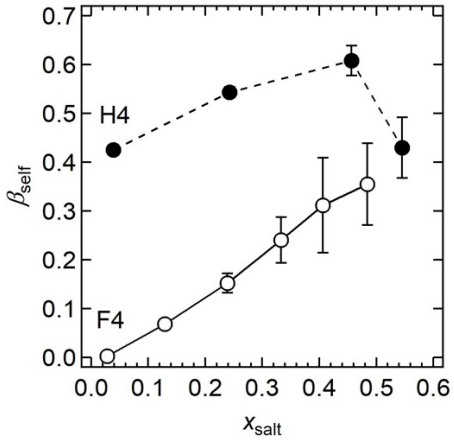


Figure 5.7. Pre-factor $\beta_{self}$ relating conductivity to self-diffusion coefficients of the ions (Equation 5.1) as a function of salt concentration for H4 (filled symbols) and F4 (open symbols).

$\beta_{self}$ is often called ionicity, and it is often argued to be a measure of the extent of dissociation of the salt ions because empirically-derived values are often less than unity. [79,77,78,76,83,88,89,90,91] This argument rests on the assumption that lower-than-expected values of conductivity are obtained because only a fraction of ions present in the system are free to migrate under applied potentials with mobilities that are controlled by self-diffusion coefficients according to the Nernst equation; when $\beta_{self}$ is low, many ions are assumed to be in neutral ion pairs. Since ion pairing and clustering increases with increasing salt concentration, we would expect $\beta_{self}$ to decrease with increasing salt concentration. This is clearly not the case in F4, implying that in this system, $\beta_{self}$ has little to do with the extent of dissociation. In other words, ionic conductivity is unrelated to self-diffusion in F4. The decrease of $\beta_{self}$ between the two highest salt concentrations in H4 may, in principle, be related to ion pairing, but more evidence is required to

establish if this explanation is correct. It is clear, however, that the polymer-ion interactions and charge transport mechanisms must be different in the two systems.

*5.4.5 Full Electrochemical Characterization and Stefan-Maxwell Coefficients*

The factors that determine the conductivity and the interactions between ions is not clear from the data in Figures 5.3-5.7. We sought to resolve this by performing additional electrochemical characterization experiments. In addition to frictional interactions, ion transport depends on thermodynamic effects that are quantified by the chemical potential of the salt. The thermodynamic contribution to ion transport, often referred to as the thermodynamic factor, is determined by the dependence of the mean molal activity coefficient of the salt, $\gamma_{\pm}$, on salt concentration (molality), and is given by $1 + \frac{\mathrm{d}\ln\gamma_{\pm}}{\mathrm{d}\ln m}$.[29] Figure 5.8 shows the dependence of the thermodynamic factor on salt concentration for H4 and F4. The data for F4 are adapted from Shah *et al.*[98] by permission of the PCCP Owner Societies. In F4, the thermodynamic factor increases monotonically with salt concentration. In H4, the thermodynamic factor is a non-monotonic function of salt concentration, reaching a maximum at $x_{\mathrm{salt}} = 0.24$. It is higher than that of F4 by one to two orders of magnitude.

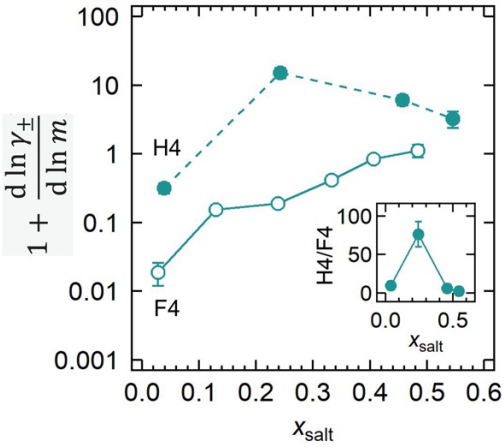


Figure 5.8. Thermodynamic factor in H4 (filled symbols) and F4 (open symbols). Inset shows the ratio of the thermodynamic factors in H4 *vs.* F4.

The salt mutual diffusion coefficient plotted in Figure 5.4 is related to the thermodynamic factor as shown in Equation 5.12,

$$D = \mathfrak{D}\frac{c_{\mathrm{T}}}{c_0}\left(1 + \frac{\mathrm{d}\ln\gamma_{\pm}}{\mathrm{d}\ln m}\right), \quad (5.12)$$

where $\mathfrak{D}$ is the salt diffusion coefficient based on a thermodynamic driving force.

The thermodynamic factor, combined with measurements of $\kappa$, $\rho_+$, and $D$, can be used to calculate the transference number, $t_+^0$, using Equation 5.8. The results are shown in Figure 5.9, where $t_+^0$ is plotted as a function of $x_{\text{salt}}$. $t_+^0$ for F4 is adapted from Shah *et al.* [98] by permission of the PCCP Owner Societies. For F4, the transference number is negative at all salt concentrations. It increases with salt concentration, reaching a maximum of -0.07 at $x_{\text{salt}} = 0.41$. At the lowest salt concentration, $x_{\text{salt}} = 0.41$, shown only in the inset for ease of comparison of other salt concentrations, $t_+^0$ is -10.8. However, in H4, the transference number is positive at low and moderate salt concentrations, reaching a maximum of 0.90 at $x_{\text{salt}} = 0.24$, but then becomes negative at $x_{\text{salt}} = 0.55$. We note that this is a very different trend from that seen in $\rho_+$ (compare Figures 5.9 and 5.3b). At all concentrations, $\rho_+$ of F4 is higher than that of H4. The opposite is true for $t_+^0$. It should be evident that $\rho_+$ is not a good approximation for the transference number in either H4 or F4.

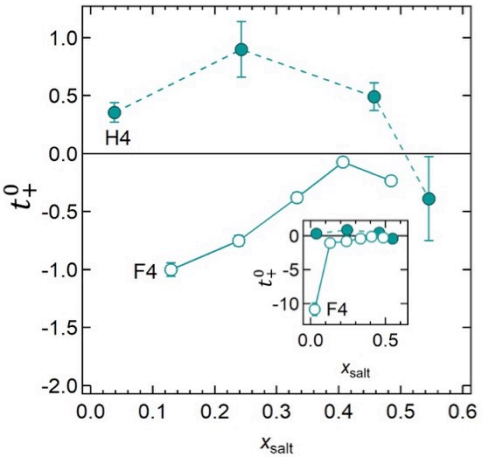


Figure 5.9. Rigorously-defined transference number, $t_+^0$ in H4 (filled symbols) and F4 (open symbols). The inset includes the data at the lowest salt concentration for F4.

The overall diffusion coefficient based on a thermodynamic driving force, $\mathfrak{D}$, depends on frictional interactions between all of the species in solution, and can be calculated using Equation 5.12 and the data in Figures 5.4 and 5.8. The ion-solvent and ion-ion frictional interactions are quantified by Stefan-Maxwell diffusion coefficients, $\mathfrak{D}_{0+}$, $\mathfrak{D}_{0-}$, and $\mathfrak{D}_{+-}$. Concentrated solution theory relates these diffusion coefficients to ion transport parameters introduced above: [29]

$$\mathfrak{D}_{0+} = \frac{-z_-}{z_+ - z_-} \frac{\mathfrak{D}}{1 - t_+^0}, \quad (5.13)$$

$$\mathfrak{D}_{0-} = \frac{z_+}{z_+ - z_-} \frac{\mathfrak{D}}{t_+^0}, \quad (5.14)$$

$$\text{and } \mathfrak{D}_{+-} = \left( \frac{-z_+ z_- c_T F^2}{\kappa RT} - \frac{z_+ - z_-}{z_+ \nu_+} \frac{c_0 t_+^0 (1 - t_+^0)}{c\mathfrak{D}} \right)^{-1}. \quad (5.15)$$

$\mathfrak{D}_{0-}$ characterizes interactions between the polymer and the anion, $\mathfrak{D}_{0+}$ between the polymer and the cation, and $\mathfrak{D}_{+-}$ between the cation and the anion. All of the parameters on the right sides of Equations 5.13-5.15 have been measured as a function of salt concentration. This enables calculation of the Stefan-Maxwell diffusion coefficients.

In Figure 5.10a, we plot $\mathfrak{D}_{0+}$ as a function of salt concentration. The inset shows the same data with a different y-axis scale for visibility of small diffusion coefficients. At low salt concentrations, $\mathfrak{D}_{0+}$ is significantly higher in H4 than in F4. At $x_{\text{salt}} = 0.24$ and above, $\mathfrak{D}_{0+}$ in H4 and F4 are very similar to each other. Given the fact that the self-diffusion coefficients of the lithium ions in H4 and F4 are very different at all salt concentrations, this agreement is perhaps surprising. This suggests that despite differences in apparent ion transport behavior, at moderate to high salt concentrations, the frictional interactions between the lithium cation and the polymer are similar in both fluorinated and non-fluorinated systems. This similarity can only be observed after thermodynamic effects have been properly accounted for using the concentrated solution theory approach.

In Figure 5.10b and its inset, we plot $\mathfrak{D}_{0-}$ as a function of salt concentration. Here we see dramatic differences between H4 and F4, indicating differences in the frictional interactions between the anion and polymer. In H4, as with $\mathfrak{D}_{0+}$, $\mathfrak{D}_{0-}$ is large and positive at low salt concentrations, then decreases rapidly, but unlike $\mathfrak{D}_{0+}$, $\mathfrak{D}_{0-}$ becomes slightly negative at $x_{\text{salt}} = 0.55$. The behavior seen in F4 is yet more complex: $\mathfrak{D}_{0-}$ is negative at all salt concentrations, but the magnitude decreases with increasing salt concentration. This complexity supports the hypothesis that one of the main differences between H4 and F4 is the presence of the fluorous effect in F4, which influences interactions between the fluorinated anion and the fluorinated chain. This is consistent with other recent studies on fluorinated ether-based electrolytes. [66]

Equation 5.3 indicates that $t_+^0$ depends only on $\mathfrak{D}_{0+}$ and $\mathfrak{D}_{0-}$. Because $\mathfrak{D}_{0+}$ of H4 and F4 are in good agreement at high salt concentrations, we conclude that the difference in $t_+^0$ observed in this regime in Figure 5.9 must be due to differences in anion interactions with the backbone which are captured in $\mathfrak{D}_{0-}$. At low salt concentrations, neither $\mathfrak{D}_{0-}$ nor $\mathfrak{D}_{0+}$ agrees between the two systems, so differences in both cation-solvent and anion-solvent interactions are responsible for the difference in transference number.

In Figure 5.10c and its insets, we plot $\mathfrak{D}_{+-}$ as a function of salt concentration. In Figures 5.10d and 5.10e, we plot the ratios of $\mathfrak{D}_{0-}$ and $\mathfrak{D}_{+-}$ to $\mathfrak{D}_{0+}$ for H4 and F4, respectively. In both H4 and F4, $\mathfrak{D}_{+-}$ is very small relative to $\mathfrak{D}_{0+}$. In F4, it is also small relative to $\mathfrak{D}_{0-}$, while in H4, $\mathfrak{D}_{+-}$ and $\mathfrak{D}_{0-}$ are similar in magnitude at high salt concentrations. In F4, $\mathfrak{D}_{+-}$ is positive at all salt concentrations, reaching a shallow maximum at intermediate salt concentrations. In H4, it is relatively large and positive at low salt concentration, then fluctuates between positive and negative at higher salt concentrations. $\mathfrak{D}_{+-}$ characterizes cation-anion interactions and is ignored in dilute solution theory due to the assumption of fully-dissociated ions. The inverse of $\mathfrak{D}_{+-}$ describes friction between the ions, so a small $\mathfrak{D}_{+-}$ indicates that there is a large amount of friction between cation and anion and that the assumption of full dissociation is likely to be invalid. The motion of cations in electrolytes depends on $\mathfrak{D}_{0+}$ and $\mathfrak{D}_{+-}$, while the motion of anions depends on $\mathfrak{D}_{0-}$ and $\mathfrak{D}_{+-}$. The smaller of the two diffusion coefficients dominates, and so we expect $\mathfrak{D}_{+-}$ to be important in both H4 and F4 due to its small magnitude. Thus, the data in Figure 5.10 indicate that concentrated solution theory is necessary to understand ion transport in both systems.

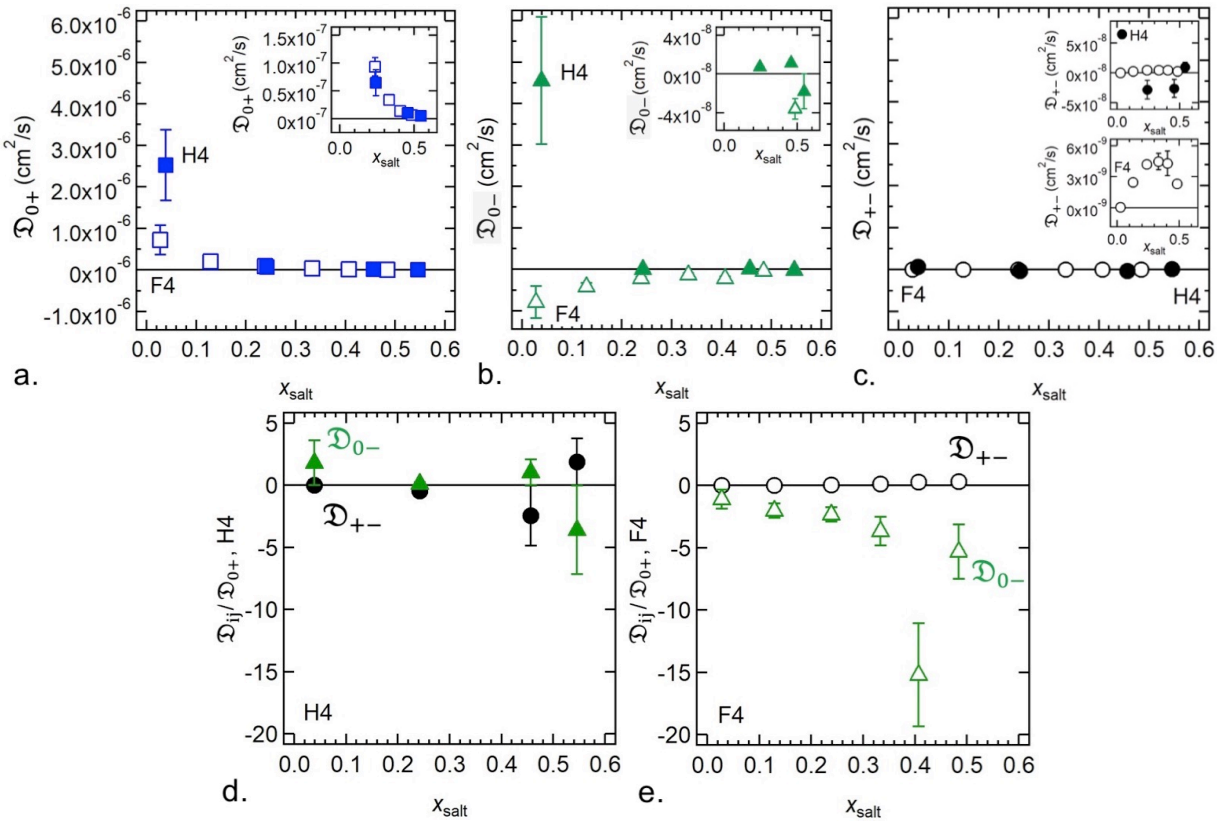


Figure 5.10. Stefan-Maxwell diffusion coefficients $\mathfrak{D}_{0+}$ (a), $\mathfrak{D}_{0-}$ (b), and $\mathfrak{D}_{+-}$ (c) calculated for H4 (filled symbols) and F4 (open symbols) as a function of salt

concentration. Insets show the same data expanded for small values of $\mathfrak{D}$. The ratio of $\mathfrak{D}_{0-}$ (green) and $\mathfrak{D}_{+-}$ (black) to $\mathfrak{D}_{0+}$ for H4 (d) and F4 (e).

*5.4.6 β Parameters and Insight Beyond Nernst-Einstein*

We can use concentrated solution theory to elucidate the underpinnings of the vastly different conductivities reported in Figure 5.3a. Concentrated solution theory provides an equation relating the ionic conductivity to the Stefan-Maxwell diffusion coefficients: [29]

$$\frac{1}{\kappa} = \frac{-RT}{c_T z_+ z_- F^2}\left(\frac{1}{\mathfrak{D}_{+-}} - \frac{c_0 z_-}{\nu_+ c(z_+\mathfrak{D}_{0+} - z_-\mathfrak{D}_{0-})}\right). \quad (5.16)$$

Equation 5.16 illustrates that conductivity is given by the addition of two diffusive contributions, one related to the frictional interactions between the cation and anion, and the other related to frictional interactions between the ions and the solvent. It is conceivable that in some systems, one of these contributions is dominant.

If the frictional interactions between ions are dominant, we can re-express Equation 5.16 in a form that is reminiscent of the Nernst-Einstein equation (Equation 5.1):

$$\kappa = -\beta_{+-}\frac{c_T z_+ z_- F^2}{RT}(\mathfrak{D}_{+-}). \quad (5.17)$$

We have introduced a pre-factor, $\beta_{+-}$, in Equation 5.17 to account for the fact that the relationship between $\kappa$ and $\mathfrak{D}_{+-}$ is obtained by ignoring frictional interactions between the ions and the solvent and is therefore certainly not expected to apply universally. $\beta_{+-}$ is similar in spirit to $\beta_{\text{self}}$ in the Nernst-Einstein equation. If the experimentally-determined values of $\kappa$ and $\mathfrak{D}_{+-}$ are such that $\beta_{+-}$ is in the vicinity of unity, then we would infer that in such a system, frictional interactions between the ions and the solvent can be ignored.

Correspondingly, if ion-solvent interactions are dominant, then we can re-express Equation 5.16 as

$$\kappa = \beta_0 \frac{F^2 c c_T}{RT c_0}(z_+^2 \nu_+ \mathfrak{D}_{0+} + z_-^2 \nu_- \mathfrak{D}_{0-}), \quad (5.18)$$

where we have introduced a pre-factor, $\beta_0$, that is similar to $\beta_{+-}$ and $\beta_{\text{self}}$. If the experimentally-determined values of $\kappa$, $\mathfrak{D}_{0+}$, and $\mathfrak{D}_{0-}$ are such that $\beta_0$ is in the vicinity of unity, then we would infer that in such a system, frictional interactions between the cation and anion can be ignored.

In the dilute limit, we can write

$$\frac{c_T \nu_+ c}{c_0} = \frac{(c_0 + \nu_+ c + \nu_- c)\nu_+ c}{c_0} = \frac{c_0 \nu_+ c}{c_0} = \nu_+ c \quad (5.19)$$

because $c \ll c_0$. In this limit, Equation 5.18 reduces to

$$\kappa = \beta_{0,c} \frac{cF^2}{RT}(z_+^2 \nu_+ \mathfrak{D}_{0+} + z_-^2 \nu_- \mathfrak{D}_{0-}), \quad (5.20)$$

where we have introduced a pre-factor, $\beta_{0,c}$, that is similar to $\beta_0$. This dilute-limit approximation leaves Equation 5.17 unchanged, so there is no analogous $\beta_{+-,c}$. Equation 5.20 is identical to Equation 5.1, the Nernst-Einstein equation, except that self-diffusion coefficients have been replaced by Stefan-Maxwell diffusion coefficients.

For a univalent salt such as LiTFSI or LiFSI, used here, where $z_+ = 1$, $z_- = -1$, and $\nu_+ = \nu_- = 1$, Equations 5.17, 5.18, 5.20, and 5.1 reduce to

$$\kappa = \beta_{+-} \frac{c_T F^2}{RT}(\mathfrak{D}_{+-}), \quad (5.21)$$

$$\kappa = \beta_0 \frac{F^2 c c_T}{RT c_0}(\mathfrak{D}_{0+} + \mathfrak{D}_{0-}), \quad (5.22)$$

$$\kappa = \beta_{0,c} \frac{cF^2}{RT}(\mathfrak{D}_{0+} + \mathfrak{D}_{0-}), \quad (5.23)$$

$$\text{and } \kappa = \beta_{self} \frac{cF^2}{RT}\left(D_{\text{self},+} + D_{\text{self},-}\right). \quad (5.24)$$

The set of equations above are Nernst-Einstein-like equations. In many respects, Equations 5.21 and 5.24 represent approximations at two ends of a spectrum. In a classical dilute electrolyte, wherein the motion of the cations and anions are entirely decoupled, i.e., the solution is thermodynamically ideal, one obtains Equation 5.24. If, on the other hand, coulombic interactions between the cations and anions dominate, one obtains Equation 5.21.

It is illustrative to examine the concentration-dependence of the newly-introduced $\beta$ pre-factors in Equations 5.21-5.24 for a classical electrolyte. For KCl in water, we obtained

values of $\kappa$ from Chambers *et al.*,[110] and values of $\mathfrak{D}_{0+}$, $\mathfrak{D}_{0-}$, and $\mathfrak{D}_{+-}$ from Newman *et al.*[29] Figure 5.11 shows calculated values of $\beta_{+-}$, $\beta_0$, and $\beta_{0,c}$ thus obtained; we were unable to find literature data for $D_{\text{self}}$ in KCl/water solutions, and so were unable to calculate $\beta_{\text{self}}$. In simple electrolytes with dissociated ions, one expects conductivity to be dominated by frictional interactions between the ions and the solvent. In this case, we expect $\beta_0$ and $\beta_{0,c}$ to be close to unity. In Figure 5.11, at low salt concentrations, we see that this is true. At $x_{\text{salt}} = 0.002$, $\beta_0$ and $\beta_{0,c}$ are both 1.0 and $\beta_{+-} = 0.19$, consistent with the expectation that, in dilute systems, cation-anion interactions are insignificant relative to ion-solvent interactions. As salt concentration increases, $\beta_{+-}$ increases, indicating the increased contributions of cation-anion interactions to conductivity. At $x_{\text{salt}} = 0.07$, $\beta_0$ is 0.75, while $\beta_{+-}$ is 0.44. This implies that frictional interactions between the ions and the solvent remain somewhat more important than cation-anion interactions even at this high salt concentration. We attach no significance to the observation that $\beta_{0,c}$ at high salt concentrations is closer to one than $\beta_0$. $\beta_{0,c}$ is necessarily greater than $\beta_0$ because $c_T/c_0$ is always greater than or equal to one (Equation 5.19).

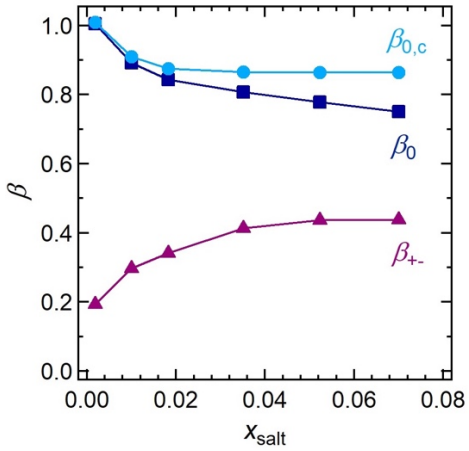


Figure 5.11. $\beta_{+-}$ (purple), $\beta_0$ (dark blue), and $\beta_{0,c}$ (light blue) pre-factors in Equations 5.21-5.23 for KCl in water as a function of salt concentration.

Figure 5.12a shows the $\beta$ pre-factors from Equations 5.21-5.24 in H4. In addition to $\beta_{+-}$, $\beta_0$, and $\beta_{0,c}$, we have included $\beta_{\text{self}}$ data from Figure 5.7. For H4 at the lowest salt concentration, $x_{\text{salt}} = 0.04$, we find that $\beta_{\text{self}} = 0.27$, $\beta_0 = 0.19$, $\beta_{0,c} = 0.20$, and $\beta_{+-} = 0.81$. These values are qualitatively different from those obtained in KCl/water, with $\beta_{+-}$ being closest to one, indicating that cation-anion interactions are more significant than ion-solvent interactions, even at very low salt concentrations. At higher salt concentrations, the magnitudes of all of the $\beta$ pre-factors other than $\beta_{\text{self}}$ are large relative to unity. These values indicate that all of the binary interactions in solution affect

conductivity, and that neglecting any one of them cannot be justified. These observations also show that conclusions regarding ionicity based on $\beta_{self}$ in H4 are erroneous. The behavior of $\beta_{+-}$, $\beta_0$, and $\beta_{0,c}$ indicate that the system cannot be thought of as having 20-40% dissociated ions diffusing freely with the remainder in neutral ion pairs; instead, there are complex interactions between ions and solvent and between cations and anions.

Figure 5.12b shows the $\beta$ pre-factors from Equations 5.21-5.24 in F4. Note the differences in y-axis scales used in Figure 5.12a and 5.12b. It is evident that $\beta_{+-}$ for F4 is unity and $\beta_0$ and $\beta_{0,c}$ are nearly zero at all salt concentrations. This implies that conductivity in F4 over the entire salt concentration range is dominated by frictional interactions between the anion and the cation. Conversely, it implies that frictional interactions between the ions and the solvent do not affect conductivity. A possible explanation is that the salt ions in F4 are present in clusters, consistent with the expectation of a lower dielectric constant of F4, [100] and ion transport occurs mainly within the clusters. For appreciable conductivity, these clusters must exhibit a percolating morphology. We note that this is consistent with the self-diffusion trends observed in Figure 5.5; if the ions form a network-like percolating morphology, then it is unsurprising that they diffuse slowly relative to the polymeric solvent, which is not part of this network. H4 is similar to a more traditional electrolyte, wherein ions are coordinated with the ether oxygens on the polymeric solvent, as evidenced by $\beta_0$ being non-zero. At low salt concentrations, a significant fraction of solvent molecules are uncoordinated and diffuse freely, leading to the trends observed in Figure 5.5. It is clear that F4 is very different from a traditional electrolyte, and in this case also that $\beta_{self}$ has little to do with ionicity. For example, at $x_{salt} = 0.48$, $\beta_{self}$ is 0.35. It would be incorrect to conclude from this that 35% of the $Li^+$ and $FSI^-$ ions are in a dissociated state in F4. In fact, the values of $\beta_{+-}$ indicate that most, if not all, of the $Li^+$ and $FSI^-$ ions are in clusters.

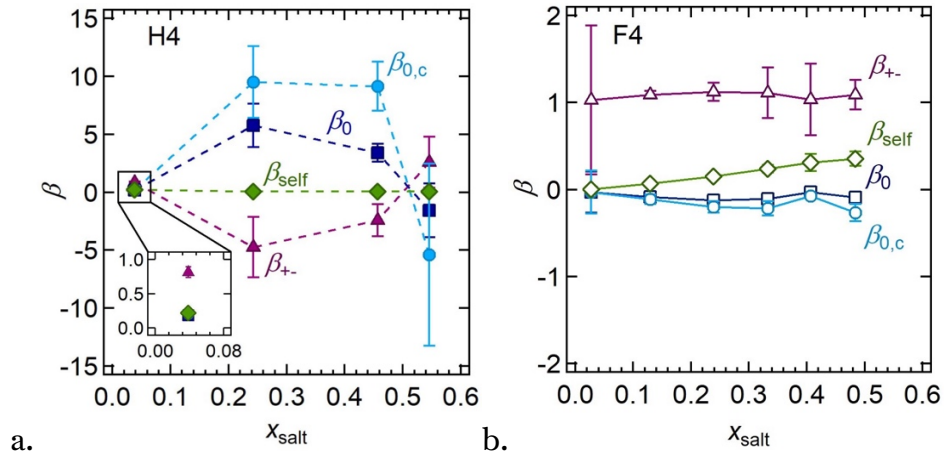


Figure 5.12. $\beta_{+-}$ (purple), $\beta_0$ (dark blue), $\beta_{0,c}$ (light blue), and $\beta_{self}$ (green) pre-factors from Equations 5.21-5.24 for H4 (a) and F4 (b) as a function of salt concentration. Inset

of (a) shows the $\beta$ pre-factors at $x_{\text{salt}} = 0.04$, with $\beta_{\text{self}}$, $\beta_0$, and $\beta_{0,c}$ all overlapping near $\beta = 0.2$.

## 5.5 Conclusions

We have used a variety of characterization techniques, including viscosity measurement, pulsed-field gradient NMR, and full electrochemical characterization, to study electrolytes made from tetraglyme mixed with LiTFSI (H4) and a fluorinated tetraglyme analog, C8-DMC, mixed with LiFSI (F4). We observe significant differences in properties, including conductivity, viscosity, and self-diffusion coefficients differing by one to two orders of magnitude, and differences in sign in the rigorously-defined transference number, $t_+^0$.

It is common in the literature, though not universal, [66,92,98] to focus on frictional interactions between the cation and the solvent to explain trends in the cation transference number. By analyzing our data using Newman's concentrated solution theory, [29] we determine that at high salt concentrations, the differences in $t_+^0$ are due to differences in $\mathfrak{D}_{0-}$, which characterizes frictional interactions between the anion and the solvent chain. This can be explained by the fact that, due to the fluorous effect, the fluorinated backbone in F4 is expected to have much stronger interactions with a fluorinated anion than tetraglyme would be expected to have.

Establishing the underpinnings of ionic conductivity was a major goal of this paper. It is common in the literature to assume that differences in conductivity arise due to differences in viscosity and self-diffusion coefficients of the ions. Quantitative differences between conductivity and self-diffusion are usually interpreted in terms of ionicity and quantified by the measured Nernst-Einstein pre-factor, $\beta_{\text{self}}$. It is therefore important to answer the three questions presented in the Introduction:

(1) Are differences in conductivity in H4 and F4 related to differences in ion self-diffusion coefficients, $D_{\text{self},+}$ and $D_{\text{self},-}$, as anticipated by Equation 5.1?
(2) Are differences in conductivity in H4 and F4 related to differences in viscosity?
(3) Is $\beta_{\text{self}}$ a measure of the extent of ion dissociation in H4 and F4?

The data presented in Figures 5.8-5.12 indicate that the answers to all three questions is "No." In both H4 and F4, ionic conductivity is not dominated by frictional interactions between individual ions and the solvent and thus it is not related to the self-diffusion coefficients of the ions. The self-diffusion coefficients themselves are greatly affected by viscosity but conductivity is not. In both H4 and F4, it is incorrect to consider the electrolytes to be a simple mixture of free ions and ion pairs, indicating that the measured $\beta_{\text{self}}$ has little to do with ionicity.

Using Newman's concentrated solution theory,[29,111] we define pre-factors that are similar in spirit to the Nernst-Einstein pre-factor, $\beta_{self}$.The newly-defined pre-factors, however, acknowledge that conductivity is controlled by three independent frictional interactions: cation-solvent, anion-solvent, and cation-anion, which are quantified using Stefan-Maxwell diffusion coefficients. The simplest situation arises when conductivity is only dependent on frictional interactions between the ions and the solvent, which is the basis of Equation 5.22 and the pre-factor $\beta_0$. To illustrate this situation, we sought an electrolyte in which the answers to the three aforementioned questions would be "yes," and in which Stefan-Maxwell diffusion coefficients had been measured. To our knowledge, however, no such electrolyte has been fully characterized. For the classical electrolyte aqueous KCl, we were unable to find measurements of ion self-diffusivities in the literature. Based on Stefan-Maxwell diffusion coefficients, however, we were able to show that the conductivity in this system can be understood in terms of $\beta_0$ in the dilute limit; $\beta_0$ is unity in the limit of low salt concentration and decreases monotonically to a value of 0.75 at $x_{salt} = 0.07$. In contrast, the conductivity of F4 electrolytes is controlled by frictional interactions between the cation and the anion. We present Equation 5.21 to describe ion transport in such systems, introducing a new pre-factor, $\beta_{+-}$. A remarkable observation is that $\beta_{+-}$ in F4 is approximately equal to unity at all salt concentrations ($x_{salt} = 0.03$ to $0.48$). We posit that such electrolytes contain transient clusters of ions and high conductivity is obtained only when the clusters form a percolating network-like structure.

## 5.6 Acknowledgements

This work was intellectually led by the Joint Center for Energy Storage Research (JCESR), an Energy Innovation Hub funded by the U.S. Department of Energy (DOE), Office of Science, Basic Energy sciences (BES), under Contract No. DEAC02-06CH11357. Electrolyte synthesis and characterization work was performed by L.S.G., D.B.S., and H.Q.N. under the supervision of N.P.B.; L.S.G. under the supervision of H.C.; and K.M.D. under the supervision of B.D.M. We thank UC Berkeley's NMR facility in the College of Chemistry (CoC-NMR) for spectroscopic assistance. Instruments in the CoC-NMR are supported in part by NIH S10OD024998. Electrolyte synthesis work was initially established by Kevin R. Olson, Sue J. Mecham, and J.M.D., who were supported by the Center for Mesoscale Transport Properties, an Energy Frontier Research Center supported by the U.S. Department of Energy, Office of Science, Basic Energy Sciences, under award #DE-SC0012673. The work of K.M.D. and B.D.M. was supported by the Assistant Secretary for Energy Efficiency and Renewable Energy, Office of Vehicle Technologies of the U.S. Department of Energy under Contract DE-AC02-05CH11231 under the Advanced Battery Materials Research (BMR) Program.

# Chapter 6: Electrochemical Characterization of PEO / LiTFSI Electrolytes Near the Solubility Limit*

## 6.1 Abstract

Polymer electrolytes are commonly studied as potential solid replacements to conventional liquid electrolytes to enable the design of rechargeable batteries with a lithium metal anode. Poly(ethylene oxide) (PEO) / lithium bis(trifluoromethanesulfonyl)imide (LiTFSI) has been studied extensively and serves as the foundation for advanced systems. We present the first full electrochemical characterization of this system at high salt concentrations above $r = 0.30$ lithium ions per ethylene oxide moiety. Above $r = 0.28$, we observe signatures of phase separation into an amorphous phase with $r = 0.28$ and a crystalline phase with $r = 0.50$. We measure the limiting current, the maximum current that can be applied to an electrolyte before the potential diverges exponentially, and find that at $r = 0.50$ the limiting current is essentially zero. This indicates that $r = 0.50$ is the solubility limit for PEO / LiTFSI. Based on this solubility limit, we use concentrated solution theory to predict the limiting current below $r = 0.50$. The theory and experiments agree qualitatively but not quantitatively because the theory was developed for single-phase systems.

## 6.2 Introduction

A key step in the development of high energy density rechargeable lithium batteries is to enable lithium metal anodes. However, conventional liquid electrolytes are unstable against lithium metal. [4–6] Ether-based polymer electrolytes, such as poly(ethylene oxide) (PEO) mixed with lithium bis(trifluoromethanesulfonyl)imide (LiTFSI) salt, are compatible with lithium metal, and are therefore commonly used as starting points in the design of next-generation polymer electrolytes. [20,64] For example, rigid PEO-based block copolymers can be used as a solid polymer electrolyte to resist dendrite growth, a common failure mechanism of lithium metal anodes. [63,112] Rational design of such systems requires a complete understanding of ion transport in PEO-based electrolytes. [25,53,113] While ionic conductivity using blocking electrodes has been measured over a broad range of concentrations, complete electrochemical characterization is restricted to salt concentrations below $r = 0.30$, where $r$ is the molar ratio of $Li^+$ to ethylene oxide in the electrolyte. [113–115]

It is essential to understand ion transport at high salt concentrations. Even when the salt concentration of an electrolyte is below $r = 0.30$, where properties are known, when current is passed through a PEO / LiTFSI electrolyte, salt accumulates at the positive

* This Chapter is adapted from Grundy, L. S.; Fu, S.; Hoffman, Z. J.; Balsara, N. P. **2022**, in preparation.

electrode,[29] which could cause this region of the electrolyte to pass into the poorly-studied salt concentration regime. To model these salt concentration profiles, a full electrochemical characterization based on Newman's concentrated solution theory is required.[29]

In this work, we study PEO / LiTFSI electrolytes with a PEO molecular weight of 275 kg/mol and LiTFSI, focusing on concentrations ranging from $r = 0.30$ to 0.50. We begin by measuring three transport parameters—the ionic conductivity, $\kappa$, current fraction, $\rho_+$, and salt diffusion coefficient, $D$. In addition, we measure the open circuit potential, $U$, using concentration cells. We observe signatures of two-phase coexistence above $r = 0.32$ in the concentration cell data. This conclusion is supported by optical microscopy experiments and differential scanning calorimetry and is qualitatively consistent previously published phase diagrams.[113]

The passage of a constant current through an electrolyte results in salt concentration gradients that can be modeled using Newman's concentrated solution theory, provided $\kappa$, $\rho_+$, $D$, and $U$ are known. We use lithium-electrolyte-lithium symmetric cells and measure cell potential as a function of time during the imposition of a current. Salt accumulates near the positive electrode and is depleted near the negative electrode. For a cell to achieve a stable voltage at long times, the salt concentration must be finite. As the salt concentration ($Li^+$) at the negative electrode approaches zero, the cell potential diverges as the electrochemical reaction $Li^+ + e^- \rightarrow Li$ cannot be sustained as the electrolyte is depleted of Li+ ions. The current at which the potential diverges exponentially due to a failure to attain a steady-state concentration profile is called the limiting current density, $i_{\mathrm{lim}}$. An approximate expression, which assumes that $D$ and $\rho_+$ are independent of salt concentration, is given by Equation 6.1,[29,49]

$$i_{\mathrm{lim}} L = \frac{2 c_{\mathrm{av}} D F}{1 - \rho_+}, \quad (6.1)$$

where $L$ is the electrolyte thickness, $F$ is Faraday's constant and $c_{\mathrm{av}}$ is the average salt concentration in the electrolyte. The salt concentration can be converted between $r$ and $c$ using the electrolyte density.[116] Since different groups are likely to use cells with different values of $L$, it is best to examine the normalized limiting current density, which is obtained by multiplying the current density by the electrolyte thickness, $L$. The limiting current density thus normalized is an intrinsic property of the electrolyte of interest.

Another mechanism for the limiting current is the salt concentration ($Li^+$) reaching a solubility limit at the positive electrode: at the solubility limit, the electrochemical reaction $Li \rightarrow Li^+ + e^-$ cannot be sustained. This is because passage of ionic current through a binary electrolyte must cause a salt concentration gradient, i.e., the salt concentration near

the positive electrode must increase, but this is forbidden if the electrolyte is at the solubility limit. The analogous expression to Equation 6.1 in the high-salt regime is given by Equation 6.2, [49]

$$i_{\lim}L = \frac{2(c_{\text{sat}} - c_{\text{av}})DF}{1 - \rho_+}, \quad (6.2)$$

where $c_{\text{sat}}$ is the salt concentration at the solubility limit. Determining equilibrium thermodynamic properties such as the solubility limit in liquid electrolytes is straightforward. In polymers, however, equilibrium phase behavior is often shrouded by crystallization kinetics. [117] PEO is a crystalline polymer: PEO / LiTFSI mixtures are known to form crystalline complexes, and there is little knowledge on chain conformations within the complexes. However, Equation 6.2 presents a simple approach for measuring $c_{\text{sat}}$ – it is the concentration at which $i_{\lim}L$ is zero (or nearly so).

In the present study, we find that at $r = 0.50$, the limiting current is essentially zero, indicating that the salt solubility limit is $r = 0.50$. Our main objective is to compare measured values of the limiting current in the vicinity of the PEO / LiTFSI solubility limit with predictions based on complete characterization with no adjustable parameters.

## 6.3 Experimental Methods

### *6.3.1 Materials*

Poly(ethylene oxide) (PEO) with a molecular weight of 275 kg/mol was purchased from polymer source. Lithium bis(trifluoromethanesulfonyl)imide (LiTFSI) salt was purchased from Sigma Aldrich. PEO and LiTFSI were dried under active evacuation for three days at 120 °C before use. Electrolytes were prepared as reported in Pesko *et al.* [25] In short, PEO and LiTFSI were mixed in the desired ratio and dissolving in anhydrous tetrahydrofuran (THF) (Sigma Aldrich) at 60 °C. After complete dissolution, the mixtures were dried on a hotplate until the THF had evaporated, and then further dried under active evacuation in a glovebox antechamber for two days at 120 °C to remove residual solvent. All sample preparation was performed in an argon glovebox maintained at sub-ppm levels of $H_2O$ and $O_2$.

### *6.3.2 Differential Scanning Calorimetry*

DSC samples were prepared by sealing 5-10 mg of electrolyte in a TZero aluminum pan. Samples were analyzed using a Thermal Advantage Q200 instrument at the Molecular Foundry at Lawrence Berkeley National Laboratory. Samples were cooled to -80 °C at 20 °C per minute, then heated to 140 °C at 1 °C per minute.

*6.3.3 Electrochemical Characterization*

Conductivity cells were constructed by filling a spacer of thickness 0.035 cm and inner diameter 0.318 cm with electrolyte. The spacer was then sandwiched between two stainless steel electrodes of thickness 0.02 cm. Nickel current collectors were affixed to the electrodes, and the cell assembly was vacuum sealed in aluminum pouch material (MTI) before being removed from the glovebox for testing. Cells used for the measurement of the current fraction, $\rho_+$, salt diffusion coefficient, $D$, and limiting current, $i_{\mathrm{lim}}$, were assembled following similar methods, except that lithium foil of thickness 0.02 cm was inserted between the electrolyte and the stainless steel. In all cases, cells were disassembled following testing, and the electrolyte thickness, $L$, was measured using a micrometer.

Ionic conductivity was measured using ac impedance spectroscopy on a BioLogic VMP3 potentiostat. Conductivity cells were annealed at 90 °C for at least two hours, until impedance measurements stabilized. After annealing, ac impedance spectroscopy was performed with an amplitude of 60 mV, and a frequency range of 1 MHz to 1 Hz. The conductivity data was fit to an equivalent circuit to extract the bulk resistance, $R_{\mathrm{b}}$, and the ionic conductivity, $\kappa$, was calculated using Equation 6.3,

$$\kappa = \frac{L}{R_{\mathrm{b}} A}, \quad (6.3)$$

where $A$ is the electrochemically active area of the electrode (based on the spacer dimensions, $A = 0.079$ cm$^2$).

Lithium symmetric cells were used for current fraction, $\rho_+$, and salt diffusion coefficient, $D$, measurements. The cells were annealed at 90 °C for at least two hours, until ac impedance measurements stabilized. Next, cells were pre-conditioned to form a stable electrode-electrolyte interface. Four pre-conditioning cycles were run for each cell, with a single cycle consisting of four hours of polarization at $I = +1$ μA (equivalent to a current density, $i = L/A$, of 13 μA/cm$^2$), four hours of rest, four hours of polarization at -1 μA, and four hours of rest. During pre-conditioning, ac impedance measurements were performed regularly to ensure stability of the bulk and interfacial resistance ($R_{\mathrm{b}}$ and $R_{\mathrm{i}}$) before proceeding.

To measure $\rho_+$, the method developed by Bruce and Vincent was used. [55,51] Cells were polarized at a constant potential of $\Delta V = +10$ mV until the current stabilized, with ac impedance measurements acquired every 20 minutes. Accounting for the potential drop at the electrode / electrolyte interface, $\rho_+$ was calculated according to Equation 6.4, [52]

$$\rho_+ = \frac{i_{ss}(\Delta V - i_\Omega R_{i,0} A)}{i_\Omega(\Delta V - i_{ss} R_{i,ss} A)}, \quad (6.4)$$

Where $i_{ss}$ is the steady-state current density, $R_{i,0}$ and $R_{i,ss}$ are the interfacial resistance initially and at steady-state, and $i_\Omega$ is defined using Equation 6.5,

$$i_\Omega = \frac{\Delta V}{R_{b,0} A + R_{i,0} A}, \quad (6.5)$$

where $R_{b,0}$ is the initial bulk resistance. This experiment was repeated at $\Delta V$ = -10 mV, +20 mV, and -20 mV to ensure reliability of the $\rho_+$ measurement.

At the end of this experiment, once a stable salt concentration gradient had been established, the cell was allowed to relax for 3 hours in a restricted diffusion experiment. [56] The relaxation of the potential was fit to

$$U(t) = k_0 + ae^{-bt}, \quad (6.6)$$

where $k_0$ is the fitted offset voltage and $a$ and $b$ are fit parameters. The salt diffusion coefficient, $D$, is then calculated using Equation 6.7,

$$D = \frac{L^2 b}{\pi^2}. \quad (6.7)$$

Concentration cells were used to measure the difference in potential between electrolytes at different concentrations, as described by Pesko *et al.* [25] In short, A channel approximately 0.3 cm wide and 2.5 cm long was filled with a reference electrolyte, PEO / LiTFSI at a salt concentration of $r$ = 0.06 Li ions per ethylene oxide moiety, in one half, and the electrolyte of interest in the other half. Each side was connected to a lithium electrode, and the potential was monitored until it reached a stable plateau, which was taken to be the potential, $U$, of that electrolyte relative to the reference. All experiments were performed at 90 °C.

### *6.3.4 Limiting Current Measurements*

Symmetric cells identical to those used for $\rho_+$ and $D$ measurements were used to measure the limiting current, with the exception that in a few cases, the electrolyte thickness was different. The annealing and pre-conditioning procedure was also identical to that described above. Next, a constant current was applied while the potential was monitored. A safety potential cutoff of 1 V was imposed. If the potential was observed to increase exponentially, this was taken as a signature that the applied current was above the limiting

current; [29] the experiment was stopped and the cell was allowed to relax. If the potential reached a stable plateau, this was taken as a signature that the applied current was below the limiting current. The limiting current was taken to be the average between the highest accessible current and the lowest inaccessible current.

### *6.3.5 Optical Microscopy*

Microscopy samples were prepared by preparing a solution of PEO and LiTFSI at the desired ratio in anhydrous THF in the glovebox. This solution was drop casted onto a standard microscope slide, which was dried on a hot plate at 60 °C for several hours, and then in the glovebox antechamber under active evacuation at 120 °C overnight. The slides were moved back into the glovebox, where they were allowed to cool. A second slide was placed on top of the sample and the edges were sealed with epoxy so that the electrolyte would not be exposed to air during analysis. Samples were left in the glovebox for several weeks, to allow the epoxy to cure and the electrolytes to equilibrate, and were not removed until immediately before imaging. During imaging, sample temperature was controlled at 90 °C using a Linkam LTS120 stage, which was calibrated using a thermocouple. Samples were equilibrated at temperature for at least 20 minutes prior to imaging. The microscope used was a Leica DC 300.

## 6.4 Results and Discussion

### *6.4.1 Differential Scanning Calorimetry*

To characterize the phase behavior of electrolytes composed of PEO with a molecular weight of 275 kg/mol mixed with LiTFSI at high salt concentrations, we performed differential scanning calorimetry (DSC). The melting points are are shown in Figure 6.1, with black dashed lines to guide the eye. Above the highest melting point at each salt concentration, an amorphous morphology is expected, while below the melting point the system is semicrystalline. These results are qualitatively similar to those presented by Lascaud *et al*, with slight quantitative differences we attribute to the difference in molecular weight (275 *versus* 4 kg/mol). [113]

We are interested in the phase behavior at 90 °C. A horizontal line drawn at $T$ = 90 °C intersects the melting curve at $r$ = 0.28. Therefore, at 90 C, we expect a homogeneous amorphous electrolyte below $r$ = 0.28. Above $r$ = 0.28, we expect semicrystalline behavior. The crystalline complex at this temperature is at $r$ = 0.5, *i.e.*, this complex has 2 ethylene oxide units and 1 LiTFSI molecule. This complex is often referred to as the $C_2$ complex. [113] We refer to it as $C_2$ ($r$ = 0.5).

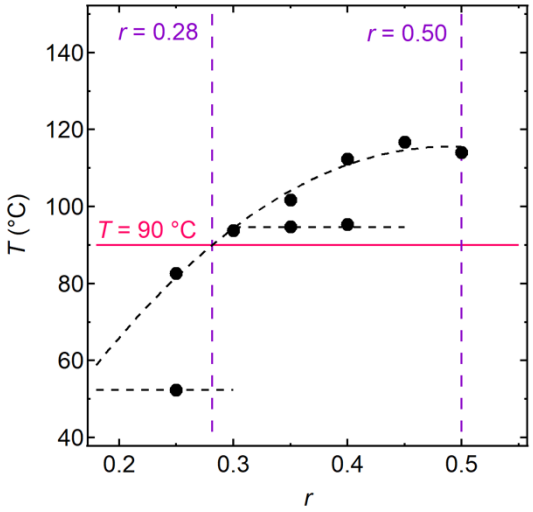


Figure 6.1. Differential scanning calorimetry results for electrolytes ranging from $r = 0.25$ to $r = 0.50$ at a heating rate of 1 °C per minute. Melting points are shown as black circles, with black dashed fit lines to guide the eye. A horizontal line at $T = 90$ °C and vertical lines at $r = 0.50$, the upper salt concentration, and $r = 0.28$, the intersection of the melting curve with $T = 90$ °C, are shown.

*6.4.2 Concentrated Solution Theory Parameters*

To study the electrochemical effects of this phase behavior, we begin by measuring the three transport properties required by Newman's concentrated solution theory. [29] The dependence of ionic conductivity, $\kappa$, current fraction, $\rho_+$, and salt diffusion coefficient, $D$ on salt concentration is shown in Figure 6.2a-c. This system has been studied previously at salt concentrations below $r = 0.30$ by Pesko *et al.*, and results from that study are reproduced here. [116] All data points below $r = 0.20$ are from Pesko *et al.* and all data points above $r = 0.30$ are from this work. The range of $0.20 < r < 0.30$ includes data from both studies to ensure continuity. All experiments were conducted at 90 °C.

The ionic conductivity, $\kappa$, measured using ac impedance spectroscopy, is shown as a function of $r$ in Figure 6.2a. As discussed elsewhere, [118] $\kappa$ is affected by both charge carrier concentration, which increases with increasing $r$, and polymer segmental motion, which slows with increasing $r$. Below $r = 0.30$, the data are fit to a functional form proposed by Mongcopa *et al.*, [118]

$$\kappa = k_0 e^{-\frac{r}{r_{max}}}, \quad (6.8)$$

where $k_0$ is a fit parameter ($k_0 = 0.582$ S/cm), and $r_{max}$ is the $r$ value at the conductivity maximum ($r_{max} = 0.075$). This is consistent with values reported elsewhere. [53] Above $r =$

0.30, however, the data are inconsistent with Equation 6.8. In this region, we use a simple linear function that is continuous with Equation 6.8 at $r = 0.30$:

$$\kappa = -0.00118r + 0.00067. \quad (6.9)$$

This change in conductivity behavior near the expected crystallization salt concentration of $r = 0.28$ supports a change in phase behavior.

Figure 6.2b shows the dependence of the current fraction, $\rho_+$, measured using the Bruce-Vincent method, [55,51] on salt concentration. The entire data set was fit to a 3rd order polynomial:

$$\rho_+ = -4.01r^3 + 6.80r^2 - 1.58r + 0.176\,. \quad (6.10)$$

The minimum in $\rho_+$ is consistent with that reported by others. [119] Figure 6.2c shows the dependence of the salt diffusion coefficient, $D$, measured using restricted diffusion, [56] on salt concentration. The entire data set was fit to a 4th order polynomial:

$$D = (-1.41 \times 10^{-5})r^4 + (1.59 \times 10^{-5})r^3 - (6.03 \times 10^{-6})r^2 + (7.28 \times 10^{-7})r + (4.00 \times 10^{-8})\,. \quad (6.11)$$

Figure 6.2d shows the open circuit potential of a concentration cell containing a reference electrolyte with $r = 0.06$ and an electrolyte of the studied $r$-value. As expected, the potential at $r = 0.06$ is zero. Below $r = 0.32$, the fit from previously-studied low-$r$ electrolytes,

$$U = 100. - 74.9m^{0.835}\,, \quad (6.12)$$

is used. The salt molality, $m$, is used instead of $r$ because these measurements are used to calculate $\frac{dU}{d\ln m}$, an important parameter in concentrated solution theory. Above $r = 0.32$, the value of $U$ plateaus at -290 ± 5 mV. These results are repeatable; at $r = 0.45$ and $r = 0.50$, multiple overlapping points appear at the same potential. If electrolytes above $r = 0.32$ behaved similarly to those at low $r$, one would expect the potential difference to continue to become more negative as the salt concentration grows increasingly different from $r = 0.06$. The plateau suggests portioning of the salt into two phases: if these coexisting phases were in equilibrium, then the salt chemical potential in the two phases would be identical and only the relative ratio of the two phases would change as a function of $r$ in the coexisting window. It is possible that the plateau is related to this, but there are two factors that we must acknowledge: (1) the coexisting crystalline and amorphous phases in polymeric systems are seldom in equilibrium, and (2) even for a one-phase

electrolyte, $U$ depends on both salt chemical potential and the transference number, according to Equation 6.13: [29]

$$\frac{dU}{d\ln m} = \frac{2RTt_-^0}{F}\left(1 + \frac{d\ln\gamma_{+-}}{d\ln m}\right), \quad (6.13)$$

where $R$ is the ideal gas constant, $t_-^0$ is the anion transference number relative to the solvent frame (or 1 - $t_+^0$), and $\gamma_{+-}$ is the mean molal activity coefficient of the salt ($1 + \frac{d\ln\gamma_{+-}}{d\ln m}$ is the thermodynamic factor, $T_f$). We note that rigorous expressions for the dependence of $U$ on $m$ for two-phase systems have not yet been derived. Based on our DSC results, one might intuitively expect the plateau in $U$ to occur in the coexistence window which begins at $r$ = 0.28. Our observation that the plateau is observed at $r$ = 0.32 is qualitatively consistent with this expectation and the difference between 0.28 and 0.32 may reflect contributions from the two factors identified above.

The coexistence of two phases explains the linearity of the ionic conductivity data at high salt concentrations: As the salt concentration increases above the point of phase separation, the composition of the two phases remains the same (and therefore retains the same ionic conductivity), and what changes is the volume fraction occupied by each phase. The conductivity is then a weighted average of the conductivity of each phase, resulting in a linear dependence of $\kappa$ on $r$.

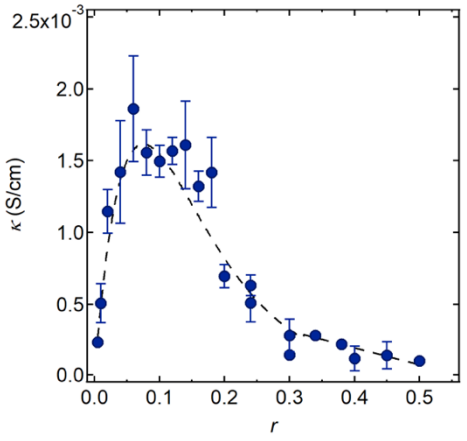


a.

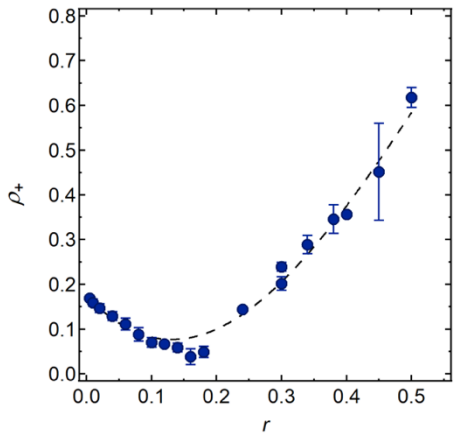


b.

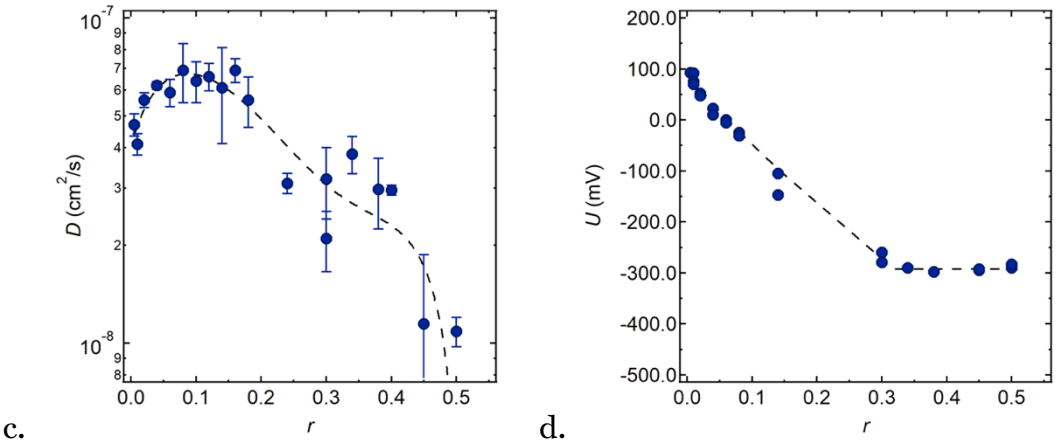


c. d.

Figure 6.2. (a) ionic conductivity, $\kappa$, (b) current fraction, $\rho_+$, (c) restricted diffusion coefficient, $D$, and (d) open circuit potential from concentration cells. All data below $r$ = 0.20 is reproduced from Pesko *et al.* [116], all data above $r$ = 0.30 is from this work, and the intermediate salt concentration range contains data from both studies. Error bars represent at least three repeats for (a-c); each point in (d) represents one concentration cell due to the large amount of material required to make a concentration cell. Dashed lines are given by Equations 6.8 and 6.9 (a), 6.10 (b), 6.11 (c), and 6.12 (d). Above $r$ = 0.28 in (d) a plateau at $U$ = -290 mV is shown. All experiments were conducted at 90 °C.

### *6.4.3 Optical Microscopy*

Figure 6.3 shows optical microscopy images taken at 90 °C of PEO / LiTFSI at $r$ = 0.30 and $r$ = 0.40. At $r$ = 0.30, the electrolyte is homogeneous and amorphous; the image shows only small patches of contrast which are due to instrument artifacts. At $r$ = 0.40, we clearly observe two phases: a crystalline phase at the center, surrounded by an amorphous phase. These results are consistent with previous microscopy studies. [114] Based on the results presented above, we propose that the amorphous region is at $r$ = 0.28, while the crystalline phase is at or above $r$ = 0.50 (2:1 EO:Li).

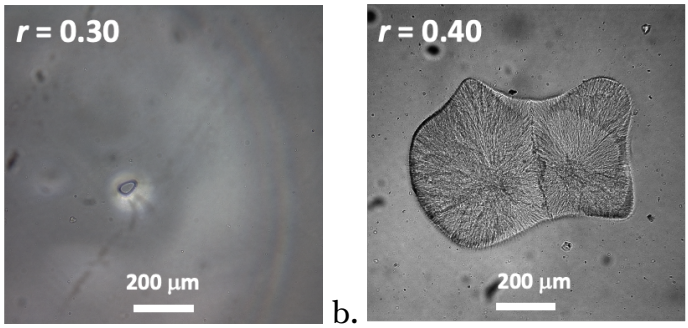


a. b.

Figure 6.3. Optical microscopy images taken at 90 °C of PEO / LiTFSI at $r$ = 0.30 and $r$ = 0.40.

*6.4.4 The Limiting Current*

To gain insight into the effects of the phase behavior indicated by Figures 6.1, 6.2, and 6.3, we measure the limiting current in high salt concentration PEO / LiTFSI electrolytes. Figure 6.4a shows the potential response of two cells with electrolytes at $r = 0.50$ to the application of the smallest current we can apply, $I = 1$ μA. We report current densities normalized by electrode electrochemically active area ($A$) and electrolyte thickness ($L$), $iL = IL/A$. In these two cells, which have slightly different thicknesses, $I = 1$ μA corresponds to $iL = 0.00068$ and 0.00069 mA/cm. Even at this very small current density, the cell potential does not reach a plateau, indicating that the limiting current is immeasurably small. Using Equation 6.2, we conclude that $r = 0.50$ is the solubility limit of the electrolyte. Optical micrographs of the $r = 0.50$ electrolyte are qualitatively similar to Figure 6.3b, indicating coexistence between an amorphous and a $C_2$ ($r = 0.5$) complex, suggesting that the coexisting phases at the solubility limit only differ in crystallinity (*i.e.* in the volume fraction of the crystalline, $C_2$ ($r = 0.5$) phase and the amorphous phase.

At salt concentrations in the vicinity of but below $r = 0.50$, we expect the limiting current to be finite. It will be reached when the salt concentration at the positive electrode approaches $r = 0.50$. Figure 6.4b shows the potential response of electrolytes at $r = 0.45$ to the application of current densities ranging from the lower limit up to $iL = 0.0031$ mA/cm. Up to $iL = 0.0014$ mA/cm, the potential plateaus, indicating that a steady-state salt concentration gradient has been reached, and the applied current density is below the limiting current. At $iL = 0.0031$, the potential diverges at long times, indicating that the applied current density is above the limiting current. We approximate the limiting current, $i_{\text{lim}}$, as the average of the highest accessible current and the lowest inaccessible current, such that for $r = 0.45$, $i_{\text{lim}}L = 0.0022$ mA/cm.

As the salt concentration decreases further, we expect the limiting current to increase. Figure 6.4c shows the response of cells with $r = 0.40$ to applied current. At $iL = 0.0018$ mA/cm, the potential reaches a plateau, indicating that the applied current is below the limiting current. However, when the current is increased to $iL = 0.0034$ mA/cm, the potential initially increases smoothly as expected before becoming jagged and ultimately falling to zero. These are standard signatures of cell failure due to a short circuit caused by lithium dendrite growth from the electrodes. Dendrite growth is increasingly prominent as the applied current increases, [120] which makes it difficult to observe the exponential potential divergence required to determine the limiting. Based on Figure 6.4c, we have a lower bound for the limiting current ($i_{\text{lim}}L > 0.0018$ mA/cm), but no upper bound.

To combat the effects of dendrite growth, in Figure 6.4d we use the same electrolyte, $r = 0.40$ in a cell with a thicker electrolyte ($L = 0.16$ cm). Because we normalize the current

density by $L$, $i_{lim}L$ does not depend on the thickness. However, we note that the time constant is proportional to $L^2$ (Equation 6.7), so the time required for the potential to plateau or diverge is higher in these experiments. The potential is also higher, because $E/L$, not $E$, is conserved. In Figure 6.4d, we observe that at $iL$ = 0.0035 mA/cm, the potential reaches a plateau, while at iL = 0.004 mA/cm and above, the potential diverges exponentially. We thus approximate $i_{lim}L$ as 0.00375 mA/cm.

As the salt concentration decreases further, we expect a higher limiting current, but dendrite growth becomes a more significant impediment. Measurements of limiting current below $r$ = 0.40 would require unwieldy material and time requirements, and we are thus unable to measure limiting currents at $r$-values that are high but below $r$ = 0.40. In the low-$r$ regime, measurements of limiting current become possible: Gribble *et al.* measured $i_{lim}L$ up to $r$ = 0.085. [57] At higher salt concentrations, they encountered similar dendrite-related issues to those reported here.

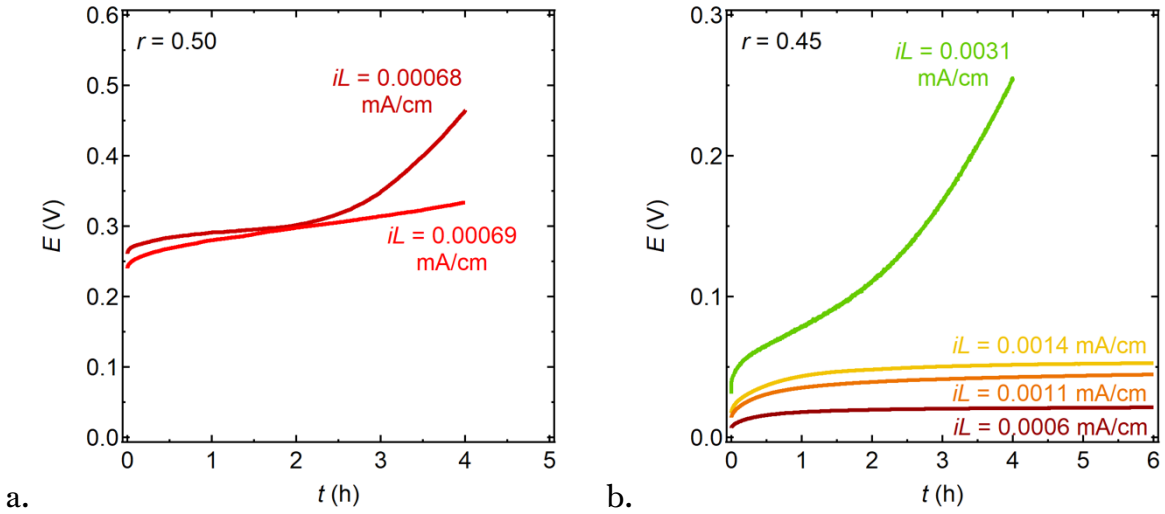

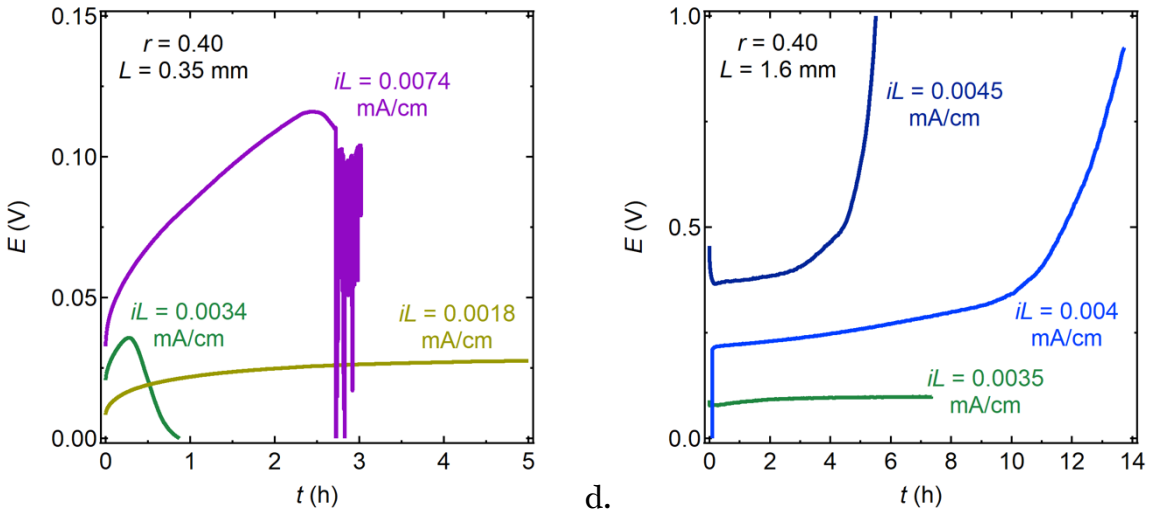


Figure 6.4. Cell potential responses to various applied current densities, $i$, normalized by cell thickness, $L$, in PEO / LiTFSI electrolytes with (a) $r = 0.50$, (b) $r = 0.45$, and (c-d) $r = 0.40$. In Figures 6.4a-c, a spacer thickness of 0.028 cm was used, while in Figure 6.4d, the spacer thickness was increased to $L = 0.16$ cm to combat cell failure due to dendrite growth.

*6.4.5 Concentrated Solution Theory and the Limiting Current*

Using concentrated solution theory, given the electrochemical and thermodynamic data reported in Figure 6.2, the salt concentration profile as a function of position in the cell ($x$) can be calculated. [47,121,122,123] To do this, we use Equation 6.14,

$$\int_{r\left(\frac{x}{L}=0\right)}^{r\left(\frac{x}{L}\right)} J_1(r)\,\mathrm{d}r = -\frac{iL}{F}\left(\frac{x}{L}\right), \qquad (6.14)$$

where $F$ is Faraday's constant and

$$J_1(r) = \kappa\left(\frac{\mathrm{d}U}{\mathrm{dln}m}\right)\left[r\left(1-\frac{1}{\rho_+}\right)z_+\nu_+F\right]^{-1}. \qquad (6.15)$$

In Equation 6.15, $z_+$ is the charge of the cation, and $\nu_+$ is the number of cations in one molecule of salt; both are unity in LiTFSI. $\frac{\mathrm{d}U}{\mathrm{dln}m}$ is calculated based on the data in Figure 6.2d. Because $\kappa$, $\frac{\mathrm{d}U}{\mathrm{dln}m}$, and $\rho_+$ all depend on $r$ through the fits given in Equations 6.8, 6.9, 6.10, and 6.12, $J_1$ is a complex function of $r$. By combining the fits for these parameters, we generate $J_1(r)$ as shown in Figure 6.5. Above $r = 0.28$, the value of $\frac{\mathrm{d}U}{\mathrm{dln}m}$ is taken to be its value at $r = 0.28$. This combination of functional forms is difficult to integrate

analytically, which is necessary to use Equation 6.14. We therefore fit the values of $J_1(r)$ to a polynomial, given by Equation 6.16:

$$J_1(r) = (-5.94 \times 10^{-4})r^8 + (1.36 \times 10^{-3})r^7 - (1.30 \times 10^{-3})r^6 + (6.75 \times 10^{-4})r^5 - (2.05 \times 10^{-4})r^4 + (3.64 \times 10^{-5})r^3 - (3.56 \times 10^{-6})r^2 + (1.52 \times 10^{-7})r + (6.53 \times 10^{-10}) . \quad (6.16)$$

The fit is shown by the dashed line in Figure 6.5.

To model the salt concentration profile, $r\left(\frac{x}{L}\right)$, at a given value of $iL$ and average salt concentration, $r_{avg}$, we start with a guess for the value of $r$ at positive electrode, $r\left(\frac{x}{L} = 0\right)$. Equation 6.14 is then used to generate an array of salt concentrations up to $r\left(\frac{x}{L} = 1\right)$. This array is then averaged; if the resulting value is higher than $r_{avg}$, the guess for $r\left(\frac{x}{L} = 0\right)$ is decreased and vice versa, and the process is repeated iteratively until the average of $r\left(\frac{x}{L}\right)$ converges to $r_{avg}$.

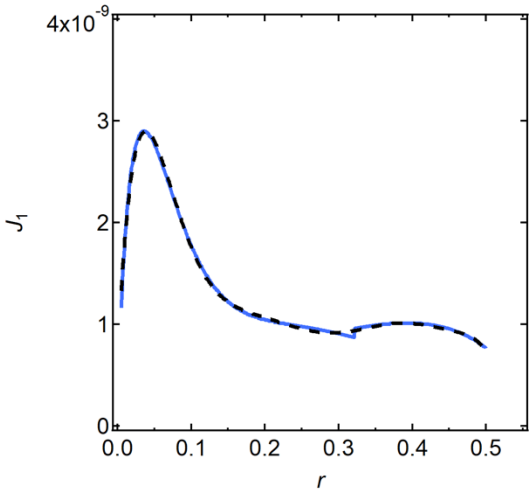


Figure 6.5. $J_1(r)$ based on Equation 6.14 and the functional forms for the transport parameters given by Equations 6.7-6.12 (blue) and the fit to $J_1(r)$ given by Equation 6.16 (dashed).

Figure 6.6a shows the theoretical salt concentration gradient generated using this method for $r_{avg} = 0.50$ and $iL = 0.00069$ mA/cm, matching the experimental conditions used in Figure 6.4a. The theoretical salt concentration gradient is very shallow, ranging from $r = 0.505$ at the positive electrode to $r = 0.495$ at the negative electrode. These calculations

indicate the magnitude of the salt concentration gradients that the cells discussed in Figure 6.4a could not reach.

To calculate the theoretical limiting current for $r = 0.45$ based on a solubility limit of $r = 0.50$, we model the concentration gradient at a variety of values of $iL$, and designate the value at which $r = 0.50$ at $\frac{x}{L} = 0$ to be $i_{\text{lim}}L$. Figure 6.6b shows the theoretical salt concentration profile for $r_{\text{avg}} = 0.45$ and $iL = 0.0087$ mA/cm, the theoretical $i_{\text{lim}}L$ from this method, in pink. In purple, we include the salt concentration profile for $iL = 0.0022$, the $i_{\text{lim}}L$ calculated based on the experimental data in Figure 6.6b. It reaches a maximum of only $r = 0.46$ at $\frac{x}{L} = 0$.

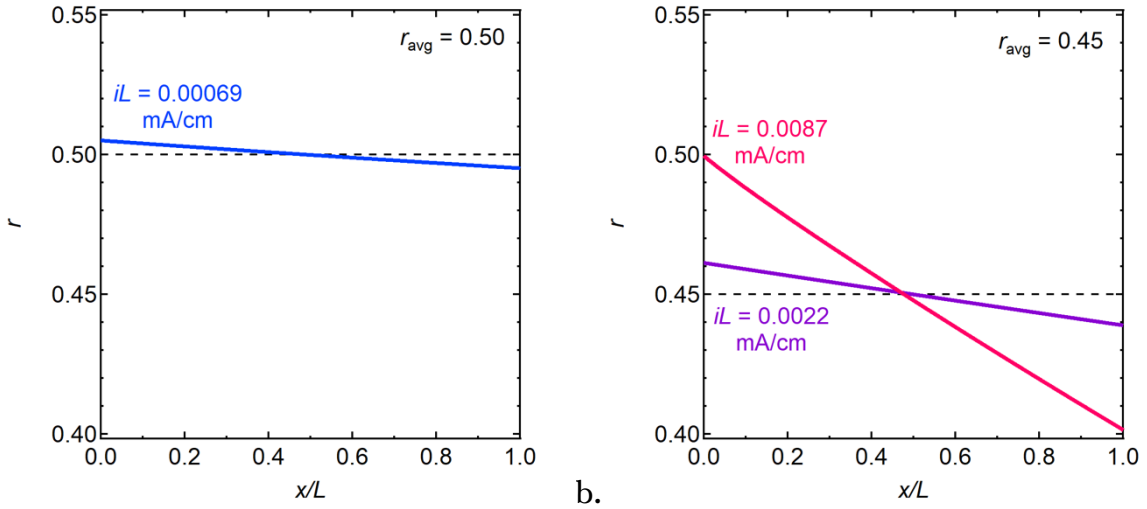


Figure 6.6. Theoretical salt concentration profiles calculated using Equation 6.14 for PEO / LiTFSI electrolytes with (a) $r_{\text{avg}} = 0.50$ and $iL = 0.00069$ mA/cm (blue) and (b) $r_{\text{avg}} = 0.45$ and $iL = 0.0022$ mA/cm (purple) and $iL = 0.0087$ mA/cm (pink). The average salt concentrations are given by a horizontal dashed line.

The theoretical limiting current based on a solubility limit of $r = 0.50$ was calculated for salt concentrations ranging from $r = 0.25$ to 0.50. The results are shown by the blue dashed line in Figure 6.7. Below $r = 0.25$, the salt concentration reaches zero at $\frac{x}{L} = 1$ while remaining below $r = 0.50$, and thus the mechanism for the limiting current is not expected to be related to the solubility limit. We have reported on this regime elsewhere, and include it in Figure 6.7 for completeness. Experimental data from Gribble *et al.* at low salt concentrations [57] and from this study for $r = 0.40$, 0.45, and 0.50 are included as black circles.

While there is qualitative agreement between theory and experiment at high salt concentrations, there are quantitative differences. The likely reason for this is the presence

of two coexisting phases in the regime of interest. To model this regime, we would need to characterize the ion transport properties of the two phases and expand the scope of concentrated solution theory. In addition, one would need to account for the non-equilibrium nature of the two phases. In general, one can conclude from the disagreement between theory and experiments in Figure 6.7 that ion transport through the phases in the vicinity of $r = 0.40$ is considerably slower than expected based on the measured transport parameters and thermodynamic factor.

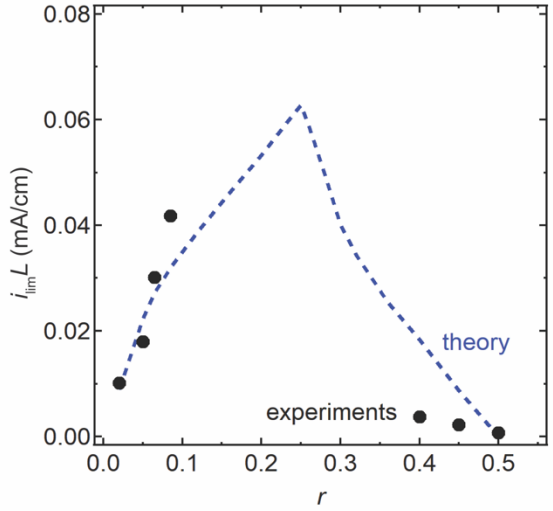


Figure 6.7. Below $r = 0.25$, Experimental $i_{\text{lim}}L$ data from Gribble *et al.* [57] (black circles) and $i_{\text{lim}}L$ predicted by concentrated solution theory and the salt concentration reaching zero at the negative electrode (blue dashed line). Above $r = 0.25$, experimental $i_{\text{lim}}L$ data based on Figure 6.4 (black circles) and $i_{\text{lim}}L$ predicted by concentrated solution theory and a salt solubility limit of $r = 0.50$ at the positive electrode (blue dashed line).

## 6.5 Conclusions

We report full electrochemical characterization of PEO / LiTFSI electrolytes above $r = 0.30$. Based on DSC, optical microscopy, ionic conductivity, and electric potential, we conclude that above $r = 0.28$, these electrolytes phase separate into an amorphous phase at $r = 0.28$ and a $C_2$ crystalline phase at $r = 0.50$. We measure the limiting current in high salt concentration electrolytes, and find that at $r = 0.50$, the limiting current is essentially zero, indicating a solubility limit has been reached. The limiting current increases with decreasing salt concentration down to $r = 0.40$. The experimental limiting currents do not match those predicted by concentrated solution theory, which we attribute to the fact that the theory does not account for the separation of the electrolyte into two distinct ion-transporting phases.

This suggests that concentrated solution theory cannot be applied to PEO / LiTFSI electrolytes above $r = 0.28$ until it is modified to account for coexisting conducting phases. This is relevant not only for electrolytes with an initial salt concentration above $r = 0.28$, but also to electrolytes at lower salt concentrations: when salt concentration gradients develop, if the salt concentration exceeds $r = 0.28$ at the salt-rich, positive electrode, the electrolyte is expected to phase separate. For practical applications, it is important to ensure that the electrolyte is single-phase at the maximum current. This value may be well below the limiting current.

## 6.6 Acknowledgements

The authors were supported by the Joint Center for Energy Storage Research (JCESR), an Energy Innovation Hub funded by the U.S. Department of Energy, Office of Science, Basic Energy Sciences, under Contract No. DEAC02-06CH11357. Work at Lawrence Berkeley National Laboratory was supported by the U.S. Department of Energy under Contract No. DE-AC02-05CH11231.

# Chapter 7: The Effect of Annealing on Grain Structure and Ionic Conductivity of Block Copolymer Electrolytes*

## 7.1 Abstract

Block copolymer electrolytes that microphase separate into rigid non-conducting domains and soft ion-conducting domains are known to exhibit stability against lithium metal anodes. In these systems, order is confined to grains with concomitant defects. When these electrolytes are annealed, the grain size typically increases, which is assumed in the literature to lead to a decrease in the ionic conductivity. In this work, we study the interplay between grain size and ionic conductivity using a block polymer electrolyte composed of a polystyrene (PS) block of molecular weight 19 kg/mol and a poly(ethylene oxide) (PEO) block of 20 kg/mol, mixed with lithium bis(trifluoromethanesulfonyl)imide (LiTFSI) salt at a variety of salt concentrations. The electrolytes have a lamellar morphology at all salt concentrations. At low salt concentrations, the average grain size before annealing is large and ionic conductivity decreases upon annealing. At high salt concentrations, however, the average grain size before annealing is small and ionic conductivity increases upon annealing.

## 7.2 Introduction

Block copolymer electrolytes are promising materials for rechargeable batteries with lithium metal anodes due to their ability to microphase separate into mechanically-rigid non-conducting domains and soft ion-conducting domains. [20] This enables independent control over the mechanical and electrical properties of the electrolyte. In microphase-separated block copolymers created in the absence of external fields, order is restricted to randomly-oriented grains, separated by grain boundaries and other defects. [124–127] While transport within coherently ordered grains has been modeled, [128,129] ion transport through a collection of grains is complex, as it depends on the nature of the defects between grains. [130,131] Simple theories such as effective medium theory proposed by Sax and Ottino assume that ion transport is independent of grain size. [128]

The grain structure of an ordered material is dependent not only on thermodynamic parameters such as temperature and composition but also on kinetic factors such as thermal history. Annealing block copolymer electrolytes can lead to grain growth due to processes such as defect annihilation. [132–134] There is, however, a limited understanding of the relationship between grain growth and molecular structure. For example, one might expect less grain growth in high molecular weight polymers due to entanglement effects and concomitant limitations on molecular mobility. To our knowledge, there is no

* This Chapter is adapted from Grundy, L. S.; Fu, S.; Galluzzo, M. D.; Balsara, N. P. **2022**, submitted.

systematic study of grain growth as a function of block copolymer molecular weight. Many more questions arise when one considers the relationship between grain growth and ionic conductivity. In a previous study on one electrolyte composed of polystyrene-*block*-poly(ethylene oxide) (SEO) mixed with lithium bis(trifluoromethane-sulfonyl)imide (LiTFSI) salt, it was found that the ionic conductivity decreased by a factor of 5 when the electrolyte was annealed. Small-angle X-ray scattering experiments indicated that the average grain size increased by a factor of 7 during annealing. [135] One possible explanation for this observation is that a collection of small randomly-oriented grains allows for a more direct path for ion transport than large randomly-oriented grains. In the latter case, one might anticipate the presence of large grains that are orthogonal to the direction of ion transport, and this may lead to less direct pathways between the electrodes. This explanation ignores the geometry of the defects and grain boundaries. [136] It is conceivable that some defects impede ion transport, while others may provide channels that enhance it. This has been observed in the literature: there is general agreement that decreasing the tortuosity of the path between electrodes increases conductivity. [131,137–139] In some cases, defects seem to enhance ionic conductivity, [135] while in others defects have been shown to decrease the ionic conductivity by blocking ion transport paths. [137,140] The result is that some work seeks to produce single-grain electrolytes, [138,140] while others seek to arrest coarsening to produce electrolytes with a grain size approaching zero. [141] Annealing may remove defects of either kind, or may also transform defects from one kind to the other. In this paper we attempt to shed light on the relationship between annealing and conductivity of block copolymer electrolytes.

We study a block copolymer electrolyte composed of a polystyrene (PS) block of molecular weight 19 kg/mol and a poly(ethylene oxide) (PEO) block of 20 kg/mol, mixed with lithium bis(trifluoromethanesulfonyl)imide (LiTFSI) salt at salt concentrations ranging from $r = 0.04$ to 0.22 lithium ions per ethylene oxide moiety. Previous work has shown that this copolymer is lamellar at all salt concentrations. [121] Over a broad range of salt concentrations, we find that the ionic conductivity decreases significantly during annealing, consistent with previous observations. [135,142] However, at high salt concentrations, ionic conductivity is unaffected by annealing. At the highest salt concentration studied, ionic conductivity increases during annealing. The presence of salt ions decreases molecular mobility, and thus one expects the average grain size to decrease with salt concentration. Our experimental observations are largely consistent with this expectation. We find that annealing samples with high salt concentrations leads to significant grain growth, but this is not accompanied by the expected decrease in ionic conductivity. This suggests that grain size is not the only parameter that affects conductivity; the nature of the defects must also be considered.

## 7.3 Experimental Methods

### *7.3.1 Materials*

This study uses a polystyrene-*block*-poly(ethylene oxide) (SEO) block copolymer with a polystyrene (PS) block of 19 kg/mol and a poly(ethylene oxide) (PEO) block of 20 kg/mol, and is denoted SEO(19-20). This polymer has been studied previously by Galluzzo *et al.* [121] The polymer was synthesized via anionic polymerization and purified and characterized as described in Teran *et al.* [14] and Hadjichristidis *et al.* [16] The electrolytes, SEO(19-20) mixed with lithium bis(trifluoromethanesulfonyl)imide (LiTFSI) salt, were prepared as described in Yuan *et al.* [143] In short, stock solutions of LiTFSI in THF and SEO in benzene were mixed to achieve the desired value of $r$ (Li ions per ethylene oxide moiety). Electrolytes were then lyophilized to remove the solvent. LiTFSI was purchased from Sigma-Aldrich and all solvents were purchased from Fisher Scientific. Electrolytes were stored and samples were prepared in an argon glovebox maintained at sub-ppm levels of $H_2O$ and $O_2$.

### *7.3.2 Ionic Conductivity Measurements*

SEO(19-20) samples for ionic conductivity measurements were prepared by pressing electrolytes into rubber spacers with an inner diameter of 3.18 mm and a thickness of 500 μm. Each spacer was placed between stainless steel electrodes of known thickness. The thickness was then measured using a micrometer to extract the exact electrolyte thickness, $L$. Nickel current collectors were attached, and the cell was sealed in polypropylene pouch material before being removed from the glovebox for testing.

Samples were attached to a heating stage initially at 90 °C and connected to a BioLogic VMP3 potentiostat. Ionic conductivity, $\kappa$, was measured using ac impedance spectroscopy with an amplitude of 80 mV and a frequency range of 1 MHz to 100 mHz. The data were fit to an equivalent circuit to extract the bulk resistance, $R_b$. Equation 7.1,

$$\kappa = \frac{L}{R_b A}, \qquad (7.1)$$

where $A$ is the electrochemically active area based on the spacer dimensions, was used to calculate $\kappa$. Impedance measurements were performed every 30 minutes during the following annealing procedure: cells were maintained at 90 °C for 40 hours, then 120 °C for 9 hours, and finally at 90 °C for 12 hours.

### *7.3.3 Small-Angle X-Ray Scattering (SAXS) Measurements*

SEO(19-20) samples for SAXS measurements were prepared by pressing electrolytes into rubber spacers with an inner diameter of 3.18 mm and a thickness of 0.072 cm. Kapton

windows of thickness 25 μm were affixed to each side of the spacer, and the samples were sealed in custom aluminum air-free sample holders. All SAXS experiments were performed at beamline 7.3.3 at the Advanced Light Source (ALS) at the Lawrence Berkeley National Laboratory [144] at an X-ray energy of 10 keV and an acquisition time of 10 seconds. During data acquisition, the sample temperature was controlled using a custom heating stage which was maintained at 90 °C for 16 hours, 120 °C for 23 hours, and 90 °C for 3 hours. Silver behenate was used to determine the beam center and sample-to-detector distance. 2D scattering patterns were collected with a Pilatus3 2M detector (Dectris Ltd.). Data were processed using PyFAI [46] and peak fitting was performed using lmfit. [145]

The thermal histories of the samples studied by SAXS and ac impedance were closely matched to enable cross-correlation between results obtained from these experiments.

## 7.4 Results and Discussion

### *7.4.1 Ionic Conductivity*

To test the effects of annealing on ionic conductivity, $\kappa$, in block copolymer electrolytes, SEO(19-20) / LiTFSI values were formulated at a variety of salt concentrations. Stainless steel symmetric cells were assembled, and ac impedance spectroscopy was performed every 30 minutes as the cells were annealed at 90 °C for 40 hours, 120 °C for 9 hours, and at 90 °C for 12 hours. In all cases, the ionic conductivity was constant with time during the first 90 °C step before the temperature was increased to 120 °C.

Figure 7.1a shows $\kappa$ versus $r$ at 90 °C at the end of the first annealing step. As a guide to the eye, a fit of the form

$$\kappa = a \cdot r \cdot e^{-b/r}, \qquad (7.2)$$

where $a$ and $b$ are fit constants, is included as a dotted line. In Figure 7.1a, $a = 0.0052$ and $b = 0.095$. The trend is consistent with descriptions elsewhere, [118] with $\kappa$ increasing with $r$ at low $r$ due to increasing charge carrier concentration, reaching a maximum at a value of $r = b$, and decreasing with $r$ at high $r$ due to decreasing segmental motion. Figure 7.1b shows $\kappa$ versus $r$ at 90 °C immediately after the decrease in temperature from 120 to 90 °C. The trend in ionic conductivity is similar to that shown in Figure 7.1a, but the values are quantitatively different due to the intervening 120 °C annealing step: in the fit to Equation 7.2, $a = 0.0033$ and $b = 0.117$. During the annealing step, the pre-factor $a$ decreased from 0.0052 to 0.0033, indicating that the ionic conductivity has generally decreased. However, the salt concentration at which the conductivity is maximized shifted

from $r$ = 0.095 to 0.117, suggesting that this decrease is not uniform with salt concentration, but instead is more pronounced at lower salt concentrations.

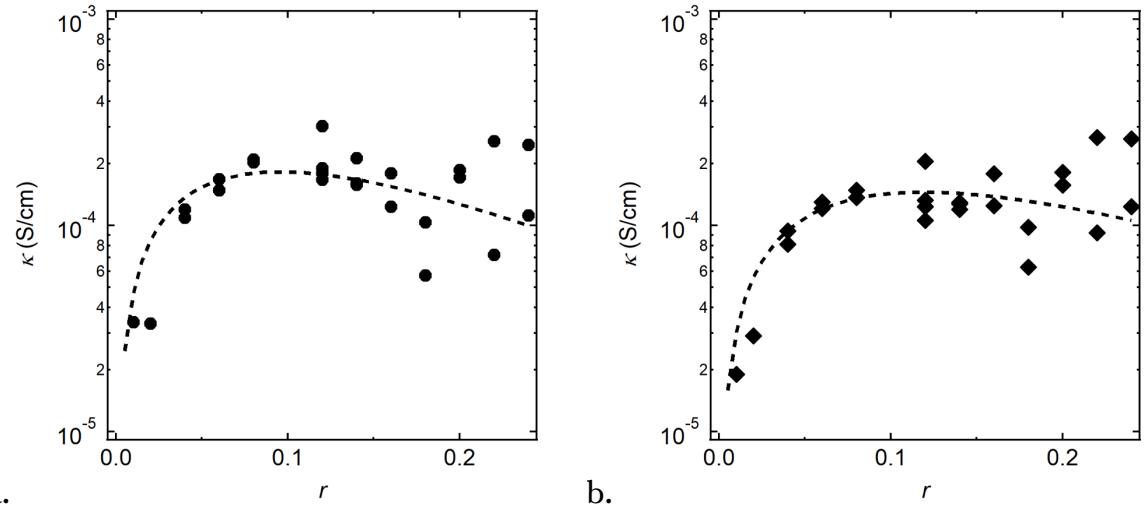


Figure 7.1. (a) Ionic conductivity, $\kappa$, measured after equilibration at 90 °C before and (b) after the 120 °C annealing step. In both Figures, the dashed line represents a fit to Equation 7.2.

Figure 7.2 shows the percent change in conductivity after *versus* before the 120 °C annealing step (*i.e.* From Figure 7.1a to Figure 7.1b). At low salt concentrations, the ionic conductivity decreases after the annealing step. This is consistent with the expectation that annealing causes an increase in grain size, which decreases the conductivity. However, at high salt concentrations, the percent change in conductivity is approximately zero. This could imply that the grains do not grow during the annealing step, or that the grain growth does not lead to an increase in conductivity.

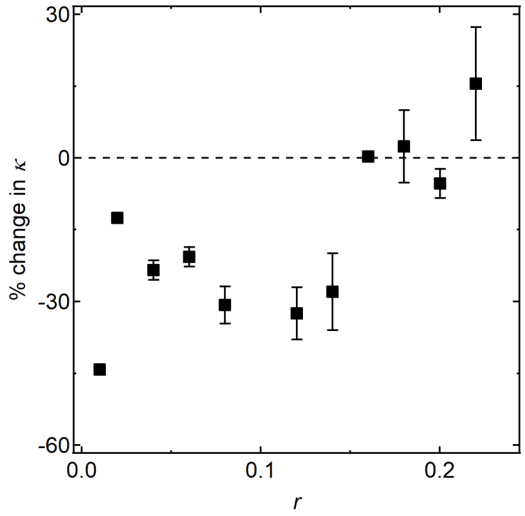


Figure 7.2. The percent change in ionic conductivity from Figure 7.1a to Figure 7.1b (after *versus* before the 120 °C annealing step)

To further investigate the effect of annealing on ionic conductivity, we examine the time-dependent ionic conductivity values during the annealing step. Figure 7.3 shows representative conductivity measurements as a function of time for low salt concentration samples at $r$ = 0.04, 0.08, 0.12, and 0.14. The conductivity increases sharply upon the temperature increase from 90 to 120 °C, decreases during the annealing step, and returns to a lower value than pre-annealing upon the temperature decrease back to 90 °C. The sharp increases and decreases in conductivity following temperature changes are expected, as conductivity is known to increase with increasing temperature. [146–148]

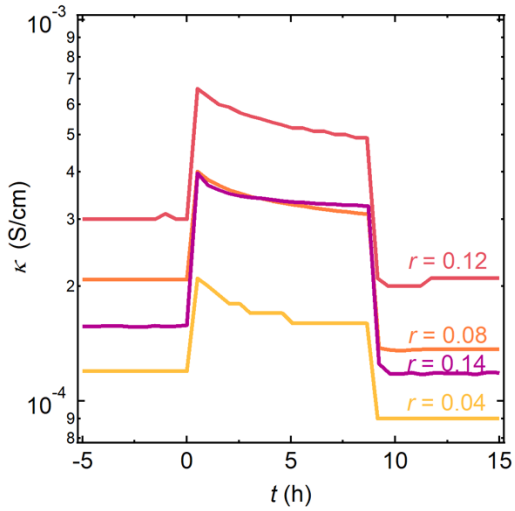


Figure 7.3. Representative conductivity vs time data for low concentration samples. $t$ = 0 is set to be the beginning of the 120 °C annealing step.

Figure 7.4 shows representative conductivity measurements as a function of time for high salt concentration samples at $r$ = 0.16, 0.18, and 0.22. The conductivity increases sharply upon the temperature increase from 90 to 120 °C at $t$ = 0 h, remains relatively flat during the annealing step, and returns to approximately its pre-annealing value upon the temperature decrease back to 90 °C at $t$ = 9 h.

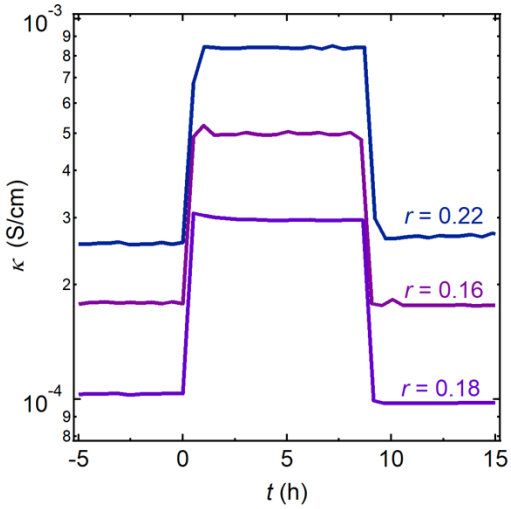


Figure 7.4. Representative conductivity *versus* time data for high concentration samples. The temperature is initially at 90 °C, increases to 120 °C at $t$ = 0 h, and decreases to 90 °C at $t$ = 9 h.

*7.4.2 Small Angle X-Ray Scattering (SAXS)*

If grain growth during the annealing step is the primary contributor to the changes in conductivity, one would conclude that the grain size must increase during the annealing step for low salt concentration samples, resulting in a decrease in conductivity, while remaining constant for the high salt concentration samples. To see whether this is the case, we use small-angle X-ray scattering (SAXS). Samples at $r$ = 0.04, 0.08, 0.12, 0.14, 0.16, 0.18, and 0.22 were exposed to a similar annealing process as that described above: 90 °C for 40 hours, 120 °C for 23 hours, and then 90 C for 3 hours. The times for the first two annealing steps were extended to ensure that the samples were allowed to fully equilibrate before the next step. During annealing, SAXS scans at multiple positions were acquired for each sample.

This polymer is lamellar at all salt concentrations, [121] so we focus only on the primary scattering peak. The peak was fit to a pseudo-Voigt model, from which the location of the primary scattering peak, $q^*$, and the full width at half-maximum, FWHM, were extracted.

The time-dependence of the domain spacing, $d$, was extracted from the scattering data using Bragg's law, [28]

$$d = \frac{2\pi}{q^*}. \qquad (7.3)$$

and the results are shown in Figure 7.5. To focus on the changes during the 120 °C annealing step, and for comparison with the conductivity data reported above, we omit the time-dependent data during the first 90 °C annealing step; the full time-dependent data can be found in Appendix A7. As reported elsewhere, $d$ increases with increasing salt concentration as the added salt swells the PEO-rich domains. [121] Figure 7.5b shows the percent change in $d$ at 90 °C before and after the annealing step. Annealing has little effect on $d$; the percent change in $d$ is 5.3% or less at all salt concentrations.

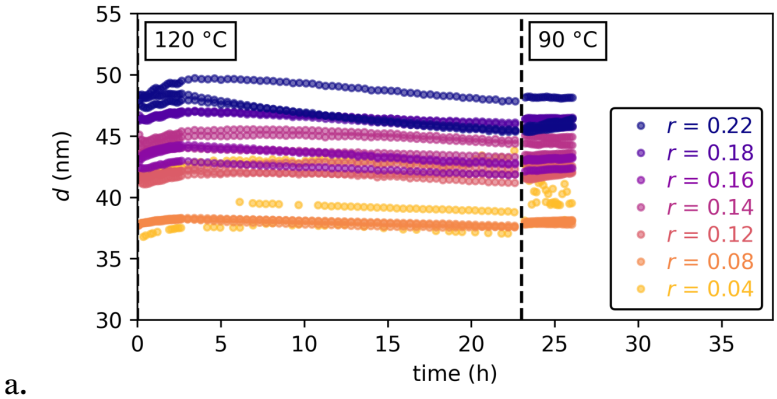


a.

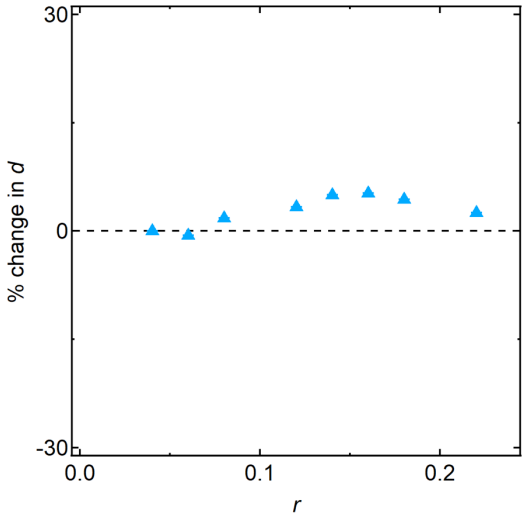


b.

Figure 7.5. (a) Domain size ($d$) as a function of time during annealing for different salt concentrations ($r$ = Li / EO) of SEO(19-20) / LiTFSI electrolytes. Low salt

concentrations are shown in yellow and orange, and high salt concentrations are shown in purple and blue. (b) The percent change in the domain spacing at 90 °C after *versus* before the 120 °C annealing step.

According to the Scherrer equation,[149] the grain size can be approximated as

$$L = \frac{2\pi K}{\text{FWHM}}, \quad (7.4)$$

where $K$ is a constant that we take to be 0.93.[150] Figure 7.6a shows this value as a function of time and salt concentration during the annealing process obtained at specific positions in the SAXS samples. In most cases, $L$ increases with time. The exception is one position on the $r = 0.04$ sample, where $L$ decreases with time. At the other positions on this sample, however, $L$ also increases with time, such that on average the change in $L$ is positive for all samples (see Figure 7.8). Figure 7.6b shows the values of $L$ from Figure 7.6a normalized by their value at the start of the 120 °C annealing step ($t = 0$). Based on Figure 7.6b, the grain growth is more pronounced in the high-$r$ samples (purple and blue traces) then in the low-$r$ samples (yellow and orange traces). If grain growth were the primary factor in conductivity changes during annealing, one would expect the conductivity to decrease significantly in the high-$r$ samples, while staying approximately the same in the low-$r$ samples. However, based on Figure 7.2, the opposite is true.

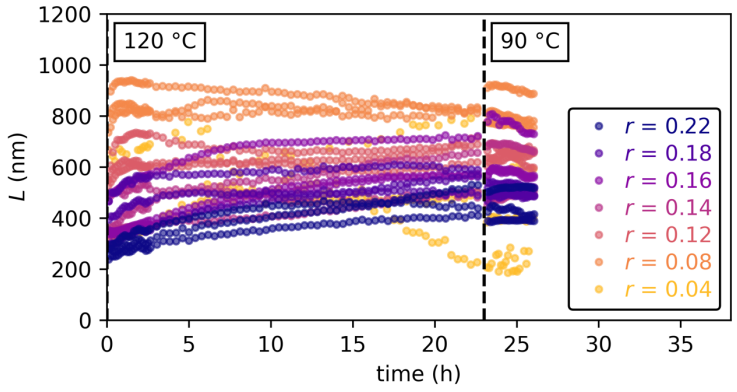


a.

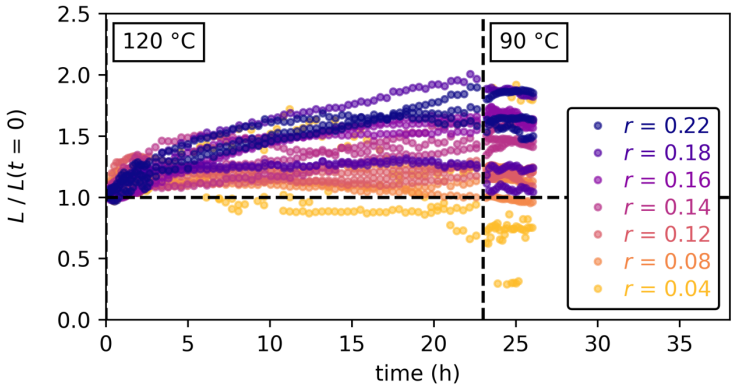


b.

Figure 7.6. (a) Average grain size, $L$, as a function of time during the annealing process, and (b) $L$ normalized by its value at the start of the 120 °C annealing step ($t$ = 0) for different salt concentrations. The color scheme matches that of Figure 7.5.

### *7.4.3 Combining Changes in Ionic Conductivity and Grain Size*

Given the time-dependent data for both grain size and ionic conductivity, we examine the relationship between the two over the first 9 hours of the 120 °C annealing step. Conductivity data was interpolated to extract conductivity values at the timepoints at which SAXS data was acquired. Figures 7.7a-g show the percent change in $\kappa$ *versus* the percent change in $L$ over time (blue is immediately after the increase to 120 °C, and dark red is after 9 hours at 120 °C) for each salt concentration. If decreases in conductivity were attributable to increases in $L$, one would observe a diagonal line with a negative slope initially (blue time points) at zero percent change $L$ and $\kappa$, with the percent change $\kappa$ steadily becoming more negative as the percent change $L$ increases (red time points). This behavior is observed only in the samples at $r$ = 0.04 and 0.14. It is also observed at early times for $r$ = 0.08 and 0.12, but after less than 1 hour, the grain size in these samples stabilizes while the ionic conductivity continues to decrease. At high salt concentrations, $r$ = 0.16, 0.18, and 0.22, very little change in ionic conductivity is observed despite significant increases in the grain size.

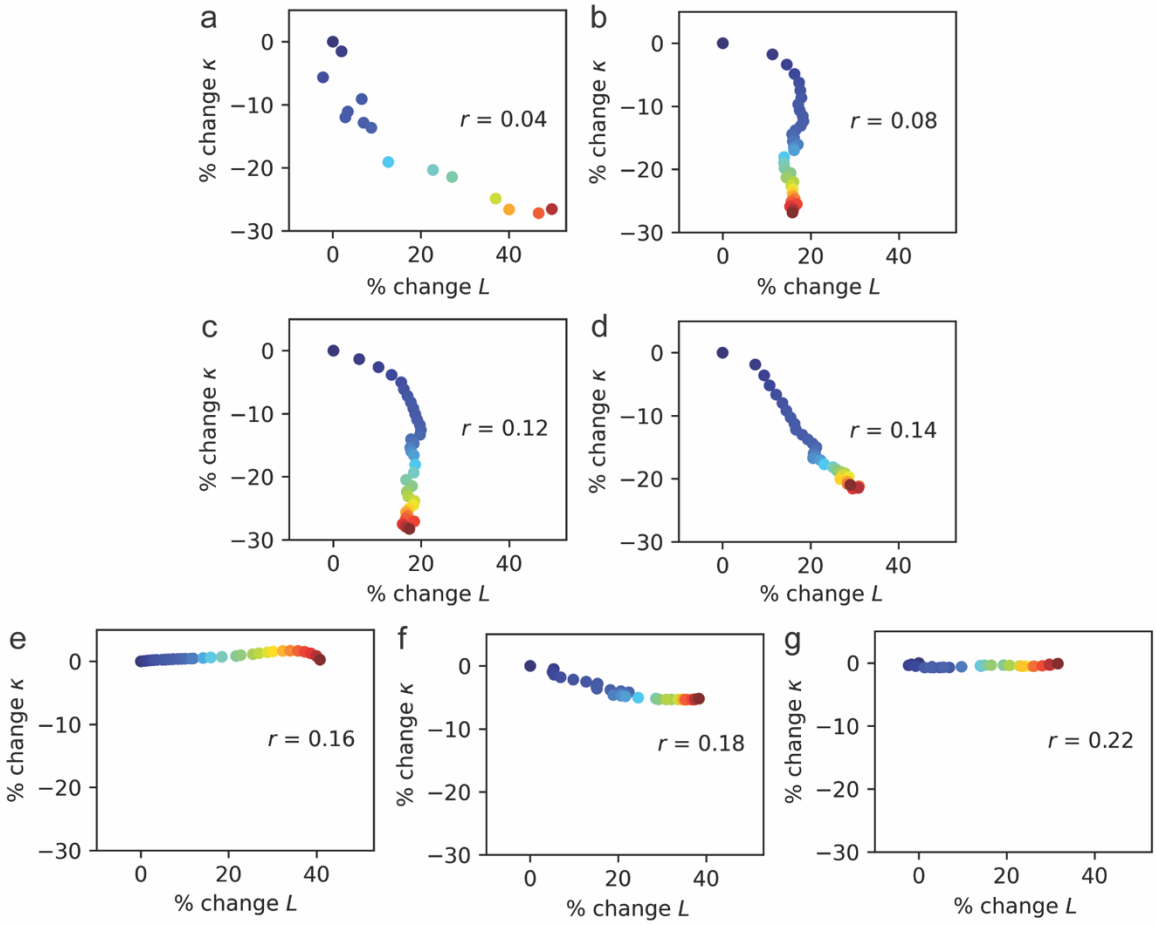


Figure 7.7. Percent change in ionic conductivity, $\kappa$, versus percent change in average grain size, $L$, during the 120 °C annealing step, with time indicated by the color: data transitions from blue at $t = 0$ h, immediately after temperature increase from 90 to 120 °C, to red after 9 hours at 120 °C.

The percent change in average grain size, $L$, after *versus* before the 120 °C annealing step is shown in Figure 7.8a, with the percent change data from Figures 7.2 and 7.5b included for comparison. $L$ increases at all salt concentrations, increasing more in the high-$r$ samples. To directly compare changes in ionic conductivity, $\kappa$, to changes in $L$, the percent changes are plotted against each other in Figure 7.8b, with the salt concentration of each point indicated by the color, corresponding to the color scheme in Figures 7.5 and 7.6 (low salt concentrations are shown in yellow and orange, transitioning to purple and blue at higher salt concentrations). The smallest increases in $L$, at low $r$, correspond to the largest decreases in $\kappa$, while the largest increases in $L$, at high $r$, correspond to almost no change in $\kappa$, or even, at $r = 0.22$, a slight increase in $\kappa$. If grain growth leading to a decrease in conductivity were the main factor in changes to the ionic conductivity, one

would expect the percent change in $\kappa$ to be negative at all salt concentrations, and monotonically decreasing, instead of increasing, with the percent change in $L$.

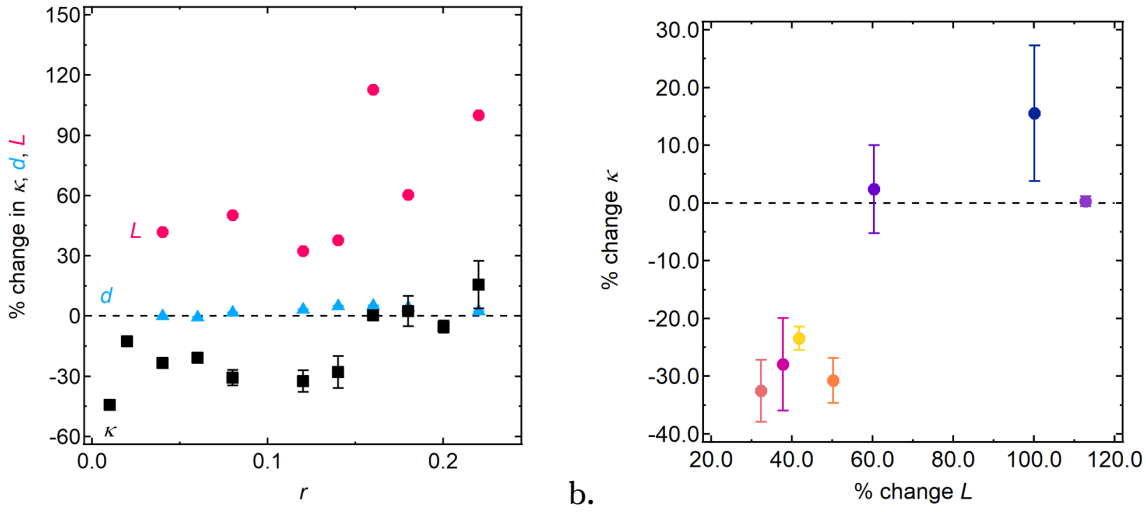


Figure 7.8. (a) Percent change in ionic conductivity, $\kappa$ (black squares), domain spacing, $d$ (blue triangles), and $L$ (pink circles) at 90 °C after *versus* before annealing at 120 °C. (b) Percent change in $\kappa$ *versus* percent change in $L$ after *versus* before annealing at 120 °C. Different salt concentrations are represented by different colored points, with the color scheme matching that of Figure 7.5 and 7.6: low salt concentrations are shown in yellow and orange ($r$ = 0.04 is yellow, 0.08 is orange, 0.12 is coral, and 0.14 is magenta), and high salt concentrations are shown in purple and blue ($r$ = 0.16 is violet, 0.18 is indigo, and 0.22 is navy).

In search of alternate explanations for our observed behavior, we plot the percent change in $\kappa$ *versus* the initial average grain size at the start of the annealing step, $L(t = 0)$ (Figure 7.9). We observe that when the grain size is initially large, the conductivity decreases upon annealing, suggesting that annealing annihilates defects that assist in ionic conductivity, perhaps by decreasing the path length. When the average grain size is initially small, however, the conductivity increases upon annealing, suggesting that annealing annihilates defects that impede ionic conductivity, perhaps by hampering ion transport between grains. At intermediate initial average grain size, the effect of annealing depends on the salt concentration: at low salt concentrations, annealing decreases the ionic conductivity, while at higher salt concentrations, annealing does not change the ionic conductivity significantly. This suggests that the initial grain size affects the relationship between average grain size and ion transport.

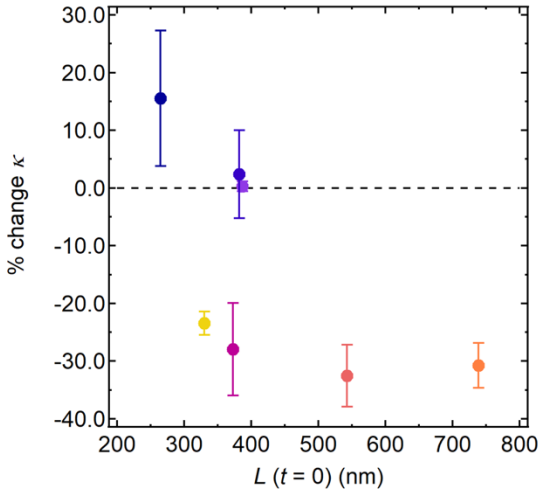


Figure 7.9. Percent change in $\kappa$ *versus* the initial value of $L$ at the start of the annealing step. The color scheme matches that in Figure 7.8b.

## 7.5 Conclusions

Block copolymer electrolytes are commonly annealed at high temperature prior to testing and use in order to obtain a reproducible grain structure. In general, annealing is expected to increase the grain size, which, based on previous work, [135] is expected to lead to a decrease in the ionic conductivity. In this work, we study the effect of a 120 °C annealing step on the conductivity of a symmetric polystyrene-*block*-poly(ethylene oxide) block copolymer of total molecular weight 39 kg/mol mixed with LiTFSI salt at salt concentrations ranging from $r = 0.04$ to 0.22 lithium ions per ethylene oxide moiety. We find that at low salt concentrations, the ionic conductivity decreases by approximately 30% during annealing at 120 °C, while at high salt concentrations the ionic conductivity does not change significantly or increases during annealing. Using SAXS, we observe that the average grain size, $L$ prior to annealing, proportional to the inverse of the full width at half-maximum of the primary scattering peak, of high salt concentration samples is significantly smaller than that of low salt concentration samples. Annealing low salt concentration samples results in a modest change in grain size (an increase between 30 and 50%) and a significant decrease in conductivity. At high salt concentrations, annealing results in a large increase in grain size (up to 113%) but conductivity remains largely unaffected. At the highest salt concentration, annealing increases conductivity by 15% in spite of a 100% increase in grain size. It is evident that the effect of annealing on ion transport is not a simple function of grain growth, but in fact depends on the initial average grain size and the character of the defects between grains. Further work quantifying the role of specific defects on ion transport in block copolymer electrolytes seems warranted.

## 7.6 Acknowledgements

The authors were supported by the Joint Center for Energy Storage Research (JCESR), an Energy Innovation Hub funded by the U.S. Department of Energy, Office of Science, Basic Energy Sciences, under Contract No. DEAC02-06CH11357. This research was completed at beamline 7.3.3 of the Advanced Light Source, which is supported by the Director of the Office of Science, Office of Basic Energy Sciences, of the U.S. Department of Energy under Contract No. DE-AC02-05CH11231.

# Chapter 8: Detection of the Order-to-Disorder Transition in Block Copolymer Electrolytes Using Quadrupolar $^{7}$Li NMR Splitting*

## 8.1 Abstract

The order-to-disorder transition temperature ($T_{ODT}$) in a series of mixtures of polystyrene-*b*-poly(ethylene oxide) (SEO) and lithium bis(trifluoromethane-sulfonyl)imide (LiTFSI) salt is identified by the disappearance of a quadrupolar $^{7}$Li NMR triplet peak splitting above a critical temperature, where a singlet is observed. The macroscopic alignment of ordered domains required to produce a quadrupolar splitting occurs due to exposure to the NMR magnetic field. Alignment is confirmed using small-angle X-ray scattering (SAXS). The $T_{ODT}$ determined by NMR is consistent with that determined using SAXS.

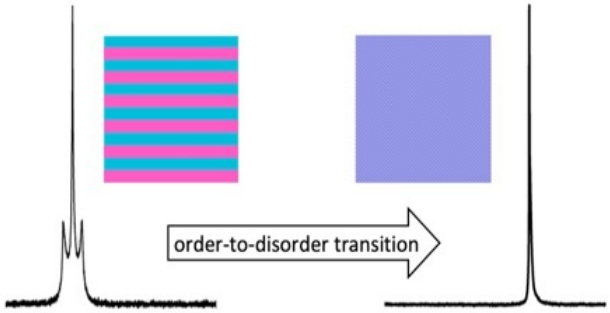


Figure 8.1. Illustration of the disappearance of quadrupolar triplet peak splitting upon disordering of an aligned lamellar block copolymer electrolyte.

## 8.2 Introduction

### *8.2.1 Order-to-Disorder Transitions in Block Copolymer Electrolytes*

Block copolymers (with or without salt added) self-assemble into a variety of ordered phases. [12,13] At sufficiently high temperatures, entropy dominates, resulting in the formation of a disordered phase. Established experimental approaches for locating the order-to-disorder transition temperature ($T_{ODT}$) include small-angle X-ray scattering (SAXS), [151,152] small-angle neutron scattering (SANS), [153] birefringence, [154] and rheology. [155,156,157,158] There is increasing interest in the properties of mixtures of block copolymers

* This Chapter is adapted from Grundy, L. S. *et al.* Detection of the Order-to-Disorder Transition in Block Copolymer Electrolytes Using Quadrupolar $^{7}$Li NMR Splitting. *ACS Macro Letters* **2019**, *8* (2), 107-112. [231]

and lithium salts due to their relevance in lithium batteries. Locating the $T_{ODT}$ in these systems is important, as microscopic morphology has a profound impact on bulk properties such as mechanical rigidity and ionic conductivity. [27,159]

### *8.2.2 $^{7}$Li NMR Spectroscopy of Block Copolymer Electrolytes*

While nuclear magnetic resonance spectroscopy (NMR) is often used to study the chemical environment of lithiated compounds, it is rarely used to study block copolymer electrolyte systems. Both naturally occurring lithium isotopes, $^{6}$Li and $^{7}$Li, can be observed using NMR, but $^{7}$Li is chosen most commonly due to its higher natural abundance and NMR sensitivity. [160] Several researchers have used NMR to study these polymer electrolytes. [160–164] In these studies, the NMR peak corresponding to lithium appears as a single line. While lithium spin-spin (scalar *J* or dipole-dipole *D*) coupling to other NMR-active nuclei such as protons ($^{1}$H) or fluorine ($^{19}$F) is possible, [165,166] to our knowledge, lithium splitting due to such coupling has never been observed in polymeric systems. Previous studies of lithium cations in polymer electrolytes report only $^{7}$Li line broadening due to heteronuclear dipolar interactions. [167]

The quadrupolar moment of the spin-3/2 $^{7}$Li nucleus enables splitting of the NMR signal into a triplet when the lithium atoms experience a non-zero average electric field gradient (EFG). [26] ($^{19}$F, however, is spin-1/2, and therefore cannot exhibit quadrupolar splitting.) A triplet peak splitting will occur only when lithium cations are sampling an EFG environment with an overall degree of alignment, as in a macroscopically aligned sample. It is therefore not surprising that in the vast majority of experiments, $^{7}$Li spectra appear as single peaks. However, recent work has demonstrated that strong magnetic fields can uniformly align the domains of block copolymers, allowing for a higher degree of average orientation. [168] Earlier work has shown that quadrupolar splitting can be used to investigate magnetic-field-aligned biological membrane bicelles [169] and alignment in polymers using labeled probe molecules, [170] including $D_2O$-swollen block copolymers aligned by a casting process, [171] but never with lithium ions in block copolymers. In previous work on aligned polymer electrolytes with magnetic fillers, quadrupolar interactions have been shown only to cause line broadening, due to a broad distribution in domain orientation. [162]

Herein, we report the presence of quadrupolar $^{7}$Li triplet spectra in lamellae-forming mixtures of block copolymers and a lithium salt oriented through exposure to the NMR magnetic field. The splittings disappear when the sample is disordered, indicating that NMR can be used to detect the order-to-disorder transition.

## 8.3 Results and Discussion

### *8.3.1 SAXS Characterization of the Order-to-Disorder Transition in SEO Electrolytes*

SAXS profiles of three electrolytes at selected temperatures are shown in Figure 8.2. The scattering from these samples was isotropic, as is typically the case for block copolymers in the absence of external fields. In Figure 8.2a, we show SAXS profiles of polystyrene-*b*-poly(ethylene oxide) (SEO) with a molecular weight of 3.3 kg mol$^{-1}$ of polystyrene (PS) and 2.6 kg mol$^{-1}$ of poly(ethylene oxide) (PEO) mixed with a lithium bis(trifluoromethanesulfonyl)imide (LiTFSI) salt at a concentration of 0.02 lithium ions per ethylene oxide (EO) moiety (SEO(3.3-2.6) $r$ = 0.02). At 75 and 89 °C, we see two scattering peaks, a sharp primary scattering peak at $q = q^* = 0.60$ nm$^{-1}$ and a higher order scattering peak at $q = 2q^*$. This indicates the presence of a lamellar phase in this temperature range. At 99 and 103 °C, we observe a single broad scattering peak due to disordered concentration fluctuations. [12,172] The scattering profile at 94 °C is a superposition of a broad peak and a narrow peak, indicating coexistence of ordered and disordered phases. This coexistence is required by the Gibbs phase rule. [173,174] Qualitatively similar results are observed for the other two electrolytes, SEO(1.7-1.4) $r$ = 0.075 (Figure 8.2b) and SEO(1.5-2.0) $r$ = 0.125 (Figure 8.2c). Based on previous studies, [14] we can assert that the ordered phases are lamellar. (The higher order peaks are outside the $q$ window of our experiment.) In these experiments, we also observe coexistence of ordered and disordered phases. In Figure 8.3, we plot the full-width at half-maximum (FWHM) of the primary scattering peak as a function of temperature. In cases where broad and sharp peaks coexist, we fit two curves and report the FWHM of the sharp peak. The temperature change that results in complete disordering of the partially ordered sample is used to define the $T_{ODT}$. For SEO(3.3-2.6) $r$ = 0.02, $T_{ODT}$ = 96.5 ± 3 °C; for SEO(1.7-1.4) $r$ = 0.075, $T_{ODT}$ = 114 ± 2 °C; and for SEO(1.5-2.0) $r$ = 0.125, $T_{ODT}$ = 114 ± 2 °C.

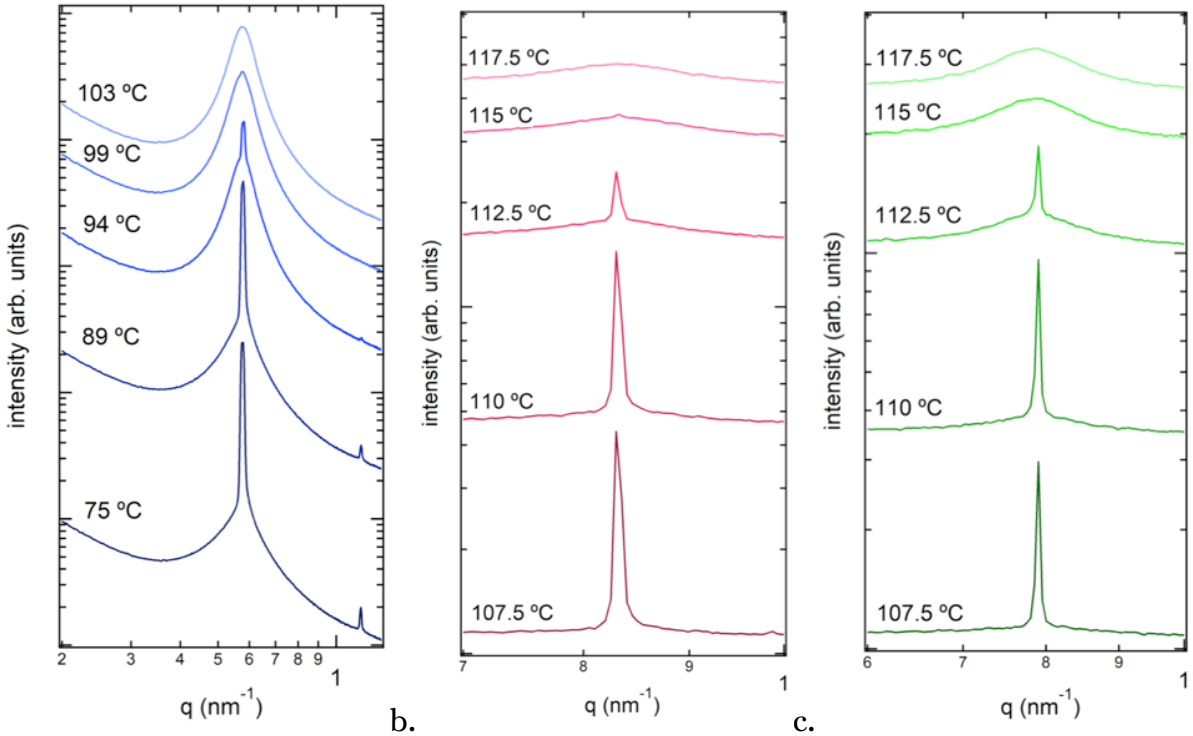


a. b. c.

Figure 8.2. SAXS profiles at a range of temperatures for SEO(3.3-2.6) $r$ = 0.02 (a), SEO(1.7-1.4) $r$ = 0.075 (b), and SEO(1.5-2.0) $r$ = 0.125 (c).

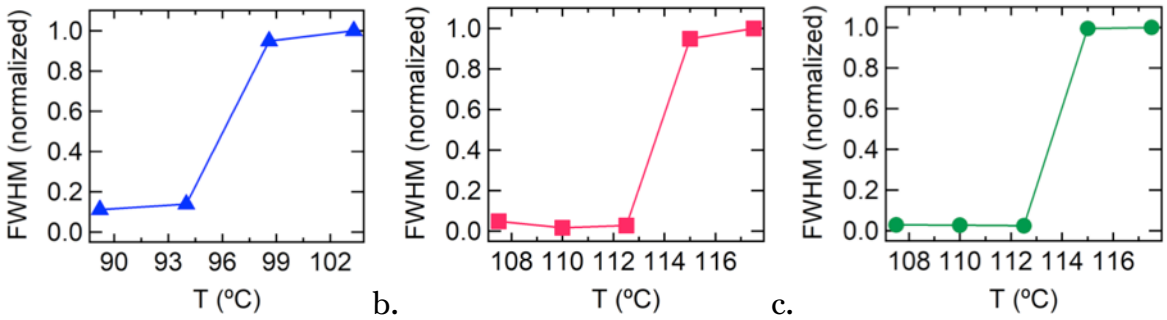


a. b. c.

Figure 8.3. Plots of the full-width at half-maximum (FWHM) of the primary scattering peak at a range of temperatures for SEO(3.3-2.6) $r$ = 0.02 (a), SEO(1.7-1.4) $r$ = 0.075 (b), and SEO(1.5-2.0) $r$ = 0.125 (c).

### *8.3.2 $^{7}$Li NMR Peak Splitting in SEO Electrolytes*

The $^{7}$Li NMR spectrum of SEO(1.7-1.4) $r$ = 0.075 taken at 90 °C on a 14.1 T instrument is shown in Figure 8.4a. The spectrum contains a primary peak and two satellites spaced 1.8 ppm (420 Hz) apart. In principle, this splitting could be due to indirect spin-spin coupling of lithium to fluorine ($^{19}$F; $I$ = 1/2), the only significantly naturally abundant NMR-observable nucleus in the anion. We therefore performed $^{19}$F-decoupled $^{7}$Li NMR, [32] and the resulting spectrum is shown in Figure 8.4b. The persistence of a triplet in this

spectrum indicates that the splitting seen in Figure 8.4a is not due to spin-spin coupling of lithium to fluorine.

Quadrupolar splitting is the most likely explanation for the presence of a triplet in the $^{7}$Li NMR spectrum, as $^{7}$Li is a spin $I = 3/2$ nucleus with a moderate quadrupole moment (-40.1 millibarn). [31] We tested this hypothesis by measuring the $^{6}$Li spectrum of SEO(1.7-1.4) $r = 0.075$, as $^{6}$Li is a spin $I = 1$ nucleus with a very weak quadrupole moment (-0.808 millibarn). If heteronuclear coupling were responsible for the splitting, the $^{6}$Li spectrum would also show a triplet with a spacing of 1.8 ppm (160 Hz), while if residual quadrupolar splitting were the cause, such a triplet would not appear in the $^{6}$Li spectrum. The result of this experiment is shown in Figure 8.4c, where only a single peak is observed. In principle, the spin $I = 1$ $^{6}$Li nucleus should exhibit doublet quadrupolar splitting, but the low quadrupole moment of $^{6}$Li causes the predicted splitting to be 26 Hz (0.36 ppm) in this case, [26] which is smaller than the spectral resolution of the measurement. Additional confirmation of our conclusion based on the $^{19}$F-decoupled $^{7}$Li and the $^{6}$Li NMR spectra can be found in the peak integrals of the $^{7}$Li spectrum: triplets caused by spin-spin coupling have a peak ratio of 1:2:1, while those caused by quadrupolar splitting have a ratio of 3:4:3. [8] When the peaks in Figure 8.4a are fit to Lorentzian curves and integrated, they have a ratio of 3.0:4.0:3.3, further indicating that the origin of the triplet peak pattern is quadrupolar.

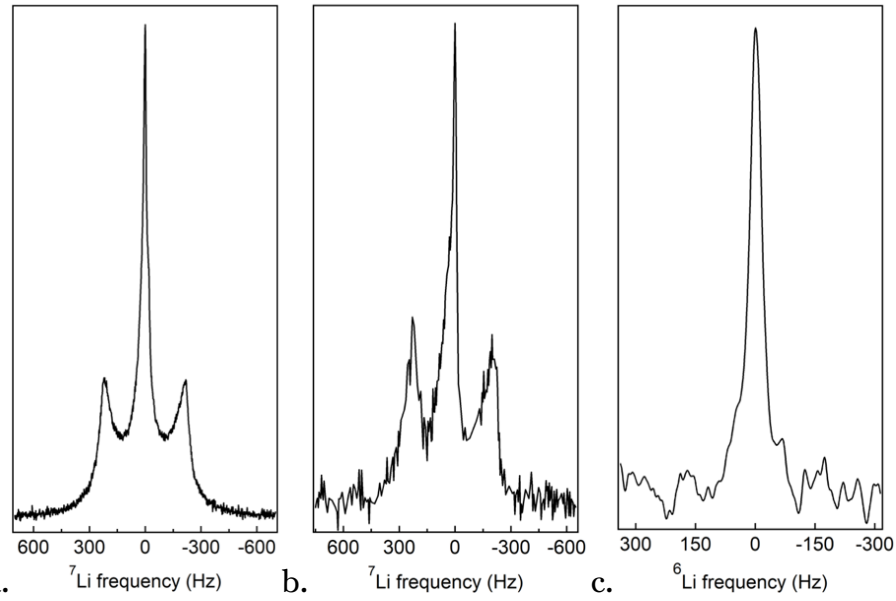


Figure 8.4. NMR spectra of SEO(1.7-1.4) $r = 0.075$ at 90 °C for $^{7}$Li (a), $^{19}$F-decoupled $^{7}$Li (b), and $^{6}$Li (c).

Our observation of quadrupolar splitting indicates interactions between the $^{7}$Li nuclei and local EFGs which could, in principle, be generated by an ordered phase composed of

alternating PS-rich and PEO-rich lamellae. However, if these lamellae were randomly oriented with respect to the applied magnetic field direction, the effect of the concomitant randomly oriented electric fields would cancel, precluding quadrupolar splitting. Therefore, the splitting in SEO(1.7-1.4) $r$ = 0.075 could arise only if the lamellae were not randomly oriented.

### *8.3.3 SAXS Measurement of Magnetic Field Alignment in SEO Electrolytes*

Recent work by Osuji and coworkers has shown that block copolymers domains can align spontaneously under an applied magnetic field, even if the chains are devoid of mesogenic units. [168] In order to test whether this is the case in SEO(1.7-1.4) $r$ = 0.075, a SAXS sample of the electrolyte was placed in an NMR tube, heated above the $T_{ODT}$ outside the magnet to erase thermal history and prior alignment, and then inserted into the 14.1 T NMR magnet, where it was cooled to 90 °C (a temperature that is below the $T_{ODT}$). After 5 min, it was rapidly removed from the NMR magnet and quenched in liquid nitrogen to lock in the morphology that was relevant for our NMR experiment. (Crystallization of the PEO-rich lamellae can distort the morphology of block copolymers. [175,176] The quench vitrifies the PEO, preventing crystallization.) The sample was then studied using SAXS, yielding the two-dimensional pattern shown in Figure 8.5a. The presence of anisotropic arcs in the SAXS pattern indicates alignment of the lamellae. The experiment was repeated for the other two electrolytes, and the results are qualitatively similar. These results are shown in the form of normalized scattering intensity in the vicinity of the primary peak, $I$, *vs.* the azimuthal angle, $\phi$, in Figure 8.5b. (Our experimental setup does not enable determination of the relationship between the magnetic field direction and $\phi$.) A control sample of SEO(1.7-1.4) $r$ = 0.075 was exposed to the same conditions but was never placed in the magnet. The SAXS pattern of this sample is more-or-less isotropic (Figure 8.5c), indicating that alignment in the other samples is a result of magnetic field exposure.

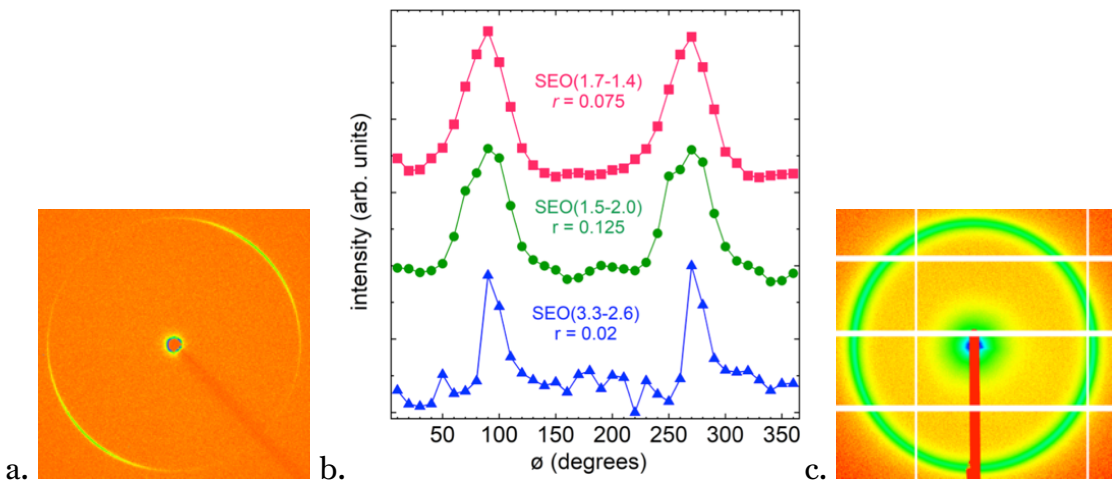


Figure 8.5. Two-dimensional SAXS profile of magnetic-field-aligned SEO(1.7-1.4) $r$ =

0.075 (a), plots of normalized scattering intensity as a function of angle, $I(\phi)$, for aligned SEO(1.7-1.4) $r$ = 0.075 (pink), SEO(1.5-2.0) $r$ = 0.125 (green), and SEO(3.3-2.6) $r$ = 0.02 (blue) (b), and the two-dimensional SAXS profile of SEO(1.7-1.4) $r$ = 0.075 not exposed to the magnetic field (c).

### *8.3.4 Comparison Between SAXS and NMR Measurements of $T_{ODT}$*

The attribution of $^7$Li NMR triplets to quadrupolar interactions caused by aligned lamellae requires this behavior to disappear in disordered samples. In Figure 8.6a, we show the NMR spectra of SEO(1.7-1.4) $r$ = 0.075 obtained at 90 and 120 °C. We define $\Delta\upsilon$ as the difference between the locations of the satellite triplet peaks. When there is no splitting, as is the case at 120 °C, $\Delta\upsilon$ is zero. Figure 8.6b presents $\Delta\upsilon$ as a function of temperature for all three electrolytes. In these measurements, samples were first annealed outside the magnet to remove any previous alignment, then inserted into the magnet, where measurements were taken upon cooling after 10 minutes of equilibration at each temperature. In all cases, the first temperature studied was above $T_{ODT}$ (as determined by SAXS). The triplet splittings appear below the $T_{ODT}$, confirming our assignment of the triplet splitting to quadrupolar interactions caused by an aligned ordered morphology which arises due to exposure to the NMR magnetic field. There is a 5 °C difference between the NMR and SAXS signatures of $T_{ODT}$ in SEO(1.7-1.4) $r$ = 0.075 and SEO(1.5-2.0) $r$ = 0.125. Given the large differences in sample geometry and instrumentation, we attribute this shift to imprecise temperature calibrations and complications arising from the presence of coexistence windows in the vicinity of the $T_{ODT}$. [173,174]

The data in Figure 8.6b show that, for a given electrolyte, $\Delta\upsilon$ is a weak function of temperature below the $T_{ODT}$. The splitting magnitude in the ordered phase likely depends on a variety of parameters, such as salt concentration, degree of alignment, ion dynamics, domain spacing, anisotropic chain stretching, and the nature of the interface between PS-rich and PEO-rich lamellae. [170,171,177] While further work is needed to elucidate the relationship between $\Delta\upsilon$ and the ordered morphology, we have established that the disappearance of NMR quadrupolar splitting is a definitive signature of the order-to-disorder transition in magnetic-field-oriented lamellae-forming block copolymer electrolytes.

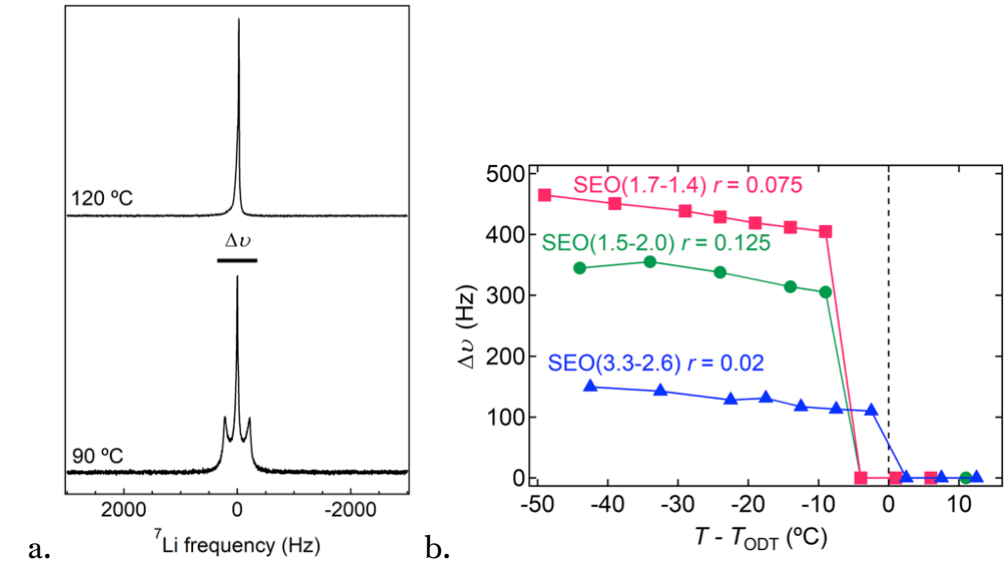


Figure 8.6. NMR spectra of SEO(1.7-1.4) r = 0.075 at 90 and 120 °C (a), and the distance between the two satellite peaks, $\Delta\upsilon$, in $^7$Li NMR quadrupolar triplets *vs.* temperature, normalized by the SAXS $T_{ODT}$, for SEO(1.7-1.4) r = 0.075 (pink), SEO(1.5-2.0) r = 0.125 (green), and SEO(3.3-2.6) r = 0.02 (blue) (b).

### *8.3.5 Determination of Alignment Direction*

All data presented thus far are compatible with the vectors normal to the lamellar planes being oriented parallel with or perpendicular to the direction of the magnetic field. To determine the direction of orientation, SAXS samples were fabricated and aligned such that the magnetic field direction was perpendicular to the eventual direction of the X-ray beam. SAXS measurements were taken, and then the samples were heated above their $T_{ODT}$ into a disordered morphology, cooled to room temperature into a randomly-oriented lamellar morphology, and analyzed again. Since SAXS signals depend on small angle-deflections along domain boundaries, signal intensity is expected to be highest when lamellar normals are perpendicular to the beam, moderate in randomly-oriented samples, and lowest when lamellar normals are parallel to the beam. In Figure 8.7, we plot the scattering invariant, $Iq^2$, *vs.* the scattering vector, $q$. The scattering invariant is directly proportional to the volume of the relevant scattering objects present and is therefore the preferred independent variable in determining relative amounts of scattering in different samples. The signal decreased upon loss of alignment, indicating that aligned samples have lamellar normals parallel to the magnetic field direction.

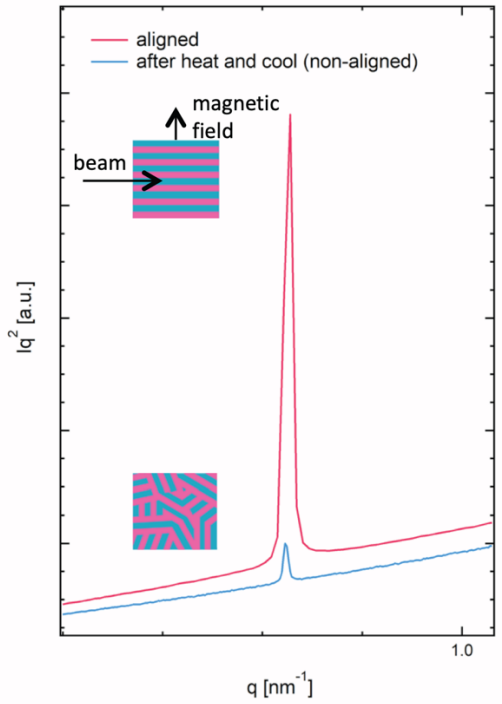


Figure 8.7. SEO(1.7-1.4) $r$ = 0.075 SAXS profile in the aligned state with the X-ray beam perpendicular to the magnetic field direction (pink), the SAXS profile of the same sample after it has been disordered and returned to a randomly-oriented morphology (blue).

*8.3.6 Persistence of Alignment*

Finally, we wished to investigate the persistence of the magnetic-field orientation. The aligned SEO(1.7-1.4) $r$ = 0.075 sample presented in Figure 8.4a was stored at room temperature in an Ar glovebox for 1 year. The dark pink open symbols in Figure 8.8 show that the degree of anisotropy in the SAXS pattern, and therefore the degree of alignment, is very similar to that present immediately after alignment, showing that the magnetic-field alignment is stable with time at room temperature. Subsequently, the sample was heated to 110 °C, just below $T_{ODT}$, and alignment was maintained (light pink closed symbols, Figure 8.8). The sample was then heated above $T_{ODT}$ and then cooled to room temperature to restore order and, as expected, alignment was erased due to the disordering step (light pink open symbols, Figure 8.8). Alignment persists over time at room temperature and up to $T_{ODT}$ and is erased by heating above $T_{ODT}$.

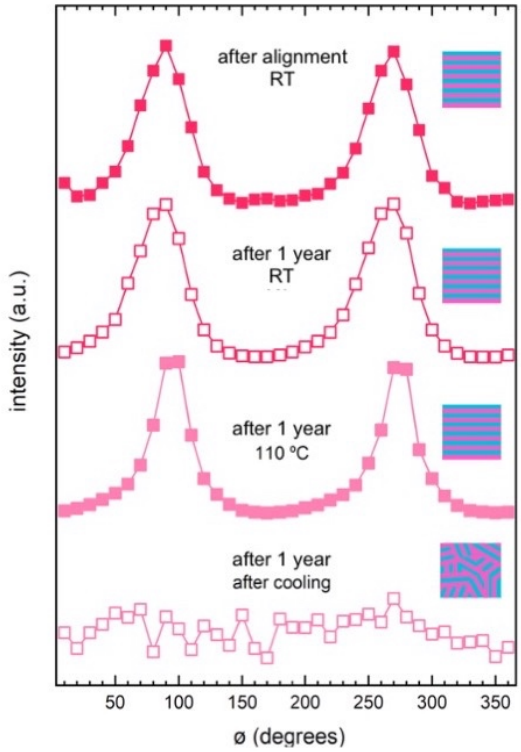


Figure 8.8. Thermal response of alignment in SEO(1.7-1.4) $r$ = 0.075. Normalized scattering intensity as a function of angle, $I(\phi)$, for aligned SEO(1.7-1.4) $r$ = 0.075 (dark pink closed symbols, reproduced from Figure 8.4b), the same sample stored at room temperature for one year (dark pink open symbols), then heated to 110 °C, immediately below $T_{ODT}$ (light pink closed symbols), then heated above $T_{ODT}$ to erase alignment and cooled to room temperature to restore (randomly-oriented) ordering (light pink open symbols).

## 8.4 Experimental Methods

### *8.4.1 Polymer Synthesis and Characterization*

The polystyrene-*b*-poly(ethylene oxide) (SEO) block copolymers in this study were synthesized, purified, and characterized using methods described by Teran et al. [14] and Hadjichristidis et al. [16] The polymers are denoted SEO($M_{PS}$–$M_{PEO}$), where $M_{PS}$ and $M_{PEO}$ are the number-averaged molecular weights of PS and PEO, respectively, in kg mol$^{-1}$.

### *8.4.2 Preparation of Electrolytes*

The salt-containing copolymers were prepared using methods described by Thelen et al. [174] Argon gloveboxes from Vacuum Atmospheres Company were used for all sample preparation. The molar ratio of lithium ions to ethylene oxide (EO) units, $r$, is used to quantify salt concentration. Table 8.1 describes the electrolytes used in this study.

Table 8.1. Characteristics of Electrolytes used in Chapter 8

| Polymer | $M_{PS}$ (kg mol$^{-1}$) | $M_{PEO}$ (kg mol$^{-1}$) | $r$ |
|---|---|---|---|
| SEO(1.7-1.4) | 1.7 | 1.4 | 0.075 |
| SEO(1.5-2.0) | 1.5 | 2.0 | 0.125 |
| SEO(3.3-2.6) | 3.3 | 2.6 | 0.020 |

*8.4.3 SAXS Measurements*

SAXS samples, consisting of electrolyte in a rubber spacer sandwiched between two Kapton windows, were prepared according to methods described by Loo et al. [178] Experiments were conducted at the Advanced Light Source beamline 7.3.3 at Lawrence Berkeley National Lab [144] and beamline 1–5 at the Stanford Synchrotron Radiation Lightsource (SSRL) at SLAC National Accelerator Laboratory. Measurements were taken upon cooling from 130 °C in steps of 2.5 °C to 60 °C, after 20 min annealing at each temperature.

*8.4.4 NMR Spectroscopy*

NMR measurements were performed at 14.1 T using a 600 MHz Bruker Avance III spectrometer with a 5 mm PABBO direct detection broad-band probe (BB-1H/D Z-GRD) and a variable temperature unit. Measurements were performed on $^{7}$Li at a resonance frequency of 233.23 MHz with a 90° pulse time of 13.5 μs at a power level of -2 dB, acquisition time of 0.4 s, and relaxation delay of 1 s, and on $^{6}$Li at a resonance frequency of 88.32 MHz with a 90° pulse time of 16.75 μs at a power level of -2 dB, acquisition time of 0.58 s, and relaxation delay of 1 s. Additionally, $^{7}$Li measurements were acquired with $^{19}$F decoupling using an inverse-gated decoupling sequence [32] on resonance with $\delta(^{19}F)$ frequencies at -78 ppm at 1.66 watts. The acquisition time was 0.114 s, and the relaxation delay 1.5 s. Before each experiment, prior to exposure to the magnetic field, samples were heated above $T_{ODT}$ and allowed to cool to remove previous alignment. When temperature was varied during NMR experiments, samples were allowed to equilibrate for 10 min at each new temperature, and the first temperature studied was above the $T_{ODT}$ determined by SAXS.

*8.4.5 SAXS Measurements of Magnetically Aligned Samples*

SAXS samples were prepared as described above and inserted into 5 mm NMR tubes in an argon glovebox. Because the polymer was protected by Kapton windows, it did not experience shear stress upon insertion into the tubes. The samples were heated above $T_{ODT}$ and annealed at 90 °C for 5 min in the same 14.1 T instrument used for NMR experiments, while control samples were exposed to the same conditions without the presence of a magnetic field. All samples were quenched at -196 °C for 5 min to prevent morphological changes upon crystallization. They were then removed from NMR tubes in an argon glovebox and analyzed with SAXS at room temperature using the methods

described above. Two-dimensional scattering profiles were divided into sectors which were integrated in the vicinity of the primary scattering peak to determine the azimuthal dependence of the scattered intensity, $I(\phi)$.

## 8.5 Conclusions

In summary, we have demonstrated that $^{7}$Li NMR can be used to locate the $T_{ODT}$ in block copolymer electrolytes. The electrolytes tested here have lamellar morphology in the ordered state, which is oriented through exposure to the strong magnetic field present in an NMR instrument. The orientation of lamellae is confirmed using SAXS. The anisotropic material environment causes NMR spectra of the quadrupolar $^{7}$Li nucleus to display a triplet splitting. The triplet becomes a singlet above the $T_{ODT}$ due to the disappearance of the anisotropic environment. The $T_{ODT}$ determined by NMR agrees well with that determined by SAXS experiments.

## 8.6 Acknowledgements

Primary funding for this work was provided by the National Science Foundation through Award DMR-1505444. Work at the Advanced Light Advanced Light Source, which is a DOE Office of Science User Facility, was supported by contract no. DE-AC02-05CH11231. Work at the Stanford Synchrotron Radiation Light Source, a user facility at SLAC National Accelerator Laboratory, was supported by the U.S. Department of Energy, Office of Science, Office of Basic Energy Sciences under contract no. DE-AC02-76SF00515. The work of L.A.M. was also supported in part by the National Science Foundation under Award DMR-1810194. We are grateful to the UC Berkeley College of Chemistry NMR Facility, and especially Hasan Celik and Nanette Jarenwattananon, for their productive conversations and help with instrumentation, and to David Halat for helpful discussions.

# Chapter 9: Orientation-Dependent Distortion of Lamellae in a Block Copolymer Electrolyte Under DC Polarization*

## 9.1 Abstract

Lithium-salt-doped block copolymers have the potential to serve as solid electrolytes in rechargeable batteries with lithium metal anodes. In this work, we use small-angle X-ray scattering (SAXS) to study the structure of polystyrene-*block*-poly(ethylene oxide) (PS-*b*-PEO) doped with bis-(trifluoromethylsulfonyl)amine lithium salt (LiTFSI) during direct current (dc) polarization experiments in lithium–lithium symmetric cells. The block copolymer studied is nearly symmetric in composition, has a total molecular weight of 39 kg $mol^{-1}$, and exhibits a lamellar morphology at all studied salt concentrations. When ionic current is passed through the electrolyte, a salt concentration gradient forms that induces a spatial gradient in the domain spacing, $d$. The dependence of $d$ on distance from the positive electrode, $x$, was determined experimentally by scanning the incident X-ray beam from one lithium electrode to the other. By studying the two-dimensional (2D) SAXS patterns as a function of azimuthal scattering angle, we find that lamellae with PS/PEO interfaces oriented perpendicular to the flow of ionic current ($LAM_{\perp}$) swell and contract to a greater degree than those with interfaces oriented parallel to the current direction ($LAM_{||}$). While domains with the $LAM_{\perp}$ do not provide direct conducting pathways between the electrodes, our analysis suggests that they play an important role in establishing the salt concentration gradient necessary for sustaining a large ionic current through greater expansion and contraction.

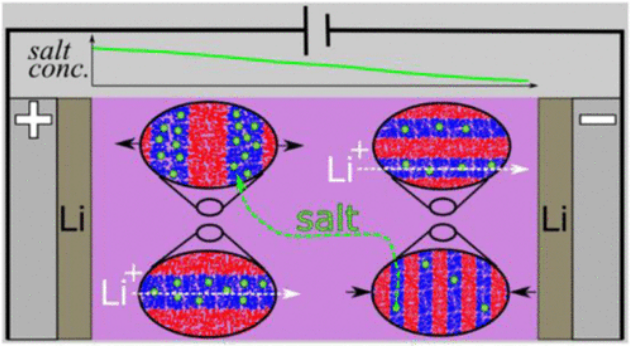


Figure 9.1. Illustration of ion transport and grain swelling of a lamellar block copolymer electrolyte during polarization for different grain orientations.

* This Chapter is adapted from Galluzzo, M. D.; Grundy, L. S. *et al.* Orientation-Dependent Distortion of Lamellae in a Block Copolymer Electrolyte under DC Polarization. *Macromolecules* **2021**, *54* (17), 7808-7821. 216

## 9.2 Introduction

Solid-state lithium metal batteries are an attractive alternative to standard lithium-ion batteries as they offer improved energy density. [1] Lithium metal has the highest theoretical specific capacity (3.86 Ah $g^{-1)}$ of any anode material for lithium-based batteries. [2,3] Nanostructured block copolymer electrolytes present one approach for enabling solid-state lithium metal batteries. [179] Polymer-based lithium metal batteries have had limited commercial success for reasons including: limited electrolyte conductivity, the need to establish new manufacturing protocols, and issues related to the reactive and pyrophoric nature of lithium metal. [180]

### *9.2.1 Rearrangement of Molecules During Polarization*

The purpose of this paper is to shed light on the nature of ion transport in nanostructured block copolymers under direct current (dc) polarization. Prior to polarization, the salt ions are uniformly distributed in all conducting domains of the block copolymer. In systems wherein both the cation and anion are mobile and the cation transference number with respect to the solvent velocity, $t_+^0$, is less than unity, the salt accumulates near the positive electrode where lithium ions enter the electrolyte and depletes at the negative electrode where lithium ions exit the electrolyte to react with (or intercalate into) the positive electrode. The result is a salt concentration gradient along the direction perpendicular to the current collectors while the total moles of salt within the entire electrolyte is conserved. This process is well understood in the case of homogeneous electrolytes. [29,181] During battery operation, we thus obtain regions of the electrolyte where the salt concentration is higher than the initial salt concentration and regions where it is lower. If the volume of the electrolyte is fixed, the inescapable conclusion is that the solvent must rearrange to accommodate the salt concentration gradient. [111] For liquid electrolytes, solvent molecules can rearrange easily, and we expect a lower concentration of solvent in regions where there is a high salt concentration and a higher concentration of solvent in regions where there is a lower salt concentration. [182,183] It is not well understood how or if this occurs in polymer electrolytes where the rearrangement of the "solvent phase" is slow. In this work, we show that this process is complex for a block copolymer electrolyte and the local lamellar orientation relative to the electrodes plays an important role. Our results indicate that the process of block copolymer rearrangement limits the maximum current that can be sustained by a block copolymer electrolyte.

### *9.2.2 in situ SAXS of SEO/LiTFSI Electrolytes*

We employ small-angle X-ray scattering (SAXS) to study the structure of a block copolymer electrolyte during dc polarization. [184–186] We focus on a system that has been well characterized in the literature: [50,187,188] polystyrene-block-poly-(ethylene oxide) (SEO) block copolymer doped with bis-(trifluoromethylsulfonyl)amine lithium salt (LiTFSI). Polystyrene (PS) provides mechanical rigidity to suppress lithium dendrite growth, while poly(ethylene oxide) (PEO) solvates and conducts lithium ions. We

previously reported similar experiments on an SEO/LiTFSI electrolyte with a PS molecular weight, $M_{PS}$, of 1.7 kg mol−1 and a PEO molecular weight, $M_{PEO}$, of 1.4 kg mol$^{-1}$, which exhibited phase transitions over the range of salt concentrations studied. [186] In this study, we used an SEO copolymer with $M_{PS}$ = 19 kg mol$^{-1}$ and $M_{PEO}$ = 20 kg mol$^{-1}$ that exhibits a lamellar morphology over all salt concentrations, measured as the molar ratio of LiTFSI to ethylene oxide moieties, r = [LiTFSI]/[EO]. Since the modulus of the electrolyte increases with molecular weight, a longer chain block copolymer is more practical for battery applications. [159] Our goal is to study the response of a practical nanostructured block copolymer electrolyte subjected to dc polarization and understand the mechanisms that limit performance. The foundation of our understanding of ion transport through nanostructured electrolytes is based on numerous studies that examine structure−property relationships. [23,27,187–194]. We extend this approach by considering the dynamic nature of these relationships when a dc current is applied.

### *9.2.3 The Limiting Current*

The maximum current that can be sustained through an electrolyte, i.e., the limiting current, $i_{lim}$, depends on the salt concentration, $r$, and the distance between electrodes, $L$. [57,48] In this work, we study electrochemical cells comprising a block copolymer electrolyte sandwiched between two lithium electrodes (i.e., lithium−lithium symmetric cells). We consider situations where a constant current is passed through the electrolyte. As concentration gradients develop, the potential drop across the electrolyte increases. Eventually, the potential drop will either stabilize at some constant value or diverge, depending on whether the applied current density is below or above the limiting current density. A stable potential is obtained if the diffusional flux of the anion down the salt concentration gradient matches the migratory flux due to the electric field; flow of ionic current for sustained periods thus requires the formation of a salt concentration gradient. The limiting current density typically coincides with the condition that the steady-state salt concentration at the negative electrode approaches zero. Above the limiting current, the potential begins to diverge because, in the absence of lithium ions at the electrode/electrolyte interface, electrons in the negative electrode begin to participate in irreversible parasitic reactions with the electrolyte. [195]

## 9.3 Experimental Methods

### *9.3.1 Materials*

The polystyrene-block-poly(ethylene oxide) (SEO) block copolymer used in this study was synthesized, purified, and characterized by methods described by Teran *et al.* [14] and Hadjichristidis *et al.* [16] The block copolymer electrolyte (polystyrene (PS) molecular weight of 19 and poly(ethylene oxide) (PEO) molecular weight of 20 kg mol$^{-1}$) was prepared following the methods reported by Yuan *et al.* [143] to produce an SEO/LiTFSI mixture with $r$ = 0.16. We use the notation SEO($xx$−$yy$) to denote SEO block copolymers with molecular weights of the PS and PEO blocks equal to $xx$ and $yy$ kg mol$^{-1}$,

respectively. Lithium metal with a nominal thickness of 0.75 mm was purchased from MTI and scraped with a nylon brush to expose a fresh lithium surface. The lithium was then cut into a 3.18 mm diameter disk and pressed at 500 psi, resulting in a disk approximately 1 cm in diameter and 0.1 mm in thickness.

### *9.3.2 Electrochemical Characterization of Conductivity and Limiting Current*

SEO samples for electrochemical measurements were prepared by placing electrolytes in annular spacers with inner diameters of 3.18 mm and hand-pressing them into pellets. Samples were hot-pressed at 90 °C to create uniform, nonporous films. The polymer sample was sandwiched between stainless steel or lithium electrodes of known thickness. The total cell thickness was measured using a micrometer before attaching nickel current collectors and sealing the cell in a polypropylene-lined aluminum pouch material. At this point, the cells were removed from the glovebox for testing. The inner diameter of the spacer and the thickness measurements allow for determination of the cell constants $A$ and $L$, the electrochemically active area and distance between electrodes, respectively.

Ionic conductivity of samples with blocking electrodes (stainless steel), $\kappa$, was measured by alternating current (ac) impedance spectroscopy at 90 °C. Prior to measurement, cells were annealed at 120 °C for at least 8 h and then cooled to 90 °C. The bulk resistance, $R_\mathrm{b}$, was determined by fitting an equivalent circuit and was used to calculate the ionic conductivity, $\kappa$, via $\kappa = \frac{L}{R_\mathrm{b}A}$.

The limiting current was measured by assembling cells with lithium electrodes and $L$ = 0.025 cm. All measurements were performed at 90 °C. The cells were polarized at a constant current until either a steady-state potential was reached or the potential diverged. After polarization, the current was set to zero and the potential relaxed until it stabilized around 0 V. For subsequent polarizations, the direction of the current was flipped.

### *9.3.3 Preparation of Electrochemical Cells for Simultaneous SAXS Experiments*

The polymer electrolytes were dried at 120 °C under active evacuation in a glovebox antechamber for 24 h prior to constructing the cells for the simultaneous SAXS and electrochemical experiments. Lithium electrodes were pressed onto stainless steel current collectors and placed in the cell assembly, which was machined out of poly(ether ether ketone) (PEEK). Polymer electrolyte was then hot-pressed between the electrodes. Set screws were used to press the stainless steel blocks closer together, until the distance between the two lithium electrodes was approximately 1.4 mm. (The distance between electrodes, $L$, was measured accurately at the beamline by X-ray transmission measurements, as detailed in Figure A9.4.) Excess polymer was then scraped away, and nickel tabs were affixed to the stainless steel blocks. A reference channel, isolated from the electrochemical channel, was also filled with the electrolyte of the same salt

concentration. The reference channel was designed so that the path length traveled through the electrolyte by the X-ray beam was identical to the electrochemical channel. The PEEK assembly was then closed and sealed in an aluminum-laminated pouch material with nickel tabs protruding. A picture of the cell assembly and dimensions is provided in Figure A9.1. After assembling the lithium–lithium symmetric cells, the samples were vacuum-annealed at 120 °C for at least 8 h. The samples were then cooled to room temperature and brought to the beamline for testing. The samples were affixed to a heating stage custom-built for simultaneous SAXS and electrochemical measurements. The samples were allowed to thermally equilibrate for 1 h at 90 °C prior to polarization and then maintained at this temperature for the duration of the experiment.

*9.3.4 Simultaneous SAXS and DC Polarization Experiments*

All simultaneous SAXS and dc polarization experiments were performed at Stanford Synchrotron Radiation Light Source (SSRL) beamline 1–5 at SLAC National Accelerator Laboratory. The sample heating stage allowed for up to three electrochemical cells to be studied simultaneously. The beam size was fixed at 700 $\mu$m ($y$-axis) by 200 $\mu$m ($x$-axis) by slits that were positioned downstream of a multilayer monochromator and toroidal focusing mirror, where the $x$-axis is parallel to the current direction. While the beam is rectangular in shape at the sample, it is focused to a point at the detector plane. Our primary focus is on the scattered peak position and intensity, which is not impacted by the beam shape. The dimensions of the lithium electrodes were 0.195 × 0.395 cm$^2$. Thus, the electrolyte formed a rectangular prism where the 0.395 cm × $L$ face was oriented with its normal parallel to the X-ray beam and the X-ray beam passed through 0.195 cm of electrolyte. Based on the direction of the current flow, we expect the sample to be uniform in structure along the $y$- and $z$-coordinates. The X-ray energy was 12 keV, and the exposure time at each position was 10 s. The x- and y-coordinates of the cell were mapped out by scanning the beam across the sample and measuring the beam-stop diode intensity. The intensity reading from the diode was approximately zero when the beam was positioned on the stainless steel current collector and nonzero when passing through the lithium metal, polymer electrolyte, or PEEK. Intensity readings were used to calculate $L$ (see Figure A9.4). Silver behenate was used to determine the beam center and sample-to-detector distance. 2D scattering patterns were captured on an SX165 CCD detector (Rayonix, LLC). The 2D scattering profiles were reduced to one-dimensional (1D) profiles using the PyFAI package for Python.[46] We performed SAXS on the reference sample simultaneously with the electrochemical samples to check for changes in the beamline conditions that could result in variations in the data. We visually inspected the cells after the experiment and found no discoloration or visible changes to the cell, indicating that beam damage was not an issue.

*9.3.5 Electrochemical Measurements*

All electrochemical measurements were made using a Biologic VMP3 potentiostat. Ac impedance measurements were made in a frequency range from 1 MHz to 100 mHz with an amplitude of 80 mV.

## 9.4 Results and Discussion

*9.4.1 Electrolyte Properties as a Function of Salt Concentration*

To understand the transient phase behavior of a block copolymer electrolyte in the presence of a salt concentration gradient between two lithium electrodes, we start by characterizing the electrolyte under quiescent conditions over the range of salt concentrations that may be encountered during polarization. LiTFSI selectively partitions into the PEO domains, [24,196,197] and this affects the thermodynamic properties of the system. [23] One consequence is that the domain spacing increases as salt is added. The domain spacing, $d$, is defined as the distance between the center of two lamellae of the same component. Using sample holders with inert Kapton windows, we performed SAXS on a series of SEO(19−20)/LiTFSI electrolytes to extract the $d$ as a function of salt concentration, $r$. The domain spacing is related to the position of the first-order scattering peak, $q^*$, by Equation 9.1:

$$d = \frac{2\pi}{q^*}. \qquad (9.1)$$

The results are presented in Figure 9.2a. The neat block copolymer ($r = 0$) has a domain spacing of 28.1 nm. The domain spacing increases rapidly with increasing salt concentration until $r = 0.04$, where $d = 35.9$ nm. Above $r = 0.06$, $d$ increases more gradually and shows an approximately linear trend with $r$ up to the highest salt concentration measured, $r = 0.36$, where $d = 52.2$ nm. Based on the data in Figure 9.2a for individual electrolytes cast at different salt concentrations, we have a straightforward approach to predict the spatial dependence of the domain spacing when a known salt concentration gradient forms across a lithium symmetric cell. This analysis, which relies on a quantitative relationship between $d$ and $r$, is enabled by empirically fitting the data. The least-squares fit using a sum of two exponential functions is given by the curve in Figure 9.2a, and the resulting expression is

$$d(\text{nm}) = 149 - 114\exp[-0.421\text{r}] - 7.09\exp[-46.3\text{r}]. \qquad (9.2)$$

Newman's concentrated solution theory allows us to predict the salt concentration and potential gradient across a lithium symmetric cell during polarization. [29,181,198]. The steady-state concentration profile, $r(x/L)$, and potential drop, $U_{ss}$, can be determined using integral relationships when the conductivity, $\kappa$, current fraction, $\rho_+$, and a term

related to the thermodynamics of the electrolyte, $\frac{\mathrm{d}U}{\mathrm{dln}m}$, are known as a function of salt concentration, where $U$ is the open-circuit potential of a concentration cell and $m$ is the salt molality. The details for modeling salt concentration profiles are discussed in several references. [10,47,57] Briefly, the salt concentration gradient at steady state, $r(x/L)$, can be determined from Equation 9.3 by an iterative process: (1) guess a salt concentration at $x/L = 0$, (2) calculate $r(x/L)$ based on the initial guess from Equation 9.3, (3) integrate $r(x/L)$ from 0 to 1 to determine the average salt concentration, and (4) iterate the initial guess until the calculated average salt concentration matches the desired value (in our case, $r = 0.16$). Equation 9.3 is given by

$$\int_{r\left(\frac{x}{L}=0\right)}^{r\left(\frac{x}{L}\right)} J_1(r)\,\mathrm{d}r = -\frac{iL}{F}\left(\frac{x}{L}\right), \qquad (9.3)$$

where $F$ is Faraday's constant and

$$J_1(r) = \kappa\left(\frac{\mathrm{d}U}{\mathrm{dln}m}\right)\left[r\left(1-\frac{1}{\rho_+}\right)z_+\nu_+F\phi_c\right]^{-1}. \qquad (9.4)$$

Here, $z_+$ is the charge number of the cation, $\nu_+$ is the number of cations into which the salt dissociates, and $\phi_c$ is the volume fraction of the conducting phase. Once $r(x/L)$ is known, the steady-state potential drop, $U_{\mathrm{ss}}$, across the electrolyte can then be calculated by solving

$$U_{\mathrm{ss}}(x) = Fz_-\nu_-\int_{r(x/L=1)}^{r(x/L=0)} J_2(r)\,\mathrm{d}r\,, \qquad (9.5)$$

where $z_-$ is the charge number of the anion and $\nu_-$ is the number of anions into which the salt dissociates and

$$J_2(r) = \left(\frac{\mathrm{d}U}{\mathrm{d}\ln m}\right)\left[r\left(1-\frac{1}{\rho_+}\right)z_+\nu_+F\phi_c\right]^{-1}. \qquad (9.6)$$

Derivations for Equations 9.6–9.9 are provided in Pesko *et al.* [47] The equations presented here are rearranged by substituting expressions for the anion transference number with respect to the solvent velocity, $t_-^0$, which is given by

$$t_-^0 = 1 - t_+^0 = -\left(\frac{1}{\rho_+}-1\right)\frac{z_+\nu_+FDc\phi_c}{\kappa}\left(\frac{\mathrm{d}U}{\mathrm{d}\ln m}\right), \qquad (9.7)$$

where $c$ is the salt concentration in moles per liter and $D$ is the salt diffusion coefficient in $cm^2\ s^{-1}$.

In previous work, we demonstrated that $\rho_+$ and $\frac{dU}{d\ln m}$ in SEO/LiTFSI electrolytes follow universal trends regardless of chain length and conducting phase volume fraction, given by Equations 9.8 and 9.9: [23]

$$\rho_+ = 0.18 - 1.7r + 6.3r^2 \qquad (9.8)$$

$$\frac{dU}{d\ln m}(\text{mV}) = -74 - 66\ln m - 13.8(\ln m)^2\,. \qquad (9.9)$$

The dependence of $\phi_c$ on $r$ is given by:

$$\phi_c = \frac{\nu_c}{\nu_c + \frac{M_{PS}M_{EO}}{M_S M_{PEO}}\nu_S}\,, \qquad (9.10)$$

where $M_{PS}$ and $M_{PEO}$ are the molecular weight of the PS and PEO blocks (19,000 and 20,000 g $mol^{-1}$, respectively), $M_S$ and $M_{EO}$ are the molar mass of the styrene and ethylene oxide monomers (104.2 and 44.05 g $mol^{-1}$, respectively), and $\nu_c$ is the molar volume of the conducting phase (PEO + LiTFSI), given by $\nu_c = \frac{M_{EO} + rM_{LiTFSI}}{\rho_c(r)}$, where $M_{LiTFSI}$ is the molar mass of the LiTFSI salt (287.075 g $mol^{-1}$). The density of the conducting phase, $\rho_c(r)$, was taken from Pesko *et al.* [25]

The implication of Equations 9.3−9.9 is that, for any SEO/LiTFSI electrolyte, we need to only measure the ionic conductivity, $\kappa$, as a function of $r$ to predict $r(x/L)$ at steady state and $U_{ss}$ for a given current density. We present κ as a function of r for SEO(19−20)/LiTFSI in Figure 9.2b based on ac impedance spectroscopy performed on cells with blocking (i.e., stainless steel) electrodes. The data presented in Figure 9.2b was obtained at 90 °C after annealing at 120 °C for 8 h. The conductivity of block copolymer electrolytes is a function of the lamellar grain size, which can change depending on the thermal history of the sample. We therefore kept the thermal history identical for all samples (see the Experimental Methods, Section 9.3). The conductivity of SEO(19−20) increases with salt concentration from the dilute limit until r = 0.10 and then plateaus at higher salt concentrations. The results are consistent with measurements on other block copolymer electrolytes that have been reported in the literature, and we defer the discussion of the relationship between κ and r to those references. [23,27,115,135,187]. We fit the conductivity following the functional form presented in Mongcopa *et al.* [118] and obtain

$$\kappa\ (\mathrm{S\ cm^{-1}}) = 0.00237r \exp\left[-\frac{r}{0.170}\right]. \qquad (9.11)$$

We can thus calculate $J_1(r)$ and $J_2(r)$ for SEO(19−20)/LiTFSI electrolytes using Equations 9.8−9.11, and the results are presented in Figure A9.2 of Appendix A9.

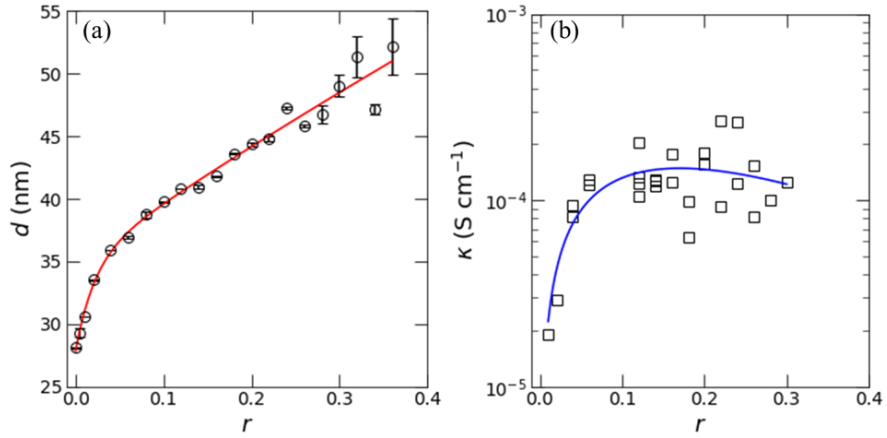


Figure 9.2. (a) Domain spacing, $d$, *vs.* molar salt concentration, $r$, for a series of SEO(19−20)/LiTFSI electrolytes at 90 °C. The electrolyte exhibits a lamellar morphology at all salt concentrations. The red line is a double exponential fit to the data given by Equation 9.2. (b) Ionic conductivity, $\kappa$, *vs.* $r$ measured from ac impedance spectroscopy in cells with blocking electrodes at 90 °C. Each data point represents a measurement from a unique cell. The blue curve is a fit to the data given by Equation 9.3. In both panels (a) and (b), the samples were annealed at 120 °C for at least 8 h and then cooled to 90 °C prior to the measurement.

We are now poised to predict salt concentration profiles at steady state and $U_{ss}$ for various current densities. We test these predictions by experimentally measuring the voltage *vs.* time behavior (at a constant polarization current) of our electrolyte with an initially uniform salt concentration of $r = 0.16$ in the long-time limit. Lithium−lithium symmetric cells were constructed with $L = 0.025$ cm. The cells were polarized at a constant current density, i, and the potential was measured. If $iL$ is below $i_{lim}L$, it is expected that the potential will plateau and reach a steady-state value, $U_{ss}$, indicating that a time-independent concentration profile is achieved. The time scale on which the cell reaches steady state is proportional to $L^2$. (For the simultaneous polarization and SAXS experiments, which we discuss in the next Section, $L \sim 0.15$ cm and the time scales are expected to be about 36 times longer relative to the cells with $L = 0.025$ cm.) If $iL$ is above $i_{lim}L$, then the potential will diverge instead of reaching a plateau. In Figure 9.3a, we plot the potential response for a series of applied current densities: $iL = 0.025$ (red trace), 0.10 (orange trace), 0.40 (yellow trace), 0.60 (green trace), 1.6 (blue trace), 3.2

(purple trace), and 6.4 $\mu$A cm$^{-1}$ (black trace). The cell potential, $U$, is the potential drop across the electrolyte. Experimentally, we measure the potential drop across the current collectors, $\Delta V$, which includes a significant contribution from the resistance at the lithium electrode/ electrolyte interfaces. We calculate the interfacial potential drop, $\Delta V_{int}$, by multiplying the interfacial resistance measured from ac impedance spectroscopy and the current ($\Delta V_{int} = R_{int} iA$). [52] The interfacial resistance was approximately constant throughout each polarization experiment, so $\Delta V_{int}$ is assumed to be independent of time (see Figure A9.5). The data in Figures 9.3a and b has been corrected by subtracting $\Delta V_{int}$ from the measured voltage ($U = \Delta V - \Delta V_{int}$). In Figure 9.3b, we plot $U_{ss}$ *vs.* $iL$ with red star makers. We see excellent agreement between the theory and experiment up to $iL$ = 3.2 $\mu$A cm$^{-1}$. At $iL$ = 6.4 $\mu$A cm$^{-1}$, the potential diverges after about 5 h in Figure 9.3a. In Figure 9.3b, we denote this experimental observation with a red dashed line that extends toward infinity above $iL$ = 3.2 $\mu$A cm$^{-1}$. We estimate $i_{lim}$ as the average between the largest sustained current density and the lowest value measured that resulted in a divergence of the potential. Thus, the normalized limiting current, $i_{lim}L$, measured experimentally is estimated to be 4.8 ± 1.6 $\mu$A cm$^{-1}$.

Using Equations 9.3−9.11, we can predict $i_{lim}$ by extrapolating to the case where the salt concentration reaches zero at the plating electrode (see Figure A9.3). [57,47,10] In Figure 9.3c, we plot the theoretically predicted limiting current for SEO(19−20)/LiTFSI electrolytes with $r$ ranging from 0.02 to 0.16 as open black circles. The limiting current normalized by the distance between electrodes, $i_{lim}L$, is plotted *vs.* $r$; we choose this format because results obtained using symmetric cells with other values of $L$ can be compared directly with the data presented here. We note that these predictions are made using no adjustable parameters. We see the expected behavior that $i_{lim}L$ increases monotonically with salt concentration from 2.12 $\mu$A cm$^{-1}$ at $r$ = 0.03 to 10.5 $\mu$A cm$^{-1}$ at $r$ = 0.16. The red star in Figure 9.3c represents the experimentally measured limiting current. The experimental value is approximately a factor of 2 lower than that predicted by concentrated solution theory. One of the motivations for the simultaneous SAXS and polarization experiments described in the next Section is to investigate the reason for this discrepancy.

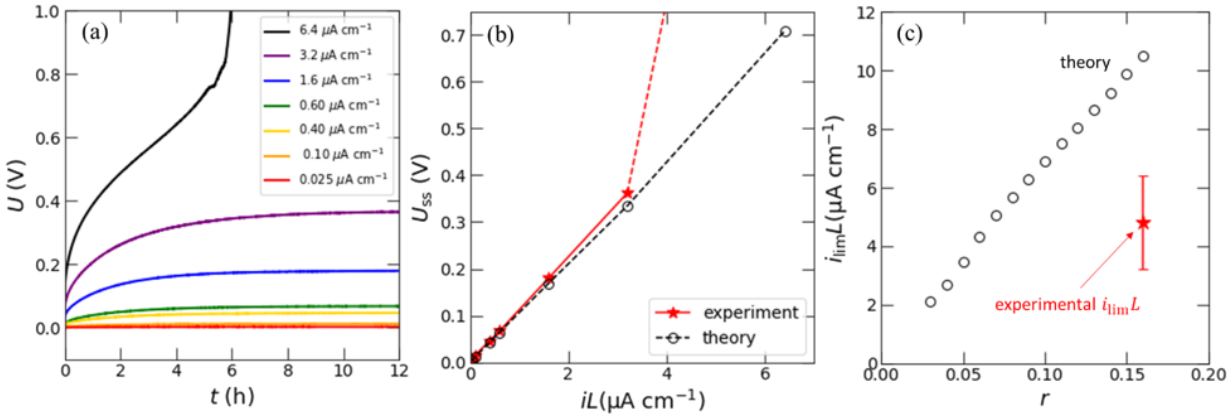


Figure 9.3. Comparison of an experimental limiting current measurement to theory. (a) Experimental measurement of the limiting current. The potential drop across the electrolyte, $U$, is plotted *vs.* time, $t$, for increasing current densities from $iL$ = 0.025 to 6.4 $\mu$A cm$^{-1}$ with $L$ = 0.025 cm. A steady-state potential, $U_{ss}$, is obtained for all currents except $iL$ = 6.4 $\mu$A cm$^{-1}$, where $U$ diverges after 5 h. We take the experimental limiting current to be the average of the lowest unsustainable current density (6.4 $\mu$A cm$^{-1}$) and the highest sustainable current density (3.2 $\mu$A cm$^{-1}$). The error bars in panel (c) depict the fact that the true value of $i_{lim}L$ may lie anywhere between these two values. (b) $U_{ss}$ *vs.* $iL$ from the experiment (red stars) and theory (black open circles). The dashed red line indicates that the steady-state potential diverges to infinity at $iL$ = 6.4 $\mu$A cm$^{-1}$. (c) Normalized limiting current, $i_{lim}L$, *vs.* molar salt concentration, $r$. Black open circles represent the predicted $i_{lim}L$ from the concentrated solution theory. The data point marked by a red star indicates the value of $i_{lim}L$ measured experimentally.

### *9.4.2 Gradients in Domain Spacing as a Function of Current Density*

To monitor the structure of the SEO(19–20) electrolyte with $r$ = 0.16 during polarization, we built a custom electrochemical cell to allow simultaneous SAXS measurements. This cell is shown schematically in Figure 9.4a. The lithium electrodes are in the $y$–$z$ plane such that the nominal direction of ionic current is parallel to the x-axis. In Figure 9.4b, we show an example of a SAXS pattern obtained from SEO(19–20), where the incident beam is oriented in the $z$-direction. Our sample, which is made by pressing the freeze-dried electrolyte into the sample holder, consists of lamellar grains oriented in different directions. The information in a 2D SAXS pattern from a collection of lamellar grains results from lamellae which have normal vectors in the plane perpendicular to the incident beam (the $x$–$y$ plane, in our case); the normal vector is defined to be perpendicular to the nominal interfaces between adjacent lamellae. [199] By scanning the beam along the $x$-axis, the 2D scattering patterns contain information about the structure of lamellae with normal vectors in the $x$–$y$ plane. In our experiment, there is a macroscopic gradient in salt concentration along the $x$-axis which forms during dc

polarization. We define the azimuthal angle, χ, in Figure 9.4b and denote χ = 0° along the y-axis, pointing upwards and increasing counterclockwise. The SAXS pattern is divided into 16 sectors as shown in Figure 9.4b, and the cartoons in each sector indicate the orientation of lamellar grains which give rise to scattering in that sector. By analyzing data at χ = 0 and 180° (as defined in Figure 9.4b), we obtain information about grains with PS-PEO interfaces oriented parallel to the flow of ionic current (we call these lamellae $LAM_{||}$ and note that their normal vectors are parallel to the *y*-axis). For χ = 90 and 270°, we obtain information about grains with PS-PEO interfaces oriented perpendicular to the flow of ionic current (we call these lamellae $LAM_{\perp}$ and note that their normal vectors are perpendicular to the *y*-axis).

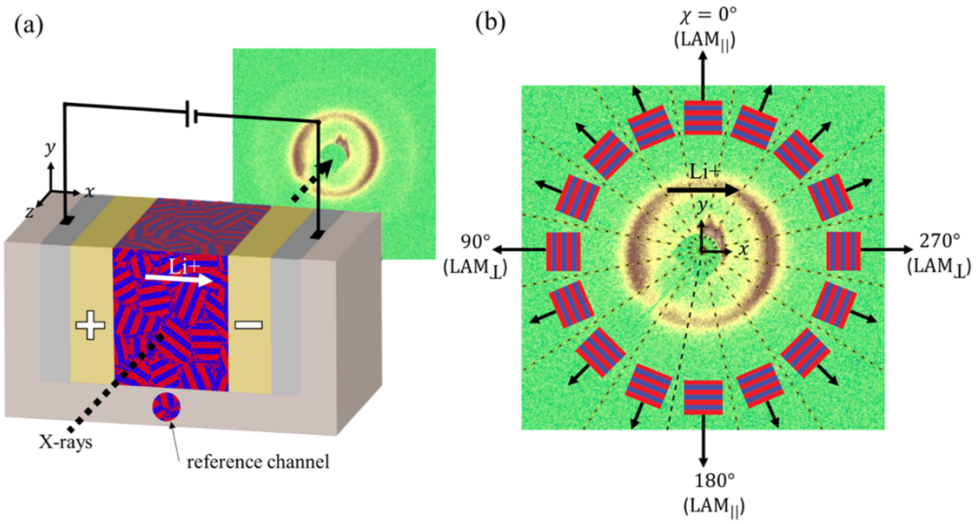


Figure 9.4. (a) Schematic representation of the simultaneous polarization and SAXS experiment. An SEO/LiTFSI electrolyte with randomly oriented grains is sandwiched between two lithium electrodes with current passing parallel to the *x*-axis. X-rays pass parallel to the *z*-axis, perpendicular to the current. Scanning the beam along the *x*-axis allows for spatial resolution between the electrodes. A reference channel filled with the electrolyte was placed next to the electrochemical cell. (b) Characteristic 2D SAXS pattern obtained from experiments. The pattern is divided into 16 sectors defined by the azimuthal angle, χ. Scattering data in each sector corresponds to lamellae oriented with the angle between the vector normal to the PEO-PS interfaces and the positive *y*-axis equal to χ. The cartoons in each sector show the lamellar orientation with their respective normal vectors.

Using the experimental geometry shown schematically in Figure 9.4, we studied three lithium−lithium symmetric cells comprising an SEO(19−20)/LiTFSI electrolyte with $r$ = 0.16 at three current densities. The beam was aligned so that the 200 $\mu$m beam dimension was along the *x*-axis of the cell (i.e., the axis perpendicular to the planar

electrodes and the direction of the ionic current flow). The 700 $\mu$m dimension was along the $y$-axis of the cell and in the center of the channel along the $y$-axis. The sample was scanned in 100 $\mu$m increments along the $x$-axis, beginning and ending over the stainless steel current collectors. When the beam was aligned over the stainless steel, the beam was completely attenuated, and the transmitted and scattered intensities were approximately zero. We used the transmitted intensity to define the coordinates and measure $L$ for each cell (see Figure A9.4). We define the initial time, $t = 0$, as the first moment of polarization. Throughout this work, we discuss the current in terms of $iL$, which is the current, $I$ ($\mu$A), divided by the electrode surface area, $A = 0.077$ cm$^2$, multiplied by the distance between electrodes, $L$ (cm).

We begin by analyzing SAXS data for cells polarized at $iL = 0.926$ $\mu$A cm$^{-1}$ (Figure 9.5a), 1.96 $\mu$A cm$^{-1}$ (Figure 9.5b), and 3.74 $\mu$A cm$^{-1}$ (Figure 9.5c). An example of a 2D SAXS pattern obtained from these experiments is presented in Figure 9.5b. A 360° azimuthal average of the data was performed to obtain 1D SAXS profiles of the scattered intensity, $I$, as a function of the scattering vector, $q$. We obtain the domain spacing by fitting the primary scattering peak to a pseudo-Voight function as described in Appendix A9 to obtain $q^*$ and calculating d from Equation 9.1. In Figure 9.5, we plot $d$ as a function of the normalized position between the electrodes, $x/L$. Lithium stripping occurs at the positive electrode where $x/L = 0$ and lithium plating occurs at the negative electrode where $x/L = 1$. The top panel in each figure (Figure 9.5a–c) shows the potential response, $U$, of the cell as a function of time. The black dashed line represents $U_{ss}$ predicted from the theory. In all cases, the measured potential stays below the predicted value and does not reach a clear plateau before the experiment was halted at $t = 48$ h, mainly due to limited access to the SAXS instrument. The rainbow color scheme in the top panel and main figure is coordinated such that the color of the data points on the $U$ *vs.* $t$ plot corresponds to the time that the data set of the d *vs.* $x/L$ was obtained. Purple data sets were obtained near the beginning of the polarization step ($t = 0$ h), and red data sets were obtained near the end ($t = 47$ h).

In Figure 9.5a, a constant current density of 6.34 $\mu$A cm$^{-2}$ was applied across a cell with L = 0.140 cm ($iL = 0.926$ $\mu$A cm$^{-1}$). At $t = 0$ h, the average domain spacing across all positions is 42.4 nm. The domain spacing is not completely uniform initially: $d = 42.3$ nm near the center of the cell and $d = 42.6$ nm near the electrodes. We suspect that this difference (less than 1% of the domain spacing) is due to uneven stress distribution on the lamella during sample preparation. This trend is also seen in Figures 9.5b and c. In Figure 9.5b, a current density of 13.5 $\mu$A cm$^{-2}$ was applied across a cell with $L = 0.145$ cm ($iL = 1.96$ $\mu$A cm$^{-1}$), and in Figure 9.5c, a current density of 27.3 $\mu$A cm$^{-2}$ was applied across a cell with $L = 0.137$ cm ($iL = 3.74$ $\mu$A cm$^{-1}$). For each cell, $d$ increases near the positive electrode where local salt concentration increases and decreases near the negative

electrode where local salt concentration decreases. The gradient in $d$ develops near the electrodes first, then propagates toward the center of the cell and becomes more linear with time. To highlight this, we drew lines through the $d$ *vs.* $x/L$ data sets corresponding to $t$ = 4.7 and 19.6 h along with the first ($t$ = 0 h) and last data ($t$ = 46.6 h) sets. The qualitative observation that the domain spacing changes first near the electrodes before propagating into the center of the cell is consistent with predictions of time-dependent concentration profiles from concentrated solution theory. [58]

As the current increases from Figures 9.5a–c, the magnitude of the domain spacing gradient increases. For the lowest current density, the difference in $d$ between the positive and negative electrodes at $t$ = 46.6 h is 1.63 nm; for the middle current density, it is 3.84 nm; and for the highest current density, it is 9.08 nm. A larger salt concentration gradient is expected for higher current densities as the flux of the anion due to migration is larger and thus a larger diffusive flux is required to match it and achieve steady state. Interestingly, the domain spacing gradients are not symmetric; the increase in domain spacing at the positive electrode is larger than the magnitude of the decrease in domain spacing at the negative electrode. This effect is most prominent for the largest current density in Figure 9.5c. For all three current densities, the point where $d$ shifts from increasing to decreasing is at a position $x/L \approx 0.6$. We next turn to Equation 9.2 to convert the measured domain spacings into local salt concentrations as they can be directly compared with theoretical predictions.

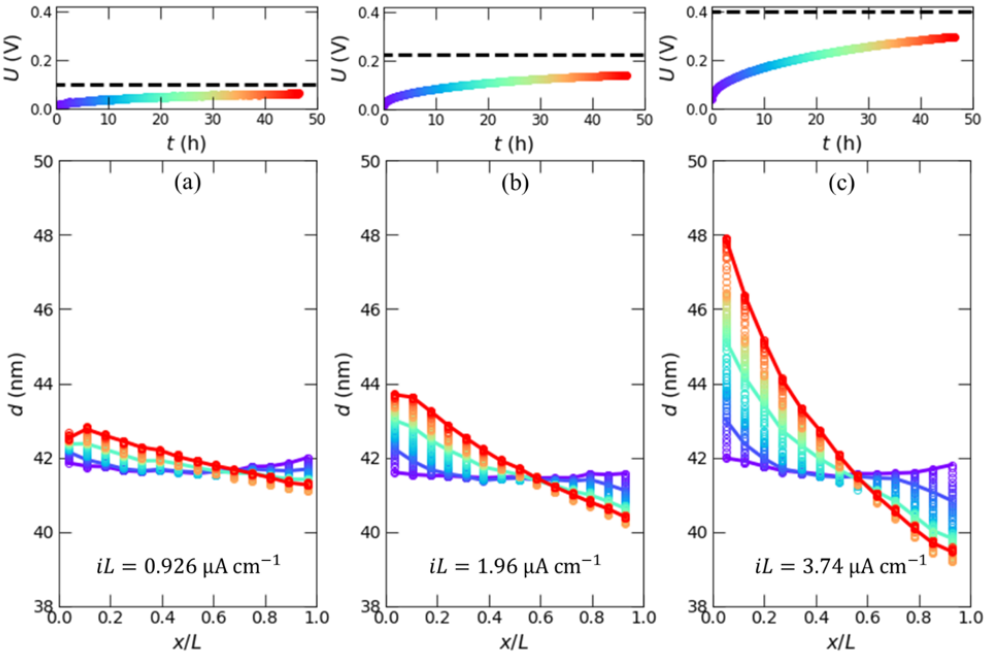


Figure 9.5. Results from simultaneous polarization and SAXS experiments at three current densities. The potential drop across the electrolyte, $U$, *vs.* time, $t$, is plotted in the

top panel of each figure. The dashed line represents the steady-state potential ($U_{ss}$) predicted from concentrated solution theory. In the main panel, the domain spacing, $d$, is plotted *vs.* normalized cell position, $x/L$, for the cell polarized at (a) $iL$ = 0.962 $\mu$A cm$^{-1}$, (b) 1.96 $\mu$A cm$^{-1}$, and (c) 3.74 $\mu$A cm$^{-1}$. The color of each data set corresponds with the $U$ *vs.* $t$ plot in the top panel. Purple data sets were obtained at the beginning of polarization ($t$ = 0 h), and red data sets were obtained at the end of polarization ($t$ = 46.6 h).

### *9.4.3 Domain Spacing as a Proxy for Salt Concentration*

For each data point in Figures 9.5a–c, we calculate a local salt concentration from Equation 9.2 to obtain $r(x/L,t)$ for each cell, and the results are plotted as data points in Figure 9.6, following the same color scheme as in Figure 9.5. The black dashed lines represent the nominal initial salt concentration ($r$ = 0.16) of the cell, and the solid black lines represent the steady-state salt concentration gradient predicted from the theory. Based on Figure 9.3a, we calculate the ratio of the current density to the limiting current, $i/i_{lim}$. Because the predicted limiting current differs significantly from the measured limiting current, we report the ratio of the applied current to both the experimental and theoretical limiting currents, $i_{lim,expt}$ and $i_{lim,theory}$, respectively. The applied current density is 20, 44, and 80% of $i_{lim,expt}$ and 9.0, 20, and 36% of $i_{lim,theory}$ for Figures 9.6a–c, respectively. In Figure 9.6a and b, we see good agreement between the experiment and the theory; the magnitude of the salt concentration near the end of the polarization experiment matches the predicted salt concentration gradient. Conversely, the agreement with $r(x/L)$ is poor in Figure 9.6c at $iL$ = 3.74 $\mu$A cm$^{-1}$.

In Figure 9.6c, using the domain spacing as a proxy for salt concentration results in local values of $r$ which are significantly greater than the theory across the entire cell. The experimental salt concentration averaged across all positions calculated from Equation 9.2 in Figure 9.6c is $r$ = 0.157 at $t$ = 0 h and $r$ = 0.186 at $t$ = 46.6 h, an increase of 18%. Because the average salt concentration must be conserved throughout the experiment, we conclude that the assumed relationship between $r$ and $d$, which was based on measurements on samples at equilibrium, is strictly valid when the magnitude of the ionic current that flows through the sample is well below the limiting current. Nevertheless, we obtain considerable insight into the origin of the observed gradients in $d$ under applied electric fields by combining equilibrium measurements of domain spacing with concentrated solution theory. Reasonable agreement is observed between the theory and experiment for $i/i_{lim,expt} < 0.5$. In this regime, we also observe good agreement between theoretical and experimental $U_{ss}$ *vs.* $iL$ data in Figure 9.3b.

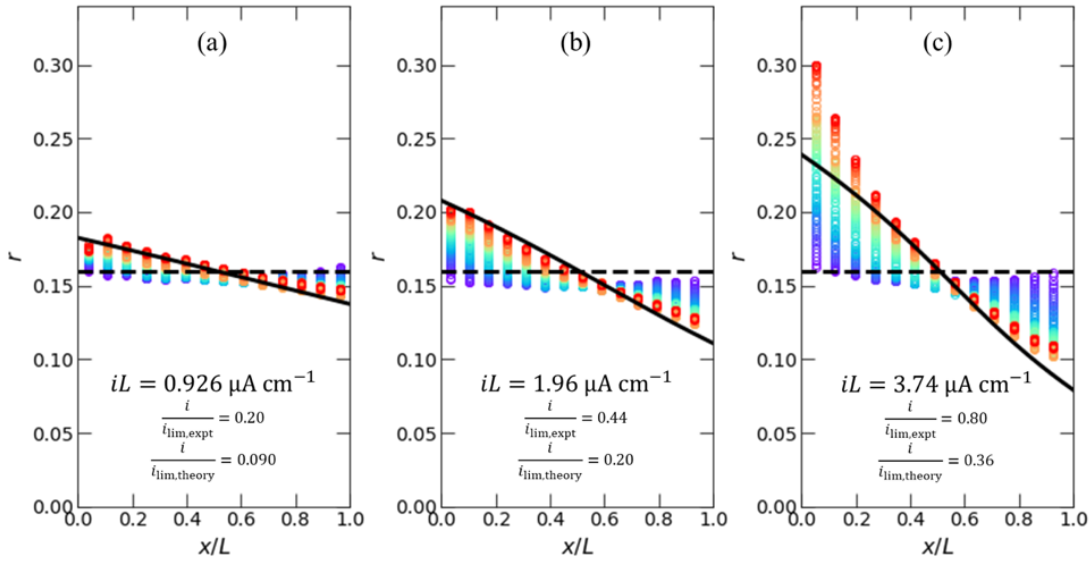


Figure 9.6. Molar salt concentration, $r$, *vs.* normalized cell position, $x/L$, based on converting the domain spacing, $d$, presented in Figure 9.5 to $r$ with Equation 9.2. We report the ratio of the applied current to the experimental limiting current, $i_{\text{lim,expt}}$, and the theoretical limiting current, $i_{\text{lim,theory}}$. Data obtained with (a) $iL = 0.926$ $\mu$A cm$^{-1}$, (b) $iL = 1.96$ $\mu$A cm$^{-1}$, and (c) $iL = 3.74$ $\mu$A cm$^{-1}$. The color scheme for each data set matches that presented in Figures 9.5a–c. The dashed black line represents the nominal initial salt concentration, $r = 0.16$. The solid black line represents the predicted steady-state salt concentration gradient from the theory.

### *9.4.4 Swelling and Contracting Lamellae at High Current Density*

To gain deeper insight into the swelling and contraction of the lamellae at high current density, we performed the following experiments. After polarizing the cell in Figure 9.5a at 0.926 $\mu$A cm$^{-1}$ for 46.6 h, we increased the current by a factor of 12: 11.1 $\mu$A cm$^{-1}$ (i.e., $i/i_{\text{lim,expt}} = 2.4$ and $i/i_{\text{lim,theory}} = 1.07$). The potential of the cell is plotted as a function of time in Figure 9.7a beginning at $t = 46.6$ h when the current was abruptly increased in a blue-to-green color scheme. At that time, the potential jumps from 0.08 to 0.2 V and then steadily increases. At $t = 58$ h, there is an inflection point and the potential diverges. A cutoff voltage was set at 1.0 V, and the cell was switched to an open circuit ($i = 0$ $\mu$A cm$^{-2}$) at $t = 61.1$ h. The potential then begins to decay, plotted in a blue-to-pink color scheme, as the concentration gradient relaxes.

Throughout the experiment, we measured $d(x/L)$ as a function of time. We define the change in domain spacing, $\Delta d$, by Equation 9.12:

$$\Delta d(x/L, t) = d(x/L, t) - d\left(\frac{x}{L}, t = 0\right). \qquad (9.12)$$

Recall that $t = 0$ is at the beginning of the first polarization step at 0.926 $\mu$A cm$^{-1}$, so the quantity $\Delta d(x/L, t)$ reflects the change in domain spacing from the quiescent, $r = 0.16$ electrolyte. In Figure 9.7b, we plot $\Delta d$ as a function of normalized position in the cell from $t = 0$ to 61.1 h. Data sets plotted with black markers represent $\Delta d$ during the initial polarization at 0.926 $\mu$A cm$^{-1}$. The magnitude of $\Delta d$ is less than 2 nm during this time (see Figure 9.5a). Data for $46.6 < t$ (h) $< 61.1$ is plotted in a blue-to-green color scheme, where the color corresponds to the *U vs. t* data in Figure 9.7a. The right axis of Figure 9.7b represents the percent change of the domain spacing from the nominal initial value of 42.4 nm (averaged over all $x/L$ at $t = 0$ h). At $x/L = 0.088$ (near the lithium stripping electrode), $\Delta d$ reaches 10.8 nm at $t = 61.1$ h, an increase of 25.4% from the quiescent state. At $x/L = 0.93$ (near the lithium plating electrode), we measure $\Delta d$ of $-4.4$ nm at $t = 61.1$ h, a decrease of 10.4% from the quiescent state. This difference between $\Delta d$ at $x/L = 0.088$ and 0.93 highlights the point that the swelling of the salt-rich lamellae is not compensated by the contracting of the salt-deficient lamellae. We take this analysis a step further by fitting the data set at $t = 61.1$ h to a fifth-order polynomial plotted as a red line in Figure 9.7b and given by

$$\Delta d = -272(x/L)^5 + 816(x/L)^4 - 955(x/L)^3 + 542(x/L)^2 - 158(x/L) + 21.0. \qquad (9.13)$$

Because the cell is operating above the limiting current, the shape of *d vs. x/L* when the potential diverges (green data set) is highly nonlinear: the gradient in *d* is most severe near the electrodes. The area under the curve (calculated by integrating Equation 9.13 from $x/L = 0$ to 1) is an average of 1.6 nm. This implies that the average increase in *d* is 1.6 nm or 3.8% from the quiescent state. Based on these significant changes in the domain spacing, it is instructive to analyze the scattering profiles more closely.

In Figure 9.7c,d, we present the 1D SAXS profiles during polarization ($t = 46-61$ h) for the $x/L = 0.088$ (highlighted by the dashed gold box in Figure 9.7b) and $x/L = 0.93$ (highlighted by the dashed purple box in Figure 9.7b) positions, respectively. We plot the scattered intensity from the sample $I_s(q)$ divided by a constant reference intensity, $I_{ref}$. $I_{ref}$ is the maximum intensity of the primary scattering peak of the reference sample (as described in the Experimental Methods, Section 9.3). The scattering from the reference sample was measured once for each data set in Figure 9.7b. We use the same color scheme in Figures 9.7c and d to denote the time of each data set. Our main interest is to investigate if there are any signatures of the lamellar structure being disrupted near the electrodes during the extreme polarization conditions. Overall, we see a shift of the primary scattering peak to lower $q$ (higher domain spacing) in Figure 9.7c, but the character of the peak remains consistent throughout the experiment. We do not observe the emergence of new peaks, indicating that the lamellar structure is preserved at all times and locations.

The gradual changes in peak intensity are attributed to the change in scattering contrast between the lamella associated with changing salt concentration in the PEO-rich domains. The same is true in Figure 9.7d as the peak shifts to higher $q$ (lower domain spacing). In Figures 9.7e and f, we show the 1D SAXS patterns obtained during the open-circuit relaxation step ($t$ = 61 through $t$ = 80 h) at x/$L$ = 0.088 and 0.93, respectively. Again, the character of the primary scattering peak is maintained as the peak position shifts toward the initial peak position prior to polarization.

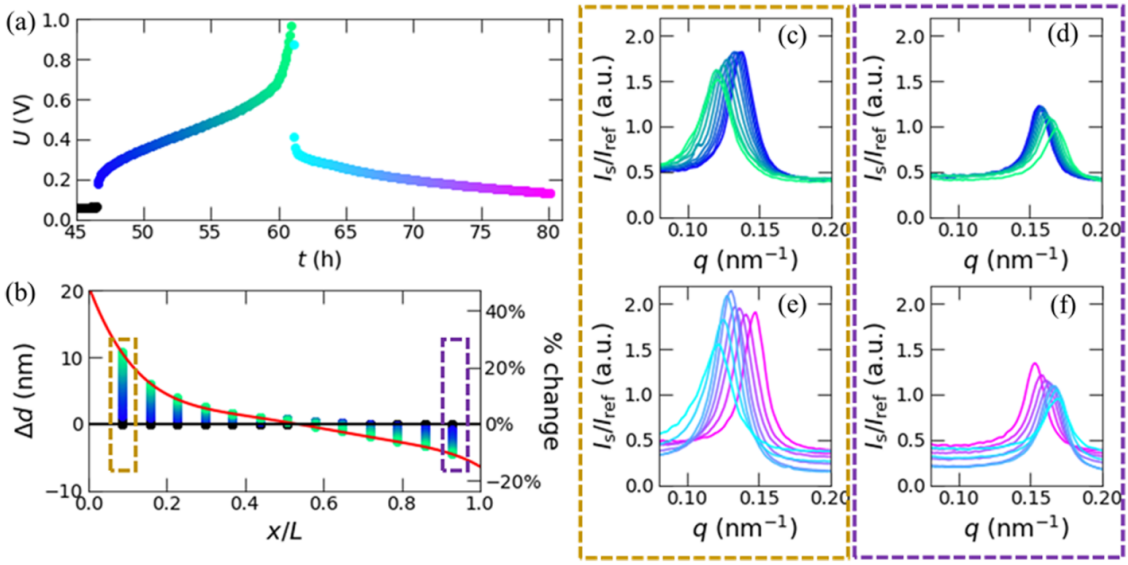


Figure 9.7. Results from simultaneous polarization and SAXS experiments performed at a current density above the limiting current, $iL$ = 11.1 $\mu$A cm$^{-1}$. The current was increased from 0.926 $\mu$A cm$^{-1}$ at $t$ = 46.6 h (data for $t$ < 46.6 h is presented in Figures 9.5a and 9.6a at the lower current density). (a) Potential drop across the electrolyte, $U$, *vs.* $t$. For 46.6 < $t$ (h) < 61.1, a constant current of $iL$ = 11.1 $\mu$A cm$^{-1}$ was applied and $U$ is plotted in a blue-to-green color scheme. At $t$ = 61.1 h, the cell was switched to an open circuit ($iL$ = 0) and the open-circuit cell potential is plotted in a blue-to-pink color scheme. (b) Change in domain spacing, $\Delta d$, defined by Equation 9.12 *vs.* $t$ for the constant current polarization for 46.6 < $t$ (h) < 61.1. Data sets plotted with black symbols were obtained during the 0.926 $\mu$A cm$^{-1}$ polarization for $t$ < 46.6 h. The blue-to-green color scheme of the remaining data set corresponds with the $U$ *vs.* $t$ plot in panel (a). The red trace is a polynomial fit to the final data set at $t$ = 61.1 h (green data points). 360° azimuthal averages of selected 2D SAXS patterns are presented in panels (c) through (e), with colors corresponding to the $U$ *vs.* $t$ data in panel (a). (c) $I(q)$ plots for 46.6 < $t$ (h) < 61.1 during the 11.1 $\mu$A cm$^{-1}$ polarization at $x/L$ = 0.088 and (d) $x/L$ = 0.93. (e) $I(q)$ plots for $t$ > 61.1 h when the cell is at open circuit measured at $x/L$ = 0.088 and (f) $x/L$ = 0.93. The gold and purple dashed boxes in panels (b) through (f) highlight data obtained at $x/L$ = 0.088 and 0.93, respectively.

*9.4.5 Lamellar Orientation Order Parameter*

To further investigate the extent to which the lamella may rearrange due to polarization, we calculated an orientation parameter for the electrolyte as a function of position and time. For each scan, the scattering pattern was divided into 36 sectors and averaged to obtain $I(q)$ for each sector. To compare the total scattered intensity for each grain orientation, $Q(\chi)$, we integrated $q^2I(q)$ over the primary scattering peak for each sector. The orientation parameter, $f$, was calculated according to Equation 9.14

$$f = \frac{3\langle\cos^2\chi\rangle - 1}{2}, \qquad (9.14)$$

using Equation 15

$$\langle\cos^2\chi\rangle = \frac{\int_0^{90} Q(\chi)\cos^2(\chi)\sin(\chi)\,\mathrm{d}\chi}{\int_0^{90} Q(\chi)\sin(\chi)\,\mathrm{d}\chi}, \qquad (9.15)$$

where 0° is defined such that it corresponds to lamellae with normal vectors perpendicular to the direction of current flow, as shown in Figure 9.4b. Our analysis is based on the commonly used Herman's orientation parameter [200–202] An orientation parameter $f = 1$ describes a lamellar sample where all grains are oriented with PS-PEO interfaces parallel to the direction of current flow. For a sample with all PS-PEO interfaces oriented perpendicular to the direction of current flow, $f = -0.5$. Randomly oriented lamellae correspond to $f = 0$.

The $Q(\chi)$ data ranges from $\chi = 0$ to 360°. In Equation 9.15, we restrict the analysis to only include data from $\chi = 0$ to 90°, which is justified by symmetry in the 2D SAXS patterns. A single lamellar grain generates identical scattering along two azimuths separated by 180°. There is an additional plane of symmetry as grains oriented with $\chi = \pm\alpha$ for $0° < \alpha < 180°$ are identical from an electrochemical standpoint. To minimize noise in the data, we thus averaged the four quadrants of our data by first adding $Q(\chi)$ from 180 to 360° to the $Q(\chi)$ from 0 to 180°. Next, we folded the resulting data, which ranges from 0 to 180°, around $\chi = 90°$, thus resulting in $Q(\chi)$ that includes data from all four quadrants with $\chi$ ranging from 0 to 90°. This data set of $Q(0 < \chi < 90°)$ was numerically integrated to obtain $\langle\cos^2\chi\rangle$ according to Equation 9.15.

The resulting orientation parameter, $f(t)$, is presented in Figure 9.8 for each position in the cell with $iL = 1.96$ $\mu$A cm$^{-1}$. Similar plots for the other two cells can be found in Figure A9.9 and are qualitatively similar. At all positions, $f$ is approximately $-0.18 \pm 0.03$,

with little change over time. This indicates that before any current is applied, the lamellar grains have a slight preference for orientations such that the PS-PEO interfaces are perpendicular to the direction of current flow. This orientation was likely introduced by the mechanical force necessary to deform the electrolyte and fill the cell. Electrochemical polarization does not affect the distribution of grain orientations. If lamellar grains were to break up and reform during electrochemical polarization, one would expect newly formed lamellae either to be randomly oriented, corresponding to $f = 0$, or to form with a new preferential orientation due to current flow. In either case, we would expect to observe $f$ which varies with time. The observation that $f$ is time-invariant suggests that the grain structure remains relatively constant throughout the experiment.

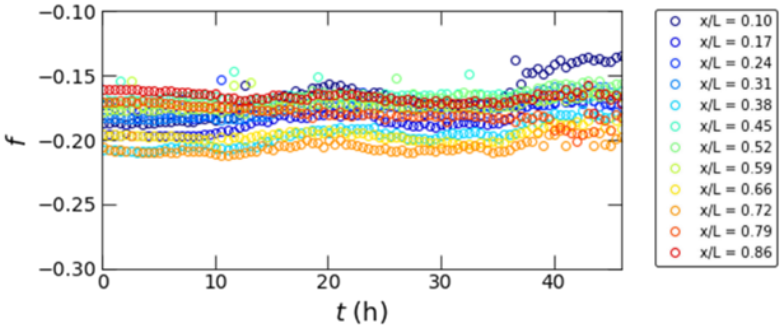


Figure 9.8. Orientation parameter, $f$, *vs.* time, $t$, for the cell polarized at $iL = 1.96$ $\mu$A cm$^{-1}$ for positions ranging from $x/L = 0.10$ to 0.86. $f$ is approximately constant with time across all positions, indicating that polarization does not induce grain alignment or dealignment.

*9.4.6 Orientation Dependence of Lamellar Distortion*

We next analyze how different orientations of lamella swell and contract in response to the salt concentration gradient. We focus our attention on the data sets obtained right before the cells are switched to open circuit. We divide the 2D scattering pattern into 16 sectors as shown in Figure 9.4b to obtain $I(q,\chi)$, where $\chi$ represents the angle at the center of the sector. We follow the same peak fitting procedure as discussed previously to obtain $d(\chi)$ from the 2D scattering plots. Before polarization, we find that $d(\chi)$ was not constant. To account for this, we redefine the quantity $\Delta d$ for a fixed position $x/L$ in Equation 9.16

$$\Delta d(\chi, t) = d(\chi, t) - d(\chi, t = 0)\,. \qquad (9.16)$$

In Figures 9.9a–c, we plot $\Delta d$ as a function of $\chi$ for each position in the cell for the cells polarized at (a) $iL = 1.96$ $\mu$A cm$^{-1}$, (b) $iL = 3.74$ $\mu$A cm$^{-1}$, and (c) $iL = 11.1$ $\mu$A cm$^{-1}$. From top to bottom, $x/L$ increases from 0.10 to 0.86. Near the positive electrode (i.e., $x/L < 0.4$), $\Delta d > 0$ for all $\chi$ and there are local maxima at $\chi = 90$ and 270°. Near the

center of the cell, $\Delta d$ is approximately equal to zero for all values of $\chi$. Near the negative electrode (i.e., $x/L > 0.6$), $\Delta d < 0$ for all $\chi$ and there are local minima at $\chi = 90$ and 270°. The results presented in Figures 9.9a–c show that grains with PS-PEO interfaces perpendicular to the flow of ionic current ($LAM_{\perp}$) undergo greater expansion (near the positive electrode) or contraction (near the negative electrode) when compared to those with PS-PEO interfaces oriented parallel to the flow of ionic current ($LAM_{||}$). To highlight this point, we plot the difference in lamella spacing between $LAM_{\perp}$ and $LAM_{||}$, $d_{LAM\perp} - d_{LAM||}$, in Figure 9.9d. The color of each data point in Figure 9.9d corresponds to the data set of the same color in Figure 9.9a–c. As the concentration gradient builds up, the $LAM_{\perp}$ near the positive electrode are swollen between 0.6 and 1.2 nm larger than $LAM_{||}$. Near the negative electrode, the $LAM_{\perp}$ are between 0.2 and 1.2 nm smaller than the $LAM_{||}$. Figures 9.8 and 9.9 indicate that the $\chi$ dependence of domain swelling and contracting is decoupled from any preferential grain orientation that was introduced during sample preparation.

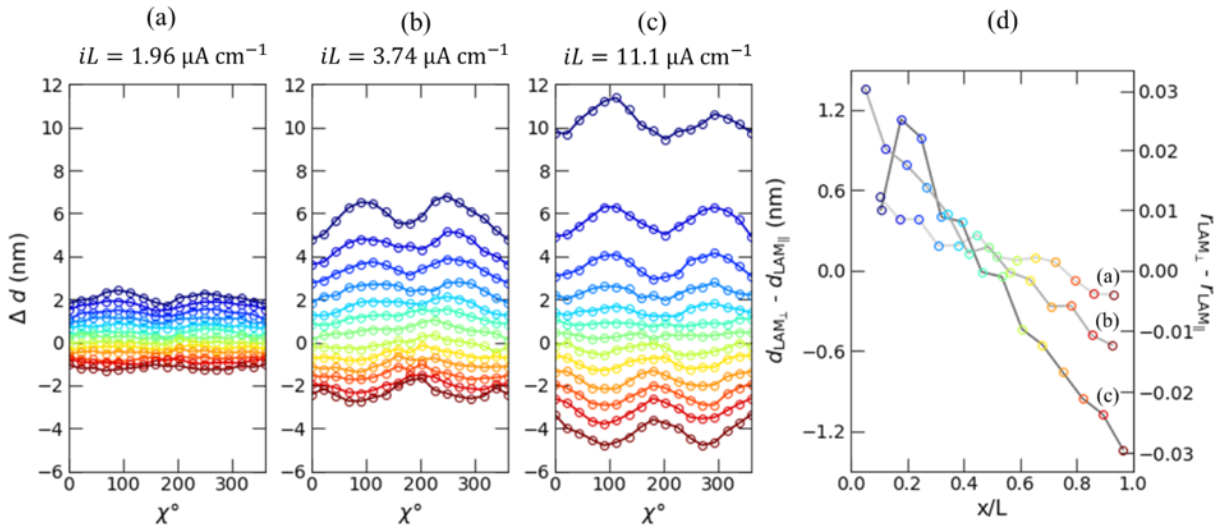


Figure 9.9. Orientation dependence of lamellar distortion. The change in domain spacing, $\Delta d$, defined by Equation 9.16 as a function of azimuthal angle, $\chi$, is plotted for each cell position for the cell polarized at (a) $iL = 1.96\ \mu A\ cm^{-1}$ at $t = 46.7$ h, (b) $iL = 3.74\ \mu A\ cm^{-1}$ at $t = 46.7$ h, and (c) $iL = 11.1\ \mu A\ cm^{-1}$ at $t = 60.7$ h. Each data set is based on the last scan taken at the end of each polarization. (d) Difference in domain spacing between $LAM_{\perp}$ and $LAM_{||}$ as a function of normalized position, $x/L$, for the three data sets in panels (a)–(c). The right axis is the difference in molar salt concentration, $r$, based on Equation 9.2. The color of each data set in panels (a)–(c) corresponds to the $x/L$ position plotted in panel (d).

The orientation-dependent distortion of lamellae shown in Figures 9.9a–d indicates that the salt that is preferentially depleted from $LAM_{\perp}$ at the negative electrode preferentially accumulates in $LAM_{\perp}$ near the positive electrode. In a randomly oriented lamellar sample, one would conclude that grains in the $LAM_{||}$ orientation contribute the most to dc conductivity relative to any other orientation, while those in the $LAM_{\perp}$ do not contribute to the dc conductivity. [203] Our analysis shows that $LAM_{\perp}$ also play a critical, but more subtle, role in ion transport. The swelling and contracting of the lamellae are required to allow the formation of a salt concentration gradient and thus sustain the applied current, and a larger portion of this volume change is accommodated by those lamellae in the $LAM_{\perp}$ orientation. While a lamellar sample with only the $LAM_{\perp}$ orientation would not be desirable as there would be no path for ionic current to pass between the electrodes, one with only the $LAM_{||}$ orientation may also be undesirable because the resistance to volume change would reduce the limiting current. Therefore, we hypothesize that a collection of lamellar grains with a distribution of orientations is likely to lead to the largest limiting current due to the need to accommodate both large ionic currents and large salt concentration gradients. Testing of this hypothesis would require control over the distribution of grain orientations prior to polarizing the cell.

We take our analysis a step further by using Equation 9.2 to estimate the local salt concentration in the lamellar grains as a function of $\chi$. The results are shown on the right axis of Figure 9.9d. Although we have discussed that the conversion from $d$ to $r$ fails quantitatively at high current densities, we do expect qualitatively that for two grains at the same $x/L$ but with different $d$, the grain with higher $d$ will have higher local $r$. Thus, by calculating $r$ *vs.* $\chi$ for each position, we get an approximation of how the salt concentration varies in grains with different orientations. Based on Figure 9.9d, $r$ is about 0.03 higher in $LAM_{\perp}$ compared to that in $LAM_{||}$ near the salt-rich electrode and about 0.03 lower near the salt-deficient electrode for the cell polarized above the limiting current at $iL = 11.1\ \mu A\ cm^{-1}$. These results suggest that salt concentration is nonuniform along all three axes ($x$, $y$, and $z$), not just along the axis of ion transport ($x$). For the $y$- and $z$-axes, the concentration heterogeneity is on the length scale of the grain size (typically a few microns), while along the $x$-axis, the concentration gradient is on the length scale of $L$. In previous work, we identified the formation of concentration hotspots in SEO(1.7–1.4). [186] This new insight suggests that the nucleation of these hotspots likely emerges from grains in the $LAM_{\perp}$ orientation where salt accumulates more heavily.

The local salt concentration within a single lamellar grain and domain spacing is intimately related. Thermodynamically, there is no reason why salt would prefer to reside in one grain over another based strictly on grain orientation relative to the current direction. We posit that the reason for preferential salt partitioning into perpendicular lamellae is related to the fact that the salt concentration gradient forms along the x-axis,

independent of the local block copolymer grain structure (salt concentration gradients also develop along the $x$-axis in homopolymer electrolytes). Thus, there is a force driving the lamellae to expand in the $x$-direction for regions near the positive electrode where $r > r_{avg}$ and contract in the $x$-direction for regions near the negative electrode where $r < r_{avg}$. This force naturally distorts lamellae that have PEO-PS interfaces oriented perpendicular to the $x$-axis ($LAM_{\perp}$). For lamellae with interfaces oriented parallel to the $x$-axis ($LAM_{||}$), this force acts parallel to the PEO-PS interfaces and therefore does not lead to additional lamellar distortions.

## 9.5 Conclusions

Concentrated solution theory provides a framework to predict the development of salt concentration gradients and the associated potential drop across the electrolyte when current is passed through a cell. This can be extended to predict the maximum current density that can be sustained through the electrolyte (i.e., the limiting current, $i_{lim}$). The prediction is based on the condition that the salt concentration reaches zero at the negative electrode where lithium plating occurs. Experimentally, we find that the limiting current in SEO(19-20)/LiTFSI at $r = 0.16$ is approximately a factor of 2 lower than that predicted from concentrated solution theory. Small-angle X-ray scattering performed on the electrolyte during dc polarization provides several key insights into the reasons for this observation. In particular, we use scattering data to track distortions of the block copolymer lamellae due to the passage of ionic current. The rearrangement of conducting and nonconducting domains is coupled to the observed limiting current: the passage of ionic current requires the lamellae to distort to accommodate the salt concentration gradient. Concentrated solution theory does not account for these effects.

The SAXS experiments show that there was a net increase in the domain spacing of the block copolymer as the salt concentration gradient develops. We observed that grains with PS-PEO interfaces oriented perpendicular to the flow of ionic current ($LAM_{\perp}$) swell and contract to a greater extent compared to those with PS-PEO interfaces oriented parallel to the flow of ionic current ($LAM_{||}$). It is obvious that $LAM_{||}$ play an important role in ion transport as the conducting domains in these grains are parallel to the direction of macroscopic ion transport. Our work indicates that $LAM_{\perp}$ also play an important role. The formation of a salt concentration gradient that must arise due to ion transport across macroscopic length scales relies on the ability of the lamellae to swell and contract. These distortions occur to a greater extent in $LAM_{\perp}$. Both $LAM_{||}$ and $LAM_{\perp}$ appear to be necessary to accommodate large ionic currents in block copolymer electrolytes.

## 9.6 Acknowledgements

This work was supported by the Assistant Secretary for Energy Efficiency and Renewable Energy, Vehicle Technologies Office, under the Advanced Battery Materials Research

(BMR) Program, of the U.S. Department of Energy under Contract No. DE-AC02-05CH11231. C.J.T., C.C., H.-G.S., and M.F.T. were supported by the Joint Center for Energy Storage Research (JCESR), an Energy Innovation Hub funded by the U.S. Department of Energy, Office of Science, Basic Energy Sciences. This research was completed at the Stanford Synchrotron Radiation Light Source, a user facility at SLAC National Accelerator Laboratory, which was supported by the U.S. Department of Energy, Office of Science, Office of Basic Energy Sciences under Contract No. DE-AC02-76SF00515. The authors also used beamline 7.3.3 of the Advanced Light Source, which is a DOE Office of Science User Facility under contract no. DE-AC02-05CH11231. The research used resources of the Advanced Photon Source and the Center for Nanoscale Materials, U.S. Department of Energy (DOE) Office of Science User Facilities operated for the DOE Office of Science by Argonne National Laboratory under Contract No. DE-AC02-06CH11357.

# Chapter 10: Inaccessible Polarization-Induced Phase Transitions in a Block Copolymer Electrolyte: An Unconventional Mechanism for the Limiting Current*

## 10.1 Abstract

Block copolymer electrolytes that microphase separate into mechanically rigid and ion-conducting domains are promising materials for lithium metal batteries. We present experimental data on a block copolymer electrolyte composed of polystyrene-block-poly(ethylene oxide) (SEO) and bis(trifluoromethanesulfonyl)imide (LiTFSI) which, under equilibrium conditions, exhibits a hexagonally-packed cylindrical (HEX) morphology at low salt concentrations and a body-centered cubic spherical (BCC) morphology at high salt concentrations. The limiting current, which causes the cell potential to diverge exponentially if exceeded, is usually reached when the salt concentration at the negative electrode approaches zero due to concentration polarization. We use *in situ* X-ray scattering to study the morphology of our SEO/LiTFSI electrolyte, which exhibits a BCC morphology at equilibrium, during polarization. We expected to obtain a HEX morphology near the negative electrode as the limiting current is approached and the salt concentration at the negative electrode approaches zero. Instead, we find that the cell potential diverges when the salt concentration at this electrode approaches the concentration at the BCC / HEX boundary at high current densities. The maximum current that can be carried by our electrolyte is thus not limited by the lack of salt at the negative electrode. Instead, it appears to be related to a phase transition that occurs readily in equilibrated samples but is inaccessible in a polarized cell.

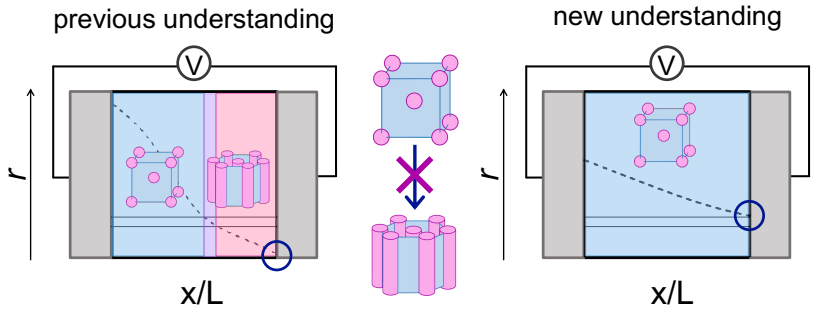


Figure 10.1. Illustration of the previous understanding of the origins of the limiting current (left) compared with the salt concentration gradient at the limiting current in this work.

* This Chapter is adapted from Grundy, L. S. *et al.* Inaccessible Polarization-Induced Phase Transitions in a Block Copolymer Electrolyte: An Unconventional Mechanism for the Limiting Current. *Macromolecules* **2022**, *in press*. [232]

## 10.2 Introduction

### *10.2.1 Block Copolymer Electrolytes*

Lithium metal is a promising anode material due to its high energy density [1] but is limited by its propensity for dendrite growth, which can lead to short-circuits. [204,205] One class of candidate electrolyte materials consists of block copolymers mixed with a lithium salt; [20] in this case, polystyrene-block-poly(ethylene oxide) (SEO), which consists of a polystyrene (PS) block and a poly(ethylene oxide) (PEO) block, mixed with lithium bis(trifluoromethanesulfonyl)imide (LiTFSI). These materials are non-reactive with lithium and are particularly notable because they phase separate into mechanically rigid (PS) and ion-conducting (PEO / LiTFSI) domains to prevent dendrite growth without inhibiting ion transport. [112] There is a long literature history characterizing the morphologies of block copolymer electrolytes as a function of molecular structure and salt concentration. The morphology of neat block copolymers has been studied extensively, and depends on the total polymer molecular weight, volume fraction of each component, and the Flory-Huggins interaction parameter between the two blocks. [13,206,207] When salt is added, the morphology also depends on the salt concentration. [14,15,208,209] The morphology of the electrolyte has a significant impact on its properties by influencing both the mechanical properties, and therefore dendrite suppression, as well as the geometry of the ion-transporting microphase, and therefore electrochemical performance. [138,210–214]

### *10.2.2 Salt Concentration Gradients*

In an electrochemical cell, the salt concentration and block copolymer electrolyte morphology are initially macroscopically uniform. However, when a current is applied, salt accumulates at the positive electrode and is depleted at the negative electrode; in other words, the salt concentration is polarized. This occurs because the anion migrates towards the positive electrode and, because it is electrochemically-inactive, accumulates there. The cation migrates towards the negative electrode, where it is reduced electrochemically and therefore does not accumulate. Due to the requirement of charge neutrality, if the salt is univalent, the concentration profile of the two ions must be identical, with an accumulation of salt at the positive electrode. The salt concentration profile can be calculated both at steady-state and as a function of time if three transport parameters — ionic conductivity, $\kappa$, cation transference number with respect to the solvent velocity, $t_+^0$, and salt diffusion coefficient, $D$ — and the thermodynamic factor, $T_\mathrm{f} = 1 + \frac{d\ln \gamma_\pm}{d\ln m}$ (where $\gamma_\pm$ is the mean molal salt activity coefficient and $m$ is the salt molality in the ion-transporting microphase), are known. [181,29,47,215] These calculations rely on Newman's concentrated solution theory, which is a continuum theory that is valid in both dilute and concentrated electrolytes, regardless of molecular-scale complexities due to factors such as partial dissociation of the ions and the formation of transient charged clusters. [29]

Recent experimental work has begun to validate predicted salt concentration profiles.[215,216,111] In a constant-current experiment, a higher applied current results in a steeper steady-state concentration gradient. The maximum accessible current density, which causes the cell potential to diverge exponentially if exceeded, is referred to as the limiting current density, $i_{\text{lim}}$, and is often approximated as the current at which the steady-state salt concentration profile reaches zero at the negative electrode.[48,49] This approach for characterizing electrolytes with two mobile charged species, developed by Newman[29] and used in the context of homogeneous liquid electrolytes,[217] has been shown to be an appropriate starting point for examining microphase separated electrolytes.[23,218,219]

As the salt concentration changes, the electrolyte properties also change. As such, to model the salt concentration profile under polarization, the above properties must be measured at a range of salt concentrations. This is done by formulating equilibrated electrolytes—using a solvent, as described in the Methods section—at various salt concentrations and performing electrochemical experiments in test cells in which small salt concentration gradients are formed to measure $\kappa$, $t_+^0$, $D$, and $T_f$. It is assumed that in a practical polarized cell with large salt concentration gradients, the properties of the region of the electrolyte at a given location correspond to the properties of the equilibrated electrolyte of the same concentration.

*10.2.3 Morphological Transitions*

In this work, we study a block copolymer electrolyte composed of polystyrene-*block*-poly(ethylene oxide) with a polystyrene molecular weight of 4.0 kg/mol and a poly(ethylene oxide) molecular weight of 22.4 kg/mol (SEO(4.0-22.4)) mixed with lithium bis(trifluoromethanesulfonyl)imide (LiTFSI) salt. All measurements were performed at 90 °C. The salt concentration is quantified using $r$, the number of lithium ions per ethylene oxide moiety. In equilibrated samples, SEO(4.0-22.4) with $r > 0.10$ exhibits a body-centered cubic spherical (BCC) morphology with PS-rich spheres in a PEO/LiTFSI-rich lattice; SEO(4.0-22.4) with $r < 0.075$ exhibits a hexagonally-packed cylindrical (HEX) morphology with PS-rich cylinders in a PEO/LiTFSI-rich lattice; and SEO(4.0-22.4) with $0.075 \leq r \leq 0.10$ exhibits a coexisting BCC and HEX morphology.

Our objective is to study electrochemically-induced phase behavior of this electrolyte in the vicinity of the limiting current. An SEO(4.0-22.4) / LiTFSI electrolyte with an average salt concentration $r_{\text{avg}} = 0.16$, and therefore a BCC morphology, was placed in a lithium-lithium symmetric cell. Using *in situ* small-angle X-ray scattering and absorbance measurements, we study the position- and time-dependent concentration and morphology of the electrolyte; the electrode/electrolyte plane is parallel to the incident beam which enables determination of morphology as a function of position on the axis along which ion transport occurs and a salt concentration gradient develops. Unexpectedly, we observe that the morphology in the entire cell is BCC, regardless of position, time, and applied

current. When the local salt concentration near the negative electrode in a cell with an initially uniform salt concentration of $r_{avg} = 0.16$ reaches $r = 0.10$, the cell potential diverges exponentially, the signature that the limiting current has been exceeded. No signature of the coexistence of HEX and BCC observed in equilibrated samples is seen in any of the *in situ* SAXS profiles obtained in the presence of ionic current. We conclude that the BCC / HEX transition observed in equilibrated samples is inaccessible under the conditions of concentration polarization in an operando cell. This indicates that block copolymer electrolyte behavior in an *in situ* electrochemical cell can be fundamentally different from that obtained in *ex situ* equilibrium experiments.

## 10.3 Experimental Methods

### *10.3.1 Materials*

The polystyrene-*block*-poly(ethylene oxide) (SEO) block copolymer used in this study has a polystyrene (PS) block molecular weight of 4.0 kg/mol and a poly(ethylene oxide) (PEO) block molecular weight of 22.4 kg/mol; it is denoted SEO(4.0-22.4). This polymer was designed specifically to study current-induced phase transitions, and not for practical applications related to the stabilization of lithium metal anodes. The polymer was synthesized using anionic polymerization techniques and purified and characterized as described in Teran *et al.* [14] and Hadjichristidis *et al.* [16] Morphological [15] and electrochemical [23] studies of this polymer have been published previously. The electrolytes, mixtures of SEO(4.0-22.4) and lithium bis(trifluoromethanesulfonyl)imide (LiTFSI) salt, were prepared following methods described in Yuan *et al.* [143] In brief, stock solutions of freeze-dried SEO(4.0-22.4) in benzene and dry LiTFSI in tetrahydrofuran were prepared in an argon glovebox and combined gravimetrically to achieve the desired lithium to polymer ratio. The mixture was then freeze-dried in an air-free lyophilizer and dried again at 120 °C overnight under active evacuation in a glovebox antechamber. LiTFSI was purchased from Sigma-Aldrich and all solvents were purchased from Fisher Scientific. Lithium metal was purchased from MTI and scraped with a nylon brush prior to use. It was cut into small squares, with side length approximately 5 mm, and pressed to 500 psi, producing discs approximately 1 cm in diameter and 0.11 mm thick, which were used as electrodes.

### *10.3.2 Electrochemical Characterization*

Electrochemical experiments, both *in situ* and *ex situ*, were performed using a BioLogic VMP3 potentiostat. For impedance spectroscopy measurements, a frequency range of 1 MHz to 100 mHz and an amplitude of 80 mV were used. Electrochemical characterization from Galluzzo *et al.* [23] was used to calculate theoretical steady-state concentration gradients. Analysis of electrochemical data was performed using EC-Lab software.

*10.3.3 Equilibrium ex situ SAXS Measurements*

To obtain morphology and domain spacing information as a function of salt concentration, SEO(4.0-22.4) / LiTFSI electrolytes were prepared at salt concentrations ranging from $r = 0.02$ to 0.35 lithium ions per ethylene oxide moiety. Each electrolyte was pressed into an annular spacer of thickness 0.72 mm and sealed between two Kapton windows of thickness 0.025 mm in an air-free aluminum sample holder in an argon glovebox. The samples were annealed at 120 °C for 24 h in a glovebox antechamber under active evacuation. Measurements were performed at beamline 1-5 at Stanford Synchrotron Radiation Light Source (SSRL) at SLAC National Accelerator Laboratory using a custom-built heating stage. Each sample was maintained at 90 °C for at least 20 min before measurement. The beam center and sample-to-detector distance were calibrated using a silver behenate (AgB) standard, and an X-ray energy of 12 keV was used. 2D scattering patterns were captured on an SX165 CCD detector (Rayonix, LLC). Data previously published by Loo *et al.* [15] were also incorporated into the analysis; these experiments used the same sample preparation and thermal history and were performed at beamline 7.3.3.[144] of the Advanced Light Source (ALS) at Lawrence Berkeley National Laboratory at an X-ray energy of 10 keV using a Pilatus3 2M detector (Dectris Ltd.). Equilibrium *ex situ* SAXS data was analyzed using the Nika macro [45] in Igor Pro.

*10.3.4 Sample Preparation for in situ SAXS Measurements*

Figure 10.2 depicts the custom-designed and machined poly(ether ether ketone) (PEEK) cells used for *in situ* SAXS measurement. The electrolyte (a) is between two stainless steel current collectors (b), each of which have lithium metal on the face that is in contact with the electrolyte. The electrode dimensions are 1.95 mm by 3.95 mm, with the 1.95 mm direction oriented parallel to the X-ray beam direction. Nickel tabs are affixed to the stainless steel current collectors. The cell thickness can be adjusted using the set screw (c); tightening the set screw during sample preparation also helps to ensure consistent melting throughout the electrolyte. In this case, the cell thickness was set to 1.1 mm. As built-in controls, two isolated sample holes are included. One contains the same electrolyte being studied (d), so that *in situ* and *ex situ* measurements can be done in parallel, and any shifts in sample-to-detector distance during the experiment can be corrected. The other contains no sample (e), which serves as the "blank" measurement needed for X-ray transmission calculations and background subtraction. Finally, the two halves of the cell are sealed with a rubber o-ring (f), screwed together (g), and sealed in pouch material. The beam is oriented normal to the face of the cell, and shifting the samples spatially allows us to probe different positions between the two electrodes.

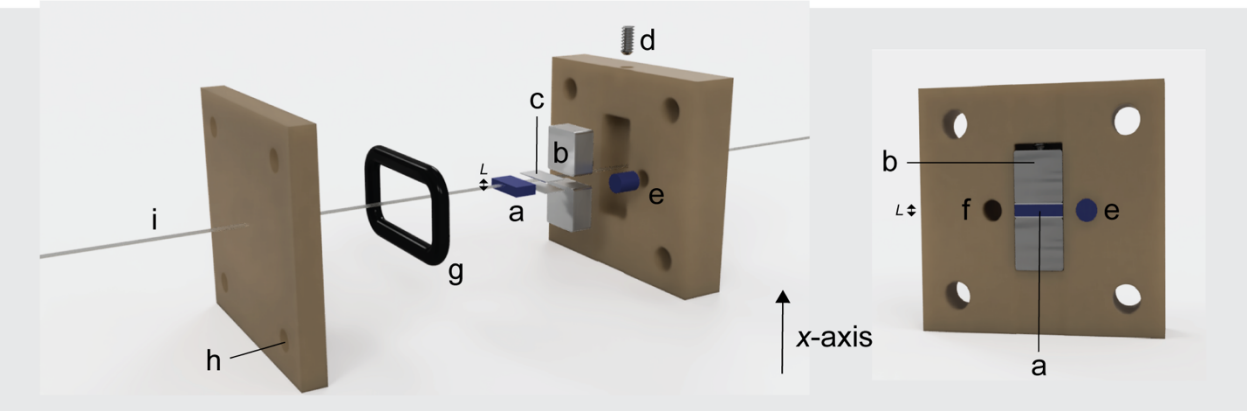


Figure 10.2. Schematic of *in situ* SAXS cell, side and front views. The electrolyte (a) is compressed between two stainless steel blocks (b). The lithium metal electrodes (c) are at the a / b boundaries. The electrolyte thickness, $L$, is controlled using a set screw (d). A reference (e) and a blank slot (f) are built in. The two halves of the cell are sealed with a rubber o-ring (g) and screwed together (h) before being sealed in pouch material. The X-ray beam (i) is shown to scale. The cell is constructed using PEEK.

Before sample preparation, the PEEK cell pieces were dried for 12 h under active evacuation in the glovebox antechamber at 120 °C to remove residual water and solvent from the washing process. The pouch material was also annealed following the same procedure to prevent any shifts in scattering from the pouch material during *in situ* SAXS experiments at high temperature. The electrolyte thickness, $L$, was measured using X-ray transmission at beamline 1-5 at Stanford Synchrotron Radiation Light Source (SSRL) at SLAC National Accelerator Laboratory after the completion of *in situ* SAXS experiments.

### *10.3.5 Experimental Procedure for in situ SAXS Measurements*

Samples were affixed to a custom-built heating stage at beamline 1-5 at Stanford Synchrotron Radiation Light Source (SSRL) at SLAC National Accelerator Laboratory and maintained at 90 °C for at least 1 h prior to polarization. The beam size was 700 $\mu$m by 200 $\mu$m, with the 200 $\mu$m direction aligned parallel to the direction of ion transport. We define the $x$-axis as parallel to the direction of ion motion; with an electrolyte thickness of $L$, the two electrodes are at $x/L = 0$ and 1. During cell polarization, a series of SAXS scans were taken at $x$ positions spaced 100 $\mu$m apart. After each traversal of the cell, the reference position, blank position, and a silver behenate sample were scanned, and a dark scan with the shutter blocking the X-ray beam was performed. The acquisition time was 10 s and was increased to 30 s every third scan to balance temporal resolution with data contrast. Scattering intensity is proportional to acquisition time, so the intensity of the 30 s scans was divided by a factor of three for comparison with the 10 s scans. Ion chambers immediately before and after the sample enable X-ray transmission calculations. 2D scattering patterns were captured on an SX165 CCD detector (Rayonix, LLC). Analysis

of *in situ* SAXS data was automated in Python using the PyFAI [46] and LMFIT [145] packages. A representative fitting result is shown in Appendix A10.

### *10.3.6 X-ray Transmission and SAXS Data Correction*

X-ray transmission is calculated using intensities from pre- ($I_0$) and post- ($I_1$) sample ion chambers. To calibrate the detector offsets, scans were acquired with the shutter blocking the X-ray beam to acquire offset values, $I_{0,\mathrm{dark}}$ and $I_{1,\mathrm{dark}}$. To account for absorption of the PEEK sample holders, pouch material, and air, a blank reference with the same components but no electrolyte was scanned, allowing $I_{0,\mathrm{blank}}$ and $I_{1,\mathrm{blank}}$ measurements. Both calibration measurements were performed with the same acquisition time as the data scans. The X-ray transmission of the electrolyte is then given by Equation 10.1,

$$\mathrm{transmission} = \frac{\left(I_{1,\mathrm{sample}} - I_{1,\mathrm{dark}}\right) \Big/ \left(I_{0,\mathrm{sample}} - I_{0,\mathrm{dark}}\right)}{\left(I_{1,\mathrm{blank}} - I_{1,\mathrm{dark}}\right) \Big/ \left(I_{0,\mathrm{blank}} - I_{0,\mathrm{dark}}\right)}. \qquad (10.1)$$

2D X-ray scattering data was also corrected using data from the blank and dark scans. First, data from the dark scan was subtracted pixel-by-pixel from all other scans to account for fixed pattern noise and dark currents in the raw images. Second, to isolate the scattering from the block copolymer electrolyte, the data from the PEEK / air blank sample was subtracted. As the scattering due to PEEK and air is attenuated by the sample absorption, these scans were corrected using the position- and time-dependent X-ray transmission (Equation 10.1) before subtraction. Finally, a correction based the on transmission was applied to remove self-absorption effects: to ensure that the scattering intensity represents the relative population of grains, each 2D SAXS image was divided by the transmission of the corresponding position and time calculated using Equation 10.1.

## 10.4 Results and Discussion

### *10.4.1 X-Ray Transmission*

To understand the behavior of SEO(4.0-22.4) / LiTFSI electrolytes during cell polarization, the X-ray transmission coefficient was calculated and block copolymer morphology was measured at a range of salt concentrations from $r = 0.02$ to $r = 0.35$. All measurements were performed at a temperature of 90 °C. The X-ray transmission of an arbitrary substance depends only on the X-ray energy and the thickness, density, and atomic composition of the sample; thus, for a given salt concentration, the X-ray transmission can be calculated with no adjustable parameters. This can be done using computational tools such as the online tool maintained by the center for X-ray optics (CXRO) [43] or offline, as described in detail in Appendix A10. [25,220–223] Figure 10.3 shows

the calculated X-ray transmission for SEO(4.0-22.4) / LiTFSI electrolytes as a function of salt concentration, $r$. The presence of LiTFSI salt increases X-ray absorption, leading to a marked decrease in transmission with increasing salt concentration at the X-ray energy and sample thickness used. This enables determination of salt concentration at any point in the cell from measurement of the X-ray transmission. We note that the X-ray transmission does not depend on the morphology or orientation of grains in a nanostructured block copolymer electrolyte. This approach to determining the salt concentration at a given location in the cell is thus independent of the local morphology.

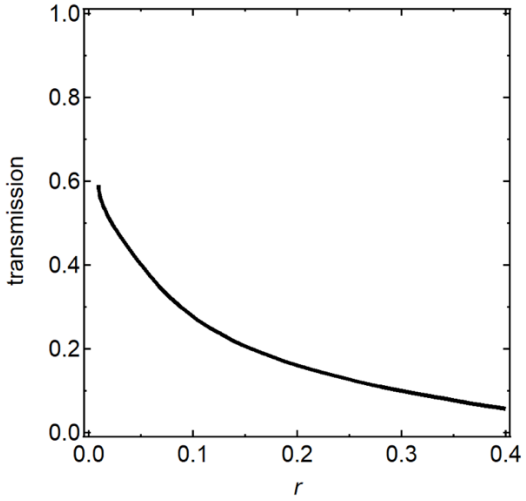


Figure 10.3. The calculated relationship between X-ray transmission and salt concentration, $r$, using the chemical composition, known thickness (1.95 mm), and mass density of SEO(4.0-22.4) / LiTFSI electrolytes. See Appendix A10 for details of the calculation.

*10.4.2 Equilibrium Morphology*

The equilibrium morphology and domain spacing of SEO(4.0-22.4) / LiTFSI electrolytes was measured at salt concentrations ranging from $r = 0.02$ to 0.35, and the results are shown in Figure 10.4. As described in the Experimental Methods section, these samples were prepared by dissolving the polymer and salt in solvent and then freeze-drying the electrolyte to remove the solvent; this process is assumed to result in the equilibrium morphology. [135,224] The domain spacing, $d$, was calculated based on the position of the primary scattering peak, $q^*$, using Bragg's law: [28]

$$d = \frac{2\pi}{q^*}. \qquad (10.2)$$

The domain spacing in Figure 10.4b increases with increasing salt concentration, as the added salt swells the PEO/LiTFSI domains. The morphology depends on the location of

additional scattering peaks: a sample with a hexagonally-packed cylindrical (HEX) morphology exhibits peaks at $q^*, \sqrt{3}q^*, \sqrt{4}q^*$, and so forth, while a sample with a body-centered cubic spherical (BCC) morphology exhibits peaks at $q^*, \sqrt{2}q^*, \sqrt{3}q^*$, and so forth.[44] Below $r = 0.075$, we observe only a HEX morphology, and above $r = 0.10$, we observe only a BCC morphology. In the range of $0.075 \leq r \leq 0.10$, two primary scattering peaks at different domain spacings are observed, with additional scattering peaks corresponding to HEX and BCC morphologies; this indicates coexistence of grains with each morphology. Representative SAXS traces are shown in Figure 10.4a.

In addition to X-ray transmission, the relationship of domain spacing and morphology to salt concentration in equilibrated SEO / LiTFSI electrolytes provides a second method to estimate salt concentration from spatially-resolved, *in situ* scattering data. Figure 10.4c shows $r$ versus $d$ (the inverse of Figure 10.4b), and logarithmic fits that are used to calculate $r$ based on $d$ for the BCC and HEX morphologies. For the BCC morphology, the root-mean-square deviation between the fit and the data, caused by scatter in the data, is 11%. The fit is given in Equation 10.3:

$$r = (1.168 \pm 0.133)\ln(d) - (3.283 \pm 0.373) \qquad (10.3).$$

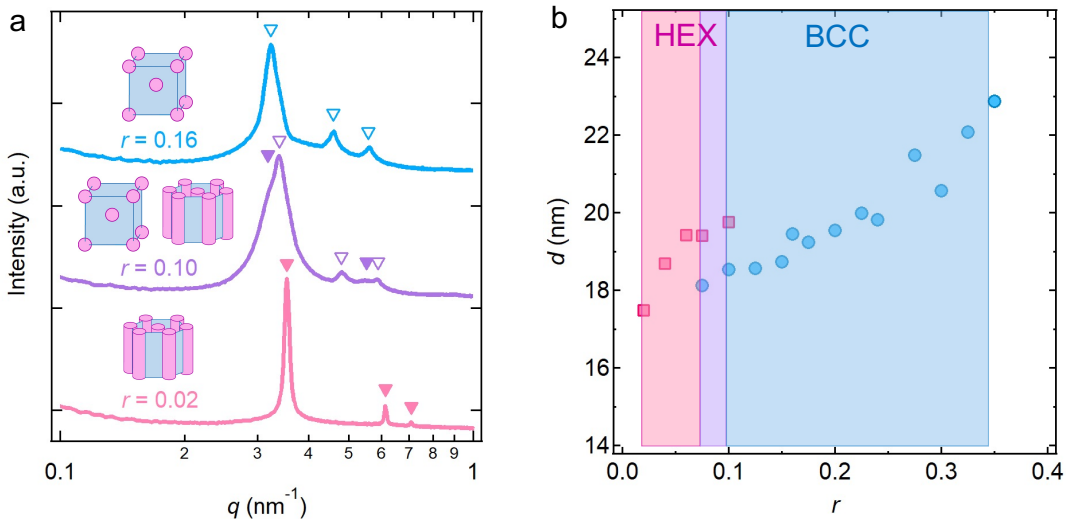

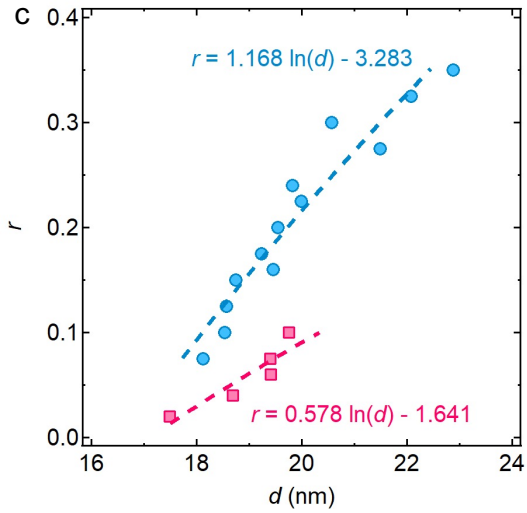


Figure 10.4. (a) SAXS traces for SEO(4.0-22.4) $r$ = 0.02 (pink), 0.10 (purple), and 0.16 (blue). Filled triangles denote peaks attributed to a hexagonally packed cylindrical (HEX) morphology, and empty triangles denote a body-centered cubic spherical (BCC) morphology. (b) Domain spacing ($d$) versus salt concentration ($r$) for SEO(4.0-22.4) / LiTFSI electrolytes; a HEX morphology is observed at and below $r$ = 0.10 and a BCC morphology is observed at and above $r$ = 0.075. (c) Salt concentration ($r$) vs domain spacing ($d$), with logarithmic fits relating $r$ to $d$.

### *10.4.3 Modeled Salt Concentration Gradients*

Using concentrated solution theory, [29] the steady-state salt concentration profile of a cell can be calculated if three transport parameters—ionic conductivity, $\kappa$, transference number with respect to the solvent velocity, $t_+^0$, and salt diffusion coefficient, $D$—and the thermodynamic factor, $T_f = 1 + \frac{d\ln \gamma_\pm}{d\ln m}$, are known. The procedure for calculating salt concentration gradients is described in Appendix A10, [10,47,123,216] and full electrochemical characterization of SEO(4.0-22.4) / LiTFSI electrolytes is reported in Galluzzo *et al.* [23] Figure 10.5a shows modeled salt concentration profiles for SEO(4.0-22.4) with an initially homogeneous salt concentration of $r$ = 0.16 at current densities, $i$, normalized by cell thickness, $L$, of $iL$ = 0.007, 0.032, and 0.041 mA/cm. The predicted limiting current is typically the current at which the salt concentration at the negative electrode reaches zero. [29] Using this method, the predicted limiting current density, scaled by the cell thickness, for SEO(4.0-22.4) / LiTFSI $r$ = 0.16 is $i_{\text{lim}}L$ = 0.041 mA/cm; see Appendix A10 for details. Based on the equilibrium morphological data reported in Figure 10.4, Figure 10.5b shows the expected morphology as a function of position for a cell polarized at $iL$ = 0.041, the theoretical limiting current.

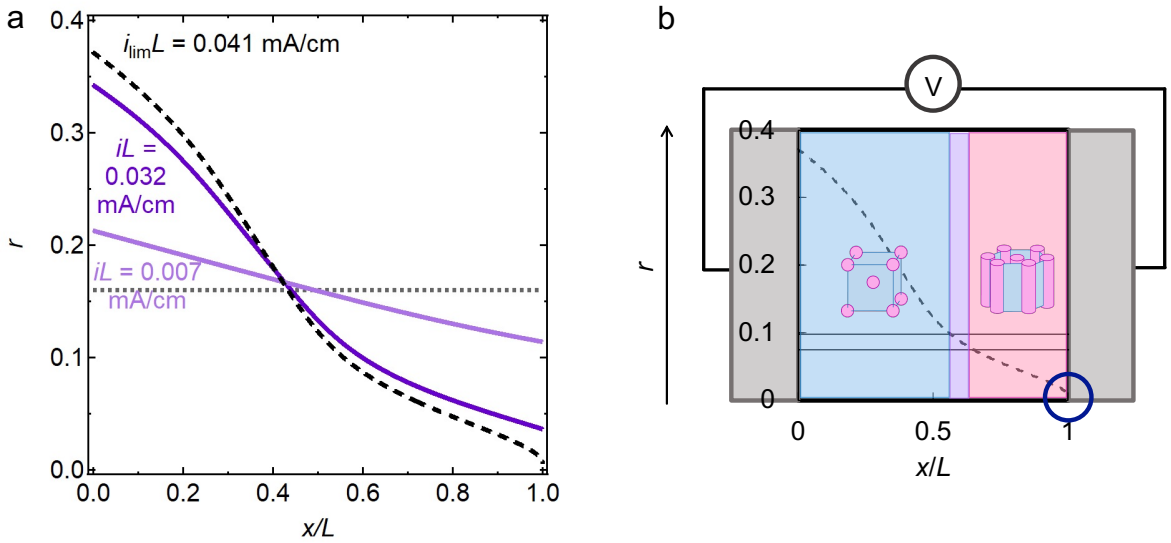


Figure 10.5. (a) Modeled salt concentration ($r$) versus normalized cell position, $x/L$, in SEO(4.0-22.4) $r$ = 0.16 at $iL$ = 0.007, 0.032, and 0.041 mA/cm, where $i$ is the current density and $L$ is the cell thickness. (b) A schematic of an electrochemical cell with the modeled salt concentration profile at $iL$ = 0.041 mA/cm, with expected morphologies based on equilibrium phase behavior reported in Figure 10.4.

*10.4.4 Electrochemical Behavior*

To measure changes in the salt concentration and morphology during electrochemical polarization, we fabricated a cell, depicted in Figure 10.2, that enables measurement of X-ray transmission and small-angle scattering as a function of position during electrochemical experiments. The electrolyte used was the same as that for which modeling results are reported in Figure 10.5: SEO(4.0-22.4) with an initial salt concentration, uniform throughout the cell, of $r_{avg}$ = 0.16. Constant dc current experiments were performed, and the potential response is shown in Figure 10.6. An initial current of $I$ = +29.6 $\mu$A was applied until the potential diverged, reaching a safety cut-off of 1 V after 2.6 h. The current direction was then flipped and decreased in magnitude to -22.2 $\mu$A, and the potential again diverged, reaching a safety cut-off of -1 V after 10.9 h (8.3 h at -22.2 $\mu$A). This indicates that both currents are above the experimental limiting current.[48] Next, the current direction was again flipped and further decreased in magnitude to +4.9 $\mu$A, before being switched to open circuit (0 $\mu$A) after 26.9 h (16 h at 4.9 $\mu$A). Measurement was stopped after 37.2 h (10.3 h at open circuit). Using an electrolyte thickness of 1.1 mm and electrode area of 7.7 mm$^2$, these applied current densities correspond to $iL$ = +0.042, -0.032, and +0.007 mA/cm.

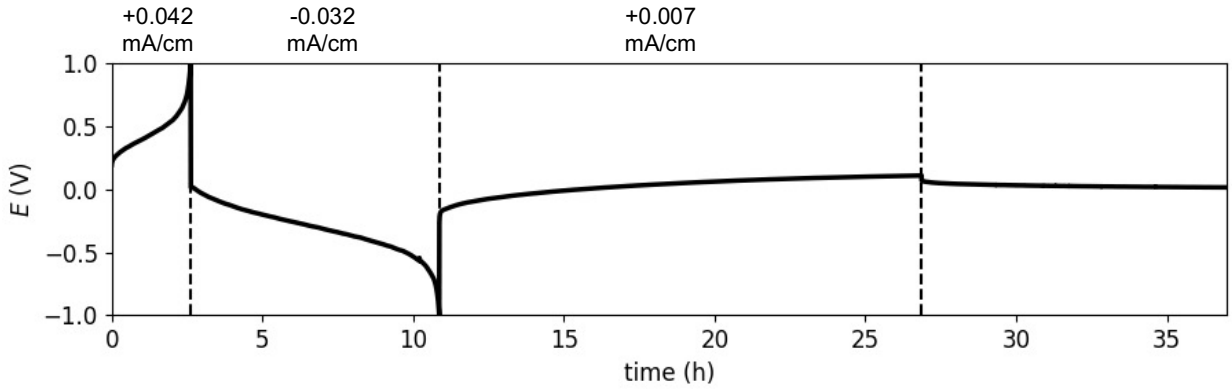


Figure 10.6. Potential response of an SEO(4.0-22.4) $r = 0.16$ cell during application of length-normalized current densities of $iL$ = +0.042, -0.032, +0.007, and 0 mA/cm.

The first applied current density in this experiment, +0.042 mA/cm, is above the predicted limiting current of 0.041 mA/cm, and so the observed divergence in potential is consistent with the theory; similarly, the third applied current density, +0.007 mA/cm, is below the theoretical limiting current, and the potential reaches a stable steady-state, as expected. However, the magnitude of the second applied current density, -0.032 mA/cm, is significantly below the predicted limiting current, but we observe a divergence in the potential. We now turn to the simultaneous X-ray transmission and scattering results to explain this disagreement between our electrochemical experiment and theoretical calculation of the limiting current.

### *10.4.5 Salt Concentration from X-Ray Transmission*

Figure 10.7a shows the X-ray transmission as a function of time during the electrochemical experiment performed in Figure 10.6. Each position in the cell is represented on a color scale, from blue near $x/L = 0$ to red near $x/L = 1$. The X-ray transmission is initially spatially uniform because the salt concentration is initially uniform. As the cell is polarized and a salt concentration gradient develops, the transmission decreases near the positive electrode as the salt concentration increases and, correspondingly, increases near the negative electrode as the salt concentration decreases.

Using the relationship depicted in Figure 10.3, the salt concentration can be calculated based on the transmission, and the results are shown in Figure 10.7b. During the first polarization at $iL$ = +0.042 mA/cm, $r$ increases near $x/L = 1$ and decreases near $x/L = 0$. When the potential diverges at 2.6 h, the salt concentration at the salt-poor electrode is slightly above $r = 0.10$. During the second polarization at $iL$ = -0.032 mA/cm, $r$ increases near $x/L = 0$ and decreases near $x/L = 1$. When the potential diverges at 10.9 h, the salt concentration at the salt-poor electrode is slightly above $r = 0.10$. During the third polarization at $iL$ = +0.007 mA/cm, $r$ increases near $x/L = 1$ and decreases near $x/L = 0$. The salt concentration remains above $r = 0.10$, and the potential does not

diverge. During the final step, where $iL$ is set to 0 mA/cm, the salt concentration approaches its starting value of $r = 0.16$ at all positions.

While the sign of the concentration gradients flips with changes in the direction of the applied current, as expected, there is a noticeable time delay between the applied current and the effect on the concentration gradients. For instance, at $t = 2.6$ h, the current is switched from positive to negative. However, $r$ at $x/L = 0.05$ continues to increase, reaching a maximum of $r = 0.23$ at $t = 3.3$ h, and $r$ at $x/L = 0.95$ continues to decrease, reaching a minimum of $r = 0.11$ at $t = 2.9$ h. The same is true at the second change in current direction: at $t = 10.9$ h, the current is switched from negative to positive, but $r$ at $x/L = 0.95$ continues to increase, reaching a maximum of $r = 0.26$ at $t = 11.6$ h, and $r$ at $x/L = 0.05$ continues to decrease, reaching a minimum of $r = 0.12$ at $t = 11.6$ h. This time delay is consistent with experiments and modeling in the literature. [225]

At both timepoints at which the potential diverges, 2.6 and 10.9 h, the salt concentration ranges from approximately $r = 0.10$ to $r = 0.25$. This is in contradiction with the expectation that, at the limiting current, the potential diverges due to the salt concentration reaching either zero or the solubility limit. We thus conclude that there is another mechanism for the limiting current in this case. Based on Figure 10.4, equilibrium morphology data indicates that as the salt concentration decreases from $r = 0.16$, polystyrene spheres in the BCC morphology are expected to begin to transform into cylinders in the HEX morphology at $r = 0.10$. Figure 10.7b contains a horizontal line at $r = 0.10$, and the salt concentration never decreases below this point, even when the potential diverges.

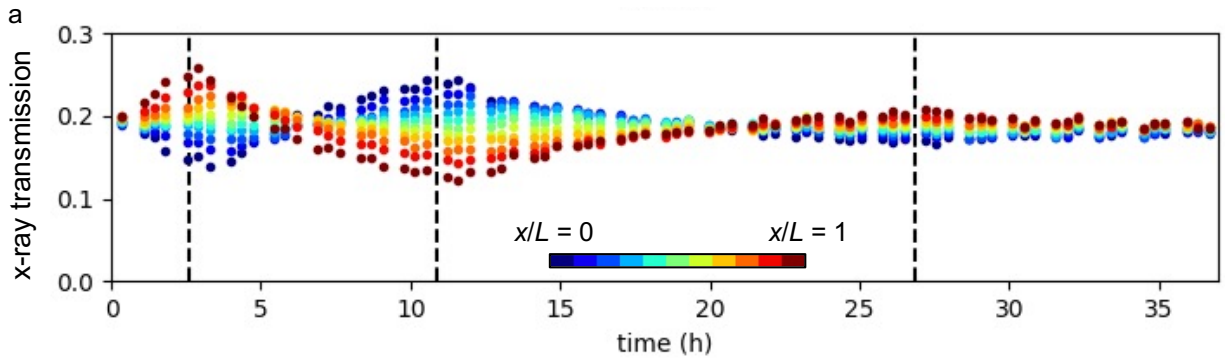

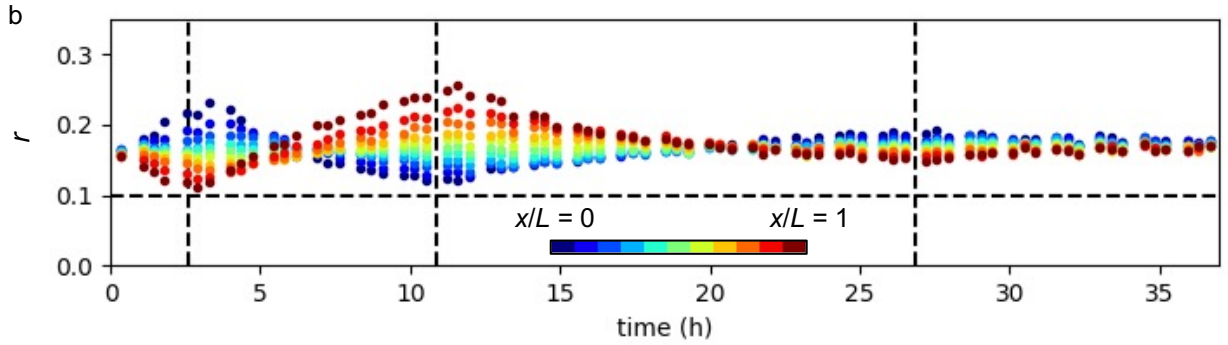


Figure 10.7. (a) X-ray transmission and (b) salt concentration ($r$) calculated based on the transmission using Figure 10.3 as a function of time during the polarization depicted in Figure 10.6. Each position in the cell is represented by a different color, from blue near $x/L = 0$ to red near $x/L = 1$. Vertical dashed lines indicate times at which the applied current was changed from $iL = +0.042$ mA/cm to $iL = -0.032$ mA/cm at 2.6 h, to $iL = +0.007$ mA/cm at 10.9 h, and to $iL = 0$ at 26.9 h. See Figure 10.11 for the presentation of this data in the form of $r$ as a function of $x/L$ instead of time for comparison with Figure 10.5.

### *10.4.6 SAXS Data*

To test the hypothesis that the limiting current is reached due to barriers to the block copolymer traversing the BCC-HEX phase transmission, we examine the SAXS data. Figure 10.8 shows representative 2D SAXS images, taken at $x/L = 0.05$ (a) and 0.95 (b) at $t = 20$ h. We observe position-dependent preferential orientation of the BCC grains, likely due to strain imposed on the electrolyte during sample preparation. We perform an azimuthal average of our scattering data, ignoring effects related to sample orientation, because the electrochemical behavior of BCC grains is expected to be independent of orientation. We note, however, that differently oriented grains appear to respond differently to polarization—see Appendix A10 for orientation-separated scattering data. Due to the azimuthal averaging, the analysis presented below ignores this.

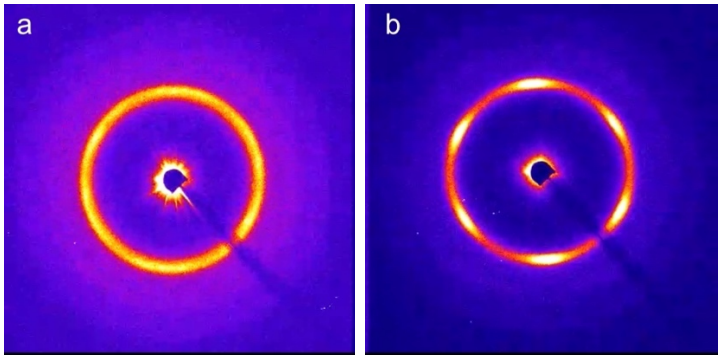


Figure 10.8. 2D scattering profiles at $x/L = 0.05$ (a) and 0.95 (b) at $t = 20$ h, showing preferential orientation of the BCC grains in (b) but not in (a). The beamstop casts a

diagonal shadow in the lower right corner of both images.

Figure 10.9 shows time-dependent reduced azimuthally-averaged scattering data. Figure 10.9a reproduces the electrochemical data from Figure 10.6, with added color mapping to indicate the time. Azimuthally-averaged SAXS data for the positions closest to each electrode, $x/L = 0.05$ and 0.95, are shown in Figures 10.9b-e and f-i, respectively (plots for other positions are shown in Appendix A10). For each position, the scattering data is shown separately for each polarization step, and the color of each trace corresponds to the color of the electric potential trace in Figure 10.9a at the time the scan was taken. In all cases, we observe a single primary scattering peak, at location $q^*$ with additional peaks at $\sqrt{2}q^*$ and $\sqrt{3}q^*$, indicating a BCC morphology. A HEX morphology would be indicated by a $\sqrt{3}q^*$ peak without a $\sqrt{2}q^*$ peak. We therefore integrate the intensity of the $\sqrt{2}q^*$ peak ($I_{\sqrt{2}}$) and compare it to the integrated intensity of the $\sqrt{3}q^*$ peak ($I_{\sqrt{3}}$). The ratio $I_{\sqrt{2}}/I_{\sqrt{3}}$ as a function of $x/L$ and time is shown in Figure 10.9j. We note that as the salt concentration changes, the volume fraction of the PEO / LiTFSI changes, which affects the structure factor; as such, $I_{\sqrt{2}}/I_{\sqrt{3}}$ is not expected to be constant with time during polarization. At early times, $I_{\sqrt{2}}/I_{\sqrt{3}}$ ranges between 1 and 2, and it increases slightly with time. This ratio would be expected to be zero for a HEX morphology. There is no indication of the appearance of a HEX morphology, even at the positions closest to the electrodes ($x/L = 0.05$ and 0.95), confirming our conclusion, based on the X-ray transmission data, that as the cell potential diverges, the electrolyte at the negative electrode fails to traverse the BCC-HEX phase transition that begins at $r = 0.10$. Previous work has observed a polarization-induced morphological transition from lamellar to gyroid morphologies;[226] more work must be performed to determine when concentration polarization leads to phase transitions and when such transitions are inaccessible, as in this study. This may include experiments using different block copolymers and salt concentrations to access different morphological transitions, experiments at different temperatures to determine the effects of kinetics, and theoretical work to probe phase transition pathways in the presence of ionic current.

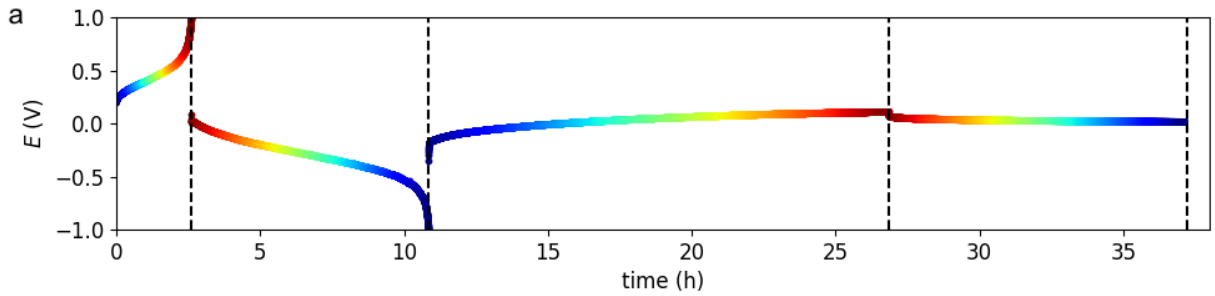

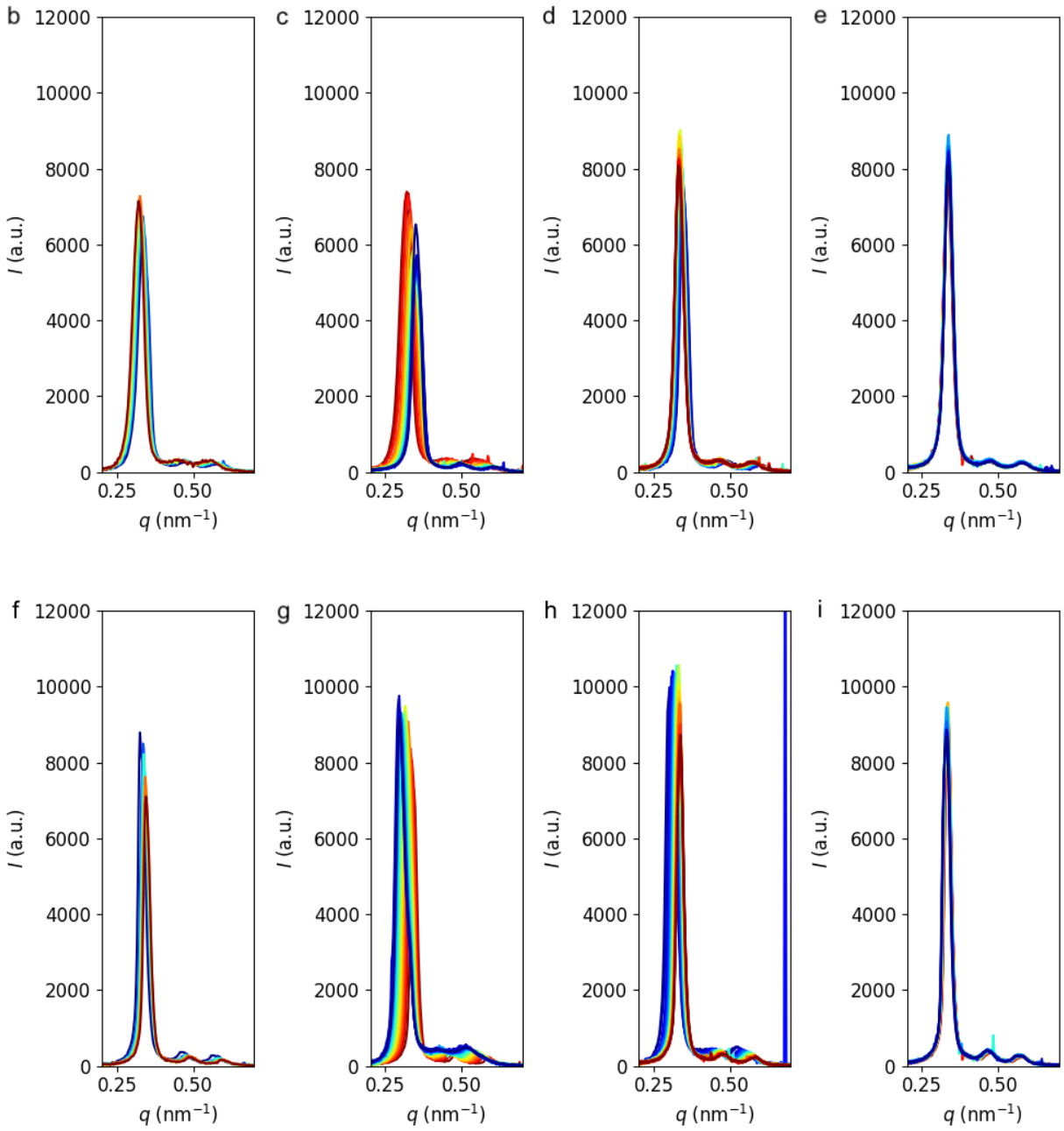
b
c
d
e
f
g
h
i
12000
10000
8000
6000
4000
2000
0
I (a.u.)
0.25
0.50
q (nm−1)

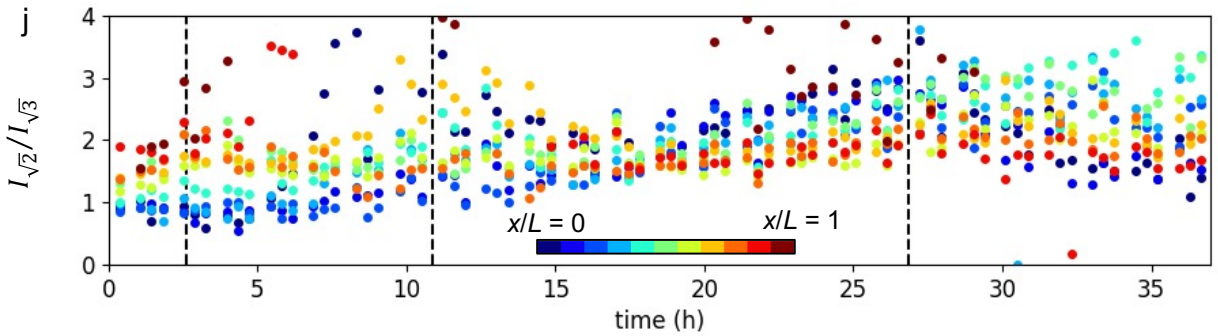


Figure 10.9. (a) Potential response of the SEO(4.0-22.4) $r_{avg}$ = 0.16 cell polarized at +0.042, -0.032, +0.007, and 0 mA/cm, reproduced from Figure 10.6. (b-e) Azimuthally-averaged SAXS patterns at $x/L$ = 0.05 for the four polarization steps depicted in Figure 10.9a; the color of each trace matches the color of the timepoint of Figure 10.9a to which it corresponds. (f-i) Azimuthally-averaged SAXS patterns at $x/L$ = 0.95 for the four polarization steps depicted in Figure 10.9a; the color of each trace matches the color of the timepoint of Figure 10.9a to which it corresponds. In (h), a stray pixel causes a non-physical spike in intensity, which can be neglected. (j) Ratio of integrated intensity of the $\sqrt{2}q^*$ peak to that of the $\sqrt{3}q^*$ peak ($I_{\sqrt{2}}/I_{\sqrt{3}}$) as a function of time; each position in the cell is represented by a different color, from blue near $x/L$ = 0 to red near $x/L$ = 1.

Using the location of the primary scattering peak, we determine the domain spacing of the BCC morphology as a function of time and position according to Equation 10.2. The results are shown in Figure 10.10a. Each position in the cell is represented by a different color, from blue near $x/L$ = 0 to red near $x/L$ = 1; the color scheme matches that in Figure 10.7. The salt concentration, and therefore the domain spacing, is initially spatially uniform. As the cell is polarized and a salt concentration gradient develops, the domain spacing increases near the positive electrode as the salt concentration increases and, correspondingly, decreases near the negative electrode as the salt concentration decreases. The polarization at the end of the second step is larger than that of the first step because of the factor of 4 increase in the time used to polarize the cell.

Using the equilibrium SAXS data presented in Figure 10.4, we calculate the salt concentration based on the domain spacing using the fits shown in Figure 10.4c, and the results are presented in Figure 10.10b. The initial salt concentration determined by this method is approximately $r$ = 0.18; the discrepancy between this and the known initial salt concentration of $r$ = 0.16 is commensurate with the 11% uncertainty of the calibration expression (Eq. 3); note the difference between the experimental data and the fit in Figure 10.4c. The data in Figure 10.10b is consistent with the data in Figure 10.7b, in which salt concentration was determined using X-ray transmission. Most significantly, the salt concentration is never found to decrease below $r$ = 0.10, which is consistent with our observation that no BCC-HEX phase transition occurs.

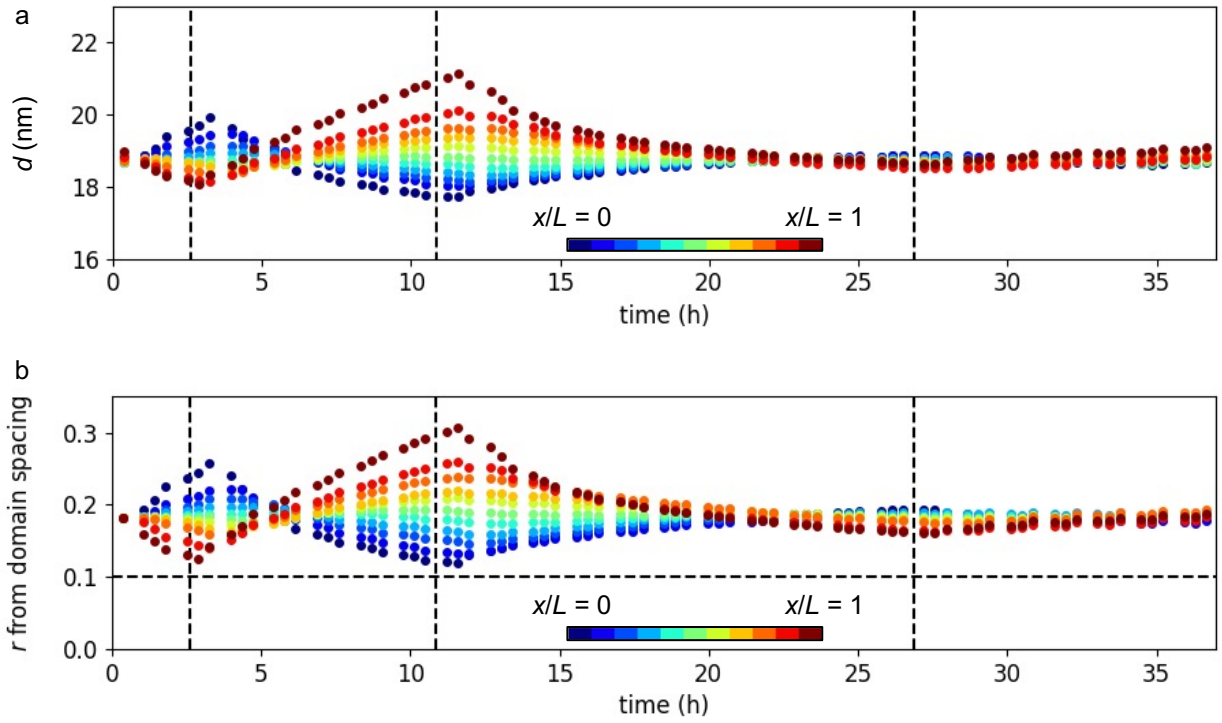


Figure 10.10. (a) Domain spacing, $d$, of the SEO(4.0-22.4) $r_{avg}$ = 0.16 electrolyte as a function of $x/L$ and time. (b) Salt concentration ($r$) calculated based on the domain spacing and Equation 10.3 as a function of $x/L$ and time. The polarization conditions are given in Figure 10.6. Each position in the cell is represented by a different color, from blue near $x/L$ = 0 to red near $x/L$ = 1. Vertical dashed lines indicate times at which the applied current was changed from $iL$ = +0.042 mA/cm to $iL$ = -0.032 mA/cm at 2.6 h, to $iL$ = +0.007 mA/cm at 10.9 h, and to $iL$ = 0 at 26.9 h.

### *10.4.7 Experimental and Modeled Salt Concentration Profiles*

The evolution of salt concentration profiles as a function of position in the cell is shown in Figure 10.11, using both methods of measuring salt concentration: X-ray transmission (Figure 10.11e-h) and domain spacing (Figure 10.11i-l). Because these profiles are driven by the applied current, we show the time-dependence of $E$ for the four steps used in this study in Figures 10.11a-d. Below these plots, we show the evolution of salt concentration as a function of $x/L$ at selected times for each polarization based on the two methods, where the color of the concentration trace corresponds to the color of the polarization data at the time at which the data was taken.

The first point to note is the similarity of the matched pairs of plots; compare Figures 10.11e and 10.11i, Figures 10.11f and 10.11j, Figures 10.11g and 10.11k, and Figures 10.11h and 10.11l. This implies excellent correspondence between the two methods used to

determine $r(x/L)$. For simplicity, we will use the transmission data to discuss Figure 10.11. During the first polarization step, which lasts for 2.6 h before the potential exceeds the cutoff potential, there is a relatively small change in local salt concentration – see Figure 10.11e. The initial profile, shown in dark blue, is relatively flat, and as time increases, the salt concentration at low $x/L$ increases as Li metal is oxidized at $x = 0$, while the concentration at high $x/L$ decreases as $Li^+$ ions are reduced at $x = L$. The final concentration profile, shown in red in Figure 10.11e, is consistent with qualitative expectations. It intersects the initial dark blue data set at $x/L = 0.4$, indicating that the concentration gradients near the positive electrode are steeper than those near the negative electrode. The current density used in this step, $iL = +0.042$ mA/cm, is above the predicted limiting current ($i_{lim}L = 0.041$ mA/cm). The dotted curve in Figure 10.11e corresponds to the steady-state concentration profile predicted using concentrated solution theory for a current density of $i_{lim}L$ (at which the salt concentration reaches $r = 0$ at the negative electrode); there is no steady-state for $i > i_{lim}$. This predicted profile is also steeper on the near the positive electrode. However, the predicted concentration gradients are much larger than the measured concentration gradients: the predicted concentrations range from $r = 0.37$ to $r = 0.0$ while the measured concentrations range from $r = 0.22$ to $r = 0.12$.

Changing the sign and decreasing the magnitude of the current ($iL = -0.032$ mA/cm) results in a longer polarization experiment which lasts for 8.3 h (from $t = 2.6$ to 10.9 h); see Figure 10.11b. The slope of the salt concentration profile, $r(x/L)$, which is negative during the previous polarization step, continues to grow during the first 1.2 h, with the salt concentration reaching a maximum of $r = 0.23$ at $x/L = 0.05$ and $t = 3.8$ h before declining in magnitude; see Figure 10.11f. At $t = 4.6$ h, the concentration profile becomes non-monotonic (see the horizontal S-shaped red and orange traces in Figure 10.11f), *i.e.*, the sign of the slope of the salt concentration gradient varies with $x/L$. At $t = 5.7$ h the slope is positive in the range $x/L < 0.14$, negative in the range $0.14 < x/L < 0.68$, and positive again for $x/L > 0.68$, this occurs because the effect of the change in applied current propagates inward from the electrodes. The change in concentration at the electrodes is more rapid than in the center of the cell. After $t = 7.5$ h, the slope of the salt concentration gradient becomes positive at all values of $x/L$. The final concentration profile, shown in dark blue, is steeper than that obtained at the end of the first polarization step due to the longer polarization time. The dotted curve in Figure 10.11f corresponds to the steady-state concentration profile predicted using concentrated solution theory for a current density $iL = -0.032$ mA/cm. The predicted concentration gradients are much larger than the measured concentration gradients, ranging from $r = 0.04$ to 0.34 while the measured concentrations range from $r = 0.12$ to 0.24.

It is interesting to note that increasing the polarization time while reducing the applied current resulted in an increase in the final concentration near the positive electrode ($x/L = 0.05$ in the first polarization step and 0.95 in the second) from 0.22 to 0.24 but had a

negligible effect on the concentration near the negative electrode, which remains at $r$ = 0.12 regardless of current density and polarization time. This is consistent with our previous statements regarding the inability of the applied electric field to induce a BCC to HEX transition which is predicted to occur if $r$ decreases below 0.10. When the theory is modified with a new constraint limiting the minimum salt concentration to $r$ = 0.10, shown by the dashed lines in Figures 10.11e and f, the predicted and experimental profiles agree quantitatively. See Appendix A10 for the details of calculation of the predicted profiles.

Figure 10.11g shows the evolution of concentration during the third step wherein a smaller current of $iL$ = +0.007 mA/cm was applied. This experiment was terminated at $t$ = 26.9 h, corresponding to 16 h of polarization in this step, after $E$ had stabilized at 0.1 V. The final concentration profile (dark red) obtained at this current density is in qualitative agreement with concentration solution theory predictions. The calculated concentrations range from $r$ = 0.11 to 0.21 while the measured concentrations range from $r$ = 0.15 to 0.19. Deviations between theory and experiment are larger near the negative electrode – this is general observation that applies to all three polarization steps.

The final step was setting the current to 0, resulting in a slow relaxation in concentration gradients as expected; see Figure 10.11h. Here the predicted steady-state concentration profile is flat (see dashed line in Figure 10.11h) and in reasonable agreement with the final measurements (dark blue). The departures between the steady-state predictions and experiments, seen most clearly in Figure 10.11l, are attributed to uncertainty in our calibration scheme (Equation 10.3).

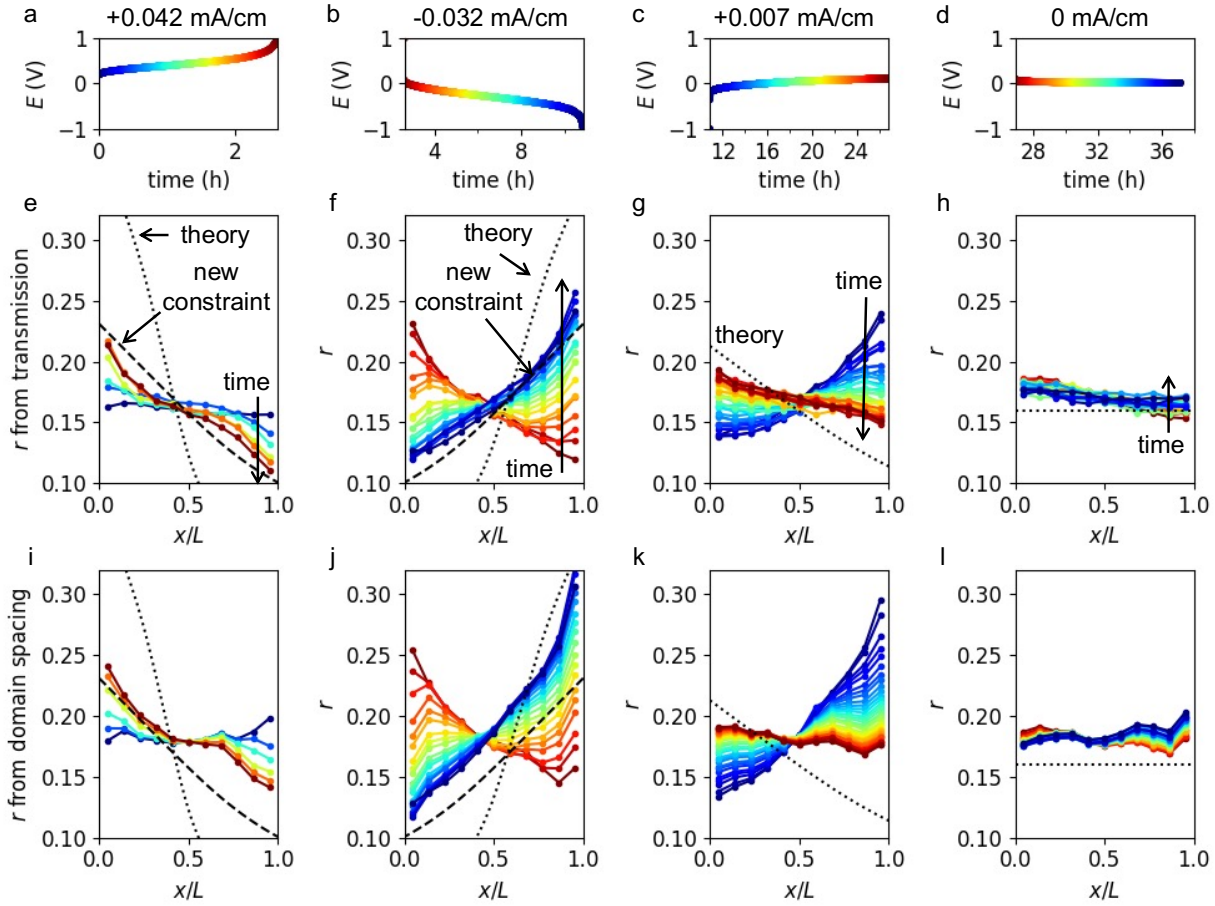


Figure 10.11. (a-d) Potential response of an SEO(4.0-22.4) $r_{avg}$ = 0.16 cell during application of length-normalized current densities of $iL$ = +0.042, -0.032, +0.007, and 0 mA/cm, reproduced from Figure 10.6. (e-h) Salt concentration as a function of position within the cell as determined from X-ray transmission, where the colors of the traces correspond to the matching point in Figures 10.11a-d. (i-l) Salt concentration as a function of position within the cell as determined from domain spacing, where the colors of the traces correspond to the matching point in Figures 10.11a-d. (e-l) include predicted concentration gradients in black dotted lines, and (e, f, i, and j) include theoretical concentration gradients with a new constraint limiting the minimum salt concentration to $r$ = 0.10 in black dashed lines. In Figures 10.11e, f, i, and j, the non-constrained predicted concentration profile is cut off by the y-axis scaling; the full profile is shown in Figure 10.5a, and a version of this Figure with wider y-axis scaling is presented in Appendix A10.

## 10.5 Conclusions

It is typically assumed that the limiting current, the highest current that an electrolyte can accommodate, occurs when the salt concentration reaches zero at the negative electrode

(Figure 10.5b). In this work, we perform dc current polarization experiments at 90 °C on a lithium symmetric cell with an electrolyte composed of polystyrene-*block*-poly(ethylene oxide) mixed with LiTFSI salt at an initially uniform concentration of $r_{avg} = 0.16$ lithium ions per ethylene oxide moiety while simultaneously measuring the X-ray transmission and small-angle scattering. We determine the salt concentration as a function of position and time using the X-ray transmission, and find that when the potential diverges, the salt concentration ranges from $r = 0.10$ to 0.25, a much narrower range than predicted based on equilibrium characterization and concentrated solution theory.

Equilibrium SAXS data indicate that as the salt concentration decreases from $r = 0.16$, one would expect a transition from a body-centered cubic spherical (BCC) morphology to a hexagonally-packed cylindrical (HEX) morphology to begin at $r = 0.10$. Our *in situ* SAXS data allows us to estimate the salt concentration based on the domain spacing of the BCC phase; these salt concentration profiles agree with those obtained using the X-ray transmission. Based on both measures of salt concentration, $r$ is never observed to decrease below a value of 0.10, even as the potential diverges (Figure 10.12).

It is evident that in the presence of an ionic current, the salt concentration in block copolymer grains initially in a BCC morphology with $r_{avg} = 0.16$ experience a barrier to a salt concentration decrease below $r = 0.10$ and the corresponding BCC-HEX phase transition that is expected under equilibrium conditions. One possible explanation for this observation is that the free energy barrier for the formation of the HEX phase cannot be overcome by the applied current. The BCC-HEX transition in some block copolymers can be accessed by changing temperature; the mechanism of this transition involves elongation of the spheres and coalescence ultimately leading to the formation of hexagonally-packed cylinders. [227] It is evident that these processes do not occur in our electrochemical cell, and the salt concentration in the vicinity of the negative electrode does not decrease below $r = 0.10$. The cell potential diverges when this point is reached, indicating that the applied current exceeds the limiting current. The limiting current in ordered electrolytes may thus arise due factors related to the self-assembly of the nanostructured morphologies rather than salt depletion at the negative electrode, a possibility that has not yet been considered in the literature. Further work is required to elucidate the relationship between applied current, cell potential, concentration gradients, and morphological transitions in nanostructured electrolytes.

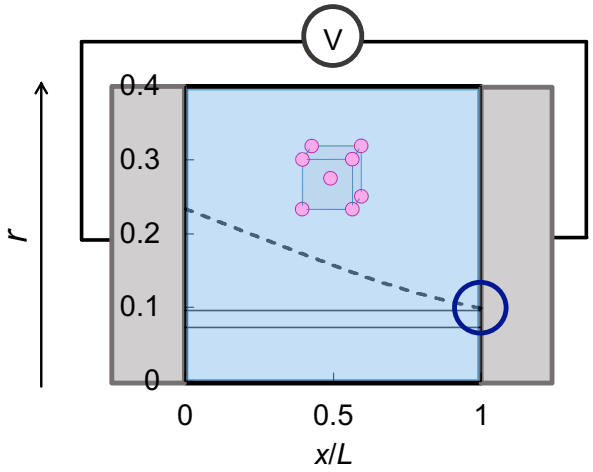


Figure 10.12. The dashed line shows the predicted salt concentration profile in a cell polarized at $iL$ = 0.010 mA/cm, the practical length-normalized limiting current density. The horizontal lines indicate equilibrium phase transitions from BCC to BCC / HEX at $r$ = 0.10 and to HEX at $r$ = 0.075 (see Figure 10.4). The limiting minimum salt concentration is $r$ = 0.10 because the BCC-HEX transition is inaccessible. This is in contrast with expectations based on equilibrium thermodynamics wherein a length-normalized limiting current density $iL$ = 0.041 mA/cm is expected, as shown in Figure 10.5b. Concentrated solution theory is used to calculate the salt concentration profile.

## 10.6 Acknowledgements

The authors were supported by the Joint Center for Energy Storage Research (JCESR), an Energy Innovation Hub funded by the U.S. Department of Energy, Office of Science, Basic Energy Sciences, under Contract No. DEAC02-06CH11357. This research was completed at the Stanford Synchrotron Radiation Light Source, a user facility at SLAC National Accelerator Laboratory, which is supported by the U.S. Department of Energy, Office of Science, Office of Basic Energy Sciences under Contract No. DE-AC02-76SF00515. The authors also used beamline 7.3.3 of the Advanced Light Source, which is supported by the Director of the Office of Science, Office of Basic Energy Sciences, of the U.S. Department of Energy under Contract No. DE-AC02-05CH11231.

# Chapter 11: Conclusions and Outlook

## 11.1 Conclusions

This Dissertation provides insight into the behavior of polymer electrolytes, which are promising candidates to enable rechargeable batteries with a highly energy-dense lithium metal anode. We studied electrolytes composed of fluorinated and non-fluorinated oligomeric liquids, poly(ethylene oxide) (PEO) homopolymers, and polystyrene-*block*-poly(ethylene oxide) (SEO) block copolymers. The electrochemical properties of interest are: ionic conductivity; salt diffusion coefficient; transference number, which is the fraction of charge that is carried by the electrochemically active cation; and limiting current, which is the maximum current that can be stably applied.

Chapter 5 explored the connections between molecular frictional interactions and continuum electrochemical properties in glyme-based liquid electrolytes. We found that cation-anion interactions, typically assumed to be negligible in dilute systems, in fact dominated ionic conductivity even at very low salt concentrations in fluorinated electrolytes. Our observations emphasize the limited applicability of ideal solution approximations, in particular the Nernst-Einstein equation, and underscore the importance of concentrated solution theory.

In Chapter 6, we applied concentrated solution theory to highly-concentrated PEO / LiTFSI electrolytes. We showed that above $r = 0.28$ lithium ions per ethylene oxide moiety, a two-phase region exists, which single-phase concentrated solution theory is not equipped to handle. We found a solubility limit at $r = 0.50$, which caused the limiting current to approach zero as the salt concentration approached $r = 0.50$. The electrochemical implications of phase behavior in PEO / LiTFSI systems had not been studied previously; from this work, we learned that phase transitions occur at salt concentrations where we did not previously expect them, and that the solubility limit is the mechanism for the limiting current in high salt concentration PEO electrolytes.

The remainder of the Dissertation focused on SEO block copolymer electrolytes. In Chapter 7, we explored the effects of annealing on ionic conductivity to test the assumption that during annealing, microstructured grains grow and this leads to a decrease in ionic conductivity as the path length between electrodes increases. We found that this assumption did not explain the observed behavior of these electrolytes. We posit that the annihilation of defects that impede ion transport also plays an important role, and that the impact of different forms of defect annihilation on ionic conductivity depends on the salt concentration and initial grain size.

Chapter 8 continued the investigation of changes to SEO grains; we found that under exposure to a strong magnetic field, lamellar SEO grains were preferentially aligned, which led to quadrupolar $^7$Li NMR splitting. This splitting disappeared above the temperature at which the system became disordered—the order-to-disorder temperature, $T_{ODT}$—and therefore provides a new method for detecting $T_{ODT}$, which is typically measured using small-angle X-ray scattering, SAXS.

In Chapters 9 and 10, we combined SAXS with electrochemical measurements to study the effect of applied current on SEO domains, and vice versa. In Chapter 9, SAXS was applied to measure time- and position-dependent domain spacing in a lamellar SEO electrolyte during polarization. As expected, we observed that during the development of salt concentration gradients, lamellae expanded near the salt-rich positive electrode and contracted near the salt-poor negative electrode. However, we also found that the change in domain spacing was orientation-dependent: lamellae that were oriented perpendicular to the direction of ion transport played a more significant role in expanding and contracting to accommodate salt concentration gradients. It is therefore possible that limitations on domain expansion and contraction could place limits on concentration polarization and thereby on the limiting current.

In Chapter 10, we uncovered yet another new mechanism for the limiting current: morphological transitions. In equilibrated samples of our SEO electrolyte, a body-centered cubic spherical (BCC) morphology was observed above $r = 0.10$; below $r = 0.10$, grains with a hexagonally-packed cylindrical (HEX) morphology were formed. We polarized a cell with an initially homogeneous salt concentration of $r = 0.16$, and therefore a BCC morphology. We found that the limiting current was reached not when the salt concentration reached zero at the salt-poor negative electrode, as is commonly expected, or a solubility limit at the salt rich-positive electrode, as in Chapter 6, but instead when the salt concentration reached $r = 0.10$. This suggests that a morphological transition that occurs in equilibrated samples may not be accessible via electrochemical polarization, and that an inaccessible phase transition can be the mechanism for the limiting current.

## 11.2 Future Directions

This work has answered several questions but raises many more. Several are outlined below.

### *11.2.1 Theoretical*

In Chapter 6, we discussed the inability of concentrated solution theory to characterize systems in which ion transport occurs through two phases. This means that if any region of a PEO-based electrolyte exceeds $r = 0.28$, we are currently unable to model its behavior. We have learned that the two coexisting phases are an amorphous phase with $r = 0.28$ and a crystalline phase with $r = 0.50$, and we have complete electrochemical

characterization of each phase. However, we have not yet derived the equations that will use these parameters. Assuming equilibrium between the two phases, it may be possible to develop a set of equations, equivalent to the single-phase concentrated solution theory, that account for multi-phase transport.

In Chapters 9 and 10, we discussed the inability of polarization to induce domain expansion or contraction past a certain limit (Chapter 9) and a phase transition (Chapter 10). While it is trivial to determine the amount of energy provided by the flowing current, we do not yet have a way to quantify the forces involved in salt-induced domain size or morphology changes. How much force is required to expand or contract lamellae by adding or removing salt? How much strain is induced by changing salt concentrations? How much energy is needed to induce a BCC-HEX morphological transition? These may be interesting starting points for future theoretical studies.

*11.2.2 Experimental*

*In situ* SAXS, used in Chapters 9 and 10 to probe position- and time-dependent X-ray scattering and transmission during cell polarization, is a new technique that allows us to look inside a functioning cell and probe why the cell fails. In Chapter 10, we found that the inaccessibility of a BCC-HEX morphological transition can limit the applicable current. Future work may probe other morphological transitions. The simplest question is whether a HEX-BCC transition is accessible—for example, if a cell with the same electrolyte starts at $r = 0.06$, in the HEX region, can the salt concentration increase above $r = 0.075$, where BCC grains are expected to form? Moving into different block copolymers, which have different phase transitions, which are accessible and which are not? Coupled with the theoretical work proposed in Section 11.2.1, the proposed *in situ* studies will provide insight into the non-equilibrium morphology of block copolymer electrolytes under polarization conditions, which will inform design decisions allowing for higher limiting currents and therefore faster charging rates.

---

This Dissertation explored electrolytes based on liquid oligomers, PEO homopolymers, and SEO block copolymers. The studies herein spanned molecular interactions and macroscopic phase behavior, shedding light on the many factors influencing electrochemical properties of polymer electrolytes. These insights will contribute to future work in designing the high-performance electrolytes needed to enable widespread implementation of alternative energy sources.

# References


1. Trahey, L.; Brushett, F. R.; Balsara, N. P.; Ceder, G.; Cheng, L.; Chiang, Y. M.; Hahn, N. T.; Ingram, B. J.; Minteer, S. D.; Moore, J. S.; Mueller, K. T.; Nazar, L. F.; Persson, K. A.; Siegel, D. J.; Xu, K.; Zavadil, K. R.; Srinivasan, V.; Crabtree, G. W. Energy Storage Emerging: A Perspective from the Joint Center for Energy Storage Research. *Proc. Natl. Acad. Sci. U.S.A.* **2020,** *117,* 12550-12557.

2. Cheng, X.-B.; Zhang, R.; Zhao, C.-Z.; Zhang, Q. Toward Safe Lithium Metal Anode in Rechargeable Batteries: A Review. *Chem. Rev.* **2017,** *117,* 10403-10473.

3. Arya, A.; Sharma, A. L. A Glimpse on All-Solid-State Li-Ion Battery (ASSLIB) Performance Based on Novel Solid Polymer Electrolytes: A Topical Review. *J. Mater. Sci.* **2020,** *55,* 6242-6304.

4. Aurbach, D. Review of selected electrode solution interactions which determine the performance of Li and Li-ion batteries. *J. Power Sources* **2000,** *89,* 206-218.

5. Aurbach, D.; Markovsky, B.; Shechter, A.; Ein-Eli, Y.; Cohen, H. A Comparative Study of Synthetic Graphite and Li Electrodes in Electrolyte Solutions Based on Ethylene Carbonate-Dimethyl Carbonate Mixtures. *J. Electrochem. Soc.* **1996,** *143* (12), 3809-3820.

6. Xu, K. Nonaqueous Liquid Electrolytes for Lithium-Based Rechargeable Batteries. *Chem. Rev.* **2004,** *104* (10), 4303-4418.

7. Ding, F.; Yu, W.; Chen, X.; Zhang, J.; Engelhard, M. H.; Zhang, Y.; Johnson, B. R.; Crum, J. V.; Blake, T. A.; Liu, X.; Zhang, J.-G. Effects of Carbonate Solvents and Lithium Salts on Morphology and Coulombic Efficiency of Lithium Electrode. *J. Electrochem. Soc.* **2013,** *160* (10), A1894-A1901.

8. Man, P. P.; Klinowski, J.; Trokiner, A.; Zanni, H.; Papon, P. Selective and non-Selective NMR Excitation of Quadrupolar Nuclei in the Solid State. *Chem. Phys. Lett.* **1988,** *151,* 143-150.

9. Barai, P.; Higa, K.; Srinivasan, V. The Electrochemical Society Impact of External Pressure and Electrolyte Transport Properties on Lithium Dendrite Growth. *J. Electrochem. Soc.* **2018,** *165* (11), A2654-A2666.

10. Frenck, L.; Veeraraghavan, V. D.; Maslyn, J. A.; Müller, A.; Ho, A. D.; Loo, W. S.; Minor, A. M.; Balsara, N. P. Effect of Salt Concentration Profiles on Protrusion Growth in Lithium-Polymer-Lithium Cells. *Solid State Ionics* **2020,** *358,* No. 115517.

11. Monroe, C.; Newman, J. The impact of elastic deformation on deposition kinetics at lithium/polymer interfaces. *J. Electrochem. Soc.* **2005,** *152* (2), A396.

12. Leibler, L. Theory of Microphase Separation in Block Copolymers. *Macromolecules* **1980,** *13* (6), 1602-1617.

13. Bates, F. S.; Fredrickson, G. H. Block Copolymer Thermodynamics: Theory and Experiment. *Annu. Rev. Phys. Chem.* **1990,** *41* (1), 525-557.

14. Teran, A. A.; Balsara, N. P. Thermodynamics of Block Copolymers with and without Salt. *J. Phys. Chem. B* **2014,** *188,* 4-17.

15. Loo, W. S.; Galluzzo, M. D.; Li, X.; Maslyn, J. A.; Oh, H. J.; Mongcopa, K. I. S.; Zhu, C.; Wang, A. A.; Wang, X.; Garetz, B. A.; Balsara, N. P. Phase Behavior of Mixtures of Block Copolymers and a Lithium Salt. *J. Phys. Chem. B* **2018,** *122,* 8065-8074.

16. Hadjichristidis, N.; Iatrou, H.; Pispas, S.; Pitsikalis, M. Anionic Polymerization: High Vacuum Techniques. *J. Polym. Sci., Part A: Polym. Chem.* **2000,** *38,* 3211-3234.

17. Quirk, R. P.; Kim, J.; Kausch, C.; Chun, M. S. Butyllithium-initiated anionic synthesis of well-defined poly(styrene-block-ethylene oxide) block copolymers with potassium salt additives. *Polym. Int.* **1996,** *39* (1), 3-10.

18. Eitouni, H. Ambient Temperature Purification of Alkylene Oxides. **2013**.

19. Teran, A. A. Block Copolymer Electrolytes: Thermodynamics, Ion Transport, and Use in Solid-State Lithium/Sulfur Cells. Ph.D. Dissertation, University of California, Berkeley, Berkeley, CA. **2013**.

20. Hallinan, D. T.; Balsara, N. P. Polymer Electrolytes. *Annu. Rev. Mater. Res.* **2013,** *43,* 503-525.

21. Gao, K. W.; Loo, W. S.; Snyder, R. L.; Abel, B. A.; Choo, Y.; Lee, A.; Teixeira, C. M.; Garetz, B. A.; Coates, G. W.; Balsara, N. P. Miscible Polyether/Poly(ether–acetal) Electrolyte Blends. *Macromolecules* **2020,** *53* (14), 5728-5739.

22. Rojas, A. A.; Thakker, K.; McEntush, K. D.; Inceoglu, S.; Stone, G. M.; Balsara, N. P. Dependence of Morphology, Shear Modulus, and Conductivity on the Composition of Lithiated and Magnesiated Single-Ion-Conducting Block Copolymer Electrolytes. *Macromolecules* **2017,** *50,* 8765-8776.

23. Galluzzo, M. D.; Loo, W. S.; Wang, A. A.; Walton, A.; Maslyn, J. A. Measurement of Three Transport Coefficients and the Thermodynamic Factor in Block Copolymer Electrolytes with Different Morphologies. *J. Phys. Chem. B* **2020,** *124,* 921-935.

24. Gomez, E. D.; Panaday, A.; Feng, E. H.; Chen, V.; Stone, G. M.; Minor, A. M.; Kisielowski, C.; Downing, K. H.; Borodin, O.; Simth, G. D.; Balsara, N. P. Effect of Ion Distribution on Conductivity of Block Copolymer Electrolytes. *Nano Lett.* **2009,** *9,* 1212-1216.

25. Pesko, D. M.; Timachova, K.; Bhattacharya, R.; Smith, M. C.; Villaluenga, I.; Newman, J.; Balsara, N. P. Negative Transference Numbers in Poly(ethylene oxide)-Based Electrolytes. *J. Electrochem. Soc.* **2017,** *164* (11), E3569-E3575.

26. Levitt, M. H. *Spin Dynamics: Basics of Nuclear Magnetic Resonance,* 2nd ed.; Wiley: New York, 2008.

27. Teran, A. A.; Mullin, S. A.; Hallinan Jr., D. T.; Balsara, N. P. Discontinuous Changes in Ionic Conductivity of a Block Copolymer Electrolyte through an Order-Disorder Transition. *ACS Macro Lett.* **2012,** *1,* 305-309.

28. Bragg, W. H.; Bragg, W. L. The Reflection of X-Rays by Crystals. *Proc. R. Soc. Lond. A* **1913,** *88,* 428-438.

29. Newman, J.; Balsara, N. P. *Electrochemical Systems,* 4th ed.; Wiley, 2021.

30. Rosman, K. J. R.; Taylor, P. D. P. Isotopic Compositions of the Elements 1997. *Pure & Appl. Chem.* **1998,** *70* (1), 217-235.

31. Pyykkö, P. Year-2017 Nuclear Quadrupole Moments. *Mol. Phys.* **2018,** *116* (10), 1328-1338.

32. Freeman, R.; Hill, H. D. W.; Kaptein, R. Proton-Decoupled NMR Spectra of Carbon-13 With the Nuclear Overhauser Effect Suppressed. *J. Magn. Reson.* **1972,** *7* (3), 327-329.

33. Philp, D. J.; Naumann, D.; Kuchel, P. W. Relative Intensities of Components of Quadrupolar-Split Multiplets in NMR Spectra: Rationale for a Simple Rule. *Concepts Magn. Reson., Part A* **2012,** *40A* (2), 90-99.

34. Stejskal, E. O.; Tanner, J. E. Spin Diffusion Measurements: Spin Echoes in the Presence of a Time-Dependent Field Gradient. *J. Chem. Phys.* **1965,** *42,* 288-292.

35. Sinnaeve, D. The Stejskal-Tanner Equation Generalized for Any Gradient Shape--An Overview of Most Pulse Sequences Measuring Free Diffusion. *Concepts Magn. Reson., Part A* **2012,** *40,* 39-65.

36. Johnson Jr., C. S. Diffusion ordered nuclear magnetic resonance spectroscopy: principles and applications. *Prog. Nucl. Magn. Reson. Spectrosc.* **1999,** *34,* 203-256.

37. Price, W. S. Pulsed-Field Gradient Nuclear Magnetic Resonance as a Tool for Studying Translational Diffusion: Part II. Experimental Aspects. *Concepts Magn. Reson.* **1998,** *10* (4), 197-237.

38. Wu, D. H.; Chen, A. D.; Johnson, C. S. An Improved Diffusion-Ordered Spectroscopy Experiment Incorporating Bipolar-Gradient Pulses. *J. Magn. Reson., Ser. A* **1995,** *115* (2), 260-264.

39. Gibbs, S. J.; Johnson, C. S. A PFG NMR Experiment for Accurate Diffusion and Flow Studies in the Presence of Eddy Currents. *J. Magn. Reson. (1969-1992)* **1991,** *93* (2), 395-402.

40. Jerschow, A.; Müller, N. Suppression of Convection Artifacts in Stimulated-Echo Diffusion Experiments, Double-Stimulated-Echo Ecperiments. *J. Magn. Reson.* **1997,** *125* (2), 372-375.

41. Holz, M. Electrophoretic NMR. *Chem. Soc. Rev.* **1994,** *23,* 165-174.

42. Timachova, K.; Newman, J.; Balsara, N. P. Theoretical Interpretation of Ion Velocities in Concentrated Electrolytes Measured by Electrophoretic NMR. *J. Electrochem. Soc.* **2019,** *166* (2), A264-A267.

43. Henke, B. L.; Gullikson, E. M.; David, J. C. X-ray Interactions: Photoabsorption, Scattering, Transmission, and Reflection at $E = 50$-30000 eV, $Z = 1$-92. *Atomic Data and Nuclear Data Tables* **1993,** *54* (2), 181-342.

44. Hamley, I.; Castelletto, V. Small-Angle Scattering of Block Copolymers. In *Soft Matter Characterization;* Springer: Dordrecht, 2008; pp 1021-1081.

45. Ilavsky, J. Nika: Software for Two-Dimensional Data Reduction. *J. Appl. Cryst.* **2012,** *45,* 324-328.

46. Kieffer, J.; Karkoulis, D. PyFAI, a Versatile Library for Azimuthal Regrouping. *J. Phys. Conf. Ser.* **2013,** *425,* No. 202012.

47. Pesko, D. M.; Feng, Z.; Sawhney, S.; Newman, J.; Srinivasan, V.; Balsara, N. P. Comparing Cycling Characteristics of Symmetric Lithium-Polymer-Lithium Cells with Theoretical Predictions. *J. Electrochem. Soc.* **2018,** *165,* A3186-A3194.

48. Maslyn, J. A.; Frenck, L.; Veeraraghavan, C. D.; Mu, A.; Ho, A. S.; Marwaha, N.; Loo, W. S.; Parkinson, D. Y.; Minor, A. M.; Balsara, N. P. Limiting Current in Nanostructured Block Copolymer Electrolytes. *Macromolecules* **2021,** *54,* 4010-4022.

49. Shah, D. B.; Kim, H. K.; Nguyen, H. Q.; Srinivasan, V.; Balsara, N. P. Comparing Measurements of Limiting Current of Electrolytes with Theoretical Predictions up to the Solubility Limit. *J. Phys. Chem. C* **2019,** *123* (39), 23872-23881.

50. Villaluenga, I.; Pesko, D. M.; Timachova, K.; Feng, Z.; Newman, J.; Srinivasan, V.; Balsara, N. P. Negative Stefan-Maxwell Diffusion Coefficients and Complete Electrochemical Transport Characterization of Homopolymer and Block Copolymer Electrolytes. *J. Electrochem. Soc.* **2018,** *165* (11), A2766-A2773.

51. Evans, J.; Vincent, C.; and Bruce, P. Electrochemical measurement of transference numbers in polymer electrolytes. *Polymer* **1987,** *28,* 2324-2328.

52. Galluzzo, M. D.; Maslyn, J. A.; Shah, D. B.; Balsara, N. P. Ohm's law for ion conduction in lithium and beyond-lithium battery electrolytes. *J. Chem. Phys* **2019,** *151,* 020901.

53. Gao, K. W.; Balsara, N. P. Electrochemical properties of poly(ethylene oxide) electrolytes above the entanglement threshold. *Solid State Ionics* **2021,** *364,* 115609.

54. Ma, Y.; Doyle, M.; Fuller, T. F.; Doeff, M. M.; De Jonghe, L. C.; Newman, J. The Measurement of a Complete Set of Transport Properties for a Concentrated Solid Polymer Electrolyte Solution. *J. Electrochem. Soc.* **1995,** *142* (6), 1859-1868.

55. Bruce, P. G.; Vincent, C. A. Steady State Current Flow in Solid Binary Electrolyte Cells. *J. Electroanal. Chem.* **1987,** *225* (1), 1-17.

56. Newman, J.; Chapman, T. W. Restricted Diffusion in Binary Solutions. *AIChE J.* **1973,** *19* (2), 343-348.

57. Gribble, D. A.; Frenck, L.; Shah, D. B.; Maslyn, J. A.; Loo, W. S.; Mongcopa, K. I. S.; Pesko, D. M.; Balsara, N. P. Comparing Experimental Measurements of Limiting Current in Polymer Electrolytes with Theoretical Predictions. *J. Electrochem. Soc.* **2019,** *166,* A3228-A3234.

58. Kim, H.-K.; Balsara, N. P.; Srinivasan, V. Continuum Description of the Role of Negative Transference Numbers on Ion Motion in Polymer Electrolytes. *J. Electrochem. Soc.* **2020,** *167,* No. 110559.

59. Mistry, A.; Grundy, L. S.; Halat, D. M.; Newman, J.; Balsara, N. P.; Srinivasan, V. Effect of Solvent Motion on Ion Transport in Electrolytes. *J. Electrochem. Soc.* **2022,** *169* (4), 040524.

60. Logan, E. R.; Gering, K. L.; Ma, X.; Dahn, J. R. Electrolyte Development for High-Performance Li-Ion Cells: Additives, Solvents, and Agreement with a Generalized Molecular Model. *Electrochem. Soc. Interface* **2019,** *28* (2), 49-53.

61. Manthiram, A. A reflection on lithium-ion battery cathode chemistry. *Nat. Commun.* **2020,** *11,* 1550.

62. Marzantowicz, M.; Dygas, J. R.; Krok, F.; Nowiński, J. L.; Tomaszewska, A.; Florjańczyk, Z.; Zygadlo-Monikowzka, E. Crystalline phases, morphology and conductivity of PEO:LiTFSI electrolytes in the eutectic region. *J. Power Sources* **2006,** *159,* 420-430.

63. Murata, K.; Izuchi, S.; Yoshihisa, Y. An overview of the research and development of solid polymer electrolyte batteries. *Electrochim. Acta* **2000,** *45,* 1501-1508.

64. Ren, X.; Zou, L.; Jiao, S.; Mei, D.; Engelhard, M. H.; Li, Q.; Lee, H.; Niu, C.; Adams, B. D.; Wang, C.; Liu, J.; Zhang, J.-G.; Xu, W. High-Concentration Ether Electrolytes for Stable High-Voltage Lithium Metal Batteries. *ACS Energy Lett.* **2019,** *4,* 896-902.

65. Wong, D. H. C.; Thelen, J. L.; Fu, Y.; Devaux, D.; Pandya, A. A.; Battaglia, V. S.; Balsara, N. P.; DeSimone, J. M. Nonflammable Perfluoropolyether-Based Electrolytes for Lithium Batteries. *PNAS* **2014,** *111* (9), 3327-3331.

66. Amanchukwu, C. V.; Yu, Z.; Kong, X.; Qin, J.; Cui, Y.; Bao, Z. A New Class of Ionically Conducting Fluorinated Ether Electrolytes with High Electrochemical Stability. *J. Am. Chem. Soc.* **2020,** *142,* 7393-7403.

67. Fan, X.; Chen, L.; Borodin, O.; Ji, X.; Chen, J.; Hou, S.; Deng, T.; Zheng, J.; Yang, C.; Liou, S.-C.; Amine, K.; Xu, K.; Wang, C. Non-flammable electrolyte enables Li-metal batteries with aggressive cathode chemistries. *Nat. Nanotechnol.* **2018,** *13,* 715-722.

68. Lin, Y.-M.; Klavetter, K. C.; Abel, P. R.; Davy, N. C.; Snider, J. L.; Heller, A.; Mullins, C. B. High performance silicon nanoparticle anode in fluoroethylene carbonate-based electrolyte for Li-ion batteries. *Chem. Commun.* **2012,** *48,* 7268-7270.

69. Hou, T.; Yang, G.; Rajput, N. N.; Self, J.; Park, S.-W.; Nanda, J.; Persson, K. A. The influence of FEC on the solvation structure and reduction reaction of $LiPF_6$/EC electrolytes and its implication for solid electrolyte interphase formation. *Nano Energy* **2019,** *64,* 103881.

70. Berger, R.; Resnati, G.; Matrangolo, P.; Weber, E.; and Hulliger, J. Organic fluorine compounds: a great opportunity for enhanced materials properties. *Chem. Soc. Rev.* **2011,** *40,* 3496-3508.

71. Self, J.; Fong, K. D.; Logan, E. R.; Persson, K. A. Ion Association Constants for Lithium Ion Battery Electrolytes from First-Principles Quantum Chemistry. *J. Electrochem. Soc.* **2019,** *166* (15), A3554-A3558.

72. Shen, K.-H.; Hall, L. M. Ion Conductivity and Correlations in Model Salt-Doped Polymers: Effects of Interaction Strength and Concentration. *Macromolecules* **2020,** *53* (10), 3655-3668.

73. Balsara, N. P.; Newman, J. Relationship between Steady-State Current in Symmetric Cells and Transference Number of Electrolytes Comprising Univalent and Multivalent Ions. *J. Electrochem. Soc.* **2015,** *162* (14), A2720-A2722.

74. Noda, A.; Hayamizu, K.; Watanabe, M. Pulsed-Gradient Spin-Echo $^{1}H$ and $^{19}F$ NMR Ionic Diffusion Coefficient, Viscosity, and Ionic Conductivity of Non-Chloroaluminate Room-Temperature Ionic Liquids. *J. Phys. Chem. B* **2001,** *105,* 4603-4610.

75. Gouverneur, M.; Schmidt, F.; Schönhoff, M. Negative effective Li transference numbers in Li salt/ionic liquid mixtures: does Li drift in the "Wrong" direction? *Phys. Chem. Chem. Phys* **2018,** *20,* 7470-7478.

76. Yoshida, K.; Tsuchiya, M.; Tachikawa, N.; Dokko, K.; Watanabe, M. Change from Glyme Solutions to Quasi-ionic Liquids for Binary Mixtures Consisting of Lithium Bis(trifluoromethanesulfonyl)amide and Glymes. *J. Phys. Chem. C* **2011,** *115,* 18384-18394.

77. Ueno, K.; Yoshida, K.; Tsuchiya, M.; Tachikawa, N.; Dokko, K.; Watanabe, M. Glyme-Lithium Salt Equimolar Molten Mixtures: Concentrated Solutions or Solvate Ionic Liquids? *J. Phys. Chem. B* **2012,** *116,* 11323-11331.

78. Zhang, C.; Ueno, K.; Yamazaki, A.; Yoshida, K.; Moon, H.; Mandai, T.; Umebayashi, Y.; Dokko, K.; Watanabe, M. Chelate Effects in Glyme/Lithium Bis(trifluoromethanesulfonyl)amide Solvate Ionic Liquids. I. Stability of Solvate Cations and Correlation with Electrolyte Properties. *J. Phys. Chem. B* **2014,** *118,* 5144-5153.

79. Schmidt, F.; Schönhoff, M. Solvate Cation Migration and Ion Correlations in Solvate Ionic Liquids. *J. Phys. Chem. B* **2020,** *124,* 1245-1252.

80. Thieu, L. M.; Zhu, L.; Korovich, A. G.; Hickner, M. A.; Madsen, L. A. Multiscale Tortuous Diffusion in Anion and Cation Exchange Membranes. *Macromolecules* **2019,** *52,* 24-35.

81. Kidd, B. E.; Forbey, S. J.; Steuber, F. W.; Moore, R. B.; Madsen, L. A. Multiscale Lithium and Counterion Transport in an Electrospun Polymer-Gel Electrolyte. *Macromolecules* **2015,** *48,* 4481-4490.

82. D'Agostino, C.; Mantle, M. D.; Mullan, C. L.; Hardacre, C.; Gladden, L. F. Diffusion, Ion Pairing and Aggregation in 1-Ethyl-3-Methylimidazolium-Based Ionic Liquids Studied by $^{1}H$ and $^{19}F$ PFG NMR: Effect of Temperature, Anion and Glucose Dissolution. *ChemPhysChem* **2018,** *19,* 1081-1088.

83. Lonergan, M. C.; Shriver, D. F.; Ratner, M. A. Polymer Electrolytes: the Importance of Ion-Ion Interactions in Diffusion Dominated Behavior. *Electrochimica Acta* **1995,** *40* (13), 2041-2048.

84. Murch, G. E. The Haven Ratio in Fast Ionic Conductors. *Solid State Ionics* **1982,** *7,* 177-198.

85. Bird, R. B.; Stewart, W. E.; Lightfoot, E. N. *Transport Phenomena;* John Wiley & Sons: New Jersey, 1960.

86. Schreiner, C.; Zugmann, S.; Hartl, R.; Gores, H. J. Fractional Walden Rule for Ionic Liquids: Examples from Recent Measurements and a Critique of the So-Called Ideal KCl Line for the Walden Plot. *J. Chem. Eng. Data* **2010,** *55,* 1784-1788.

87. Pinkert, A.; Ang, K. L.; Marsh, K. N.; Pang, S. Density, viscosity and electrical conductivity of protic alkanolammonium ionic liquids. *Phys. Chem. Chem. Phys.* **2011,** *13,* 5136-5143.

88. Chintapalli, M.; Timachova, K.; Olson, K. R.; Mecham, S. J.; Devaux, D.; DeSimone, J. M.; Balsara, N. P. Relationship between Conductivity, Ion Diffusion, and Transference Number in Perfluoropolyether Electrolytes. *Macromolecules* **2016,** *49,* 3508-3515.

89. Boden, N.; Leng, S. A.; Ward, I. M. Ionic conductivity and diffusivity in polyethylene oxide/electrolyte solutions as models for polymer electrolytes. *Solid State Ionics* **1991,** *45,* 261-270.

90. Hayamizu, K.; Aihara, Y.; Arai, S.; Price, W. S. Diffusion, conductivity and DSC studies of a polymer gel electrolyte composed of cross-linked PEO, gamma-butyrolactone and $LiBF_4$. *Solid State Ionics* **1998,** *107,* 1-12.

91. Bocharova, V.; Sokolov, A. P. Perspectives for Polymer Electrolytes: A View from Fundamentals of Ionic Conductivity. *Macromolecules* **2020,** *53* (11), 4141-4157.

92. Dewing, B. L.; Bible, N. G.; Ellison, C. J.; Mahanthappa, M. K. Electrochemically Stable, High Transference Number Lithium Bis(malonato)borate Polymer Solution Electrolytes. *Chem. Mater.* **2020,** *32* (9), 3794-3804.

93. Diederichsen, K. M.; Fong, K. D.; Terrell, R. C.; Persson, K. A.; McCloskey, B. D. Investigation of Solvent Type and Salt Addition in High Transference Number Nonaqueous Polyelectrolyte Solutions for Lithium Ion Batteries. *Macromolecules* **2018,** *51* (21), 8761-8771.

94. Lu, Y.; Tikekar, M.; Mohanty, R.; Hendrickson, K.; Ma, L.; Archer, L. A. Stable Cycling of Lithium Metal Batteries Using High Transference Number Electrolytes. *Adv. Energy Mater.* **2015,** *5,* 1402073.

95. Landesfeind, J.; Gasteiger, H. A. Temperature and Concentration Dependence of the Ionic Transport Properties of Lithium-Ion Battery Electrolytes. *J. Electrochem. Soc.* **2019,** *166* (14), A3079-A3097.

96. Vardner, J. T.; Ling, T.; Russell, S. T.; Perakis, A. M.; He, Y.; Brady, N. W.; Kumar, S. K.; West, A. C. Method of Measuring Salt Transference Numbers in Ion-Selective Membranes. *J. Electrochem. Soc.* **2017,** *164* (13), A2940-A2947.

97. Craig, N.; Mullin, S. A.; Pratt, R.; Crane, G. B. Determination of Transference Number and Thermodynamic Factor by use of Anion-Exchange Concentration Cells and Concentration Cells. *J. Electrochem. Soc.* **2019,** *166* (13), A2769-A2775.

98. Shah, D. B.; Nguyen, H. Q.; Grundy, L. S.; Olson, K. R.; Mecham, S. J.; DeSimone, J. M.; Balsara, N. P. Difference between approximate and rigorously measured transference numbers in fluorinated electrolytes. *Phys. Chem. Chem. Phys.* **2019,** *21,* 7857-7866.

99. Dees, D. W.; Battaglia, V. S.; Redey, L.; Henriksen, G. L.; Atanasoski, R.; Belanger, A. Toward standardizing the measurement of electrochemical properties of solid-state electrolytes in lithium batteries. *J. Power Sources* **2000,** *89,* 249.

100. Olson, K. R.; Wong, D. H. C.; Chintapalli, M.; Timachova, K.; Janusziewicz, R.; Daniel, W. F. M.; Mecham, S.; Sheiko, S.; Balsara, N. P.; DeSimone, J. M. Liquid perfluoropolyether electrolytes with enhanced ionic conductivity for lithium battery applications. *Polymer* **2016,** *100,* 126-133.

101. Shah, D. B.; Olson, K. R.; Karny, A.; Mecham, S. J.; DeSimone, J. M.; Balsara, N. P. Effect of Anion Size on Conductivity and Transference Number of Perfluoroether Electrolytes with Lithium Salts. *J. Electrochem. Soc.* **2017,** *164* (14), A3511-A3517.

102. Maitra, A.; Heuer, A. Cation Transport in Polymer Electrolytes: A Microscopic Approach. *Phys. Rev. Lett.* **2007,** *98* (22), 227802.

103. Watanabe, M.; Nagano, S.; Sanui, K.; Ogata, N. Estimation of $Li^+$ Transport Number in Polymer Electrolytes by the Combination of Complex Impedance and Potentiostatic Polarization Measurements. *Solid State Ionics* **1988,** *28-30,* 911-917.

104. Vanag, V. K.; Epstein, I. R. Cross-diffusion and pattern formation in reaction-diffusion systems. *Phys. Chem. Chem. Phys.* **2008,** *11,* 897-912.

105. Clunie, J. C.; Burns, N. L.; Baird, J. K. Nernst-Hartley evaluation of the interdiffusion coefficient of aqueous nickel sulfamate using new measurements of the equivalent conductances of the ions. *J. Electroanal. Chem.* **1992,** *328,* 317-320.

106. Heintz, A.; Ludwig, R.; Schmidt, E. Limiting diffusion coefficients of ionic liquids in water and methanol: a combined experimental and molecular dynamics study. *Phys. Chem. Chem. Phys.* **2011,** *13,* 3268-3273.

107. Hartley, G. S. *Philos. Mag.* **1931,** *12,* 473.

108. Einstein, A. Investigations on the theory of brownian movement. *Leipzig, Ann. Phys.* **1905,** *17,* 549.

109. Vorotyntsev, M. A.; Zinovyeva, V. A.; Picquet, M. Diffusional transport in ionic liquids: stokes-einstein relation or 'sliding sphere' model ? Ferrocene (Fc) in imidazolium liquids. *Electrochim. Acta* **2010,** *55,* 5063.

110. Chambers, J. F.; Stokes, J. M.; Stokes, R. H. Conductances of Concentrated Aqueous Sodium and Potassium Chloride Solutions at 25C. *J. Phys. Chem.* **1956,** *60* (7), 985-986.

111. Steinrück, H.-G.; Takacs, C. J.; Kim, H.-K.; Mackanic, D. G.; Holladay, B.; Cao, C.; Narayanan, S.; Dufresne, E. M.; Chushkin, Y.; Ruta, B.; Zontone, F.; Will, J.; Borodin, O.; Sinha, S. K.; Srinivasan, V.; Toney, M. F. Concentration and Velocity Profiles in a Polymeric Lithium-Ion Battery Electrolyte. *Energy Environ. Sci.* **2020,** *13,* 4312-4321.

112. Maslyn, J. A.; Loo, W. S.; McEntush, K. D.; Oh, H. J.; Harry, K. J.; Parkinson, D. Y.; Balsara, N. P. Growth of Lithium Dendrites and Globules through a Solid Block Copolymer Electrolyte as a Function of Current Density. *J. Phys. Chem. C* **2018,** *122* (47), 26797-26804.

113. Lascaud, S.; Perrier, M.; Vallée, A.; Besner, S.; Prud'homme, J. Phase Diagrams and Conductivity Behavior of Poly(ethylene oxide)-Molten Salt Rubbery Electrolytes. *Macromolecules* **1994,** *27,* 7649-7477.

114. Marzantowicz, M.; Krok, F.; Dygas, J. R.; Florjańczyk, Z.; Zygadł0-Monikowska, E. The influence of phase segregation on properties of semicrystalline PEO:LiTFSI electrolytes. *Solid State Ionics* **2008,** *179,* 1670-1678.

115. Chintapalli, M.; Le, T. N. P.; Venkatesan, N. R.; Mackay, N. G.; Rojas, A. A.; Thelen, J. L.; Chen, X. C.; Devaux, D.; Balsara, N. P. Structure and Ionic Conductivity of Polystyrene-Block-Poly(Ethylene Oxide) Electrolytes in the High Salt Concentration Limit. *Macromolecules* **2016,** *49,* 1770-1780.

116. Pesko, D. M.; Sawhney, S.; Newman, J.; Balsara, N. P. Comparing Two Electrochemical Approaches for Measuring Transference Numbers in Concentrated Electrolytes. *J. Electrochem. Soc.* **2018,** *165* (13), A3014-A3021.

117. Keller, A.; Hikosaka, M.; Rastogi, S.; Toda, A.; Barham, P. J.; Goldbeck-Wood, G. An approach to the formation and growth of new phases with application to polymer crystallization: effect of finite size, metastability, and Ostwald's rule of stages. *J. Mater. Sci.* **1994,** *29,* 2579-2604.

118. Mongcopa, K. I. S.; Tyagi, M.; Mailoa, J. P.; Samsonidze, G.; Kozinsky, B.; Mullin, S. A.; Gribble, D. A.; Watanabe, H.; Balsara, N. P. Relationship between Segmental Dynamics Measured by Quasi-Elastic Neutron Scattering and Conductivity in Polymer Electrolytes. *ACS Macro Lett.* **2018,** *7,* 504-508.

119. Pożycka, K.; Marzantowicz, M.; Dygas, J. R.; Krok, F. Ionic Conductivity and Lithium Transference Number of Poly(Ethylene Oxide):LiTFSI System. *Elecrochim. Acta* **2017,** *227,* 127-135.

120. Monroe, C.; Newman, J. Dendrite Growth in Lithium/Polymer Systems: A Propagation Model for Liquid Electrolytes under Galvanostatic Conditions. *J. Electrochem. Soc.* **2003,** *150* (10), A1377-A1384.

121. Galluzzo, M. D.; Grundy, L. S.; Takacs, C. J.; Cao, C.; Steinrueck, H.-G.; Fu, S.; Rivas Valdez, M. A.; Toney, M. F.; Balsara, N. P. Orientation-Dependent Distortion of Lamellae in a Block Copolymer Electrolyte under DC Polarization. *Macromolecules* **2021,** *54,* 7808-7821.

122. Frenck, L.; Veeraraghavan, V. D.; Maslyn, J. A.; Muller, A; Ho, A. D.; Loo, W. S.; Minor, A. M.; Balsara, N. P. Effect of Salt Concentration Profiles on Protrusion Growth in Lithium-Polymer-Lithium Cells. *Solid State Ionics* **2020,** *358,* No. 115517.

123. Goyal, P.; Monroe, C. W. New Foundations of Newman's Theory for Solid Electrolytes: Thermodynamics and Transient Balances. *J. Electrochem. Soc.* **2017,** *164* (11), E3647-E3660.

124. Hashimoto, T.; Nagatoshi, K.; Todo, A.; Hasegawa, H.; Kawai, H. Domain-Boundary Structure of Styrene-Isoprene Block Copolymer Films Cast from Toluene Solutions. *Macromolecules* **1974,** *7* (3), 364-373.

125. Gido, S. P.; Gunther, J.; Thomas, E. L.; Hoffman, D. Lamellar diblock copolymer grain boundary morphology. 1. Twist boundary characterization. *Macromolecules* **1993,** *26* (17), 4506-4520.

126. Dai, H. J.; Balsara, N. P.; Garetz, B. A.; Newstein, M. C. Grain Growth and Defect Annihilation in Block Copolymers. *Phys. Rev. Lett.* **1996,** *77,* 3677.

127. Li, X.; Martínez-González, J. A.; Guzmán, O.; Ma, X.; Park, K.; Zhou, C.; Kambe, Y.; Jin, H. M.; Dolan, J. A.; Nealey, P. F.; de Pablo, J. Sculpted grain boundaries in soft crystals. *Sci. Adv.* **2019,** *5,* eaax9112.

128. Sax, J.; Ottino, J. M. Modeling of Transport of Small Molecules in Polymer Blends: Application of Effective Medium Theory. *Polym. Eng. Sci.* **1983,** *23* (3), 165-176.

129. Shen, K.-H.; Brown, J. R.; Hall, L. M. Diffusion in Lamellae, Cylinders, and Double Gyroid Block Copolymer Nanostructures. *ACS Macro Lett.* **2018,** *7* (9), 1092-1098.

130. Young, W.-S.; Epps, T. H. Ionic Conductivities of Block Copolymer Electrolytes with Various Conducting Pathways: Sample Preparation and Processing Considerations. *Macromolecules* **2012,** *45* (11), 4689-4697.

131. Kim, O.; Jo, G.; Park, Y. J.; Kim, S.; Park, M. J. Ion Transport Properties of Self-Assembled Polymer Electrolytes: The Role of Confinement and Interface. *J. Phys. Chem. Lett* **2013,** *4,* 2111-2117.

132. Harrison, C.; Adamson, D. H.; Cheng, Z.; Sebastian, J. M.; Sethuraman, S.; Huse, D. A.; Register, R. A.; Chaikin, P. M. Mechanisms of Ordering in Striped Patterns. *Science* **2000,** *290* (5496), 1558-1560.

133. Ryu, H. J.; Fortner, D. B.; Lee, S.; Ferebee, R.; De Graef, M.; Misichronis, K.; Avgeropoulos, A.; Bockstaller, M. R. Role of Grain Boundary Defects During Grain Coarsening of Lamellar Block Copolymers. *Macromolecules* **2013,** *46* (1), 204-215.

134. Ren, J.; Zhou, C.; Chen, X.; Dolejsi, M.; Craig, G. S. W.; Rincon Delgadillo, P. A.; Segal-Peretz, T.; Nealey, P. F. Engineering the Kinetics of Directed Self-Assembly of Block Copolymers toward Fast and Defect-Free Assembly. *ACS Appl. Mater. Interfaces* **2018,** *10* (27), 23414-23423.

135. Chintapalli, M.; Chen, X. C.; Thelen, J. L.; Teran, A. A.; Wang, X.; Garetz, B. A.; Balsara, N. P. Effect of Grain Size on the Ionic Conductivity of a Block Copolymer Electrolyte. *Macromolecules* **2014,** *47,* 5424-5431.

136. Chintapalli, M.; Higa, K.; Chen, X. C.; Srinivasan, V.; Balsara, N. P. Simulation of Local Ion Transport in Lamellar Block Copolymer Electrolytes Based on Electron Micrographs. *J. Polym. Sci., Part B: Polym. Phys.* **2017,** *55,* 266-274.

137. Arges, C. G.; Kambe, Y.; Dolejsi, M.; Wu, G.-P.; Segal-Pertz, T.; Ren, J.; Cao, C.; Graig, G. S. W.; Nealey, P. F. Interconnected ionic domains enhance conductivity in microphase separated block copolymer electrolytes. *J. Mater. Chem. A* **2017,** *5,* 5619.

138. Majewski, P. W.; Gopinadhan, M.; Jang, W.-S.; Lutkenhaus, J. L.; Osuji, C. O. Anisotropic Ionic Conductivity in Block Copolymer Membranes by Magnetic Field Alignment. *J. Am. Chem. Soc.* **2010,** *132* (49), 17516-17522.

139. Majewski, P. W.; Gopinadhan, M.; Osuji, C. O. Understanding anisotropic transport in self-assembled membranes and maximizing ionic conductivity by microstructure alignment. *Soft Matter* **2013,** *9,* 7106-7116.

140. Kambe, Y.; Arges, C. G.; Czaplewski, D. A.; Dolejsi, M.; Krishnan, S.; Stoykovich, M. P.; de Pablo, J. J.; Nealey, P. F. Role of Defects in Ion Transport in Block Copolymer Electrolytes. *Nano Lett* **2019,** *19,* 4684-4691.

141. Schulze, M. W.; McIntosh, L. D.; Hillmyer, M. A.; Lodge, T. P. High-Modulus, High-Conductivity Nanostructured Polymer Electrolyte Membranes via Polymerization-Induced Phase Separation. *Nano Lett.* **2014,** *14,* 122-126.

142. Mullin, S. A.; Teran, A. A.; Yuan, R.; Balsara, N. P. Effect of Thermal History on the Ionic Conductivity of Block Copolymer Electrolytes. *J. Polym. Sci., Part B: Polym. Phys.* **2013,** *51,* 927-934.

143. Yuan, R.; Teran, A. A.; Gurevitch, I.; Mullin, S. A.; Wanakule, N. S.; Balsara, N. P. Ionic Conductivity of Low Molecular Weight Block Copolymer Electrolytes. *Macromolecules* **2013,** *46,* 914-921.

144. Hexemer, A.; Bras, W.; Glossinger, J.; Schaible, E.; Gann, E.; Kirian, R.; MacDowell, A.; Church, M.; Rude, B.; Padmore, H. A. SAXS/WAXS/GISAXS Beamline with Multilayer Monochromator. *J. Phys.: Conf. Ser.* **2010,** *247,* 1-11.

145. Newville, M.; Stensitzki, T.; Allen, D. B.; Ingargiola, A. LMFIT: Non-Linear Least-Square Minimization and Curve-Fitting for Python. *Zenodo* **2014.**

146. Teran, A. A.; Tang, M. H.; Mullin, S. A.; Balsara, N. P. Effect of molecular weight on conductivity of polymer electrolytes. *Solid State Ionics* **2011,** *203* (1), 18-21.

147. Devaux, D.; Bouchet, R.; Glé, D.; Denoyel, R. Mechanism of ion transport in PEO/LiTFSI complexes: Effect of temperature, molecular weight and end groups. *Solid State Ionics* **2012,** *227,* 119-127.

148. Hoffman, Z. J.; Shah, D. B.; Balsara, N. P. Temperature and concentration dependence of the ionic transport properties of poly(ethylene oxide) electrolytes. *Solid State Ionics* **2021,** *370,* 115751.

149. Scherrer, P. Estimation of the Size and Structure of Colloidal Particles by Rontgen Rays. *Nachrichten von der K. Gesellschaft der Wissenschaften zu Gottingen, Math. Phys. Klasse* **1918,** *i,* 322-323.

150. Smilgies, D.-M. Scherrer grain-size analysis adapted to grazing incidence scattering with area detectors. *J. Appl. Crystallogr.* **2009,** *42,* 1030-1034.

151. Gervais, M.; Gallot, B. Phase Diagram and Structural Study of Polystyrene−Poly(ethylene oxide) Block Copolymers, 1. *Makromol. Chem.* **1973,** *171,* 157-178.

152. Sakamoto, N.; Hashimoto, T. Order-Disorder Transition of Low Molecular Weight Polystyrene-block-Polyisoprene. 1. SAXS Analysis of Two Characteristic Temperatures. *Macromolecules* **1995,** *28* (20), 6825-6834.

153. Bates, F. S.; Rosedale, J. H.; Fredrickson, G. H. Fluctuation Effects in a Symmetric Diblock Copolymer Near the Order-Disorder Transition. *J. Chem. Phys.* **1990,** *92* (10), 6255-6270.

154. Balsara, N. P.; Perahia, D.; Safinya, C. R.; Tirrell, M.; Lodge, T. P. Birefringence Detection of the Order-to-Disorder Transition in Block Copolymer Liquids. *Macromolecules* **1992,** *25* (15), 3896-3901.

155. Chung, C. I.; Gale, J. C. Newtonian Behavior of a Styrene- Butadiene-Styrene Block Copolymer. *J. Polym. Sci., Polym. Phys. Ed.* **1976,** *14,* 1149-1156.

156. Han, C. D.; Kim, J.; Kim, J. K. Determination of the Order- Disorder Transition Temperature of Block Copolymers. *Macromolecules* **1989,** *22* (1), 383-394.

157. Adams, J. L.; Graessley, W. W.; Register, R. A. Rheology and the Microphase Separation Transition in Styrene-Isoprene Block Copolymers. *Macromolecules* **1994,** *27* (21), 6026-6032.

158. Rosedale, J. H.; Bates, F. S. Rheology of Ordered and Disordered Symmetric Poly(ethylenepropylene)-poly(ethylene) Diblock Copolymers. *Macromolecules* **1990,** *23* (8), 2329-2338.

159. Singh, M.; Odusanya, O.; Wilmes, G. M.; Eitouni, H. B.; Gomez, E. D.; Patel, A. J.; Chen, V. L.; Park, M. J.; Fragouli, P.; Iatrou, H.; Hadjichristidis, N.; Cookson, D.; Balsara, N. P. Effect of Molecular Weight on Mechanical and Electrical Properties of Block Copolymer Electrolytes. *Macromolecules* **2007,** *40* (13), 4578-4585.

160. Abbrent, S.; Greenbaum, S. Recent Progress in NMR Spectroscopy of Polymer Electrolytes for Lithium Batteries. *Curr. Opin. Colloid Interface Sci.* **2013,** *18,* 228-244.

161. Dai, Y.; Wang, Y.; Greenbaum, S. G.; Bajue, S. A.; Golodnitsky, D.; Ardel, G.; Strauss, E.; Peled, E. Electrical, Thermal, and NMR Investigation of Composite Solid Electrolytes Based on PEO, LiI and High Surface Area Inorganic Oxides. *Electrochim. Acta* **1998,** *43* (10-11), 1557-1561.

162. Golodnitsky, D.; Livshits, E.; Kovarsky, R.; Peled, E.; Shung, S. H.; Suarez, S.; Greenbaum, S. G. New Generation of Ordered Polymer Electrolytes for Lithium Batteries. *Electrochem. Solid-State Lett.* **2004,** *7* (11), A412-A415.

163. Trease, N. M.; Köster, T. K.-J.; Grey, C. P. In Situ NMR Studies of Lithium Ion Batteries. *Electrochem. Soc. Interface* **2011,** *20* (3), 69-73.

164. Timachova, K.; Villaluenga, I.; Cirrincione, L.; Gobet, M.; Bhattacharya, R.; Jiang, X.; Newman, J.; Madsen, L. A.; Greenbaum, S. G.; Balsara, N. P. Anisotropic Ion Diffusion and Electrochemically Driven Transport in Nanostrucured Block Copolymer Electrolytes. *J. Phys. Chem. B* **2018,** *122* (4), 1537-1544.

165. Günther, H. Selected Topics from Recent NMR Studies of Organolithium Compounds. *J. Braz. Chem. Soc.* **1999,** *10* (4), 241-262.

166. Fernández, L.; Oña-Burgos, P.; Armbruster, F.; Krummenacher, L.; Breher, F. $^{7}$Li,$^{15}$N Heteronuclear Multiple Quantum Shift Correlation--a Fast and Reliable 2D NMR Method on Natural Abundant Nuclei. *Chem. Commun.* **2009,** *18,* 2586-2588.

167. Pawlicka, A.; Donoso, J. P.; Abbrent, S.; Greenbaum, S. In *Polymer Electrolytes: Fundamentals and Applications;* Sequeria, C., Santos, D., Eds.; Woodhead: Cambridge, 2010; pp 112-118 and 278-313.

168. Rokhlenko, Y.; Gopinadhan, M.; Osuji, C. O.; Zhang, K.; O'Hern, C. S.; Larson, S. R.; Gopalan, P.; Majewski, P. W.; Yager, K. G. Magnetic Alignment of Block Copolymer Microdomains by Intrinsic Chain Anisotropy. *Phys. Rev. Lett.* **2015,** *115,* 258302.

169. Prosser, R. S.; Evanics, F.; Kitevski, J. L.; Al-Abdul-Wahid, M. S. Current Applications of Bicelles in NMR Studies of Membrane-Associated Amphiphiles and Proteins. *Biochemistry* **2006,** *45* (28), 8453-8465.

170. Deloche, B.; Samulski, E. T. Short-Range Nematic-like Orientational Order in Strained Elastomers: A Deuterium Magnetic Resonance Study. *Macromolecules* **1981,** *14* (3), 575-581.

171. Hou, J.; Li, J.; Madsen, J. A. Anisotropy and Transport in Poly(arylene ether sulfone) Hydrophilic-Hydrophobic Block Copolymers. *Macromolecules* **2010,** *43* (1), 347-353.

172. Bates, F. S.; Rosedale, J. H.; Fredrickson, G. H.; Glinka, C. J. Fluctuation-Induced First-Order Transition of an Isotropic System to a Periodic State. *Phys. Rev. Lett.* **1988,** *61* (19), 2229-2232.

173. Nakamura, I.; Balsara, N. P.; Wang, Z. G. First-Order Disordered-to-Lamellar Phase Transition in Lithium Salt-Doped Block Copolymers. *ACS Macro Lett.* **2013,** *2* (6), 478-481.

174. Thelen, J. L.; Teran, A. A.; Wang, X.; Garetz, B. A.; Nakamura, I.; Wang, Z. G.; Balsara, N. P. Phase Behavior of a Block Copolymer/Salt Mixture through the Order-to-Disorder Transition. *Macromolecules* **2014,** *47* (8), 2666-2673.

175. Loo, Y.; Register, R. A.; Ryan, A. J. Modes of Crystallization in Block Copolymer Microdomains: Breakout, Templated, and Confined. *Macromolecules* **2002,** *35* (6), 2365-2374.

176. Ho, R. M.; Lin, F. H.; Tsai, C. C.; Lin, C. C.; Ko, B. T.; Hsiao, B. S.; Sics, I. Crystallization-Induced Undulated Morphology in Polystyrene-b-Poly(L-lactide) Block Copolymer. *Macromolecules* **2004,** *37* (16), 5985-5994.

177. Wang, Y.; Gao, J.; Dingemans, T. J.; Madsen, L. A. Molecular Alignment and Ion Transport in Rigid Rod Polyelectrolyte solutions. *Macromolecules* **2014,** *47* (9), 2984-2992.

178. Loo, W. S.; Jiang, X.; Maslyn, J. A.; Oh, H. J.; Zhu, C.; Downing, K. H.; Balsara, N. P. Reentrant Phase Behavior and Coexistence in Asymmetric Block Copolymer Electrolytes. *Soft Matter* **2018,** *14,* 2789-2795.

179. Tu, Z.; Nath, P.; Lu, Y.; Tikekar, M. D.; Archer, L. A. Nanostructured Electrolytes for Stable Lithium Electrodeposition in Secondary Batteries. *Acc. Chem. Res.* **2015,** *48,* 2947-2956.

180. Isikli, S.; Ryan, K. M. Recent Advances in Solid-State Polymer Electrolytes and Innovative Ionic Liquids Based Polymer Electrolyte Systems. *Curr. Opin. Electrochem.* **2020,** *21,* 188-191.

181. Doyle, M.; Fuller, T. F.; Newman, J. The Importance of the Lithium Ion Transference Number in Lithium/Polymer Cells. *Electrochim. Acta* **1994,** *39,* 2073-2081.

182. Liu, J.; Monroe, C. W. Solute-Volume Effects in Electrolyte Transport. *Electrochim. Acta* **2014,** *135,* 447-460.

183. Nyman, A.; Behm, M.; Lindbergh, G. Electrochemical Characterisation and Modelling of the Mass Transport Phenomena in $LiPF_6$-EC-EMC Electrolyte. *Electrochim. Acta* **2008,** *53,* 6356-6365.

184. Mullin, S. A.; Stone, G. M.; Teran, A. A.; Hallinan, D. T.; Hexemer, A.; Balsara, N. P. Current-Induced Formation of Gradient Crystals in Block Copolymer Electrolytes. *Nano Lett.* **2012,** *12,* 464-468.

185. Möhl, G. E.; Metwalli, E.; Müller-Buschbaum, P. In Operando Small-Angle X-Ray Scattering Investigation of Nanostructured Polymer Electrolyte for Lithium-Ion Batteries. *ACS Energy Lett.* **2018,** *3,* 1525-1530.

186. Galluzzo, M. D.; Loo, W. S.; Schaible, E.; Zhu, C.; Balsara, N. P. Dynamic Structure and Phase Behavior of a Block Copolymer Electrolyte under Dc Polarization. *ACS Appl. Mater. Interfaces* **2020,** *12,* 57421-57430.

187. Sharon, D.; Bennington, P.; Webb, M. A.; Deng, C.; De Pablo, J. J.; Patel, S. N.; Nealey, P. F. Molecular Level Differences in Ionic Solvation and Transport Behavior in Ethylene Oxide-Based Homopolymer and Block Copolymer Electrolytes. *J. Am. Chem. Soc.* **2021,** *143,* 3180-3190.

188. Shen, K.-H.; Brown, J. R.; Hall, L. M. Diffusion in Lamellae, Cylinders, and Double Gyroid Block Copolymer Nanostructures. *ACS Macro Lett.* **2018,** *7,* 1092-1098.

189. Zhang, Z.; Krajniak, J.; Ganesan, V. A Multiscale Simulation Study of Influence of Morphology on Ion Transport in Block Copolymeric Ionic Liquids. *Macromolecules* **2021,** *54,* 4997-5010.

190. Delhorbe, V.; Bresser, D.; Mendhil-Jakani, H.; Rannou, P.; Bernard, L.; Gutel, T.; Lyonnard, S.; Picard, L. Unveiling the Ion Conduction Mechanism in Imidazolium-Based Poly(Ionic Liquids): A Comprehensive Investigation of the Structure-to-Transport Interplay. *Macromolecules* **2017,** *50,* 4309-4321.

191. Sethuraman, V.; Mogurampelly, S.; Ganesan, V. Multiscale Simulations of Lamellar PS-PEO Block Copolymers Doped with $LiPF_6$ Ions. *Macromolecules* **2017,** *50,* 4542-4554.

192. Young, W. S.; Epps, T. H. Ionic Conductivities of Block Copolymer Electrolytes with Various Conducting Pathways: Sample Preparation and Processing Considerations. *Macromolecules* **2012,** *45,* 4689-4697.

193. Irwin, M. T.; Hickey, R. J.; Xie, S.; So, S.; Bates, F. S.; Lodge, T. P. Structure-Conductivity Relationships in Ordered and Disordered Salt-Doped Diblock Copolymer/Homopolymer Blends. *Macromolecules* **2016,** *49,* 6928-6939.

194. Kambe, Y.; Arges, C. G.; Czaplewski, D. A.; Dolejski, M.; Krishnan, S.; Stoykovich, M. P.; De Pablo, J. J.; Nealey, P. F. Role of Defects in Ion Transport in Block Copolymer Electrolytes. *Nano Lett.* **2019,** *19,* 4684-4691.

195. Chu, K. T.; Bazant, M. Z. Electrochemical Thin Films at and above the Classical Limiting Current. *J. Appl. Math.* **2005,** *65,* 1485-1505.

196. Gilbert, J. B.; Lui, M.; Shelton, C. K.; Rubner, M. F.; Cohen, R. E.; Epps, T. H. Determination of Lithium-Ion Distributions in Nanostructured Block Polymer Electrolyte Thin Films by X-Ray Photoelectron Spectroscopy Depth Profiling. *ACS Nano* **2015,** *9,* 512-520.

197. Gartner, T. E.; Morris, M. A.; Shelton, C. K.; Dura, J. A.; Epps, T. H. Quantifying Lithium Salt and Polymer Density Distributions in Nanostructured Ion-Conducting Block Polymers. *Macromolecules* **2018,** *51,* 1917-1926.

198. Wang, A. W.; Gunnardottir, A. B.; Fowdon, J.; Pasta, M.; Grey, C. P.; Monroe, C. W. Potentiometric MRI of a Superconcentrated Lithium Electrolyte: Testing the Irreversible Thermodynamics Approach. *ACS Energy Lett.* **2021,** *6,* 3086-3095.

199. Wang, H.; Newstein, M. C.; Krishnan, A.; Balsara, N. P.; Garetz, B. A.; Hammouda, B.; Krishnamoorti, R. Ordering Kinetics and Alignment of Block Copolymer Lamellae under Shear Flow. *Macromolecules* **1999,** *32,* 3695-3711.

200. Samuels, R. J. *Structured Polymer Properties;* Wiley, 1974.

201. Wilkes, G. L. *Encyclopedia of Polymer Science and Engineering,* 2nd ed.; Wiley: New York, 1988; Vol. 14.

202. White, J. L. *Encyclopedia of Polymer Science and Engineering,* 2nd ed.; Wiley: New York, 1988; Vol. 10.

203. Sax, J.; Ottino, J. M. Modeling of Transport of Small Molecules in Polymer Blends: Application of Effective Medium Theory. *Polymer. Eng. Sci.* **1983,** *23,* 165-176.

204. Takeda, Y.; Yamamoto, O.; Imanishi, N. Lithium Dendrite Formation on a Lithium Metal Anode from Liquid, Polymer and Solid Electrolytes. *Electrochemistry* **2016,** *4,* 210-218.

205. Aurbach, D.; Zinigrad, E.; Cohen, Y.; Teller, H. A Short Review of Failure Mechanisms of Lithium Metal and Lithiated Graphite Anodes in Liquid Electrolyte Solutions. *Solid State Ionics* **2002,** *148,* 405-416.

206. Cochran, E. W.; Garcia-Cervera, C. J.; Fredrickson, G. H. Stability of the Gyroid Phase in Diblock Copolymers at Strong Segregation. *Macromolecules* **2006,** *39* (7), 2449-2451.

207. Arora, A.; Qin, J.; Morse, D. C.; Delaney, K. T.; Fredrickson, G. H.; Bates, F. S.; Dorfman, K. D. Broadly Accessible Self-Consistent Field Theory for Block Polymer Materials Discovery. *Macromolecules* **2016,** *49* (13), 4675-4690.

208. Brown, J. R.; Seo, Y.; Hall, L. M. Ion Correlation Effects in Salt-Doped Block Copolymers. *Phys. Rev. Lett.* **2018,** *120* (12), 127801.

209. Qin, J.; de Pablo, J. J. Ordering Transition in Salt-Doped Diblock Copolymers. *Macromolecules* **2016,** *49* (9), 3630-3638.

210. Irwin, M. T.; Hickey, R. J.; Xie, S.; So, S.; Bates, F. S.; Lodge, T. P. Structure-Conductivity Relationships in Ordered and Disordered Salt-Doped Diblock Copolymer/Homopolymer Blends. *Macromolecules* **2016,** *49* (18), 6928-6939.

211. Cho, B. K.; Jain, A.; Gruner, S. M.; Wiesner, U. Mesophase Structure-Mechanical and Ionic Transport Correlations in Extended Amphiphilic Dendrons. *Science* **2004,** *305* (5690), 1598-1601.

212. Shen, K.-H.; Brown, J. R.; Hall, L. M. Diffusion in Lamellae, Cylinders, and Double Gyroid Block Copolymer Nanostructures. *ACS Macro Lett.* **2018,** *7* (9), 1092-1098.

213. Kim, O.; Kim, S. Y.; Lee, J.; Park, M. J. Building Less Tortuous Ion-Conduction Pathways Using Block Copolymer Electrolytes with a Well-Defined Cubic Symmetry. *Chem. Mater.* **2016,** *28* (1), 318-325.

214. Kong, X.; Rudnicki, P. E.; Choudhury, S.; Bao, Z.; Qin, J. Dendrite Suppression by a Polymer Coating: A Coarse-Grained Molecular Study. *Adv. Funct. Mater.* **2020,** *30,* 1910138.

215. Wang, A. A.; Gunnarsdottir, A. B.; Fawdon, J.; Pasta, M.; Grey, C. P.; Monroe, C. W. Potentiometric MRI of a Superconcentrated Lithium Electrolyte: Testing the Irreversible Thermodynamics Approach. *ACS Energy Lett.* **2021,** *6* (9), 3086-3095.

216. Galluzzo, M. D.; Grundy, L. S.; Takacs, C. J.; Cao, C.; Steinrück, H.-G.; Fu, S.; Rivas Valdez, M. A.; Toney, M. F.; Balsara, N. P. Orientation-Dependent Distortion of Lamellae in a Block Copolymer Electrolyte under DC Polarization. *Macromolecules* **2021,** *54,* 7808-7821.

217. Hou, T.; Monroe, C. W. Composition-dependent thermodynamic and mass-transport characterization of lithium hexafluorophosphate in propylene carbonate. *Electrochim. Acta* **2020,** *332,* 135085.

218. Sethi, G. K.; Frenck, L.; Sawhney, S.; Chakraborty, S.; Villaluenga, I.; Balsara, N. P. Effect of microphase separation on the limiting current density in hybrid organic-inorganic copolymer electrolytes. *Solid State Ionics* **2011,** *368* (1), 115702.

219. Chen, T.-L.; Lathrop, P. M.; Sun, R.; Elabd, Y. A. Lithium-Ion Transport in Poly(ionic liquid) Diblock Copolymer Electrolytes: Impact of Salt Concentration and Cation and Anion Chemistry. *Macromolecules* **2021,** *54,* 8780-8797.

220. Thompson, A.; Linday, I.; Attwood, D.; Liu, Y.; Gullikson, E.; Pianetta, P.; Howells, M.; Robinson, A.; Kim, K.-J.; Scofield, J.; Kirz, J.; Underwood, J.; Kortright, J.; Williams, G.; Winick, H. *X-ray Data Booklet;* Center for X-Ray Optics and Advanced Light Source: Berkeley, CA, 2009.

221. Berger, M. J.; Hubbell, J. H.; Seltzer, S. M.; Chang, J.; Coursey, J. S.; Sukumar, R.; Zucker, D. S.; Olsen, K. XCOM: photon cross section database. http://www.nist.gov/pml/data/xcom/index.cfm (accessed June 17, 2022).

222. Brunetti, A.; Sanchez del Rio, M.; Golosio, B.; Simionovici, A.; Somogyi, A. A library for X-ray–matter interaction cross sections for X-ray fluorescence applications. *Spectrochim. Acta, Part B* **2004,** *59* (10-11), 1725-1731.

223. Schoonjans, T.; Brunetti, A.; Golosio, B.; Sanchez del Rio, M.; Sole, V. A.; Ferrero, C.; Vincze, L. The xraylib library for X-ray–matter interactions. Recent developments. *Spectrochim. Acta, Part B* **2011,** *66* (11-12), 776-784.

224. Mullin, S. A.; Teran, A. A.; Yuan, R.; Balsara, N. P. Effect of Thermal History on the Ionic Conductivity of Block Copolymer Electrolytes. *J. Polym. Sci., Part B: Polym. Phys.* **2013,** *51,* 927-934.

225. Georen, P.; Adebahr, J.; Jacobsson, P.; Lindbergh, G. Concentration Polarization of a Polymer Electrolyte. *J. Electrochem. Soc.* **2002,** *149* (8), A1015.

226. Galluzzo, M. D.; Loo, W. S.; Schaible, E.; Zhu, C.; Balsara, N. P. Dynamic Structure and Phase Behavior of a Block Copolymer Electrolyte under dc Polarization. *ACS Appl. Mater. Interfaces* **2020,** *12,* 57421-57430.

227. Sota, N.; Hashimoto, T. Process and kinetics of order–order transition from bcc-sphere to hex-cylinder in polystyrene-block-polyisoprene-block-polystyrene: Time-resolved SAXS and TEM studies. *Polymer* **2005,** *46,* 10392-10404.

228. Hoffman, Z. J.; Shah, D. B.; Balsara, N. P. Temperature and concentration dependence of the ionic transport properties of poly(ethylene oxide) electrolytes. *Solid State Ionics* **2021,** *370,* 115751.

229. Berger, M. J.; Hubbell, J. H.; Seltzer, S. M.; Chang, J.; Coursey, J. S.; Sukumar, R.; Zucker, D. S.; Olsen, K. XCOM: photon cross section database. http://www.nist.gov/pml/data/xcom/index.cfm.

230. Grundy, L. S.; Shah, D. B.; Nguyen, H. Q.; Diederichsen, K. M.; Celik, H.; DeSimone, J. M.; McCloskey, B. D.; Balsara, N. P. Impact of Frictional Interactions on Conductivity, Diffusion, and Transference Number in Ether- and Perfluoroether-Based Electrolytes. *J. Electrochem. Soc.* **2020,** *167,* 120540.

231. Grundy, L. S.; Sethi, G. K.; Galluzzo, M. D.; Loo, W. S.; Maslyn, J. A.; Teran, A. A.; Thelen, J. L.; Timachova, K.; Reimer, J. A.; Madsen, L. A.; Balsara, N. P. Detection of the Order-to-Disorder Transition in Block Copolymer Electrolytes Using Quadrupolar $^{7}$Li NMR Splitting. *ACS Macro. Lett.* **2019,** *8,* 107-112.

232. Grundy, L. S.; Galluzzo, M. D.; Loo, W. S.; Fong, A. Y.; Balsara, N. P.; Takacs, C. P. Inaccessible Polarization-Induced Phase Transitions in a Block Copolymer Electrolyte: An Unconventional Mechanism for the Limiting Current. *Macromolecules* **2022,** *in press*.

# Index

# Appendix A5: Supplemental Information from Chapter 5

Table A5.1 shows the directly-measured electrochemical properties, $\kappa$, $\rho_+$, $D$, and $\frac{\mathrm{d}\,U}{\mathrm{d}\ln m}$, and calculated electrochemical properties, $1+\frac{\mathrm{d}\ln\gamma_\pm}{\mathrm{d}\ln m}$ and $t_+^0$.

Table A5.1. Electrochemical properties for electrolytes studied in Chapter 5

| | $x_{salt}$ | $\kappa$ x$10^5$ (S/cm) | $\rho_+$ | $D$ x$10^8$ (cm$^2$/s) | $\frac{\mathrm{d}\,U}{\mathrm{d}\ln m}$ (V) | $1+\frac{\mathrm{d}\ln\gamma_\pm}{\mathrm{d}\ln m}$ | $t_+^0$ |
|---|---|---|---|---|---|---|---|
| H4 | 0.04 | 90. | 0.75 | 110 | 0.011 | 0.32 | 0.36 |
| | 0.24 | 322 | 0.61 | 33 | 0.081 | 15 | 0.90 |
| | 0.46 | 193 | 0.22 | 18 | 0.15 | 6.1 | 0.49 |
| | 0.55 | 81 | 0.15 | 15 | 0.24 | 3.3 | -0.39 |
| F4 | 0.03 | 0.06 | 0.97 | 34 | 0.35 | 0.019 | -1.00 |
| | 0.13 | 3.3 | 0.89 | 17 | 0.44 | 0.15 | -0.75 |
| | 0.24 | 8.1 | 0.77 | 10 | 0.56 | 0.19 | -0.38 |
| | 0.33 | 9.9 | 0.71 | 7.8 | 0.94 | 0.42 | -0.07 |
| | 0.41 | 9.6 | 0.67 | 6.1 | 1.50 | 0.85 | -0.23 |
| | 0.48 | 6.7 | 0.67 | 5.4 | 2.29 | 1.1 | -1.00 |

Table A5.2 shows the measured viscosity values.

Table A5.2. Viscosity measurements for electrolytes studied in Chapter 5

| | $x_{salt}$ | $\eta$ (Pas) |
|---|---|---|
| H4 | 0.04 | 0.004 |
| | 0.07 | 0.005 |
| | 0.14 | 0.006 |
| | 0.24 | 0.014 |
| | 0.32 | 0.025 |
| | 0.39 | 0.043 |
| | 0.49 | 0.081 |
| F4 | 0.00 | 0.014 |
| | 0.03 | 0.017 |
| | 0.13 | 0.036 |
| | 0.24 | 0.098 |
| | 0.33 | 0.231 |
| | 0.41 | 0.458 |
| | 0.48 | 1.340 |

Appendix A5: Supplemental Information from Chapter 5

Figure A5.1 shows the *T1* relaxation constants measured by inversion recovery in H4 (a) and F4 (b). In F4, $^{19}$F *T1* constants are reported for both the polymeric solvent and for the $FSI^-$ anion.

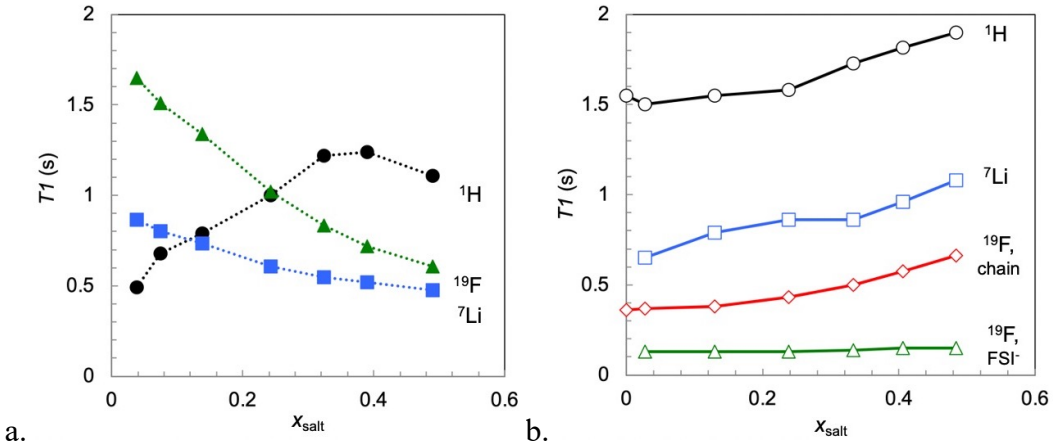


Figure A5.1. *T1* relaxation constants for H4 (a) and F4 (b) as a function of salt concentration. Proton data are black circles, lithium data are blue squares, and fluorine anion data are green triangles. In F4, the fluorine chain *T1* times were also measured, and are shown with red diamonds.

Figure A5.2 shows an example Stejskal-Tanner plot for Li self-diffusion from PFG-NMR for H4 at $x_{salt} = 0.04$. We plot the natural logarithm of the signal attenuation, $E$, *vs.* all contents of the exponential of Equation 5.9 except $D_{self,+}$. The magnitude of the slope of the fit line is $D_{self,+}$, which in this case is 1.53x10$^{-6}$ cm$^2$/s.

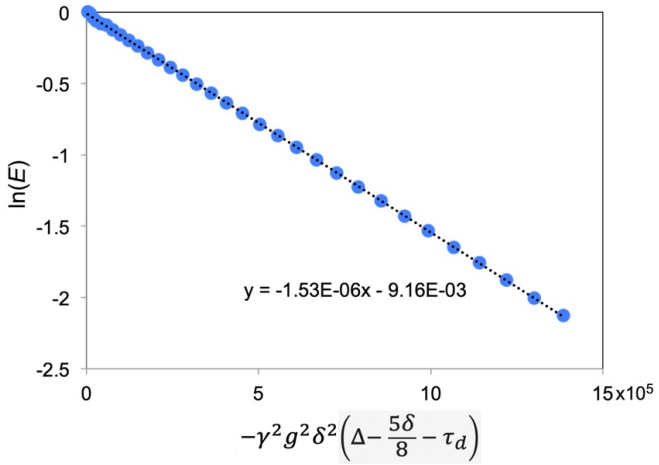


Figure A5.2. Example Stejskal-Tanner plot for $D_{self,+}$ of H4 at $x_{salt} = 0.04$. Blue circles are the measured data points as $g$ is varied, and the dotted line is the fit used to determine $D_{self,+}$.

# Appendix A6: Supplemental Information from Chapter 6

## A6.1 Full Electrochemical Characterization of PEO 275k / LiTFSI Above $r = 0.30$

Tables A6.1-A6.4 contain the electrochemical characterization data shown in Figure 6.2, so that this data may be readily used in future studies. Table A6.4 also contains data from concentration cells at higher temperatures. These experiments were performed because in Figure 6.2d, we observed a plateau in potential above $r = 0.32$, which we propose is due to phase separation. If the temperature is increased, it is possible that the phases might mix, thus removing the plateau and causing the potential to decrease with $r$. Below $r = 0.30$, the potential does not depend on temperature.[228] Above $r = 0.30$, we find that the potential still plateaus at 120 °C, but at a slightly lower potential (-314 *versus* -290 mV) perhaps indicating that the two-phase region begins at a higher salt concentration. At 140 °C, the plateau seems to disappear. However, these experiments could not be repeated safely; lithium metal is safe at this temperature, as is the electrolyte, but our pouch material becomes brittle. This could be an interesting route for future work, but a new sealing mechanism would need to be developed.

Table A6.1. Ionic conductivity data shown in Figure 6.2a

| $r$ | $\kappa$ (S/cm) | error |
|---|---|---|
| 0.20 | 6.95E-04 | 8.15E-05 |
| 0.24 | 6.32E-04 | 7.23E-05 |
| 0.30 | 2.83E-04 | 1.14E-04 |
| 0.34 | 2.85E-04 | 1.08E-05 |
| 0.38 | 2.22E-04 | 9.43E-06 |
| 0.40 | 1.24E-04 | 8.66E-05 |
| 0.45 | 1.44E-04 | 9.31E-05 |
| 0.50 | 1.06E-04 | 3.97E-06 |

Table A6.2. Current fraction data shown in Figure 6.2b

| $r$ | $\rho_+$ | error |
|---|---|---|
| 0.30 | 0.239 | 0.010 |
| 0.34 | 0.289 | 0.020 |
| 0.38 | 0.346 | 0.032 |
| 0.40 | 0.356 | 0.006 |
| 0.45 | 0.452 | 0.108 |
| 0.50 | 0.618 | 0.022 |

Table A6.3 Salt diffusion coefficient data shown in Figure 6.2c

| $r$ | $D$ (cm$^2$/s) | error |
|---|---|---|
| 0.30 | 3.20E-08 | 7.93E-09 |
| 0.34 | 3.82E-08 | 5.04E-09 |
| 0.38 | 2.97E-08 | 7.26E-09 |
| 0.40 | 2.96E-08 | 1.04E-09 |
| 0.45 | 1.15E-08 | 7.26E-09 |
| 0.50 | 1.09E-08 | 1.14E-09 |

Table A6.4 Concentration cell data high-$r$ PEO 275k / LiTFSI electrolytes

| $r$ | $U$ (mV) (90 °C) | U (mV) (120 °C) | U (mV) (140 °C) |
|---|---|---|---|
| 0.34 | -290 | | |
| 0.38 | -298 | -307 | |
| 0.40 | | | -338 |
| 0.45 | -294.95 | | |
| 0.45 | -292.09 | | |
| 0.50 | -290 | -320 | -480 |
| 0.50 | -283.36 | | |

The data in Figure 6.2 can be used to calculate the transference number relative to the solvent velocity, $t_+^0$, according to Equation 4.8, and the thermodynamic factor, $T_f$, according to Equation 4.12. Figure A6.1 shows the results. However, recall the discussion in Chapter 6: concentrated solution theory applies only to homogeneous electrolytes at equilibrium, which may not be the case here due to phase separation. Therefore, the physical meaning of these results is unclear.

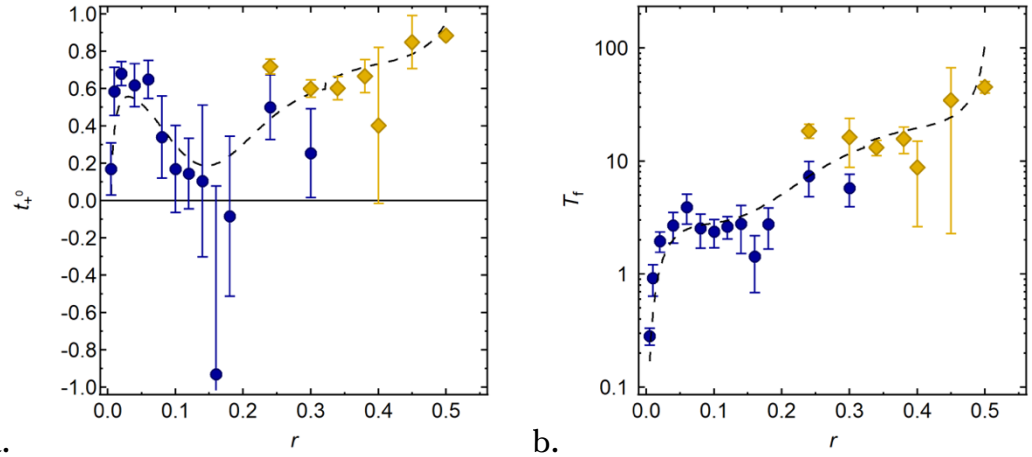


a. b.

Figure A6.1. (a) Calculated transference number, $t_+^0$, and (b) thermodynamic factor, $T_f$,

based on the measurements in Figure 6.2. $\frac{dU}{dln(m)}$ is set to its value at $r = 0.28$ for all salt concentrations in the two-phase region. Error bars are propagated error from the measurements in Figure 6.2 according to methods in Gao *et al.* [53] Dashed lines represent the combination of the fits given by Equations 6.8-6.12. Blue data points are reported in Pesko *et al.*, [116] while yellow data points are new in this study.

## A6.2 Microscopy Results

Figure 6.3 shows optical microscopy images at $r = 0.30$ and $r = 0.40$. Similar images were taken at a wider range of salt concentrations, and the results are shown in Figure A6.3. At $r = 0.30$ and below, the sample is fully amorphous. At $r = 0.40$ and above, there are amorphous ($r = 0.33$) and crystalline ($r = 0.50$) regions. The image at $r = 0.35$ is ambiguous: we do not observe clear evidence of crystallization, but we would expect the volume fraction of $r = 0.50$ regions to be very small. This image is therefore inconclusive.

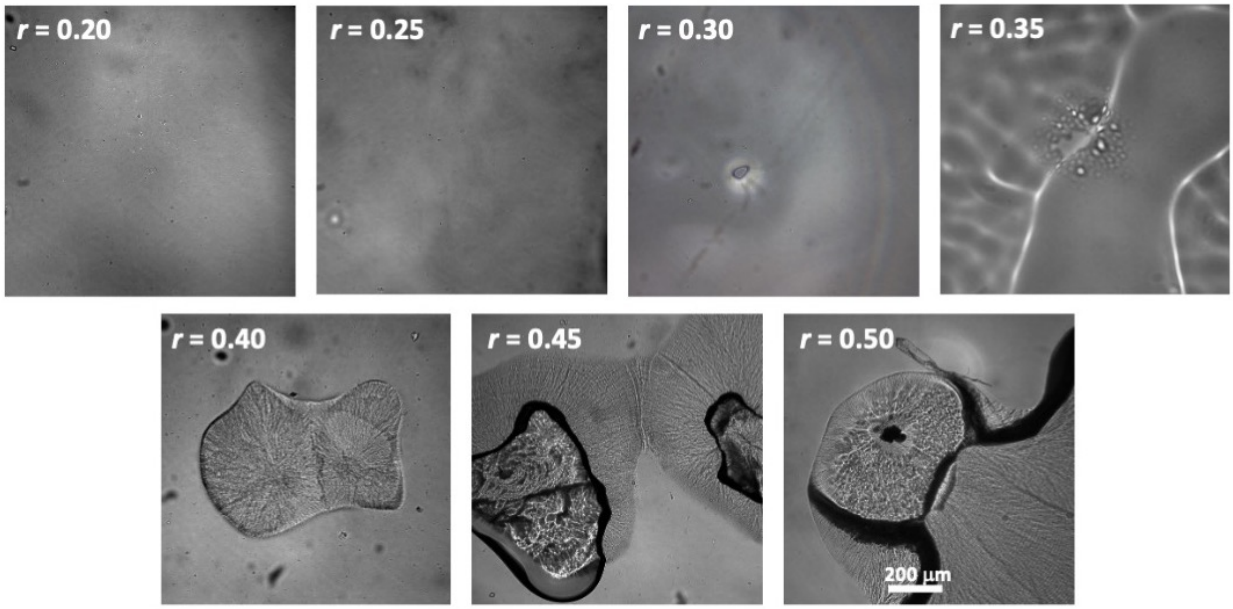


Figure A6.2. Optical microscopy images of PEO 275k / LiTFSI samples at $r = 0.20$, 0.25, 0.30, 0.35, 0.40, 0.45, and 0.50 taken at 90 °C. The sample preparation and experimental procedures are the same as those discussed in Chapter 6.

## A6.3 Dendrite Growth in Limiting Current Experiments

In Gribble *et al.*, [57] limiting current is reported in PEO / LiTFSI up to $r = 0.085$, while in Figure 6.4 we report limiting current beginning at $r = 0.50$ and decreasing down to $r = 0.40$. Both above $r = 0.085$ and below $r = 0.40$, these experiments fail due to the prevalence of lithium dendrite growth leading to cell short circuits. The data showing this is given in Figure A6.3. Figure A6.3a shows constant-current experiments in PEO 275k

/ LiTFSI for $r$ = 0.14, and Figure A6.3b shows constant-current experiments in PEO 275k / LiTFSI for $r$ = 0.35. In all cases, the potential neither plateaus nor diverges exponentially, but instead becomes jagged followed by a cell short-circuit, indicating dendrite growth.

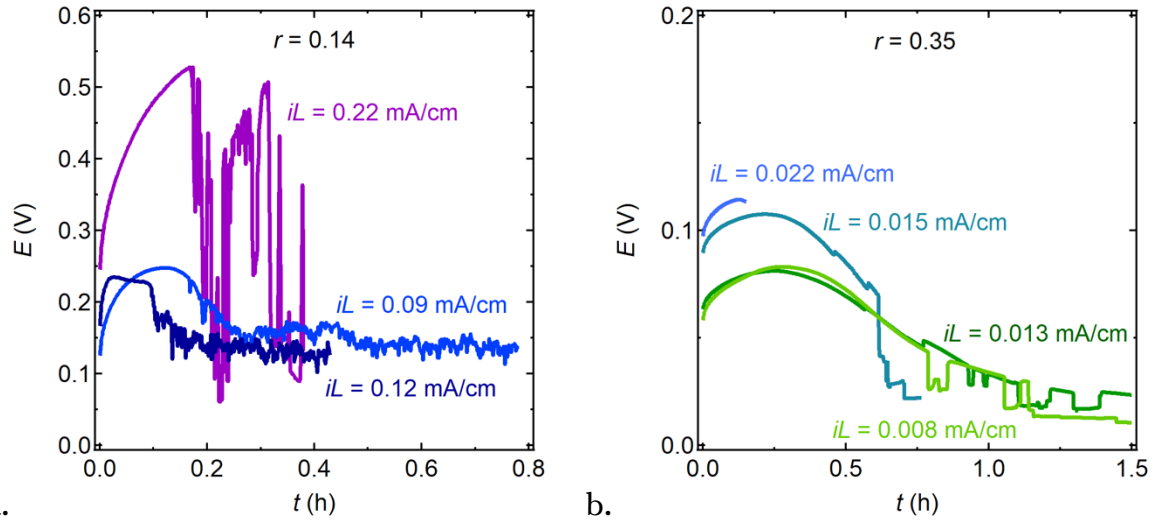


Figure A6.3. Cell potential responses to various applied current densities, $i$, normalized by cell thickness, $L$, in PEO / LiTFSI electrolytes with (a) $r$ = 0.14, (b) $r$ = 0.35.

## A6.4 WAXS Results in PEO / LiTFSI at High Salt Concentrations

In addition to the electrochemical, theoretical, and microscopy results presented in Chapter 6, we also performed wide-angle X-ray scattering (WAXS) experiments to characterize the phase behavior of our electrolytes. The WAXS results, taken at 90 °C on heating, are shown in Figure A6.4. At $r$ = 0.40 and below, no peaks are observed, which is a signature of an amorphous regime. At $r$ = 0.45 and 0.50, crystalline peaks are observed. No crystallization was observed on cooling, and when the same samples were analyzed using three weeks later, no peaks were observed. This suggests that the crystallization kinetics in this system are an important factor, making it difficult to compare results across techniques with different sample preparation requirements.

Appendix A6: Supplemental Information from Chapter 6

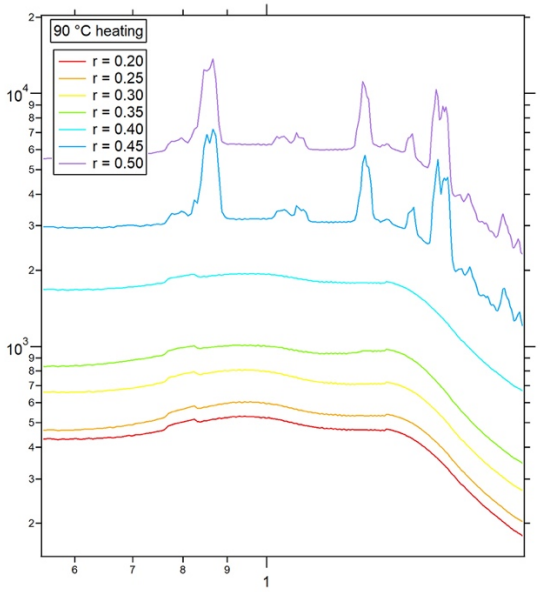


Figure A6.4. WAXS performed at beamline 7.3.3. at the Advanced Light Source at Lawrence Berkeley National Lab at 90 °C on heating.

# Appendix A7: Supplemental Information from Chapter 7

In Figures 7.5 and 7.6, we show time-dependent SAXS data during annealing, starting at $t = 0$, where $t = 0$ is the time at which the temperature is increased from 90 °C to 120 °C. We omitted data during the first 16 hours, during which the temperature was maintained at 90 °C. The full time series is shown in Figure A7.1: Figure A7.1a is analogous to Figure 7.5a, and Figures A7.1b and A7.1c are equivalent to Figures 7.6a and 7.6b. Note that in many samples in Figure A7.1b and A7.1c, the grain size, $L$, decreases during the first 90 °C annealing step. This runs counter to the assumption that annealing generally causes an increase in grain size. However, recall that $L$ is defined to be inversely proportional to the peak width (Equation 7.4); it is possible that there is another explanation for the peak broadening during this step which is not related to $L$.

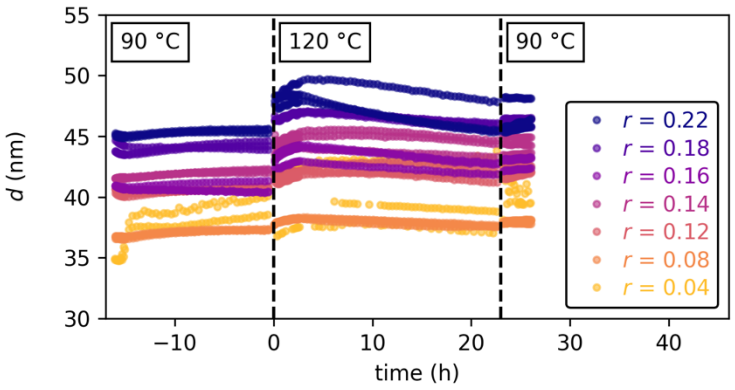


a.

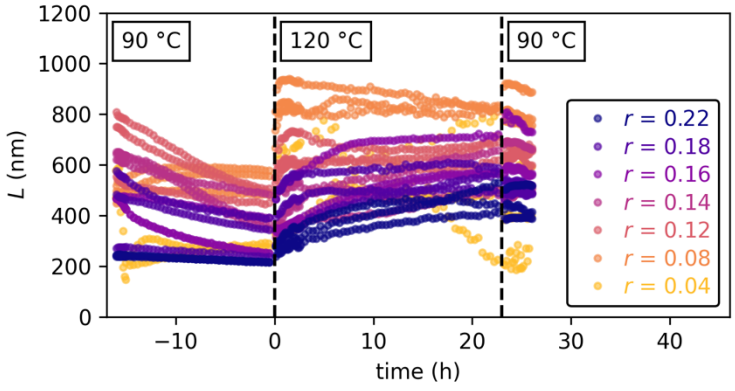


b.

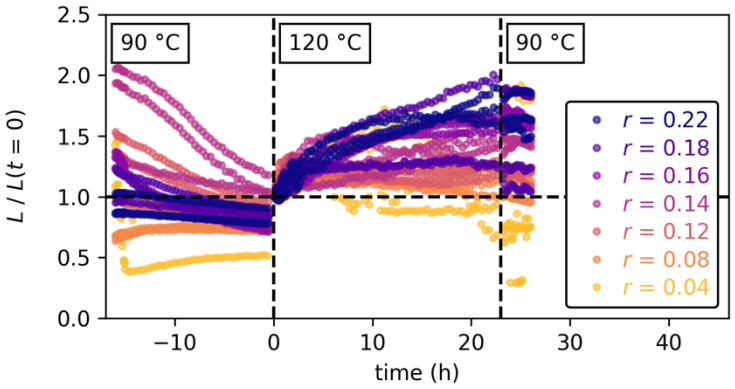


c.

Figure A7.1. (a) Domain size ($d$) as a function of time during annealing for different salt concentrations ($r$ = Li / EO) of SEO(19-20) / LiTFSI electrolytes. (b) Grain size, $L$, as a function of time during the annealing process, and (c) $L$ normalized by its value at the start of the 120 °C annealing step ($t$ = 0) for different salt concentrations. In all three panels, low salt concentrations are shown in yellow and orange, and high salt concentrations are shown in purple and blue. Data above $t$ = 0 are reproduced from Figures 7.5 and 7.6.

The general goal of this Chapter is to compare changes in ionic conductivity ($\kappa$) with changes in grain size ($L$). This comparison is done with a variety of methods of data presentation. One that was not included in the chapter is showing the changes in $L$ and $\kappa$ as a function of time on the same axes; this is presented in Figure A7.2. Note that the inverse of the full width at half-maximum (1/FWHM) is used in place of $L$, so these data differ from those above by a factor of $2\pi$ (Equation 7.4). The same data is presented more concisely in Figure 7.7.

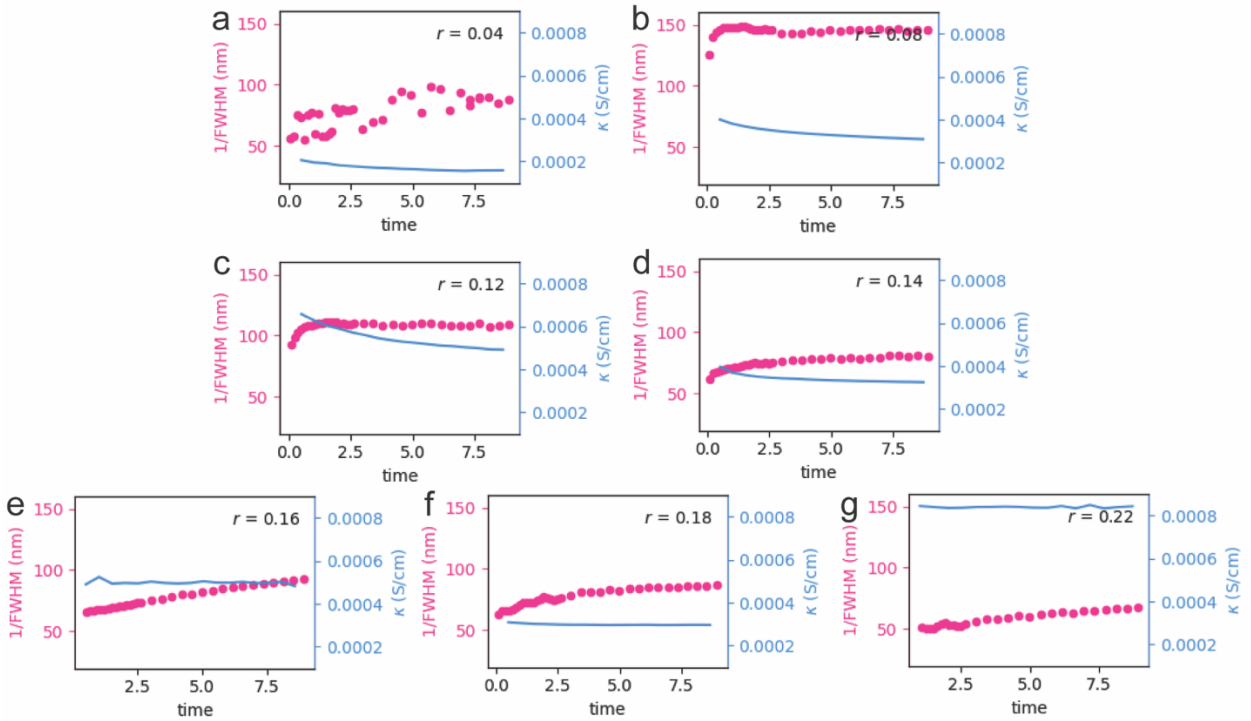


Figure A7.2. The inverse of the full width at half maximum of the primary SAXS scattering peak (pink) and the ionic conductivity ($\kappa$) as a function of time for SEO(19-20) electrolytes with $r$ = 0.04, 0.08, 0.12, 0.14, 0.16, 0.18, and 0.22.

# Appendix A9: Supplemental Information from Chapter 9

## A9.1 Supporting Discussion

### *A9.1.1 Data Fitting*

The scattering intensity as a function of the scattering vector, $I(q)$, data was fit using a Levenberg-Marquardt nonlinear least-squares algorithm. The 2D scattering profiles were reduced to 1D profiles using the pyFAI package as part of the Python programming language. Data was reduced to $I(q)$ based on either a 360° azimuthal average or by sector averages, as described in Chapter 9. In all cases, the fitting procedure was the same regardless of whether the $I(q)$ data represented a 360° azimuthal average or a 20° sector average. The $I(q)$ data was fit to the sum of a pseudo-Voigt function and a background function given by Equation A9.1 in the range $0.05 < q\ (\mathrm{nm}^{-1}) < 0.3$:

$$I(q) = I_{\mathrm{pV}}(q) + I_{\mathrm{bkg}}(q) \tag{A9.1}$$

$I_{\mathrm{pV}}(q)$ is a pseudo-Voigt function given by:

$$I_{\mathrm{pV}}(q) = A[\eta G(q) + (1-\eta)L(q)], \tag{A9.2}$$

where $A$ is the area under the curve, $\eta$ is the Gaussian fraction. $G(q)$ is the Gaussian component of the fit given by Equation A9.3 and $L(q)$ is the Lorentzian component of the fit given by Equation A9.4:

$$G(q) = \frac{2}{w}\left(\frac{\ln 2}{\pi}\right)^{0.5} \exp\left[\frac{-4\ln 2\,(q-q^*)^2}{w^2}\right] \tag{A9.3}$$

$$L(q) = \frac{\frac{w}{2\pi}}{(q-q^*)^2 + \left(\frac{w}{2}\right)^2} \tag{A9.4}$$

where $w$ is the peak width (*i.e.*, full width at half maximum) and $q^*$ is the position of the primary scattering peak. For fitting the background, we used:

$$I_{\mathrm{bkg}}(q) = y_{b0} + y_{b1} \exp\left[\frac{y_{b2}}{q}\right]. \tag{A9.5}$$

In Equation A9.1, the fitted parameters are: $\eta$, $w$, $q^*$, $y_{b0}$, $y_{b1}$, and $y_{b2}$. The value of $\eta$ lies between 0 and 1. The value of $q^*$ was used to calculate the domain spacing, $d$, by Equation 9.1.

*A9.1.2 Beam Center Correction*

The beam center position drifted slightly over the course of the experiment by about 40 $\mu$m in the vertical direction. The nominal beam center position was determined using a silver behenate sample. When calculating the $\chi$ dependence of the primary scattering peak position, $q^*$, we expect there should be symmetry in the peak position $q^*$ about 180° such that $q^*(\chi) = q^*(\chi + 180°)$. When analyzing the data with the nominal beam position, determined using a silver behenate sample at the beginning of the experiment, we found that this was not true for most scans. This showed that the beam center position drifted throughout the experiment as a function of time. To correct for this, we corrected the nominal beam center for each scan so that the values of $q^*$ were symmetric about 180°; these are the data presented in Figure 9.9a-c.

## A9.2 Supporting Figures

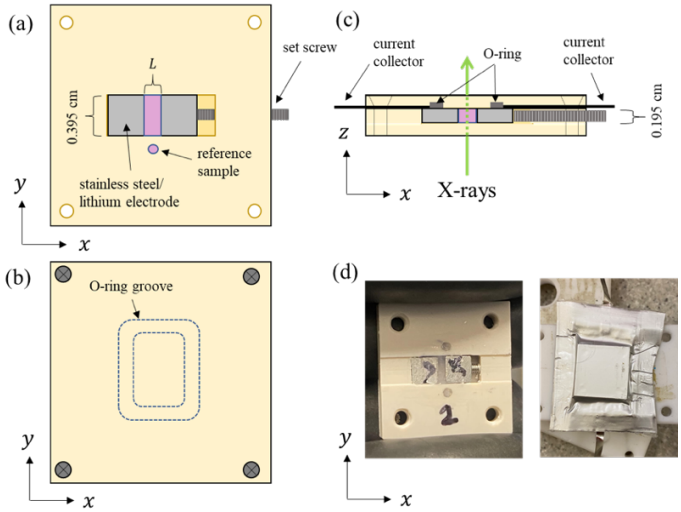


Figure A9.1. Schematic of the cell designed for simultaneous SAXS polarization experiments.

(a) Schematic representation of the bottom plate in the two-part PEEK sample holder. Two stainless steel blocks sit in a channel cut into the PEEK. The blocks have lithium metal pressed on the inside face to serve as electrodes. Polymer electrolyte (pink) is hot-pressed between the blocks, and a set screw is used to adjust the distance between the blocks and create an air free sample. The length of the polymer channel along the *y*-axis is 0.395 cm and the distance between electrodes (width of the polymer channel) was measured in Figure A9.4 for each sample. The thickness of the polymer channel is 0.195 cm (as shown in part c). The reference sample is isolated from the electrochemical channel and consist of a cylindrical channel cut into the PEEK, also with thickness of 0.195 cm. In this view, the X-rays would pass into the page along the *z*-axis. The holes near the four corners of the sample holder are tapped to allow the top plate to attach with tapered screws. (b) Top plate of the two-part PEEK sample holder. The top plate screws into the bottom plate and secures the tabs to the stainless-steel blocks which are used to make electrical connections. The dashed lines show the hidden O-ring groove which is cut into the side of the plate which contacts the bottom plate. A Viton O-ring is used to seal the cell around the polymer channel. (c) View of the cell in the *x*-*z* plane of a slice taken through the center of the cell. The dimensions of the lithium electrodes are 0.395 × 0.195 cm. Dashed lines indicate the location of the tapered screws. Current collectors (nickel foil) are secured to the stainless-steel blocks by a Viton O-ring which also serves to seal the area around the polymer channel. The green arrow indicates the direction which X-rays pass during the experiment. (d) Left panel: picture of the bottom plate (shown schematically in part a) loaded with polymer electrolyte in both the reference channel and

electrochemical channel. This cell had two reference channels but only one was used for measurements during the experiment. Right panel: picture of an assembled cell sealed in aluminum laminated pouch material. The nickel tabs protrude out of the pouch and connect to the potentiostat.

$$J_1 = \kappa\left(\frac{d\,U}{d\ln m}\right)\left[r\left(1-\frac{1}{\rho_+}\right)F\phi_c\right]^{-1} \qquad J_2 = -\left(\frac{d\,U}{d\ln m}\right)[r(1-\rho_+)F\phi_c]^{-1}$$

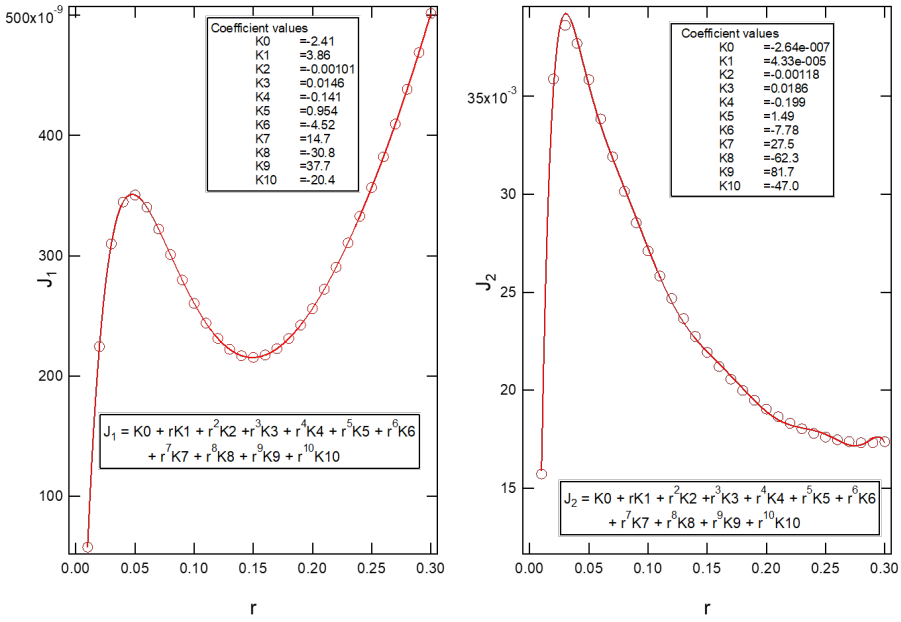


Figure A9.2. Integral parameters used for calculating salt concentration gradients and steady state potentials from concentrated solution theory using the methodology discussed in Chapter 9. (a) Calculated values for $J_1$ as a function of $r$ plotted with open circles. Equation 9.4 is reproduced above the plot. The red line is a fit to the data given by the 10th order polynomial and the fit equation and resulting coefficient values are provided. (b) Calculated values for $J_2$ as a function of $r$ plotted with open circles. Equation 9.6 is reproduced above the plot. The red line is a fit to the data given by the 10th order polynomial and the fit equation and resulting coefficient values are provided.

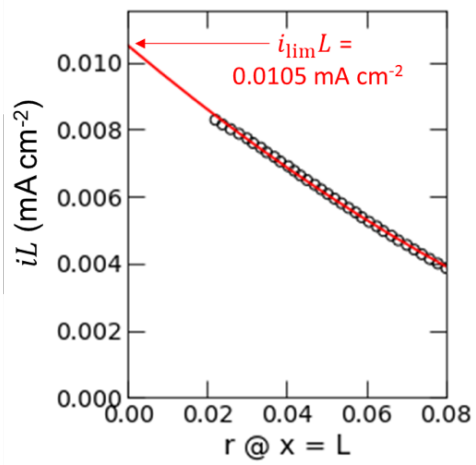


Figure A9.3. Example calculation of the limiting current based on an average salt concentration of $r = 0.16$. Salt concentration gradients are predicted for increasingly large currents until the salt concentration at $x/L = 1$ reaches the lower bound of the model. The bottom axis is the value of $r$ at $x/L = 1$ for the current density ($iL$) plotted on the left axis. The red curve is a polynomial fit and is extrapolated to $r = 0$ at $x/L = 1$. The current at the $y$-intercept is the limiting current. This calculation was repeated for each salt concentration in Figure 9.3c.

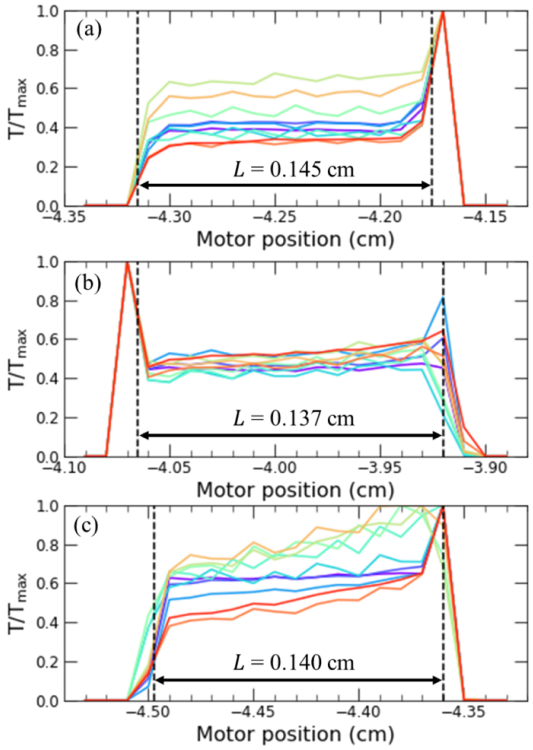


Figure A9.4. Transmission *vs.* motor position for cell (a), (b), and (c), which correspond to the cells in Figure 9.5a, 9.5b, and 9.5c, respectively. The transmission is given by the intensity recorded from the ion counter at the beam stop divided by the intensity from the ion counter upstream of the sample. We normalize the transmission by the maximum transmission for each data set. The color of each data set corresponds to the data in Figure 9.5.

Where $T/T_{\max} = 0$, the beam is centered over the stainless-steel electrode. Where $T/T_{\max} > 0$, the beam is passing through polymer and/or lithium metal. In some cases, there is a peak in the data when the beam is centered over the lithium metal (lithium metal has very low electron density and results in high transmission). In other cases, this peak is not observed which likely indicates that the beam was not directly centered over the lithium metal at any of the positions sampled. The dashed lines represent the motor position for $x/L = 0$ (left most dashed line) and $x/L = 1$ (right-most dashed line). The distance between electrodes, $L$, is calculated as the distance between the two dashed lines and is reported in the figure for each cell. The increase in $T/T_{\max}$ from left to right (to varying degrees in Figures a-c based on the magnitude of polarization) is due to the salt concentration gradient. LiTFSI has high electron density, so we expect lower $T/T_{\max}$ at the salt rich electrode.

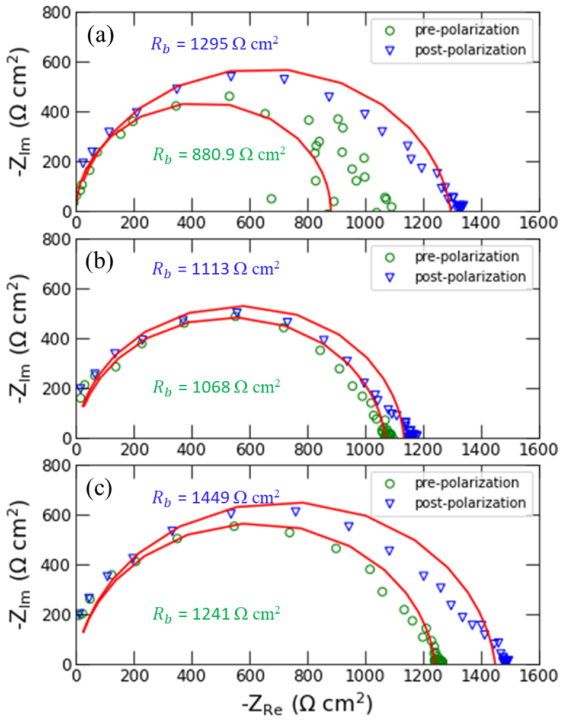


Figure A9.5. Nyquist plots obtained from ac impedance spectroscopy performed on cells (a), (b), and (c) which correspond to the data in Figure 9.5a, 9.5b, and 9.5c, respectively. Green circles represent data points obtained prior to polarization ($t < 0$ h). Blue triangles represent data points obtained after polarization and subsequent open circuit relaxation ($t > 80$ h). Red lines are fits to the data using a resistor and constant phase element in parallel as the equivalent circuit.

In all cases, we only observe one semi-circle. The fitted resistance is reported in the figure. Prior to polarization, the conductivity calculated from the resistance is 1.62 x $10^{-3}$ S cm-1 for cell (a), 1.48 x $10^{-3}$ S $cm^{-1}$ for cell (b), and 1.13 x 10-3 S $cm^{-1}$ for cell (c). These values are in good agreement with the conductivity measured from cells with blocking electrodes (Figure 9.2b). The conductivity of SEO(19-20)/LiTFSI as a function of $r$ is given by Equation 9.11: at $r = 0.16$, $\kappa = 1.48$ x $10^{-3}$ S $cm^{-1}$. Therefore, we can assume that the contribution of the interface to the total resistance of the cell is relatively small and explains why we cannot deconvolute it from the Nyquist plots. We thus assume that $\Delta V_{int} = 0$ for the cells designed for simultaneous polarization/SAXS experiments. The increase in resistance at the end of the experiment may be due to an increase in the interfacial resistance or due to the lingering presence of a salt concentration gradient (in general, the measured resistance decreases as the salt concentration gradient relaxes).

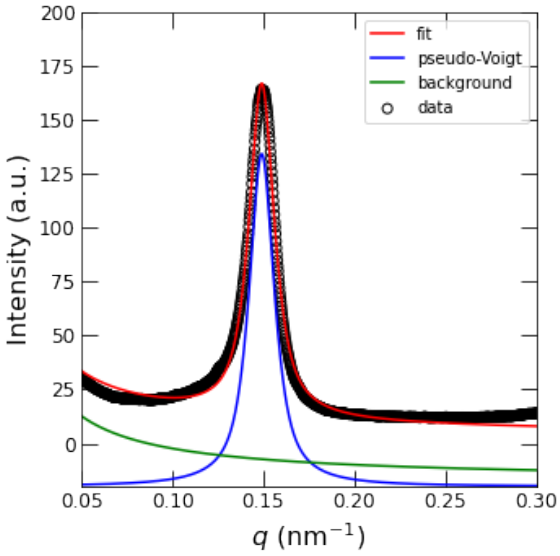


Figure A9.6. Example fit of one of the 1D SAXS profiles obtained from a 360° azimuthal average of the 2D SAXS profile. The data set corresponds to the cell polarized at 2.13 $\mu$A cm$^{-1}$ at t = 34.6 h and $x/L = 0.51$. The black open circles represent the raw data, and the red curve is the total fit given by Equation A9.1. The pseudo-Voigt fit is shown in blue (given by Equation A9.2) and the background (given by Equation A9.3) is shown in green and is offset by -20 a.u. for clarity.

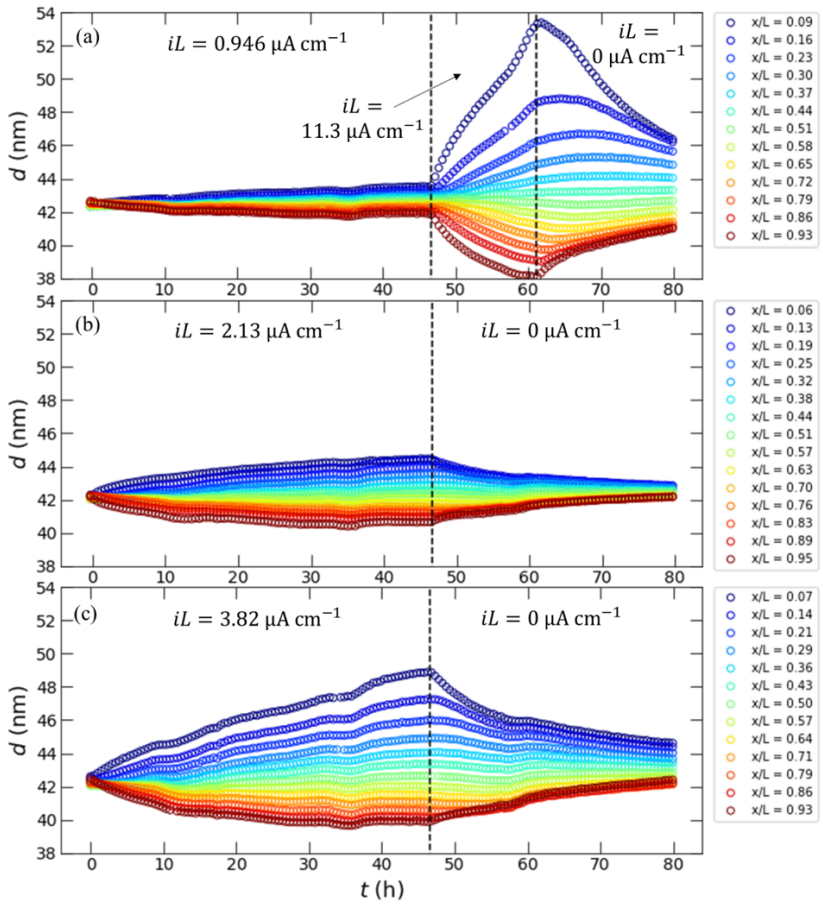


Figure A9.7. Domain spacing, $d$, as a function of time, $t$. The vertical dashed lines divide the plots into sections and indicate changes in the electrochemical conditions. The color of each data set corresponds to the position of the cell given in the legend on the right side of the plot. (a) Left section: $iL$ = 0.946 $\mu$A cm$^{-1}$, middle section: $iL$ = 11.3 $\mu$A cm$^{-1}$, right section $iL$ = 0 $\mu$A cm$^{-1}$ (*i.e.,* open circuit) (b) Left section: $iL$ = 2.13 $\mu$A cm$^{-1}$, right section: $iL$ = 0 $\mu$A cm$^{-1}$ (*i.e.,* open circuit) (c) Left section: $iL$ = 3.82 $\mu$A cm$^{-1}$, right section: $iL$ = 0 $\mu$A cm$^{-1}$ (*i.e.,* open circuit). The left section of each plot was reported as $d$ vs $x/L$ plots in Figure 9.5. The middle section of part (a) was the basis of Figure 9.7b.

The change in $d$ during open circuit was not discussed in Chapter 9. In general, $d$ converges towards the original $d$ at $t$ = 0. In all cases, there is still a spatial gradient in $d$ at $t$ = 80 h, which indicates that we do not reach equilibrium on the time scale of the experiment, but we would expect $d$ to eventually become independent of position at longer times.

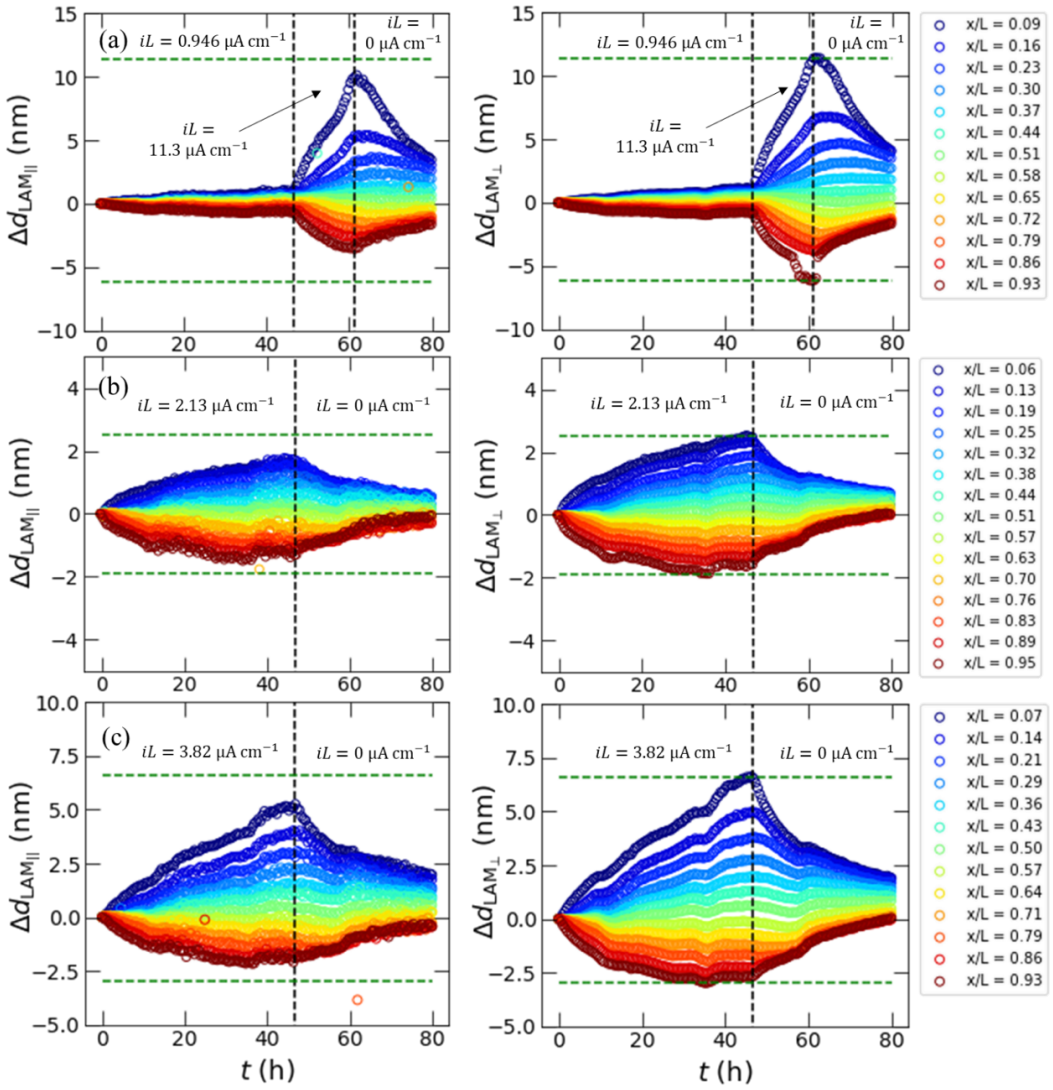


Figure A9.8. Change in domain spacing, $\Delta d$, for $LAM_{||}$ (left panels) and $LAM_{\perp}$ (right panels) as a function of time, $t$. $\Delta d$ is defined by Equation 9.16, where $\chi = 0$ and 180° correspond to $LAM_{||}$ and $\chi = 90$ and 270° correspond to $LAM_{\perp}$. The vertical dashed lines divide the plots into sections and indicate changes in the electrochemical conditions. The color of each data set corresponds to the position of the cell given in the legend on the right side of the plot. (a) Left section: $iL = 0.946$ $\mu$A cm$^{-1}$, middle section: $iL = 11.3$ $\mu$A cm$^{-1}$, right section $iL = 0$ $\mu$A cm$^{-1}$ (*i.e.,* open circuit) (b) Left section: $iL = 2.13$ $\mu$A cm$^{-1}$, right section: $iL = 0$ $\mu$A cm$^{-1}$ (*i.e.,* open circuit) (c) Left section: $iL = 3.82$ $\mu$A cm$^{-1}$, right section: $iL = 0$ $\mu$A cm$^{-1}$ (*i.e.,* open circuit). The green dashed lines represent the maximum and minimum $\Delta d_{LAM_{\perp}}$ based on the data in the right plots. We draw the green lines at the same value of $\Delta d$ on the left plot to highlight the point that $LAM_{\perp}$ are distorted more than $LAM_{||}$.

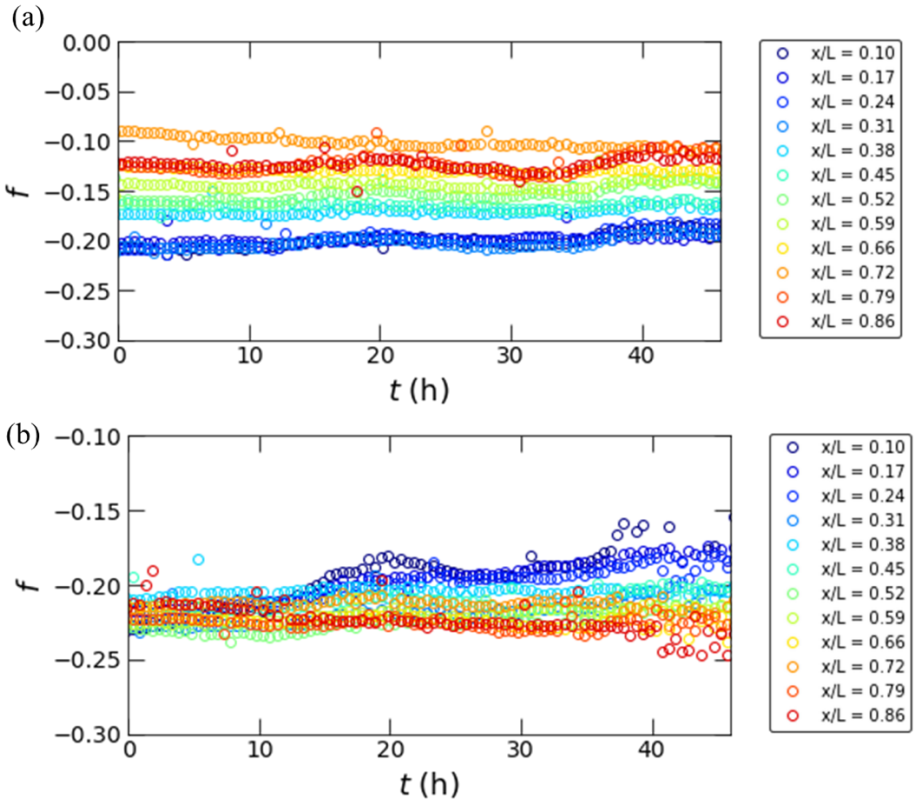


Figure A9.9. Orientation parameter, $f$, *vs.* time, $t$. $f$ is defined by Equations 9.14 and 9.15 for the cell polarized at (a) 0.926 μA cm$^{-1}$ and (b) 3.74 μA cm$^{-1}$.

$f$ is approximately constant with time across all positions, indicating that polarization does not induce grain alignment or dealignment in any of the samples, even at very high polarizations (middle section of part (a)). We exclude data very close to the electrodes because the beam partially passes through the lithium electrode at these positions, and some sectors of the 2D scattering patterns contain artifacts, resulting in noisy data. However, because the beam spans 200 μm along the x-axis, most of the sample is accounted for by the positions listed in the legends.

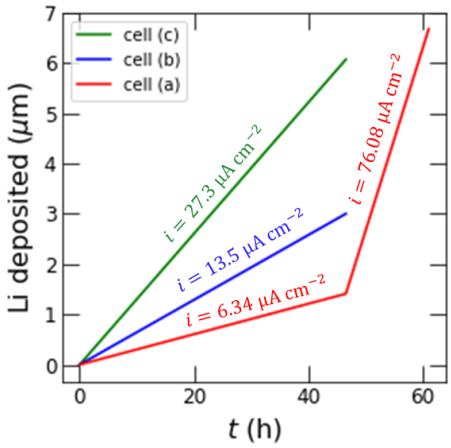


Figure A9.10. Calculation of the thickness of lithium deposited during polarization. The cell in Figures 9.5a and 9.7 is shown in red at the two different current densities used in the experiments. The cells in Figure 9.5b and 9.5c are shown in blue and green, respectively. The amount of lithium deposited is less that 7 $\mu$m for all three cells.

The cell thicknesses are on the order of 1400 $\mu$m and the beam samples a 200 $\mu$m region along the $x$-coordinate of the cell. Therefore, the shifting of the cell positions due to the stripping and plating of the lithium is relatively small and we do not account for it in our definitions of the cell positions.

# Appendix A10: Supplemental Information from Chapter 10

## A10.1 Example Peak Fitting Result

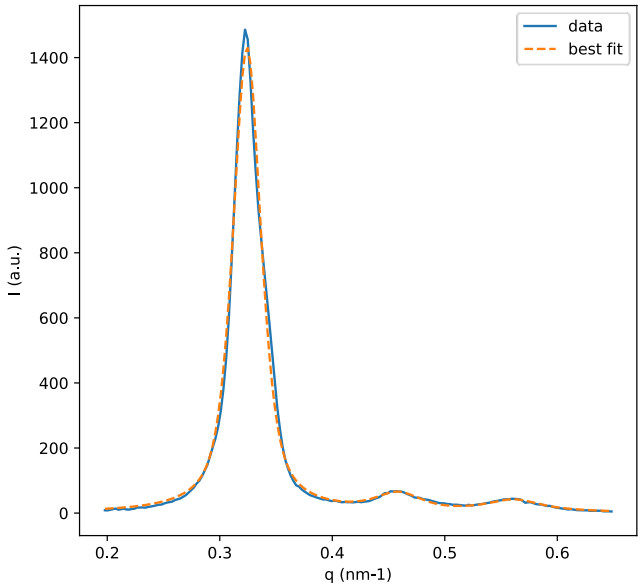


Figure A10.1. A representative azimuthally averaged SAXS trace (at $t = 0$, $x/L = 0.41$) (blue solid) and the fitting result obtained using lmfit (orange dashed). The model is set to obtain three pseudo-Voigt peaks, where the first is at $q^*$ and the second and third are at $\sqrt{2}q^*$ and $\sqrt{3}q^*$. The location of $q^*$ and the broadness and integral of each peak is fit.

## A10.2 Relationship between X-ray transmission and $r$ in SEO electrolytes

The X-ray transmission, $\frac{I}{I_0}$, is determined by

$$\frac{I}{I_0} = e^{-\mu\rho d} \quad , \quad \text{(A10.1)}$$

where $\mu$ is the mass absorption coefficient, $\rho$ is the mass density, and $d$ is the sample thickness. [220] The mass absorption coefficient depends on the chemical composition of the sample via a weighted average of the absorption cross-sections of the atoms:

$$\mu = N_A \sum_i \frac{x_i \sigma_{ai}}{w_i} , \quad \text{(A10.2)}$$

where $N_A$ is Avogadro's number, and $x_i$, $\sigma_{ai}$, and $w_i$ are the mole fractions, absorption cross sections, and atomic weights, respectively, of the constituent atoms. The LiTFSI salt has a chemical composition of $LiC_2S_2O_4NF_6$. SEO(4.0-22.4) has a mass ratio of PS to PEO of 4.0 to 22.4; given monomeric weights of 104.1 and 44.05 g/mol for styrene and ethylene oxide, respectively, this translates to a molar ratio, $m$, of 0.0756 styrene repeat units per ethylene oxide repeat unit; i.e., the chemical composition of SEO(4.0-22.4), normalized to one ethylene oxide repeat unit, is $(C_8H_8)_{0.0756}(C_2H_40)$. The salt concentration, $r$, is defined as the number of lithium ions per ethylene oxide repeat unit. Thus, for a known value of $r$, the total electrolyte chemical composition for an SEO electrolyte is $(C_8H_8)_m(C_2H_4O)(LiC_2S_2O_4NF_6)_r$ – this allows calculation of the values of $x_i$, which are shown in Table S1 for a general SEO electrolyte with styrene : ethylene oxide monomer molar ratio $m$ and salt concentration $r$. The scattering cross section of each element depends on the X-ray energy; these have been tabulated by NIST, [229] and can be accessed using the xraylib database. [222,223] In these experiments, the X-ray energy is 12 keV, and the resulting values of $\sigma_{ai}$ are shown in Table A10.1.

Table A10.1. Values of the mole fractions ($x_i$) and X-ray absorption cross sections ($\sigma_{ai}$) for SEO(4.0-22.4) / LiTFSI electrolytes at 12 keV.

| element | $x_i$ | $\sigma_{ai}$ (cm$^2$/g) |
|---|---|---|
| C | $2 + 8m + 2r$ | 1.132 |
| H | $4 + 8m$ | 0.001470 |
| O | $1 + 4r$ | 3.098 |
| Li | $r$ | 0.06666 |
| S | $2r$ | 28.25 |
| N | $r$ | 1.899 |
| F | $6r$ | 4.336 |

The density is calculated according to Equation A10.3,

$$\rho = \phi_c\rho_c + (1 - \phi_c)\rho_{PS}\,, \qquad \text{(A10.3)}$$

where $\rho_{PS}$ is the density of polystyrene (104.1 g/mol), $\rho_c$ is the density of the PEO/LiTFSI conducting phase, and $\phi_c$ is the volume fraction of the conducting phase. The density of the conducting phase, $\rho_c$, depends on the salt concentration, and can be fit to Equation A10.4,

$$\rho_c(r) = 1.714r + 1.161\,, \qquad \text{(A10.4)}$$

where $\rho_c$ is in units of g/mL, using data published in the literature.[25] The volume fraction of the conducting phase, $\phi_c$, is calculated using Equation A10.5,

$$\phi_c = \frac{v_c}{v_c + \frac{M_{PS}M_{EO}}{M_S M_{PEO}} v_S} \quad , \qquad \text{(A10.5)}$$

where $M_{PS}$ and $M_{PEO}$ are the molecular weights of the PS and PEO, respectively, blocks of the block copolymer (4,000 g/mol and 22,400 g/mol, respectively), $M_S$ is the molar mass of the styrene repeat unit (104.1 g/mol), $M_{EO}$ is the molar mass of the ethylene oxide repeat unit (44.05 g/mol), $v_S$ is the molar volume of styrene (0.167 nm$^3$), and $v_c$ is the molar volume of the conducting (PEO/LiTFSI) phase,

$$v_c = \frac{M_{EO} + rM_{LiTFSI}}{\rho_c(r)} , \qquad \text{(A10.6)}$$

where $M_{LiTFSI}$ is the molecular weight of LiTFSI (287.075 g/mol). Note that this density calculation assumes that the density of the PEO / LiTFSI phase in an SEO / LiTFSI electrolyte matches that of a homopolymer PEO / LiTFSI electrolyte, and the density of the PS phase in an SEO / LiTFSI electrolyte matches that of homopolymer PS; given local stresses during polarization, this may be a source of error.[123]

The values of $\mu$ (calculated using Equation A10.2 and the data in Table A10.1), $\rho$ (calculated using Equations A10.3- A10.6), and $d$ (1.95 mm) can then be inserted into Equation A10.1 to produce an analytical relationship between the X-ray transmission, $\frac{I}{I_0}$, and the salt concentration, $r$, in an SEO / LiTFSI electrolyte. Alternatively, an online tool such as that provided by the center for X-ray optics [43] can be used to calculate the transmission directly given the chemical composition, $\rho$, $d$, and the X-ray energy, with the same results. The relationship between X-ray transmission for SEO(4.0-22.4) / LiTFSI electrolytes and the salt concentration, $r$, is shown in Figure A10.2.

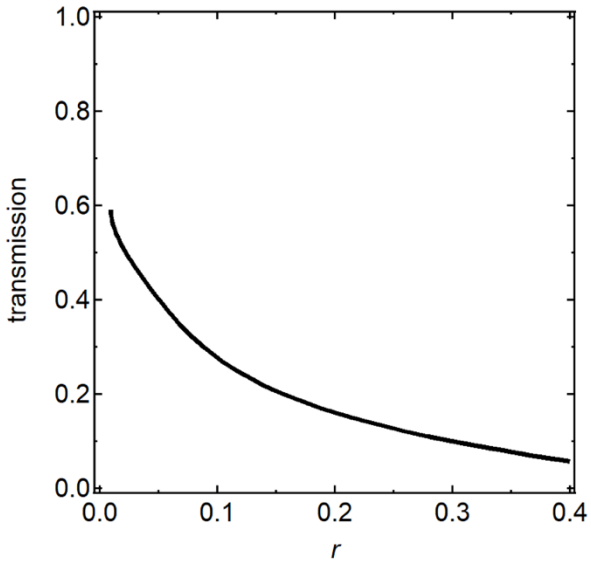


Figure A10.2. The calculated relationship between X-ray transmission and salt concentration, $r$, using Equations A10.1-A10.6 and Table A10.1.

## Concentrated Solution Theory Predictions of Salt Concentration Gradients

Newman's concentrated solution theory [29] can be used to model the steady-state salt concentration gradient in electrolytes ($r(x/L)$, where $r$ is the molar salt concentration, $x$ is the position in the cell, and $L$ is the cell thickness, such that $x/L$ ranges between zero and one) as a function of the applied current density, $i$, given measurements of the ionic conductivity, $\kappa$, diffusion coefficient, $D$, and current fraction, $\rho_+$. For SEO(4.0-22.4), these measurements are reported in Galluzzo *et al.* [23]

In the literature, [47,10] Equation A10.7,

$$\int_{r(x/L=0)}^{r(x/L)} \frac{D(r)c(r)}{rt_-^0(r)} = -\frac{iL}{F}(x/L), \qquad \text{(A10.7)}$$

where $t_-^0$ is the anion transference number with respect to the solvent velocity, or 1 - $t_+^0$. However, due to the challenges in measuring $t_+^0$, it is convenient to perform a rearrangement. $t_+^0$ is related to other transport parameters according to Equation A10.8, [29]

$$t_+^0 = 1 + \left(\frac{1}{\rho_+} - 1\right)\frac{(z_+\nu_+)FDc\phi_c}{\kappa}\left(\frac{d\ln(m)}{dU}\right), \qquad \text{(S8)}$$

where $z_+$ and $\nu_+$ are the cation charge and number of cations into which the salt dissociates (both are 1 for univalent salts), $c$ is the molal concentration, $\phi_c$ is the volume fraction of the conducting phase, given in Equation A10.5, and $\frac{\mathrm{d}U}{\mathrm{dln}m}$ is related to the thermodynamics of the system. Rearranging Equation A10.7 using Equation A10.8, we obtain

$$\int_{r\left(\frac{x}{L}=0\right)}^{r\left(\frac{x}{L}\right)} J_1(r)\,\mathrm{d}r = -\frac{iL}{F}\left(\frac{x}{L}\right), \qquad \text{(A10.9)}$$

where

$$J_1(r) = \kappa\left(\frac{\mathrm{d}U}{\mathrm{dln}m}\right)\left[r\left(1-\frac{1}{\rho_+}\right)z_+\nu_+F\phi_c\right]^{-1}. \qquad \text{(A10.10)}$$

$J_1(r)$ can be fit to a functional form based on previously-measured parameters as a function of $r$. For SEO(4.0-22.4), using parameters reported in Galluzzo et al., [23] $J_1(r)$ was calculated and fit to a polynomial, given by Equation A10.11. The calculated and fit $J_1(r)$ curves are shown in Figure A10.3.

$$J_1(r) = -0.00130r^9 + 0.000652r^8 + 0.00181r^7 - 0.00243r^6 + 0.00134r^5 - 0.000400r^4 + 6.85\times10^{-5}r^3 - 6.43\times10^{-6}r^2 + 2.73\times10^{-7}r - 1.43\times10^{-9} \qquad \text{(A10.11)}$$

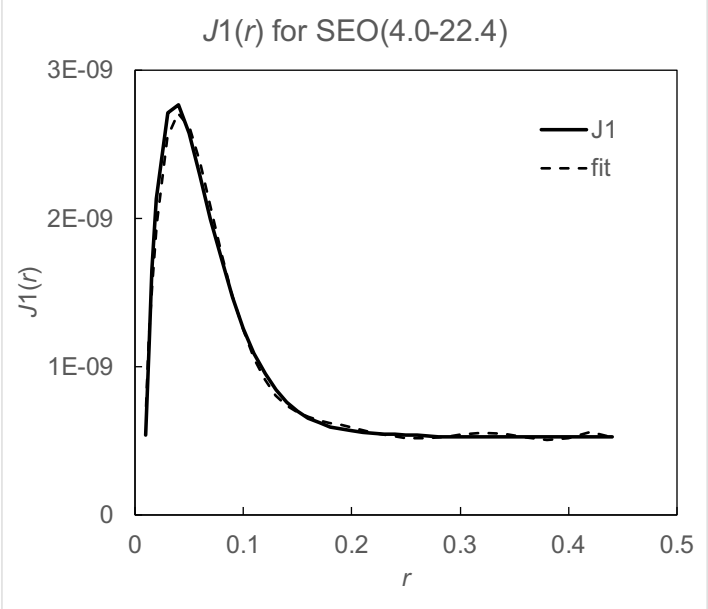


Figure A10.3. $J_1(r)$ calculated using transport and thermodynamic properties and Equation A10.10 (solid line) and the functional fit used in predictions of salt concentration gradients (dashed line).

Then, for a given current, $i$, a salt concentration at $x/L = 0$, $r(x/L = 0)$, is assumed, and Equation A10.9 is used to calculate $r(x/L)$ for all values of $x$, thus generating a salt concentration profile. This salt concentration profile can then be integrated to obtain the average salt concentration. If this is not equal to the known initial salt concentration, the guess for $r(x/L)$ is modified, and the process is completed until the salt concentration converges.

### A10.3 Two-Dimensional SAXS Data for All Positions

In Figure 10.9, we show the azimuthally averaged SAXS patterns of the positions at each end of the cell, $x/L = 0.05$ and 0.95. Here, we show the same data for all positions.

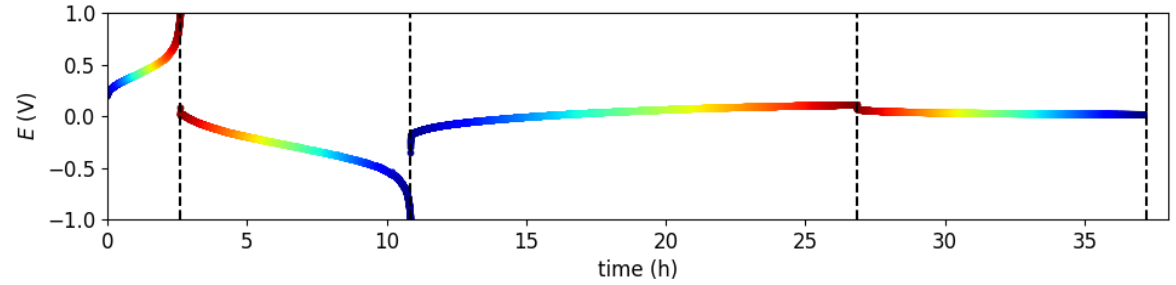


a.

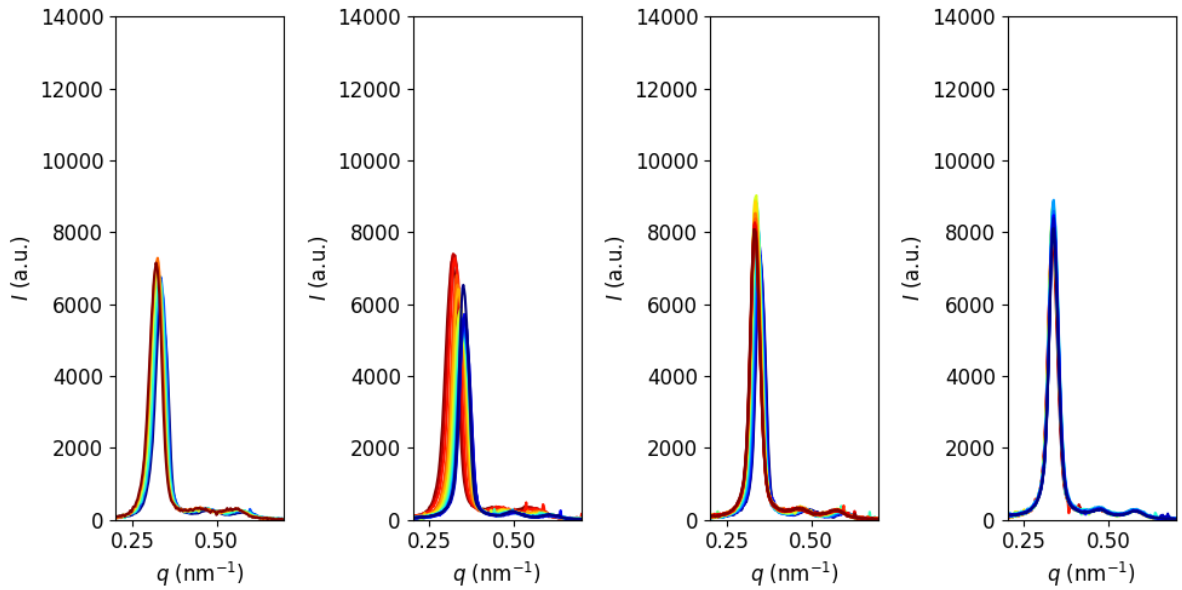


b.

c.

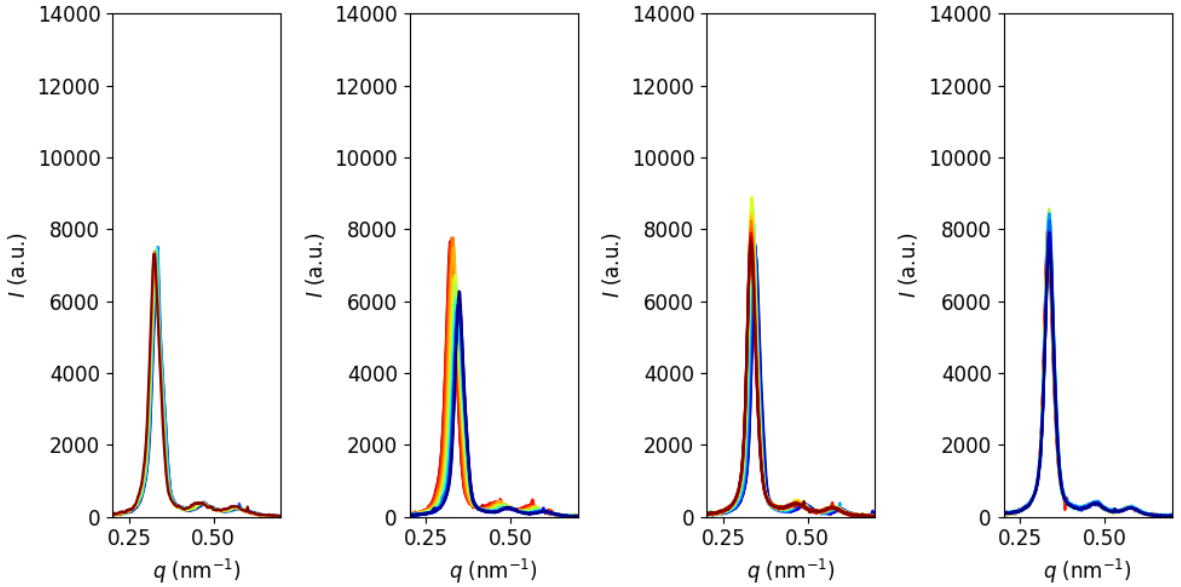
14000
12000
10000
8000
6000
4000
2000
0
I (a.u.)
0.25
0.50
q (nm$^{-1}$)

d.

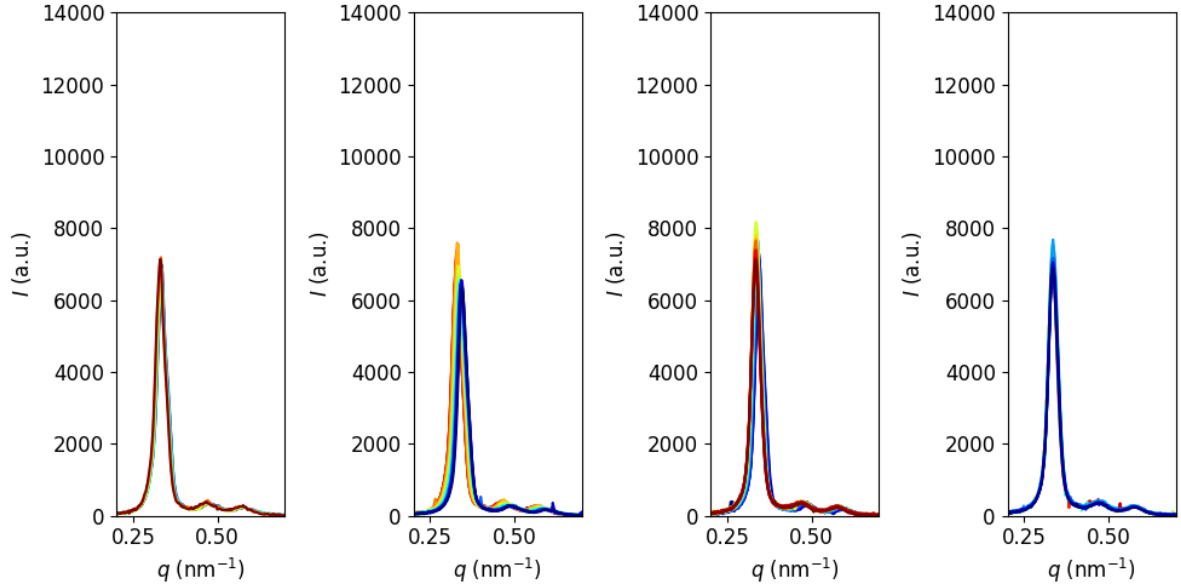
14000
12000
10000
8000
6000
4000
2000
0
I (a.u.)
0.25
0.50
q (nm$^{-1}$)

e.

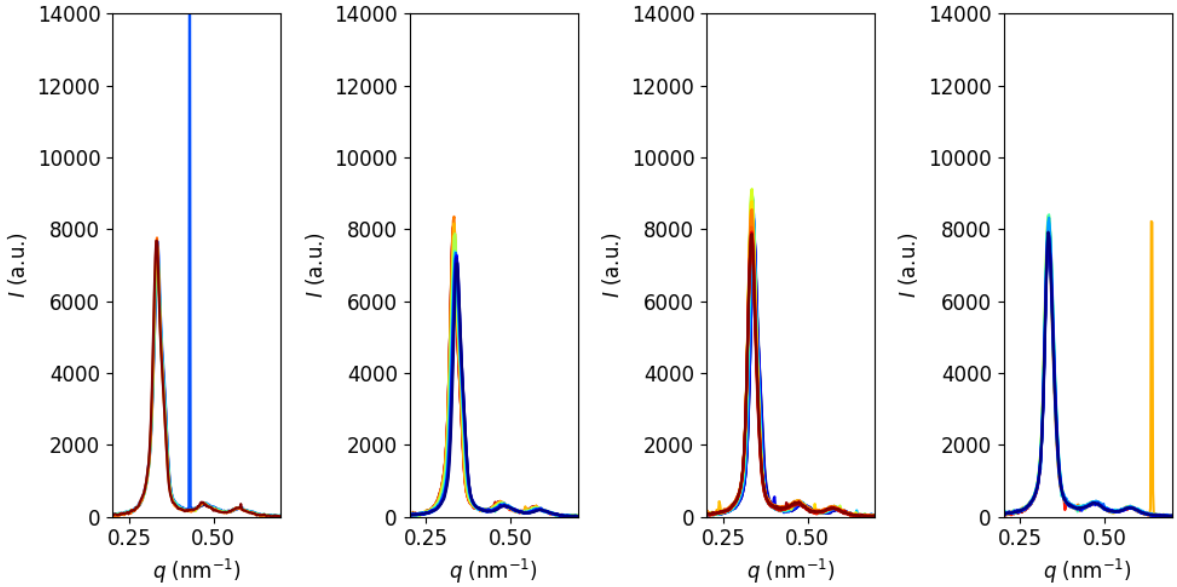
14000
12000
10000
8000
6000
4000
2000
0
I (a.u.)
0.25
0.50
q (nm$^{-1}$)

f.

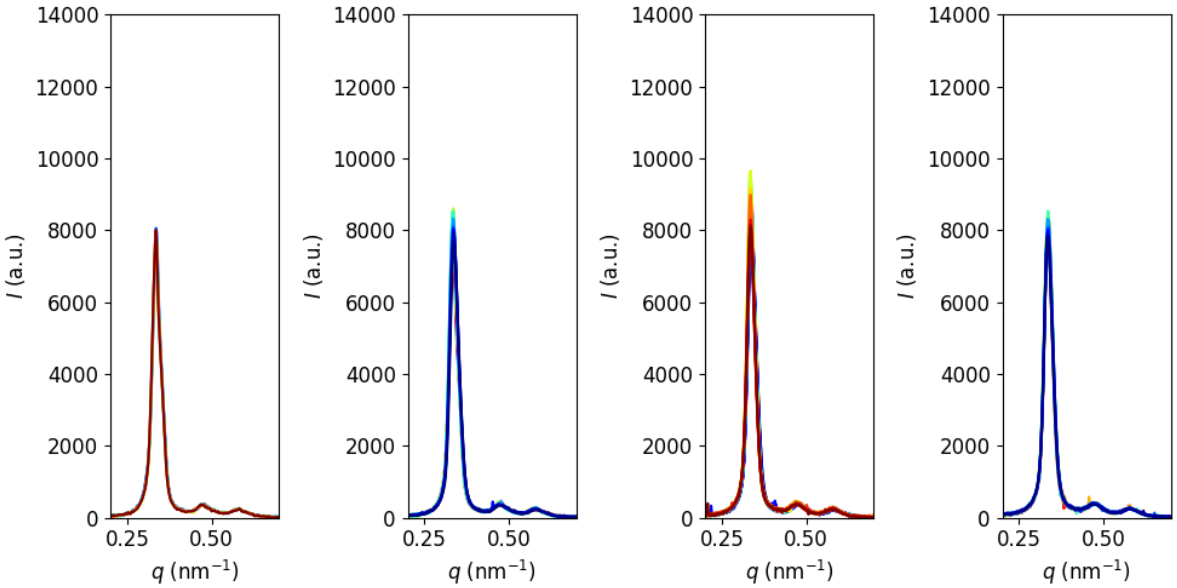
14000
12000
10000
8000
6000
4000
2000
0
I (a.u.)
0.25
0.50
q (nm$^{-1}$)

g.

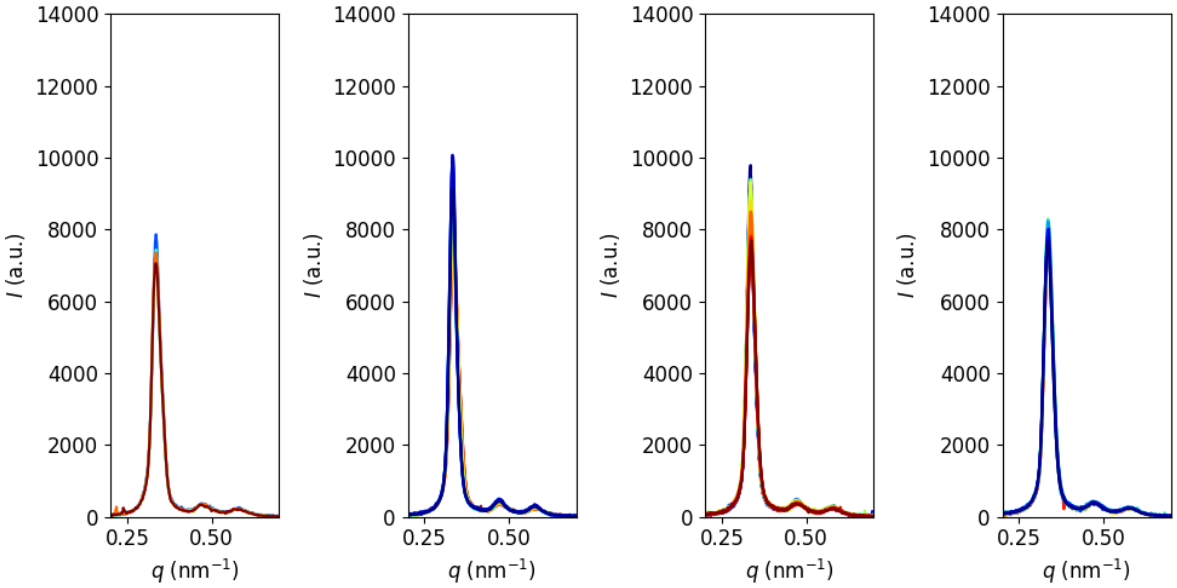
14000
12000
10000
8000
6000
4000
2000
0
I (a.u.)
0.25
0.50
q (nm$^{-1}$)

h.

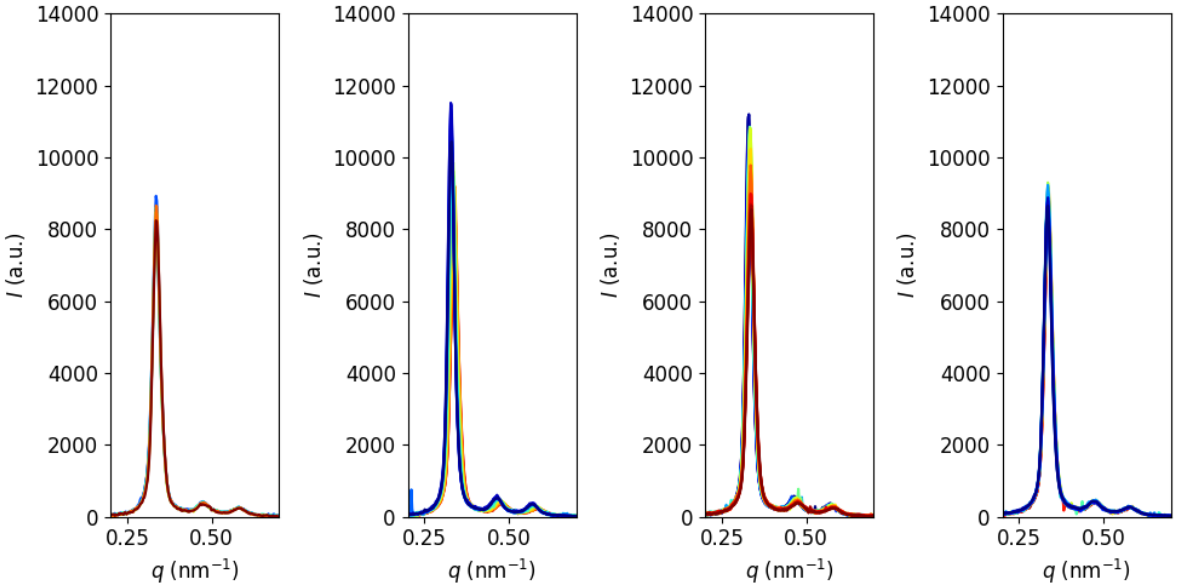
14000
12000
10000
8000
6000
4000
2000
0
I (a.u.)
0.25
0.50
q (nm$^{-1}$)

i.

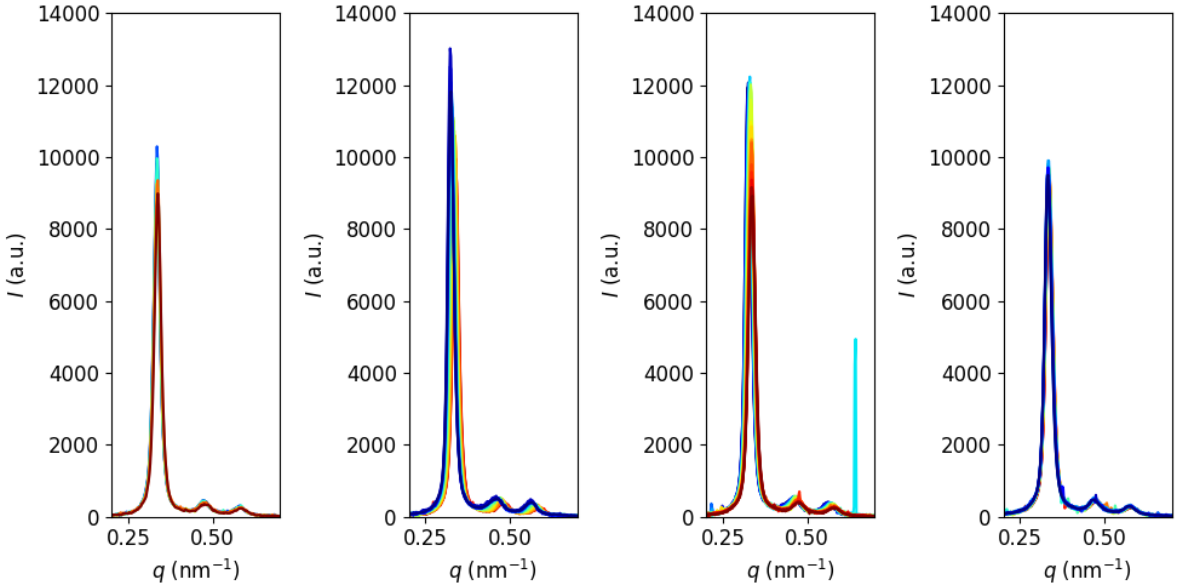
14000
12000
10000
8000
6000
4000
2000
0
I (a.u.)
0.25
0.50
q (nm$^{-1}$)

j.

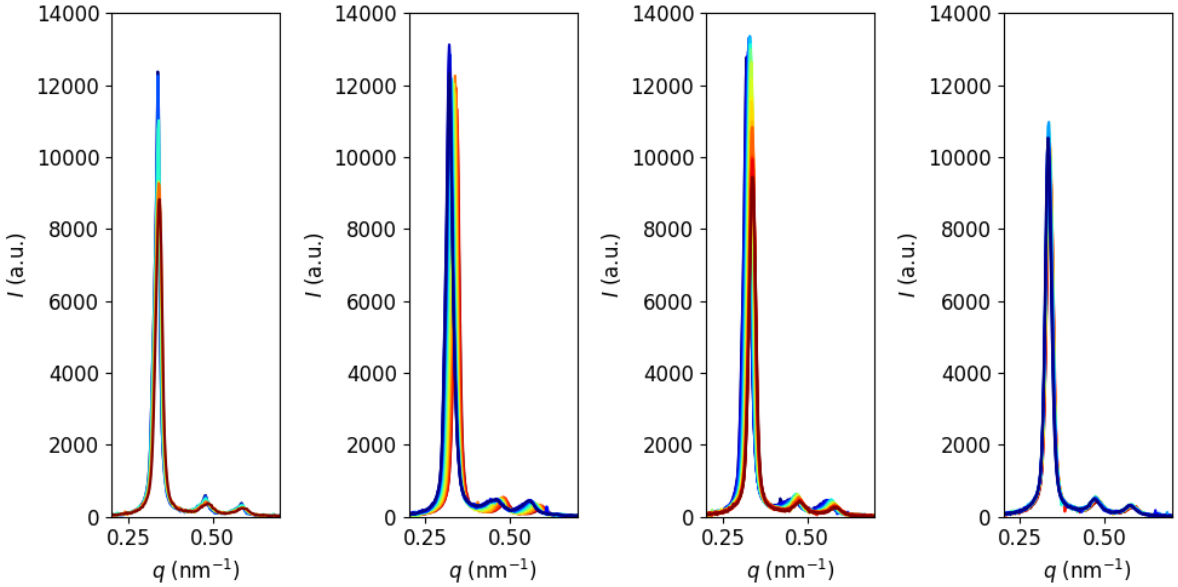
14000
12000
10000
8000
6000
4000
2000
0
I (a.u.)
0.25
0.50
q (nm$^{-1}$)

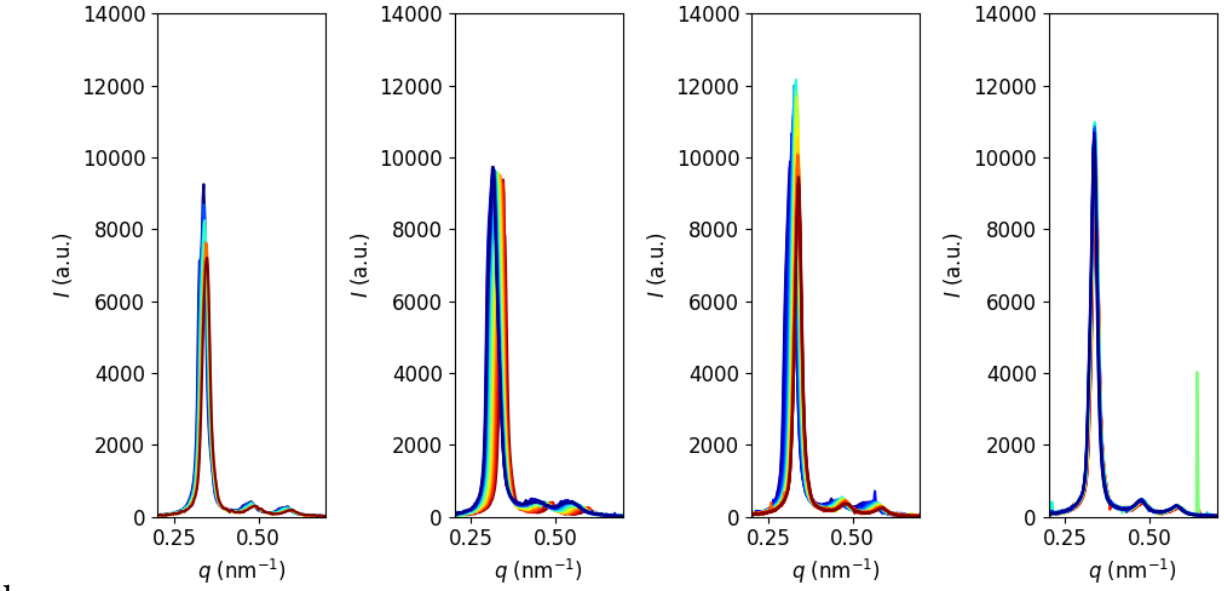


k.

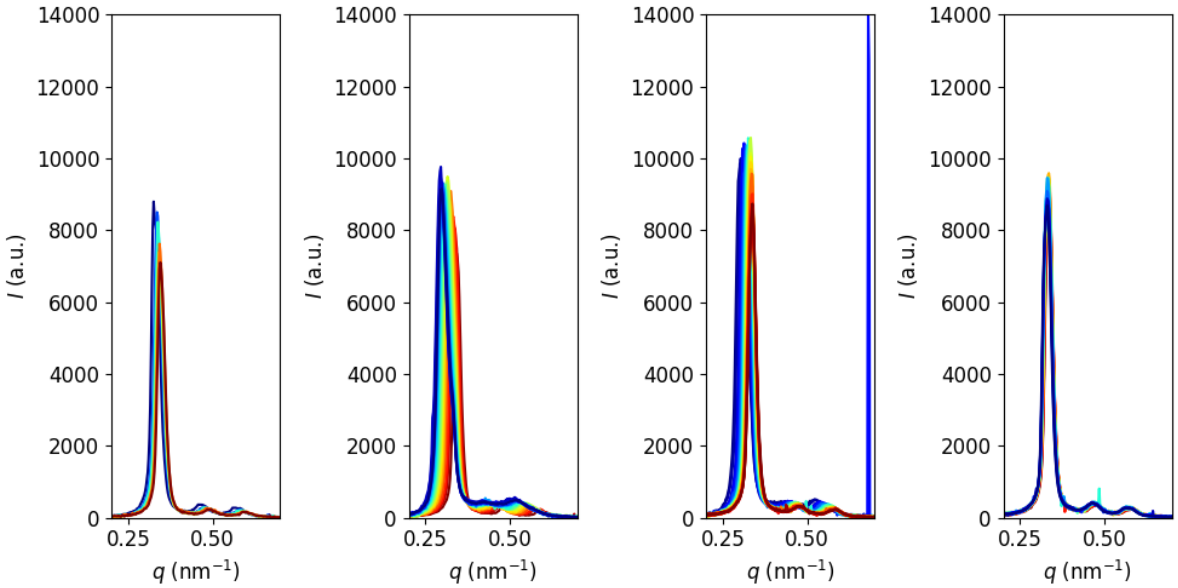


l.

Figure A10.4. Potential response of the SEO(4.0-22.4) $r_{avg}$ = 0.16 cell polarized at +0.042, -0.032, +0.007, and 0 mA/cm, reproduced from Figure 10.6 (a). Azimuthally-averaged SAXS patterns at $x/L$ = 0.05 (b), 0.14 (c), 0.23 (d), 0.32 (e), 0.41 (f), 0.5 (g), 0.59 (h), 0.68 (i), 0.77 (j), 0.86 (k), and 0.95 (l) for the four polarization steps depicted in Figure A10.4a; the color of each trace matches the color of the timepoint of Figure A10.4a to which it corresponds.

## A10.4 Orientation-Dependent Response to Polarization

The orientation-dependence of scattering can be quantified using the azimuthal angle, χ. In Chapter 10 and thus far in Appendix A10, we report azimuthally averaged scattering information, where we have averaged over all values of χ to obtain $I(q)$. The BCC morphology has a majority ion-transporting (PEO / LiTFSI) phase, with polystyrene spheres interspersed; we do not expect the orientation of the BCC morphology to impact ion transport significantly. However, we note that during polarization, we observe changes in the scattering pattern that depend on the azimuthal angle, indicating that the strain applied to the BCC grains during polarization affects differently-oriented grains differently, as we have observed previously with lamellar grains. [216]

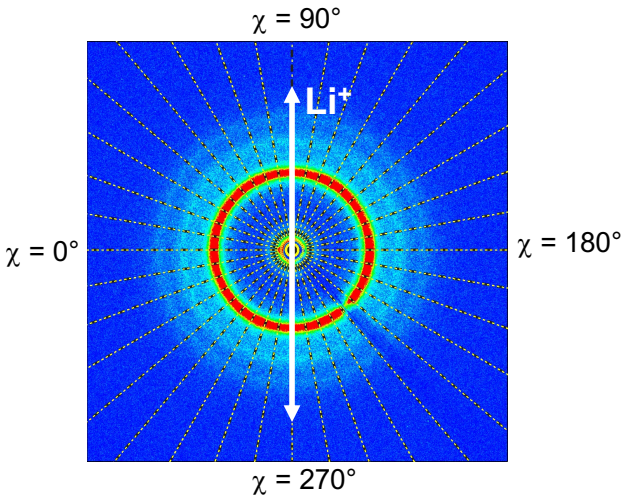


Figure A10.5. A representative 2D SAXS scan ($t$ = 0, $x/L$ = 0.41; the same image azimuthally integrated and fit in Figure A10.1) divided into 36 sectors, with azimuthal angle, χ, labeled. The direction of ion transport is up and down, between χ = 90 and 270°. The shadow around χ = 225° is attributed to the beamstop.

Figure A10.5 shows an example two-dimensional SAXS pattern divided into 36 sectors. An azimuthal angle of zero (χ = 0°) is defined as the left side of the image, with ion transport being in the vertical direction (along the χ = 90° axis). Due to the symmetry of the BCC morphology, scattering at χ = 0 and 180° is expected to be equivalent, as is scattering at χ = 90 and 270°. Therefore, to examine scattering in the horizontal direction, we average four sectors: the two on either size of χ = 0° and the two on either side of χ = 180°. This represents scattering in the direction perpendicular to ion transport. To examine scattering in the vertical direction, we average four sectors: the two on either size of χ = 90° and the two on either side of χ = 270°. This represents scattering in the direction parallel to ion transport. For ease of comparison of the intensity, we normalize the sector-averaged intensity by multiplying it by 9, *i.e.* the total number of sectors divided

by the number of sectors averaged in this analysis. Thus, if the scattering were isotropic, the intensity of these traces would match the intensity of those shown in Figure A10.4. The results are shown in Figure A10.6 for each position. In general, we observe more significant changes to both the peak location and peak intensity at $\chi = 90$ and 270° than at $\chi = 0$ and 180°, which could imply that strain applied in the direction of ion transport by the development of a concentration gradient anisotropically distorts the BCC grains in that direction.

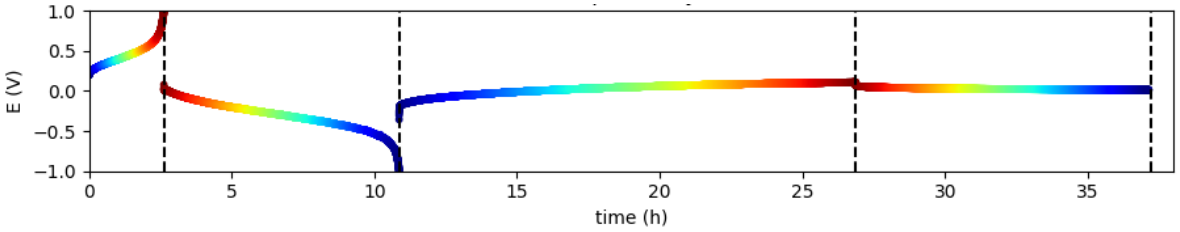


a.

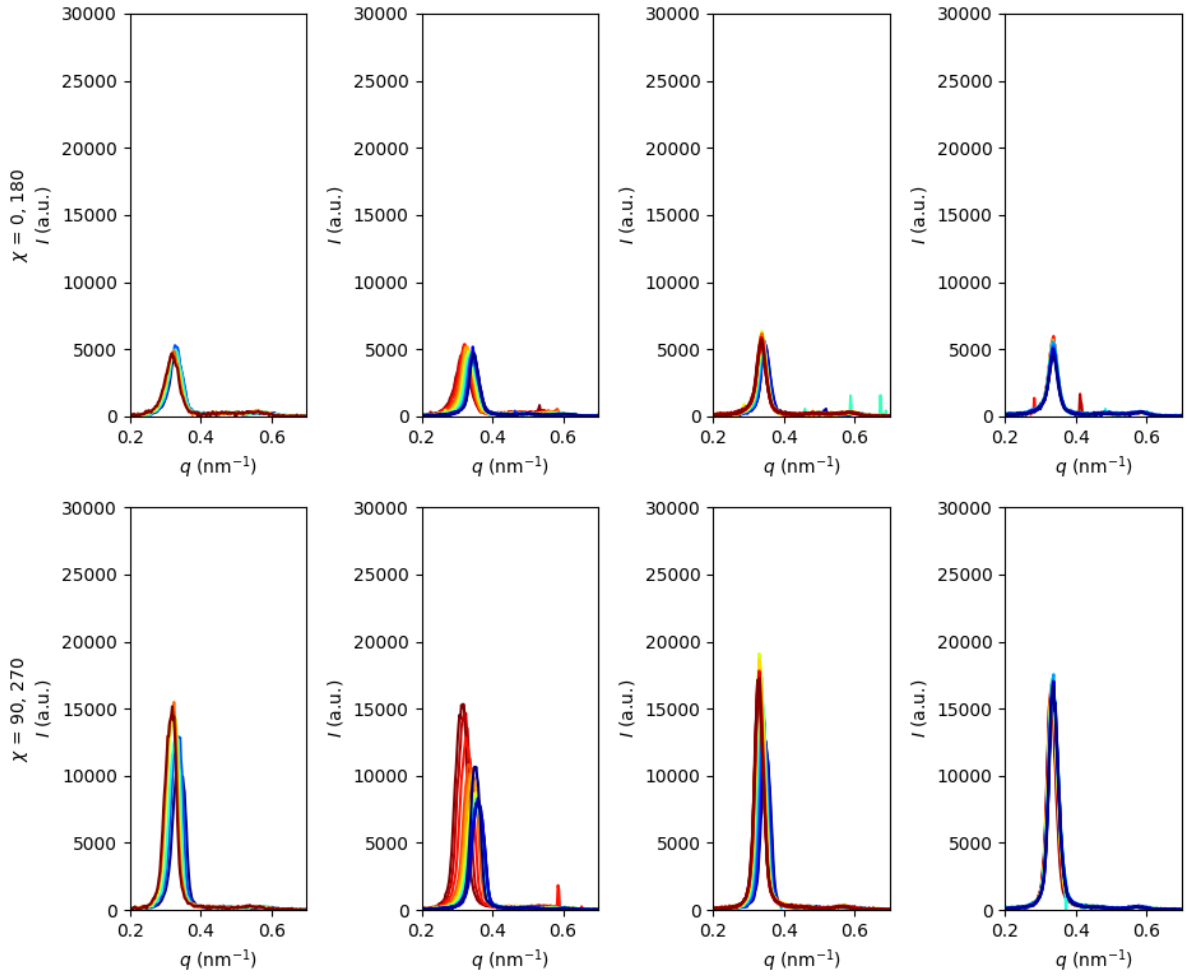


b.

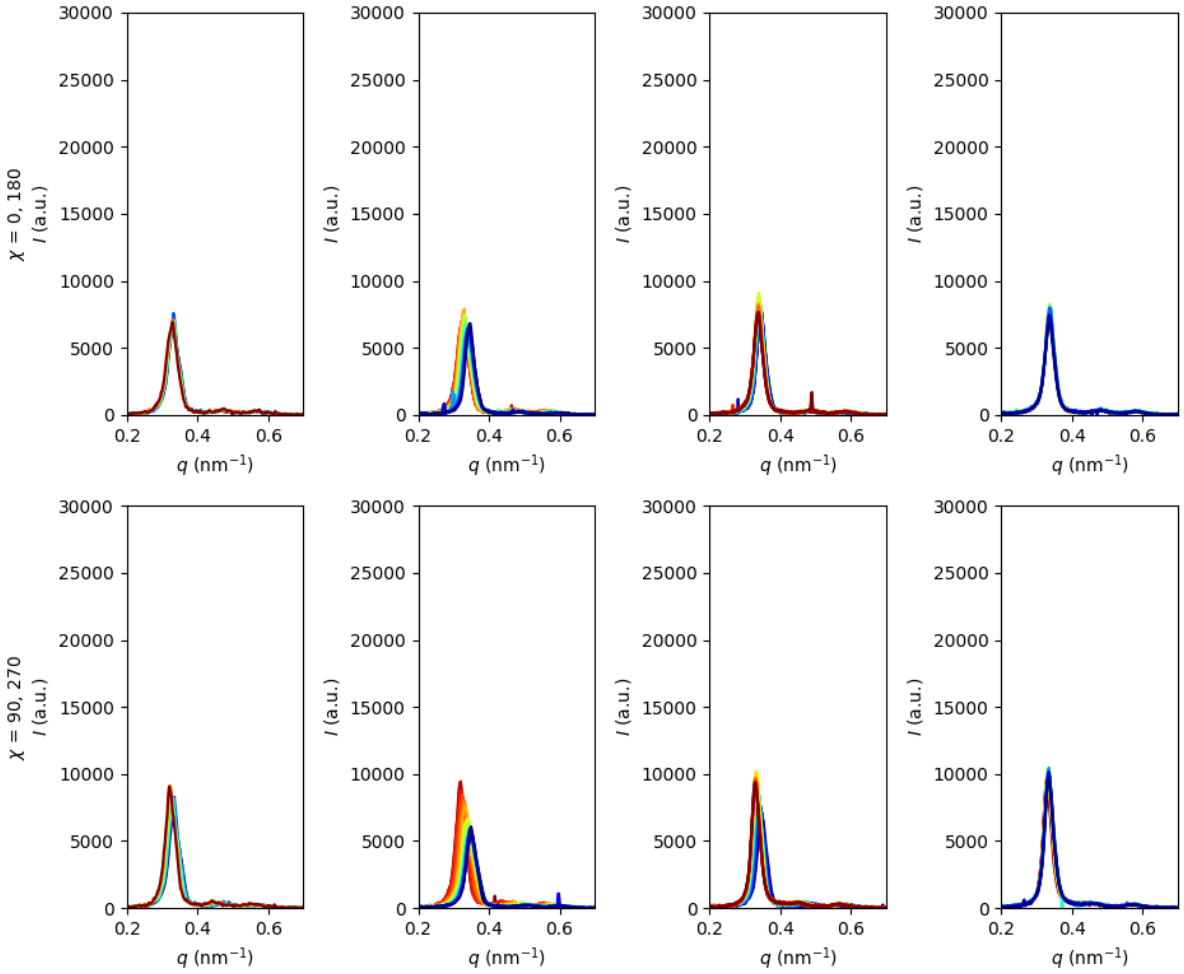
χ = 0, 180
χ = 90, 270
I (a.u.)
q (nm⁻¹)
0
5000
10000
15000
20000
25000
30000
0.2
0.4
0.6

c.

d.

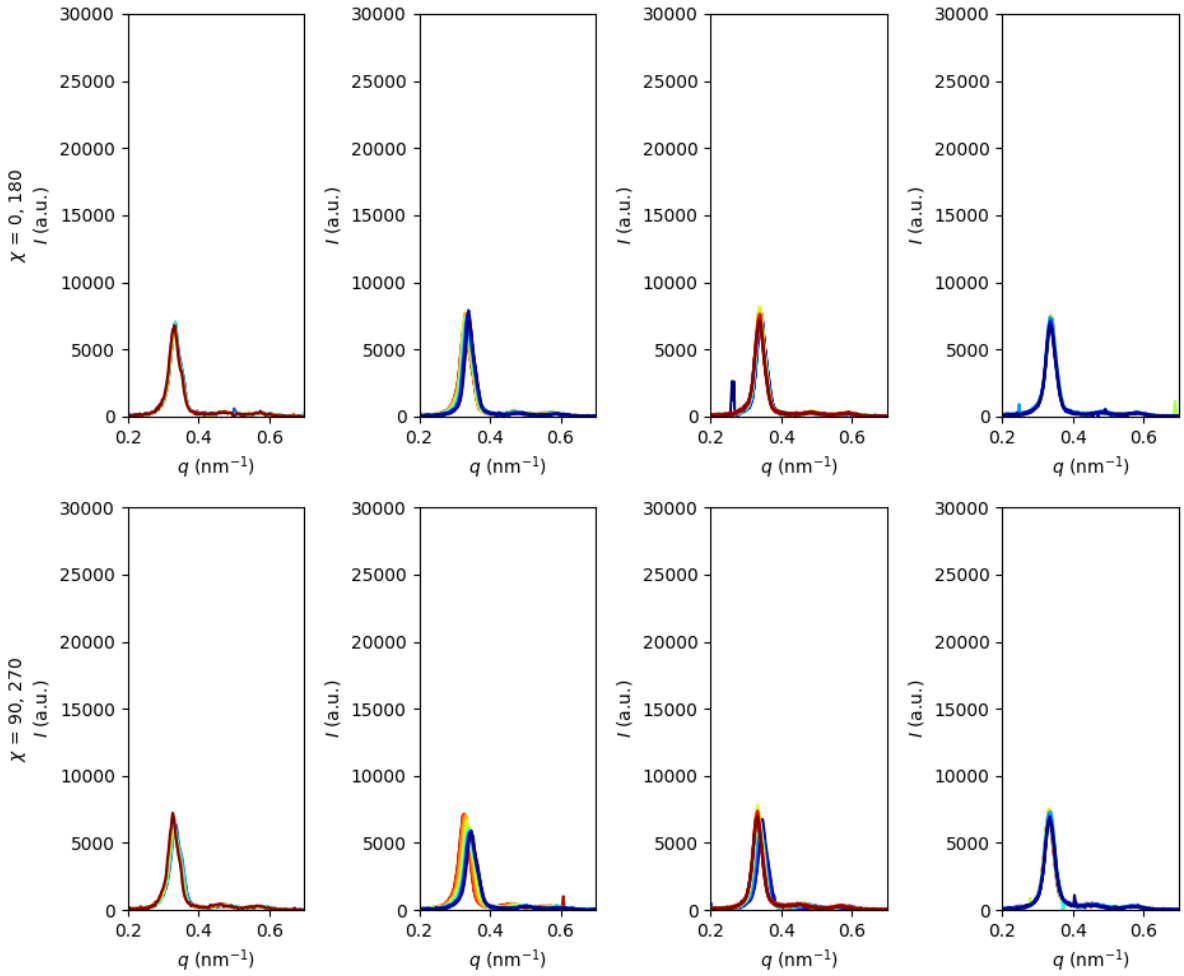
χ = 0, 180
χ = 90, 270
I (a.u.)
q (nm⁻¹)
30000
25000
20000
15000
10000
5000
0
0.2
0.4
0.6

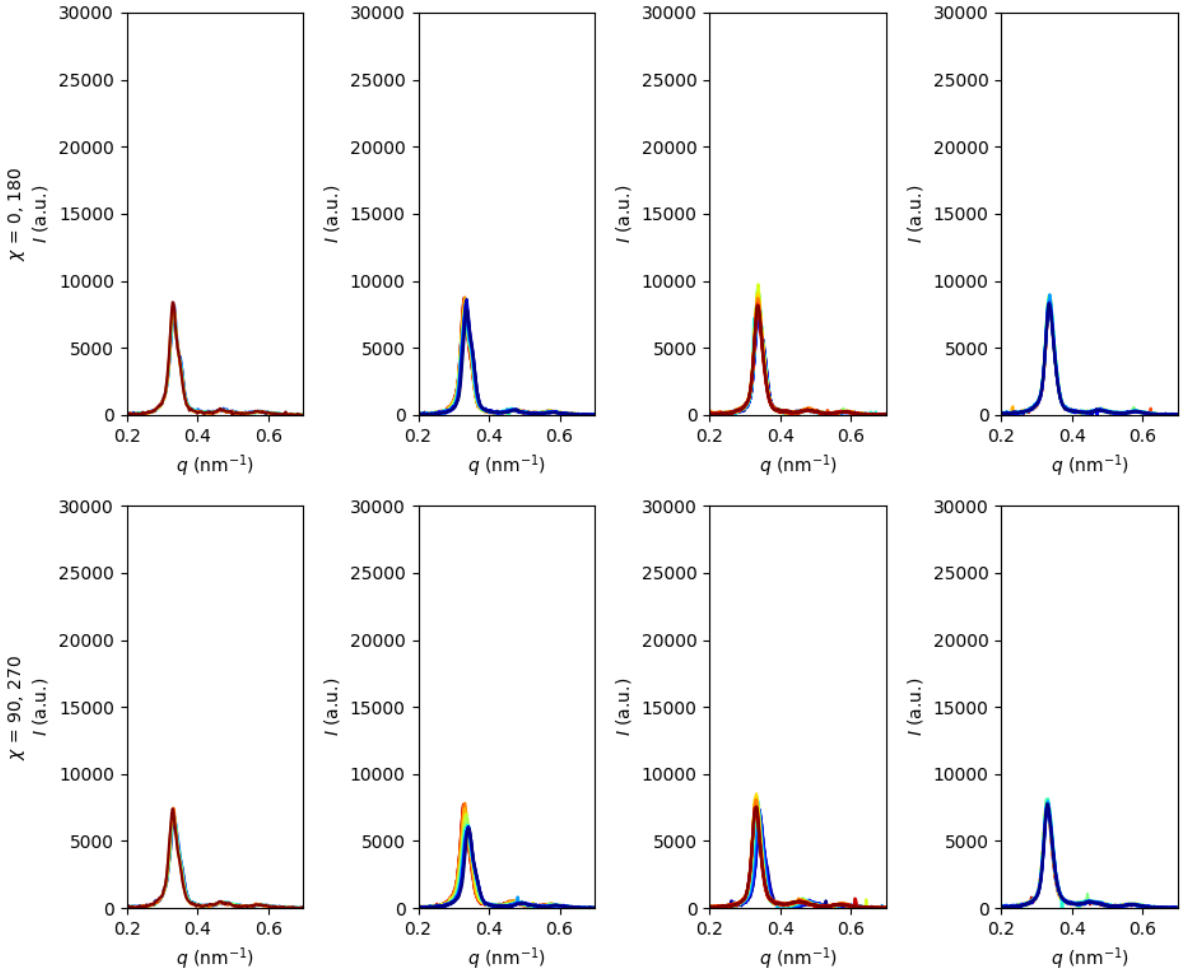
χ = 0, 180
χ = 90, 270
I (a.u.)
q (nm⁻¹)
30000
25000
20000
15000
10000
5000
0
0.2
0.4
0.6

e.

f.

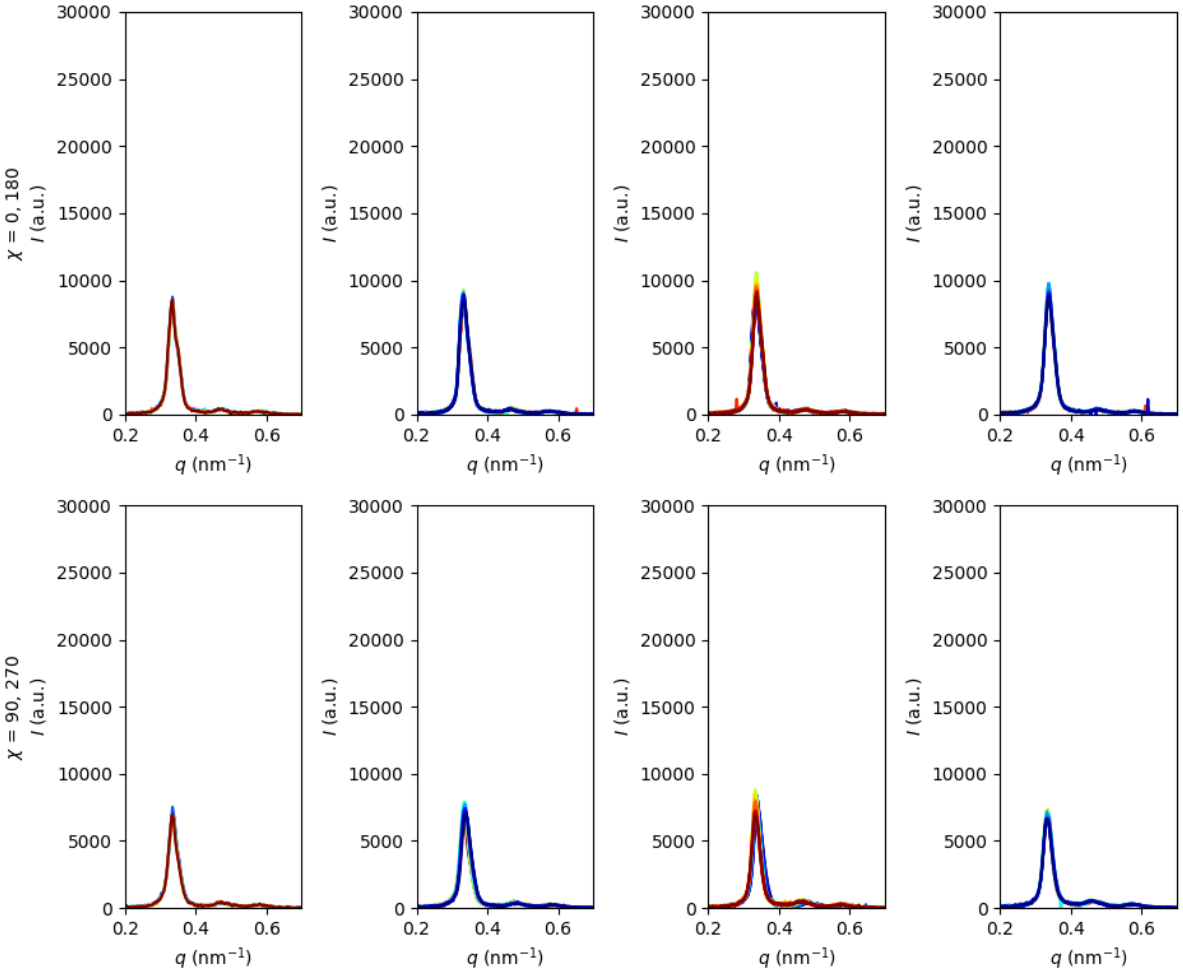
χ = 0, 180
χ = 90, 270
I (a.u.)
q (nm⁻¹)
0
5000
10000
15000
20000
25000
30000
0.2
0.4
0.6

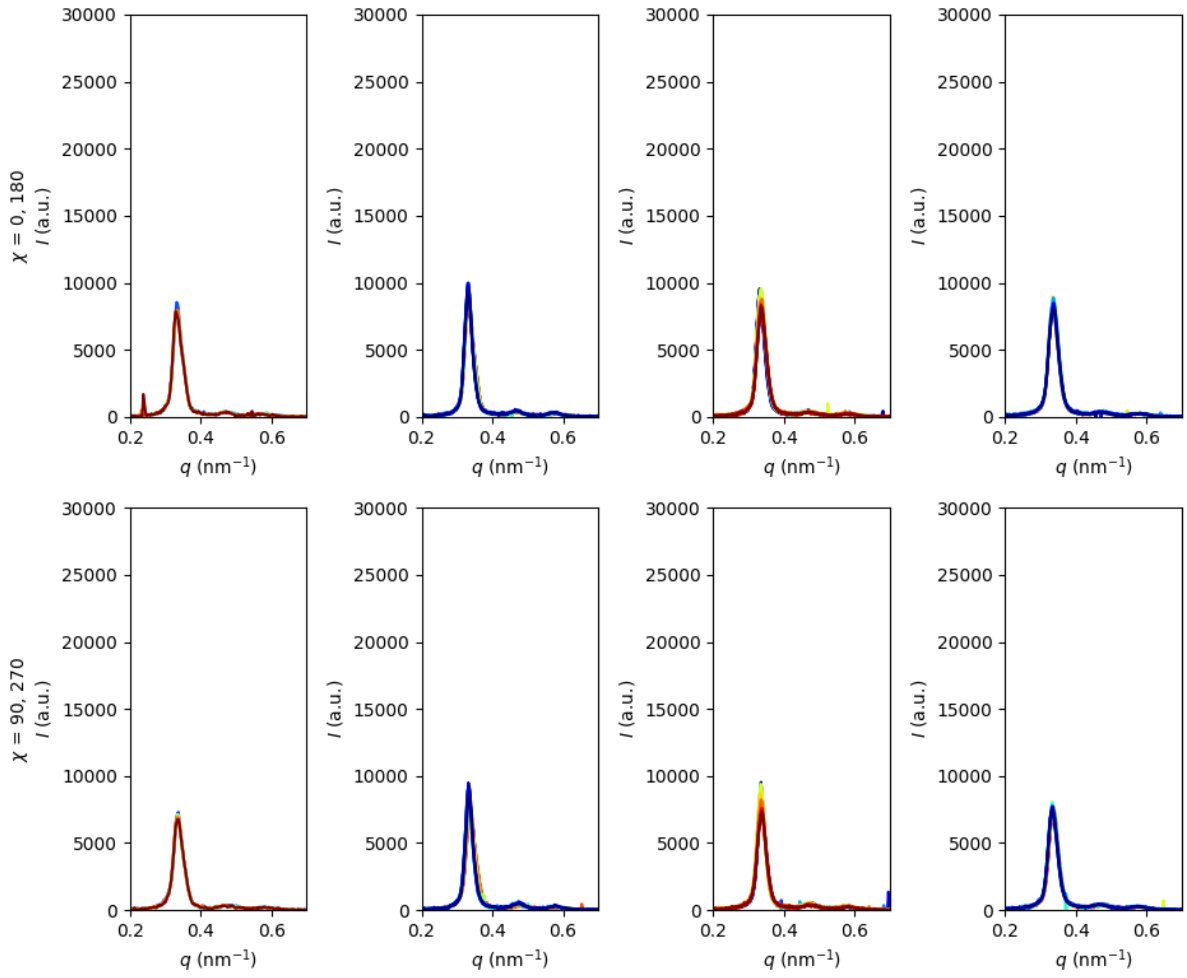
χ = 0, 180
χ = 90, 270
I (a.u.)
q (nm⁻¹)
0
5000
10000
15000
20000
25000
30000
0.2
0.4
0.6

g.

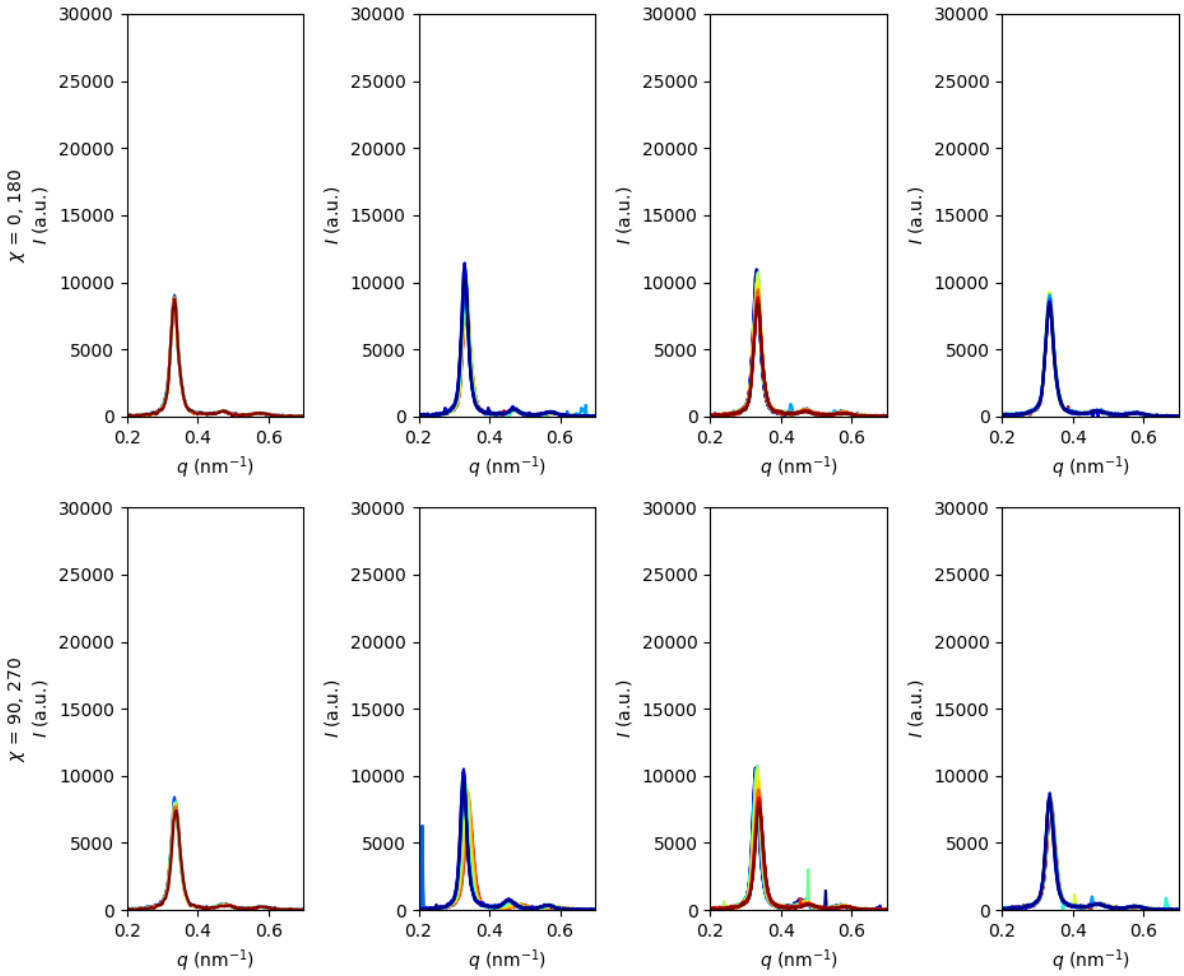
χ = 0, 180
χ = 90, 270
I (a.u.)
q (nm⁻¹)
0
5000
10000
15000
20000
25000
30000
0.2
0.4
0.6

h.

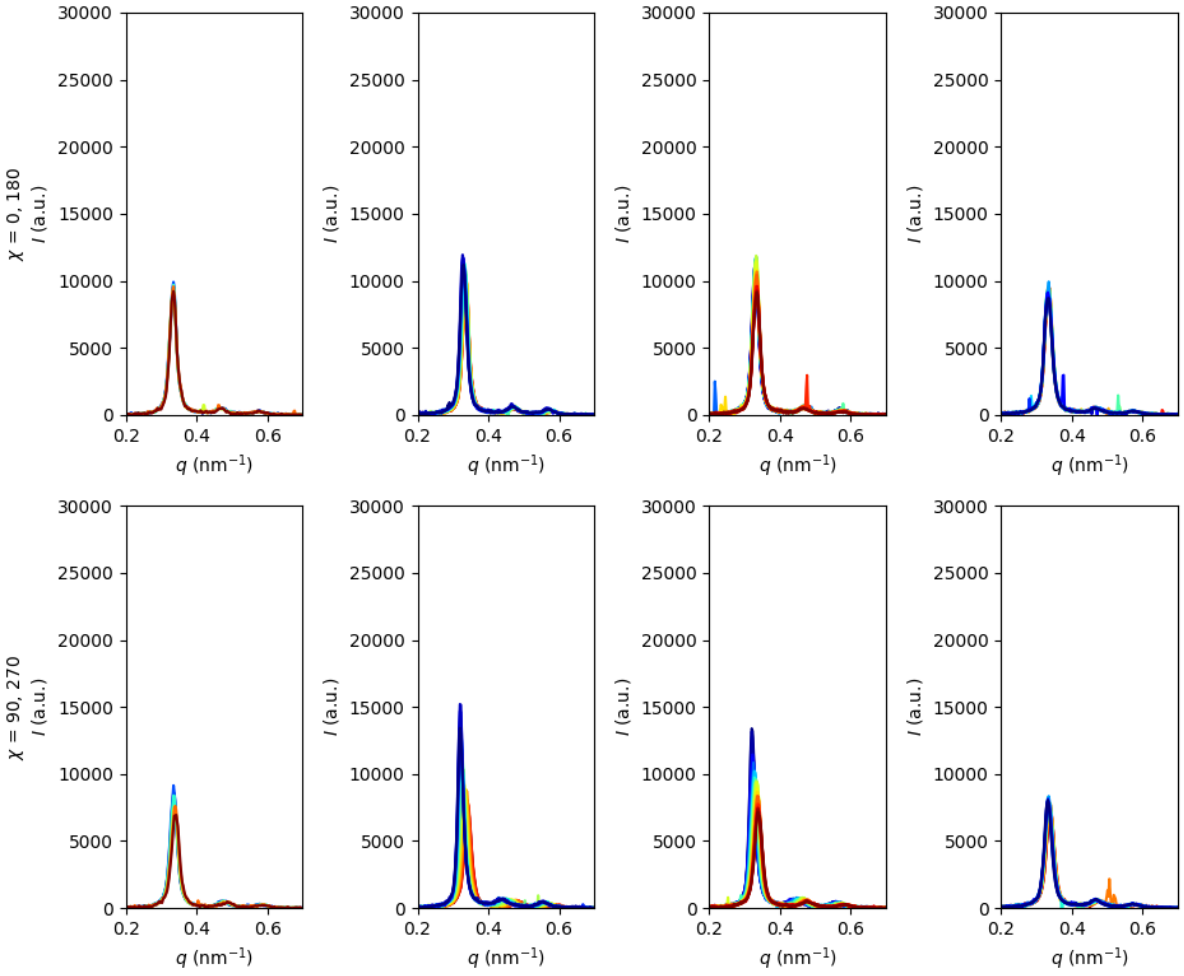
χ = 0, 180
χ = 90, 270
I (a.u.)
q (nm⁻¹)
0
5000
10000
15000
20000
25000
30000
0.2
0.4
0.6

i.

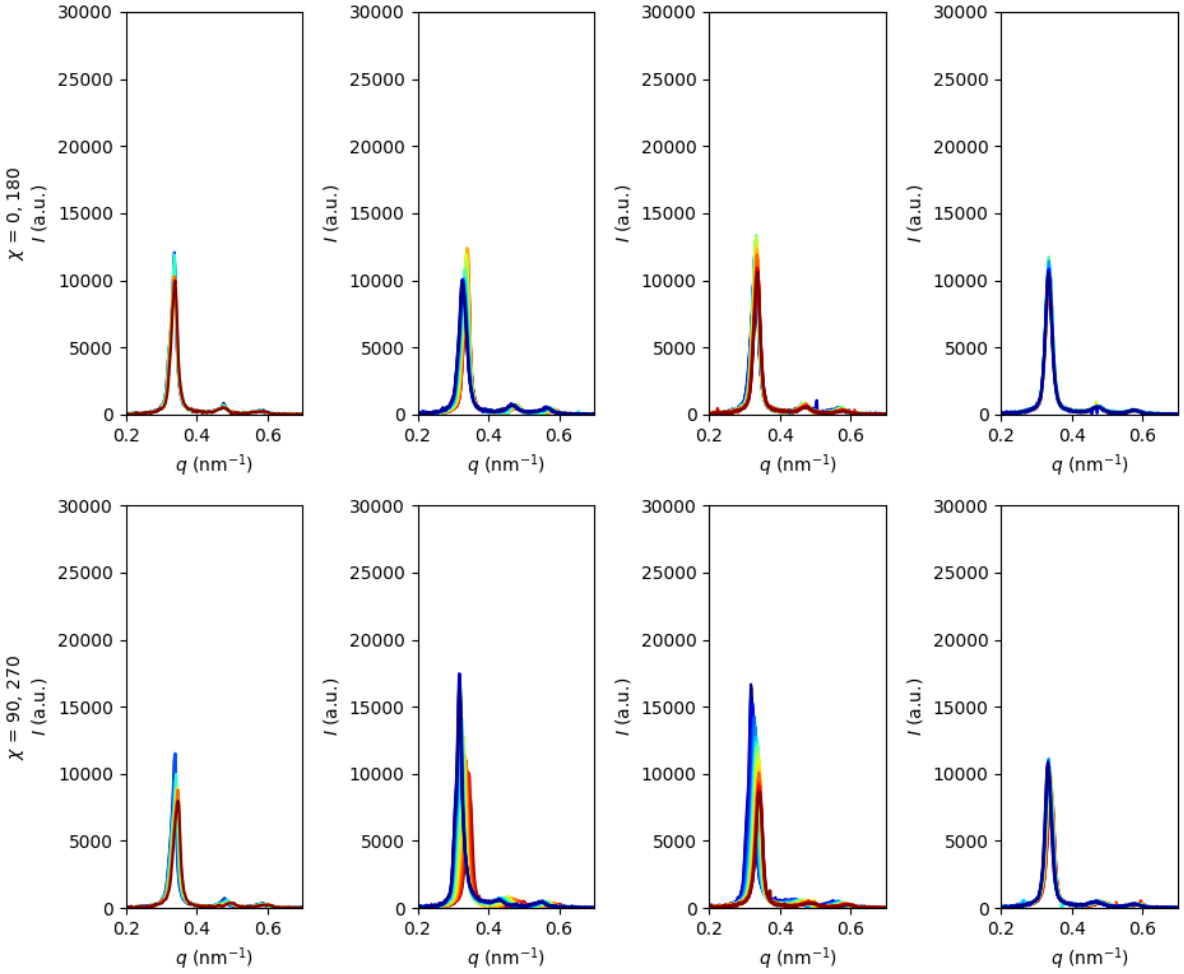
χ = 0, 180
χ = 90, 270
I (a.u.)
q (nm⁻¹)
0
5000
10000
15000
20000
25000
30000
0.2
0.4
0.6

j.

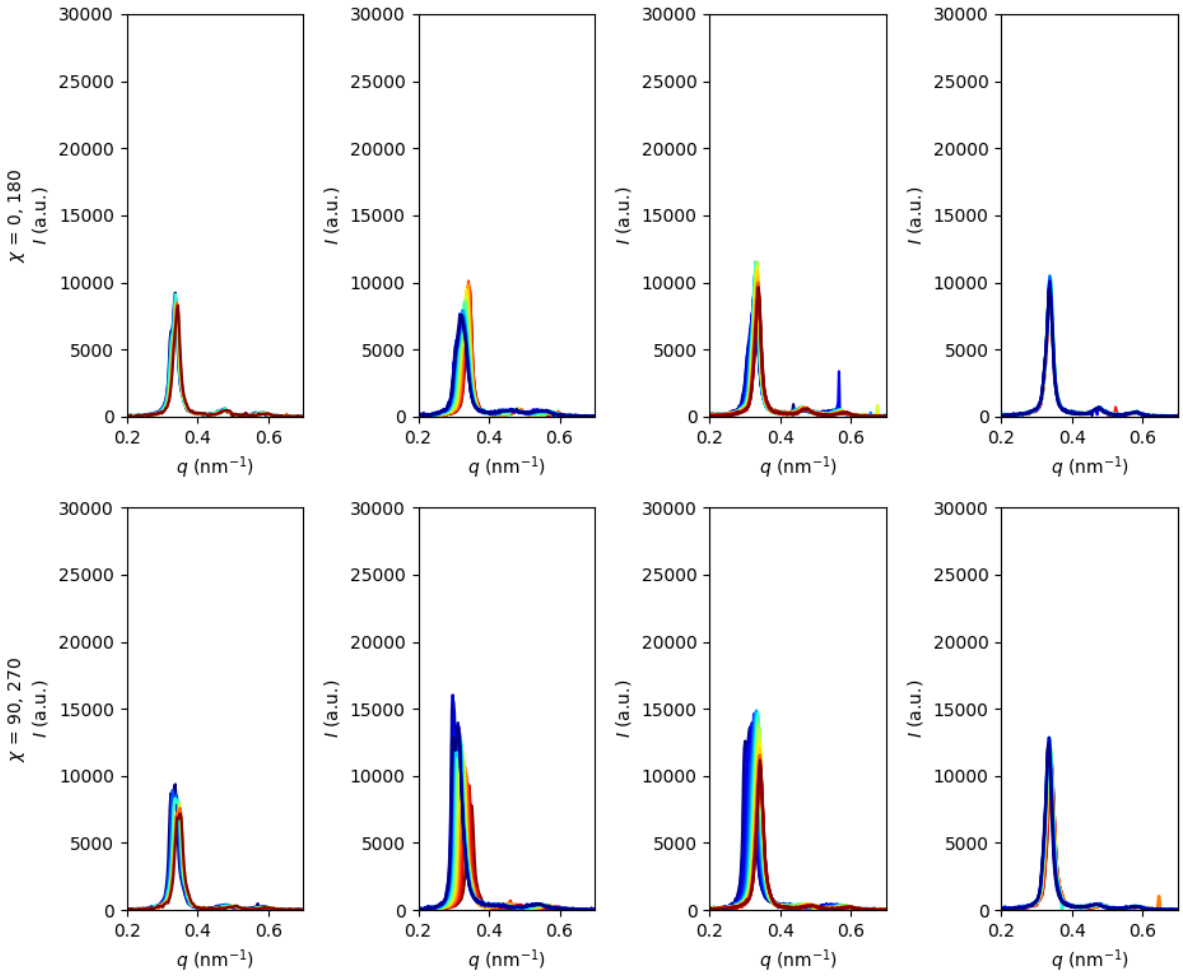
χ = 0, 180
χ = 90, 270
I (a.u.)
q (nm⁻¹)
0
5000
10000
15000
20000
25000
30000
0.2
0.4
0.6

k.

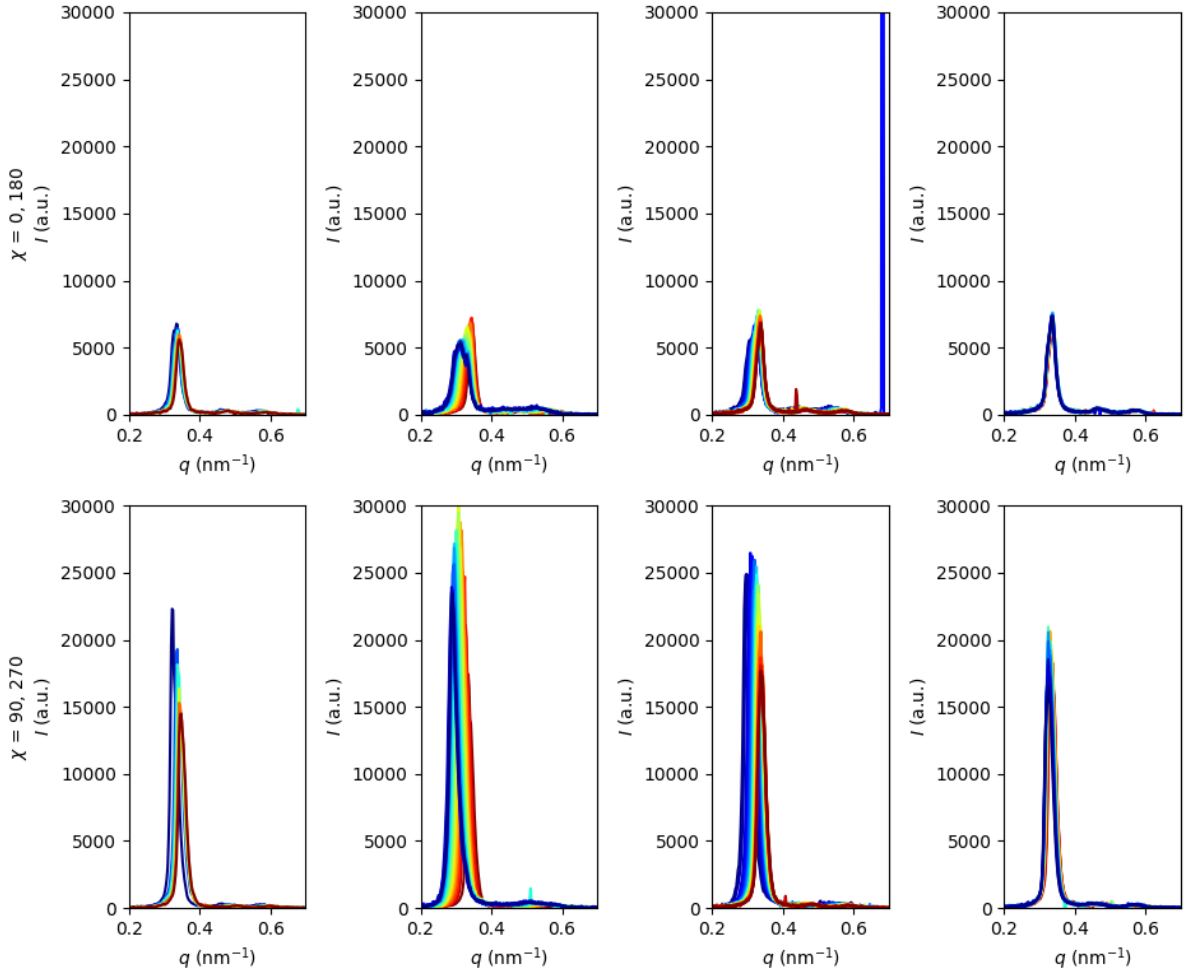


l.

Figure A10.6. Potential response of the SEO(4.0-22.4) $r_{avg}$ = 0.16 cell polarized at +0.042, -0.032, +0.007, and 0 mA/cm, reproduced from Figure 10.6 (a). SAXS patterns at $x/L$ = 0.05 (b), 0.14 (c), 0.23 (d), 0.32 (e), 0.41 (f), 0.5 (g), 0.59 (h), 0.68 (i), 0.77 (j), 0.86 (k), and 0.95 (l) for the four polarization steps depicted in Figure A10.6a; the color of each trace matches the color of the timepoint of Figure A10.6a to which it corresponds. For each position, SAXS patterns are averaged for an azimuthal angle χ range of -10 to 10 and 170 to 190 (top), and 80 to 100 and 260 to 280 (bottom). See Figure A10.5 for a map of azimuthal angles.

## A10.5 Expanded Version of Figure 10.11

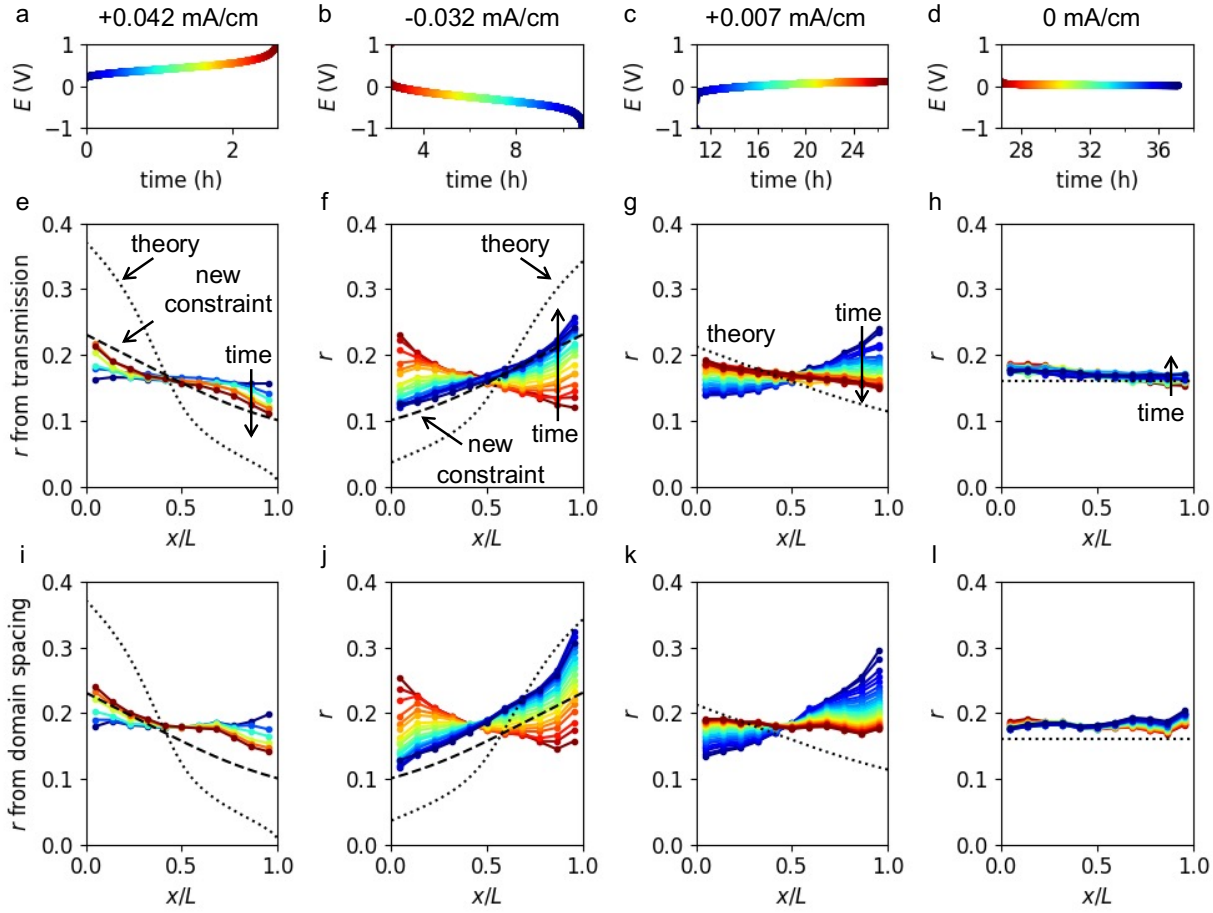


Figure A10.7. A version of Figure 10.11 with wider y-axis scaling in parts (e)-(l), enabling visualization of the entire non-constrained predicted salt concentration profile.

# Appendix B: Data Analysis Tools

## B1. Introduction to Processing Small Angle X-Ray Scattering (SAXS) Data

Small-angle X-ray scattering (SAXS) data is typically acquired in the form of a two-dimensional image, which is essentially an array of the intensity at each pixel of the detector, and accompanying data, often in the form of a text file, including acquisition time and ion chamber readings necessary for calculation of X-ray transmission. As described in Chapter 3, this data must be processed to calculate the transmission and morphology of the sample.

## B2. Using the Nika Macro in Igor Pro

To process data using Igor Pro, we use the Nika macro, installation instructions for which can be found on the Nika website. [45] It is worth noting that the Igor software requires a paid subscription; PyFAI (section B3) is free, but has a steeper learning curve and requires comfort with coding in Python.

Once the Nika macro is installed, in Igor, go to Macros and select "Load Irena and Nika." If it does not appear automatically, go to "SAS 2D" and select "Main panel" to open the panel used to select and process data. On this panel, push "Select data path" and navigate to the folder in which SAXS data is stored. Under image type, select the relevant type, typically ".tif" or "Pilatus," depending on the detector used. Enter the appropriate X-ray energy and pixel size; this depends on the beamline and detector used.

Before data can be processed, the workfile must be calibrated. This requires processing specially-acquired calibration scans—for SAXS, the typical calibrant is silver behenate (AgB) and for WAXS, it is lanthanum hexaboride ($LaB_6$). Go to "SAS 2D" and select "Beam center and Geometry cor." On the panel that appears, push "Select path to data" and navigate to the path where calibration scans are stored. Select the image you wish to use and push "Make Image." A two dimensional image should appear; adjust the sliders in the bottom left of the refinement panel until the AgB ring is visible.

Select the "BeamCntr" tab. Below the image, there should be a small panel which includes cursors; drag the "x" next to "A" to the approximate center of the ring. In the "BeamCntr" tab, select "Read Cursor A" to set the center position. In the "Calibrant" tab, select "Ag behenate" from the drop-down menu. Typically, only the first ring of the AgB scattering is visible—in this case, de-select all but the "Use d1?" box. Manually adjust the number next to "d1 =" such that the fit ring approximately lines up with the scattering ring. Adjust "width" such that the entirety of the peak is contained within the red lines around the fit peak.

Select the "Refinement" tab. Typically, it is best to start with only "Refine beam center" and "Refine Sa-Det distance" (sample-to-detector distance) selected. Select "Run refinement"—the program will now adjust the beam center and sample-to-detector distance to match the peak in the data. This can be run several times to reach a good fit. If necessary, "Refine tilts" can then be selected to further correct for tilt of the detector. Once the fit is satisfactory, close the image window and the refinement panel.

The macro can also be used to create a mask to remove the effect of the beamstop or dark spots in the detector. To do this, go to "SAS 2D" and select "Create mask." In the panel, navigate to the appropriate data folder and select the appropriate data type. Select a representative data scan and click "Make Image." Select Start MASK Draw" and use the provided tools to draw shapes over the beamstop and dark areas of the detector. Choose an appropriate name and click "Save MASK," then close the panel and image.

We are now ready to begin analyzing data. In the main panel, under "Par," select "Dezinger 2D Data?" to automatically remove outliers caused by rogue detector pixels. Under "Mask," select "Use Mask?" and load the previously-created mask file. Under "Sect.," select "Use?" and choose "Q space?" Here, we can make choices about our azimuthally averaging; this panel can be used to create sector averages, for example. For a typical full azimuthal average, select "Max num points?" for maximum resolution and select "Do circular average?" Finally, select "Create 1D graph?"

At this point, the workfile can be saved, so that this process needs to be repeated only once per beamtime.

Select the desired file(s) to be processed, and choose "Convert sel. Files 1 at time." The images will appear one at a time, and a graph of Intensity vs Q vector will be created. This graph can be modified to fit the desired aesthetics. Alternatively, the intensity for each scan is saved as a wave in Igor, which can be manipulated into future graphs.

For peak fitting with Igor, with a graph open, under "Analysis" select "Packages," then "Multipeak Fitting," then "Multipeak Fitting 2." In the window that appears, select "From Target" and choose which graph trace to analyze. Select "Continue." In the new window that appears, zoom into the relevant area and select "Auto-locate Peaks Now." If needed, adjust the sensitivity of auto-location using the options under the "+" icon, and modify the baseline format and delete extraneous peaks. Click "OK," then "Do Fit." If the fitting appears sufficient, select "Peak Results" to obtain the location, amplitude, and area of each peak.

For many applications with tractable amounts of data, the above process should be sufficient. However, for larger amounts of data and more complex analysis, automation becomes necessary.

## B3. Automation of *in situ* SAXS Data Analysis

### *B3.1 Automation of in situ SAXS Data Acquisition*

Before we can analyze the data, we need to acquire it. Below is an example macro to do so, run in July 2021 at beamline 1-5 at SSRL, which acquires the data analyzed in Chapter 10. Note that we must first manually locate the positions of interest in each sample, which we then input into the macro. It is worth thinking carefully about how to name each scan acquired in order to parse the data easily during analysis. An example filename would be P2_s3_scan1_y10.tif, which would indicate position 2 on stage 3 (the third set of samples run) at the first scan (the first loop through all of the positions) and the 10$^{th}$ position. The line that acquires the data changes with changes to the detector, so this should be checked before each beamtime.

```
  1 # Set the directories. note this is slightly different for the two detectors
  2 dir_mar = "Jul2021/stage3/s3_mar" #Leave off the last '/'
  3 dir_pilatus = "~/data/Jul2021/stage3/s3_platus" #No trailing '/'. Note the
use of the ~/data/ This is different than the mar
  4 pd save
  5 ####
  6
  7 # number of scans to loop through
  8 numscans = 500
  9
 10 # Time in seconds to count for both detectors
 11 # we do 10 sec acquisition, with 30 sec every 3 scans
 12 count_time_slow = 30
 13 count_time_fast = 10
 14
 15 # setting the positions of the center of the electrochemically active area
 16 # and the centers of the polymer reference and air holes
 17 P2_xcen = -34.7
 18 P2_ycen = -134.4
 19 P2_xr = -38.15
 20 P2_yr = -134.6
 21 P2_xa  = -31.3
 22 P2_ya  = -135.2
 23
 24 P4_xcen = 46.1
 25 P4_ycen = -135.8
 26 P4_xr = 42.6
 27 P4_yr = -136.3
```

```
 28 P4_xa  = 49.4
 29 P4_ya  = -136.8
 30
 31 P6_xcen = 127.5
 32 P6_ycen = -138.45
 33 P6_xr = 124.1
 34 P6_yr = -138.9
 35 P6_xa  = 130.9
 36 P6_ya  = -139.1
 37
 38 # setting the positions of the reference samples
 39 AgB_xcen = 6.3
 40 AgB_ycen = -136.3
 41
 42 SBA_xcen = 87.5
 43 SBA_ycen = -138
 44
 45 LaB_xcen = 167.5
 46 LaB_ycen = -139.3
 47
 48
 49 # Set the output directory of the pilatus images. Sadly, this will be
somewhat painful to parse
 50 # later. The name of the file will actually come from the current newfile
and the scans will
 51 # increase linearly. No other control over the name is yet possible.
 52 pd_out_tmp = sprintf("pd savepath %s", dir_pilatus )
 53 p pd_out_tmp
 54 eval(pd_out_tmp)
 55
 56 #########
 57 # Enable the detectors both as counters
 58 mar_enable
 59 pd enable
 60 #########
 61
 62
 63 ## do a bunch of scans
 64 for (scan = 35; scan < numscans; scan++) {
 65
 66 # start by displaying the temperature, as a check
 67 showtemp
 68
 69 # set the count time
 70 if (scan % 3 == 0) {
 71 count_time = count_time_slow
 72 }
```

```
 73 if (scan % 3 != 0) {
 74 count_time = count_time_fast
 75 }
 76 p "count time"
 77 p count_time
 78
 79 # acquire dark data (shutter closed)
 80 umv rail3_x P2_xcen
 81 umv rail3_y P2_ycen
 82 umvr rail3_y -2
 83 sclose
 84 filename = sprintf("mar netroot %s/dark_s3_scan%d", dir_mar, scan)
 85 eval(filename)
 86 loopscan 1 count_time
 87 sopen
 88
 89 ## start with position 2
 90
 91           # move to the center
 92           umv rail3_x P2_xcen
 93           umv rail3_y P2_ycen
 94           # move to the bottom
 95           umvr rail3_y -0.7
 96
 97           # scan through, incrementing position after each scan
 98           for (i = 0; i<16 ; i++) {
 99              filename = sprintf("mar netroot %s/P2_s3_scan%d_y%d", dir_mar,
scan, i)
100                eval(filename)
101                loopscan 1 count_time
102
103                umvr rail3_y 0.1
104           }
105
106           # scan the reference
107           umv rail3_x P2_xr
108           umv rail3_y P2_yr
109            filename = sprintf("mar netroot %s/P2_s3_scan%d_ref", dir_mar,
scan)
110           eval(filename)
111           loopscan 1 count_time
112
113           # scan the air
114           umv rail3_x P2_xa
115           umv rail3_y P2_ya
116            filename = sprintf("mar netroot %s/P2_s3_scan%d_air", dir_mar,
scan)
```

```
117           eval(filename)
118           loopscan 1 count_time
119
120 ## take AgB each time
121     umv rail3_x AgB_xcen
122     umv rail3_y AgB_ycen
123
124     filename = sprintf("mar netroot %s/AgB_s3_scan%d", dir_mar, scan)
125     eval(filename)
126     loopscan 1 count_time
127
128 ## start with position 4, same idea as position 2
129
130           umv rail3_x P4_xcen
131           umv rail3_y P4_ycen
132           # this cell is longer so we move down farther
133           umvr rail3_y -0.9
134
135           # we also acquire more positions
136           for (i = 0; i<19 ; i++) {
137              filename = sprintf("mar netroot %s/P4_s3_scan%d_y%d", dir_mar,
scan, i)
138                eval(filename)
139                loopscan 1 count_time
140
141                umvr rail3_y 0.1
142           }
143
144           umv rail3_x P4_xr
145           umv rail3_y P4_yr
146            filename = sprintf("mar netroot %s/P4_s3_scan%d_ref", dir_mar,
scan)
147           eval(filename)
148           loopscan 1 count_time
149
150           umv rail3_x P4_xa
151           umv rail3_y P4_ya
152            filename = sprintf("mar netroot %s/P4_s3_scan%d_air", dir_mar,
scan)
153           eval(filename)
154           loopscan 1 count_time
155
156 ## take SBA each time
157     umv rail3_x SBA_xcen
158     umv rail3_y SBA_ycen
159
160     filename = sprintf("mar netroot %s/SBA_s3_scan%d", dir_mar, scan)
```

```
161     eval(filename)
162     loopscan 1 count_time
163
164 ## start with position 6, same idea as positions 2 and 4
165
166           umv rail3_x P6_xcen
167           umv rail3_y P6_ycen
168           umvr rail3_y -0.7
169
170           for (i = 0; i<16; i++) {
171              filename = sprintf("mar netroot %s/P6_s3_scan%d_y%d", dir_mar,
scan, i)
172                eval(filename)
173                loopscan 1 count_time
174
175                umvr rail3_y 0.1
176           }
177
178           umv rail3_x P6_xr
179           umv rail3_y P6_yr
180            filename = sprintf("mar netroot %s/P6_s3_scan%d_ref", dir_mar,
scan)
181           eval(filename)
182           loopscan 1 count_time
183
184           umv rail3_x P6_xa
185           umv rail3_y P6_ya
186            filename = sprintf("mar netroot %s/P6_s3_scan%d_air", dir_mar,
scan)
187           eval(filename)
188           loopscan 1 count_time
189
190 ## take LaB each time
191     umv rail3_x LaB_xcen
192     umv rail3_y LaB_ycen
193
194     filename = sprintf("mar netroot %s/LaB_s3_scan%d", dir_mar, scan)
195     eval(filename)
196     loopscan 1 count_time
197 }
198
199 # Disable detectors as counter
200 mar_disable
201 pd disable
202
203 # done
```

*B3.2 Setting up Python and PyFAI*

Before proceeding further, a working knowledge of Python coding and running code on your machine is required. There are a number of resources and tutorials online; stop here and ensure that you can run "Hello World" on your machine, and establish basic familiarity with Python syntax. For simplicity, I usually create .py files using Sublime Text and run them from the command prompt of my PC. The code I have written requires a variety of packages—the command "pip install [package]" should be sufficient for all of them. Variations of the code below were used to generate the figures in Chapter 10; the code used to generate the figures in Chapter 9 was conceptually similar but less sophisticated and efficient, so is not included here.

Processing SAXS data using PyFAI requires similar calibration information as using Igor; this information is stored in a .poni (point of normal incidence) file. When PyFAI is installed, it comes with a GUI called "pyFAI-calib2" which, combined with a calibration scan of silver behenate, can be used to generate the poni file. An example poni file (used for the data analysis in Chapter 10) is reproduced below:

```
1-5_calib_3.poni
# Nota: C-Order, 1 refers to the Y axis, 2 to the X axis
# Calibration done at Fri Jan 15 16:52:21 2021
poni_version: 2
Detector: RayonixSx165
Detector_config: {"pixel1": 7.9e-05, "pixel2": 7.9e-05}
Distance: 2.92
Poni1: 0.0815256
Poni2: 0.07944577
Rot1: 0.0
Rot2: 0.0
Rot3: 0.0
Wavelength: 1.031396709368607e-10
```

*B3.3 X-Ray Transmission*

The following code reads in the text files storing the metadata (in particular, the readings from the ion chambers) and calculates the X-ray transmission. It requires dark scans (to calibrate the zero value of the ion chambers) and scans of the empty holes (to isolate the transmission of the electrolyte, removing the effects of the PEEK sample holder, etc.) See Chapter 3 for the theory. Of course, all code will need to be modified to account for the relevant file names and other factors; this is intended only as a starting point.

```
ioncounts.py
  1 #### WRITTEN BY LORENA GRUNDY
  2 #### DECEMBER 2021
  3
```

```
 4 import numpy as np
 5 import matplotlib.pyplot as plt
 6 import pandas as pd
 7 import csv
 8 import os
 9 import os.path
10 from os import path
11 import math
12 import time
13
14 start = time.time()
15
16 # using chemical composition and density, I calculated the transmission as
a function of r
17 # then inverted it to be able to calculate r given transmission
18 def getr(t):
19               r   =   10.6394*math.pow(t,4)   -   18.2321*math.pow(t,3)   +
12.0484*math.pow(t,2) - 3.92919*t + 0.588828
20     return r
21
22 # find how many scans there are in order to size the dataframes
23 # the three positions are named P2, P4, and P6
24 P2_maxscan = 0
25 P4_maxscan = 0
26 P6_maxscan = 0
27
28 # incrementing the maxscan variables to find the highest number
29 for file in os.listdir():
30     if 'scan' in file and 'y' in file:
31         cell = file.split('_')[0]
32         scan = file.split('_')[2].split('scan')[1]
33         pos = file.split('_')[3].split('y')[1]
34
35         if (cell == 'P2' and int(scan) > P2_maxscan):
36             P2_maxscan = int(scan)
37         if (cell == 'P4' and int(scan) > P4_maxscan):
38             P4_maxscan = int(scan)
39         if (cell == 'P6' and int(scan) > P6_maxscan):
40             P6_maxscan = int(scan)
41
42 # because of some weird stuff, I had to make the csv of mon counts of the
dark scans separately,
43 # so just reading it in here
44 # (mon is post-sample ion counter)
45 dark = pd.read_csv(r'stage3_dark.csv',index_col = 1)
46 # because of more weird stuff, I had to calculate the dark i1 separately,
normally would just
```

```
# read it from the dark scans
# (i1 is pre-sample ion counter)
P2_darki1 = pd.read_csv(r'P2_darki1.csv',index_col = 0)
P4_darki1 = pd.read_csv(r'P4_darki1.csv',index_col = 0)
P6_darki1 = pd.read_csv(r'P6_darki1.csv',index_col = 0)

# create DataFrames for transmission, r-value, corrected transmission
# (this is the one we care about) and air and reference hole transmissions
P2_t = pd.DataFrame(index = range(0, P2_maxscan+1, 1), columns = range(0,21,1))
P2_r = pd.DataFrame(index = range(0, P2_maxscan+1, 1), columns = range(0,21,1))
P2_c = pd.DataFrame(index = range(0, P2_maxscan+1, 1), columns = range(0,21,1))
P2_air = pd.DataFrame(index = range(0, P2_maxscan+1, 1), columns = range(0,1,1))
P2_ref = pd.DataFrame(index = range(0, P2_maxscan+1, 1), columns = range(0,1,1))
P4_t = pd.DataFrame(index = range(0, P4_maxscan+1, 1), columns = range(0,21,1))
P4_c = pd.DataFrame(index = range(0, P4_maxscan+1, 1), columns = range(0,21,1))
P4_r = pd.DataFrame(index = range(0, P4_maxscan+1, 1), columns = range(0,21,1))
P4_air = pd.DataFrame(index = range(0, P4_maxscan+1, 1), columns = range(0,1,1))
P4_ref = pd.DataFrame(index = range(0, P4_maxscan+1, 1), columns = range(0,1,1))
P6_t = pd.DataFrame(index = range(0, P6_maxscan+1, 1), columns = range(0,21,1))
P6_c = pd.DataFrame(index = range(0, P6_maxscan+1, 1), columns = range(0,21,1))
P6_r = pd.DataFrame(index = range(0, P6_maxscan+1, 1), columns = range(0,21,1))
P6_air = pd.DataFrame(index = range(0, P6_maxscan+1, 1), columns = range(0,1,1))
P6_ref = pd.DataFrame(index = range(0, P6_maxscan+1, 1), columns = range(0,1,1))
P6_mon = pd.DataFrame(index = range(0, P6_maxscan+1, 1), columns = range(0,1,1))

#variables to store counters
i1 = 0.0
mon = 0.0
transmission = 0.0
Ar_transmission = 0.99
air_transmission = 0.0
```

```
ref_transmission = 0.0
relative_transmission = 0.0
darki1 = 0

# read in each file
# this chunk of code just deals with the air hole scans
for file in os.listdir():
    # only read in air hole scans (will be used for correction)
    # ("txt in file" is so we look at the metadata not the SAXS image)
    if 'scan' in file and 'air' in file and 'txt' in file:
        # parse file name
        cell = file.split('_')[0]
        scan = file.split('_')[2].split('scan')[1]

        # read text file as string
        fileObject = open(file, "r")
        fileString = fileObject.read()

        # since the dark i1 value depends on the position in this case (it wouldn't normally)
        # pick the right one to read in
        if cell == 'P2':
              darki1 = P2_darki1.loc[int(scan),"0"]
        if cell == 'P4':
              darki1 = P4_darki1.loc[int(scan),"0"]
        if cell == 'P6':
              darki1 = P6_darki1.loc[int(scan),"0"]

        # parse counters using string stuff, save to variables
        i1 = float(fileString.split(', ')[3].split('i1')[1].split('=')[1])
        # subtract off the relevant dark value
        i1 -= darki1
      mon = float(fileString.split(', ')[4].split('mon')[1].split('=')[1])
        mon -= dark.loc[int(scan),"mon"]
        # calculate transmission
        transmission = mon/i1

        #record air transmission in the dataframe
        if cell == 'P2':
            P2_air.at[int(scan),0] = transmission
        if cell == 'P4':
            P4_air.at[int(scan),0] = transmission
        if cell == 'P6':
            P6_air.at[int(scan),0] = transmission

# I wanted to calculate the transmission of the AgB (reference) over time
```

```
# to check for beam stability. This doesn't factor into any of the data analysis
# but I'm saving it for posterity
 AgB = pd.DataFrame(index = range(0, P2_maxscan+1, 1), columns = range(0,1,1))
for file in os.listdir():
    #populate AgB frames
    if 'scan' in file and 'AgB' in file and 'txt' in file:
        # parse file name
        cell = file.split('_')[0]
        scan = file.split('_')[2].split('scan')[1]
        if int(scan) > 68:
            continue

        #read text file as string
        fileObject = open(file, "r")
        fileString = fileObject.read()
        #parse counters
        timestr = fileString.split('time: ')[1].split('#')[0]
        AgB.at[int(scan),"time"] = timestr

        i1 = float(fileString.split(', ')[3].split('i1')[1].split('=')[1])
        AgB.at[int(scan),"i1 raw"] = i1
        i1 -= P2_darki1.loc[int(scan),"0"]

      mon = float(fileString.split(', ')[4].split('mon')[1].split('=')[1])
        AgB.at[int(scan),"mon raw"] = mon
        mon -= dark.loc[int(scan),"mon"]

        transmission = mon/i1

        #record air transmission in the dataframe
        AgB.at[int(scan),"transmission"] = transmission
        AgB.at[int(scan),"i1"] = i1
        AgB.at[int(scan),"mon"] = mon
AgB.to_csv('AgB.csv')

# now we're going to go through all the reference holes (polymer isolated from echem)
# and calculate their transmission
for file in os.listdir():
    if 'scan' in file and 'ref' in file and 'txt' in file:

        # parse file name
        cell = file.split('_')[0]
        scan = file.split('_')[2].split('scan')[1]

```

```
167         #read text file as string
168         fileObject = open(file, "r")
169         fileString = fileObject.read()
170         #parse counters
171         if cell == 'P2':
172               darki1 = P2_darki1.loc[int(scan),"0"]
173         if cell == 'P4':
174               darki1 = P4_darki1.loc[int(scan),"0"]
175         if cell == 'P6':
176               darki1 = P6_darki1.loc[int(scan),"0"]
177 
178         #parse counters
179         i1 = float(fileString.split(', ')[3].split('i1')[1].split('=')[1])
180         i1 -= darki1
181        mon = float(fileString.split(', ')[4].split('mon')[1].split('=')[1])
182         mon -= dark.loc[int(scan),"mon"]
183         transmission = mon/i1
184 
185          # now we have the air transmission from above, so we can use that
to correct the
186         # sample transmission so we get only the transmission of the polymer
itself
187         if cell == 'P2':
188             air_transmission = P2_air.loc[int(scan),0]
189         if cell == 'P4':
190             air_transmission = P4_air.loc[int(scan),0]
191         if cell == 'P6':
192             air_transmission = P6_air.loc[int(scan),0]
193 
194         transmission /= air_transmission
195         transmission /= Ar_transmission
196 
197         if cell == 'P2':
198             P2_ref.at[int(scan),0] = transmission
199         if cell == 'P4':
200             P4_ref.at[int(scan),0] = transmission
201         if cell == 'P6':
202             P6_ref.at[int(scan),0] = transmission
203 
204 # now we're ready to go through the actual positions!
205 for file in os.listdir():
206       # only look at the scans that have "y" in it because those are the
position ones
207     if 'scan' in file and 'y' in file and 'txt' in file:
208 
209         # parse file name
210         cell = file.split('_')[0]
```

```
211         scan = file.split('_')[2].split('scan')[1]
212         pos = file.split('_')[3].split('y')[1]
213
214         #read text file as string
215         fileObject = open(file, "r")
216         fileString = fileObject.read()
217
218         # get the right dark info
219         if cell == 'P2':
220               darki1 = P2_darki1.loc[int(scan),"0"]
221         if cell == 'P4':
222               darki1 = P4_darki1.loc[int(scan),"0"]
223         if cell == 'P6':
224               darki1 = P6_darki1.loc[int(scan),"0"]
225
226         # parse counters, subtract dark, and calculate transmission
227         i1 = float(fileString.split(', ')[3].split('i1')[1].split('=')[1])
228         i1 -= darki1
229       mon = float(fileString.split(', ')[4].split('mon')[1].split('=')[1])
230         mon -= dark.loc[int(scan),"mon"]
231         transmission = mon/i1
232
233         # put uncorrected transmission into dataframes
234         # this is kinda useless
235         if cell == 'P2':
236             P2_t.at[int(scan),int(pos)] = transmission
237         if cell == 'P4':
238             P4_t.at[int(scan),int(pos)] = transmission
239         if cell == 'P6':
240             P6_t.at[int(scan),int(pos)] = transmission
241            # for some reason I also just collected the mon count as f(time)
242             # I think this was to test the stability of the ion counters
243             P6_mon.at[int(scan),int(pos)] = mon
244
245         # find the relevant air and ref transmission from the csvs we made
above
246         if cell == 'P2':
247             air_transmission = P2_air.loc[int(scan),0]
248             ref_transmission = P2_ref.loc[int(scan),0]
249         if cell == 'P4':
250             air_transmission = P4_air.loc[int(scan),0]
251             ref_transmission = P4_ref.loc[int(scan),0]
252         if cell == 'P6':
253             air_transmission = P6_air.loc[int(scan),0]
254             ref_transmission = P6_ref.loc[int(scan),0]
255
256       # correct for the air hole (so now we have the corrected transmission)
```

```
257         transmission /= air_transmission
258         transmission /= Ar_transmission
259 
260         # calculate r from the transmission using the functions defined at
top
261         r = getr(transmission)
262 
263         #put corrected transmission into dataframes
264         if cell == 'P2':
265             P2_c.at[int(scan),int(pos)] = transmission
266         if cell == 'P4':
267             P4_c.at[int(scan),int(pos)] = transmission
268         if cell == 'P6':
269             P6_c.at[int(scan),int(pos)] = transmission
270 
271         # constrain r to the realm of reason
272         if (r < 0):
273             r = 0
274         if (r > 0.5):
275             r = 0
276 
277 # store dataframes as csvs
278 P2_air.to_csv('P2_air_transmission.csv')
279 P4_air.to_csv('P4_air_transmission.csv')
280 P6_air.to_csv('P6_air_transmission.csv')
281 
282 P2_t.to_csv('P2_raw_transmission.csv')
283 P4_t.to_csv('P4_raw_transmission.csv')
284 P6_t.to_csv('P6_raw_transmission.csv')
285 
286 P2_c.to_csv('P2_transmission.csv')
287 P4_c.to_csv('P4_transmission.csv')
288 P6_c.to_csv('P6_transmission.csv')
289 
290 P2_r.to_csv('P2_r_transmission.csv')
291 P4_r.to_csv('P4_r_transmission.csv')
292 P6_r.to_csv('P6_r_transmission.csv')
293 
294 P2_ref.to_csv('P2_ref_transmission.csv')
295 P4_ref.to_csv('P4_ref_transmission.csv')
296 P6_ref.to_csv('P6_ref_transmission.csv')
297 
298 P6_mon.to_csv('P6_mon.csv')
299 
300 end = time.time()
301 print("time elapsed: ")
302 print(end-start)
```

In later versions of the data acquisition process at SSRL, the metadata is stored in csv files. In this case, lines 205-231 become:

```
for file in os.listdir():
   if 'loop' in file and '_y' in file and 'csv' in file:
         print(file)

         # parse file name
         cell = file.split('_')[0]
         scan = file.split('_')[2].split('loop')[1]
         pos = file.split('_')[3].split('y')[1]

         # we took some practice scans with loop1000
         # I don't want to deal with those
         if int(scan) >= 1000:
               continue

         # read counters
         tempdf = pd.read_csv(file)
         i1 = float(tempdf.iat[0,4])
         mon = float(tempdf.iat[0,5])

         # find appropriate dark
         darki1 = float(dark.loc[int(scan),"i1"])
         darkmon = float(dark.loc[int(scan),"mon"])

         # correct for dark
         i1 -= darki1
         mon -= darkmon
         transmission = mon/i1
```

The code above creates csv files, such as "P6_r_transmission.csv," containing a row for each loop through the positions, a column for each position, and, in each cell, the *r*-value based on the X-ray transmission as per the theory described in Chapters 3 and 10.

### *B3.4 Image Processing*

As described in Chapter 3, several processes need to be applied to the two-dimensional SAXS images. First, in "subtract.py," the dark image is subtracted in order to zero the detector, and a transmission-corrected blank image is subtracted. The image is then corrected by the transmission value at that position and time.

subtract.py

```
#### WRITTEN BY LORENA GRUNDY
#### DECEMBER 2021
```

```
#### make sure to run ioncounts.py first so that you have the transmission values

import numpy as np
import matplotlib.pyplot as plt
import pandas as pd
import csv
import os
import os.path
from os import path
import math
import time
from PIL import Image as pil
import imageio

start = time.time()

# create dataframe to store transmission values
transmission_df = pd.read_csv(r'P6_transmission.csv',index_col = 0)

#scan through the positions
for file in os.listdir():
    # we want to read in the SAXS images this time, so need tif in the file name
     # we want to read in the raw ones, not subtracted or integrated (that will come later)
    # this time I'm only looking at the P6 data
    if 'scan' in file and 'y' in file and 'P6' in file and 'tif' in file and 'sub' not in file and 'int' not in file:

        # parse file name
        cell = file.split('_')[0]
        scan = file.split('_')[2].split('scan')[1]
        pos = file.split('_')[3].split('y')[1]

        print(file)

        #read tif file as array
        scan_image = np.asarray(pil.open(file), dtype = np.float32)

        # get the relevant transmission value
        transmission = transmission_df.loc[int(scan),pos]

        # find the relevant dark image to subtract and read it in
        dark_name = "dark_s3_scan" + scan + "_0001.tif"
        dark_image = np.asarray(pil.open(dark_name), dtype = np.float32)

```

```
46          # find the relevant blank image (air hole) to correct for and read
it in
47          blank_name = cell + "_s3_scan" + scan + "_air_0001.tif"
48          blank_image = np.asarray(pil.open(blank_name), dtype = np.float32)
49
50          # what to name subtracted image (basically, append "sub")
51          subtracted_name = cell + "_s3_scan" + scan + "_y" + pos + "_sub.tif"
52
53           # subtract the dark image, and the sample transmission times the
dark-corrected blank
54          # this transmission-correction is so that we only subtract for the
amount of blank scattering
55          # that is not absorbed by the polymer
56                        subtracted_image   =   (scan_image   -   dark_image)   -
transmission*(blank_image - dark_image)
57
58          # save subtracted image as image
59           imageio.imwrite(subtracted_name,np.asarray(subtracted_image, dtype
= np.float32))
60
61           # we're also going to save images with an additional transmission
correction
62          # this is so that the observed scattering intensity represents only
the population densities
63              # and is not skewed by the salt concentration and therefore
transmission
64          subtracted_corrected_name = cell + "_s3_scan" + scan + "_y" + pos +
"_sub_corr.tif"
65
66          subtracted_corrected_image = subtracted_image / transmission
67
68
imageio.imwrite(subtracted_corrected_name,np.asarray(subtracted_corrected_ima
ge, dtype = np.float32))
69
70 end = time.time()
71 print("time elapsed: ")
72 print(end-start)
```

In integrate.py, we use the images generated by subtract.py, along with the poni file, to translate our images into q-space using PyFAI. The result is saved as a tif file, where instead of $x$- and $y$-axes, the data is stored on $\chi$- and $q$-axes.

integrate.py

```
 1 #### WRITTEN BY LORENA GRUNDY
 2 #### DECEMBER 2021
```

```
#### make sure to run subtract.py first so that you have the subtracted images to integrate
#### and note that subtract.py relies on having run ioncounts.py to get the ion counts
#### you will also need the poni file to provide information about sample-to-detector distance etc
#### which you can get via PyFAI

import numpy as np
import matplotlib.pyplot as plt
import pandas as pd
import csv
import os
import os.path
from os import path
import math
import time
from PIL import Image as pil
import imageio
import pyFAI, fabio

start = time.time()

# number of azimuthal slices to make
# please make this divisible by 4!
nslices = 36
# number of q-rings to make
nrings = 1024

# make the azimuthal imtegrator based on the poni file
ai = pyFAI.load("1-5_calib_3.poni")

# make sure you've already run subtract.py to get PEEK subtracted images
# scan through the subtracted images:
for file in os.listdir():
    # in this iteration we're only looking at the transmission-corrected subtracted images
    # change to "sub.tif" if you want the non-transmission-corrected subtracted images
    if 'P6' in file and 'scan' in file and 'sub_corr.tif' in file:

        # parse file name
        cell = file.split('_')[0]
        scan = file.split('_')[2].split('scan')[1]
        pos = file.split('_')[3].split('y')[1]

        print(file)
```

```
45
46          #read tif file as array
47          img_array = np.asarray(pil.open(file), dtype = np.float32)
48
49          # run the azimuthal integrator with the parameters we've set
50           integrated_image, q_values, chi_values = ai.integrate2d(img_array,
nrings,  nslices,  unit="q_nm^-1",  method='IntegrationMethod(2d  int,  pseudo
split, histogram, cython)')
51
52          # name the integrated file;
53            # we're going to save it as a tif because that's just the most
efficient way to save a matrix of numbers
54               integrated_name  =  cell  +  "_s3_scan"  +  scan  +  "_y"  +  pos  +
"_int_corr.tif"
55
56          # every third scan, we used 30 second exposure instead of 10 second
57            # I'm just gonna divide those images by 3 so that the intensity
should be the same for all images
58          if int(scan) % 3 == 0:
59              integrated_image = integrated_image / 3
60
61          # save as tif
62           imageio.imwrite(integrated_name,np.asarray(integrated_image, dtype
= np.float32))
63
64 # save the chi values and q values corresponding to the slices, so we have
an x-axis for our later analysis
65 np.savetxt('chi_values.csv', chi_values, delimiter = ", ")
66 np.savetxt('q_values.csv', q_values, delimiter = ", ")
67
68 end = time.time()
69 print("time elapsed: ")
70 print(end-start)
```

Finally, in fitting.py, we perform an azimuthal average by summing across all rows of our integrated images, then use the lmfit [145] package to create a BCC model consisting of three peaks, at $q^*$, $\sqrt{2}q^*$ and $\sqrt{3}q^*$, where the location of the primary scattering ($q^*$) peak is adjustable. The domain spacing is then used to calculate the *r*-value based on *ex situ* scattering data. In this version of the code, only the domain spacing and *r*-value are saved; however, the full peak fitting information is available, enabling calculation of, for example, the ratio of the integrals of the $\sqrt{2}q^*$ and $\sqrt{3}q^*$ peaks (see Chapter 10).

fitting.py

```
1 #### WRITTEN BY LORENA GRUNDY
2 #### FEBRUARY 2022
3 #### run subtract.py and integrate.py to generate corrected images
```

```
 4
 5 import numpy as np
 6 import matplotlib.pyplot as plt
 7 import pandas as pd
 8 import csv
 9 import os
10 import os.path
11 from os import path
12 import math
13 import time
14 from PIL import Image as pil
15 import imageio
16
17 from lmfit.models import PseudoVoigtModel
18
19 start = time.time()
20
21 # for SEO(4-22.4), function to calculate r from domain spacing based on ex
situ scattering
22 def getr(d):
23     r = 1.168*math.log(d) - 3.283
24     return r
25
26 # make sure you have run integrate.py to get integrated images
27
28 # read in q-values
29 q_values = np.genfromtxt('q_values.csv', delimiter=',')
30
31 # constrain q from 0.2 to 1 nm-1
32 qmin = 0.2
33 qmax = 1
34 min_index = 0
35 max_index = 0
36 for i in range(0, 1024):
37     if q_values[i] < qmin:
38         min_index = i
39     if q_values[i] > qmax:
40         max_index = i
41         break
42
43 q_values = q_values[min_index:max_index]
44
45 ### define BCC model
46
47 peak1 = PseudoVoigtModel(prefix = 'p1_')
48 peak2 = PseudoVoigtModel(prefix = 'p2_')
49 peak3 = PseudoVoigtModel(prefix = 'p3_')
```

```
50
51 bccmod = peak1 + peak2 + peak3
52
53 # guess for primary peak for r = 0.16 SEO(4-22.4):
54 guess_qstar = 0.33
55
56 # set guesses for the start values of the parameters
57 pars = bccmod.make_params()
58 pars['p1_center'].set(value=guess_qstar, min=0.25, max=0.45)
59 pars['p1_sigma'].set(value=0.01)
60 pars['p1_amplitude'].set(value=30)
61
62 # for a BCC morphology, the second peak must be at root2 of the first peak
63 # this line enforces that constraint
64 pars['p2_center'].set(value=pars['p1_center']*math.pow(2,0.5))
65 pars['p2_sigma'].set(value=0.01)
66 pars['p2_amplitude'].set(value=3)
67 pars.add('p2_center', expr = 'p1_center*(2**0.5)')
68
69 # for a BCC morphology, the third peak must be at root3 of the first peak
70 # this line enforces that constraint
71 pars['p3_center'].set(value=pars['p1_center']*math.pow(3,0.5))
72 pars['p3_sigma'].set(value=0.01)
73 pars['p3_amplitude'].set(value=3)
74 pars.add('p3_center', expr = 'p1_center*(3**0.5)')
75
76 # initialize the model
77 init = bccmod.eval(pars, x = q_values)
78
79 P6_d = pd.DataFrame()
80 P6_r = pd.DataFrame()
81 P6_d0 = pd.DataFrame()
82 P6_r0 = pd.DataFrame()
83
84 # scan through integrated images
85 for file in os.listdir():
86     # to scan through all integrated images for P6
87     if 'P6' in file and 'y' in file and 'int.tif' in file:
88
89         # parse file name
90         cell = file.split('_')[0]
91         scan = file.split('_')[2].split('scan')[1]
92         pos = file.split('_')[3].split('y')[1]
93
94         # only examine positions within the electrolyte
95         if int(pos) < 2 or int(pos) > 12:
96             continue
```

```
97
98          if int(scan) > 75:
99              continue
100
101         print(file)
102
103         # read tif file as array
104         img_array = np.asarray(pil.open(file), dtype = np.float32)
105         # azimuthal average
106         I_values = np.sum(img_array, axis = 0)
107         I_values = I_values[min_index:max_index]
108
109         out = bccmod.fit(I_values, pars, x = q_values)
110
111         # when un-commented, this code generates a plot
112         # which allows visual inspection of the fit quality
113         """residual = I_values - out.best_fit
114
115         plt.plot(q_values, I_values)
116         plt.plot(q_values, out.init_fit, '--', label='initial fit')
117         plt.plot(q_values, out.best_fit, '-', label='best fit')
118         plt.legend()
119         plt.show()
120
121         plt.plot(q_values, residual)
122         plt.show()"""
123
124         # read the location of the primary peak
125         qstar = out.best_values['p1_center']
126         # convert to domain spacing
127         d = 2*3.14159/qstar
128         # convert to r using the function defined above
129         r = getr(d)
130         print("primary scattering peak: " + str(d) + " nm")
131         print("r value: " + str(r))
132
133         P6_d.at[int(scan),int(pos)] = d
134         P6_r.at[int(scan),int(pos)] = r
135
136         # when un-commented, this line prints the fit data
137         # print(out.fit_report(min_correl=0.5))
138
139 # save the results of both domain spacing and r to csv files
140 P6_d.to_csv('P6_dspacing.csv')
141 P6_r.to_csv('P6_rvalue_from_d.csv')
142 end = time.time()
143 print("time elapsed: ")
```

```
144 print(end-start)
```

As mentioned previously, the code included in this section is the code that was used for the analysis in Chapter 10, as it is a more refined version of the code used for Chapter 9. However, Chapter 9 includes calculation of Herman's orientation parameter, which is not included in Chapter 10. The code snippet below shows how this calculation was done.

```
 1 #### Lorena Grundy
 2 #### March 2021
 3
 4 # in preceding code, images were processed and transformed using PyFAI
 5 # similar to what is done in subtract.py
 6 # the boolean "failed" was set to True if fitting the azimuthally-averaged
data failed
 7 # so as not to try this more complex analysis on bad data
 8
 9         # make an array where invariants of each slice are stored
10         inv_chi = np.zeros(nslices)
11         herman = 2.0
12
13         if failed == False:
14             # calculate the invariant of each slice
15             for i in range(nslices):
16                 try:
17                      # fitting was done with a home-made fitting algorithm
imported
18                     # this should be done using lmfit in future.
19                         params, q_cut, I_cut, I_cut_fit, I_cut_fit_peak =
fit.peak_fit(q_values_A, I[i], ShowBkgFit = False, ShowFit = False)
20                      # calculate the invariant of each slice, normalize by
total intensity
21                          inv_chi[i] = np.sum(I_cut_fit_peak*q_cut*q_cut) /
intensity
22                 except:
23                     inv_chi[i] = 0.0
24
25             # ------ implement Herman orientation --------- #
26             # fold up inv_chi to utilize all data (we will only integrate 0
to 90 degrees)
27             fold_len = int(nslices/4)
28
29             folded = np.zeros(fold_len)
30             for i in range(0, fold_len):
31                 folded[i] += inv_chi[i]
32                 folded[i] += inv_chi[i + fold_len*2]
33                 folded[i] += inv_chi[fold_len*2 - i - 1]
34                 folded[i] += inv_chi[nslices - i - 1]
```

```
35
36              # variables to store information
37              num = 0.0
38              denom = 0.0
39               # shift by 90 degrees to match the conventional definition of
zero (decide whether or not you want to do this)
40              shift = np.pi/2
41              # implementing equations 9.14 and 9.15
42              for i in range(0, fold_len):
43                                                                      num    +=
folded[i]*np.cos(chi_radians[i]+shift)*np.cos(chi_radians[i]+shift)*np.sin(ch
i_radians[i]+shift)
44                  denom += folded[i]*np.sin(chi_radians[i]+shift)
45              # "herman" is the value of the orientation parameter, which can
now be stored
46              herman = (3*(num/denom) - 1)/2
```

### *B3.5 Electrochemical Data*

Electrochemical experiments are typically controlled using EC-Lab installed on a PC, resulting in the data being stored in EC-Lab files. In EC-Lab, these can be converted to text files. Using echem.py, we can translate these text files into elapsed time from whatever we designate as $t = 0$, and can combine multiple text files into one dataframe, which we can save as a csv for ease of plotting later.

echem.py

```
#### WRITTEN BY LORENA GRUNDY
#### December 2021

# using EC-Lab, first save desired electrochem files as .txt

import numpy as np
import matplotlib.pyplot as plt
import pandas as pd
import csv
import os
import os.path
from os import path
import math
import time
import datetime

# create dataframe for all electrochem data
P2_echem = pd.DataFrame(index = range(0, 1, 1), columns = range(0,1,1))

# set the time from which all other times will be subtracted
P2_startTuple = (2021, 7, 5, 16, 23, 44, 0, 0, 0)
```

```
P2_startTime = time.mktime(P2_startTuple)

# variables in which to save time data
d = 0
mo = 0
h = 0
m = 0
s = 0
i = 0

# open the first text file and save each data point to the dataframe
for line in open("P6_0_01_CP_C16.txt"):
  # disregard the label
  if line.split('/')[0] == "time":
        continue

  # parse the time
  date = line.split(" ")[0]
  mo = int(date.split('/')[0])
  d = int(date.split('/')[1])
  y = int(date.split('/')[2])
  timestr = line.split(" ")[1].split("       ")[0]
  h = int(timestr.split(':')[0])
  m = int(timestr.split(':')[1])
  s = int(timestr.split(':')[2].split('.')[0])
  scan_tuple = (y, mo, d, h, m, s, 0, 0, 0)
  scan_mk = time.mktime(scan_tuple)

  # subtract the start time
  elapsed = scan_mk - P2_startTime

  # convert to hours
  elapsed = elapsed/(60*60)

  # read in the potential
  potential = line.split("       ")[1].split("\n")[0]

  # save the date, time, potential, and elapsed time to the dataframe
  P2_echem.at[i, "date"] = date
  P2_echem.at[i, "time"] = timestr
  P2_echem.at[i, "potential"] = potential
  P2_echem.at[i, "elapsed"] = elapsed

  # increment to the next line
  i = i + 1

# print the elapsed time as of the end of the first text file
```

```
# this is useful in recording after how much time the conditions were changed
print(elapsed)

# repeat the same process for the other steps in the electrochem sequence
# (i.e. the other electrochem text files)
for line in open("P6_0_02_CP_C16.txt"):
  if line.split('/')[0] == "time":
        continue
  date = line.split(" ")[0]
  mo = int(date.split('/')[0])
  d = int(date.split('/')[1])
  y = int(date.split('/')[2])
  timestr = line.split(" ")[1].split("       ")[0]
  h = int(timestr.split(':')[0])
  m = int(timestr.split(':')[1])
  s = int(timestr.split(':')[2].split('.')[0])
  scan_tuple = (y, mo, d, h, m, s, 0, 0, 0)
  scan_mk = time.mktime(scan_tuple)
  elapsed = scan_mk - P2_startTime
  elapsed = elapsed/(60*60)
  potential = line.split("       ")[1].split("\n")[0]
  P2_echem.at[i, "date"] = date
  P2_echem.at[i, "time"] = timestr
  P2_echem.at[i, "potential"] = potential
  P2_echem.at[i, "elapsed"] = elapsed
  i = i + 1
print(elapsed)
for line in open("P6_0_restart_01_CP_C16.txt"):
  if line.split('/')[0] == "time":
        continue
  date = line.split(" ")[0]
  mo = int(date.split('/')[0])
  d = int(date.split('/')[1])
  y = int(date.split('/')[2])
  timestr = line.split(" ")[1].split("       ")[0]
  h = int(timestr.split(':')[0])
  m = int(timestr.split(':')[1])
  s = int(timestr.split(':')[2].split('.')[0])
  scan_tuple = (y, mo, d, h, m, s, 0, 0, 0)
  scan_mk = time.mktime(scan_tuple)
  elapsed = scan_mk - P2_startTime
  elapsed = elapsed/(60*60)
  potential = line.split("       ")[1].split("\n")[0]
  P2_echem.at[i, "date"] = date
  P2_echem.at[i, "time"] = timestr
  P2_echem.at[i, "potential"] = potential
```

```
115   P2_echem.at[i, "elapsed"] = elapsed
116   i = i + 1
117 print(elapsed)
118 for line in open("P6_0_restart_02_CP_C16.txt"):
119   if line.split('/')[0] == "time":
120         continue
121   date = line.split(" ")[0]
122   mo = int(date.split('/')[0])
123   d = int(date.split('/')[1])
124   y = int(date.split('/')[2])
125   timestr = line.split(" ")[1].split("       ")[0]
126   h = int(timestr.split(':')[0])
127   m = int(timestr.split(':')[1])
128   s = int(timestr.split(':')[2].split('.')[0])
129   scan_tuple = (y, mo, d, h, m, s, 0, 0, 0)
130   scan_mk = time.mktime(scan_tuple)
131   elapsed = scan_mk - P2_startTime
132   elapsed = elapsed/(60*60)
133   potential = float(line.split("       ")[1].split("\n")[0])
134   P2_echem.at[i, "date"] = date
135   P2_echem.at[i, "time"] = timestr
136   P2_echem.at[i, "potential"] = potential
137   P2_echem.at[i, "elapsed"] = elapsed
138   i = i + 1
139 print(elapsed)
140 for line in open("P6_0_restart_03_OCV_C16.txt"):
141   if line.split('/')[0] == "time":
142         continue
143   date = line.split(" ")[0]
144   mo = int(date.split('/')[0])
145   d = int(date.split('/')[1])
146   y = int(date.split('/')[2])
147   timestr = line.split(" ")[1].split("       ")[0]
148   h = int(timestr.split(':')[0])
149   m = int(timestr.split(':')[1])
150   s = int(timestr.split(':')[2].split('.')[0])
151   scan_tuple = (y, mo, d, h, m, s, 0, 0, 0)
152   scan_mk = time.mktime(scan_tuple)
153   elapsed = scan_mk - P2_startTime
154   elapsed = elapsed/(60*60)
155   potential = float(line.split("       ")[1].split("\n")[0])
156   P2_echem.at[i, "date"] = date
157   P2_echem.at[i, "time"] = timestr
158   P2_echem.at[i, "potential"] = potential
159   P2_echem.at[i, "elapsed"] = elapsed
160   i = i + 1
161
```

```
# save the dataframe to a csv
P6_echem.to_csv("P6_echem.csv")
```

*B3.6 Converting to Elapsed Time*

The electrochemistry data has been converted to elapsed time. However, the SAXS data is stored in csv files in which the rows are numbered by how many loops have been taken through the positions. It would be simplest to re-number these rows according to the time at which that loop started. However, this is imprecise, in that it approximates all scans in a given loop as having occurred at the time that loop started. The following file, fulltime.py, creates a csv where the rows are loops and the columns are positions, and each cell stores the elapsed time at which that scan was taken. This is used later as the x-axis values in the plots.

fulltime.py

```
#### WRITTEN BY LORENA GRUNDY
#### December 2022

import pandas as pd
import time
import datetime
import numpy as np
import matplotlib.pyplot as plt
import csv
import os
import os.path
from os import path
import math

P2_time = pd.DataFrame()

#scan through the actual positions
for file in os.listdir():
    if 'scan' in file and 'y' in file and 'txt' in file and 'P2' in file:

        # parse file name
        cell = file.split('_')[0]
        scan = file.split('_')[2].split('scan')[1]
        pos = file.split('_')[3].split('y')[1]

        #read text file as string
        fileObject = open(file, "r")
        fileString = fileObject.read()

        #parse time
        timestr = fileString.split('time: ')[1].split(' 2021')[0]

```

```
33          #put time string into dataframe
34          P2_time.at[int(scan),int(pos)] = timestr
35
36  # this csv stores the time strings for each scan
37  P2_time.to_csv('P2_fulltimes.csv')
38
39  # make a csv for the elapsed time for each scan
40  P2_hours = pd.DataFrame(index = range(0,1,1), columns = range(0,1,1))
41
42  # set the start time
43  start_tuple = (2021, 7, 5, 16, 23, 44, 0, 0, 0)
44  start_mk = time.mktime(start_tuple)
45
46  # creating variables to store the data
47  # (values at this point are meaningless)
48  d = 0
49  mo = 11
50  h = 0
51  m = 0
52  s = 0
53  date = ""
54  scan_tuple = (2021, 7, 4, 15, 40, 29, 0, 0, 0)
55  scan_mk = time.mktime(dark_start_tuple)
56  elapsed = 0.0
57
58  # now we will go through the time strings and convert them
59  # to elapsed time
60  titles = list(P2_time.columns.values)
61
62  for index, row in P2_time.iterrows():
63     for name in titles:
64          # parse the date strings
65           date = row[name]
66           d = int(date.split(' ')[2])
67           h = int(date.split(' ')[3].split(':')[0])
68           m = int(date.split(' ')[3].split(':')[1])
69           s = int(date.split(' ')[3].split(':')[2].split(' ')[0])
70
71          # turn it into a time
72           scan_tuple = (2021, 7, d, h, m, s, 0, 0, 0)
73           scan_mk = time.mktime(scan_tuple)
74
75          # calculate the elapsed time, convert to hours, store it
76           elapsed = scan_mk - dark_start_mk
77           elapsed = elapsed/(60*60)
78           P2_hours.at[index,name] = elapsed
79
```

```
80 # sort the dataframe and save it
81 P2_hours.sort_index(axis = 0, inplace = True)
82 P2_hours.sort_index(axis = 1, inplace = True)
83 P2_hours.to_csv('P2_hours.csv')
```

*B3.7 Plotting the Raw SAXS Data*

To generate $I(q)$ plots as a function of time, we first need to translate our integrated images to csv files. The following code, make_integrated_csv.py, creates three csv files for each position, each with $q$-values as the index column and loop number as the column titles: the first includes the four sectors around $\chi = 0°$ and 180°, the second includes the four sectors around $\chi = 90°$ and 270°, and the third averages across all $\chi$. The sector averaged data is multiplied by nine (because it is four out of the 36 sectors) for ease of comparison of the intensity.

make_integrated_csv.py

```
  1 #### WRITTEN BY LORENA GRUNDY
  2 #### February 2022
  3
  4 import numpy as np
  5 import matplotlib.pyplot as plt
  6 import pandas as pd
  7 import csv
  8 import os
  9 import os.path
 10 from os import path
 11 import math
 12 import time
 13 from PIL import Image as pil
 14 import imageio
 15
 16 start = time.time()
 17
 18 # make sure you have run integrate.py to get integrated images
 19
 20 # read in q-values
 21 q_values = np.genfromtxt('q_values.csv', delimiter=',')
 22
 23 # constrain q from 0.2 to 1 nm-1
 24 qmin = 0.2
 25 qmax = 1
 26 min_index = 0
 27 max_index = 0
 28 for i in range(0, 1024):
 29     if q_values[i] < qmin:
 30         min_index = i
```

```
    if q_values[i] > qmax:
        max_index = i
        break

q_values = q_values[min_index:max_index]

# make dataframes for each position
# set q as the index row
P6_y2 = pd.DataFrame()
P6_y2['q'] = q_values
P6_y2.set_index('q', inplace = True)
P6_y3 = pd.DataFrame()
P6_y3['q'] = q_values
P6_y3.set_index('q', inplace = True)
P6_y4 = pd.DataFrame()
P6_y4['q'] = q_values
P6_y4.set_index('q', inplace = True)
P6_y5 = pd.DataFrame()
P6_y5['q'] = q_values
P6_y5.set_index('q', inplace = True)
P6_y6 = pd.DataFrame()
P6_y6['q'] = q_values
P6_y6.set_index('q', inplace = True)
P6_y7 = pd.DataFrame()
P6_y7['q'] = q_values
P6_y7.set_index('q', inplace = True)
P6_y8 = pd.DataFrame()
P6_y8['q'] = q_values
P6_y8.set_index('q', inplace = True)
P6_y9 = pd.DataFrame()
P6_y9['q'] = q_values
P6_y9.set_index('q', inplace = True)
P6_y10 = pd.DataFrame()
P6_y10['q'] = q_values
P6_y10.set_index('q', inplace = True)
P6_y11 = pd.DataFrame()
P6_y11['q'] = q_values
P6_y11.set_index('q', inplace = True)
P6_y12 = pd.DataFrame()
P6_y12['q'] = q_values
P6_y12.set_index('q', inplace = True)

# first we will average the four sectors around chi = 0 and 180
# scan through integrated images
for file in os.listdir():
    if 'int_corr.tif' in file and 'P6' in file and 'y' in file:

```

```
        # parse file name
        cell = file.split('_')[0]
        scan = file.split('_')[2].split('scan')[1]
        pos = file.split('_')[3].split('y')[1]

        print(file)

        # read tif file as array
        img_array = np.asarray(pil.open(file), dtype = np.float32)

        # only use the rows corresponding to the two sectors around chi = 0
        # and the two sectors around chi = 180
        I_values = (img_array[0,:] + img_array[35,:] + img_array[17,:] + img_array[18,:])*9
        I_values = I_values[min_index:max_index]

        # save the averaged I array to the relevant dataframe
        if pos == '2':
            P6_y2[int(scan)] = I_values
        if pos == '3':
            P6_y3[int(scan)] = I_values
        if pos == '4':
            P6_y4[int(scan)] = I_values
        if pos == '5':
            P6_y5[int(scan)] = I_values
        if pos == '6':
            P6_y6[int(scan)] = I_values
        if pos == '7':
            P6_y7[int(scan)] = I_values
        if pos == '8':
            P6_y8[int(scan)] = I_values
        if pos == '9':
            P6_y9[int(scan)] = I_values
        if pos == '10':
            P6_y10[int(scan)] = I_values
        if pos == '11':
            P6_y11[int(scan)] = I_values
        if pos == '12':
            P6_y12[int(scan)] = I_values

# sort and save the dataframes
P6_y2.sort_index(axis = 1, inplace = True)
P6_y2.to_csv('P6_y2_zerodeg_corr.csv')
P6_y3.sort_index(axis = 1, inplace = True)
P6_y3.to_csv('P6_y3_zerodeg_corr.csv')
P6_y4.sort_index(axis = 1, inplace = True)
```

```
P6_y4.to_csv('P6_y4_zerodeg_corr.csv')
P6_y5.sort_index(axis = 1, inplace = True)
P6_y5.to_csv('P6_y5_zerodeg_corr.csv')
P6_y6.sort_index(axis = 1, inplace = True)
P6_y6.to_csv('P6_y6_zerodeg_corr.csv')
P6_y7.sort_index(axis = 1, inplace = True)
P6_y7.to_csv('P6_y7_zerodeg_corr.csv')
P6_y8.sort_index(axis = 1, inplace = True)
P6_y8.to_csv('P6_y8_zerodeg_corr.csv')
P6_y9.sort_index(axis = 1, inplace = True)
P6_y9.to_csv('P6_y9_zerodeg_corr.csv')
P6_y10.sort_index(axis = 1, inplace = True)
P6_y10.to_csv('P6_y10_zerodeg_corr.csv')
P6_y11.sort_index(axis = 1, inplace = True)
P6_y11.to_csv('P6_y11_zerodeg_corr.csv')
P6_y12.sort_index(axis = 1, inplace = True)
P6_y12.to_csv('P6_y12_zerodeg_corr.csv')

# now do the same thing for the four sectors corresponding to
# chi = 90 and 270
# scan through integrated images
for file in os.listdir():
    if 'int_corr.tif' in file and 'P6' in file and 'y' in file:

        # parse file name
        cell = file.split('_')[0]
        scan = file.split('_')[2].split('scan')[1]
        pos = file.split('_')[3].split('y')[1]

        print(file)

        #read tif file as array
        img_array = np.asarray(pil.open(file), dtype = np.float32)
        # pick the four sectors corresponding to chi = 90 and 270
          I_values = (img_array[8,:] + img_array[9,:] + img_array[26,:] +
img_array[27,:])*9
        I_values = I_values[min_index:max_index]

        # add to dataframe
        if pos == '2':
            P6_y2[int(scan)] = I_values
        if pos == '3':
            P6_y3[int(scan)] = I_values
        if pos == '4':
            P6_y4[int(scan)] = I_values
        if pos == '5':
            P6_y5[int(scan)] = I_values
```

```
        if pos == '6':
            P6_y6[int(scan)] = I_values
        if pos == '7':
            P6_y7[int(scan)] = I_values
        if pos == '8':
            P6_y8[int(scan)] = I_values
        if pos == '9':
            P6_y9[int(scan)] = I_values
        if pos == '10':
            P6_y10[int(scan)] = I_values
        if pos == '11':
            P6_y11[int(scan)] = I_values
        if pos == '12':
            P6_y12[int(scan)] = I_values

# sort and save dataframes
P6_y2.sort_index(axis = 1, inplace = True)
P6_y2.to_csv('P6_y2_90deg_corr.csv')
P6_y3.sort_index(axis = 1, inplace = True)
P6_y3.to_csv('P6_y3_90deg_corr.csv')
P6_y4.sort_index(axis = 1, inplace = True)
P6_y4.to_csv('P6_y4_90deg_corr.csv')
P6_y5.sort_index(axis = 1, inplace = True)
P6_y5.to_csv('P6_y5_90deg_corr.csv')
P6_y6.sort_index(axis = 1, inplace = True)
P6_y6.to_csv('P6_y6_90deg_corr.csv')
P6_y7.sort_index(axis = 1, inplace = True)
P6_y7.to_csv('P6_y7_90deg_corr.csv')
P6_y8.sort_index(axis = 1, inplace = True)
P6_y8.to_csv('P6_y8_90deg_corr.csv')
P6_y9.sort_index(axis = 1, inplace = True)
P6_y9.to_csv('P6_y9_90deg_corr.csv')
P6_y10.sort_index(axis = 1, inplace = True)
P6_y10.to_csv('P6_y10_90deg_corr.csv')
P6_y11.sort_index(axis = 1, inplace = True)
P6_y11.to_csv('P6_y11_90deg_corr.csv')
P6_y12.sort_index(axis = 1, inplace = True)
P6_y12.to_csv('P6_y12_90deg_corr.csv')

# finally, we will do the full azimuthal average
# scan through integrated images
for file in os.listdir():
    if 'int_corr.tif' in file and 'P6' in file and 'y' in file:

        # parse file name
        cell = file.split('_')[0]
        scan = file.split('_')[2].split('scan')[1]
```

```
216         pos = file.split('_')[3].split('y')[1]
217 
218         print(file)
219 
220         #read tif file as array
221         img_array = np.asarray(pil.open(file), dtype = np.float32)
222 
223         # sum over all rows (all chi values)
224         I_values = np.sum(img_array, axis = 0)
225         I_values = I_values[min_index:max_index]
226 
227         # add to the dataframe
228         if pos == '2':
229             P6_y2[int(scan)] = I_values
230         if pos == '3':
231             P6_y3[int(scan)] = I_values
232         if pos == '4':
233             P6_y4[int(scan)] = I_values
234         if pos == '5':
235             P6_y5[int(scan)] = I_values
236         if pos == '6':
237             P6_y6[int(scan)] = I_values
238         if pos == '7':
239             P6_y7[int(scan)] = I_values
240         if pos == '8':
241             P6_y8[int(scan)] = I_values
242         if pos == '9':
243             P6_y9[int(scan)] = I_values
244         if pos == '10':
245             P6_y10[int(scan)] = I_values
246         if pos == '11':
247             P6_y11[int(scan)] = I_values
248         if pos == '12':
249             P6_y12[int(scan)] = I_values
250 
251 # sort and save the dataframes
252 P6_y2.sort_index(axis = 1, inplace = True)
253 P6_y2.to_csv('P6_y2_azimuthavg_corr.csv')
254 P6_y3.sort_index(axis = 1, inplace = True)
255 P6_y3.to_csv('P6_y3_azimuthavg_corr.csv')
256 P6_y4.sort_index(axis = 1, inplace = True)
257 P6_y4.to_csv('P6_y4_azimuthavg_corr.csv')
258 P6_y5.sort_index(axis = 1, inplace = True)
259 P6_y5.to_csv('P6_y5_azimuthavg_corr.csv')
260 P6_y6.sort_index(axis = 1, inplace = True)
261 P6_y6.to_csv('P6_y6_azimuthavg_corr.csv')
262 P6_y7.sort_index(axis = 1, inplace = True)
```

```
P6_y7.to_csv('P6_y7_azimuthavg_corr.csv')
P6_y8.sort_index(axis = 1, inplace = True)
P6_y8.to_csv('P6_y8_azimuthavg_corr.csv')
P6_y9.sort_index(axis = 1, inplace = True)
P6_y9.to_csv('P6_y9_azimuthavg_corr.csv')
P6_y10.sort_index(axis = 1, inplace = True)
P6_y10.to_csv('P6_y10_azimuthavg_corr.csv')
P6_y11.sort_index(axis = 1, inplace = True)
P6_y11.to_csv('P6_y11_azimuthavg_corr.csv')
P6_y12.sort_index(axis = 1, inplace = True)
P6_y12.to_csv('P6_y12_azimuthavg_corr.csv')

end = time.time()
print("time elapsed: ")
print(end-start)
```

This code generates plots of the azimuthally-averaged $I(q)$ data, separated by polarization step and color coded to match the electrochemistry data at the time that the scan was taken (see Figure 10.9).

make_SAXSPlot.py

```
#### LORENA GRUNDY
#### December 2022

#### run make_integrated_csv.py first

import matplotlib.pyplot as plt
from matplotlib.offsetbox import AnchoredText
from matplotlib.offsetbox import AnnotationBbox
from matplotlib.offsetbox import TextArea
import pandas as pd
import numpy as np
import math
from matplotlib.ticker import (MultipleLocator, AutoMinorLocator)

# set figure font size
plt.rcParams.update({'font.size': 12})

# set y range
intensity_upper = 12000
# set q range
q_lower = 0.2
q_upper = 0.7

# make a separate figure for each position
for position in range(2, 13):

```

```
27  # generate colors for each scan so that for each echem step
28  # the colors go from red to blue, then blue to red, etc
29  start_scan = 0
30  end_scan = 5
31  num_scans = end_scan - start_scan + 1
32  colors1 = plt.cm.jet(np.linspace(0,1,num_scans))
33  start_scan2 = end_scan+1
34  end_scan2 = 24
35  num_scans = end_scan2 - start_scan2 + 1
36  colors2 = plt.cm.jet(np.linspace(0,1,num_scans))
37  colors2 = np.flipud(colors2)
38  start_scan3 = end_scan2+1
39  end_scan3 = 56
40  num_scans = end_scan3 - start_scan3 + 1
41  colors3 = plt.cm.jet(np.linspace(0,1,num_scans))
42  start_scan4 = end_scan3+1
43  end_scan4 = 75
44  num_scans = end_scan4 - start_scan4 + 1
45  colors4 = plt.cm.jet(np.linspace(0,1,num_scans))
46  colors4 = np.flipud(colors4)
47
48  # set up the figure dimensions
49  fig = plt.figure(tight_layout = True, figsize = (10, 8))
50  axs = fig.add_gridspec(3, 4)
51
52  # read in the relevant dataframe for this position
53  # generated by make_integrated_csv.py
54  readme = 'P6_y' + str(position) + '_azimuthavg_corr.csv'
55
56  #setting up P2 figure
57  p2_T = pd.read_csv(readme,index_col = 0)
58  ax1 = fig.add_subplot(axs[1:3, 0:1])
59  ax1.plot(p2_T)
60  ax2 = fig.add_subplot(axs[1:3, 1:2])
61  ax2.plot(p2_T)
62  ax3 = fig.add_subplot(axs[1:3, 2:3])
63  ax3.plot(p2_T)
64  ax4 = fig.add_subplot(axs[1:3, 3:4])
65  ax4.plot(p2_T)
66
67  # opacity for all but the last trace of each step
68  # set to 1 for fully opaque
69  # zero to only see the last trace
70  a = 0.1
71
72  # set aesthetics for the first graph
73  for i, line in enumerate(ax1.get_lines()):
```

```
74          line.set_marker('')
75          # make it disappear if it's not relevant to this step
76          if (int(i) < start_scan or int(i) > end_scan):
77                line.set_marker("")
78                line.set_linestyle("none")
79          # set the color if it is in this step
80          else:
81                line.set_marker('')
82                line.set_color(colors1[int(i - start_scan)])
83          # make it more transparent if it's not the last step
84          if (int(i) < end_scan):
85                line.set_alpha(a)
86
87    # do the same for the other graphs
88    for i, line in enumerate(ax2.get_lines()):
89          line.set_marker('')
90          if (int(i) < start_scan2 or int(i) > end_scan2):
91                line.set_marker("")
92                line.set_linestyle("none")
93          else:
94                line.set_marker('')
95                line.set_color(colors2[int(i - start_scan2)])
96          if (int(i) < end_scan2):
97                line.set_alpha(a)
98    for i, line in enumerate(ax3.get_lines()):
99          line.set_marker('')
100         if (int(i) < start_scan3 or int(i) > end_scan3):
101               line.set_marker("")
102               line.set_linestyle("none")
103         else:
104               line.set_marker('')
105               line.set_color(colors3[int(i - start_scan3)])
106         if (int(i) < end_scan3):
107               line.set_alpha(a)
108   for i, line in enumerate(ax4.get_lines()):
109         line.set_marker('')
110         if (int(i) < start_scan4 or int(i) > end_scan4):
111               line.set_marker("")
112               line.set_linestyle("none")
113         else:
114               line.set_marker('')
115               line.set_color(colors4[int(i - start_scan4)])
116         if (int(i) < end_scan4):
117               line.set_alpha(a)
118
119   # remove legends, add axis labels
120   ax1.set_xlabel('$\it{q}$' + ' (nm' + '$^{-1}$' + ')')
```

```
ax1.set_ylabel('$\it{I}$' + ' (a.u.)')
ax1.set_ylim(0,intensity_upper)
ax1.set_xlim(q_lower,q_upper)
ax2.set_xlabel('$\it{q}$' + ' (nm' + '$^{-1}$' + ')')
ax2.set_ylabel('$\it{I}$' + ' (a.u.)')
ax2.set_ylim(0,intensity_upper)
ax2.set_xlim(q_lower,q_upper)
ax3.set_xlabel('$\it{q}$' + ' (nm' + '$^{-1}$' + ')')
ax3.set_ylabel('$\it{I}$' + ' (a.u.)')
ax3.set_ylim(0,intensity_upper)
ax3.set_xlim(q_lower,q_upper)
ax4.set_xlabel('$\it{q}$' + ' (nm' + '$^{-1}$' + ')')
ax4.set_ylabel('$\it{I}$' + ' (a.u.)')
ax4.set_ylim(0,intensity_upper)
ax4.set_xlim(q_lower,q_upper)


# set up the electrochem

# elapsed hours at which the electrochem changes
dash = 2.621
dash2 = 10.864
dash3 = 26.864
dash4 = 37.2

counts1 = 0
counts2 = 0
counts3 = 0
counts4 = 0

# count the points during each step
p2 = pd.read_csv(r'P6_echem.csv',index_col = 0)
for j in range(0, len(p2.index)):
      elapsed = float(p2.loc[j, "elapsed"])
      if elapsed < dash:
            counts1 += 1
      if elapsed > dash and elapsed < dash2:
            counts2 += 1
      if elapsed > dash2 and elapsed < dash3:
            counts3 += 1
      if elapsed > dash3:
            counts4 += 1

# set up the colors, so that they will match with the SAXS data
colors1 = plt.cm.jet(np.linspace(0,1,counts1))
colors2 = plt.cm.jet(np.linspace(0,1,counts2))
colors2 = np.flipud(colors2)
```

```
168   colors3 = plt.cm.jet(np.linspace(0,1,counts3))
169   colors4 = plt.cm.jet(np.linspace(0,1,counts4))
170   colors4 = np.flipud(colors4)
171
172   colors5 = np.append(colors1, colors2, axis = 0)
173   colors6 = np.append(colors5, colors3, axis = 0)
174   colors = np.append(colors6, colors4, axis = 0)
175
176   # time bounds
177   xlower = 0
178   xupper = 38
179
180   # potential bounds
181   ylower = -1
182   yupper = 1
183
184   eplot = fig.add_subplot(axs[0, 0:4])
185
186   # read in the electrochem data and plot it
187   p2 = pd.read_csv(r'P6_echem.csv',index_col = 0)
188   times = p2['elapsed']
189   currents = p2['current']
190   p2.index = times
191   eplot.scatter(times, currents, c = colors, s = 10)
192
193   # add the dashed lines
194   eplot.plot([dash,dash],[ylower,yupper], color = 'black',linestyle =
'dashed')
195   eplot.plot([dash2,dash2],[ylower,yupper], color = 'black',linestyle =
'dashed')
196   eplot.plot([dash3,dash3],[ylower,yupper], color = 'black',linestyle =
'dashed')
197   eplot.plot([dash4,dash4],[ylower,yupper], color = 'black',linestyle =
'dashed')
198
199   # set the limits
200   eplot.set_xlim(xlower,xupper)
201   eplot.set_ylim(ylower,yupper)
202
203   # remove legends, add axis labels
204   eplot.set_xlabel('time (h)')
205   eplot.set_ylabel('$\it{E}$' + ' (V)')
206
207   # add a title so we can tell what position this is
208   titlestring = "P6, position y" + str(position) + '\n'
209   plt.title(titlestring)
210
```

```
211    #go
212    plt.show()
```

Analogously, we can make plots using the sector-averaged data. The concept is similar, except now there will be two rows of SAXS plots for each position: one row corresponding to $\chi = 0°$ and 180°, and another corresponding to $\chi = 90°$ and 270° (see Figure A10.6).

make_sectorsPlot.py

```
  1 #### LORENA GRUNDY
  2 #### December 2022
  3
  4 #### run make_integrated_csv.py first
  5
  6 import matplotlib.pyplot as plt
  7 from matplotlib.offsetbox import AnchoredText
  8 from matplotlib.offsetbox import AnnotationBbox
  9 from matplotlib.offsetbox import TextArea
 10 import pandas as pd
 11 import numpy as np
 12 import math
 13 from matplotlib.ticker import (MultipleLocator, AutoMinorLocator)
 14
 15 # set y range
 16 intensity_upper = 15000
 17
 18 for position in range(2, 13):
 19
 20    # generate colors for each scan so that for each echem step
 21    # the colors go from red to blue, then blue to red, etc
 22    start_scan = 0
 23    end_scan = 5
 24    num_scans = end_scan - start_scan + 1
 25    colors1 = plt.cm.jet(np.linspace(0,1,num_scans))
 26    start_scan2 = end_scan+1
 27    end_scan2 = 24
 28    num_scans = end_scan2 - start_scan2 + 1
 29    colors2 = plt.cm.jet(np.linspace(0,1,num_scans))
 30    colors2 = np.flipud(colors2)
 31    start_scan3 = end_scan2+1
 32    end_scan3 = 56
 33    num_scans = end_scan3 - start_scan3 + 1
 34    colors3 = plt.cm.jet(np.linspace(0,1,num_scans))
 35    start_scan4 = end_scan3+1
 36    end_scan4 = 75
 37    num_scans = end_scan4 - start_scan4 + 1
 38    colors4 = plt.cm.jet(np.linspace(0,1,num_scans))
 39    colors4 = np.flipud(colors4)
```

```
40
41  # set up the figure dimensions
42  fig = plt.figure(tight_layout = True, figsize = (9.5, 7))
43  axs = fig.add_gridspec(5, 4)
44
45  # read in the relevant dataframe for this position
46  # generated by make_integrated_csv.py
47  # this time we are looking at the chi = 0 sectors
48  readme = 'P6_y' + str(position) + '_zerodeg_corr.csv'
49
50  #setting up P2 figure
51  p2_T = pd.read_csv(readme,index_col = 0)
52  ax1 = fig.add_subplot(axs[1:3, 0:1])
53  ax1.plot(p2_T)
54  ax2 = fig.add_subplot(axs[1:3, 1:2])
55  ax2.plot(p2_T)
56  ax3 = fig.add_subplot(axs[1:3, 2:3])
57  ax3.plot(p2_T)
58  ax4 = fig.add_subplot(axs[1:3, 3:4])
59  ax4.plot(p2_T)
60
61  # set aesthetics
62  for i, line in enumerate(ax1.get_lines()):
63        line.set_marker('')
64        # make it disappear if it's not in this step
65        if (int(i) < start_scan or int(i) > end_scan):
66              line.set_marker("")
67              line.set_linestyle("none")
68        # set the color
69        else:
70              line.set_marker('')
71              line.set_color(colors1[int(i - start_scan)])
72  for i, line in enumerate(ax2.get_lines()):
73        line.set_marker('')
74        if (int(i) < start_scan2 or int(i) > end_scan2):
75              line.set_marker("")
76              line.set_linestyle("none")
77        else:
78              line.set_marker('')
79              line.set_color(colors2[int(i - start_scan2)])
80  for i, line in enumerate(ax3.get_lines()):
81        line.set_marker('')
82        if (int(i) < start_scan3 or int(i) > end_scan3):
83              line.set_marker("")
84              line.set_linestyle("none")
85        else:
86              line.set_marker('')
```

```
87                line.set_color(colors3[int(i - start_scan3)])
88    for i, line in enumerate(ax4.get_lines()):
89          line.set_marker('')
90          if (int(i) < start_scan4 or int(i) > end_scan4):
91                line.set_marker("")
92                line.set_linestyle("none")
93          else:
94                line.set_marker('')
95                line.set_color(colors4[int(i - start_scan4)])
96
97    # remove legends, add axis labels
98    ax1.set_xlabel('q')
99    ax1.set_ylabel('I (zero degrees)')
100   ax1.set_ylim(0,intensity_upper)
101   ax2.set_xlabel('q')
102   ax2.set_ylabel('I')
103   ax2.set_ylim(0,intensity_upper)
104   ax3.set_xlabel('q')
105   ax3.set_ylabel('I')
106   ax3.set_ylim(0,intensity_upper)
107   ax4.set_xlabel('q')
108   ax4.set_ylabel('I')
109   ax4.set_ylim(0,intensity_upper)
110
111   ################################
112   # now do exactly the same thing but for the 90 degree sectors
113
114   readme = 'P6_y' + str(position) + '_90deg_corr.csv'
115
116   #setting up P2 figure
117   p2_T = pd.read_csv(readme,index_col = 0)
118   ax5 = fig.add_subplot(axs[3:5, 0:1])
119   ax5.plot(p2_T)
120   ax6 = fig.add_subplot(axs[3:5, 1:2])
121   ax6.plot(p2_T)
122   ax7 = fig.add_subplot(axs[3:5, 2:3])
123   ax7.plot(p2_T)
124   ax8 = fig.add_subplot(axs[3:5, 3:4])
125   ax8.plot(p2_T)
126
127   # set aesthetics
128   for i, line in enumerate(ax5.get_lines()):
129         line.set_marker('')
130         if (int(i) < start_scan or int(i) > end_scan):
131               line.set_marker("")
132               line.set_linestyle("none")
133         else:
```

```
134                 line.set_marker('')
135                 line.set_color(colors1[int(i - start_scan)])
136     for i, line in enumerate(ax6.get_lines()):
137           line.set_marker('')
138           if (int(i) < start_scan2 or int(i) > end_scan2):
139                 line.set_marker("")
140                 line.set_linestyle("none")
141           else:
142                 line.set_marker('')
143                 line.set_color(colors2[int(i - start_scan2)])
144     for i, line in enumerate(ax7.get_lines()):
145           line.set_marker('')
146           if (int(i) < start_scan3 or int(i) > end_scan3):
147                 line.set_marker("")
148                 line.set_linestyle("none")
149           else:
150                 line.set_marker('')
151                 line.set_color(colors3[int(i - start_scan3)])
152     for i, line in enumerate(ax8.get_lines()):
153           line.set_marker('')
154           if (int(i) < start_scan4 or int(i) > end_scan4):
155                 line.set_marker("")
156                 line.set_linestyle("none")
157           else:
158                 line.set_marker('')
159                 line.set_color(colors4[int(i - start_scan4)])
160
161     # remove legends, add axis labels
162     ax5.set_xlabel('q')
163     ax5.set_ylabel('I (90 degrees)')
164     ax5.set_ylim(0,intensity_upper)
165     ax6.set_xlabel('q')
166     ax6.set_ylabel('I')
167     ax6.set_ylim(0,intensity_upper)
168     ax7.set_xlabel('q')
169     ax7.set_ylabel('I')
170     ax7.set_ylim(0,intensity_upper)
171     ax8.set_xlabel('q')
172     ax8.set_ylabel('I')
173     ax8.set_ylim(0,intensity_upper)
174
175
176     ##########################
177     # set up the electrochem figure
178
179     # elapsed hours at which the electrochem changes
180     dash = 2.621
```

```
dash2 = 10.864
dash3 = 26.864
dash4 = 37.2

counts1 = 0
counts2 = 0
counts3 = 0
counts4 = 0

# count the points during each step
p2 = pd.read_csv(r'P6_echem.csv',index_col = 0)
for j in range(0, len(p2.index)):
      elapsed = float(p2.loc[j, "elapsed"])
      if elapsed < dash:
            counts1 += 1
      if elapsed > dash and elapsed < dash2:
            counts2 += 1
      if elapsed > dash2 and elapsed < dash3:
            counts3 += 1
      if elapsed > dash3:
            counts4 += 1

# set up the colors to match the SAXS data traces
colors1 = plt.cm.jet(np.linspace(0,1,counts1))
colors2 = plt.cm.jet(np.linspace(0,1,counts2))
colors2 = np.flipud(colors2)
colors3 = plt.cm.jet(np.linspace(0,1,counts3))
colors4 = plt.cm.jet(np.linspace(0,1,counts4))
colors4 = np.flipud(colors4)

colors5 = np.append(colors1, colors2, axis = 0)
colors6 = np.append(colors5, colors3, axis = 0)
colors = np.append(colors6, colors4, axis = 0)

# time bounds
xlower = 0
xupper = 38

# potential bounds
ylower = -1
yupper = 1

eplot = fig.add_subplot(axs[0, 0:4])

# read in the electrochem data and plot it
p2 = pd.read_csv(r'P6_echem.csv',index_col = 0)
times = p2['elapsed']
```

```
228   currents = p2['current']
229   p2.index = times
230   eplot.scatter(times, currents, c = colors, s = 10)
231
232   # add the dashed lines
233   eplot.plot([dash,dash],[ylower,yupper], color = 'black',linestyle =
'dashed')
234   eplot.plot([dash2,dash2],[ylower,yupper], color = 'black',linestyle =
'dashed')
235   eplot.plot([dash3,dash3],[ylower,yupper], color = 'black',linestyle =
'dashed')
236   eplot.plot([dash4,dash4],[ylower,yupper], color = 'black',linestyle =
'dashed')
237
238   # set the limits
239   eplot.set_xlim(xlower,xupper)
240   eplot.set_ylim(ylower,yupper)
241
242   # remove legends, add axis labels
243   eplot.set_xlabel('time (h)')
244   eplot.set_ylabel('E (V)')
245
246   # add a title
247   titlestring = "P6, position y" + str(position)
248   plt.title(titlestring)
249
250   #go
251   plt.show()
```

*B3.8 Plotting Processed Data*

The below code takes the csv files generated by ioncounts.py and generates a four-row figure containing the electrochemistry results, X-ray transmission, $r$-value generated by transmission, and a heat map in which the $y$-axis is position ($x/L$), the $x$-axis is time, and each point is color-coded to indicate the time (see Figure 10.7). This fourth plot has not been published as of the current writing; it was generated to facilitate comparison with theoretical calculations, which is ongoing. [59] Figure B3.1 shows an example of the plot generated by this code. This code processes only the transmission data: with minor changes to the csv filenames and axis scaling, it can easily be modified to process the domain spacing data (see Figure 10.10).

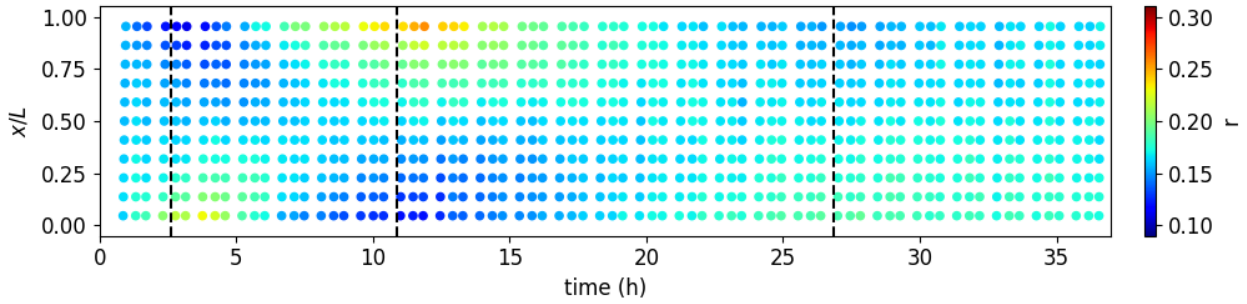


Figure B3.1. Heatmap showing the salt concentration, color-coded on a spectrum from low-$r$ (blue) to high-$r$ (red) as a function of position ($x/L$) and time, which was generated by fullplot_P6.py. The data shown is that used in Chapter 10: it is the same data presented in Figure 10.7 but presented as a heatmap.

fullplot_P6.py

```
#### LORENA GRUNDY
#### December 2021

import matplotlib.pyplot as plt
from matplotlib.offsetbox import AnchoredText
from matplotlib.offsetbox import AnnotationBbox
from matplotlib.offsetbox import TextArea
import pandas as pd
import numpy as np
from PIL import Image

plt.rcParams.update({'font.size': 8})

# where to put a dashed line
# indicating polarization conditions changed
dash = 2.621
dash2 = 10.864
dash3 = 26.864
dash4 = 37.2

# time bounds
xlower = 0
xupper = 37

# potential bounds
ylower = -1
yupper = 1

fig = plt.figure(constrained_layout = True, figsize = (7,7 - 7/4))
axs = fig.subplots(4, 1)

```

```
# setting up echem figure
p6_echem = pd.read_csv(r'P6_echem.csv',index_col = 0)
# use elapsed time as x-axis
times = p6_echem['elapsed']
p6_echem.index = times
currents = p6_echem['current']
axs[0].plot(times, currents, color = 'black', linewidth = 1.5)

# dashed lines
 axs[0].plot([dash,dash],[ylower,yupper], color = 'black',linestyle = 'dashed')
 axs[0].plot([dash2,dash2],[ylower,yupper], color = 'black',linestyle = 'dashed')
 axs[0].plot([dash3,dash3],[ylower,yupper], color = 'black',linestyle = 'dashed')
 axs[0].plot([dash4,dash4],[ylower,yupper], color = 'black',linestyle = 'dashed')

# set limits
axs[0].set_xlim(xlower,xupper)
axs[0].set_ylim(ylower,yupper)

# remove legends, add axis labels
axs[0].set_xlabel('time (h)')
axs[0].set_ylabel('$\it{E}$' + ' (V)')


##############################################################################
# transmission

# set up the colors for the different positions
num_points = 11
colors3 = plt.cm.jet(np.linspace(0,1,num_points))
colors6 = ['black']*22
for i in range (0, 11):
  colors6[i+2] = colors3[i]

# where to put a dashed line
# indicating polarization conditions changed
P6_d1 = 2.62
P6_d2 = 10.865
P6_d3 = 26.865
dash4 = 37.2

# time bounds
xlower = 0
xupper = 37
```

```
 74
 75 # transmission bounds
 76 ylower = 0
 77 yupper = 0.3
 78
 79 # set up transmission figure
 80 p6 = pd.read_csv(r'P6_transmission.csv',index_col = 0)
 81 times = pd.read_csv(r'stage3_dark_hours.csv', index_col = 0)
 82 new_index = times['1'].to_list()
 83 del new_index[-1]
 84 del new_index[-1]
 85 p6.index = new_index
 86 p6.to_csv('p6_transmission_hours.csv')
 87 a6 = p6.plot(kind='line',ax=axs[1])
 88 a6.vlines(x = [P6_d1, P6_d2, P6_d3, dash4], ymin = 0, ymax = yupper, colors
= 'black',
 89   linestyles = 'dashed')
 90
 91 # set bounds
 92 a6.set_xlim(xlower,xupper)
 93 a6.set_ylim(ylower,yupper)
 94
 95 # set aesthetics
 96 for i, line in enumerate(a6.get_lines()):
 97   line.set_marker('.')
 98   line.set_markersize(8)
 99   line.set_color(colors6[i])
100   # ignore the positions that are outside the electrolyte
101   line.set_linestyle("none")
102   if(i == 0 or i == 1 or i == 13 or i == 14 or i == 15):
103         line.set_marker("")
104   if(i == 21):
105         line.set_linestyle("dashed")
106         line.set_marker("")
107
108 # remove legends, add axis labels
109 a6.get_legend().remove()
110 a6.set_xlabel('time (h)')
111 a6.set_ylabel('transmission')
112
113
##############################################################################
114 # r from transmission
115
116 num_points = 11
117 colors3 = plt.cm.jet(np.linspace(0,1,num_points))
118 colors6 = ['black']*22
```

```
for i in range (0, 11):
  colors6[i+2] = colors3[i]

# where to put a dashed line
# indicating polarization conditions changed
P6_d1 = 2.62
P6_d2 = 10.865
P6_d3 = 26.865
dash4 = 37.2

# time bounds
xlower = 0
xupper = 37

# r bounds
ylower = 0
yupper = 0.35

# set up figure for r from transmission
p6 = pd.read_csv(r'P6_r_transmission.csv',index_col = 0)
times = pd.read_csv(r'stage3_dark_hours.csv', index_col = 0)
new_index = times['1'].to_list()
del new_index[-1]
del new_index[-1]
p6.index = new_index
p6.to_csv('p6_r_transmission_hours.csv')
a6 = p6.plot(kind='line',ax=axs[2])
a6.vlines(x = [P6_d1, P6_d2, P6_d3, dash4], ymin = 0, ymax = yupper, colors
= 'black',
  linestyles = 'dashed')
# add a horizontal line at r = 0.1
a6.hlines(y = [0.1], xmin = xlower, xmax = xupper, colors = 'black',
  linestyles = 'dashed')

# set limits
a6.set_xlim(xlower,xupper)
a6.set_ylim(ylower,yupper)

# set aesthetics
for i, line in enumerate(a6.get_lines()):
  line.set_marker('.')
  line.set_markersize(8)
  line.set_color(colors6[i])
  line.set_linestyle("none")
  if(i == 0 or i == 1 or i == 13 or i == 14 or i == 15):
        line.set_marker("")
  if(i == 21):
```

```
165         line.set_linestyle("dashed")
166         line.set_marker("")
167 
168 # remove legends, add axis labels
169 a6.get_legend().remove()
170 a6.set_xlabel('time (h)')
171 a6.set_ylabel('$\it{r}$' + ' from transmission')
172 
173 
##############################################################################
174 # colorscale plot (Aashutosh)
175 
176 # ignore positions out of bounds
177 lower_position = 2
178 upper_position = 12
179 xlower = -0.05
180 xupper = 1.05
181 
182 #0 and 5, 6 and 23
183 minscan = 0
184 maxscan = 75
185 
186 dash = 2.621
187 dash2 = 10.864
188 dash3 = 26.864
189 dash4 = 37.2
190 
191 concentrations = pd.read_csv(r'P6_r_transmission.csv',index_col = 0)
192 times = pd.read_csv(r'P6_hours.csv',index_col = 0)
193 
194    concentrations.drop(concentrations.columns[[16,17,18,19,20]],    axis=1,
inplace=True)
195 
196 # translating the positions into x/L
197                                 correct_columns                                =
[0.04545,0.1364,0.2273,0.3182,0.4091,0.5,0.5909,0.6818,0.7727,0.8636,0.9545]
198 new_columns = np.zeros(len(concentrations.columns))
199 # ignoring the positions out of bounds
200 for i in range(0, len(new_columns)):
201   if i < lower_position:
202         new_columns[i] = -1
203   elif i > upper_position:
204         new_columns[i] = 2
205   else:
206         new_columns[i] = correct_columns[i - lower_position]
207 concentrations.columns = new_columns
208 times.columns = new_columns
```

```
209
210 colorplot = pd.DataFrame()
211
212 # make a dataframe containing each time, position, and r as columns
213 positions = list(concentrations.columns.values)
214 scans = list(concentrations.index.values)
215 #print(scans)
216 for i, position in enumerate(positions):
217   # ignore the positions out of bounds
218   if position < 0 or position > 1:
219         continue
220   else:
221         for j, scan in enumerate(scans):
222               # create a unique identifier to prevent overwriting
223               label_str = str(i) + str(j)
224               label = int(label_str)
225               if concentrations.loc[scan,position] > 0.4:
226                     continue
227               if concentrations.loc[scan,position] < 0.09:
228                     continue
229               if scan > maxscan or scan < minscan:
230                     continue
231               # populate the dataframe
232               else:
233                     colorplot.at[label, "position"] = position
234                     colorplot.at[label, "time"] = times.loc[scan,position]
235                     colorplot.at[label,                "r"]                =
concentrations.loc[scan,position]
236
237 colorplot.to_csv("P6_columnized.csv")
238
239 # make the heatmap
240  tryme  =  colorplot.plot.scatter(y  =  "position",x  =  "time",c  =  "r",s  =
20,colormap = 'jet', ax = axs[3], vmin = 0.09, vmax = 0.31)
241
242   tryme.plot([dash,dash],[xlower,xupper],   color   =   'black',linestyle   =
'dashed')
243   tryme.plot([dash2,dash2],[xlower,xupper],   color   =   'black',linestyle   =
'dashed')
244   tryme.plot([dash3,dash3],[xlower,xupper],   color   =   'black',linestyle   =
'dashed')
245   tryme.plot([dash4,dash4],[xlower,xupper],   color   =   'black',linestyle   =
'dashed')
246
247 tryme.set_ylim(xlower,xupper)
248 tryme.set_xlim(0,37)
249
```

```
250 # remove legends, add axis labels
251 tryme.set_ylabel('$\it{x}$' + "/" + '$\it{L}$')
252 tryme.set_xlabel('time (h)')
253
254 fig.align_ylabels(axs)
255
256 # save the figure as a high-resolution tif file
257 fig.savefig('transmission.tiff',dpi = 600)
258 # display the figure
259 plt.show()
```

We also invert the data to create concentration profiles, with $r$ on the $y$-axis and position, $x/L$, on the $x$-axis, with time represented by the color of the trace (see Figure 10.11). This is the function of the next program, make_concPlot_gridded.py. It also divides the electrochemical data into four separate figures for ease of visualization with the concentration profiles.

make_concPlot_gridded.py

```
  1 # LORENA GRUNDY
  2 # February 2022
  3
  4 import matplotlib.pyplot as plt
  5 from matplotlib.offsetbox import AnchoredText
  6 from matplotlib.offsetbox import AnnotationBbox
  7 from matplotlib.offsetbox import TextArea
  8 import pandas as pd
  9 import numpy as np
 10 import math
 11 from matplotlib.ticker import (MultipleLocator, AutoMinorLocator)
 12
 13 # do we want to add dashed lines for the calculated steady-state profile?
 14 addssconc = True
 15
 16 plt.rcParams.update({'font.size': 8})
 17
 18 # setting up the colors for the SAXS data
 19 # to match the electrochem
 20 start_scan = 0
 21 end_scan = 5
 22 num_scans = end_scan - start_scan + 1
 23 colors1 = plt.cm.jet(np.linspace(0,1,num_scans))
 24 start_scan2 = end_scan+1
 25 end_scan2 = 24
 26 num_scans = end_scan2 - start_scan2 + 1
 27 colors2 = plt.cm.jet(np.linspace(0,1,num_scans))
 28 colors2 = np.flipud(colors2)
```

```
start_scan3 = end_scan2+1
end_scan3 = 56
num_scans = end_scan3 - start_scan3 + 1
colors3 = plt.cm.jet(np.linspace(0,1,num_scans))
start_scan4 = end_scan3+1
end_scan4 = 75
num_scans = end_scan4 - start_scan4 + 1
colors4 = plt.cm.jet(np.linspace(0,1,num_scans))
colors4 = np.flipud(colors4)

# positions to use
lower_position = 2
upper_position = 12
# x/L goes from 0 to 1
xlower = 0
xupper = 1

# r-value range
ylower = 0.1
yupper = 0.32

fig = plt.figure(tight_layout = True, figsize = (7, 5))
axs = fig.add_gridspec(5, 4)

# reading in the csvs for r from transmission and r from d-spacing
p2 = pd.read_csv(r'P6_r_transmission.csv',index_col = 0)
p6rd = pd.read_csv(r'P6_3_rvalue_from_d.csv',index_col = 0)
#sort by rows
p6rd.sort_index(axis = 0, inplace = True)
#sort by columns
p6rd = p6rd[['2', '3', '4', '5', '6', '7', '8', '9', '10', '11', '12']]

# re-labeling the columns from y2, y3 etc to their x/L values
new_columns = np.zeros(len(p2.columns))
                                correct_columns                                 =
[0.04545,0.1364,0.2273,0.3182,0.4091,0.5,0.5909,0.6818,0.7727,0.8636,0.9545]
for i in range(0, len(new_columns)):
  if i < lower_position:
        new_columns[i] = -1
  elif i > upper_position:
        new_columns[i] = 2
  else:
        new_columns[i] = correct_columns[i - lower_position]
p2.columns = new_columns
p2.drop([-1,2], axis=1, inplace=True)

# same thing but now for the d-spacing
```

```
new_columns = np.zeros(len(p6rd.columns))
for i in range(0, len(new_columns)):
  if i+2 < lower_position:
        new_columns[i] = -1
  elif i+2 > upper_position:
        new_columns[i] = 2
  else:
        new_columns[i] = correct_columns[i]
p6rd.columns = new_columns

# transpose the data frame so that rows are positions now
# and plot them
p2_T = p2.transpose()
p6rd_T = p6rd.transpose()
ax1 = fig.add_subplot(axs[1:3, 0:1])
ax1.plot(p2_T)
ax1.set_xlim(xlower,xupper)
ax1.set_ylim(ylower,yupper)
ax2 = fig.add_subplot(axs[1:3, 1:2])
ax2.plot(p2_T)
ax2.set_xlim(xlower,xupper)
ax2.set_ylim(ylower,yupper)
ax3 = fig.add_subplot(axs[1:3, 2:3])
ax3.plot(p2_T)
ax3.set_xlim(xlower,xupper)
ax3.set_ylim(ylower,yupper)
ax4 = fig.add_subplot(axs[1:3, 3:4])
ax4.plot(p2_T)
ax4.set_xlim(xlower,xupper)
ax4.set_ylim(ylower,yupper)
ax5 = fig.add_subplot(axs[3:5, 0:1])
ax5.plot(p6rd_T)
ax5.set_xlim(xlower,xupper)
ax5.set_ylim(ylower,yupper)
ax6 = fig.add_subplot(axs[3:5, 1:2])
ax6.plot(p6rd_T)
ax6.set_xlim(xlower,xupper)
ax6.set_ylim(ylower,yupper)
ax7 = fig.add_subplot(axs[3:5, 2:3])
ax7.plot(p6rd_T)
ax7.set_xlim(xlower,xupper)
ax7.set_ylim(ylower,yupper)
ax8 = fig.add_subplot(axs[3:5, 3:4])
ax8.plot(p6rd_T)
ax8.set_xlim(xlower,xupper)
ax8.set_ylim(ylower,yupper)

```

```
# opacity for all but the last scan of each polarization step
# set to 0 to only see divergence / steady state profile
a = 1

# set aesthetics
for i, line in enumerate(ax1.get_lines()):
  line.set_marker('.')
  # ignore any positions not relevant to this polarization step
  if (int(i) < start_scan or int(i) > end_scan):
        line.set_marker("")
        line.set_linestyle("none")
  # set the marker, color, and transparency
  else:
        line.set_marker('.')
        line.set_color(colors1[int(i - start_scan)])
        if (int(i) < end_scan):
              line.set_alpha(a)
# same thing repeated for all the other figures...
for i, line in enumerate(ax2.get_lines()):
  line.set_marker('.')
  if (int(i) < start_scan2 or int(i) > end_scan2):
        line.set_marker("")
        line.set_linestyle("none")
  else:
        line.set_marker('.')
        line.set_color(colors2[int(i - start_scan2)])
        if (int(i) < end_scan2):
              line.set_alpha(a)
for i, line in enumerate(ax3.get_lines()):
  line.set_marker('.')
  if (int(i) < start_scan3 or int(i) > end_scan3):
        line.set_marker("")
        line.set_linestyle("none")
  else:
        line.set_marker('.')
        line.set_color(colors3[int(i - start_scan3)])
        if (int(i) < end_scan3):
              line.set_alpha(a)
for i, line in enumerate(ax4.get_lines()):
  line.set_marker('.')
  if (int(i) < start_scan4 or int(i) > end_scan4):
        line.set_marker("")
        line.set_linestyle("none")
  else:
        line.set_marker('.')
        line.set_color(colors4[int(i - start_scan4)])
        if (int(i) < end_scan4):
```

```
169                 line.set_alpha(a)
170 for i, line in enumerate(ax5.get_lines()):
171   line.set_marker('.')
172   if (int(i) < start_scan or int(i) > end_scan):
173         line.set_marker("")
174         line.set_linestyle("none")
175   else:
176         line.set_marker('.')
177         line.set_color(colors1[int(i - start_scan)])
178         if (int(i) < end_scan):
179               line.set_alpha(a)
180 for i, line in enumerate(ax6.get_lines()):
181   line.set_marker('.')
182   if (int(i) < start_scan2 or int(i) > end_scan2):
183         line.set_marker("")
184         line.set_linestyle("none")
185   else:
186         line.set_marker('.')
187         line.set_color(colors2[int(i - start_scan2)])
188         if (int(i) < end_scan2):
189               line.set_alpha(a)
190 for i, line in enumerate(ax7.get_lines()):
191   line.set_marker('.')
192   if (int(i) < start_scan3 or int(i) > end_scan3):
193         line.set_marker("")
194         line.set_linestyle("none")
195   else:
196         line.set_marker('.')
197         line.set_color(colors3[int(i - start_scan3)])
198         if (int(i) < end_scan3):
199               line.set_alpha(a)
200 for i, line in enumerate(ax8.get_lines()):
201   line.set_marker('.')
202   if (int(i) < start_scan4 or int(i) > end_scan4):
203         line.set_marker("")
204         line.set_linestyle("none")
205   else:
206         line.set_marker('.')
207         line.set_color(colors4[int(i - start_scan4)])
208         if (int(i) < end_scan4):
209               line.set_alpha(a)
210
211 # if we want to plot the calculated steady-state profiles, read them in
212 # make sure to populate the ssconc csv file based on the theory
213 if addssconc == True:
214   p6_ssconc = pd.read_csv(r'P6_ssconc.csv',index_col = 0)
215
```

```
216    ax2_newx = 1 - p6_ssconc['x32'].values
217    ax42_newx = 1 - p6_ssconc['x42'].values
218    ax0096_newx = 1 - p6_ssconc['x0096'].values
219
220 # 0096 is the new limiting current profile with the constraint at r = 0.1
221 add0096 = True
222 addssconc = True
223
224 # add the curves to the graphs
225 if addssconc == True:
226    ax2_newx = 1 - p6_ssconc['x32'].values
227    p6_ssconc = pd.read_csv(r'P6_ssconc.csv',index_col = 0)
228
229    # first polarization
230    ax1.plot(p6_ssconc['x41'], p6_ssconc['y41'], color = "black", linestyle
= "dotted")
231    if add0096:
232          ax1.plot(p6_ssconc['x0096'], p6_ssconc['y0096'], color = "black",
linestyle = "dashed")
233
234    # second polarization
235    ax2.plot(ax2_newx,  p6_ssconc['y32'],  color  =  "black",  linestyle  =
"dotted")
236    if add0096:
237          ax2.plot(ax0096_newx,   p6_ssconc['y0096'],   color   =   "black",
linestyle = "dashed")
238
239    # third
240    ax3.plot(p6_ssconc['x007'], p6_ssconc['y007'], color = "black", linestyle
= "dotted")
241    # fourth
242    ax4.plot([xlower,xupper],[0.16,0.16],  color  =  "black",  linestyle  =
"dotted")
243
244    ## same for domain spacing-based profiles
245    ax5.plot(p6_ssconc['x41'], p6_ssconc['y41'], color = "black", linestyle
= "dotted")
246    if add0096:
247          ax5.plot(p6_ssconc['x0096'], p6_ssconc['y0096'], color = "black",
linestyle = "dashed")
248    #ax1.plot(p6_ssconc['x42'], p6_ssconc['y42'], color = "black", linestyle
= "dashed")
249    ax6.plot(ax2_newx,  p6_ssconc['y32'],  color  =  "black",  linestyle  =
"dotted")
250    if add0096:
251          ax6.plot(ax0096_newx,   p6_ssconc['y0096'],   color   =   "black",
linestyle = "dashed")
```

```
252    ax7.plot(p6_ssconc['x007'], p6_ssconc['y007'], color = "black", linestyle
= "dotted")
253    ax8.plot([xlower,xupper],[0.16,0.16],  color  =  "black",  linestyle  =
"dotted")
254
255 # remove legends, add axis labels
256 ax1.set_xlabel('$\it{x}$' + "/" + '$\it{L}$')
257 ax1.set_ylabel('$\it{r}$' + ' from transmission')
258 ax1.set_yticks([0.1,0.15, 0.2, 0.25, 0.3])
259 ax2.set_xlabel('$\it{x}$' + "/" + '$\it{L}$')
260 ax2.set_ylabel('$\it{r}$')
261 ax2.set_yticks([0.1,0.15, 0.2, 0.25, 0.3])
262 ax3.set_xlabel('$\it{x}$' + "/" + '$\it{L}$')
263 ax3.set_ylabel('$\it{r}$')
264 ax3.set_yticks([0.1,0.15, 0.2, 0.25, 0.3])
265 ax4.set_xlabel('$\it{x}$' + "/" + '$\it{L}$')
266 ax4.set_ylabel('$\it{r}$')
267 ax4.set_yticks([0.1,0.15, 0.2, 0.25, 0.3])
268 ax5.set_xlabel('$\it{x}$' + "/" + '$\it{L}$')
269 ax5.set_ylabel('$\it{r}$' + ' from domain spacing')
270 ax5.set_yticks([0.1,0.15, 0.2, 0.25, 0.3])
271 ax6.set_xlabel('$\it{x}$' + "/" + '$\it{L}$')
272 ax6.set_ylabel('$\it{r}$')
273 ax6.set_yticks([0.1,0.15, 0.2, 0.25, 0.3])
274 ax7.set_xlabel('$\it{x}$' + "/" + '$\it{L}$')
275 ax7.set_ylabel('$\it{r}$')
276 ax7.set_yticks([0.1,0.15, 0.2, 0.25, 0.3])
277 ax8.set_xlabel('$\it{x}$' + "/" + '$\it{L}$')
278 ax8.set_ylabel('$\it{r}$')
279 ax8.set_yticks([0.1,0.15, 0.2, 0.25, 0.3])
280
281 ##########################
282 # setting up the echem figure
283
284 dash = 2.621
285 dash2 = 10.864
286 dash3 = 26.864
287 dash4 = 37.2
288
289 # setting up the colors to match the concentration profiles
290 counts1 = 0
291 counts2 = 0
292 counts3 = 0
293 counts4 = 0
294
295 p2 = pd.read_csv(r'P6_echem.csv',index_col = 0)
296 for j in range(0, len(p2.index)):
```

```
297   elapsed = float(p2.loc[j, "elapsed"])
298   if elapsed < dash:
299         counts1 += 1
300   if elapsed > dash and elapsed < dash2:
301         counts2 += 1
302   if elapsed > dash2 and elapsed < dash3:
303         counts3 += 1
304   if elapsed > dash3:
305         counts4 += 1
306
307 colors1 = plt.cm.jet(np.linspace(0,1,counts1))
308 colors2 = plt.cm.jet(np.linspace(0,1,counts2))
309 colors2 = np.flipud(colors2)
310 colors3 = plt.cm.jet(np.linspace(0,1,counts3))
311 colors4 = plt.cm.jet(np.linspace(0,1,counts4))
312 colors4 = np.flipud(colors4)
313
314 colors5 = np.append(colors1, colors2, axis = 0)
315 colors6 = np.append(colors5, colors3, axis = 0)
316 colors = np.append(colors6, colors4, axis = 0)
317
318 # time range
319 xlower = 0
320 xupper = 38
321
322 # potential range
323 ylower = -1
324 yupper = 1
325
326
327 # set up 4 electrochem figures, one for each polarization step
328 eplot1 = fig.add_subplot(axs[0, 0:1])
329 eplot2 = fig.add_subplot(axs[0, 1:2])
330 eplot3 = fig.add_subplot(axs[0, 2:3])
331 eplot4 = fig.add_subplot(axs[0, 3:4])
332
333 # read in the electrochem
334 p2 = pd.read_csv(r'P6_echem.csv',index_col = 0)
335 times = p2['elapsed']
336 currents = p2['current']
337
338 # we need to split up the 4 figures based on the index where it changes
339 # so we need to find those indices
340 index2 = 0
341 index3 = 0
342 index4 = 0
343
```

```
344 # find indexes of dashes
345 for i in range(0, len(times)):
346   if times[i] < dash:
347         index2 = i
348   if times[i] < dash2:
349         index3 = i
350   if times[i] < dash3:
351         index4 = i
352
353 # splitting up the data into the four steps
354 times1 = times[0:index2+1]
355 currents1 = currents[0:index2+1]
356 colors1 = colors[0:index2+1]
357 times2 = times[index2+1:index3+1]
358 currents2 = currents[index2+1:index3+1]
359 colors2 = colors[index2+1:index3+1]
360 times3 = times[index3+1:index4+1]
361 currents3 = currents[index3+1:index4+1]
362 colors3 = colors[index3+1:index4+1]
363 times4 = times[index4+1:len(times)]
364 currents4 = currents[index4+1:len(times)]
365 colors4 = colors[index4+1:len(times)]
366
367 # make the figures
368 eplot1.scatter(times1, currents1, c = colors1, s = 2)
369 eplot2.scatter(times2, currents2, c = colors2, s = 2)
370 eplot3.scatter(times3, currents3, c = colors3, s = 2)
371 eplot4.scatter(times4, currents4, c = colors4, s = 2)
372
373 # set the limits
374 eplot1.set_xlim(xlower,dash)
375 eplot2.set_xlim(dash,dash2)
376 eplot3.set_xlim(dash2,dash3)
377 eplot4.set_xlim(dash3,xupper)
378
379 eplot1.set_ylim(ylower,yupper)
380 eplot2.set_ylim(ylower,yupper)
381 eplot3.set_ylim(ylower,yupper)
382 eplot4.set_ylim(ylower,yupper)
383
384 # set the tick marks
385 eplot1.set_xticks(np.arange(0, dash, 2))
386 eplot2.xaxis.set_major_locator(MultipleLocator(4))
387 eplot2.xaxis.set_minor_locator(MultipleLocator(2))
388 eplot3.xaxis.set_major_locator(MultipleLocator(4))
389 eplot3.xaxis.set_minor_locator(MultipleLocator(2))
390 eplot4.xaxis.set_major_locator(MultipleLocator(4))
```

```
eplot4.xaxis.set_minor_locator(MultipleLocator(2))

# remove legends, add axis labels
eplot1.set_xlabel('time (h)')
eplot1.set_ylabel('$\it{E}$' + " (V)")
eplot1.set_xticks([0, 1, 2])
eplot1.xaxis.set_minor_locator(MultipleLocator(1))
eplot2.set_xlabel('time (h)')
eplot2.set_ylabel('$\it{E}$' + " (V)")
eplot2.set_xticks([4, 6, 8, 10])
eplot2.xaxis.set_minor_locator(MultipleLocator(1))
eplot3.set_xlabel('time (h)')
eplot3.set_ylabel('$\it{E}$' + " (V)")
eplot3.set_xticks([12, 18, 24])
eplot3.xaxis.set_minor_locator(MultipleLocator(1))
eplot4.set_xlabel('time (h)')
eplot4.set_ylabel('$\it{E}$' + " (V)")
eplot4.set_xticks([28, 32, 36])
eplot4.xaxis.set_minor_locator(MultipleLocator(1))

# save the resulting figure as a high-resolution tif file
fig.savefig("gridded.tiff",dpi = 600)

# display the figure
plt.show()
```

## B4. Data Analysis for Chapter 7

In Chapter 7, we acquire SAXS data at a variety of positions over time; this is similar to the electrochemical *in situ* SAXS described in the preceding section, but because we are interested in different parameters—namely, the grain size—the analysis procedure is different.

### *B4.1 Fitting the Data*

The below program reads in the acquired SAXS scans, fits the peaks using lmfit,, [145] and saves the domain spacing and full width at half-maximum at the primary scattering peak into csv files, which will later be parsed and plotted.

fitting.py

```
# fitting domain spacing and FWHM of annealing SAXS data
# Lorena wrote this 10/22/2021

# also need 733_calib.poni (calibrated using AgB data at this beamtime)

# output:
```

```
 7 # peak.csv has index column indicating total time elapsed,
 8 # one column per position, containing domain spacing in nm
 9
10 # fwhm.csv is the full width at half maximum of the primary peak in A^-1
11
12 import pyFAI, pyFAI.detectors, pyFAI.azimuthalIntegrator, silx, fabio
13 import numpy as np
14 import matplotlib.pyplot as plt
15 import pandas as pd
16 import csv
17 from scipy import optimize
18 import os
19 import os.path
20 from os import path
21 import math
22 import SAXS_peak_fit as fit
23 import time
24
25 from lmfit.models import PseudoVoigtModel
26 from lmfit.models import ExponentialModel
27 from lmfit.models import LinearModel
28
29 # timing how long to let this run
30 start = time.time()
31
32 # number of azimuthal slices to make
33 # we're going to average these together anyway so I'm making it small
34 nslices = 1
35 # number of q-rings to make
36 nrings = 8192
37
38 # calibrated poni file
39 ai = pyFAI.load("733_calib.poni")
40
41 # peak_df will store domain spacing, fwhm_df will store fwhm
42 peak_df = pd.DataFrame(index = range(0, 1, 1), columns = range(0,1,1))
43 fwhm_df = pd.DataFrame(index = range(0, 1, 1), columns = range(0,1,1))
44
45 # for data processing as the data comes in, the above two lines can be
replaced
46 # by the four below so as only to process the new data (and remove
duplicates)
47 """peak_df = pd.read_csv(r'peak_lmfit.csv',index_col = 0)
48 fwhm_df = pd.read_csv(r'fwhm_lmfit.csv',index_col = 0)
```

```
49
50 peak_df = peak_df[~peak_df.index.duplicated(keep='first')]
51 fwhm_df = fwhm_df[~fwhm_df.index.duplicated(keep='first')]"""
52
53 # starting guesses for location of primary scattering peak (based in igor
analysis)
54 # leading zero because there's a dumb first column that we don't care about
55 guesses = [0, 0.0157, .0152, .0168, .0154, .015, .0156, .0143, .0138]
56
57 # open each file
58 for file in os.listdir():
59     # ignore the irrelevant ones
60     if 'edf' in file:
61         if 'test' in file:
62             continue
63
64         # parse file name
65         position = file.split('_')[2]
66         pos_num = int(position.split('P')[1])
67         sub_position = file.split('_')[3]
68         day = int(file.split('_')[1].split('day')[1])
69         # string corresponding to the name of the position (e.g. P1_1)
70         position_str = position+'_'+sub_position
71
72         # parse the time
73         hour = int(file.split('_')[4].split('h')[0])
74         minute = file.split('_')[5].split('m')[0]
75         second = file.split('_')[6].split('s')[0]
76
77         # add 24 hours when appropriate if we've passed midnight
78         if hour < 13 and day == 1:
79             hour = hour + 24
80         if hour < 6 and day == 2:
81             hour = hour + 24
82
83         # use the parsed time information to get the total time passed
84         # since the whole experiment started (1:40 pm on 10/22)
85         # note that for now, t = 0 is the start of the initial 90C step
86         timepassed = 0.0
87         timepassed = timepassed + (day - 1)*24
88         timepassed = timepassed + (hour - 13)
89         timepassed = timepassed + (float(minute) - 40)/60
90         timepassed = timepassed + (float(second))/(60*60)
91
```

```
 92          # uncomment these lines if you want to print each file name as you
analyze it
 93          """print(timepassed)
 94          print(file)"""
 95
 96          # this part turns the image into something pyFAI can deal with
 97          img = fabio.open(file)
 98          img_array = img.data
 99
100         # this creates arrays which are the q and chi values given the slice
numbers above
101          # I is a 2-D array with I as a function of chi and q
102         I, q_values, chi_values = ai.integrate2d(img_array, nrings, nslices,
unit="q_nm^-1", method='IntegrationMethod(2d int, pseudo split, histogram,
cython)')
103
104          # sum in the appropriate axis to give 1-D averaged I(q)
105          I_q = np.sum(I, axis = 0)
106
107          # initializing domain spacing and fwhm variables
108          d = 0.0
109          fwhm = 0.0
110
111             # get the correct guess peak location depending on the salt
concentration (position)
112          guess_qstar = 10*guesses[pos_num]
113
114          # put appropriate bounds on q and slice the data accordingly
115          qmin = 0.1
116          qmax = 0.24
117          min_index = 0
118          max_index = 0
119          for i in range(0, 1024):
120              if q_values[i] < qmin:
121                  min_index = i
122              if q_values[i] > qmax:
123                  max_index = i
124                  break
125
126          q_values = q_values[min_index:max_index]
127          I_values = I_q[min_index:max_index]
128
129           # define the model: exponential background, pseudo-voigt primary
peak
```

```
130         bkg = ExponentialModel(prefix='bkg_')
131         pars = bkg.guess(I_values, x=q_values)
132
133         peak1 = PseudoVoigtModel(prefix = 'p1_')
134         pars.update(peak1.make_params())
135
136         pars['p1_center'].set(value=guess_qstar, min=0.1, max=0.2)
137         pars['p1_sigma'].set(value=0.01)
138         pars['p1_amplitude'].set(value=30, min = 0)
139
140        # sometimes the data is imperfect, so we actually fit two overlapping
peaks
141         # instead of one primary scattering peak
142         peak2 = PseudoVoigtModel(prefix = 'p2_')
143         pars.update(peak2.make_params())
144
145         # peak 2 will be at a smaller q*
146         guess_peak2 = guess_qstar - 0.02
147         pars['p2_center'].set(value=guess_peak2, min=0.1, max=0.2)
148         pars['p2_sigma'].set(value=0.01)
149         pars['p2_amplitude'].set(value=30, min = 0)
150
151         model = peak1 + bkg
152         init = model.eval(pars, x = q_values)
153
154         # fit I(q) to pull out d and fwhm
155         out = model.fit(I_values, pars, x = q_values)
156         # turn q* into d in nm
157         q_star = out.best_values['p1_center']
158         d = 2*np.pi/q_star
159         # fwhm in nm^-1
160         fwhm = 2*out.best_values['p1_sigma']
161
162          print("P1: q = " + str(out.best_values['p1_center']) + ", amp = "
+     str(out.best_values['p1_amplitude'])     +     ",     sig     =     "     +
str(out.best_values['p1_sigma']))
163          print("P2: q = " + str(out.best_values['p2_center']) + ", amp = "
+     str(out.best_values['p2_amplitude'])     +     ",     sig     =     "     +
str(out.best_values['p2_sigma']))
164
165            # take the biggest peak, and impose restrictions on what is
reasonable to accept
```

```
166          if (out.best_values['p2_sigma'] < out.best_values['p1_sigma'] and
out.best_values['p2_amplitude']   >   0.6*out.best_values['p1_amplitude'])   or
out.best_values['p2_amplitude'] > 6*out.best_values['p1_amplitude']:
167              print("P2!")
168              q_star = out.best_values['p2_center']
169              d = 2*np.pi/q_star
170              # fwhm in nm^-1
171              fwhm = 2*out.best_values['p2_sigma']
172
173                          if   out.best_values['p1_amplitude']   <   25   and
out.best_values['p2_amplitude'] < 25:
174              print("too small!")
175              d = math.nan
176              fwhm = math.nan
177
178          # unomment these lines to show plots of each scan and its fit
179          """plt.plot(q_values, I_values, label='data')
180          plt.plot(q_values, out.init_fit, '--', label='initial fit')
181          plt.plot(q_values, out.best_fit, '--', label='best fit')
182          plt.axvline(x=q_star, color = "black", linestyle = "dashed")
183          plt.legend()
184
185          plt.xlabel('q (nm-1)')
186          plt.ylabel('I (a.u.)')
187          plt.show()"""
188
189          # impose restrictions on d and fwhm
190          if d < 30 or d > 50:
191              d = math.nan
192
193          if fwhm > 0.05:
194              print(fwhm)
195              fwhm = math.nan
196              d = math.nan
197              print(fwhm)
198
199        print(out.best_values['p2_amplitude'] / out.best_values['p2_sigma'])
200          if out.best_values['p2_amplitude'] / out.best_values['p2_sigma'] >
4000:
201              print("nope")
202              fwhm = math.nan
203              d = math.nan
204
205          # put the values into the dataframes
```

```
206         peak_df.at[str(timepassed),str(position_str)] = d
207         fwhm_df.at[str(timepassed),str(position_str)] = fwhm
208 
209 # export as csvs
210 peak_df.to_csv('peak_lmfit.csv')
211 fwhm_df.to_csv('fwhm_lmfit.csv')
212 
213 # print how long this code took to run
214 end = time.time()
215 totaltime = round((end - start), 1)
216 print("time elapsed: ", totaltime, " seconds or")
217 totaltime = round((end - start)/60.00, 1)
218 print("              ", totaltime, " minutes")
```

### *B4.2 Plotting the Data*

The below code reads in the csv files generated above and generates Figure A7.1. With $x$-axis scaling and minor spacing adjustments, the same code was used to generate Figures 7.5a and 7.6. This code adjusts the time scaling so that $t = 0$ is at the start of the 120 °C annealing step. It also converts the 1/FWHM data generated by the fitting code into $L$ by following the Scherrer equation (Equation 7.4)—see line 170.

plotting.py

```
  1 # make plots of d-spacing and FWHM data
  2 # Lorena wrote this 10/22/2021
  3 
  4 # dependencies:
  5 # takes in peak.csv and fwhm.csv which have:
  6 # index column: time passed
  7 # one column per position, with peak location (nm) or fwhm (A-1)
  8 # these can be generated using get_data.py
  9 
 10 import matplotlib.pyplot as plt
 11 from matplotlib import colors as c
 12 import pandas as pd
 13 import numpy as np
 14 import math
 15 
 16 # times where things change
 17 # time temp switches to 120
 18 # 06:00 on Saturday 10/23 (day 2)
 19 t_120 = 16.33
 20 # time temp switches back to 90
 21 # 05:00 on Sunday 10/24 (day 3)
```

```
t_90 = 39.33

# correcting the above to assign t = 0 to the start of the 120C step
t_120_zeroed = 0
t_90_zeroed = t_90 - t_120

# get a spectrum of 8 colors to code the different salt concentrations
# can change the colormap to plt.cm.[whatever]
colors = plt.cm.plasma(np.linspace(0,1,8))
colors = np.flipud(colors)
colors = np.delete(colors, (0), axis = 0)

# set x-axis ranges
xlower = -17
xupper = 24

# set y-axis ranges
# d-spacing
ylower = 30
yupper = 55

# fwhm in A-1
fwlower = 0
fwupper = .05

# 1/fwhm in nm
fwi_lower = 0
fwi_upper = 1200

# normalized values
normlower = 0
normupper = 2.5

# make a figure with 3 subplots
fig, axs = plt.subplots(nrows = 3, ncols = 1, sharex=False, tight_layout =
True, figsize = (5, 8))

### normalize FWHM

# read in FWHM csv
fwhm_df_norm = pd.read_csv(r'fwhm_lmfit_2.csv',index_col = 0)
# sort FWHM by time
fwhm_df_norm.index.name="time"
fwhm_df_norm.sort_values(by = 'time', inplace = True)
```

```
# find index of first time value > 0 so that we can normalize by the FWHM we find there
# (i.e. the first time after the temp increase)
index_120 = np.argmax(fwhm_df_norm.index.values>0)

# subtract t_120 from all of the times so that t = 0
# is when the temperature switches from 90 to 120
# only need to run this once, because it re-saves the csvs with the correct times
# comment out if running code repeatedly.
test = pd.read_csv(r'fwhm_lmfit.csv',index_col = 0)
oldtimes = test.index.values
newtimes = np.zeros(len(oldtimes))
for i in range(0, len(newtimes)):
    newtimes[i] = oldtimes[i] - t_120
test['newtimes'] = newtimes
test.set_index(newtimes, drop = True, inplace = True)
test.drop('newtimes',axis = 1, inplace = True)
test.to_csv('fwhm_lmfit_2.csv')
fwhm_df_norm.to_csv('fwhm_lmfit_2.csv')

# get the columns in the dataframe
columns = list(fwhm_df_norm.columns.values)
# for each column, normalize it
for i in range(1, 25):
    column = fwhm_df_norm[columns[i]].to_numpy()
    # look for the first reasonable value that comes after the switch to 120
    cropped = column[index_120:]
    init = next(x for x in cropped if ((not math.isnan(x)) and x > 0.0 and x < 0.019))
    # normalize by it, replace the column
    column = column / init
    fwhm_df_norm[columns[i]] = column
# we ran a sample with r = 0.06 (P2), but the data was bad - drop it
fwhm_df_norm.drop(['P2_1','P2_2','P2_3'],axis = 1, inplace = True)

# save the normalized one to a csv
fwhm_df_norm.to_csv('fwhm_lmfit_normalized_2.csv')

### turn the fwhm (A-1) into 1/fwhm (nm)
# similar method to above except what's in the loop
fwhm_df_inverse = pd.read_csv(r'fwhm_lmfit_2.csv',index_col = 0)
# drop the r = 0.06 data from this, too
```

```
fwhm_df_inverse.drop(['P2_1','P2_2','P2_3'],axis = 1, inplace = True)
# sort by time
fwhm_df_inverse.index.name="time"
fwhm_df_inverse.sort_values(by = 'time', inplace = True)

columns = list(fwhm_df_inverse.columns.values)
for i in range(1, 22):
    column = fwhm_df_inverse[columns[i]].to_numpy()
    # for every value in the column, replace it with 1/itself if possible
    for j in range (0, len(column)):
            x = column[j]
            # don't divide by zero. note 1/nan = nan so that's fine.
            if x == 0:
                    column[j] = math.nan
            else:
                    column[j] = 1/x
    fwhm_df_inverse[columns[i]] = column
fwhm_df_inverse.to_csv('fwhm_lmfit_inverted_2.csv')

# normalize FWHM inverted
# this is exactly the same as the normalization of fwhm except how we define
a reasonable value
fwhm_df_inverse_norm = pd.read_csv(r'fwhm_lmfit_inverted_2.csv',index_col
= 0)
# sort FWHM by time
fwhm_df_inverse_norm.index.name="time"
fwhm_df_inverse_norm.sort_values(by = 'time', inplace = True)

columns = list(fwhm_df_inverse_norm.columns.values)
for i in range(1, 22):
    column = fwhm_df_inverse_norm[columns[i]].to_numpy()
    cropped = column[index_120:]
    init = next(x for x in cropped if ((not math.isnan(x)) and x > 5.26))
    #print(init)
    column = column / init
    fwhm_df_inverse_norm[columns[i]] = column
fwhm_df_inverse_norm.to_csv('fwhm_lmfit_inverted_normalized_2.csv')

# find highest present time to set upper limit of x-axis
maxtime = np.max(fwhm_df_norm.index.values)
# shift by a bit to make room for the legends
xupper = maxtime + 20

#transparency of the points, so we can see them if they overlap
```

```
147 a = 0.6
148
149 # setting up d-spacing figure
150 p1_df = pd.read_csv(r'peak_lmfit_2.csv',index_col = 0)
151
152 # subtract t_120 from all of the times so that t = 0
153 # is when the temperature switches from 90 to 120
154 # as above, also only need to do this once.
155 oldtimes = p1_df.index.values
156 newtimes = np.zeros(len(oldtimes))
157 for i in range(0, len(newtimes)):
158     newtimes[i] = oldtimes[i] - t_120
159 p1_df['newtimes'] = newtimes
160 p1_df.set_index(newtimes, drop = True, inplace = True)
161 p1_df.drop('newtimes',axis = 1, inplace = True)
162
163 p1_df.drop(['P2_1','P2_2','P2_3'],axis = 1, inplace = True)
164 p1 = p1_df.plot(kind='line', ax=axs[0], alpha = a)
165
166 # setting up fwhm or 1/fwhm figure
167 p2_df = pd.read_csv(r'fwhm_lmfit_inverted_2.csv',index_col = 0)
168 # scaling the FWHM data according to the Scherrer equation to convert
169 # 1/FWHM to L
170 p2_df = p2_df*5.84
171 p2 = p2_df.plot(kind='line', ax=axs[1], alpha = a)
172
173 # setting up normalized fwhm or 1/fwhm figure
174 p3_df = pd.read_csv(r'fwhm_lmfit_inverted_normalized_2.csv',index_col = 0)
175 p3 = p3_df.plot(kind='line', ax=axs[2], alpha = a)
176
177 # set axis limits
178 p1.set_xlim(xlower,xupper)
179 p2.set_xlim(xlower,xupper)
180 p3.set_xlim(xlower,xupper)
181
182 p1.set_ylim(ylower,yupper)
183 p2.set_ylim(fwi_lower,fwi_upper)
184 p3.set_ylim(normlower,normupper)
185
186 # set aesthetics for all three charts
187 for i, line in enumerate(p1.get_lines()):
188     line.set_marker('.')
189     # i = 0 is the weird line that I'm not sure why it exists (not real
data)
```

```
    if i == 0:
            line.set_marker("")
    else:
            # this will make it so that all 3 positions from the same salt concentration match
            line.set_color(colors[int((i-1)/3)])
    line.set_linestyle("")
for i, line in enumerate(p2.get_lines()):
    line.set_marker('.')
    if i == 0:
            line.set_marker("")
    else:
            line.set_color(colors[int((i-1)/3)])
    line.set_linestyle("")
for i, line in enumerate(p3.get_lines()):
    line.set_marker('.')
    if i == 0:
            line.set_marker("")
    else:
            line.set_color(colors[int((i-1)/3)])
    line.set_linestyle("")

# create legend
handles, labels = p1.get_legend_handles_labels()
# these are the labels corresponding to the 7 salt concentrations
newlabels = ['$\it{r}$' + " = 0.04",'$\it{r}$' + " = 0.08",'$\it{r}$' + " = 0.12", '$\it{r}$' + " = 0.14", '$\it{r}$' + " = 0.16", '$\it{r}$' + " = 0.18", '$\it{r}$' + " = 0.22"]
# making a list of handles to make the legend
newhandles = handles[0:7]
for i, line in enumerate(p1.get_lines()):
    # set the 8 handles to be every 3rd line
    if (i-1)%3 == 0:
            newhandles[int((i-1)/3)] = line
# reverse the order so it matches the order of domain spacings
newhandles.reverse()
newlabels.reverse()
# putting the legend on all 3 figures. If there's a figure we don't want a legend on, change to:
# p1.get_legend().remove()
p1.legend(newhandles, newlabels, loc = 'lower right', edgecolor = 'black', framealpha = 1, handletextpad = 0.2, labelspacing = 0.3, labelcolor = "mec")
p2.legend(newhandles, newlabels, loc = 'lower right', edgecolor = 'black', framealpha = 1, handletextpad = 0.2, labelspacing = 0.3, labelcolor = "mec")
```

```
228 p3.legend(newhandles, newlabels, loc = 'lower right', edgecolor = 'black',
framealpha = 1, handletextpad = 0.2, labelspacing = 0.3, labelcolor = "mec")
229
230 # label the axes
231 p1.set_xlabel('time (h)')
232 p1.set_ylabel('$\it{d}$' + " (nm)")
233 p2.set_xlabel('time (h)')
234 p2.set_ylabel('$\it{L}$' + " (nm)")
235 p3.set_xlabel('time (h)')
236 p3.set_ylabel('$\it{L}$' + " / " + "$\it{L}$" + "($\it{t}$ = 0)")
237
238 # add vertical lines where things change
239 p1.axvline(x=t_120_zeroed, color = "black", linestyle = "dashed")
240 p2.axvline(x=t_120_zeroed, color = "black", linestyle = "dashed")
241 p3.axvline(x=t_120_zeroed, color = "black", linestyle = "dashed")
242 p1.axvline(x=t_90_zeroed, color = "black", linestyle = "dashed")
243 p2.axvline(x=t_90_zeroed, color = "black", linestyle = "dashed")
244 p3.axvline(x=t_90_zeroed, color = "black", linestyle = "dashed")
245 # on the normalized figure, add a vertical line at y = 1
246 p3.axhline(y = 1, color = "black", linestyle = "dashed")
247
248 ### adding labels to those vertical lines
249
250 # how far to shift to the right
251 timeoffset = 1.5
252 # how far to shift down for each label
253 p1y = 1.4
254 p2y = 0.0003
255 # comment the below line out to change it to something appropriate for FWHM
256 # instead of .1/FWHM
257 p2y = 70
258 # since p2 might switch between fwhm and 1/fwhm, this will make it easier
259 p2top = fwi_upper
260 p3y = 0.15
261 # how transparent to make each label
262 labela = 0.4
263
264 # label backgrounds and edge colors
265 fc = c.to_rgba('white')
266 ec = c.to_rgba('black')
267 # setting background transparency
268 fc = fc[:-1] + (labela,)
269
270 # add the three labels for each figure
```

```
271             p1.text(timeoffset+xlower,yupper-p1y,'90                \N{DEGREE
SIGN}C',horizontalalignment='left',      verticalalignment       =       "top",
bbox=dict(facecolor=fc, edgecolor = ec))
272          p1.text(t_120_zeroed+timeoffset,yupper-p1y,'120            \N{DEGREE
SIGN}C',horizontalalignment='left',      verticalalignment       =       "top",
bbox=dict(facecolor=fc, edgecolor = ec))
273           p1.text(t_90_zeroed+timeoffset,yupper-p1y,'90             \N{DEGREE
SIGN}C',horizontalalignment='left',      verticalalignment       =       "top",
bbox=dict(facecolor=fc, edgecolor = ec))
274              p2.text(timeoffset+xlower,p2top-p2y,'90               \N{DEGREE
SIGN}C',horizontalalignment='left',      verticalalignment       =       "top",
bbox=dict(facecolor=fc, edgecolor = ec))
275           p2.text(t_120_zeroed+timeoffset,p2top-p2y,'120            \N{DEGREE
SIGN}C',horizontalalignment='left',      verticalalignment       =       "top",
bbox=dict(facecolor=fc, edgecolor = ec))
276            p2.text(t_90_zeroed+timeoffset,p2top-p2y,'90             \N{DEGREE
SIGN}C',horizontalalignment='left',      verticalalignment       =       "top",
bbox=dict(facecolor=fc, edgecolor = ec))
277             p3.text(timeoffset+xlower,normupper-p3y,'90             \N{DEGREE
SIGN}C',horizontalalignment='left',      verticalalignment       =       "top",
bbox=dict(facecolor=fc, edgecolor = ec))
278          p3.text(t_120_zeroed+timeoffset,normupper-p3y,'120         \N{DEGREE
SIGN}C',horizontalalignment='left',      verticalalignment       =       "top",
bbox=dict(facecolor=fc, edgecolor = ec))
279           p3.text(t_90_zeroed+timeoffset,normupper-p3y,'90          \N{DEGREE
SIGN}C',horizontalalignment='left',      verticalalignment       =       "top",
bbox=dict(facecolor=fc, edgecolor = ec))
280
281 # aligning and adjusting aesthetics
282 plt.subplots_adjust(hspace=0.4)
283 fig.align_ylabels()
284
285 # saving the figures as a 300 dpi tif file
286 fig.savefig('fullplot_fulltime_plasma.tif', dpi = 300)
287 #go
288 plt.show()
```

Figure 7.7 plots the percent change in ionic conductivity versus percent change in grain size, $L$, during the 120 °C annealing step, with time indicated by the color. The code below, timeiscolors.py, shows how this was done. The times at which SAXS scans were acquired were used, and conductivity data was interpolated to find the approximate ionic conductivity at the time of the SAXS scan.

timeiscolors.py

```
# Lorena Grundy
# generates figures for each salt concentration. k and fwhm are plotted against
# each other, and time is represented by colors

import matplotlib.pyplot as plt
from matplotlib import colors as c
import pandas as pd
import numpy as np
import math
from matplotlib.offsetbox import AnchoredText

# I copied the times from the relevant parts of the csv generated by the previous code - there are many zeroes because the arrays include all times that any scan was taken, not necessarily at the position of interest. Data is not reproduced below in the Dissertation for the sake of length.
# yes this is horribly inefficient, I'm sorry
times = np.array([0.06555556,...,22.62638889])
fw04 = np.array([56.5316274952424,...,0])
fw06 = np.array([0,33.8785738891763,...,0])
fw08 = np.array([0,0,0,0,0,125.665577257814,...,0])
fw12 = np.array([0,0,0,0,0,0,0,0,92.8844389399061,...,0])
fw14 = np.array([0,0,0,0,0,0,0,0,0,0,0,61.9026446377989,...,0])
fw16 = np.array([0,0,0,0,0,0,0,0,0,0,0,0,0,0,64.9932366954674,...,0])
fw18 = np.array([0,0,0,0,0,0,0,0,0,0,0,0,0,0,0,0,62.8127499162287,...,0])
fw22 = np.array([0,0,0,0,0,0,0,0,0,0,0,0,0,0,0,0,0,0,0,0,0,0,45.1244600294301,...,77.7662868008214])

# we're going to crop each of these to remove the zeros and select our time interval
fw04_cropped = np.array([])
fw06_cropped = np.array([])
fw08_cropped = np.array([])
fw12_cropped = np.array([])
fw14_cropped = np.array([])
fw16_cropped = np.array([])
fw18_cropped = np.array([])
fw22_cropped = np.array([])

times04_cropped = np.array([])
times06_cropped = np.array([])
times08_cropped = np.array([])
```

```
37 times12_cropped = np.array([])
38 times14_cropped = np.array([])
39 times16_cropped = np.array([])
40 times18_cropped = np.array([])
41 times22_cropped = np.array([])
42
43 done04 = False
44 done06 = False
45 done08 = False
46 done12 = False
47 done14 = False
48 done16 = False
49 done18 = False
50 done22 = False
51
52 start04 = 0.0
53 start06 = 0.0
54 start08 = 0.0
55 start12 = 0.0
56 start14 = 0.0
57 start16 = 0.0
58 start18 = 0.0
59 start22 = 0.0
60
61 # do the sifting through and removing
62 # (actually adding the non-bad ones to empty arrays above)
63 # again it is terribly inefficient that I am doing it this way
64 # this also goes through and converts from L to percent change in L
65 for i in range(0, 1812):
66     if times[i] < 9:
67             if fw04[i] != 0:
68                     if done04 == False:
69                             fw04_cropped = np.append(fw04_cropped, 0)
70                             done04 = True
71                             start04 = fw04[i]
72                     else:
73                             fw_cng = 100*(fw04[i] - start04)/start04
74                             fw04_cropped = np.append(fw04_cropped, fw_cng)
75                     times04_cropped = np.append(times04_cropped, times[i])
76             if fw06[i] != 0:
77                     if done06 == False:
78                             fw06_cropped = np.append(fw06_cropped, 0)
79                             done06 = True
80                             start06 = fw06[i]
```

```
                else:
                        fw_cng = 100*(fw06[i] - start06)/start06
                        fw06_cropped = np.append(fw06_cropped, fw_cng)
                times06_cropped = np.append(times06_cropped, times[i])
        if fw08[i] != 0:
                if done08 == False:
                        fw08_cropped = np.append(fw08_cropped, 0)
                        done08 = True
                        start08 = fw08[i]
                else:
                        fw_cng = 100*(fw08[i] - start08)/start08
                        fw08_cropped = np.append(fw08_cropped, fw_cng)
                times08_cropped = np.append(times08_cropped, times[i])
        if fw12[i] != 0:
                if done12 == False:
                        fw12_cropped = np.append(fw12_cropped, 0)
                        done12 = True
                        start12 = fw12[i]
                else:
                        fw_cng = 100*(fw12[i] - start12)/start12
                        fw12_cropped = np.append(fw12_cropped, fw_cng)
                times12_cropped = np.append(times12_cropped, times[i])
        if fw14[i] != 0:
                if done14 == False:
                        fw14_cropped = np.append(fw14_cropped, 0)
                        done14 = True
                        start14 = fw14[i]
                else:
                        fw_cng = 100*(fw14[i] - start14)/start14
                        fw14_cropped = np.append(fw14_cropped, fw_cng)
                times14_cropped = np.append(times14_cropped, times[i])
        if fw16[i] != 0:
                if times[i] > 0.5:
                        if done16 == False:
                                fw16_cropped  =  np.append(fw16_cropped,
0)
                                done16 = True
                                start16 = fw16[i]
                        else:
                                fw_cng = 100*(fw16[i] - start16)/start16
                                fw16_cropped  =  np.append(fw16_cropped,
fw_cng)
                        times16_cropped   =   np.append(times16_cropped,
times[i])
```

```
122             if fw18[i] != 0:
123                     if done18 == False:
124                             fw18_cropped = np.append(fw18_cropped, 0)
125                             done18 = True
126                             start18 = fw18[i]
127                     else:
128                             fw_cng = 100*(fw18[i] - start18)/start18
129                             fw18_cropped = np.append(fw18_cropped, fw_cng)
130                     times18_cropped = np.append(times18_cropped, times[i])
131             if fw22[i] != 0:
132                     if times[i] > 1:
133                             if done22 == False:
134                                     fw22_cropped  =  np.append(fw22_cropped,
0)
135                                     done22 = True
136                                     start22 = fw22[i]
137                             else:
138                                     fw_cng = 100*(fw22[i] - start22)/start22
139                                     fw22_cropped  =  np.append(fw22_cropped,
fw_cng)
140                             times22_cropped   =   np.append(times22_cropped,
times[i])
141
142 # make arrays for conductivity
143 k04 = np.array([])
144 k06 = np.array([])
145 k08 = np.array([])
146 k12 = np.array([])
147 k14 = np.array([])
148 k16 = np.array([])
149 k18 = np.array([])
150 k22 = np.array([])
151
152 # given fits to conductivity data at 120C, make arrays of conductivity data
153 # corresponding to the times at which we have SAXS data
154 # this does the "percent change" calculation as well
155 for i in range(0, times04_cropped.size):
156     t_0 = times04_cropped[0]
157     k_0 = 2.8314e-8*t_0**4 - 5.8364e-7*t_0**3 + 5.0257e-6*t_0**2 - 2.4846e-
5*t_0 + 2.170e-4
158     t = times04_cropped[i]
159     kfit = 2.8314e-8*t**4 - 5.8364e-7*t**3 + 5.0257e-6*t**2 - 2.4846e-5*t +
2.170e-4
160     k_chg = 100*(kfit - k_0)/k_0
```

```
    if k_chg > -20 and fw04_cropped[i] > 20:
            k_chg = 1000
    k04 = np.append(k04, k_chg)
for i in range(0, times06_cropped.size):
    t_0 = times06_cropped[0]
    k_0 = 4.1225e-8*t_0**4 - 9.4530e-7*t_0**3 + 8.1015e-6*t_0**2 - 3.4758e-5*t_0 + 3.4447e-4
    t = times06_cropped[i]
    kfit = 4.1225e-8*t**4 - 9.4530e-7*t**3 + 8.1015e-6*t**2 - 3.4758e-5*t + 3.4447e-4
    k_chg = 100*(kfit - k_0)/k_0
    k06 = np.append(k06, k_chg)
for i in range(0, times08_cropped.size):
    t_0 = times08_cropped[0]
    k_0 = -9.5821e-9*t_0**5 + 2.7103e-7*t_0**4 - 3.0225e-6*t_0**3 + 1.7184e-5*t_0**2 - 5.7692e-5*t_0 + 4.2557e-4
    t = times08_cropped[i]
    kfit = -9.5821e-9*t**5 + 2.7103e-7*t**4 - 3.0225e-6*t**3 + 1.7184e-5*t**2 - 5.7692e-5*t + 4.2557e-4
    k_chg = 100*(kfit - k_0)/k_0
    k08 = np.append(k08, k_chg)
for i in range(0, times12_cropped.size):
    t_0 = times12_cropped[0]
    k_0 = 3.2089e-8*t_0**4 - 9.4446e-7*t_0**3 + 1.1040e-5*t_0**2 - 6.8414e-5*t_0 + 6.8854e-4
    t = times12_cropped[i]
    kfit = 3.2089e-8*t**4 - 9.4446e-7*t**3 + 1.1040e-5*t**2 - 6.8414e-5*t + 6.8854e-4
    k_chg = 100*(kfit - k_0)/k_0
    k12 = np.append(k12, k_chg)
for i in range(0, times14_cropped.size):
    t_0 = times14_cropped[0]
    k_0 = 9.6761e-8*t_0**4 - 2.1360e-6*t_0**3 + 1.6991e-5*t_0**2 - 6.0617e-5*t_0 + 4.1962e-4
    t = times14_cropped[i]
    kfit = 9.6761e-8*t**4 - 2.1360e-6*t**3 + 1.6991e-5*t**2 - 6.0617e-5*t + 4.1962e-4
    k_chg = 100*(kfit - k_0)/k_0
    k14 = np.append(k14, k_chg)
for i in range(0, times16_cropped.size):
    t_0 = times16_cropped[0]
    k_0 = 0.1*(-1.5317e-7*t_0**4 + 2.2357e-6*t_0**3 - 1.0167e-5*t_0**2 + 2.3443e-5*t_0 + 3.2603e-3)
    t = times16_cropped[i]
```

```
    kfit = 0.1*(-1.5317e-7*t**4 + 2.2357e-6*t**3 - 1.0167e-5*t**2 + 2.3443e-5*t + 3.2603e-3)
    k_chg = 100*(kfit - k_0)/k_0
    k16 = np.append(k16, k_chg)
for i in range(0, times18_cropped.size):
    t_0 = times18_cropped[0]
    k_0 = 1.3940e-8*t_0**4 - 3.4096e-7*t_0**3 + 3.0801e-6*t_0**2 - 1.2200e-5*t_0 + 3.1370e-4
    t = times18_cropped[i]
    kfit = 1.3940e-8*t**4 - 3.4096e-7*t**3 + 3.0801e-6*t**2 - 1.2200e-5*t + 3.1370e-4
    k_chg = 100*(kfit - k_0)/k_0
    k18 = np.append(k18, k_chg)
for i in range(0, times22_cropped.size):
    t_0 = times22_cropped[0]
    k_0 = -1.4185e-8*t_0**5 + 4.1212e-7*t_0**4 - 4.4459e-6*t_0**3 + 2.1893e-5*t_0**2 - 4.7836e-5*t_0 + 8.7489e-4
    t = times22_cropped[i]
    kfit = -1.4185e-8*t**5 + 4.1212e-7*t**4 - 4.4459e-6*t**3 + 2.1893e-5*t**2 - 4.7836e-5*t + 8.7489e-4
    k_chg = 100*(kfit - k_0)/k_0
    k22 = np.append(k22, k_chg)

# set bounds
fwhm_min = -10
fwhm_max = 53
k_min = -30
k_max = 5

# make the figure
fig = plt.figure(constrained_layout = True, figsize = (5,8))
axs = fig.subplots(4, 2)

# set what will be plotted and the aesthetics
mapchoice = 'jet'
size = 20
axs[0][0].scatter(x = fw04_cropped, y = k04, c = times04_cropped, s = size, cmap = mapchoice)
axs[0][1].scatter(x = fw06_cropped, y = k06, c = times06_cropped, s = size, cmap = mapchoice)
axs[1][0].scatter(x = fw08_cropped, y = k08, c = times08_cropped, s = size, cmap = mapchoice)
axs[1][1].scatter(x = fw12_cropped, y = k12, c = times12_cropped, s = size, cmap = mapchoice)
```

```
231 axs[2][0].scatter(x = fw14_cropped, y = k14, c = times14_cropped, s = size,
cmap = mapchoice)
232 axs[2][1].scatter(x = fw16_cropped, y = k16, c = times16_cropped, s = size,
cmap = mapchoice)
233 axs[3][0].scatter(x = fw18_cropped, y = k18, c = times18_cropped, s = size,
cmap = mapchoice)
234 axs[3][1].scatter(x = fw22_cropped, y = k22, c = times22_cropped, s = size,
cmap = mapchoice)
235
236 # label the plots
237 names = [['$\it{r}$' + " = 0.04",'$\it{r}$' + " = 0.06"],['$\it{r}$' + " =
0.08",'$\it{r}$' + " = 0.12"],['$\it{r}$' + " = 0.14",'$\it{r}$' + " =
0.16"],['$\it{r}$' + " = 0.18",'$\it{r}$' + " = 0.22"]]
238
239 # apply aesthetic choices
240 for i in range (0, 2):
241     for j in range (0, 4):
242             axs[j][i].set_ylim(k_min,k_max)
243             axs[j][i].set_xlim(fwhm_min,fwhm_max)
244             axs[j][i].set_ylabel("% change " + r'$\kappa$')
245             axs[j][i].set_xlabel("% change " + '$\it{L}$')
246
247             ax = AnchoredText(names[j][i], frameon = False, loc = "center
right")
248             axs[j][i]. add_artist(ax)
249
250 # save the plot as a 300 dpi tif file
251 fig.savefig('timeiscolors_percentchange.tif', dpi = 300)
252 plt.show()
```

The End